



Paton, Kirsty Anne (2023) *Studies of hybrid pixel detectors for use in Transmission Electron Microscopy*. PhD thesis.

<https://theses.gla.ac.uk/83925/>

Copyright and moral rights for this work are retained by the author

A copy can be downloaded for personal non-commercial research or study, without prior permission or charge

This work cannot be reproduced or quoted extensively from without first obtaining permission from the author

The content must not be changed in any way or sold commercially in any format or medium without the formal permission of the author

When referring to this work, full bibliographic details including the author, title, awarding institution and date of the thesis must be given

Enlighten: Theses

<https://theses.gla.ac.uk/>
research-enlighten@glasgow.ac.uk

Studies of Hybrid Pixel Detectors for Use in Transmission Electron Microscopy



University
of Glasgow

Kirsty Anne Paton

Materials and Condensed Matter Physics Group
&
Particle Physics Experimental Group
School of Physics and Astronomy
University of Glasgow

Submitted in partial fulfilment of the requirements for the Degree of
Doctor of Philosophy

January 2023

Abstract

Hybrid pixel detectors (HPDs) are a class of direct electron detectors that have been adopted for use in a wide variety of experimental modalities across all branches of electron microscopy. Nevertheless, this does not preclude the possibility of further improvement and optimisation of their performance for specific applications and increasing the range of experiments for which they are suitable. The aims of this thesis are two-fold. Firstly, to develop a more comprehensive understanding of the current generation HPDs using Si sensors, with a view to optimising their design. Secondly, to determine the advantages of alternative sensor materials that, in principle, should improve the performance of HPDs in transmission electron microscopy (TEM) due to their increased stopping power.

The three chapters review the relevant theoretical background. This includes the physics underpinning the performance of semiconductor-based sensors in electron microscopy as well as the operation of detectors more generally and the theory underlying the metrics used to evaluate detector performance in Chapter 1. In Chapter 2, TEM as a key tool in the study of nano- and atomic scale systems is also introduced, along with an overview of the detector technologies used in TEM. Also presented as part of the background material in Chapter 3 is a description of the experimental methods and software packages used to acquire the results presented in the latter half of the thesis.

Chapter 4, the first results chapter, presents a comparison of the performance of Medipix3 detectors with Si sensors with various combination of pixel pitch and sensor thickness for 60 keV and 200 keV electrons. In Chapter 5, simulations of the interactions of electrons with energies ranging from 30-300 keV with GaAs:Cr and CdTe/CZT, two of the most viable alternatives to Si for use in the sensors of HPDs, are compared with simulations of the interactions of electrons with Si. A comparative study of the performance of a Medipix3 device with GaAs:Cr sensor with that of a Si sensor of the same thickness and pixel pitch for electrons with energies ranging from 60-300 keV is presented in Chapter 6. Also included in this Chapter are the results of investigations into the defects present in the GaAs:Cr sensor material and how these affect device performance. These consist of confocal scanning transmission electron microscopy scans used to estimate the size and shape of individual pixels and how these relate to the linearity of pixels' response, as well as studies of how the efficacy of a standard flat field depends on the incident electron flux. In the final results chapter, the focus shifts to preliminary measurements of the response of an integrating detector with GaAs:Cr sensor to electrons. These initial experimental measurements prompted further simulations investigating how the backside contact of GaAs:Cr sensors can be improved when using electrons.

Declaration

This thesis is a record of research carried out by myself within the Materials and Condensed Matter Physics and Particle Physics Experimental groups in the School of Physics and Astronomy at the University of Glasgow from 2017 - 2022. The work described herein is my own, with the exception of the following:

- The Synopsis `sde` and `sdevice` scripts used to simulate the electric fields in Si sensors, described in Chapter 3 and used to produce results presented in Chapter 4 were adapted from scripts kindly provided by Mr. Ben Cline of the STFC Detector Group.
- The Geant4 package (Medipix-EM) used to simulate the interactions of electrons with different sensor materials, described in Chapters 3 and 5 and used to generate results presented in Chapters 5 and 7 was adapted from source code provided by Dr Eduardo Nebot del Busto of Quantum Detectors Ltd., which was itself adapted from the Geant4 advanced “microelectronics” example [1].
- Data acquired with the Medipix3 GaAs:Cr detector installed on the Titan 80-300 (S)TEM at Karlsruhe Institute of Technology was acquired with the assistance of Dr Xiaoke Mu.
- Confocal STEM scans acquired using the ARM 200 cF STEM at the University of Glasgow were acquired with the assistance of Dr Damien McGrouther.
- The hardware used to install detectors based on the Medipix3 ASIC onto the Tecnai T20 TEM and ARM 200 cF (S)TEM at the University of Glasgow, as well as the hardware used to install such detectors on the Titan 80-300 (S)TEM at Karlsruhe Institute of Technology (all described in Chapter 3) was developed in collaboration with Dr Damien McGrouther, Dr Dzmitry Maneuski, Ms Nadia Bassiri, Mr Michael Perreur-Lloyd and Mr David Doak.
- The hardware used to install the HEXITEC detector on the Tecnai T20 TEM at the University of Glasgow, described in Chapter 7 was developed by the STFC Detector Group.
- Experiments investigating the response of the HEXITEC detector to 60 keV and 80 keV electrons, presented were performed with the assistance of Dr Matthew C. Veale and Dr Daniel Pooley. The ^{241}Am data used to calibrate the HEXITEC detector, also discussed in Chapter 7, was acquired by Dr Matthew C. Veale.

Some of the work in Chapters 4 and 6 can be found in the following paper:

1. **K. A. Paton**, M. C. Veale, X. Mu, C. S. Allen, D. Maneuski, Kübel C., V. O'Shea, A. I. Kirkland, D. McGrouther (2021). *Quantifying the performance of a hybrid pixel detector with GaAs:Cr sensor for transmission electron microscopy*. *Ultramicroscopy*, 227, 113298. (Reference [2].)

Additionally, during the time in which this research was conducted, I contributed to the following papers:

1. G. Paterson, R. W. H. Webster, A. Ross, **K. A. Paton**, T. Macgregor, D. McGrouther, M. Nord (2020). *Fast Pixelated Detectors in Scanning Transmission Electron Microscopy. Part II: Post-Acquisition Data Processing, Visualization, and Structural Characterization*. *Microscopy and Microanalysis*, 26(5), 944-963. (Reference [3].)
2. M. Nord, R. W. H. Webster, **K. A. Paton**, S. McVitie, D. McGrouther, I. MacLaren, G. Paterson (2020). *Fast Pixelated Detectors in Scanning Transmission Electron Microscopy. Part I: Data Acquisition, Live Processing, and Storage*. *Microscopy and Microanalysis*, 26(4), 653-666. (Reference [4].)

The data presented in this thesis, which is not already publicly available at reference [5] as part of the publication of reference [2], is available upon reasonable request.

This thesis has not been submitted elsewhere for any other degree or qualification.

Acknowledgements

Firstly, I would like to express my thanks to my primary supervisor, Dr Damien McGrouther for providing me with the opportunity and funding to undertake a PhD. I am grateful to him for his kindness and patience on a number of occasions and for enabling me to become an independent researcher. Likewise, I am also grateful to my second supervisor, Dr Dzmitry Alexandrovich Maneuski for all his advice over the past few years and for always being willing to listen to my latest idea and to help me with setting things up in the detector lab.

The wider Materials and Condensed Matter Physics and Particle Physics Experimental research groups that I have worked across over the past few years have been great sources of support and fun. In particular, I would like to express my thanks to Dr Donald MacLaren, for invaluable feedback when preparing talks presented at the Microscience Microscopy Congress 2019 and EMAG 2020, the latter of which was jointly awarded the prize for best student presentation, and for general microscopy and career-related advice. I am similarly grateful to Prof. Val O'Shea for feedback in advance of a talk given at the International Workshop on Radiation Imaging Detectors 2019 and for encouraging me in my next steps of my career. My thanks are also due to Dr Ian MacLaren for always being interested in and willing to support detector-related work and to Prof. Stephen McVitie for promoting a friendly and supportive research environment. Although the COVID-19 pandemic intervened, I am also thankful to Dr Amalio Pacheco Fernandez for encouraging me to get away from my desk and have a proper lunch break from time to time. The research presented in this thesis would not have been possible the use of the microscopy facilities within the Materials and Condensed Matter Physics group. I am therefore greatly indebted to Dr Sam McFadzean, Mr Colin How and Mr William Smith for all their efforts to keep the microscopes running and helping me with all my various microscope-related (mis-)adventures. Along similar lines, I am grateful to Dr Richard Bates and Mr Frederick Doherty for their willingness to let me run off with various bits of equipment from the Particle Physics Experimental labs.

My research would also not have been possible without the various detectors I have been given to characterise, as well as assistance installing them on microscopes. Thanks is therefore due to Ms Nadia Bassiri, Mr Michael Perreur-Lloyd and Mr David Doak for their help developing and manufacturing hardware to mount detectors on microscopes. I owe particular thanks to Dr Matthew Veale for providing me with the GaAs:Cr devices characterised as part of this work, for helping to introduce me to, and promote my work within the high- Z sensors community and for helping

with all things detector-related over the course of my PhD. I am grateful to the STFC Detector Development group as a whole, in particular Dr Matthew Wilson, for developing the hardware used to install HEXITEC devices on the Tecnai T20 TEM at Glasgow. Thanks also to Dr Matthew Veale and Dr Daniel Pooley for assisting with the acquisition of data with the HEXITEC system.

Quantum Detectors Ltd. have supported me in my research by lending me the 500 μm thick 55 μm Si Medipix3 detector characterised as part of this work as well as funding travel to Karlsruhe Institute of Technology and Rutherford Appleton Laboratory for the purposes of undertaking experimental work. I would like to express my particular thanks to Dr Eduardo Nebot del Busto for helping to familiarise me with the Merlin readout system and for sharing code that formed the basis of the programme used to perform the simulations presented in Chapters 5 and 7. I am grateful also to Dr Olivia Sleator for helping to arrange the visit to Karlsruhe and to Dr Liam O’Ryan for providing an outside perspective on my work and reminding me that the key thing was to simply “have enough”.

Over the course of my PhD I have been fortunate enough to undertake visits to other research groups. I would therefore like to express my thanks to Prof. Christian Kubel and Dr Xiaoke Mu at Karlsruhe Insitute of Technology for allowing me use of the Titan 80-300 (S)TEM to acquire 300 keV data with the Medipix3 GaAs:Cr device. I am also grateful to the hospitality of Dr Jonas Weissenreider, Dr Gaolong Cao and Dr Shaozheng Ji when I visited their lab at Royal Institute of Technology at Stockholm. While sadly none of the data made it into this thesis, it was a tremendously educational experience.

My thanks to all my various office mates over the years as well as the other PhD students and postdocs who have come and gone over the years, who have helped celebrate the successes and cheered me up during the difficult patches. In particular, thanks to Dr Bianca Sala, for introducing me to both the concept of a “thesis tree” and the cows at Pollock Country Park, as well as for Zoom knitting sessions and general fun. Thanks also to Dr Kayla Fallon and Ms Rebecca Cummings for lockdown walks and Zoom breaks; Dr John Halpin for cycling and rock climbing trips; Dr Robert Webster for microscope chat and willingness to listen to me rant; Dr Laura Clark for career-related advice and encouragement as well as willingness to work together on weird and wonderful microscope alignments; and to Dr Aurelio Hierro Rodriguez giving me an opportunity to brush up my Spanish from time to time. Thanks too to the Beans on Roast club for the regular Zoom coffee breaks during lockdown, which did much to help me get through that strange time. Special thanks goes to Dr Gary Paterson, for always being willing to discuss an idea or a problem, and for inviting me to collaborate on various projects.

Above all, I would like to express my thanks to my family, without whose support it would not have been possible for me to embark upon a PhD, let alone complete one. I am especially grateful to my parents¹ for letting me ignore any and all filial

¹ While it seems absurdly informal to refer to my parents by their full names and title, given that I’ve carried on the joke (such as it is) for everyone else, it seems rude to not do it for them to. So: here’s to Mr Neil R. Paton and Mrs Anne Marie Paton, without whom none of this could have happened.

obligations while I've been writing up and to to my sister-in-law, Mrs Aimée A. Kerr, for reminding me to look after myself and for arranging a series of very thoughtful gifts while I was in the final stages of my PhD to help me with this, often aided by my nieces, Miss Flora R. K. Paton and Miss Mairi B. K. Paton. Lastly, I am particularly grateful to my brother Mr Christopher H. Paton: he has always set the bar high, but has also always helped me pass it.

This project was funded by the Science and Technology Facilities Council under grant number ST/P002471/1 (Next² TEM Detection - Investigation of Hybrid Pixel Detectors for future Transmission Electron Microscopy imaging). Additional funding for use of the Titan 80-300 (S)TEM was provided by the Deutsche Forschungsgemeinschaft under grant number MU 4276/1-1.

Contents

List of Figures	xv
List of Tables	xxxv
List of Acronyms and Abbreviations	xxxvii
List of Symbols	xli
1 Radiation Detectors	1
1.1 Introduction	1
1.2 Interactions of Radiation with Matter	1
1.2.1 Interactions of Electrons	2
1.2.2 Interactions of X-Rays	8
1.3 Principles of Detector Operation	10
1.4 Semiconductor-Based Sensors	15
1.4.1 Basics Properties of Semiconductors	15
1.4.2 Key Semiconductor Structures	22
1.5 Metrics for Evaluating Detector Performance	31
1.5.1 General Performance Metrics	31
1.5.2 Evaluating the Performance of Imaging Detectors	35
1.6 Summary	42
2 Detectors in the Context of Electron Microscopy	45
2.1 Introduction	45
2.2 Why Electron Microscopy?	45
2.3 Constituent Components of Electron Microscopes	50
2.3.1 Electron Sources and Guns	51
2.3.2 Electron Lenses	55
2.4 Anatomy and Operation of a (S)TEM	58
2.5 Survey of Detector Technologies Used in Electron Microscopy	66
2.5.1 Traditional Detector Technologies	66
2.5.2 The Direct Electron Detector Revolution	71
2.5.3 HPDs and High- <i>Z</i> Sensors	82
2.6 Summary	88

3	Methods and Materials	91
3.1	Introduction	91
3.2	Detectors and Associated Hardware	91
3.2.1	The Medipix3RX ASIC	91
3.2.2	Overview of Devices and Associated Hardware	95
3.3	Experimental Methods	99
3.3.1	Spectral Measurements and Calibration of Detectors	99
3.3.2	Measurement of MTF, NPS and DQE	102
3.3.3	Linearity of Response	107
3.3.4	Detector Mapping with Confocal STEM	111
3.4	Electron-Matter Interactions and Detector Response Simulation	118
3.4.1	Simulation Packages Based on the Geant4 Framework	118
3.4.2	Simulation of Si Sensors with Synopsys TCAD	123
3.5	Summary	126
4	Counting Detectors with Si Sensors	127
4.1	Introduction	127
4.2	Spectral Measurements	127
4.2.1	Experimental Measurements	128
4.2.2	Comparison with Simulations	134
4.3	MTF and DQE Measurements	141
4.3.1	Experimental Measurements	141
4.3.2	Electron Energy and Trajectory	147
4.3.3	Sensor Thickness	149
4.3.4	Pixel Pitch	152
4.4	Linearity of Response	155
4.5	Summary	159
5	Simulations of High-Z Sensor Materials	165
5.1	Introduction	165
5.2	Methods	165
5.3	Results and Discussion	169
5.4	Summary and Conclusions	179
6	Characterisation of a Counting Detector with GaAs:Cr Sensor	181
6.1	Introduction	181
6.2	Spectral Measurements	181
6.3	MTF and DQE Measurements	184
6.4	Linearity of Response	200
6.5	Investigation of Defects	207
6.6	Summary	226

7 Investigating a Spectroscopic Detector with GaAs:Cr Sensor	229
7.1 Introduction	229
7.2 Overview of the HEXITEC ASIC	230
7.3 Methods and Experimental Apparatus	231
7.3.1 Detector and Associated Hardware	231
7.3.2 Calibration with γ -rays	233
7.4 Results of Experiments with Electrons	236
7.5 Simulations Incorporating Contacts	241
7.6 Summary	247
8 Conclusions and Future Work	249
8.1 Introduction	249
8.2 Results and Conclusions	249
8.2.1 Si Sensors	249
8.2.2 High- Z Sensor Materials	252
8.3 Future Work	256
8.4 Summary	262
Appendices	265
Bibliography	277

List of Figures

1.1	An illustration of how electrons can be scattered by atoms. When scattered by atomic electrons the angle of scattering, θ is typically small and may or may not involve the transfer of energy to the atomic electron. If the incident electron is scattered by the atomic nucleus, then the angle of scattering can be much larger, to the extent that the incident electron is deflected by a full 180° and “backscattered”. Although less important from the perspective of electron interactions with detectors, when discussing electron interactions with a sample within TEM, electrons that are not backscattered are regarded as “forward scattered”. Whenever the incident electron is deflected there is a possibility of it producing Bremsstrahlung, though in this example only the backscattered electron is marked as having produced in X-ray photon.	4
1.2	The mechanisms by which the ionisation of an atom by a high-energy incident electron produces characteristic (a) X-rays and (b) Auger electrons. In (a), the incident electron (1) displaces the K-shell electron as a secondary electron (2), which is replaced by an electron from the L_3 shell, leading to the emission of a characteristic X-ray. Steps (1) and (2) are the same in (b), but the ejected K-shell electron is replaced from an electron from the L_1 shell (3), the excess energy of which is transferred to an electron in the L_3 shell, which then escapes as an Auger electron (4). Redrawn from [20].	7
1.3	An illustration of Compton scattering, one of the ways in which X-rays interact with matter. The relation between the scattering angle θ of the incident photon is related to the photon’s loss of energy by Equation 1.15.	9
1.4	An illustration of the difference between (a) the electric field due to an application of a bias to a detector system (E_D) and (b) the weighting field (E_W) for a single electrode determined by holding the electrode of interest at 1V and all other electrodes at ground (GND). The system shown in this example could be a semiconductor-based strip or pixelated detector such as those studied in this thesis.	12

1.5 A diagram showing a typical signal processing chain for a detector system: signal carriers created in the sensor induce a transient current pulse on the readout electrodes; a CSA converts these into voltage steps (ΔV), which are then shaped. If the system is a spectroscopic detector, the height of these voltage pulses is then converted into an ADC code as part of the readout process; if an integrating detector then the voltage pulse is integrated over, with the result converted into an ADC code. In the latter kind of system, it may be the case that that the area under the voltage pulse is integrated, without any shaping taking place. However, if the system in question is a counting detector, a counter is incremented if the height of the voltage pulses surpasses a reference voltage. At readout time, the number of counts recorded is readout by the data acquisition (DAQ) system and stored. 14

1.6 Figure showing the differences between the band structure for insulators, metals, semimetals and semiconductors. Redrawn from [31]. . . 17

1.7 Diagram showing how impurity atoms can add a (a) hole or (b) electron to the lattice depending on difference between the number of expected valence electrons for the lattice site the atom occupies and the number of valence electrons the impurity atom has. In both (a) and (b) the impurity has replaced a Si atom, which has 4 valence electrons. In (a) the B atom has only 3 valence electrons, and so its presence creates an extra hole in the valence band while in (b) the As atom has 5 valence electrons and so it adds an extra free electron to the conduction band. Redrawn from [31]. 18

1.8 An illustration of how the Fermi level is changed by the presence of dopants. In the case of n-type material, the presence of the ionised donor atoms means the Fermi level is effectively moved upwards towards the conduction band. Similarly, for p-type material the ionised acceptor atoms mean the Fermi level is moved downwards towards the valence band relative to its position for intrinsic material. Redrawn from [31]. 19

1.9 Figure showing different types of point defects possible in a crystal lattice. These include lattice sites missing an atom (vacancy), impurity atoms taking up a lattice site or taking up an interstitial position and Frenkel defects which consists of complexes of interstitial atoms and vacancies. Redrawn from [33]. 20

1.10 Diagrams of p-type and n-type material and their band structure (a) prior to being brought into contact and (b) after being brought into contact to form a pn-junction and having reached thermal equilibrium. 23

1.11 Diagrams of (a) an abrupt, one-sided pn-junction that approximates a sensor formed by implantation of acceptor atoms to form p-type wells in n-type bulk; (b) the associated distribution of space charge in the depletion volume of such a structure, where x_p and x_n are the widths of the depleted areas on the p-side and the n-side of the junction and N_A and N_D the concentrations of the acceptor and donor atoms in the p-type and n-type volumes; (c) the associated built-in electric field across the depletion volume, which is purely in the x -direction with a maximum value of $E_{x,M}$ and (d) the built-in potential of such a structure. Redrawn from [33]. 24

1.12 Figure of a pn-junction and its band structure with (a) no external bias applied), (b) a forward bias applied and (c) a reverse bias applied. Redrawn from [33]. 27

1.13 Figures showing the band structure of a surface barrier when (a) the metal and semiconductor have just been brought into contact and (b) the structure has reached equilibrium so the energy bands on the semiconductor side of the interface have bent to meet the energy bands of the metal. Redrawn from reference [31]. 29

1.14 Diagrams showing the band structure of a surface barrier when the semiconductor is (a) n-type or (b) p-type and no bias is applied; (c) n-type or (d) p-type and the devices are forward-biased; and (e) n-type or (f) p-type and the devices are reverse-biased. Redrawn from [31]. The polarity of the bias applied to an n-type device is the reverse of that applied to the p-type for a given outcome i.e. the bias applied to an n-type device to reverse bias it will forward bias a p-type device and vice versa. 31

1.15 Difference in detector performance on the basis of whether its dead time can be regarded as non-paralyzable or paralyzable. In the former case, the detector deadtime is not increased by the arrival of events within the deadtime of a prior event so that while the third and fifth events are missed the sixth event is registered. In the case of a paralyzable detector, the deadtime is extended by an event occurring within the deadtime of an earlier event, so that the third, fifth and sixth events are missed. Redrawn from [6]. 33

1.16 Illustration of a linear, shift-invariant system. In (a), the system input is represented as a pulse at x_0 , which leads to a system output in the form of the IRF centred at x_0 in (b). In the event of there being multiple inputs at one time as in (c), the output is simply the sum of the IRFs as in (d); these individual IRFs are the same independent of the position of the input pulse. 36

1.17 A hypothetical example of the MTF of a system illustrating of how it describes a system’s ability to reproduce contrast. In this example, $MTF(\omega)$ is reduced at high spatial frequencies so that contrast at low spatial frequencies (i.e. large features in the input image) is reproduced faithfully, while there is a reduction in contrast for small features in the input that correspond to high spatial frequencies. 37

1.18 An illustration of the idea of sampling and how undersampling a signal can lead to aliasing. In (a) the signal is sampled at the Nyquist frequency and can just be reproduced in (b), while in (c) the same signal is undersampled so that the reconstructed signal in (d) is one with a frequency less than a quarter of the original. Information corresponding to the original signal will therefore be mixed-in with information contained in any signals with this lower frequency that are also detected by a system with the sampling rate used in (c). 39

1.19 Figures showing the theoretical response of an square pixel detector: in (a) the PSF is a tophat function one pixel wide, which corresponds to the MTF shown in (b), which also shows the squared MTF; (c) shows the corresponding NPS while in (d) the resulting DQE is plotted, which is identical to MTF^2 41

1.20 The (a) MTF, (b) NPS and (c) DQE of a square pixel detector when aliasing is a factor for various degrees of blurring, while (d) - (f) shows the same again without any aliasing. Panel (e) also effectively shows MTF^2 for the various degrees of blurring considered. 42

2.1 Plots of the non-relativistic and relativistic de Broglie wavelength of an electron as a function of accelerating voltage. At accelerating voltages greater than ~ 100 kV the disparity between the wavelengths calculated by accounting for and by discounting relativistic effects becomes significant. 46

2.2 A demonstration of how the ability to resolve two separate Airy disks depends on how closely spaced they are. In (a) they are clearly distinguishable while in (b) they are just resolvable with the maxima of the two disks coinciding with the first minimum of the other. In (c) it is not possible to distinguish the two separate disks and a single, large disk is observed. 47

- 2.3 Illustration of Bragg diffraction at angle θ from lattice planes with spacing d in (a) real space in one dimension and (b) as a two dimensional slice through reciprocal space, wherein lattice planes become points in the reciprocal lattice. The difference between the incident wavevector \mathbf{k} and scattered wavevector \mathbf{k} is equal to a reciprocal lattice vector G from Equation 1.21. The plane of reciprocal lattice points that contain O and are perpendicular to the beam is known as the zero-order Laue zones (ZOLZ), with the planes parallel to this known as the HOLZ. The first and second of these are specifically the first-order and second-order Laue zones (FOLZ and SOLZ). 49
- 2.4 Diagrams illustrating the ways in which electrons can be thought of as interacting with samples. In (a), electrons are shown as a beam of incident particles some of which pass straight through the sample, while others are scattered and in some cases produce secondary quanta, while in (b), the way in which the sample modulates the amplitude and phase of the incident electron wave is described by the sample transmission function $f(\mathbf{r})$. Adapted from reference [20]. 50
- 2.5 A schematic of the gun assembly of a typical thermionic emitter. The primary potential difference is between the source (cathode) and anode plate, while the bias on Wehnelt modifies the electric field so that electrons are focused into a crossover with diameter d_0 with a divergence angle of α_0 . Redrawn from reference [20]. 52
- 2.6 A basic diagram of a FEG. The two anodes together act as an electrostatic lens that focuses electrons into a very small crossover. An extra lens may sometimes be added underneath the two anodes. Redrawn from reference [20]. 53
- 2.7 (a) Cross-section of a typical magnetic lens composed of two polepieces. These are in the hole down the centre of the lens. Due to resistive heating of the copper coils water cooling is also a key component of the lens system. Although (a) shows the ray paths as straight lines, in reality electrons have a helical trajectory as shown in (b). The effect of the magnetic field is that electrons pass through points P and P' on the optic axis, spiralling round the optic axis once in between [20]. . . 56

- 2.8 Ray diagrams showing the effects of spherical and chromatic aberration. In an ideal lens (a), the ray paths that emanate from point P in the object plane converge at point Gaussian image plane and there is no deformation in the form of the wave front. In (b) the further off-axis the wave front is, the more strongly focused it is, so that point P in the object plane expands to a disk at point P' in the Gaussian image plane of the lens. The diameter of the disk in the Gaussian image plane is larger than of the disk associated with P in the Plane of Least Confusion, which is the plane in which electrons are best focused. Chromatic aberration in (c) means that electrons with the primary energy E_0 are focused to point P' , but electrons with less energy are focused to a point in planes closer to the lens. The plane in which the disk associated with point P is narrowest is therefore prior to the Gaussian Image Plane. 57
- 2.9 Illustration of the key components of a TEM and STEM and the ray paths associated with electron waves in the two instruments. The electron wavefunction formalism describing how images are formed in the two instruments is also noted. Whereas in a TEM the sample can be directly imaged in the detector plane, in a STEM, the image formed depends on the intensity of the electrons scattered into different regions of the detector plane. Note that the column depicted here is a generic one and does not correspond to any particular microscope, though it largely mimics that of the ARM 200 cF at the University of Glasgow. Inspired by reference [74]. 59
- 2.10 A ray diagram showing post-sample alignment for a TEM operating in diffraction mode. The key difference between the microscope in imaging and diffraction mode is the strength of the intermediate lenses. To select the area of the sample that contributes to the diffraction pattern, an aperture is inserted in the image plane of the objective lens (which is conjugate with the sample plane) known as the selected area diffraction (SAD) aperture. Adapted from reference [20]. 61
- 2.11 Optical arrangements for (a) bright-field (b) dark-field and (c) phase-contrast imaging in TEM. In (a) the electrons that pass through the objective aperture and contribute to image formation are those that have been transmitted directly through the sample while in (b) the incident beam has been tilted so that the electrons that are on-axis (and therefore least affected by lens aberrations) post sample are those that have been scattered by the sample. In (c) both on and off-axis electrons contribute to image formation. Adapted from [20]. 64
- 2.12 Ray diagram illustrating the principle of reciprocity as it applies to BF STEM and conventional HRTEM. Redrawn from reference [78]. 65

- 2.13 Schematic of a CCD pixel. Charge generated in the thin sensor layer is collected by potential wells defined by a MOS structure. The depth of the well can be altered by changing the potential applied to the gate. 68
- 2.14 Illustration of the readout scheme for a CCD camera. Every third gate in the row of pixels is connected to the same potential (ϕ_0 , ϕ_1 and ϕ_2 , thereby creating a periodic potential underneath the gates. Electrons are collected in the minima of these (the potential wells) as seen in (a). By changing the potential at the gates, the shape and depth of the wells can be altered, moving electrons along the row to the readout anode, as seen in (b)-(e). Adapted from reference [31]. 69
- 2.15 Figure of an optically-coupled CCD camera showing how photons produced by the interaction of the incident electron with the scintillator scatter laterally and are collected by CCD pixels remote from the entry point of the electron in the scintillator causing blurring in the images recorded. 70
- 2.16 Schematic of a scintillator optically-coupled to a PMT such as might be used as a BF detector in STEM. Electrons produced at the photocathode via the photoelectron effect are multiplied by being accelerated into and colliding with a series of dynodes. The electrons produced at each dynode being also being multiplied at subsequent dynodes via the same process. 71
- 2.17 Views of a MAPS pixel using three transistors: (a) shows a cross section of a typical MAPS pixel, which is defined by the n-type well that collects electrons, is shown while (b) shows a simplified circuit diagram.. Electrons generated in the epitaxial p⁻ diffuse to the n-well. Prior to device exposure, transistor T1 is switched on, which charges the stray capacitance at node A. During exposure, the capacitor is discharged by an amount proportional to the signal induced on the n-well diode. T2 and T3, the row and column-select transistors readout the signal to the external ADC [153]. Both panels adapted from reference [154]. 76
- 2.18 Figure showing a single HPD pixel. An external bias is applied to the backside of the sensor, which ensures rapid readout of charge carriers produced by incident electrons. For devices used in electron microscopy, the sensor is typically at least 300 μm thick, though when using, 300 keV electrons a thicker sensor is required. The pixel pitch is defined by the spacing of the bump-bond pads. The ASIC contains all the signal-pro is bump-bonded to the ASIC. Not drawn to scale. 77

- 3.1 Schematic of the circuitry of a single Medipix3 pixel. Pixels can communicate with their immediate neighbours (at both their corners and along their edges) depending on the mode of operation it is set to work in. For example, the schematic shows how the central pixel “E” can communicate with its neighbours A, B, D, F, H, and I at its top left and bottom right corners when the detector is operating in CSM. Redrawn from references [177, 248, 249]. 93
- 3.2 Illustration of how different values of I_{Krum} affect the voltage pulse produced by the semi-gaussian shaper. For a given signal induced on a pixel, and assuming all other pixel settings remain the same, then higher values of I_{Krum} will cause the voltage pulse to return to baseline more quickly, leading to a shorter pulse with a reduced peak. If the counting threshold voltage remains the same, then using a higher value of I_{Krum} can cause signals that would otherwise surpass the threshold to not be counted. 93
- 3.3 An illustration of how the CSM algorithm works. In (a), an incident photon has arrived in the central pixel but the charge it has created has been registered by three neighbouring pixels as well. Copies of the voltage pulses that are produced in each pixel are sent to summing nodes that can effectively be regarded as being at the corners of each pixel. The summed voltage pulses in the top right node surpass TH1, and the central pixel is the one that has registered the longest voltage pulse, so that in (b) the hit is assigned to the central pixel. Redrawn from reference [177]. 94
- 3.4 Photographs of (a) the CERN Medipix3 chipboard and (b) the DLS Medipix3 chipboard. In both (a) and (b) the detector (chip) is glued to the PCB, with power, commands and readout of the chip occurring through the bump bond wires that connect the PCB electronics to input/output pads on the chip. The bias to the sensor is supplied through a separate wire marked "HV". Power to the board itself as well as connection to the DAQ system is via a very-high density cable interconnect (VHDCI) connector. In the case of (a), the bias voltage is limited to that which can supplied via the VHDCI connector, while in (b) the lemo connector can be used to supply a bias sourced from an external high voltage unit. 96

- 3.5 Photographs of the assembly used to install Medipix3 devices on a Tecnai T20 TEM: (a) shows an overhead view; (b) and (c) show side views while (d) shows the view of the chassis that faces outward when it is installed on a microscope. A knife-edge that can be slid in front of the chip for MTF measurements (described in Section 3.3.2) is marked in (a) as is an interconnect board which acts as a vacuum feed through connecting the detector PCB to the external VHDCI connector. Also marked in (a) and (d) are the Lemo cable and external Lemo connections used to provide an external bias to the sensor (marked in (c)) and connecting to the Faraday cup (marked (b)). The brass block marked in (b) is positioned in a recess and secured with Ag thermal vacuum paste so it acts as an efficient heat sink while still being movable to accommodate different PCB layouts. 97
- 3.6 Photograph of the Tecnai T20 at the University of Glasgow, used for the majority of experimental measurements presented in this thesis. The components of the microscope column described in Chapter 2 are labelled, along with the camera chamber and the SIS Megaview Camera. For the purposes of acquiring data with Medipix3 devices, the SIS Megaview Camera was removed and the 35mm port that it normally occupied used for the temporary installation of the chassis shown in Figure 3.5. 98
- 3.7 Photographs of the chassis used to install a Medipix3 device with GaAs:Cr sensor on the Karlsruhe Titan 80 - 300 (S)TEM and Glasgow ARM 200 (S)TEM: (a) and (b) show overhead views while (c) shows a side view and (d) the outward facing part of the chassis when installed on a microscope. The shutter (marked in (a)) has an edge which is at an angle to the chip (marked in (b)) so that it can be used as a knife-edge for MTF measurements, as described in Section 3.3.2. This shutter can be moved back and forth while the detector is in vacuum using the mechanism marked in (d). The bias to the sensor is provided by a Fast ComTech SHQ124M high voltage power supply, connected by a series of Lemo connections incorporating a vacuum feed-through. The feed-through connecting the PCB and the external VHDCI connector took the form a Kapton flex-cable. 99
- 3.8 Schematic of an X-ray tube and diagram of the experimental set-up used for calibrating the counting threshold of Medipix3-type devices with fluorescence X-rays. X-rays are produced by electrons accelerated towards a W anode (the spinning of which increases the area with which the electron beam has to interact). Those X-rays that escape the tube through a window in the lead shielding strike a fluorescence target which is at an angle of approximately 45° to both the tube and the detector. Lead shielding with appropriately placed pinholes minimised the exposure of the detector to stray X-rays. Note that experimental apparatus is not drawn to scale. 100

- 3.9 Examples of the key steps of calibrating the threshold energy of a Medipix3 device. In (a) a plot of the sum counts recorded of TH1 values in terms of DAC when the device was exposed to fluorescence X-rays produced from a Ba target. (b) shows the absolute value of the associated differential of (a). The photopeak in (b) is fitted with a Gaussian distribution, and this peak photon energy along with those from two other spectra are plotted in (c). A straight line is fit to this to determine the calibration, which is applied to the data in (b) to produce a spectrum in terms of energy in (d). 103
- 3.10 Illustration of how a knife-edge set at an angle to the rows or columns of a pixelated detector makes it possible to measure an oversampled ESF. In (a), a perfectly straight edge is set at angle relative to the pixel rows, so that rearranging the intensities recorded by pixels in order of the distance of the pixel from the edge-position is equivalent to plotting the intensities of the pixels in each column in order of the row they are located as seen in (b). 105
- 3.11 An illustration of the process by which a given detector's MTF was measured. Beginning with (a), an image of the knife-edge with a flat field correction applied, an appropriate portion of a knife-edge image is identified, which is shown in close-up in (b). The pixel values are rearranged in order of their distance from the knife-edge and are plotted as in (c). This is then fit with Equation 3.2, which is used to calculate the MTF according to Equation 3.3, seen in (d). For comparison, the MTF obtained by using the raw ESF data in 3.3 is also plotted in (d). 106
- 3.12 The process by which the NNPS of a detector was determined: (a) a single noise image and (b) the corresponding 2D noise power spectrum and (c) the 2D NPS obtained by averaging over the 2D NPS of 128 noise images. The contrast limits of (b) and (c) are the same, and it can be seen that (b) is much noisier than (c), highlighting the importance of averaging over many individual NPS. The radial average of (c) yields the 1D NPS in (d). The peak seen at ω_N in (d) is indicative of aliasing and this can also be seen in (b) and (c) in the middle of the edges of the 2D NPS. (e) shows a plot of the normalised variance of binned noise images plotted against binning factor. It can be seen that this reaches a plateau value, taken to be $NPS(0)$. The value of $NPS(0)$ was calculated as the average of the final thirty points, and is marked in orange. Along with (e), this is used to produce the NNPS shown in (f). 108
- 3.13 Illustration of how the area of the beam spot and its error. In (a) a close-up of an image of the beam spot is seen and in (b) the Otsu thresholded image. The image in (c) shows the result of applying a binary dilatation process to the mask in (b), while (d) shows the difference between (b) and (c). The sum of the pixels marked in white in (d) is taken to be the error in the area of (b). 110

- 3.14 Ray diagram of a microscope aligned for the purposes of a confocal STEM scan of a pixelated detector. The pre-sample optics are aligned as in STEM, while the post-sample optics are aligned as they would be in TEM, so that an image of the scanned probe in the sample plane is projected onto the detector. 112
- 3.15 Illustration of the procedure used to calibrate the magnification of the probe when imaged in the plane of the Medipix3 detector. In (a), the sum of the images recorded by the detector over the course of the confocal STEM scan of the calibration sample is shown; this is akin to the summed diffraction pattern of a 4D-STEM scan and is the full scan of the sample projected onto the detector. A close-up of the scan area marked in (a) is shown in (b), which is annotated with the line along which the intensity was measured, which is plotted in (c). The variation in the intensity profile in (c) due to the repeats used to calculate the average size of one of the repeats in the detector plane is marked. Along the measured profile line, the average repeat distance was measured as being 14.4 pixels. This corresponded to a distance of $791 \mu\text{m}$ in the detector plane, taking into account the pixel pitch. 114
- 3.16 Figures showing how the raw 4D confocal STEM scans were processed to produce pixel maps. (a) shows a single frame recorded by the detector, which corresponds to a single dwell point in the scan, while (b) shows a close-up of the beam spot seen in (a), with the weighted centre-of-mass marked. (c) shows a sample of the data set obtained by processing the frames recorded by the detector. Note that all points in the scan for which the beam is identified as having been incident in a given pixel, i.e. as having the same (floored) values of detY and detX , have the same pixel label. An image of the pixel label value at each scan point, as shown in (d) can be used to identify the boundaries of the detector pixels in the scan, which can then be overlaid on the sum image as a guide as shown in (e). 117
- 3.17 Schematic showing how the different components of the Allpix² framework relate to one another and how they relate to the detector and physical processes being simulated. The framework core includes components common to all modules used in a simulation chain both those that are instantiated once for a simulation (i.e. unique modules) and those that are instantiated for each detector in the simulation. An example of the former is the module that defines the simulation geometry, while those modules in green are all modules that must be instantiated for each individual detector, with the exception of the output module. Pink arrows indicate information relating to detector modules; the grey arrows correspond to logging information; and the blue arrows represent the bi-directional exchange of messages between the core and individual modules in the simulation chain. Adapted from reference [276]. 122

- 4.1 Spectra for electrons with energies from 60 keV - 200 keV recorded by Medipix3 detectors operating in SPM with (a) 300 μm thick and 55 μm pitch (b) 300 μm thick and 110 μm pitch and (c) 500 μm thick 55 μm pitch Si sensors. 129
- 4.2 Spectra for electrons with energies from 60-200 keV recorded by the Medipix3 detector with (a) a 300 μm thick Si sensor and 55 μm pixel pitch; (b) a 110 μm pixel pitch and 300 μm thick Si sensor; and (c) a 500 μm thick Si sensor and 55 μm pixel pitch. All devices were set to operate in CSM. 131
- 4.3 Comparisons of the simulated and experimental spectra for a Medipix3 detector with a 300 μm thick Si sensor and 55 μm pixel pitch exposed to 60 keV electrons with the detector operating in (a) SPM and (b) CSM; exposed to 200 keV and the detector operating in (c) SPM and (d) CSM. 135
- 4.4 Sum confocal STEM scan image of the Medipix3 detector installed on the Glasgow ARM 200 cF (S)TEM using 200 keV electrons. The detector operated in SPM and used a low counting threshold just above the detector's intrinsic noise level. The same scan was shown in close-up in Figure 3.16(e). While variation in the number of counts due to increased number of pixels recording incident electrons when the beam is at the edge of a pixel, there is also a variation in the intensity at lengthscales on the order of a few pixels that are likely due to variation in the thickness of the entrance window. This is not seen in flat field images of the same sensor. There also appears to be a region with fewer counts due to a piece of detritus on the sensor. 138
- 4.5 Spectra produced by simulating the response of a 300 μm thick Si sensor with 55 μm pitch exposed to (a) and (b) 60 keV electrons and (c) and (d) 200 keV electrons. In (a) and (d), spectra have been generated on the basis of the energy registered by individual pixels. For (c) and (d), spectra were constructed based on the sum signal recorded by pixel clusters, which identified as those pixels that recorded any signal and were neighbouring in a two-connected sense. Spectra have been broken down on the basis of whether or not the energy deposited in the pixel or cluster (as appropriate) was due to the primary electron (PE) that was absorbed or backscattered by the sensor; a combination of the primary electron (absorbed or backscattered) and secondary electrons that are absorbed by the sensor (SE) or another combination of particle and interaction types (labeled "Other") 140

- 4.6 MTFs of the three Si Medipix3 devices exposed to 60 keV electrons when operating in SPM using counting thresholds of (a) ~ 12 keV, (b) ~ 30 keV and (c) ~ 48 keV. The corresponding DQE are shown in (d) - (f). Spatial frequencies are stated in terms of ω_N of the $55\mu\text{m}$ pitch detectors; $0.5\omega_N$ therefore represents the Nyquist frequency of the $110\mu\text{m}$ pixel pitch. The MTF of a idealised square pixel detector with is plotted in (a)-(c) and the corresponding DQE plotted in (d)-(f) as a cooperator. 142
- 4.7 MTFs of the three Medipix3 detectors with Si sensors in SPM when using a counting threshold of (a) ~ 12 keV, (b) 59 keV and (c) ~ 118 keV. (d) - (f) show the devices' DQE for the same counting thresholds. As in 4.6, frequencies are stated in terms of ω_N of the $55\mu\text{m}$ pitch detectors and the MTF and DQE of a "ideal" square pixel detector is plotted as appropriate for ease of comparison. The primary electron energy was 200 keV. 143
- 4.8 Plots of the dependence of the MTF and DQE as summarised by the values of $\text{MTF}(\omega_N)$, $\text{DQE}(0)$ and $\text{DQE}(\omega_N)$ on counting threshold for the three Si Medipix3 devices. In turn, the panels show the dependence of $\text{MTF}(\omega_N)$ for (a) 60 keV and (b) 200 keV electrons; the dependence of $\text{DQE}(0)$ on threshold for (c) 60 keV and (d) 200 keV electrons; and the dependence of $\text{DQE}(\omega_N)$ on counting threshold for (e) 60 keV and (f) 200 keV electrons. The insets of panels (b) and (f) show close-ups of the data for the $55\mu\text{m}$ pitch results. 145
- 4.9 Probability distributions of the deposition of a certain amount of energy at a given point along the trajectory of the primary electron in Si for primary electron energies of (a) 60 keV and (b) 200 keV. Each column has been normalised to its own sum, so that for each position along the x -axis, the distribution in y represents the probability of depositing a given amount of energy at that position along the electron's trajectory. 149
- 4.10 Plots of σ , the standard deviation σ of the Gaussian distribution describing the effects of diffusion on the position of a hole in a Si sensor depending on the depth at which the hole was created in the sensor, depending on the sensor thickness and the applied bias. 152
- 4.11 MTFs of devices with $110\mu\text{m}$ and $55\mu\text{m}$ pixel pitch when (a) both devices register incident quanta only in the pixel in which they enter the sensor; their effective pixel pitch is calculated using Equation 4.3 with $E_T/E_0=1/6$ for (b) $\Delta=0.5$, (c) $\Delta=1.5$ and (d) $\Delta=2$, where Δ is expressed as a fraction of the width of the smaller physical pixel pitch. This ratio of E_T/E_0 could represent a threshold of 10 keV for 60 keV electrons or, given the maximum amount of energy deposited in individual pixels by 200 keV electrons, ~ 20 keV for 200 keV electrons. 154

- 4.12 Plots of the count rate curves for the three Medipix3 detectors as a function of incident 200 keV electron flux when operating in SPM with a counting threshold of 12 keV and an I_{Krum} setting of 10 DAC. Also plotted are the predicted count rates as a function of incident flux based on the fitted values of τ and g_τ for the three detectors as well as the response of a perfectly linear detector. The shaded regions indicate the uncertainty of the predicted count rates due to the errors on the fitted parameters. As no data was collected with the 500 μm thick sensor above an incident flux of 1.5×10^5 electrons/pixel/s, the predicted count-rate for this device at higher levels of incident electron flux is an extrapolation based on the fit made to the lower incident flux data. This has been plotted as a dashed line to distinguish it from the predicted count-rate for the regime in which experimental data was acquired. 157
- 5.1 2D histograms of the energy distribution of 300 keV electrons averaged over the 20 000 simulated events in (a) Si, (b) GaAs and (c) CdTe. The contour lines mark the distance from the impact point at which 50%, 90% and 99% of the energy is deposited. 168
- 5.2 Average radii of the contours containing (a) 50%, (b) 90% and (c) 99% of the energy deposited by electrons ranging in primary energy from 30 keV to 300 keV in Si, GaAs and CdTe sensors. 170
- 5.3 Results of the analysis of simulations investigating how electron backscatter depends on primary electron energy (E_0) and sensor material. In (a), the fraction of electrons backscattered for different sensor materials and values of E_0 are plotted, while in (b), the ratio of the average energy deposited E_{Mean} to E_0 is plotted. The data in (b) can be broken down further on the basis of whether the primary electron is (c) absorbed or (d) backscattered from the sensor. 172
- 5.4 Fraction of the average amount of energy deposited in the target by the incident primary electrons, secondary electrons and X-rays produce for primary electron energies ranging from 30 keV to 300 keV in (a) Si, (b) GaAs and (c) CdTe sensors. 173
- 5.5 Radii of the contours containing 50% of the energy deposited by primary electrons, secondary electrons and X-rays in (a) Si, (b) GaAs and (c) CdTe targets. 174
- 5.6 Radii of the contours containing 90% of the energy deposited by primary electrons and secondary quanta in (a) Si, (b) GaAs and (c) CdTe targets. 175
- 5.7 Radii of the 99% energy contours for primary electrons, secondary electrons and X-rays in (a) Si, (b) GaAs and (c) CdTe targets. 176

5.8	Figure showing the average energy deposition due to (a) all particles; (b) primary electrons; (c) secondary electrons and (d) X-rays. In (a)-(d), the circles plotted have radii corresponding to the average radii of the contours containing 50%, 90% and 99% of the average amount deposited by the appropriate type of particles for that Figure.	178
6.1	Spectra recorded by the Medipix3 device with a GaAs:Cr sensor operating in (a) SPM and (b) CSM. The spectra have been normalised so that the area under each of them is unity.	182
6.2	(a) MTF and (b) DQE measurements at selected thresholds with the Si device operating in SPM for 60 keV electrons; (c) MTF and (d) DQE measurements for the GaAs:Cr detector under the same conditions. . .	185
6.3	MTF for (a) Si and (c) GaAs:Cr detectors operating in SPM with selected counting thresholds for 80 keV electrons; the corresponding DQE results for (b) the Si device and (d) the GaAs:Cr device.	186
6.4	(a) MTF and (b) DQE at selected thresholds for a Si device operating in SPM for 120 keV electrons; (c) MTF and (d) DQE for a GaAs:Cr detector in SPM for 120 keV electrons at selected thresholds.	188
6.5	200 keV SPM (a) MTF and (b) DQE at selected thresholds for a Si detector at selected thresholds and selected (c) MTF and (d) DQE for a GaAs:Cr device under the same conditions.	189
6.6	(a) MTF and (b) DQE at selected thresholds for a GaAs:Cr Medipix3 device operating in SPM for 300 keV electrons.	190
6.7	$MTF(\omega_N)$ for (a) Si and (b) GaAs:Cr devices as a function of counting threshold when operating in SPM for electrons with energies ranging from 60-300 keV.	192
6.8	$MTF(\omega_N)$ as a function of counting threshold when operating in CSM with electrons energies in the range of 60 keV - 300 keV for (a) the Si sensor and (b) the GaAs:Cr device.	193
6.9	Dependence of $DQE(0)$ on counting threshold for (a) the Si Medipix3 device and (b) the Medipix3 detector with GaAs:Cr sensor, both operating in SPM for incident electrons with energies from 60 keV to 300 keV.	195
6.10	$DQE(0)$ as a function of counting threshold using electrons ranging in energy from 60 keV to 300 keV for (a) the Si device and (b) GaAs:Cr device operating in CSM.	197
6.11	Dependence of $DQE(\omega_N)$ on counting threshold for (a) Si and (b) GaAs:Cr devices operating in SPM for electrons with energies ranging from 60 keV to 300 keV.	199
6.12	Dependence of $DQE(\omega_N)$ on counting threshold for (a) Si and (b) GaAs:Cr detectors in CSM for electrons with energies from 60 keV to 300 keV.	200

- 6.13 Count rate of the Si and GaAs:Cr Medipix3 devices exposed to increasing incident flux of 120 keV electrons with both devices using an I_{Krum} setting of 10 DAC. The shading indicates the error on the fit to the data, based on the propagation of the errors calculated for the fitted parameters. 201
- 6.14 Count rate of the Si and GaAs:Cr Medipix3 detectors as a function of incident flux of 200 keV electrons when I_{Krum} is set to (a) 10 DAC, (b) 130 DAC and (c) 250 DAC. The uncertainty on the fit to the data was determined by propagating the errors on the fitted parameters. As in Figure 4.12, the predicted count rate for the Si sensor at incident flux above 1.5×10^5 electrons/pixel/s is an extrapolation based on the parameters found by fitting Equation 4.4 to the data points obtained at lower incident flux. For clarity, the predicted count rate of the sensor at incident flux $> 1.5 \times 10^5$ electrons/pixel/s has been plotted as a dashed line in (a)-(c) 202
- 6.15 Dependence of the Si and GaAs:Cr detectors deadtime (τ), on I_{Krum} for (a) 120 keV electrons and (b) 200 keV electrons; the dependence of the τg_{τ} product of the two detectors for (c) 120 keV and (d) 200 keV electrons. 204
- 6.16 Dependence of the count rate of the GaAs:Cr and Si detectors on I_{Krum} for (a) 120 keV electrons at an incident flux of $5.3 \pm 0.9 \times 10^3$ electrons/pixel/s (GaAs:Cr) and $5.4 \pm 0.1 \times 10^3$ electrons/pixel/s (Si) (b) 200 keV electrons at an incident flux of $4.8 \pm 0.2 \times 10^3$ electrons/pixel/s (GaAs:Cr) and $4.5 \pm 0.1 \times 10^3$ electrons/pixel/s (Si), (c) 120 keV at an incident flux of $4.9 \pm 0.2 \times 10^5$ electrons/pixel/s (GaAs:Cr) and $4.4 \pm 0.2 \times 10^5$ electrons/pixel/s (Si) and (d) 200 keV electrons at an incident flux of $3.49 \pm 0.08 \times 10^5$ electrons/pixel/s (GaAs:Cr) and $1.38 \pm 0.07 \times 10^5$ electrons/pixel/s (Si). 206
- 6.17 Mean-normalised flat field images recorded by (a) the Medipix3 device with $500 \mu\text{m}$ Si sensor and $55 \mu\text{m}$ pitch characterised in Chapter 3 (b) the Medipix3 GaAs:Cr device, both exposed to 200 keV electrons; (c) shows histograms of the intensities in (a) and (b); (d) - (e) show close-ups of ROI marked in (b) that showcase examples of different types of defects seen in the GaAs:Cr sensor. 208
- 6.18 Flat field exposures of the GaAs:Cr detector operating in SPM with a counting threshold of 12.7 ± 0.1 keV when using (a) 200 keV and (b) 300 keV electrons with the regions from which sub-pixel confocal STEM maps were obtained marked. (c) shows the map acquired with 200 keV electrons and (d) that acquired with 300 keV electrons. Images in (a) - (d) are all normalised to their mean pixel intensity value and set to have the same contrast limits. 209

- 6.19 Close-ups of the regions of the sensor from which confocal STEM maps were acquired for the (a) 200 keV and (b) 300 keV datasets. Marked in (a) and (b) are several ROI. ROI B is shown in close-up in (c) for 200 keV electrons, (e) 300 keV electrons; ROI C is shown in close-up in (g) for 200 keV electrons and (i) 300 keV electrons; and ROI D is shown in close-up in (k) for 200 keV and (m) 300 keV electrons. Also shown are sum confocal STEM maps of ROI B for (d) 200 keV and (f) 300 keV electrons; of ROI C for (h) 200 keV and (j) 300 keV electrons; of ROI D for (l) 200 keV and (n) 300 keV electrons. 211
- 6.20 Pixel response maps for the pixel marked in (a) light blue, (c) red, (e) purple, (g) green and (i) yellow in Figures 6.19(c)-(f) generated from the 200 keV confocal STEM scans. (b), (d), (f), (h) and (j) show the same again but generated from the 300 keV dataset. The pixel response map for the pixel marked in dark blue in Figures 6.19(g)-(j) is seen in (k) for 200 k and (l) for 300 eV electrons. 213
- 6.21 Maps of pixel areas as determined on the basis of the 300 keV confocal STEM dataset for (a) the full portion of the sensor form which the 300 keV confocal STEM dataset was acquired, (b) ROI B, (c) ROI C, (d), ROI D and (e) ROI A. The selected POI previously marked in Figures 6.19(c) - (j) are also marked where appropriate in (b), (c) and (e). The light purple pixel marked in ROI C in (c) is also marked in ROI D in (d) to aid comparison with Figures 6.24. 215
- 6.22 Plot of the mean-normalised pixel intensities in the region of the 300 keV flat field image shown in Figure 6.18(b), against the corresponding pixel area as determined from the 300 keV confocal STEM scan of that same region of the GaAs:Cr sensor. 216
- 6.23 Close-ups of ROI B of the GaAs:Cr exposed to 120 keV electrons at an incident flux of (a) $1 \pm 0.1 \times 10^4$ electrons/pixel/s, (b) $3.2 \pm 0.2 \times 10^4$ electrons/pixel/s, (c) $1.44 \pm 0.08 \times 10^5$ electrons/pixel/s, (d) $3.3 \pm 0.2 \times 10^5$ electrons/pixel/s and (e) $5.4 \pm 0.3 \times 10^5$ electrons/pixel/s, all with I_{Krum} set to 10 DAC. The same ROI still exposed to incident flux of $5.4 \pm 0.3 \times 10^5$ electrons/pixel/s but with I_{Krum} set to 50 DAC is shown in (f). Plots of the count rate of the pixels marked in (g) blue, (h) red, (i) purple, (j) green and (k) yellow are plotted as a function of incident 120 keV electron flux for selected values of I_{Krum} 217

- 6.24 Close-ups of ROI A of the GaAs:Cr detector when I_{Krum} is set 10 DAC exposed to incident flux of 200 keV electrons of (a) $1 \pm 0.2 \times 10^3$ electrons/pixel/s, (b) $1.78 \pm 0.04 \times 10^4$ electrons/pixel/s, (c) $1.03 \pm 0.02 \times 10^5$ electrons/pixel/s, (d) $3.80 \pm 0.09 \times 10^5$ electrons/pixel/s; an incident flux of $3.80 \pm 0.09 \times 10^5$ electrons/pixel/s with I_{Krum} set to (e) 50 DAC and (f) 100 DAC. The images in (a)-(f) are all normalised to their mean value and have the same contrast limits set; the inset histograms of the normalised pixel intensities have x -limits of 0-2 normalised counts and y -limits of 0-200 pixels. (g) shows a plot of the standard deviation of the mean-normalised intensities recorded in ROI A as a function of the I_{Krum} setting used; in (h) plots of the standard deviation of the mean normalised intensities recorded in ROI A as a function of incident 200 keV electron flux for selected I_{Krum} settings are shown; while in (i) plots of the count rate of the pixel marked in purple in (a)-(f) as a function of incident 200 keV electron flux for selected values of I_{Krum} are plotted. 220
- 6.25 Images same ROI A exposed to 120 keV electrons at a flux of (a) and (e) $9.2 \pm 0.2 \times 10^3$ electrons/pixel/s; (b) and (f) $4.41 \pm 0.07 \times 10^4$ electrons/pixel/s; (c) and (g) $8.5 \pm 0.1 \times 10^4$ electrons/pixel/s; and (d) and (h) $1.57 \pm 0.02 \times 10^5$ electrons/pixel/s. Images (a) - (d) have had a flat field correction applied for which the flat field has been acquired under an incident flux of $9.2 \pm 0.2 \times 10^3$ electrons/pixel/s, while images in (e) - (h) have had a flat field correction applied for which the flat field data was acquired with an incident electron flux of $1.57 \pm 0.02 \times 10^5$ electrons/pixel/s. All images have been normalised to their average pixel value. In (d) and (e), lines along which the intensity profile was measured are marked, and these are plotted in (i). The standard deviations of the images in (a) - (d) are plotted as a function of image to flat field flux in (j), while those of images (e) - (h) are plotted in (k). 223
- 6.26 (a)-(c) Images of the knife-edge placed at three different positions relative to the GaAs:Cr detector and acquired with 300 keV electrons; (d), (f) and (h) show close-ups of the ROIs marked in (a)-(c) with a flat field correction applied; (e), (g) and (i) show the same ROI in (d), (f) and (g) without the flat field correction applied. 224
- 6.27 (a)-(c) show the different positions at which the knife-edge was positioned relative to the GaAs:Cr sensor when it was mounted on the Titan 80-300 (S)TEM and exposed to 300 keV electrons with the regions that were used to determine the MTF marked, while (d) shows the corresponding MTFs. 225

- 7.1 Schematic of the signal processing circuitry present on a single HEXITEC pixel. Charge induced on the pixel Input Pad is amplified and converted into a voltage step by the preamplifier (marked as “Preamp”), which is shaped and filtered by a CR-RC shaper (labelled “Shaper” and “Filter”). The risetime of the resulting voltage pulse is $\sim 2\mu\text{s}$, while the return to baseline is $8\mu\text{s}$ [308]. Redrawn from [307]. 230
- 7.2 Photographs of the assembly used to install a HEXITEC detector on the Tecnai T20 TEM: (a) overhead shot of the PCB on which the chip is installed and which is within the vacuum of the microscope’s detector chamber; (b) photograph of the exterior face of the assembly facing away from the microscope, with the ethernet and DB15 connectors for interfacing with the DAQ computer and external temperature monitoring units respectively; and (c) side-view of the full assembly. The photographs have been cropped close to the objects of interest to remove extraneous background details. 232
- 7.3 Illustration of the procedure used to perform a pixel-by pixel calibration of the HEXITEC detector. (a) shows the reference spectrum formed by summing all pixel clusters due to individual events, with search ranges for selected photopeaks marked. In (b), the spectrum recorded by a single pixel is shown, along with the threshold used to determine the upper limit of the 59.5 keV photopeak, and hence the search range for this peak in the individual pixel spectrum. (c) shows a the difference in the position of the 59.5 keV between the exemplar individual pixel spectrum (marked in blue) and the summed reference spectrum (marked in purple). In (d), the new, scaled search ranges for selected photopeaks in the individual pixel spectrum are shown. (e) shows the calibration curve based on the position of the photopeaks found in the individual pixel spectrum shown in (b)-(d), along with the line fitted to this data. In (f), the calibrated spectrum formed using all events registered by the detector is shown. Adapted from reference [311] 234
- 7.4 Images recorded by the HEXITEC device exposed to (a) ^{241}Am , (b) 60 keV electrons and (c) 80 keV electrons. These images have been formed by identifying the weighted CoM of each pixel cluster and assigning to each pixel the number of clusters identified as having their WCoM in that pixel. The resulting images were then normalised to their mean pixel value, and all three images in (a)-(c) have the same contrast limits. (e) - (f) show the spectra corresponding to the images in (a) - (c) 237
- 7.5 Mean-normalised sum images recorded by the HEXITEC detector exposed to (a) ^{241}Am source (b) 60 keV electrons and (c) 80 keV electrons with regions along which line profiles were measured shown in (d) marked. The width of these regions is the width over which the line profiles were averaged. 238

- 7.6 Images acquired by the HEXITEC detector when exposed to (a) ^{241}Am source (b) 60 keV and (c) 80keV electrons showing the locations of ROI 1 (red) and ROI 2 (purple). ^{241}Am spectra recorded in (d) ROI 1 and (g) ROI 2; 60 keV electron spectra recorded in (e) ROI 1 and (h) ROI 2; 80 keV electron spectra recorded in (f) ROI 1 and (i) ROI 2. 239
- 7.7 Results of simulations for which the GaAs target had backside contacts consisting of $0.1\ \mu\text{m}$ thick layer of Ni and Au layers of varying thicknesses ranging from $0.45\ \mu\text{m}$ - $0.55\ \mu\text{m}$ in thickness. The fraction of primary electrons backscattered from (a) the backside contact and (b) the sensor; the ratio of the average energy deposited E_{Mean} to primary electron energy when the primary electron is (c) absorbed by the sensor, (d) backscattered from the sensor or (e) backscattered from the backside contact. 243
- 7.8 Analysis of simulations of a GaAs sensor equipped with backside contacts composed of varying thicknesses and combinations of Al and Ni. Plotted as a function of primary electron energy E_0 are (a) the fraction of electrons backscattered from the contact; (b) the fraction of electrons backscattered from the sensor; (c) the sum fraction of electrons backscattered from the device; the ratio of the average energy E_{Mean} to E_0 when electrons are (d) backscattered from the contact; (e) backscattered from the sensor; and (f) absorbed in the sensor. Relevant results from simulations of electron interactions with a GaAs sensor with no backside contact are reproduced from Figure 5.3 as a comparator. 245
- 7.9 Plots of the average radii of the (a) 50% (b) 90% and (c) 99% deposition contours in a GaAs sensor with a selection of backside contacts composed of different combinations of Al and Ni. The average radii of the 50%, 90% and 99% energy deposition contours for a GaAs sensor with no backside contact are reproduced from Figure 5.2 for the sake of comparison. 247

List of Tables

- 2.1 Table summarising the current generation of MAPS devices for use in (S)TEM. The 4D-Camera is not presently commercially available, being a custom, system developed in-house for use on the TEAM 0.5 microscope for the Molecular Foundry at the Lawrence Berkeley National Laboratory [135]. At the same time, the K2 and K3 series of detectors grew out of in-house systems built for the TEAM project [136], while the Falcon series of detectors arose from developments in monolithic device technologies made at the UK STFC Detector Group at the Rutherford Appleton Laboratory [137]. It is therefore possible there will be a commercial version of the 4D-Camera in the not distant future. Note that those applications listed for which there is no citation associated are included on the basis that the manufacturer advertises the detector for this application. A lack of citations is not necessarily cause for skepticism regarding the suitability of the detector for the application in question being in some cases is attributable to the newness of the product. 73
- 2.2 Table summarising the current generation of HPDs for use in (S)TEM. Note that in the case of the Medipix3 and Timepix3 detectors that there are a number of commercial vendors that have licensing agreements to sell systems based around the Medipix3 and/or Timepix3 technology into their detector systems. Likewise, several of the DECTRIS products (the ELA, SINGLA and QUADRO) are based around the EIGER ASIC developed at the Paul Scherrer Institut, with Gatan's STELA in turn being based around the ELA. The same caveats attached to those applications that are listed without a citation noted for Table 2.1. . . . 78
- 2.3 Table summarising key properties of semiconductors suitable for the detection of ionising radiation and that have been investigated for use with HPDs. Properties listed include the energy required to create an electron-hole pair $\epsilon_{e,h}$ and the charge carrier mobility lifetime products for electrons ($\mu_e\tau_e$) and holes ($\mu_h\tau_h$). It should be noted that in references [205] and [206] that the $\mu_h\tau_h$ product is inferred on the basis of simulation, as the small values of μ_h mean proper determination of $\mu_h\tau_h$ is not feasible. 84

3.1	Table listing fluorescence targets used for the calibration of the thresholds of Medipix3 devices in various modes of operations. Where possible, the K_α and K_β peaks would be fitted separately in order to increase the number of points in the calibration curve; even in instances where only two targets are listed, there were a minimum of three points in the calibration curve.	102
4.1	Positions of peaks identified via fitting of the spectra recorded by the different Si sensors and presented in Figures 4.1(b) and Figures 4.2(a)-(c).	133
4.2	Resolution of those peaks identified in Figures 4.1(b) and Figures 4.2(a)-(c) for which a single peak could be identified and fit with a single Gaussian.	133
4.3	Fitted values of the deadtime (τ) and the deadtime gain (g_τ) and their product for the three Medipix3 detectors operating in SPM with an I_{Krum} setting of 10 DAC and a counting threshold of ~ 12 keV for 200 keV electrons.	158
6.1	Resolution of the Medipix3 GaAs:Cr detector operating in CSM for those primary electron energies for which a single peak corresponding to the primary electron energy could be identified.	183
6.2	Positions of peaks identified via fitting the spectra recorded by the Medipix3 GaAs:Cr detector operating in CSM.	184
7.1	Energy of the primary electron peaks in the spectra recorded by the GaAs:Cr HEXITEC assembly exposed to 60 keV and 80 keV electron when taking the spectra from the full sensor and for the selected ROI shown in Figures 7.4(b) and (c).	241

List of Acronyms and Abbreviations

Symbols

1D One-Dimensional

2D Two-Dimensional

4D Four-Dimensional

4D-STEM Four-Dimensional Scanning Transmission Electron Microscopy

5D-STEM Five-Dimensional Scanning Transmission Electron Microscopy

A

ABF Annular Bright Field

ADC Analogue-to-Digital Converter

ADF Annular Dark Field

ADU Analogue-to-digital units

ARM Atomic Resolution Microscope

ASIC Application Specific Integrated Circuit

B

BF Bright Field

BFP Back Focal Plane

C

CBED Convergent Beam Electron Diffraction

CCD Charge-Coupled Device

CERN Conseil Européen pour la Recherche Nucléaire (European Organisation for Nuclear Research)

CMOS Complementary metal-oxide semiconductor

CR Capacitance-Resistor

cryoEM Cryogenic Electron Microscopy

CSA Charge-Sensitive Amplifier

CSM Charge Summing Mode

D

DAC Digital-to-Analogue Converter

DAQ Data Acquisition

DED Direct Electron Detector

DLS Diamond Light Source Ltd.

DPC	Differential Phase Contrast
DQE	Detective Quantum Efficiency
E	
EELS	Electron Energy-Loss Spectroscopy
EMPAD	Electron Microscope Pixel Array Detector
ET	Electron tomography
F	
FEG	Field Emission Gun
FOLZ	First-Order Laue Zone
FOV	Field of View
FPGA	Field-Programmable Gate Array
FWHM	Full Width Half Maximum
H	
HAADF	High-Angle Annular Dark Field
HOLZ	Higher-Order Laue Zone
HPD	Hybrid Pixel Detector
HRTEM	High-Resolution Transmission Electron Microscopy
HV	High Voltage
I	
IRF	Impulse Response Function
K	
KIT	Karlsruhe Institute of Technology
L	
LEEM	Low-Energy Electron Microscopy
M	
MAPS	Monolithic Active Pixel Sensor
microED	Micro Electron Diffraction
MOS	Metal-Oxide-Semiconductor
MTF	Modulation Transfer Function
N	
NEQ	Noise Equivalent Quanta
NIST	National Institute of Standards and Technology
NNPS	Normalised Noise Power Spectrum
NPS	Noise Power Spectrum
P	
PCB	Printed Circuit Board
PEEM	Photoemission Electron Microscopy

PMT	Photo-Multiplier Tube
pn-CCD	PN-Junction/Fully-Depleted Charge-Coupled Device
POI	Pixel of Interest
PSF	Point Spread Function
R	
RC	Resistor-Capacitor
ROI	Region of Interest
S	
(S)TEM	(Scanning) Transmission Electron Microscope/Microscopy
SEM	Scanning Electron Microscope
SOLZ	Second-Order Laue Zone
SPA	Single Particle Analysis
SPM	Single Pixel Mode
STEM	Scanning Transmission Electron Microscope/Microscopy
T	
TCAD	Technology-Aided Computer Design
TEM	Transmission Electron Microscope/Microscopy
ToA	Time-of-Arrival
ToT	Time-over-Threshold
V	
VHDCI	Very High Density Cable Interconnect
W	
WSCS	Wide-Sense Cyclostationary
WSS	Wide-Sense Stationary
X	
XFEL	X-ray Free Electron Laser
Z	
ZOLZ	Zero-Order Laue Zone

List of Symbols

Latin

A	Atomic mass; aperture function
A^*	(Effective) Richardson constant of a material
a	Function describing a sample as an amplitude object
a	Full Width Half Maximum (FWHM)
a_x	Effective pixel pitch in x
B_r	Component of magnetic field in radial direction
b_s	Experimentally determined parameter used in the calculation of the cross section of the ionisation of shell s by an incident electron
B_z	Component of magnetic field in z -direction
c	Speed of light in vacuum: $3 \times 10^8 \text{ ms}^{-1}$
C_5	Coefficient of 5th-order spherical aberration
C_c	Coefficient of chromatic aberration
C_F	Feedback capacitance
C_{In}	Contrast in an input image to a system
C_{Out}	Contrast in a system's output image
C_s	Coefficient of (third-order) spherical aberration
c_s	Experimentally determined parameter used in the calculation of the cross section of the ionisation of shell s by an incident electron
d	Generic signal; lattice spacing
d_0	Diameter of gun crossover
d_A	Diameter of the Airy disk
d_c	Diameter of disk due to chromatic aberration
D_e	Electron diffusion constant
D_h	Hole diffusion constant
d_n	Number of counts given incident quanta n
d_s	Diameter of disk due to spherical aberration
E	Energy; envelope function
E'	Ratio of primary electron energy to electron rest mass
E_0	The initial energy of the primary electron energy
E_{C_s}	Critical ionisation energy of shell s
E_D	Drift electric field
E_F	Fermi level energy

E_g	Bandgap energy
E_i	Intrinsic Fermi level energy
E_{SE}	Secondary electron energy
E_T	Counting threshold energy
\mathbf{E}_W	Weighting field for Schockley-Ramo theorem
F	Fano factor
f	Focal length; sample transmission function
$f(\theta)$	Atomic scattering factor
$F(\theta)$	Structure factor
F_e	Electron flux
F_h	Hole flux
$f_i(\theta)$	Atomic scattering factor of the i -th atom
G	Generation rate
\mathbf{G}	Reciprocal lattice vector
H	Microscope transfer function in Fourier space
h	Planck's constant; microscope transfer function in real space
I	Current
i	Generic point or pixel
I_{Det}	Intensity in the detector plane of a microscope
I_{Krum}	Current
I_m	Mean excitation potential
j	Current density
\mathbf{j}_e	Electron current density
\mathbf{j}_h	Hole current density
j_s	Saturation current density
K	Constant of proportionality linking number of quanta incident on a detector, n , and registered number of quanta, m
\mathbf{k}	Wavevector
\mathbf{k}'	Wavevector post-scattering
k_B	Boltzmann's constant
\mathbf{k}_F	Wavevector corresponding to the Fermi level
M	Generic integer
m	Number of quanta detected
m_0	Rest mass of the electron: 511 keV
m_e	Electron effective mass
m_h	Hole effective mass
N	Number density
n	Number of incident quanta
N_D	Density of bulk dopant atoms
N_D	Density of donor atoms
n_e	Electron density
n_i	Intrinsic charge carrier density

n_{in}	Incident particle flux
n_{out}	Count rate
n_s	Number of electrons in shell s
O	Origin
P	Generic point in sample/object plane of a lens/imaging system
p	Momentum
p_h	Hole density
Q	Sum charge
q	Charge; quanta
R	Recombination rate
r	Position vector
r_0	Classical electron radius
r_A	Radius of the Airy disk
R_E	Energy resolution
s	Inner shell
T	Characteristic function; temperature
t	Time
T_C	Large Area Contrast Transfer Function
V	Voltage, potential, bias
v	Velocity
V_{bd}	Breakdown bias
V_{bi}	Built-in potential
V_{dep}	Depletion bias
W	Width of depletion volume of a pn-junction
x	Position
x_0	Pixel pitch
Z	Atomic number
Greek	
B	Brightness
Γ	Fluorescence yield
Φ	Work function of a material
Φ_{B_n}	Potential barrier for an electron at a metal-semiconductor (n-type) interface
Φ_{B_p}	Potential barrier for an electron at a metal-semiconductor (p-type) interface
Φ_m	Work function of a metal
Φ_{Red}	Reduced work function of a material
Φ_s	Work function of a semiconductor
X	Aberration function in Fourier space
Ψ_T	Transmitted/post-sample electron wavefunction in Fourier space
Ω	Solid angle
α	Fine structure constant
α_0	Angle of electron wavefront/ray path relative to the optic axis; collection semi-angle of an aperture or lens

α_1	Semi-angle of convergence
β	The ratio of a velocity, v to the speed of light in vacuum, c
γ	Parameter depending on electron shell and element that determines fluorescence yield
η	Ratio of photon energy to rest energy of the electron
θ	Angle of deflection or scattering
θ_0	Screening parameter
κ	Constant of proportionality linking atomic number Z to the probability of photoelectric absorption $_{PE}$
λ	Wavelength
μ	Refractive index
μ_e	Electron mobility
μ_h	Hole mobility
ν	Frequency
ν_0	Highest possible frequency
ξ	Exponent relating atomic number, Z , to the cross section of an X-ray of a given energy undergoing photoelectric absorption, σ_{PE}
ρ_h	Electron density
ρ_h	Hole density
σ	Error; standard deviation
σ_B	Number of Bremsstrahlung X-rays
σ_{I_s}	Cross section of the ionisation of shell s
σ_{PE}	Cross section of an X-ray of a given energy undergoing photoelectric absorption
τ	Detector deadtime
τ_C	Mean free lifetime
τ_{Diff}	Differentiator time constant
τ_e	Electron recombination lifetime
τ_G	Generation lifetime
τ_h	Hole recombination lifetime
τ_{Int}	Integrator time constant
τ_R	Recombination lifetime
χ	Electron affinity
ψ_E	Electrostatic potential
ψ_{Im}	Electron wavefunction in image plane in real space
ψ_{In}	Incident electron wavefunction in real space
ψ_P	Probe electron wavefunction in real space
ψ_T	Transmitted/post-sample electron wavefunction in real space
ψ_W	Weighting potential for Schockley-Ramo theorem
ω	Spatial frequency
ω_0	Generic spatial frequency
ω_N	Nyquist spatial frequency
ϵ_0	Permittivity of free space
ϵ_s	Dielectric constant

1

Radiation Detectors

1.1 Introduction

The performance of imaging detectors used in transmission electron microscopy (TEM) is fundamentally determined by the interactions of electrons with matter, as well as how such devices transfer the signal produced by incident primary electrons and any secondary quanta they produce. This chapter therefore begins with an outline of the physics governing the interactions of electrons with matter relevant to the detection of electrons with energies typically used in current generation TEM (60-300 keV), as well as the interactions of secondary quanta produced by the interactions of electrons. It then proceeds to give an overview of the basic principles of detector operation. Modern detector technologies used in electron microscopy, including the detectors that have been investigated in this thesis, typically use semiconductors for either part or the entirety of the sensor that converts incident electrons into an electrical signal. Consequently, this chapter also includes an outline of the physics of semiconductors, focusing on how they are used to detect ionising radiation. This is followed by discussion of metrics for evaluating detector performance, with a particular focus on how the performance of imaging detectors can be quantified.

1.2 Interactions of Radiation with Matter

Electrons with can interact with matter through a variety of mechanisms, both elastic and inelastic. Some of these interactions can give rise to secondary quanta that can also go on to interact with matter through various mechanisms. It is this variety of interaction mechanisms, along with the inherently stochastic nature of both the interactions of the primary electrons and any secondary quanta, that present a challenge to the design and optimisation of detectors for electron microscopy. With

respect to the generation of signal, it is the inelastic interaction mechanisms that are relevant, as it is only by depositing energy in a sensitive volume that electrons are able to produce signal. However, elastic mechanisms are important from the perspective of the spatial spread of the signal produced, as they enable primary electrons to travel further in a detector's sensitive volume than would be the case if all interactions were via inelastic mechanisms. The production of secondaries and their interaction mechanisms are also worth consideration for the same reason. Both elastic and inelastic electron interactions are discussed in Section 1.2.1, while the interactions of secondary quanta, namely X-rays, are described in Section 1.2.2.

1.2.1 Interactions of Electrons

The first inelastic interaction mechanism for primary electrons are collisions with the bound atomic electrons in an absorbing volume, mediated by the Coulomb interaction. For most charged particles the rate of energy loss due to this mechanism is described by the Bethe-Bloch Equation, but in the case of electrons two modifications must be made [6]. First, it is necessary to take into account the indistinguishability of the primary electron and the bound electron; second, the equal masses involved in the collisions mean the usual assumption that the primary particle is undeflected as a result of the interaction does not hold. These two modifications give rise to Equation 1.1, for which T is defined in Equation 1.2 [7]:

$$-\left\langle \frac{dE}{dx} \right\rangle_{coll} = \frac{2\pi N e^4}{m_0 v^2} Z T \quad (1.1)$$

$$T = \log \left(\frac{m_0 v^2 E}{2 I_m^2 (1 - \beta^2)} \right) - \left(2\sqrt{1 - \beta^2} - 1 + \beta^2 \right) \log(2) + 1 - \beta^2 + \frac{1}{8} (1 - \sqrt{1 - \beta^2})^2 \quad (1.2)$$

In Equations 1.1 and 1.2, the various mathematical symbols have the following associated meanings associated with them:

- I_m - The mean excitation potential of the absorber, effectively the average orbital frequency multiplied by Planck's constant. This is usually experimentally determined for a given material.
- m_0 - The rest mass of the electron.
- β - Ratio of the velocity of the incident electron, v , to the speed of light, c .
- N - The number density of the absorbing material.
- Z - The atomic number of the absorbing material.

It should be noted that Equation 1.1 is only valid as an expression for the mean rate of energy loss when $E \gg I_m$. For lower electron energies that are on the order of I_m (which typically is on the order of 10-1000 eV), a modified form of Equation 1.1 is more suitable [8]. However, as the range of primary electron energies considered in this thesis (60-300 keV) are much higher than this, the modified form would only be relevant once the electrons have already lost the overwhelming majority of their energy and Equation 1.1 is the most suitable approximation in the context of the present work.

Electrons can also lose energy radiatively, through the production of Bremsstrahlung X-rays when they are deflected (i.e. accelerated) due to interactions with atoms, as shown in Figure 1.1. The rate of energy loss due to this process is described by Equation 1.3, where $\sigma(E_0, \nu)$ is the cross-section for an electron of initial energy E_0 emitting a photon of frequency ν , and ν_0 is the highest frequency photon that the electron could emit i.e. a photon with energy equal to the primary electron's initial energy [9]. There are only two cases in which there is an analytical solution to the integral in Equation 1.3. The first is when the primary electron's initial energy is much greater compared to its rest mass (511keV) but not so great that the screening of the atomic nucleus by bound electrons is significant. The second case is when the primary electron's initial energy $E_0 \gg 137m_0^2Z^{-\frac{1}{3}}$, which indicates that screening of the nucleus is complete. Neither of these conditions are met by electrons with energies typically used in TEM though, of the two, the first condition is closer to being fulfilled by electrons in the energy range under consideration in the present work. Equation 1.4, which is the result of solving the integral in Equation 1.3 for the first case is therefore an approximation for electrons with those energies typically used in a TEM.

$$-\left\langle \frac{dE}{dx} \right\rangle_{rad} = N \int_0^{\nu_0} h \nu \sigma(E_0, \nu) d\nu \quad (1.3)$$

$$-\left\langle \frac{dE}{dx} \right\rangle_{rad} = \frac{NEZ^2e^4}{137m_0^2c^4} \left(4 \ln \left(\frac{2E}{m_0c^2} \right) - \frac{4}{3} \right) \quad (1.4)$$

The simplest expression for the cross section of the generation of Bremsstrahlung is given in Equation 1.5, where $\sigma_B(E)$ is the number of X-rays of energy E produced per incident electron per atom per cm^2 per unit solid angle, while the other symbols have their usual meanings [10]. The overall rate of energy loss for the incident electron is the sum of the rate of the stopping power for Coulomb interactions and for radiative losses. For both mechanisms, the rate of energy loss is proportional to the atomic number of the material in which the electron is travelling but it increases linearly with Z for losses due to Coulomb interactions and quadratically for radiative losses. However, even for materials with higher values of Z , the generation of Bremsstrahlung is not the dominant mechanism of energy loss for electrons with the energies that are typically used in electron microscopy. Overall, the amount of energy lost by electrons

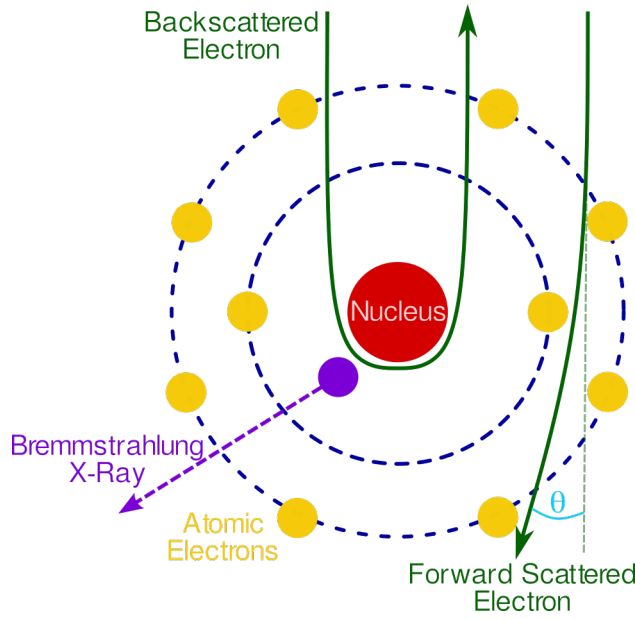


Figure 1.1: An illustration of how electrons can be scattered by atoms. When scattered by atomic electrons the angle of scattering, θ is typically small and may or may not involve the transfer of energy to the atomic electron. If the incident electron is scattered by the atomic nucleus, then the angle of scattering can be much larger, to the extent that the incident electron is deflected by a full 180° and “backscattered”. Although less important from the perspective of electron interactions with detectors, when discussing electron interactions with a sample within TEM, electrons that are not backscattered are regarded as “forward scattered”. Whenever the incident electron is deflected there is a possibility of it producing Bremsstrahlung, though in this example only the backscattered electron is marked as having produced in X-ray photon.

via Bremsstrahlung in TEM is very small compared to the energy loss due to Coulomb collisions, with the ratio of energy loss due to Coulomb interactions to that due to Bremsstrahlung production given by Equation 1.6 [9]. Taking, for example, a 300 keV electron in a sensor where the average value of Z is 50 (such as a CdTe or CZT sensor), the energy lost due to Bremsstrahlung production would be $< 2\%$ of that lost due to Coulomb interactions. Both the value of Z and the electron energy used in this example are the upper limits of the ranges considered in this thesis, so this value represents the upper limit on the amount of energy loss due to the production of Bremsstrahlung expressed as a percentage of the energy lost due to Coulomb interactions.

$$\sigma_B(E) = \frac{1.43 \times 10^{-21} Z^2 (E_0 - E)}{4\pi EE_0} \quad (1.5)$$

$$\frac{-\langle dE/dx \rangle_{coll}}{-\langle dE/dx \rangle_{rad}} = \frac{E_0 Z}{1600 m_0 c^2} \quad (1.6)$$

In addition to the two inelastic interactions outlined above, electrons can also be scattered by the nuclei of atoms. Although such scattering events are also mediated by the Coulomb interaction, primary electrons can be deflected through much larger angles when they undergo scattering with a nucleus, i.e. Rutherford scattering, than

when they scatter with an electron. An approximation for the Rutherford scattering differential cross section, for a given angle of deflection θ , is defined in Equation 1.7 [11]. This expression accounts for both relativistic effects and, through the inclusion of the screening parameter θ_0 (defined in Equation 1.8), the effect of atomic electrons screening the nucleus from the primary electrons. The parameter α depends on the heaviness of the element and has been calculated as $Z/137$ for lighter elements, though heavier elements require more specific calculation. Due to this variation in α , no analytical expression exists for the exact Rutherford cross section and simplified forms (such as that of Bethe and Ashkin [12]) are used for calculations in practice.

$$\frac{d\sigma_R(\theta)}{d\Omega} = \frac{Z^2 e^4}{16E_0^2} \frac{1}{\left| \sin^2\left(\frac{\theta}{2}\right) + \frac{\theta_0^2}{4} \right|^2} \left| 1 - \beta^2 \sin^2\frac{\theta}{2} + \pi\alpha\beta \left[\sin\frac{\theta}{2} - \sin^2\frac{\theta}{2} \right] \right| \quad (1.7)$$

$$\theta_0 = 0.1167Z^{1/3}E_0^{1/2} \quad (1.8)$$

Rutherford scattering interactions are elastic in the sense that the net kinetic energy and momentum of the nucleus and the primary electron are conserved, although the electron may still transfer energy to the nucleus as part of the scattering interaction. The dependence of the energy transferred to the nucleus, ΔE , on the scattering angle is expressed in Equation 1.9, in which A is the atomic mass of the nucleus¹ [13]. From the perspective of the spatial spread of signal, this energy loss is unimportant as it does not produce electrical signal. However, if the energy transferred to the nucleus of an atom exceeds the atom's displacement energy (which depends on the atom and the nature of its chemical bonds with its neighbours), then Rutherford scattering can lead to the nucleus being displaced from its position in the absorbing volume. Thus Rutherford scattering can be important with respect to damage to the sensor and any associated readout electronics that are exposed to incident (or high-energy secondary) electrons. The highest energies typically used in TEM, i.e. 300 keV, exceed the threshold for knock-on damage to crystalline Si (used for the sensors of many devices) due to Rutherford scattering [14, 15]. This is not usually regarded as a problem for Si as the lattice is able to anneal itself [16], but damage to the SiO₂ components of the electronics can limit device lifetime [17–19].

$$\Delta E = \frac{E_0(E_0 + 1.02)}{496A} \sin\left(\frac{\theta}{2}\right) \quad (1.9)$$

In addition to the aforementioned Bremsstrahlung X-rays, electrons can generate further secondary radiation through their interaction with an absorbing material. By transferring energy to bound atomic electrons through Coulomb scattering, they can produce secondary electrons and X-rays of specific energies that are characteristic

¹ It should be noted that for this expression to be valid, E_0 and ΔE must be in units of MeV.

of the elements composing the absorber (unlike the continuum of X-ray energies produced in the case of Bremsstrahlung). When an incident electron transfers sufficient energy to an inner-shell electron, the latter electron can escape the attractive potential of the atom, leaving the atom in an excited, ionised state. For the atom to return to its ground state, the inner-shell vacancy must be filled, which can be done by an electron in a higher energy shell dropping down in energy. This transition entails emitting an X-ray with an energy equal to the energy difference between the two electron orbitals. X-rays produced in this manner have energies defined by the energies of the atom's electron orbitals and the differences between them; they are therefore associated with specific elements, which is why they are described as being characteristic of a specific element. Both characteristic X-rays and Bremsstrahlung X-rays can go on to interact with the sensor and deposit their energy in the sensor via the mechanisms outlined in section 1.2.2.

An alternative to the production of a characteristic X-ray is the generation of an Auger electron. The process of producing an Auger electron is the same as producing a characteristic X-ray except that the energy difference between the high-energy shell and the lower-energy vacancy is transferred to an electron in the high-energy shell, enabling it to also escape, rather than going into the production of an X-ray. Figure 1.2(b) illustrates the production processes for both characteristic X-rays and Auger electrons and how they differ. An expression for σ_{I_s} , the cross-section for the ionisation of a particular inner-shell s is given in Equation 1.10 [21, 22]. In this Equation, E_{C_s} is the critical ionisation energy of the shell under consideration; b_s and c_s are parameters that are fitted to experimentally determined cross section data for the shell s ; and n_s is the number of electrons in that shell. More specific expressions for the ionisation of particular orbitals are also possible [13]. The fraction of ionisation events that lead to the production of characteristic X-rays, as opposed to Auger electrons, is quantified by the fluorescence yield, Γ , a common expression for which is stated in Equation 1.11 and in which γ is a parameter that depends on the electron shell and element under consideration [20]. Lighter elements, which have small binding energies, have a larger fluorescence yield than heavier elements. Consequently, the typical energies of Auger electrons range from a few hundred eV to a few keV.

$$\sigma_{I_s} = \left(\frac{\pi e^4 b_s n_s}{\left(\frac{m_0 v^2}{2}\right) E_{C_s}} \right) \left(\log \left(c_s \frac{m_0 v^2}{2 E_{C_s}} \right) - \log(1 - \beta^2) - \beta^2 \right) \quad (1.10)$$

$$\Gamma = \frac{Z^4}{\gamma + Z^4} \quad (1.11)$$

Both the production of characteristic X-rays and the production of Auger electrons are triggered by the escape of an inner-shell electron made possible by the transfer of energy from an incident electron. It is also possible for high-energy incident electrons

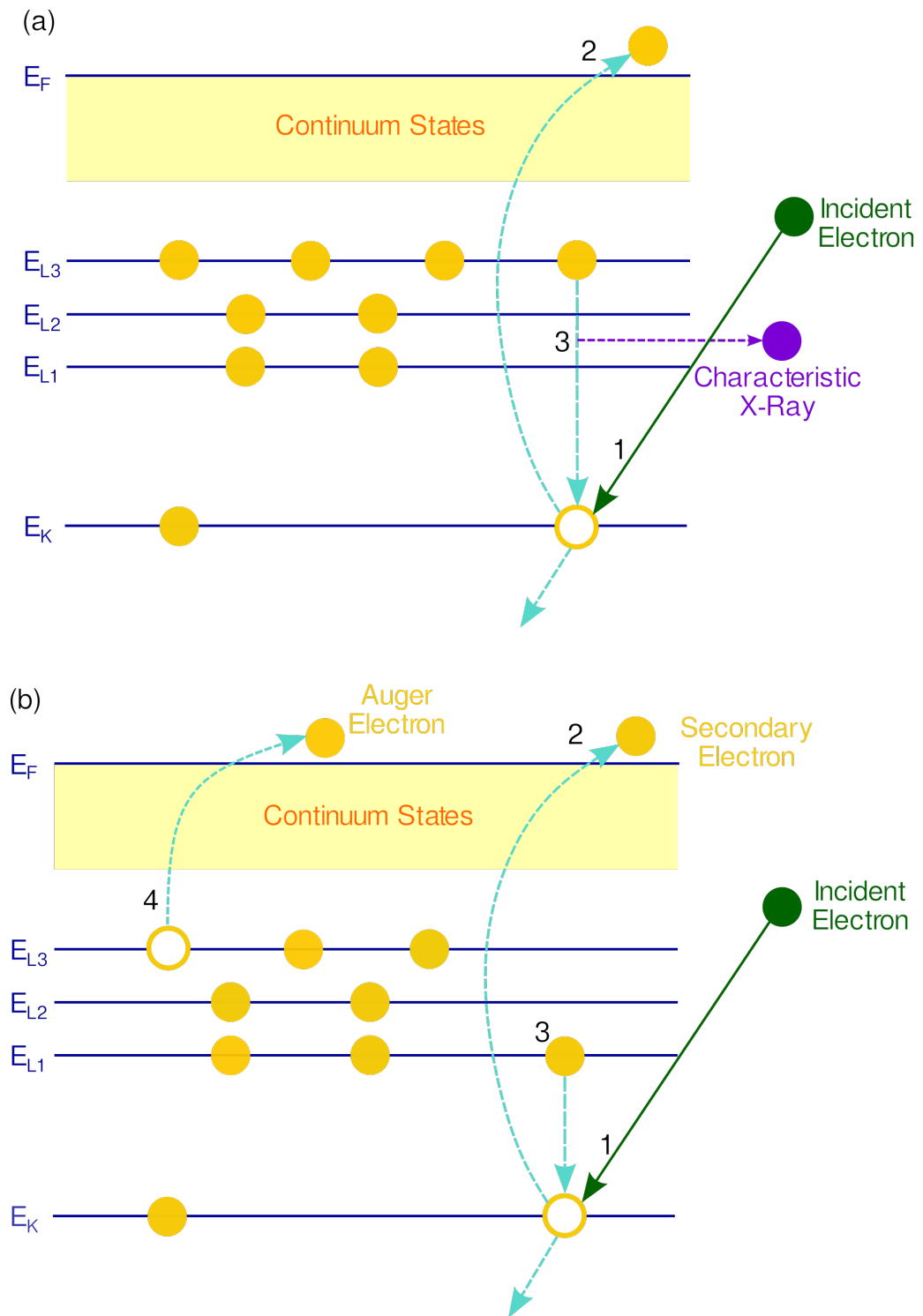


Figure 1.2: The mechanisms by which the ionisation of an atom by a high-energy incident electron produces characteristic (a) X-rays and (b) Auger electrons. In (a), the incident electron (1) displaces the K-shell electron as a secondary electron (2), which is replaced by an electron from the L_3 shell, leading to the emission of a characteristic X-ray. Steps (1) and (2) are the same in (b), but the ejected K-shell electron is replaced from an electron from the L_1 shell (3), the excess energy of which is transferred to an electron in the L_3 shell, which then escapes as an Auger electron (4). Redrawn from [20].

to enable the escape of one of the weakly bound outer-shell electrons in a similar manner, though without the need to fill a vacancy in an inner shell and the subsequent emission of a characteristic X-ray or Auger electron. The free electrons that are produced by the interaction of high-energy electrons with bound atomic electrons, be they electrons that are ejected directly or Auger electrons that are produced as a consequence, may all be regarded as secondary electrons. The cross section for the transfer of energy up to 50 eV to weakly bound electrons and consequent generation of slow secondary electrons is stated in Equation 1.12 [23]. Here, $|\mathbf{k}_F|$ is the magnitude of the wavevector corresponding to the energy of the Fermi level of the absorber, E_F ; E_{SE} the energy of the secondary electron; and E_0 the primary electron energy as usual. The low energy of slow secondary electrons (and, consequently, their small range, ≈ 5 nm) means they are fairly unimportant in the spatial spread of signal in a sensitive volume. Fast secondary electrons, which may have energies from 50eV up to E_0 , have long been recognised as important in the lateral spread of signal in electron imaging devices [24]. The cross section for fast secondary electrons is given in Equation 1.13 [25], in which E is the energy of the secondary electron after the collision; $\epsilon = \Delta E/E_0$; and $E' = E_0/m_0$. All types of secondary electron may go onto interact with the absorbing volume via the mechanisms outlined above and, assuming they have enough energy to do so, produce further secondary electrons and X-rays.

$$\sigma(E_{SE}) = \frac{e^4 |\mathbf{k}_F|^3}{3\pi E_0 (E_{SE} - E_F)^2} \quad (1.12)$$

$$\frac{d\sigma}{d\epsilon} = \frac{\pi e^4}{E^2} \left| \frac{1}{\epsilon^2} + \frac{1}{(1-\epsilon)^2} + \left(\frac{E'}{E'+1} \right)^2 - \frac{2E'+1}{(E'+1)^2 \epsilon(1-\epsilon)} \right| \quad (1.13)$$

1.2.2 Interactions of X-Rays

X-rays produced by the interactions of electrons with the sensor can go onto interact with the sensor through several mechanisms. The primary mechanism for low values of Z and low X-ray energies is photoelectric absorption. This entails the X-ray depositing all its energy in an atom, leading to the ejection of a photoelectron from one of the atom's bound shells. The energy of this photoelectron will be the difference between its binding energy and the energy of the X-ray. Its ejection from the atom creates a vacancy in one of the atom's orbitals, which is filled either through the capture of a free electron or through the rearrangement of the electrons still bound to the atom (or some combination of the two). This, in turn, can lead to the generation of a characteristic X-ray or, alternatively, an Auger electron. These X-rays can go on to interact with the absorbing volume themselves, contributing to the (lateral) spread of signal [6, 7].

There is no single expression for the cross-section σ_{PE} of an X-ray of a given energy, E_0 , undergoing photoelectric absorption with an atom of a particular element.

However, Equation 1.14 provides an approximation where κ is a constant of proportionality and the exponent ξ is a value that varies between 4 and 5 depending on the photon's energy [6]. For a given element, the cross-section typically increases as the photon's energy approaches the binding energy of particular electron shell, with it then decreasing substantially once the photon's energy is less than that binding energy and electrons in that shell are no longer accessible for the purposes of the photoelectric interaction. More specific approximations are possible for photoelectric absorption involving a particular electron shell [26].

$$\sigma_{PE}(E) \approx \kappa \frac{Z^\xi}{E^{3.5}} \quad (1.14)$$

Photons may also deposit their energy via Compton scattering, which consists of the incident photon scattering with a bound electron in the sensor, thereby being deflected and transferring a portion of its energy to the electron. This process is illustrated in Figure 1.3, while Equation 1.15 relates the post-scattering energy $h\nu'$ of a photon with an initial frequency ν to the angle θ at which it scatters with a bound electron. Equation 1.16 is the Klein-Nishina formula which expresses the differential cross section for Compton scattering for a given value of θ . In this expression, r_0 is the classical electron radius and η is defined as $h\nu/m_0c^2$ [6, 7].

$$h\nu' = \frac{h\nu}{1 + \frac{h\nu}{m_0c^2}(1 - \cos\theta)} \quad (1.15)$$

$$\frac{d\sigma}{d\Omega} = Zr_0^2 \left(\frac{1}{1 + \zeta(1 - \cos\theta)} \right)^2 \left(\frac{1 + \cos^2\theta}{2} \right) \left(1 + \frac{\zeta^2(1 - \cos\theta)^2}{(1 + \cos^2\theta)[1 + \zeta(1 - \cos\theta)]} \right) \quad (1.16)$$

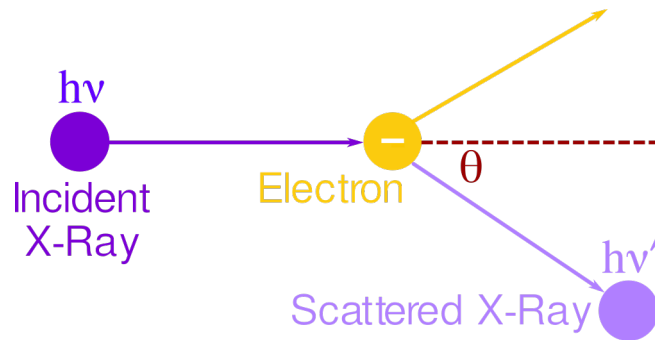


Figure 1.3: An illustration of Compton scattering, one of the ways in which X-rays interact with matter. The relation between the scattering angle θ of the incident photon is related to the photon's loss of energy by Equation 1.15.

The likelihood of an X-ray photon interacting via photoelectric absorption increases with Z but decreases with increasing photon energy. At higher photon energies, for a given value of Z , Compton scattering becomes more probable. Photons of a sufficiently high energy (1.02MeV, twice m_0) can also undergo pair-production. This

process entails the photon, under the influence of the Coulomb field of a nucleus, becoming an electron-positron pair, with the photon's energy in excess of 1.02MeV being split equally between the electron and the positron [6]. However, for the range of energies relevant to the present work, pair-production can be ignored as an interaction mechanism. Photoelectric absorption is the most important inelastic interaction photons have with matter in the context of the present work given the average value of Z of the sensors considered.

X-rays may also undergo Rayleigh scattering, whereby photons are scattered by an atom as a whole. This process is sometimes referred to as "coherent" scattering, as the atomic electrons act together in a coherent manner. No energy is transferred from the photon to the atom as part of this process, but it does cause a deflection in the photon's path [7].

1.3 Principles of Detector Operation

Fundamentally, the role of a detector is to convert incident quanta into an electrical signal that can be stored, processed and analysed to gain insight into the processes that gave rise to the primary quanta. In the case of electron microscopy, the processes of interest are those mechanisms by which monochromatic electrons of a given energy have interacted with a sample, giving rise to a spatially varying distribution of electrons (of potentially varying energy) that provides insight into the physical and chemical properties of a sample. This requires a sensitive volume (i.e. a sensor) that responds in some way to incident radiation in a way that can be measured, usually in the form of an electrical signal. In the case of ionising radiation such as electrons, the design of the sensor normally takes advantage of the ionising properties of the incident radiation to produce an electrical current in the form of electrons and holes (as in a semiconductor as will be discussed in Section 1.4) or electrons and ions (as in the case of a gaseous detector).

Conversion of incident radiation into an electrical signal can either be direct or indirect. An example of the former would be incident radiation generating an electrical current in a semiconductor-based sensor (such as those studied in this thesis) while an example of the latter would be incident radiation producing photons in a scintillator, which are then converted to an electrical signal either in semiconductor-based sensor or via the photoelectric effect. The conversion processes of indirect detectors add extra noise to the signal produced by incident quanta, if only due to the variation in the number of signal carriers produced at each conversion due to the inherently stochastic nature of such mechanisms. Such conversion processes also tend to be inherently lossy, leading to degradation of signal. Furthermore, in the case of imaging detectors, conversion processes often involve scattering of quanta and

the lateral spread of signal, which has adverse consequences for the performance of imaging detectors. Specific examples of indirect and direct detectors used in electron microscopy will be discussed in Chapter 2.

Whether the process of converting incident radiation into an electrical signal is direct or indirect, the overall response of a detector is the charge Q produced by the conversion processes. In practice this is registered by the readout electronics as a transient current $I(t)$, as the charge takes time to move towards the readout electrodes (usually under the influence of an electric field).

$$\nabla^2\psi_{\mathbf{E}} = \frac{\rho}{\epsilon_s} \quad (1.17)$$

The electric field and associated electrostatic potential acting on the charge carriers that compose the signal depend on the geometry of the electrodes and physical properties of the volume in which the charge carriers move. Poisson's Equation (1.17) relates the electric potential $\psi_{\mathbf{E}}$ to the charge density and the dielectric constant for the sensor material ϵ_s . The electric field that acts on charge carriers, \mathbf{E}_D , is simply $-\nabla\psi_{\mathbf{E}}$. Solutions of these equations require that the boundary conditions due to a particular sensor geometry are considered. An additional boundary condition is imposed if there is a voltage V between the readout electrodes, namely that the value of $\psi_{\mathbf{E}}$ must change by V between the electrodes [6, 16, 27].

The movement of a charge carrier (with charge q) due to the electric field induces charge on the electrodes. The charge induced a specific electrode can be determined using the Schockley-Ramo theorem (Equation 1.18) [28]. This states that the charge Q induced on an electrode due the motion of a charge carrier is the product of the charge q with the difference in an artificial weighting potential, ψ_W at the beginning and end of the charge's path $\Delta\psi_W$. This is distinct from any electrostatic potential in the volume and does not represent a physical quantity; rather it is a notional potential field that would exist (given a specific geometry) for that specific electrode if it were held at unit potential while all other electrodes were held at ground and all other charge (including space charge) removed. The weighting potential for a given electrode is therefore found by solving Poisson's equation for this theoretical scenario, and ranges in value from 1 at the electrode of interest and 0 at all other electrodes [6].

$$Q = q\Delta\psi_W \quad (1.18)$$

$$I = q\mathbf{v} \cdot \mathbf{E}_W \quad (1.19)$$

An alternative way of stating the Schockley-Ramo theorem is Equation 1.19, which relates the instantaneous current I induced by charge q travelling at velocity v at a point where the electrode's weighting field is \mathbf{E}_W . The weighting field for

an electrode is simply the derivative of its weighting potential and is therefore an artificial construct with no physical significance. Figure 1.4 illustrates the difference between the physical electric field that usually exists when a detector is operational and a bias applied to the sensor (Figure 1.4(a)) and the weighting field that is used in determining the induced, instantaneous current, for the central electrode of a detector with the same geometry (Figure 1.4(b)). Also marked in Figure 1.4(b) are the corresponding potentials at which the electrodes are held and that define the weighting potential for the central electrode.

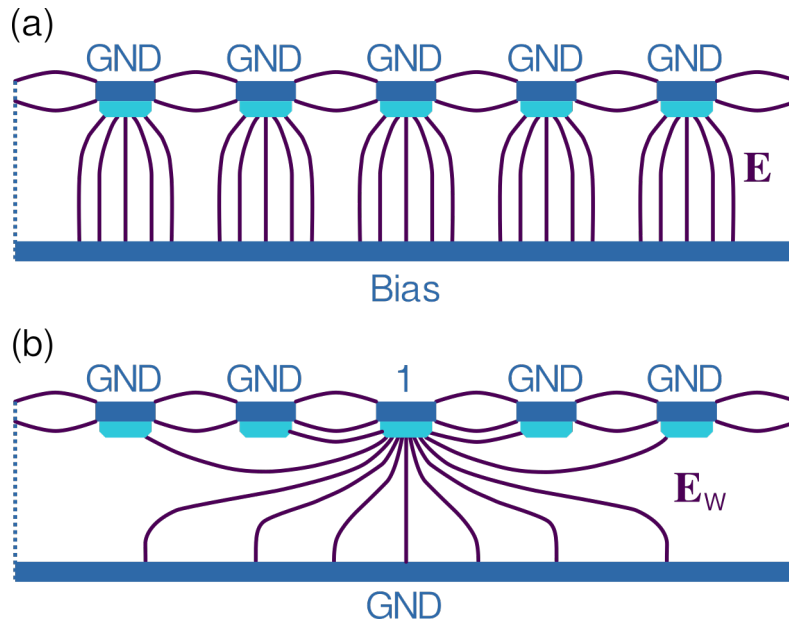


Figure 1.4: An illustration of the difference between (a) the electric field due to an application of a bias to a detector system (E_D) and (b) the weighting field (E_W) for a single electrode determined by holding the electrode of interest at 1V and all other electrodes at ground (GND). The system shown in this example could be a semiconductor-based strip or pixelated detector such as those studied in this thesis.

The current produced must usually be amplified further prior to processing and digitisation in a series of steps that is shown in Figure 1.5. Initial amplification of the induced current is achieved using a charge-sensitive amplifier (CSA), which produces a voltage step that is proportional to the integral of the current pulse i.e. the total charge, Q , produced in the sensitive element. The voltage step produced, $\Delta V = Q/C_F$, where C_F is the feedback capacitance used in the amplifier circuit [6, 16]

This voltage step is further amplified and shaped into a voltage pulse using a shaping amplifier (often referred to as the “shaper”). The aim of shaping the voltage pulse is to minimise the tail of the voltage pulse produced (and so minimise the likelihood of voltage pulses due to sequential events overlapping with one another). At the same time, the shaping process ensures the pulse characteristics (e.g. peak height, pulse length and total area under the pulse) are representative of the total charge induced due to the incident quantum of radiation. A large range of configurations are

possible, with the most basic consisting of a capacitor-resistor (CR) circuit followed by a resistor-capacitor (RC) circuit in what is known as a CR-RC circuit. The RC circuit has the effect of integrating the input signal assuming that the time constant, τ_{Int} , of the circuit is large relative to the temporal duration of the input signal and acts as a low-pass filter; otherwise the input is approximately equal to the input. It is therefore marked as an “Integrator” in Figure 1.5. Likewise, the CR circuit differentiates the voltage pulse, so that it is often referred to as a “Differentiator” and labelled as such in Figure 1.5. If the time constant of the CR circuit, τ_{Diff} , is small compared to the length of the input signal, then the output of the circuit is proportional to the time derivative of the input and the circuit acts as a high-pass filter; otherwise the output is again approximately equal to the input. The combination of the two circuits in an CR-RC configuration leads to a voltage peak with a rise time equal to τ_{Int} , while the time taken for the peak to the baseline level is equal to τ_{Diff} . Further refinement of the shape of the voltage pulse is possible by using a CR circuit followed by a number of CR circuits, with four RC circuits being sufficient to give the resulting voltage pulse a Gaussian form [6].

There are two main options for processing the voltage pulse. The first is to measure and record the maximum height of the voltage pulse. For such systems discrimination between noise and legitimate events can be done in post-processing. Such detectors are known as integrating detectors. The second option is to count the pulse if it exceeds a pre-set threshold, V_{Disc} in Figure 1.5, in the case of an integral discriminator, or if it falls between two thresholds as in the case of a differential discriminator. Detectors that fall into the second category are known as counting detectors, and more complex variations are possible, such as recording other pulse parameters including the time during which it is higher than than (one of) the counting threshold(s) or the time at which the pulse crossed (one of) the counting threshold(s). Discrimination between legitimate events and noise is also possible with the former configuration in post-processing, assuming that the overall resolution of the system and analogue-to-digital converter (ADC) is sufficient to form a spectrum on the basis of pulse height with sufficient detail [6, 27].

Detectors that count individual events belong to a broader class of detectors known as “quantum” detectors [29]. One advantage of quantum detectors is the suppression of any low-frequency system noise by setting the threshold that a signal has to surpass in order to be counted above the level of any such noise. They also have perfectly linear behaviour over their full dynamic range, the extent of which is limited only by the bit-depth of the electronics. Finally, if more than one threshold is implemented or, better still measurement of the energy associated with a count is possible, then it is feasible to discriminate between events of different energies. Integrating detectors, on the other hand, cannot distinguish between high levels of signal caused by one high energy event and or by multiple low-level events, which

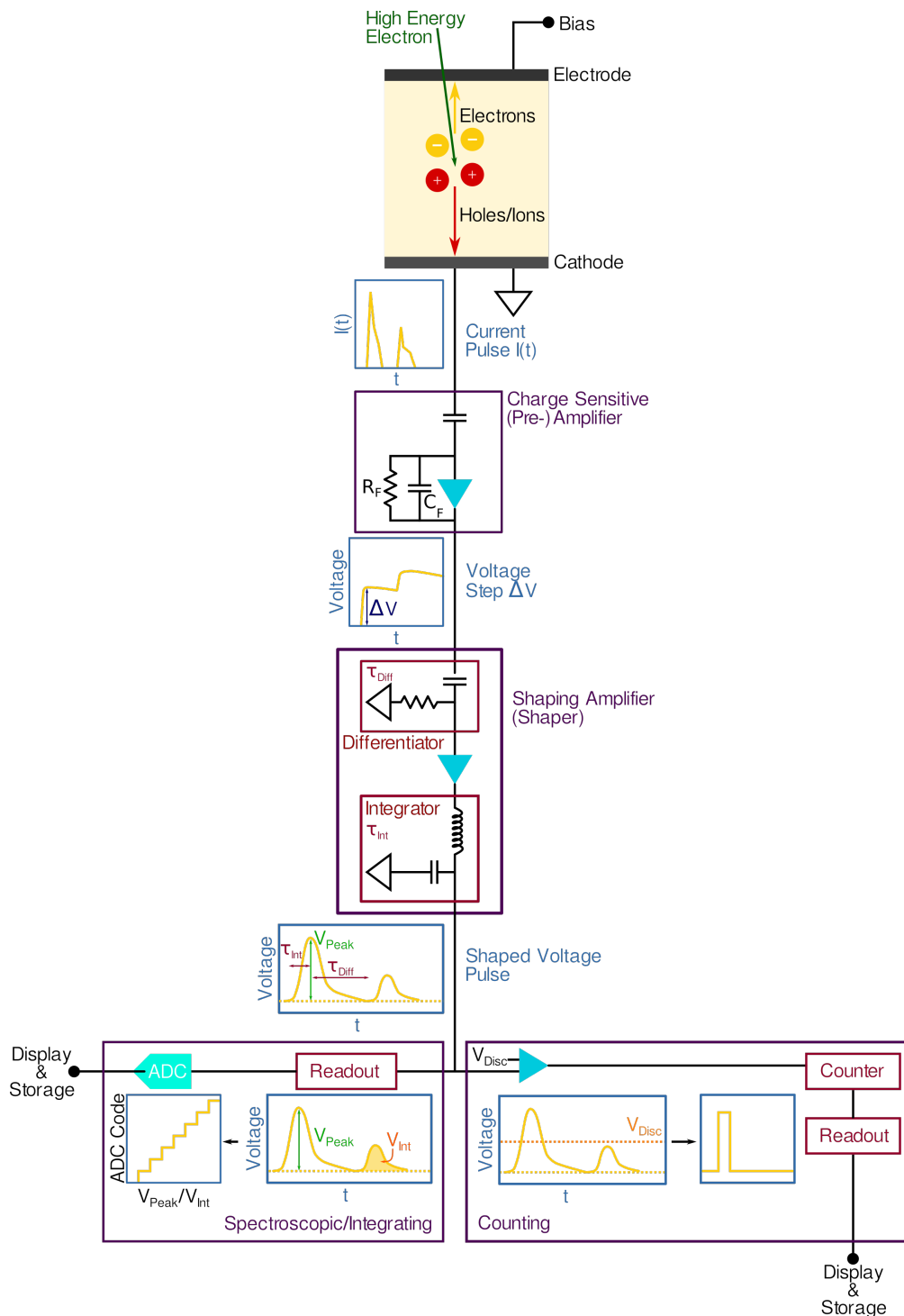


Figure 1.5: A diagram showing a typical signal processing chain for a detector system: signal carriers created in the sensor induce a transient current pulse on the readout electrodes; a CSA converts these into voltage steps (ΔV), which are then shaped. If the system is a spectroscopic detector, the height of these voltage pulses is then converted into an ADC code as part of the readout process; if an integrating detector then the voltage pulse is integrated over, with the result converted into an ADC code. In the latter kind of system, it may be the case that the area under the voltage pulse is integrated, without any shaping taking place. However, if the system in question is a counting detector, a counter is incremented if the height of the voltage pulses surpasses a reference voltage. At readout time, the number of counts recorded is readout by the data acquisition (DAQ) system and stored.

may be critical information when interpreting the data recorded. For an imaging detector to be regarded as a quantum detector, an additional requirement is that each incident quantum is counted by only one pixel. In cases where multiple pixels register the incident quanta, then the detector may still be regarded as a quantum detector if the hit can be allocated to a single pixel. Although in some instances, and with careful calibration, indirect detectors can be quantum detectors, in general most quantum detectors are direct detectors as the direct conversion of quanta to electrical signal greatly facilitates the discrimination of genuine signal from background noise and distinguishing between events of different energies.

1.4 Semiconductor-Based Sensors

The detectors studied as part of the present work all use semiconductors for the sensor that converts incident electrons into an electrical signal. This is also true of the majority of detector technologies currently in use in TEM, although in the case of some older technologies the semiconductor sensor does not directly detect incident electrons but instead converts an intermediate signal carrier into an electrical signal. Furthermore, one of the key areas of investigation is determining the advantages and disadvantages of using different semiconductor materials in the sensor of HPDs in TEM. Consequently, this section reviews the physics of semiconductors to give the background necessary to both motivate and interpret the research undertaken for this thesis. This consists of an overview of the key properties of semiconductors in Section 1.4.1 and a description of the semiconductor structures that underpin the sensors of the devices studied as part of the current work in Section .

1.4.1 Basics Properties of Semiconductors

Whether a crystalline material is a semiconductor depends on the structure and occupancy of the energy bands that describe the states that electrons in the crystal may occupy. The energy states that atomic electrons may occupy are not continuous and instead take the form of bands of permitted energy states separated by discontinuities. These discontinuities arise due to the way in which loosely bound atomic electrons interact with the ion lattice. Per the de Broglie relation (equation 1.20), the momentum \mathbf{p} , and therefore energy of the electrons, depends on \mathbf{k} , the electron wavevector. The gaps between bands of permitted energy states occur when the value of \mathbf{k} satisfies the Bragg condition (equation 1.21), given the spacing of the crystal lattice and resulting set of reciprocal lattice vectors \mathbf{G} [30].

$$\mathbf{h} = \hbar\mathbf{k} \tag{1.20}$$

$$(\mathbf{k} + \mathbf{G})^2 = k^2 \quad (1.21)$$

The valence band is the highest energy band that is fully occupied at 0K, and represents the energy states of electrons in the outer shells of specific lattice sites, while the conduction band is the first energy band above the valence band and corresponds to those electrons that are able to move throughout the crystal [6]. These are the two most important bands in accounting for the conductivity of a crystal and whether it can be regarded as a semiconductor. Although a crystal can have multiple energy bands with energy gaps between them, the term “bandgap” and corresponding energy E_g usually (and will henceforth be used to) refer to the energy gap between the valence and conduction bands.

Crystalline solids can be sorted into four categories depending on the nature of their bandgap and the occupancy of their conduction and valence bands [30–32]. These are illustrated in Figure 1.6. In cases where the lowest point of the conduction band is higher than the highest part of the valence band but the conduction band is still partially occupied by electrons at 0 K (i.e. the Fermi level lies in the conduction band) then the material is a metal. For semimetals, the conduction band is also partially occupied but only because the bottom of the conduction band is slightly lower than the top of the valence band, leading to a small number of electrons occupying the lowest states of the conduction band. Those crystals for which the Fermi level lies between the valence and conduction bands and for which the bandgap is sufficiently large that it is not feasible for electrons to be excited to the conduction band by any mechanism are insulators.

If, however, the bandgap is sufficiently small that electrons can be excited to the conduction band either thermally or, of most relevance to the present discussion, through the transference of energy from incident radiation, then the crystal in question is a semiconductor. Those semiconductors that have the lowest point of the conduction band at the same position in momentum space as the highest part of the valence band are known as direct semiconductors, as electrons can be directly excited from the valence band to the conduction band without any change in momentum. Indirect semiconductors have the highest part of the valence band at a different point from the lowest part of the conduction band. As such, electrons can still be excited to the valence band, but this process requires a change in the electron’s momentum. This is facilitated by intermediate states in the bandgap. For both direct and indirect semiconductors, it is this ability to produce current in response to incident radiation, that makes them suitable for use as the sensors of radiation detectors.

The current produced is not just due to the electrons excited to the conduction band. When electrons (in both semiconductors and semimetals) occupy states in the conduction band they leave behind a “hole” in the valence band. Electrons in the

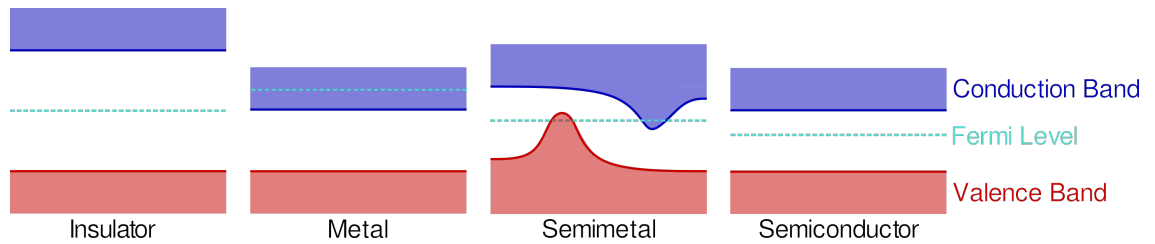


Figure 1.6: Figure showing the differences between the band structure for insulators, metals, semimetals and semiconductors. Redrawn from [31].

conduction band have, as would be expected, their usual charge of $-e$, while holes have a charge of $+e$. As charge-carriers, holes contribute to the current produced by the action of ionising radiation in a semiconductor (as well as current due to thermally-generated electron-hole pairs). Both electrons in the conduction band and holes in the valence band can be regarded as quasi-particles with effective masses that depend on their crystal momentum, i.e. the momentum they have by virtue of being in a crystal under the influence of the lattice potential. The effective mass of both electrons and holes (m_e and m_h) depends on their direction of motion relative to the crystal axis [31]. As electrons and holes occupy different energy states and hence have different values of $E(k)$, the effective masses of electrons and holes for a given direction of motion will be different.

Semiconductors can be classified as intrinsic or extrinsic depending on the source of their charge carriers. In intrinsic semiconductors, there are no impurities or (due to the extreme difficulty in impurity-free crystals growing crystals, especially those of a significant size) there are very few impurities. The effect of impurities, if they have a different number of valence electrons from the atoms that ordinarily compose the crystal lattice, is to add electrons to the conduction band or to add holes to the valence band. For a semiconductor to be regarded as intrinsic, the number of impurities must be much smaller than the number of thermally generated electron-hole pairs at room temperature, to the extent that the simplifying assumption that all electron-hole pairs are produced only by excitation of electrons from the valence band to the conduction band is valid.

In practice, it is usually the case that impurities are purposely introduced to alter the properties of the semiconductor. This process is called doping and entails introducing atoms of an element so that (ideally) they occupy a lattice site that should not feature atoms of that particular element. If the dopant atoms have a greater number of valence electrons than the atom that should occupy the site it is on, then it donates extra electrons to the conduction band and is known as a donor. Those dopant atoms that have fewer than expected valence electrons can be the cause of additional holes in the valence band by failing to provide the expected number of electrons and form the full set of covalent bonds anticipated at that lattice site by the neighbouring atoms. These two basic types of doping are illustrated in Figure 1.7.

When a crystal is doped with donor atoms, it has an excess of electrons and is known as n-type. If a crystal is doped with acceptor atoms then it is called p-type and has an excess of holes. In both types, the charge carrier type of which there is an excess is known as the majority charge carrier, while the other type of which there are fewer is the minority charge carrier. Most dopants are purposely chosen so that the number of valence atoms differs from that of the regular lattice atoms by one. Such dopants are known as shallow donors/acceptors and are typically all fully ionised at room temperature. When the dopants are almost all fully ionised, the Fermi level is effectively moved, as is shown in Figure 1.8. The densities of electrons and holes in doped material (n_e and p_h) can be calculated using Equations 1.22 and 1.23, in which n_i and E_i are the charge carrier density and the Fermi energy of undoped (i.e. intrinsic) material respectively, while k_B and T have their usual meanings of Boltzmann's constant and temperature. It should also be noted that it is possible to have impurities that add more than one electron or hole when fully ionised, and these require more complicated treatment than that outlined here. This is also true of very high levels of doping or cases of simultaneous doping with donors and acceptor atoms [31].

$$n_e = n_i \exp\left(\frac{E_F - E_i}{k_B T}\right) \quad (1.22)$$

$$n_h = n_i \exp\left(\frac{E_i - E_F}{k_B T}\right) \quad (1.23)$$

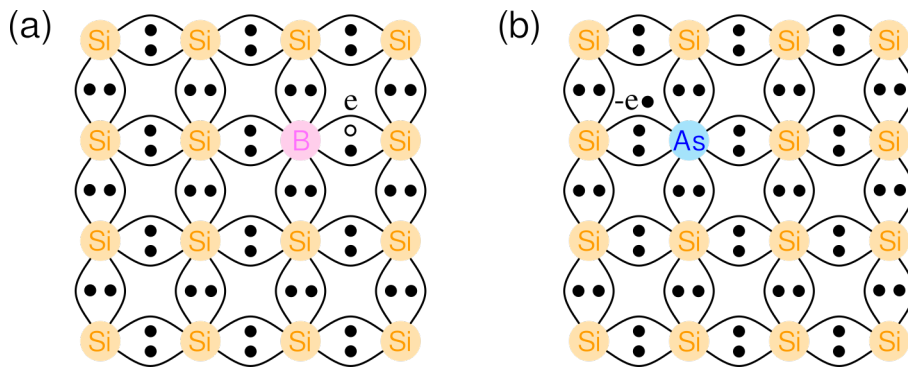


Figure 1.7: Diagram showing how impurity atoms can add a (a) hole or (b) electron to the lattice depending on difference between the number of expected valence electrons for the lattice site the atom occupies and the number of valence electrons the impurity atom has. In both (a) and (b) the impurity has replaced a Si atom, which has 4 valence electrons. In (a) the B atom has only 3 valence electrons, and so its presence creates an extra hole in the valence band while in (b) the As atom has 5 valence electrons and so it adds an extra free electron to the conduction band. Redrawn from [31].

Although detailed discussion of other types of impurities beyond shallow donors and acceptors is beyond the scope of the present discussion, it is worth mentioning the consequences of such impurities as well as other types of defects that can feature

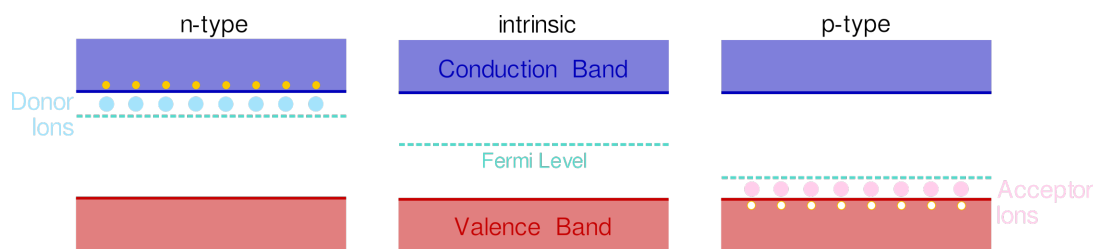


Figure 1.8: An illustration of how the Fermi level is changed by the presence of dopants. In the case of n-type material, the presence of the ionised donor atoms means the Fermi level is effectively moved upwards towards the conduction band. Similarly, for p-type material the ionised acceptor atoms mean the Fermi level is moved downwards towards the valence band relative to its position for intrinsic material. Redrawn from [31].

in semiconductors and their effects on device performance. Potential “point” defects, illustrated in Figure 1.9, include vacancies (empty lattice sites), interstitials (the presence of extra atoms between regular lattice sites) and Frenkel defects (assemblies of interstitials next to vacancies). In cases of high densities of point defects, it is possible for groups of them to cluster together to create defect clusters. Defect clusters may also be formed by the migration and agglomeration of point defects and other impurities in the crystal lattice (depending on temperature). These defect clusters can have their own local charge concentrations and local electric fields that attract or repel charge carriers depending on the profile of the defect cluster’s charge distribution and the charge carrier type [31]. In addition to these point defects, more complex defects, such as dislocations in the crystal lattice, are also possible.

Compound semiconductors can also feature defects whereby the wrong type of atom is present on a given lattice site; e.g. in the case of CdTe, a Cd atom occupies a lattice site that should feature a Te atom. The challenges of growing high-quality compound crystals mean that compound semiconductors usually feature a higher density of defects and impurities than is the case with single-element crystals such as Si. Both substitution defects and impurities that differ in the number of valence electrons from the regular lattice atom by more than one are capable of a variety of different charge states, whereas shallow donors and acceptors are capable of only two charge states (neutral and ionised). Consequently, crystals that feature substitution defects and “deep” donors or acceptors are more likely to have a greater density of energy states in the bandgap. Of these, the worst kind are those that are close to the middle of the bandgap, as these are most effective at facilitating the thermal generation of electron-hole pairs and the recombination of electron-hole pairs produced by incident radiation.

All types of defects can disrupt the movement of electrons and holes through the crystal lattice and therefore have an adverse affect on the performance of a device. As will be discussed below and in section 1.5, rapid and complete collection of charge produced by incident electrons improves both device deadtime and energy resolution.

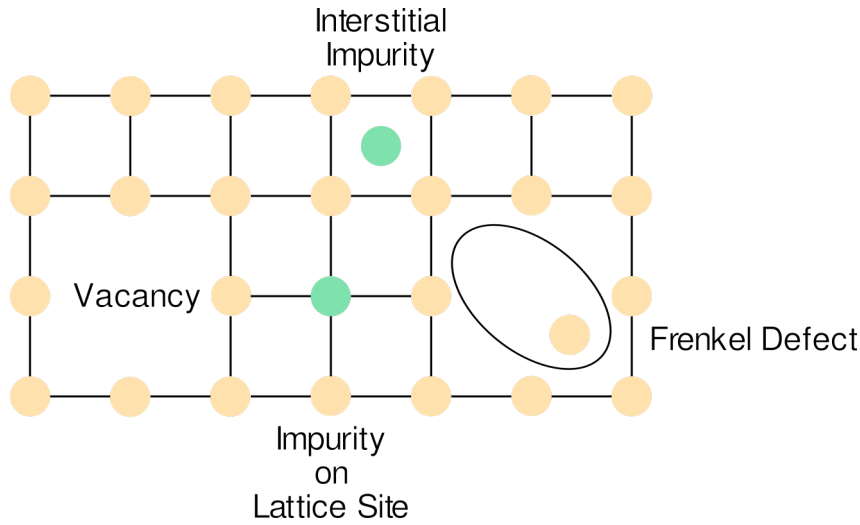


Figure 1.9: Figure showing different types of point defects possible in a crystal lattice. These include lattice sites missing an atom (vacancy), impurity atoms taking up a lattice site or taking up an interstitial position and Frenkel defects which consists of complexes of interstitial atoms and vacancies. Redrawn from [33].

There are several Figures of merit that can be used to quantify the charge transport properties of a semiconductor material. One is the lifetime of charge carriers, which is important from the perspective of ensuring that signal charge is fully collected by the electrodes without any loss due to electrons and holes recombining with one another. Of specific importance here is the recombination lifetime τ_R , which represents the time constant for the return of a system to equilibrium after a source of excess charge carriers (e.g. incident ionising radiation) is removed. It is distinct from the generation lifetime τ_G , which represents the time constant for the return of a system to equilibrium after that equilibrium has been disrupted by the removal of charge carriers (e.g. due to the application of an external electric field). However, the generation lifetime of a material is closely linked to the generation of thermal current in the depletion regions of semiconductor-based devices, including the sensitive volumes of many semiconductor-based radiation detectors [31, 33].

$$\mathbf{v}_e = \frac{-e\tau_c}{m_e} \mathbf{E} = -\mu_e \mathbf{E} \quad (1.24)$$

$$\mathbf{v}_h = \frac{e\tau_c}{m_h} \mathbf{E} = \mu_h \mathbf{E} \quad (1.25)$$

The other figure of merit, the charge carrier mobility, relates to the three different mechanisms by which electrons and holes can move through the crystal lattice. First, there is the random motion of electrons and holes that occurs even when the crystal is at equilibrium. Electrons and holes moving in this way have no net displacement in any given direction. Their motion is interrupted due to scattering events with imperfections in the lattice and impurities. The frequency of these scattering events

can be characterised using the mean free lifetime τ_C . A greater density of defects results in a shorter mean free lifetime [31, 33].

The mean free lifetime is proportional to the charge carrier mobility, which dictates the charge carrier response to the application of an electric or magnetic field. When such an external field is applied, electrons and holes are said to be “drifted” in a specific direction (as dictated by the field) with a net displacement. This is the second transport mechanism. In the case of an electric field, the mobilities of electrons and holes, μ_e and μ_h , are the constants of proportionality between the velocities of electrons and holes to the applied electric field as can be seen in Equations 1.24 and 1.25. It should be noted that these Equations only hold up to a certain electric field strength; at high electric fields, the velocity of electrons and holes tends towards a plateau value [31, 33].

The motion of electrons and holes under the influence of magnetic fields is not relevant to the work presented in this thesis, whereas their motion due to diffusion, the third transport mechanism, is important. In cases where there is an inhomogeneous distribution of charge-carriers, the effect of the random motion of the charge-carriers over time is to even-out the charge-carrier distribution, for the simple reason that it is more probable for charge-carriers to move from a region of high charge-carrier density to a region of low charge-carrier density. The diffusion of charge-carriers can be described using the diffusion Equation, which is stated for both electrons and holes in Equations 1.26 and 1.27, in which ρ_e and ρ_h are the densities of electrons and holes. These Equations describe how the flux of electrons and holes (F_e and F_h) are linked to the gradient of the electron and hole densities by the constants of diffusion (D_e and D_h) for electron and holes respectively. Linking the mobility and diffusion constant of a given charge carrier are the Einstein Equations, given for electrons and holes in Equations 1.28 and 1.29 [31, 33].

$$F_e = -D_e \nabla \rho_e \quad (1.26)$$

$$F_h = -D_h \nabla \rho_h \quad (1.27)$$

$$D_e = \frac{k_B T}{e} \mu_e \quad (1.28)$$

$$D_h = \frac{k_B T}{e} \mu_h \quad (1.29)$$

These two key Figures of merit, the recombination lifetime of a charge carrier and its mobility are often quoted as a product that summaries the transport properties of a given charge carrier. Together, these two numbers summarise the ease with which a given charge carrier type travels across the lattice and how long they have to do so before they recombine with a counterpart. Combining the different transport

mechanisms gives rise to expressions for the electron and hole current densities, \mathbf{j}_e and \mathbf{j}_h , stated in Equations 1.30 and 1.31 [31, 33].

$$\mathbf{j}_e = e\mu_e n \mathbf{E} + eD_e \nabla \rho_e \quad (1.30)$$

$$\mathbf{j}_h = e\mu_h n \mathbf{E} - eD_h \nabla \rho_h \quad (1.31)$$

When in operation, semiconductor-based sensors are often not operating under steady-state conditions. The variation in the flux of incident quanta mean there is variation in the generation of electrons and holes, which can then recombine and move through the sensitive volume. Equations 1.32 and 1.33 are the continuity Equations for electrons and holes, which relate the change in electron and hole concentrations in an infinitesimal point with the rate at which electrons and holes enter the volume as well as the rate at which they are produced (G) and the rate at which they recombine (R).

$$\frac{\delta \rho_e}{\delta t} = G - R + \frac{1}{e} \nabla \cdot \mathbf{J}_e \quad (1.32)$$

$$\frac{\delta \rho_h}{\delta t} = G - R - \frac{1}{e} \nabla \cdot \mathbf{J}_h \quad (1.33)$$

1.4.2 Key Semiconductor Structures

In the previous section, the physical properties of semiconductors were discussed, as well as how these properties made them suitable for the detection of ionising radiation. However, to be effective radiation detectors, semiconductors must typically be processed and used to fabricate specific devices or structures that are optimised for the purposes of this task. In this section the physical properties of some basic semiconductor-based structures used in detector systems are outlined.

The most basic such structure is the pn-junction. When a portion of p-type material is brought into contact with a portion of n-type material, the excess charge carriers of each block of material will diffuse across the interface due to the large gradients in charge concentration on either side of the junction. As holes from the p-type material move into the n-type material, negative acceptor ions near the interface on the side of the p-type material are left uncompensated. Similarly, positive donor ions near the interface on the n-type side are left uncompensated by the diffusion of electrons from the n-type region to the p-type region. This gives rise to a region of negative space charge on the p-type side of the junction and a region of positive space charge on the n-type side of the boundary, across which there is an electric field directed from the region of positive space charge to the area of negative space charge. Free charge-carriers in either region of fixed space charge are therefore drifted by the electric field into the regions in which they are the majority carrier (e.g. holes are drifted to

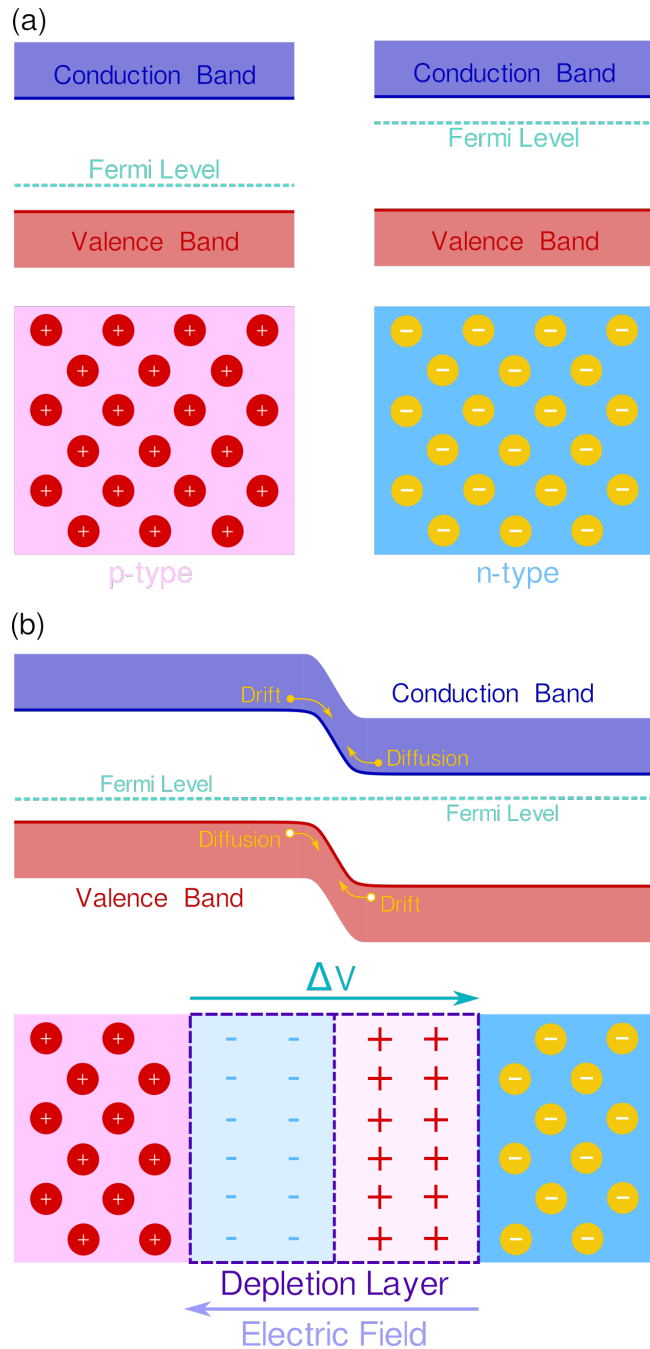


Figure 1.10: Diagrams of p-type and n-type material and their band structure (a) prior to being brought into contact and (b) after being brought into contact to form a pn-junction and having reached thermal equilibrium.

the p-type region). Thus electrons and holes are drifted in opposite directions to the directions of travel of the electrons and holes that diffuse across the junction. The steady-state that therefore arises at thermal equilibrium is that there is, in principle, no net current, as the diffusion current cancels out the drift current. Together, the volumes of negative and positive space charge are known as the depletion region as it has been depleted of any free charge carriers. This steady-state situation is illustrated Figure 1.10, as well as how the band structures of the p-type and n-type material changes at the boundary between the two materials and in the depletion volume.

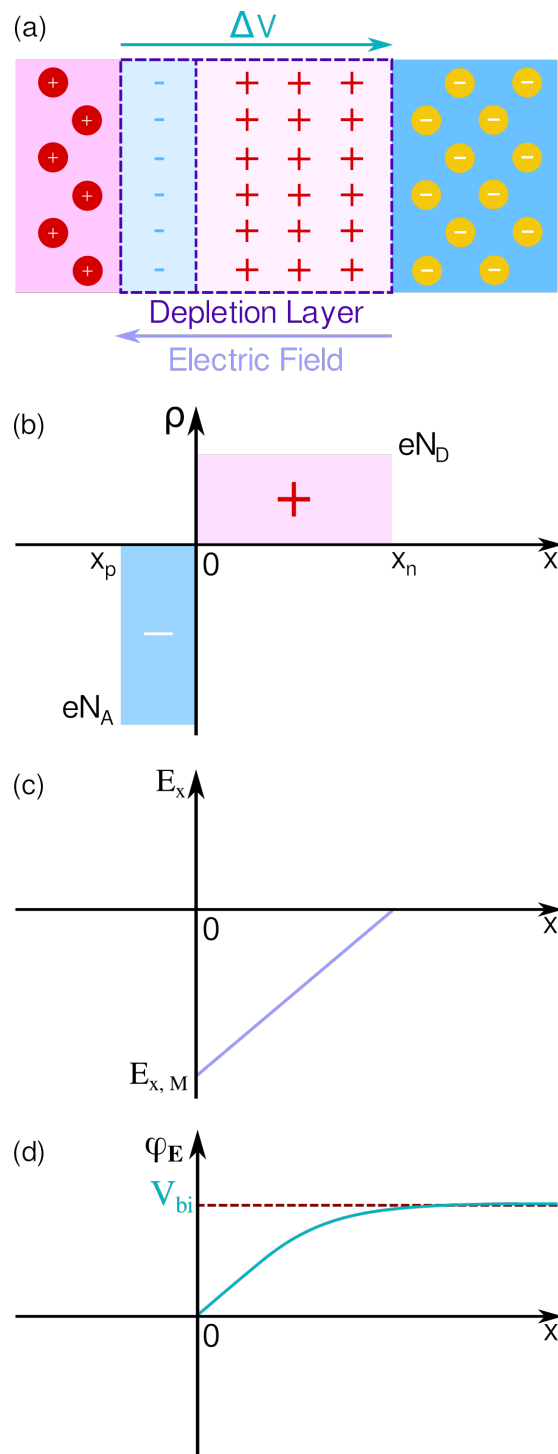


Figure 1.11: Diagrams of (a) an abrupt, one-sided pn-junction that approximates a sensor formed by implantation of acceptor atoms to form p-type wells in n-type bulk; (b) the associated distribution of space charge in the depletion volume of such a structure, where x_p and x_n are the widths of the depleted areas on the p-side and the n-side of the junction and N_A and N_D the concentrations of the acceptor and donor atoms in the p-type and n-type volumes; (c) the associated built-in electric field across the depletion volume, which is purely in the x -direction with a maximum value of $E_{x,M}$ and (d) the built-in potential of such a structure. Redrawn from [33].

Many Si sensors used for imaging purposes, including the Si sensors considered in this thesis, can be regarded as abrupt junctions, i.e. pn-junctions formed by implanting one type of doped material in a much larger volume of the other kind of bulk material via diffusion or low-energy ion implantation. The devices studied as part of the current work are p-in-n sensors, that is sensors produced by forming shallow implants of p-type material in bulk n-type material. This reflects the devices that were readily available for study. Although the devices studied in this thesis can, in principle, use n-in-p Si sensors [34], the manufacture of such sensors entails an additional processing step, namely p-stop implants and/or p-spray to ensure sufficient isolation of the n-type implants [35]. Without this, positive charge in the SiO₂ layer of such sensors induces the accumulation of electrons at the SiO₂-Si interface, causing an increase in inter-pixel capacitance and shorting of the pixels. Additionally, a guard ring structure must be implanted on the side of the p-type implant as well as the side of the n-type pixel implants, to prevent the implants from coming into contact with the sides of the sensor, which due to mechanical damage during the sensor manufacturing process are conductive. For p-in-n sensors, guard rings are necessary only on the side of the p-type implants. These additional manufacturing steps increase the cost of sensor manufacture, so that n-in-p Si sensors are typically only used when necessary. This is limited to instances where signal processing electronics are sensitive to electron signals only (rather than the hole signal) or where the sensor is to be used in a very high-radiation environment (e.g. the inner part of the ATLAS detector at the large hadron collider), in which the ability of n-type pixel implants to perform better than p-type pixel implants after the sensor has been irradiated is advantageous [16, 36].

Figure 1.11(a) shows an abrupt p-in-n junction, while Figure 1.11(b) illustrates the distribution of the space charge in such a junction. In such a device, the electric field takes the form of that stated in Equation 1.34 in which \mathbf{E}_m is the maximum electric field, is defined in Equation 1.35, and N_D is the doping concentration of the bulk region, in this example N_D , the concentration of donor atoms. As shown in Figure 1.11(c), the maximum of the electric field occurs at the junction interface ($x = 0$). The width W of the depletion volume is appropriately equal to the width of the n-type bulk material, x_n and is stated in Equation 1.36. The built-in bias across the junction V_{bi} , which is marked in Figure 1.11(d), is the difference between the electrostatic potential of the neutral p-type and n-type regions outside the depletion volume,. The electrostatic potential across the junction depends on both W and V_{bi} , as can be seen in Equation 1.38.

$$\mathbf{E}(x) = -\mathbf{E}_m + \frac{eN_Bx}{\epsilon_s}\hat{\mathbf{x}} \quad (1.34)$$

$$\mathbf{E}_m = \frac{eN_BW}{\epsilon_s}\hat{\mathbf{x}} \quad (1.35)$$

$$W \approx x_n = \sqrt{\frac{2\epsilon_s}{eN_D} V_{bi}} \quad (1.36)$$

$$V_{bi} = \frac{eN_A x_p^2}{2\epsilon_s} + \frac{eN_D x_n^2}{2\epsilon_s} = \frac{1}{2} |\mathbf{E}_m| W \quad (1.37)$$

$$\psi_{\mathbf{E}}(x) = \frac{V_{bi} x}{W} \left(2 - \frac{x}{W} \right) \quad (1.38)$$

The depletion region of a pn-junction is ideal for detecting incident ionising radiation. Incident quanta of radiation deposit their energy in the depletion region, producing signal carriers in the form of electron-hole pairs. These are drifted by the built-in electric field across the pn-junction, forming a current pulse that can be read-out and processed assuming appropriate electrical contacts at either side of the pn-junction. The lack of current flowing across the pn-junction means that in principle the only current registered should be that due to incident radiation, making detection of incident quanta straightforward.

$$W \approx \sqrt{\frac{2\epsilon_s}{eN_D} V_{bias}} \quad (1.39)$$

$$\mathbf{E}_m \approx \sqrt{\frac{eN_D}{\epsilon_s} V_{bias}} \hat{\mathbf{x}} \quad (1.40)$$

In practice, such junctions are typically operated with a bias applied. The junction can be forward-biased, by applying a positive potential to the p-type side and a negative potential to the n-side. However, this has the effect of shrinking the depletion volume and reducing the potential difference across the depletion volume, as is shown in Figure 1.12. Reverse biasing the junction increases the width of the depletion volume and increases the potential difference across the junction. Revised expressions for the width of and electric field in an abrupt, one-sided junction with a bias applied are stated in Equations 1.39 and 1.40 respectively [16].

Detectors based on a pn-junction structure are usually operated with sufficient bias applied that the full volume of the device (i.e. the full volume of the p-type and n-type regions) is depleted. The bias necessary to achieve this is known as the depletion bias, V_{dep} . Often a bias in excess of V_{dep} is applied, which has the effect of increasing the linearity of the electric field lines within the depletion volume. Such a device is said to be overdepleted and at each point in the device a constant of $(V - V_{dep})/d$ is added to the electric field. At very high biases, there will be an electrical breakdown as charge-carriers are accelerated to sufficiently high-speeds so as to generate more electron-hole pairs and trigger an avalanche effect. The breakdown bias, V_{bd} of an abrupt, one-sided junction can be estimated using Equation 1.41, though this is only valid for devices where the bulk doping has an initial concentration of $2 \times 10^{15} \text{cm}^{-3}$.

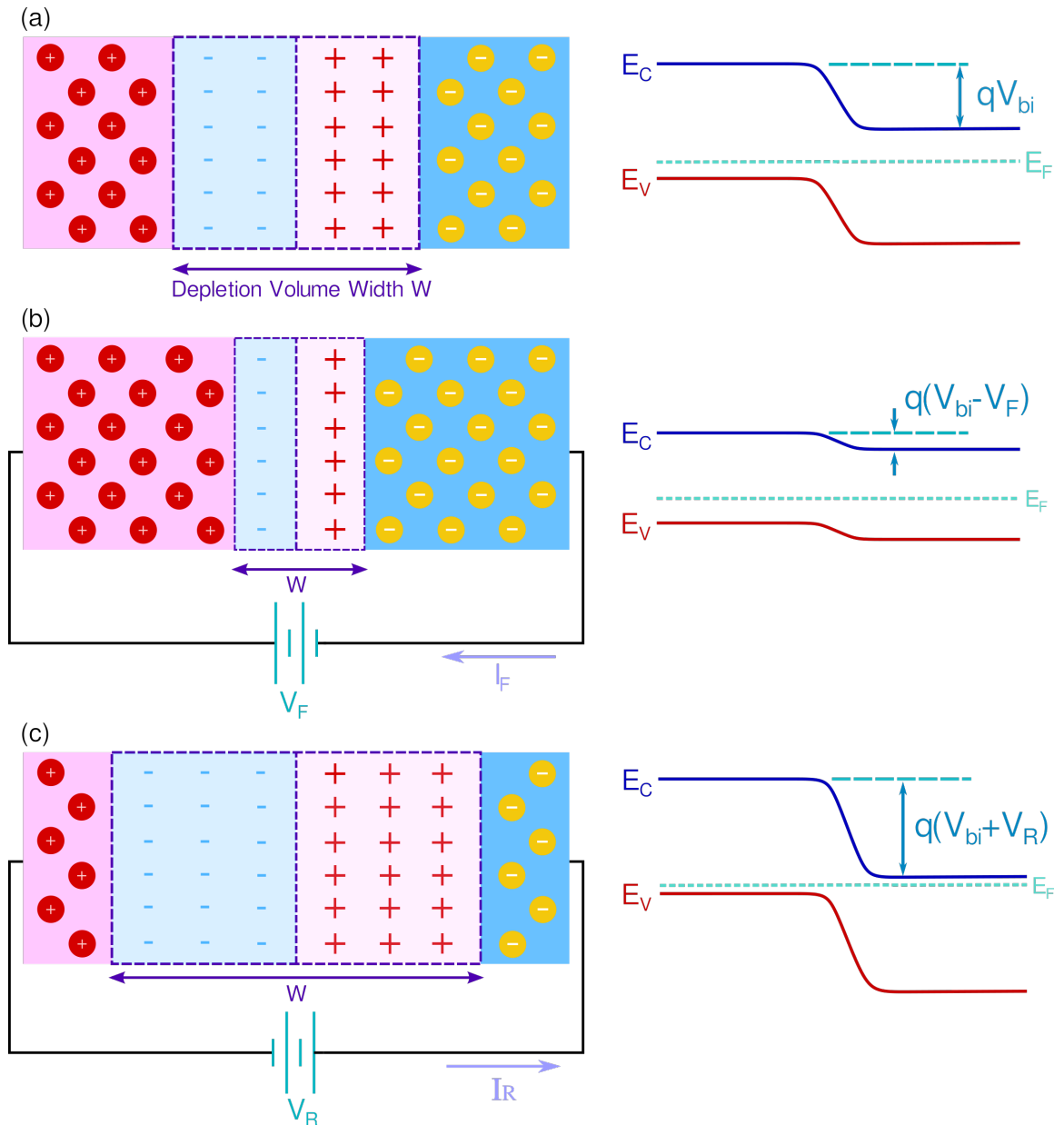


Figure 1.12: Figure of a pn-junction and its band structure with (a) no external bias applied), (b) a forward bias applied and (c) a reverse bias applied. Redrawn from [33].

For material that has a lower initial doping concentration then breakdown of the junction will occur at a lower bias due to imperfections close to the junction and higher fields at the corners of the implants [16].

$$V_{bd} \approx 5.3 \times 10^{13} N_B^{-3/4} \quad (1.41)$$

The leakage current, which in effect is a form of background noise to current pulses due to incident radiation, is primarily due to thermally generated electron-hole pairs in the depletion region. A second, very minor contribution to the leakage current is the diffusion of minority charge carriers into the depletion region, which is not balanced out by the drift. Additionally, any semiconductor device will have some

finite conductivity, which means the application of a bias will give rise to a leakage current. This means that the resistivity of the material used in the formation of the device is an important consideration, as the lower this is the higher the leakage current for a given bias will be observed, which may obscure signal. Leakage current is also produced at the edges of the junction due to the large voltage gradients that exist over relatively short distances [6].

The other key basic semiconductor-based structure is the metal-semiconductor contact or Schottky contact². When a metal is brought into contact with semiconductor crystal of intermediate doping, a surface barrier with rectifying properties not dissimilar to the pn-junction is formed. Indeed, such structures can act as detectors of ionising radiation in a similar way to a pn-junction. The GaAs:Cr sensors studied as part of this work are examples of such devices, though as the contact resistance of these devices is low relative to the resistance of the semiconductor itself, the contacts on these sensors are, strictly speaking, ohmic contacts [31,33]. Metal-semiconductor structures also arise when metal contacts are used as electrodes at either side of a pn-junction for reading out the signal caused by incident radiation.

The energy necessary to move an electron from the Fermi level of the metal contact to the vacuum level is the metal's workfunction Φ_m . In addition to its own workfunction Φ_s , the semiconductor also has an electron affinity χ . This is the energy needed to elevate an electron from the bottom of the semiconductor's conduction band to the vacuum level. Unlike Φ_s , this is an intrinsic property of the semiconductor, whereas Φ_s depends on the doping level, as this affects the position of the Fermi level in a semiconductor.

Figure 1.13(a) shows the energy band structures of a metal and n-type semiconductor prior to the formation of a contact, with Φ_m and Φ_s marked as well as χ . At the boundary between the metal and the semiconductor, the Fermi levels of the two materials must align with one another when they are in thermal equilibrium. This entails the energy bands on the semiconductor bending in the region proximate to the boundary as part of the formation of the contact, shown in Figure 1.13(b).

Within the bulk of the metal itself, the number of free charge carriers is so great that the electric field can be regarded as zero. However, surface-charge will build up at the boundary with the semiconductor. This compensates for the space-charge on the semiconductor side of the interface that develops due to the rearrangement of charge carriers in response to the bending of the energy bands. The bending of the energy bands and rearrangement of charge leads to a barrier at the metal-semiconductor interface.

The difference between Φ_m and χ is the barrier Φ_{B_n} that an electron in the metal must overcome to reach the semiconductor. For an n-type semiconductor, the barrier

² This may also be referred to as a surface-barrier or a Schottky barrier in some texts.

that an electron in the metal must overcome to reach the semiconductor is this is $\Phi_{B_n} = \Phi_m - \chi$ (marked in Figure 1.13(a)), while for an p-type semiconductor this would be $\Phi_{B_p} = E_g - (\Phi_m - \chi)$ (marked in Figure 1.14(b)).

The barrier height going from the semiconductor to the metal is equal to the difference between Φ_m and Φ_s . For n-type semiconductors, $\Phi_m > \Phi_s$ and for p-type semiconductors the reverse is true. Consequently, as Φ_s depends on the position of the Fermi level in the semiconductor, which in turn depends on the doping concentration of the semiconductor. As such, the level of doping must be chosen such as to ensure a contact is possible given the value of Φ_m .

To form rectifying, Schottky contacts, Φ_{B_n} or $\Phi_{B_p} \gg k_B T$, which is usually achieved by using doping concentration that is less than the density of states in the conduction or valence band (as appropriate) [33]. For Ohmic contacts where the doping level is very high, the width of the barrier narrows, and current from the semiconductor to the metal can be dominated by tunnelling of charge carriers through the barrier. At lower doping concentrations, the thermionic current dominates, as is the case for Schottky contacts, and the present treatment of metal-semiconductor structures takes this to be the case [31, 33].

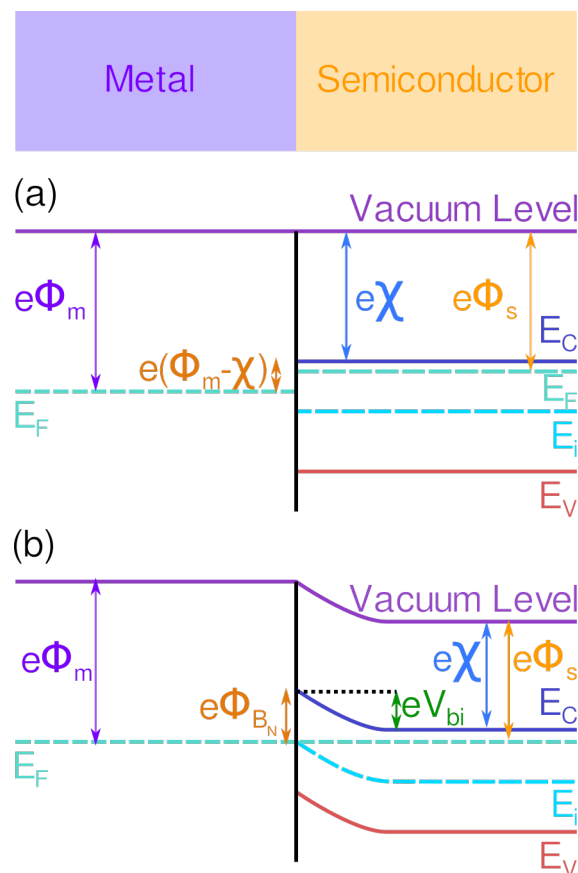


Figure 1.13: Figures showing the band structure of a surface barrier when (a) the metal and semiconductor have just been brought into contact and (b) the structure has reached equilibrium so the energy bands on the semiconductor side of the interface have bent to meet the energy bands of the metal. Redrawn from reference [31].

Applying a bias to a metal-semiconductor structure will not change the height of the barrier for electrons in the metal going to the semiconductor. The flow of current from the metal to the semiconductor is therefore fixed. However, the difference in the electrostatic potential across the barrier is changed by an applied voltage. As is shown in Figure 1.14, a forward bias will reduce the potential difference, while a reverse bias will increase it. The polarity that gives reverse and forward bias depends on whether the semiconductor is n-type or p-type as can be seen by comparing Figures 1.14(c)-(f). In equilibrium, the current from the semiconductor to the metal is exactly equal to the current in the opposite direction. Applying a reverse bias increases the current from the semiconductor to the metal, while a forward bias causes a decrease.

The resulting behaviour is like that of an abrupt, one-sided pn-junction, and many of the physical characteristics of a metal-semiconductor junction (including the distribution of space charge, electrostatic potential and electric field) can be modelled in the same way. The characteristics of a p-in-n sensor (discussed above) are those of an n-type semiconductor with metal contact, while those of an n-in-p sensor are those of a structure with a p-type semiconductor.

The current density j is therefore a function of applied bias and temperature and is stated in Equation 1.42, for which j_s , the saturation current, is defined in Equation 1.43. In the latter Equation, A^* is the effective Richardson constant of the semiconductor used in the device [33].

$$j = j_s \left(\exp\left(\frac{eV}{k_B T}\right) - 1 \right) \quad (1.42)$$

$$j_s = A^* T^2 \exp\left(\frac{\Phi_{BN}}{k_B T}\right) \quad (1.43)$$

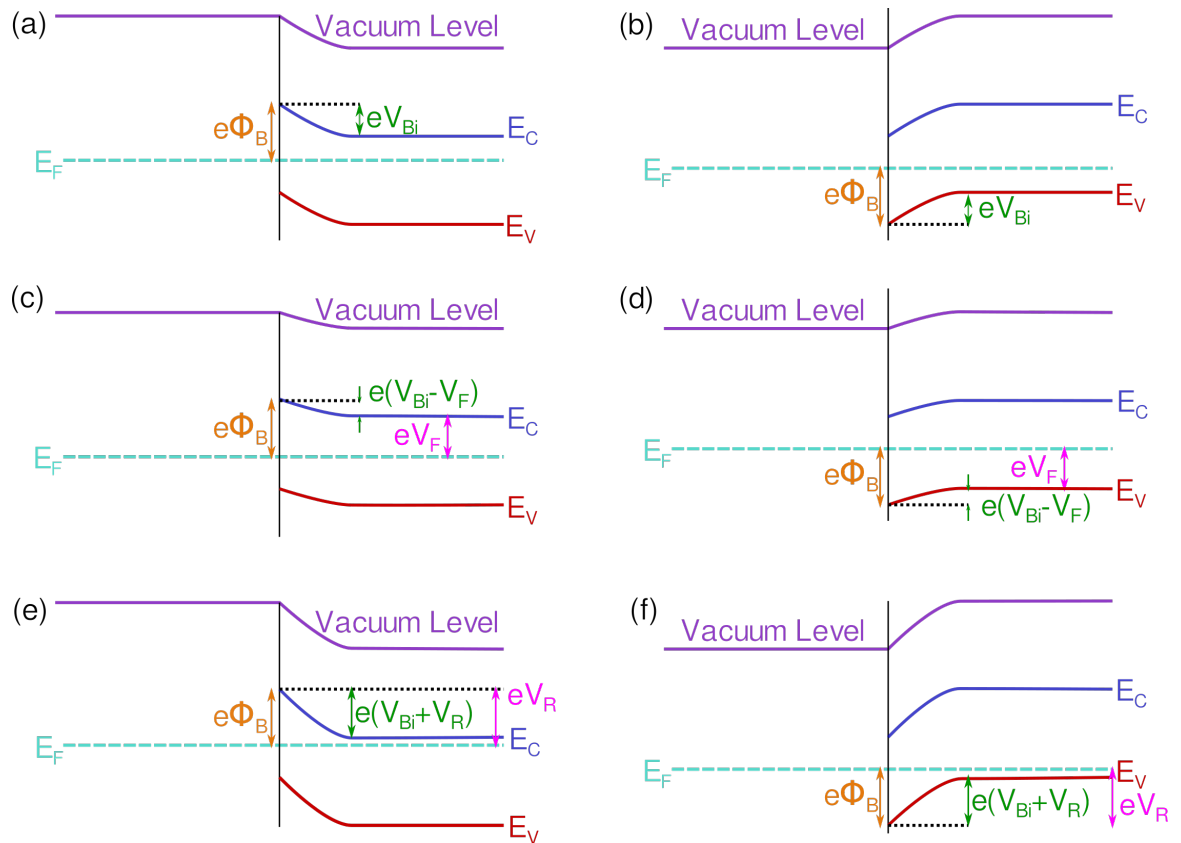


Figure 1.14: Diagrams showing the band structure of a surface barrier when the semiconductor is (a) n-type or (b) p-type and no bias is applied; (c) n-type or (d) p-type and the devices are forward-biased; and (e) n-type or (f) p-type and the devices are reverse-biased. Redrawn from [31]. The polarity of the bias applied to an n-type device is the reverse of that applied to the p-type for a given outcome i.e. the bias applied to an n-type device to reverse bias it will forward bias a p-type device and vice versa.

1.5 Metrics for Evaluating Detector Performance

1.5.1 General Performance Metrics

For detectors that are capable of measuring the energy of incident quanta, or even for those that are only capable of discriminating between events that deposit different amounts of energy, a critical figure of merit is the system's energy resolution R_E . This quantifies a detector's ability to distinguish between different amounts of energy deposited in its sensor. The energy resolution of a detector for a given type of particle of a given energy is defined in Equation 1.44, where FWHM refers to the full width half maximum of the peak in an energy spectrum recorded by the detector due to that type of particle. Assuming the peak can be described by a Gaussian distribution, then the FWHM is 2.35σ , where σ is the standard deviation of the Gaussian distribution.

At a fundamental level, a detector's energy resolution is determined by the statistics of signal-carrier production in the detector system. Even in the event of all incident quanta of a given type and primary energy depositing all their energy in the sensor, the number of signal carriers produced by the particle-sensor interactions will vary from

event to event due to the stochastic nature of the processes by which incident radiation interacts with the sensor and produces signal carriers. The number of signal-carriers produced by incident radiation of a given type and energy will fluctuate around a mean value M , equal to E_0 divided by the average amount of energy required to generate one signal carrier (which in the case of semiconductor sensors is an electron-hole pair). To a first approximation, the variation in the number of signal carriers that are produced by a given event type can be described by Poisson statistics, for which σ is \sqrt{M} . Substituting this into Equation 1.44 produces Equation 1.45, which describes the limit to a detector's energy resolution as predicted by assuming that it is only limited by the statistical variation in the number of signal carriers produced by incident quanta of a given energy.

In practice, the energy resolution of semiconductor-based detectors do not conform to that predicted by Poisson statistics and the deviation of a detector from this expected behaviour is quantified by the Fano factor F [37]. This is defined as the ratio of the observed variance of M to the variance of M predicted by Poisson statistics. Equation 1.46 expresses this revised prediction for detector energy resolution. The deviation in Poisson statistics arises because only part of the energy deposited in the sensor goes towards the production of electron-hole pairs; most energy contributes to the excitation of the lattice and the production of phonons. Another consequence of this is that the average amount of energy needed to create an electron-hole pair is more than the bandgap energy, typically $\approx 3E_G$.

$$R_E = \frac{\text{FWHM}}{M} \quad (1.44)$$

$$R_E|_{\text{Poisson}} = \frac{2.35}{\sqrt{M}} \quad (1.45)$$

$$R_E|_{\text{Statistical}} = 2.35\sqrt{\frac{F}{M}} \quad (1.46)$$

Although the variation in signal carriers produced by incident radiation of a given type is the primary determinant of a detector's energy resolution, other factors that affect energy resolution are noise in the signal-processing electronics and variation in the collection of signal carriers. A detector's energy resolution is optimal when the sensor is able to absorb all of an incident particle's energy, as this maximises the number of signal-carriers produced for a given energy (which minimises the relative variation in signal carriers) and also means that the same net amount of energy is deposited on the sensor. Events where only part of the primary particle's energy is deposited in the sensor, due to the backscatter from or transmission through the sensor, have an adverse impact on energy resolution as they lead to a variation in the amount of energy deposited in the sensor. Similarly, events where the primary particle

first produces secondary quanta that escape or that deposit their energy in a separate event have an adverse impact on detector energy resolution. In the case of imaging detectors, as each pixel (usually) operates independently, deposition of an incident particle's energy across multiple pixels has an adverse affect of energy resolution, whether this be due to the lateral spread in signal from the primary particle itself or the generation of secondaries that deposit energy in other pixels.

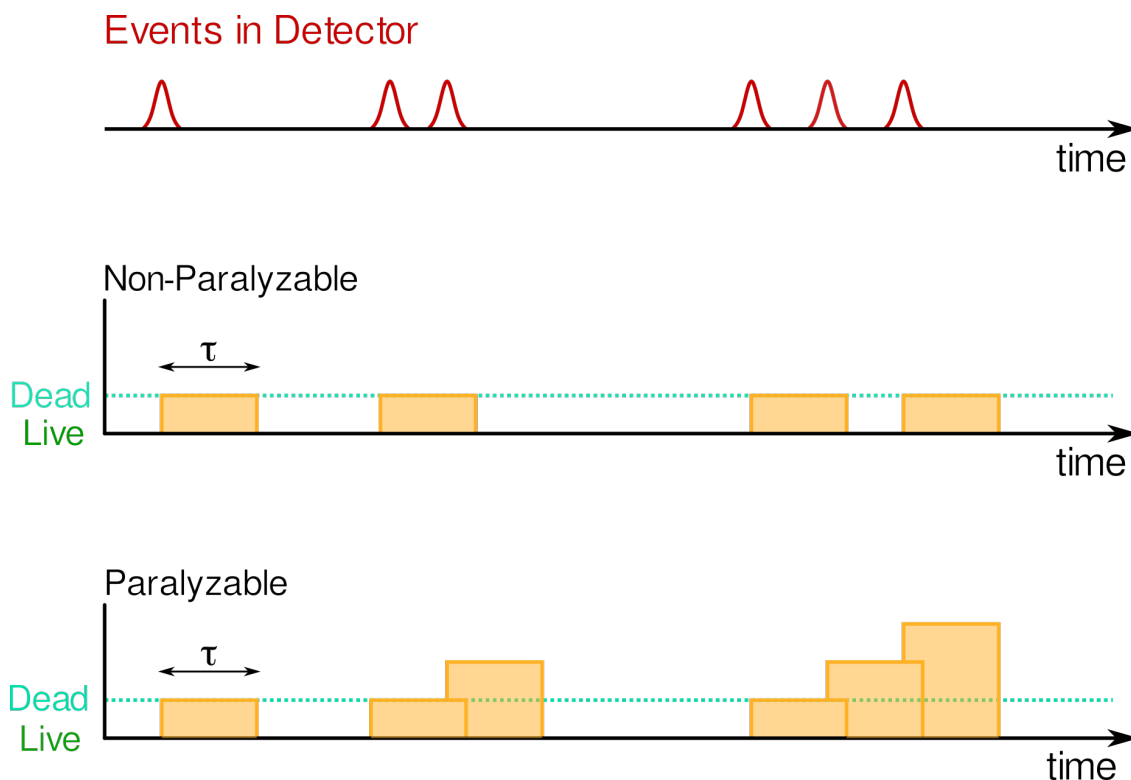


Figure 1.15: Difference in detector performance on the basis of whether its dead time can be regarded as non-paralyzable or paralyzable. In the former case, the detector deadtime is not increased by the arrival of events within the deadtime of a prior event so that while the third and fifth events are missed the sixth event is registered. In the case of a paralyzable detector, the deadtime is extended by an event occurring within the deadtime of an earlier event, so that the third, fifth and sixth events are missed. Redrawn from [6].

Another key detector performance metric is linearity of response. This refers to the extent to which the detector response to incident radiation is linearly related to the input quanta. Ideally, one incident particle should be registered as one event such that the number of incident particles n is equal to the number of particles detected m . If this is not the case, then a second-best scenario is that these be related by some constant of proportionality K such that $m = Kn$ over the full dynamic range of the detector. Related to linearity of response is the efficiency of a system and its deadtime. The latter quantity refers to the time the system is not sensitive to incident radiation as it is processing the signal, while the former is the ratio of the number of particles detected to the number of incident particles m/n .

In cases of high particle flux, significant numbers of particles can go undetected as they arrive during the deadtime following the arrival of a prior particle, reducing the system's efficiency. In some systems, the signal due to consecutive events can “pile-up” leading to a single count being registered with energy $E_1 + E_2$ when it should measure two events with energies E_1 and E_2 respectively, introducing distortions in the energy spectrum recorded. The detector dead time is therefore important with respect to a detector's energy resolution, with a shorter deadtime leading to an improved energy resolution and linearity when the flux of incident particles is high.

The effect of deadtime on a detector's response can generally be regarded as paralyzable or non-paralyzable. In the non-paralyzable case, the period of time that the detector is non-responsive (after a particle has arrived) is taken to be fixed. Particles that arrive during the detector's deadtime are simply not counted, without any adverse impact beyond this undercounting (and consequent adverse impact of detector efficiency). Such detectors can effectively be regarded as insensitive to the signal due to any particles that arrive while they are already processing an earlier event. However, in the paralyzable case, particles that arrive during the dead time extend the period during which the detector is non-responsive. This occurs because the signal due to the subsequent particle(s) is able, in some way, to overlap that of the prior particle(s) so that, from the perspective of the detector's signal processing electronics, there is one prolonged signal due to single particle, rather than several signals corresponding to separate quanta. Such overlap of events can occur if e.g. the voltage pulse produced by the analogue signal processing electronics in response to an event has not returned to ground when the voltage pulse of a subsequent event is produced, so that the latter is superimposed on the tail end of the former, effectively extending it in time.

The two different cases are illustrated in Figure 1.15. For detectors that can be modelled as non-paralyzable, the true arrival rate of incident particles n_{in} can be calculated using Equation 1.47, where n_{out} is the recorded count rate and τ the system's dead time for a single event. In the case of paralyzable detectors, the relation between the arrival rate and the recorded count rate is expressed in Equation 1.48 [6].

$$n_{in} = \frac{n_{out}}{1 - n_{out}\tau} \quad (1.47)$$

$$n_{out} = n_{in}e^{-n_{in}\tau} \quad (1.48)$$

There exist alternative models of detector deadtime as, in reality, the response of most detectors lies somewhere between the idealised responses of paralyzable and non-paralyzable detectors [38], though the standard paralyzable detector model has generally been found suitable for use with the detectors studied in this thesis [39] and for similar devices characterised for use in TEM [40].

1.5.2 Evaluating the Performance of Imaging Detectors

Additional criteria are required to evaluate and compare the performance of imaging detectors. The performance of an imaging detector depends not only on its ability to reproduce the contrast in the image incident upon it but also its ability to reproduce the noise in the image it records. Contrast refers to the relative difference in intensity between two points in an image. It is defined in Equation 1.49, where $E\{q(\mathbf{r}_i)\}$ is the expected number of quanta (or intensity) at point i in an image. In principle, a detector's ability to reproduce contrast is quantified by the Large Area Contrast Transfer function T_C . This is the ratio of the contrast between two points in the output image, C_{Out} , and the contrast between the same two points in the input image, C_{In} [41]. Noise is the stochastic variance in an image and is defined as $\sigma_d^2 = E\{|\Delta d|^2\}$, where Δd is the difference between the recorded signal d and the expected value of d , $E\{d\}$ [42].

$$C = \frac{E\{q(\mathbf{r}_2)\} - E\{q(\mathbf{r}_1)\}}{\frac{1}{2}(E\{q(\mathbf{r}_2)\} + E\{q(\mathbf{r}_1)\})} \quad (1.49)$$

However, these metrics are limited in their ability to quantify a system's performance. The Large Area Gain Transfer function fails to capture the dependence of contrast transfer on the size of the feature that is being reproduced, with the contrast of small features transferring worse than that of large features. The definition of noise given above similarly fails to account for any spatial correlations in the noise as well as how noise at different lengthscales is reproduced.

The ability of a system to transfer noise and signal depending on the size of the features in the image captured can be described using Fourier-based analysis. This requires that the system under consideration be both linear and shift-invariant³. For a system to be considered linear, it must satisfy the following conditions:

1. Have a characteristic function $S\{\}$ such that for any input $h(x)$, the system produces an output $S\{h(x)\}$.
2. For any two inputs $h_1(x)$ and $h_2(x)$, the response of the system is $S\{h_1(x) + h_2(x)\} = S\{h_1(x)\} + S\{h_2(x)\}$.
3. For any constant A , the response of the system must be $S\{Ah(x)\} = AS\{h(x)\}$.

The response of a linear system to a (theoretical) input pulse described by a Dirac δ -function $\delta(x - x_0)$ is described by its Impulse Response Function (IRF) such that $IRF(x, x_0) = S\{\delta(x - x_0)\}$. For any input that can be expressed as a superposition of Dirac δ -functions, the output of a linear system will be a superposition of IRFs,

³In practice, no system is perfectly linear, and the assumption of a linear system is always, to a certain extent, an approximation.

one for each input impulse. If a system is shift-invariant, then the form of the IRF does not depend on where the input impulse is registered so that how a feature is reproduced in the recorded image will be the same independent of where in the image it is. This can be expressed mathematically as $IRF(x, x_0) = IRF(x - x_0)$. The response of a linear and shift-invariant system and the idea of the IRF is illustrated in Figure 1.16. In the context of two-dimensional (2D) imaging systems, the IRF is commonly referred to as the system's point spread function (PSF). The response of a linear, shift-invariant system to a signal is described by the convolution of its IRF with the input signal, assuming that the system is an entirely deterministic one. If the system is stochastic, then the convolution of the system's IRF with the input signal describes only the expected response [41].

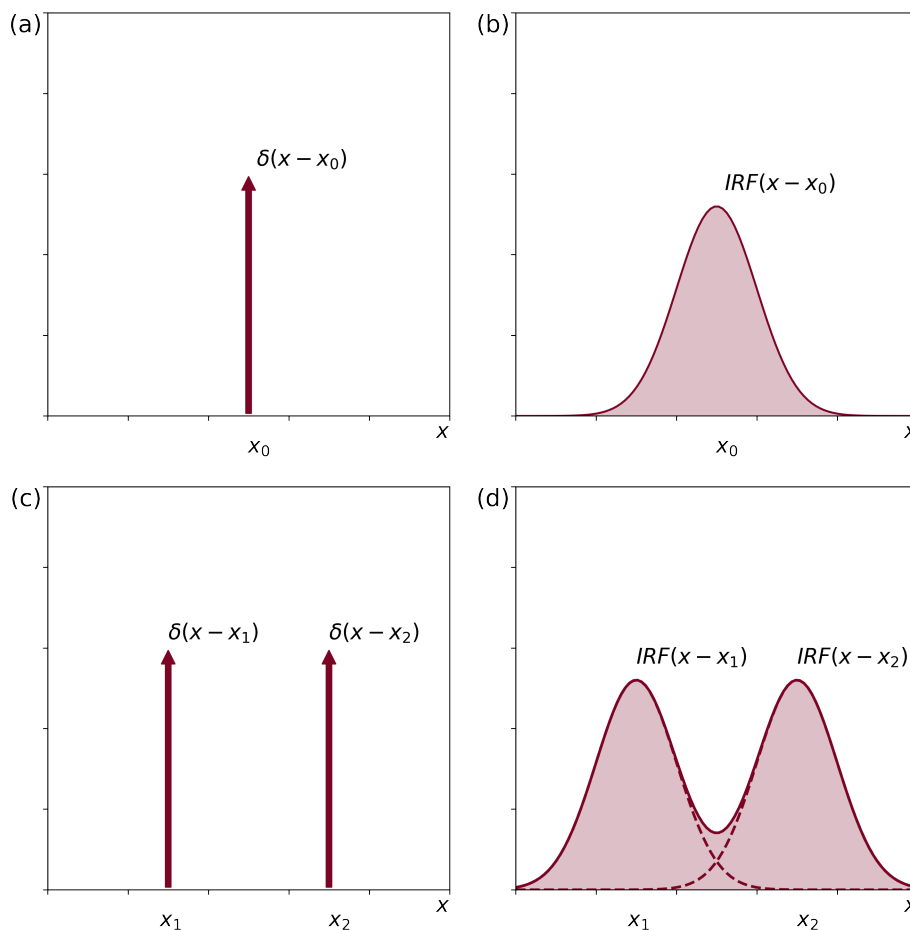


Figure 1.16: Illustration of a linear, shift-invariant system. In (a), the system input is represented as a pulse at x_0 , which leads to a system output in the form of the IRF centred at x_0 in (b). In the event of there being multiple inputs at one time as in (c), the output is simply the sum of the IRFs as in (d); these individual IRFs are the same independent of the position of the input pulse.

In the Fourier domain, the IRF corresponds to the system's characteristic function $T(\omega)$, where ω refers to spatial frequency. The characteristic function is usually complex thereby providing a complete description of the system's response, including

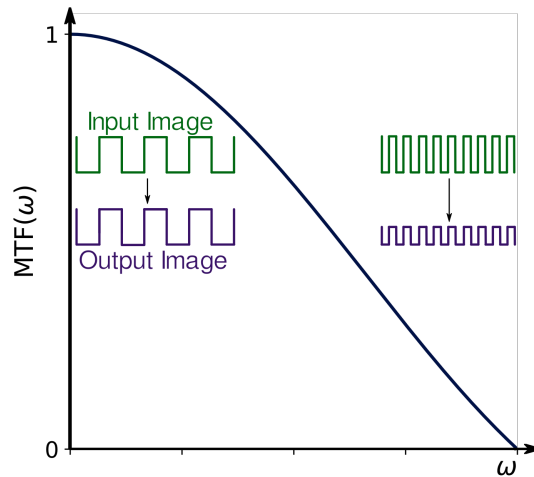


Figure 1.17: A hypothetical example of the MTF of a system illustrating of how it describes a system's ability to reproduce contrast. In this example, $MTF(\omega)$ is reduced at high spatial frequencies so that contrast at low spatial frequencies (i.e. large features in the input image) is reproduced faithfully, while there is a reduction in contrast for small features in the input that correspond to high spatial frequencies.

the transfer of both phase and contrast in the image. In the context of the present work, the transfer of phase is not of interest, as the phase information in the input is automatically lost because the detector can only record the spatial distribution of the intensity of the input quanta. Consequently, the most relevant and commonly used metric to describe an imaging detector's capacity to transfer contrast (or modulation in the image intensity) is the Modulation Transfer Function (MTF). This is defined in Equation 1.50 and illustrated in Figure 1.17 [41, 43].

$$MTF(\omega) = \frac{|T(\omega)|}{T(0)} \quad (1.50)$$

For a pixelated detector, the signal registered by each pixel is proportional to the number of incident quanta that interact with each pixel. Consequently, each pixel can be regarded as integrating over the quanta that are incident upon it. In one dimension⁴, this is expressed by Equation 1.51, where d_i is the signal recorded by the i -th pixel; K a constant of proportionality linking the the quanta q that interact with pixel i and the signal registered by pixel i ; and where Π function is a top-hat function with width a_x centred on the point ix_0 where x_0 is the distance between the centres of two pixels that are adjacent. The top-hat function is formally defined for for the purposes of the present context in Equation 1.52. More generally the signal as in Equation 1.53.

$$d_i = K \int_{-\infty}^{\infty} q(x) \Pi\left(\frac{x - ix_0}{a_x}\right) dx \quad (1.51)$$

⁴ For simplicity, the theory describing the performance of imaging detectors will be described in one dimension, x , though of course the detectors characterised in this thesis are two dimensional. The definitions provided can be extended to two dimensions without difficulty.

$$\Pi\left(\frac{x}{a_x}\right) = \begin{cases} 1, & \text{for } -a_x/2 \leq x \leq a_x/2 \\ 0, & \text{otherwise} \end{cases} \quad (1.52)$$

$$d(x) = Kq(x) * \Pi\left(\frac{-x}{a_x}\right) \quad (1.53)$$

The signal recorded by a detector is equivalent to d_x evaluated at the centre of each physical pixel, so that the signal recorded by pixel i is $d_i = d(x)|_{x=ix_0}$ while d_x itself represents the detector signal prior to sampling. Equation 1.53 makes clear that this presampling signal is the convolution of the aperture defined by the effective pixel width with the distribution of quanta $q(x)$ incident upon the detector. (The effective pixel width can be equal to the physical pixel width but need not be; it can be smaller if there are regions of the pixel that are insensitive to incident quanta and larger if pixels can register quanta that enter the sensor in another pixel.) The characteristic function of a pixelated detector is therefore the Fourier transform of the function describing the effective pixel; as this is a top-hat, this means the presampling MTF of a pixelated detector is $|\text{sinc}(a_x\omega)|$.

Noise is a random variable and to apply Fourier-analysis to a system's transfer of image noise, two further criteria, in addition to linearity and shift invariance, must be fulfilled. First, the processes that give rise to noise in both the system input and the system output must be wide-sense stationary (WSS), which means that the mean and variance as well as the autocovariance of the noise must be stationary with respect to the spatial variable x . Second, the system must be ergodic, which means that its spatial expectation value is equivalent to its ensemble expectation value [41, 42]. If these criterion are fulfilled, then Fourier transform of the autocovariance of the presampling signal is the system's Noise Power Spectrum (NPS), which describes the system's ability to transfer noise in the spatial frequency domain. This is also known as the Wiener spectrum [44] and is stated in Equation 1.54, where $FT\{\Delta d(x)\}$ is the Fourier transform of the difference between the expected value of the signal $d(x)$ ($E\{d(x)\}$) and the recorded value of $d(x)$ in the region $-X/2 \leq x \leq X/2$ [43].

$$\text{NPS}_d(\omega) = \lim_{X \rightarrow \infty} \frac{1}{X} E\{|FT\{\Delta d(x)\}|^2\} \quad (1.54)$$

Although the idea of sampling has been alluded to above, its effects have not been included on the metrics used to quantify detector performance. The maximum sampling frequency of a system is determined by the spacing of its pixels. This is known as the Nyquist frequency ω_N and is defined as $1/2x_0$. Frequencies up to the Nyquist frequency can be faithfully reproduced by a digital imaging system (though reproduction may be affected by the variation in contrast and noise transfer across different spatial frequencies), but features at frequencies above this will be mixed in with features at lower frequencies, as is shown in Figure 1.18. Specifically, features

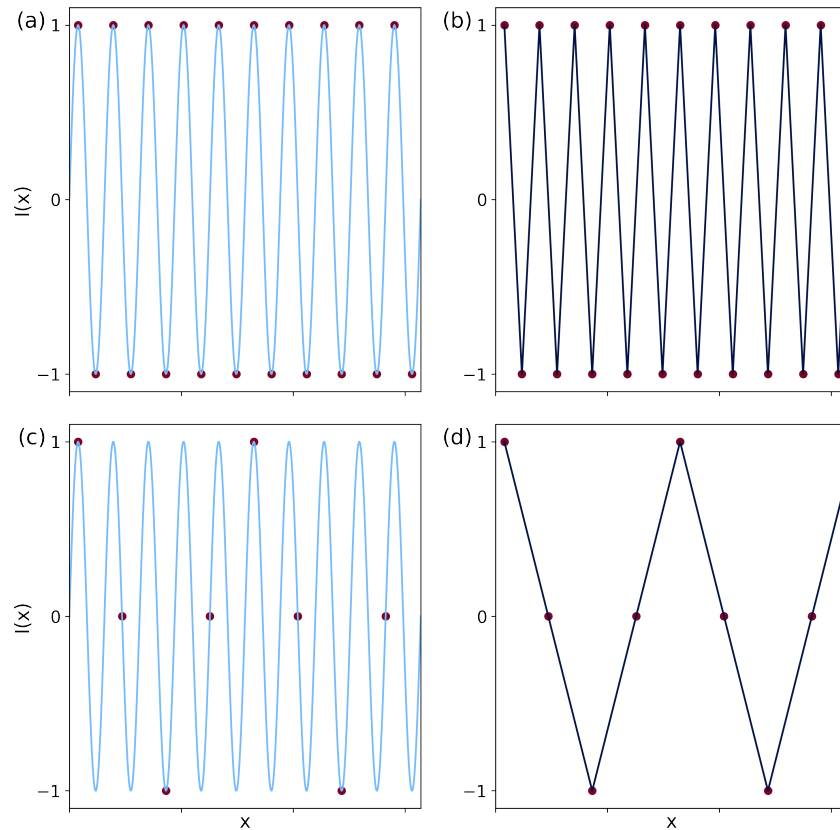


Figure 1.18: An illustration of the idea of sampling and how undersampling a signal can lead to aliasing. In (a) the signal is sampled at the Nyquist frequency and can just be reproduced in (b), while in (c) the same signal is undersampled so that the reconstructed signal in (d) is one with a frequency less than a quarter of the original. Information corresponding to the original signal will therefore be mixed-in with information contained in any signals with this lower frequency that are also detected by a system with the sampling rate used in (c).

with a frequency at $m\omega_0$ (where M is an integer $\neq 1$) will be mixed in with features at frequency ω_0 . This is known as aliasing and, in the event of aliasing, the original “presampling” signal cannot be recovered from the sampled signal [41,45,46]. While it is possible to measure a detector’s presampling MTF, as will be described in Chapter 3, this is not feasible in the case of the NPS. Consequently a detector’s noise transfer properties must be quantified using the post-sampling, or digital, NPS. The sampled noise cannot be regarded as a WSS process, though, if the incident noise can be regarded as a WSS process, the sampled noise can be described as a wide-sense cyclostationary (WSCS) process. This means the expectation and correlation functions must be shift invariant with respect to the pixel pitch x_0 . This is a random process for which the expectation and correlation functions are invariant to a shift of Mx_0 for any integer M [42]. The NPS of such a system (and therefore the postsampling, or digital, NPS of an imaging detector) is defined in Equation 1.55, where $\text{NPS}_d(\omega)$ is the NPS of a WSS system defined in Equation 1.54 [41].

$$\text{NPS}_{d^\dagger}(\omega) = \frac{1}{x_0^2} \text{NPS}_d(\omega) * \sum_{M=-\infty}^{\infty} \delta\left(\omega - \frac{M}{x_0}\right) \quad (1.55)$$

While the MTF and NPS describe a system's ability to transfer contrast and noise, they do not give a measure of the system's overall efficiency. The Noise Equivalent Quanta (NEQ) of a system is a measure of the effective number of quanta per unit area used by the system at each spatial frequency and is defined in Equation 1.56 [47]. This is defined in Equation 1.56, where n is the mean number of input quanta per unit area. However, the more commonly used figure of merit for quantifying system efficiency in electron microscopy is the Detective Quantum Efficiency (DQE) [48, 49]. This is a measure of the effective proportion of incident quanta that contribute to the image's signal-to-noise ratio (SNR). For a given value of n , it is defined as the ratio of the NEQ to n . Assuming that the average output signal of the system is d_n for average uniform input n then the system's large-area gain factor G is defined as d_n/n . For a linear system, $|T(\omega)| = g\text{MTF}(\omega)$. Consequently, if there is no additive or multiplicative system noise, then the NEQ and DQE will be independent of n , and the DQE can be expressed as Equation 1.57.

$$\text{NEQ}(n, \omega) = \frac{|nT(\omega)|^2}{\text{NPS}(\omega)} \quad (1.56)$$

$$\text{DQE}(\omega) = \frac{\bar{d}_n^2 \text{MTF}^2(\omega)}{n \text{NPS}(\omega)} \quad (1.57)$$

As the detectors studied in this thesis all have square pixels, it is worth considering the theoretical response of a square pixel detector that counts all incident quanta in the entry pixel only, so that $d_n = n$ and $a_x = x_0$. This is often used as a benchmark of performance when characterising detectors for a particular application [40, 48–51], and will be used as such in the later chapters of this work. The PSF and MTF of such a device are plotted in Figures 1.19(a) and (b). For such a detector, the noise recorded by individual pixels is uncorrelated, so that the NPS is equal to unity across all spatial frequencies, shown in Figure 1.19(c). On the basis of Equation 1.57, this yields the DQE that is plotted in Figure 1.19(d), which is 0.42 at ω_N .

However, it must be noted that the DQE of a square pixel detector can be better than that obtained when incident quanta are only counted by the entry pixel. Although there is a deterioration in the PSF when incident quanta are counted by more than one pixel, and increased blurring in the produced image, this can have a beneficial affect on the DQE. If the blurring process can be regarded as a deterministic one, which can still be the case if the underlying physical processes are themselves stochastic, then, in the presence of aliasing, the blurring will suppress the NPS to a greater extent than it does the MTF so that the DQE is enhanced. This means that the DQE can surpass the ideal square-pixel DQE described above and plotted in Figure 1.19(d) [48].

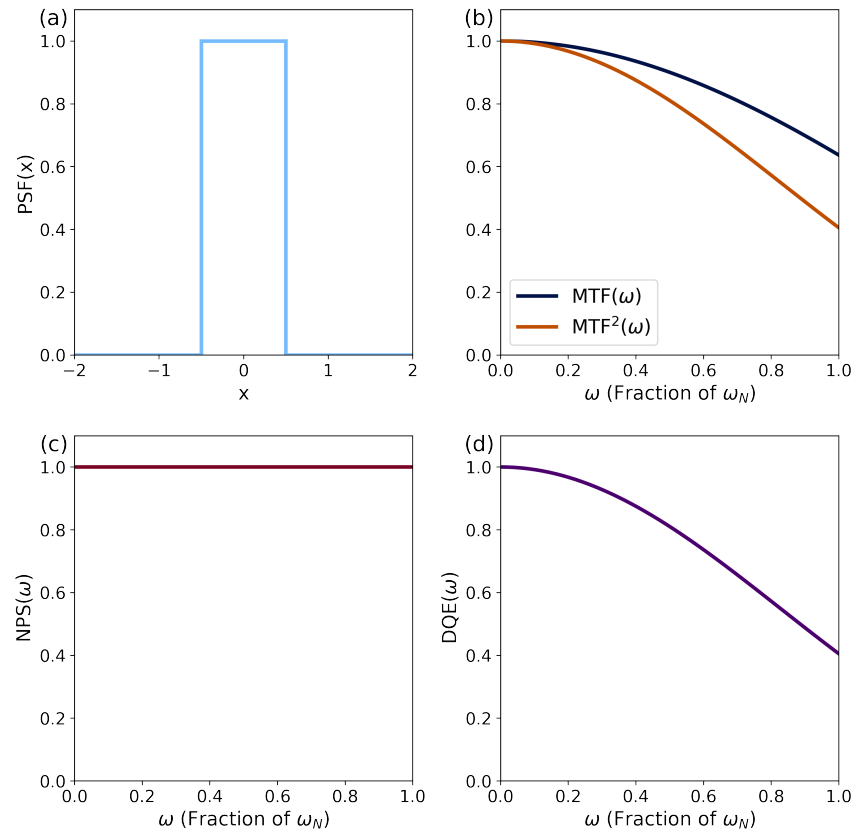


Figure 1.19: Figures showing the theoretical response of an square pixel detector: in (a) the PSF is a tophat function one pixel wide, which corresponds to the MTF shown in (b), which also shows the squared MTF; (c) shows the corresponding NPS while in (d) the resulting DQE is plotted, which is identical to MTF^2 .

Figure 1.20 illustrates how different degrees of blurring affect the MTF, NPS and DQE of a square pixel detector when aliasing is and is not considered. Comparing Figures 1.20(a) and (d), it can be seen aliasing makes no difference to the MTF. For a given degree of blurring, NPS obtained when the signal is not aliased is equal to the MTF^2 , as can be seen by comparing the NPS obtained in the case of no blurring in Figure 1.20(d) with Figure 1.19(b)). This also means that the DQE in the aliased case for a given degree of blurring is equivalent to dividing the NPS in 1.20(c) with that in Figure 1.20(d). It can be seen that although that in both Figures 1.20(c) and (d), blurring reduces the NPS and MTF^2 , it causes a greater reduction relative to the non-blurring case in the aliased NPS, leading to an increase in the DQE as seen in Figure 1.20(e). Higher degrees of blurring lead to a greater improvement in DQE at intermediate spatial frequencies in Figure 1.20(e), though the value of $DQE(\omega_N)$ tends towards a maximum 0.5 as the degree of blurring increases.

In cases where there is no aliasing, which would correspond to cases where the rate of sampling matched the smallest features in both the image and noise incident upon the detector, the NPS and MTF would be identical, and the DQE would be unity across all spatial frequencies independent of the degree of blurring, as seen in Figure

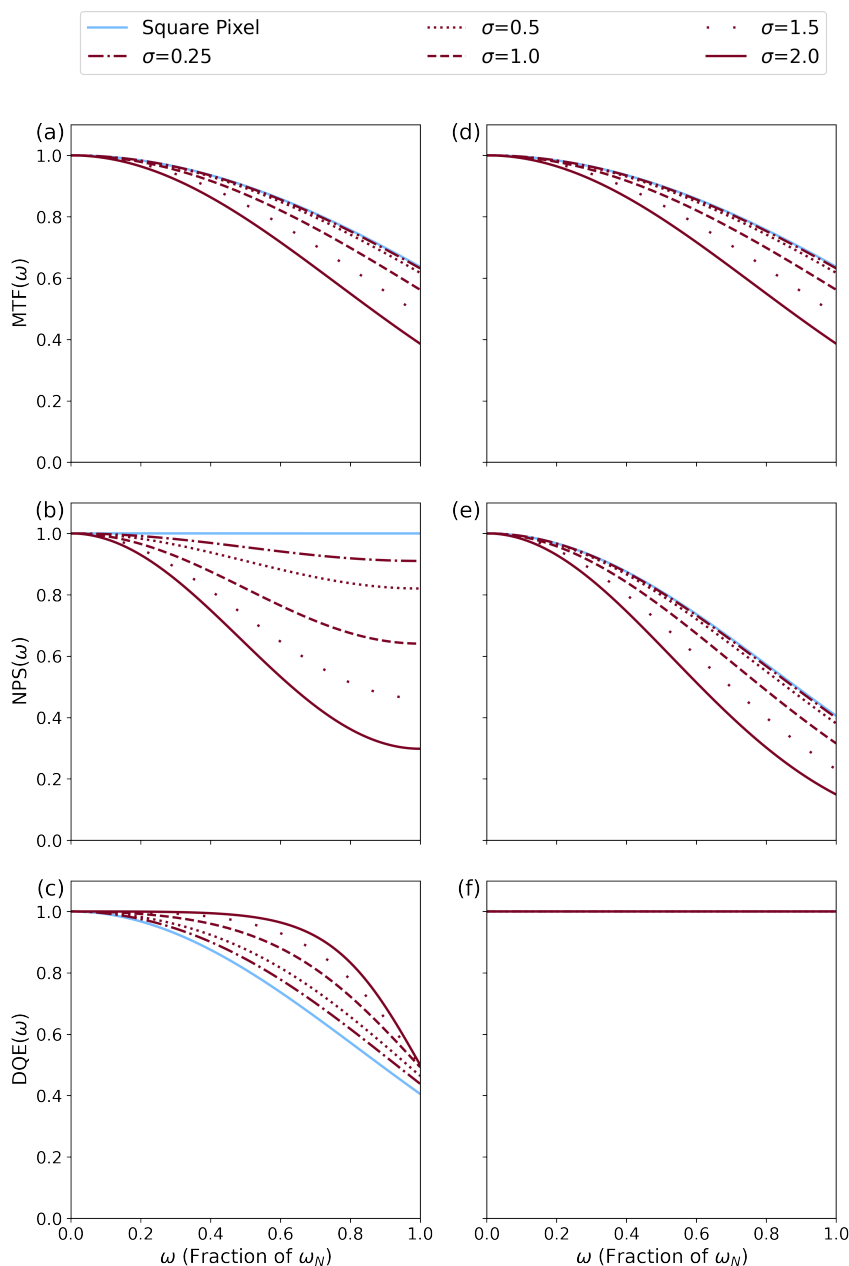


Figure 1.20: The (a) MTF, (b) NPS and (c) DQE of a square pixel detector when aliasing is a factor for various degrees of blurring, while (d) - (f) shows the same again without any aliasing. Panel (e) also effectively shows MTF^2 for the various degrees of blurring considered.

1.20(f). This would correspond to a detector that was able to sample the image and noise upon it at such a high frequency that the signal it recorded was not aliased. However, physically realising such a detector is not feasible due to the small length scales (nanometre and below) over which noise can be correlated.

1.6 Summary

As a prelude to presenting studies characterising the performance of various detectors for use in TEM, this chapter has reviewed the key physics underpinning detector oper-

ation and performance. This has included the physics of how electrons interact with matter, as this dictates how electrons generate signal in a detector's sensor. As part of this, the ways in which X-rays, which can be produced by the interactions of electrons with matter, can deposit their energy in a sensitive volume have also been outlined. This has been followed by a review of the basic principles of detector operation, including how electrical signals produced by incident radiation are typically formed and processed. The devices studied as part of the present work all use semiconductor-based sensors, and consequently, this chapter has included an overview of the relevant fundamentals of semiconductors as well as a discussion of the key semiconductor structures that underpin and/or approximate the devices studied. This provides the necessary background to reviewing the specific detector technologies used in TEM and studied as part of the current work, which will be described in Chapters 3 and 4. Finally, the Figures of merit used to quantify the performance of detectors have been described, with a view to laying the groundwork for understanding the experimental techniques described in Chapter 4 and the results presented in Chapters 5-8.

2

Detectors in the Context of Electron Microscopy

2.1 Introduction

Having given an overview of relevant aspects of detector technology and performance, this chapter considers the use of imaging detectors in electron microscopy, specifically TEM. This is with a view to contextualising and motivating the studies presented in this thesis. In order to fully appreciate the advantages and disadvantages of different detector technologies used in TEM and the suitability of different detectors for particular applications, it is helpful to understand the operation of a (scanning) transmission electron microscope ((S)TEM). As such, this chapter starts with an overview of TEM, beginning with why a TEM is such a powerful tool that has been utilised in so many fields in Section 2.2. This is followed by a description of key components of any electron microscope in Section 2.3, namely electron sources and electron lenses, while Section 2.4 describes the basic operation of a (S)TEM. Where appropriate, specific links are made to the microscopes used to perform the measurements presented in this thesis. Finally, a review of different detector technologies used in electron microscopy is presented in Section 2.5. This includes discussion of how direct detection technologies have opened up new experimental modalities in electron microscopy as well as developments in new sensor materials, the use of which in the context of electron microscopy makes up the bulk of the research presented in this thesis.

2.2 Why Electron Microscopy?

In Chapter 1, the concept of wave-particle duality was alluded to in the context of discussing how the behaviour of semiconductors arises from the interactions of weakly

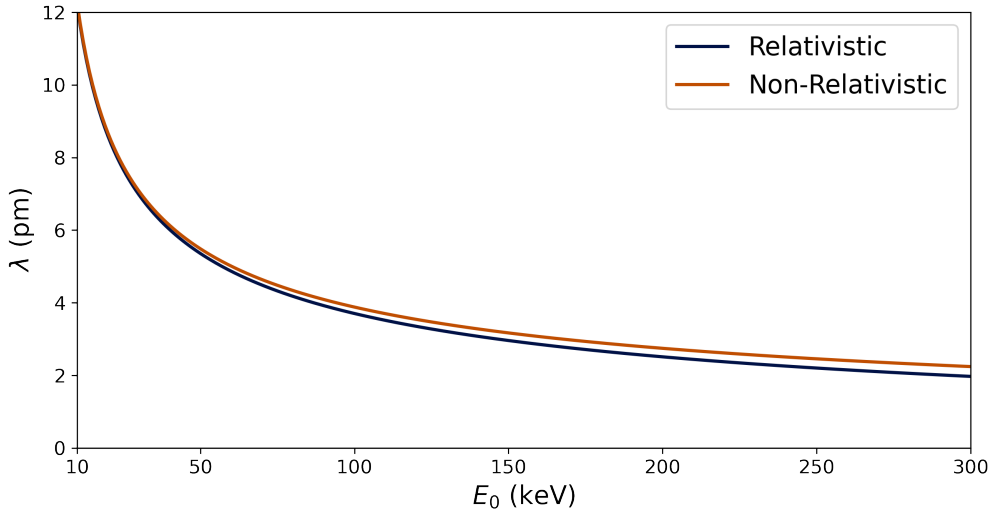


Figure 2.1: Plots of the non-relativistic and relativistic de Broglie wavelength of an electron as a function of accelerating voltage. At accelerating voltages greater than ~ 100 kV the disparity between the wavelengths calculated by accounting for and by discounting relativistic effects becomes significant.

bound atomic electrons with the interactions of the ion lattice in a crystalline material. To understand this, it is necessary to regard electrons as waves, rather than particles. Likewise, to appreciate the operation of a TEM and the motivation for using one, it is necessary to understand electrons as waves. The idea that all particles can act as waves and vice-versa was first put forward by de Broglie and is summarised by Equation 2.1 [52]. This relates the wavelength λ of a particle to its momentum¹.

$$\lambda = \frac{h}{|\mathbf{p}|} \quad (2.1)$$

By accelerating electrons, one can obtain radiation with wavelengths that are on the order of a picometre, as is shown in Figure 2.1. This matters for several reasons. At a fundamental level, the resolution of any lens (and hence of any microscope) is limited by the physics of diffraction. Waves passing through a circular aperture (be that defined by a lens or otherwise) with a collection semi-angle α_1 are diffracted by the aperture so that a single point P in the object plane broadens into an Airy disk [53]. Two points in the object plane of a lens can only be said to be resolvable in the image plane of the lens if it is possible to distinguish between the Airy disks. The Rayleigh criterion states that if the intensity due to the overlap in the two disks is $\leq 80\%$ of the maximum intensity then the disks can be resolved. This corresponds to the situation whereby the maximum of one disk coincides with the first minimum of the other, as illustrated in Figure 2.2.

¹ Although effectively already stated in Equation 1.20, the form of Equation 2.1 emphasises the notion of the particle wavelength which is most relevant here.

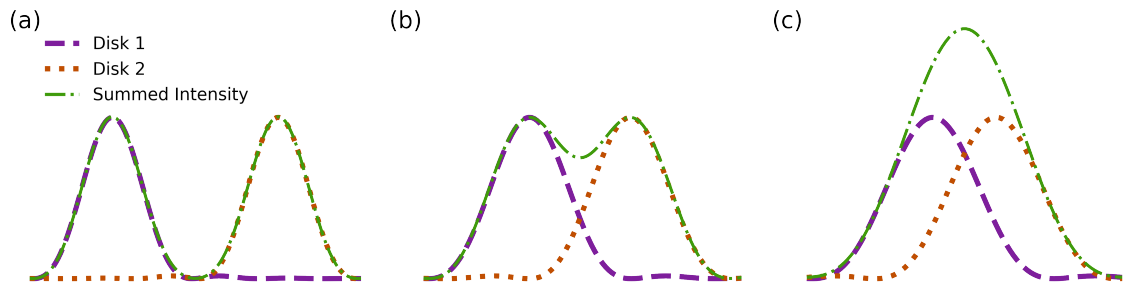


Figure 2.2: A demonstration of how the ability to resolve two separate Airy disks depends on how closely spaced they are. In (a) they are clearly distinguishable while in (b) they are just resolvable with the maxima of the two disks coinciding with the first minimum of the other. In (c) it is not possible to distinguish the two separate disks and a single, large disk is observed.

The radius of an Airy disk at its first minimum is $r_A = 0.61\lambda/\alpha_1$. Note that this is a simplification of Equation 2.2, in which μ is the refractive index of the medium in which the wave travels, which holds if μ is 1 and α_1 is small. The smaller the wavelength of the incident radiation, the smaller the value of r_A and the closer the two disks (and their associated points in the image plane) can be and still be distinguishable. In STEM, the resolution limit is slightly different, although it arises from the same underlying cause, as resolution is determined by the size of the electron probe as this determines the sample volume from which signal is generated. The dimensions of the probe are also diffraction-limited, though it is usual to define the probe size in terms of its diameter, so that the probe size as defined by $d_A = 1.22\lambda/\alpha_1$.

$$r_A = \frac{0.61\lambda}{\mu \sin \alpha_1} \quad (2.2)$$

When electrons are accelerated to velocities $\geq 0.1c$, relativistic effects must be considered and Equation 2.3 must be used to determine the electron wavelength. The discrepancy between wavelength obtained when relativistic effects are accounted for and when they are not included is shown in Figure 2.1. Electrons accelerated through a voltage of 300 keV have a wavelength of 1.97 pm, whereas for light in the middle of the visible light spectrum (e.g. green light with a wavelength of 550 nm) is on the order of 300 nm. Exact values in both cases of r_A would depend on the value of α_1 . Using electrons therefore makes it possible to image objects at far smaller lengthscales than would be the case with visible light².

$$\lambda = \frac{h}{\sqrt{2m_0eV\left(1 + \frac{eV}{2m_0c^2}\right)}} \quad (2.3)$$

²Note that limit imposed by diffraction is generally not the factor limiting resolution in electron microscopy, but rather lens aberrations, as will be discussed in Section 2.3.2.

A second reason that the small wavelength of electrons is important relates to diffraction. Diffraction patterns produced by the scattering of an incident wave with a sample can yield invaluable information about the structure of a sample. Each atom in a sample has an atomic scattering factor $f(\theta)$, which describes the amplitude of an incident wave that is scattered by angle θ by that atom when it is isolated. For a crystalline sample with a unit cell composed of i atoms, each of which have atomic coordinates x_i , y_i and z_i and atomic scattering factor $f_i(\theta)$, then the structure factor $F(\theta)$ describes the amplitude of the wave that is scattered by θ given the atomic planes with Miller indices h , k and l that define the crystal structure. This is stated in Equation 2.4. The intensity of the scattered wave is simply the square of its amplitude. Consequently, by analysing the position and intensities of diffracted beams it is possible to gain profound insight into the structure and composition of a sample, and diffraction-based studies are a cornerstone of crystallography.

$$F(\theta) = \sum_i f_i(\theta) e^{2\pi i(hx_i + ky_i + lz_i)} \quad (2.4)$$

The condition for Bragg diffraction has also already been raised in Chapter 1 in the discussion of the origin of the bands of allowed energy states in crystalline materials and stated in Equation 1.21. Restating it in one dimension as in Equation 2.5 underlines the importance of the wavelength of the incident radiation, where M is the integer reflecting the order of diffraction. In order for Bragg diffraction to occur, λ must be less than $2d$, where d is the spacing between planes of atoms in as marked in Figure 2.3(a). Consequently, to acquire diffraction patterns relating to structures with lengthscales ≤ 1 nm, the radiation used must have wavelengths < 2 nm. In practice, smaller wavelengths are preferable to ensure diffraction from the smallest lattice spacings and structural features and to maximise the number of lattice planes for which the Bragg condition is satisfied.

$$M\lambda = 2d\sin\theta \quad (2.5)$$

This latter point can be understood by considering diffraction space as in Figure 2.3(b). The Ewald sphere [54] describes the range of possible scattered wavevectors \mathbf{k}' for an incident wave with wavevector \mathbf{k} . Its origin of the reciprocal lattice, O , is defined by the incident wavevector \mathbf{k} , and the Ewald sphere is centred on the point that is $-\mathbf{k}$ away from O . The reciprocal lattice points with which the Ewald sphere intersects represent all the lattice points for which the Bragg condition is met. Consequently, the smaller the wavelength of the incident radiation, the greater the number of Bragg spots in the resulting diffraction pattern, as the radius of the sphere is inversely proportional to the radiation wavelength. The very small wavelengths of electrons with energies typically used in TEM means that the sphere is effectively planar with regard to the reciprocal lattice points and many diffraction spots can be obtained, which facilitates

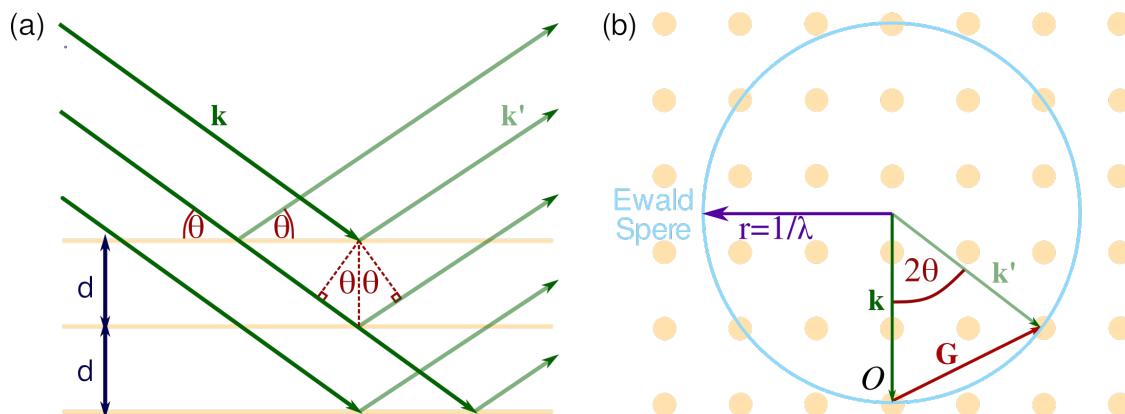


Figure 2.3: Illustration of Bragg diffraction at angle θ from lattice planes with spacing d in (a) real space in one dimension and (b) as a two dimensional slice through reciprocal space, wherein lattice planes become points in the reciprocal lattice. The difference between the incident wavevector k and scattered wavevector k' is equal to a reciprocal lattice vector G from Equation 1.21. The plane of reciprocal lattice points that contain O and are perpendicular to the beam is known as the zero-order Laue zones (ZOLZ), with the planes parallel to this known as the HOLZ. The first and second of these are specifically the first-order and second-order Laue zones (FOLZ and SOLZ).

structural analysis. One drawback of the Ewald sphere being effectively planar with regard to the reciprocal lattice is that scattering from the higher order Laue zones (HOLZ), which provides three-dimensional (3D) structural information, occurs at very high angles that may not be subtended by the detector used to record (parts of) the diffraction pattern. Converging the incident beam to obtain a convergent beam electron diffraction (CBED) pattern and/or tilting the sample can overcome this.

The above advantages depend on understanding electrons as waves, the amplitude and phase of which are modulated by interactions of the sample. Thinking of electrons again as particles, as was the case in Section 1.2, another reason for using electrons to study both material and biological samples at nanometre and below lengthscales is the fact they interact strongly with matter. Although this is what makes optimising detector technologies for them challenging, it also means that a wide range of signals are generated by the interactions of electrons with the sample. Figure 2.4 illustrates both paradigms for understanding electron-sample interactions, with some of the signals produced by electron-sample interactions marked in panel (a). Elastically scattered electrons, along with the direct beam, are used for imaging and diffraction, the specifics of which will be discussed in Section 2.4. Auger electrons and (with the exception of Bremsstrahlung) X-rays are characteristic of the elements that produced them and can be used to determine the elemental composition of a sample. The same is also true of inelastically scattered electrons, as the energy lost will depend on the elements present and the chemical bonds between different atoms species. Studying the spectra of inelastically scattered electrons is known as electron energy loss spectroscopy (EELS) [55]. Cathodoluminescence refers to the photons produced

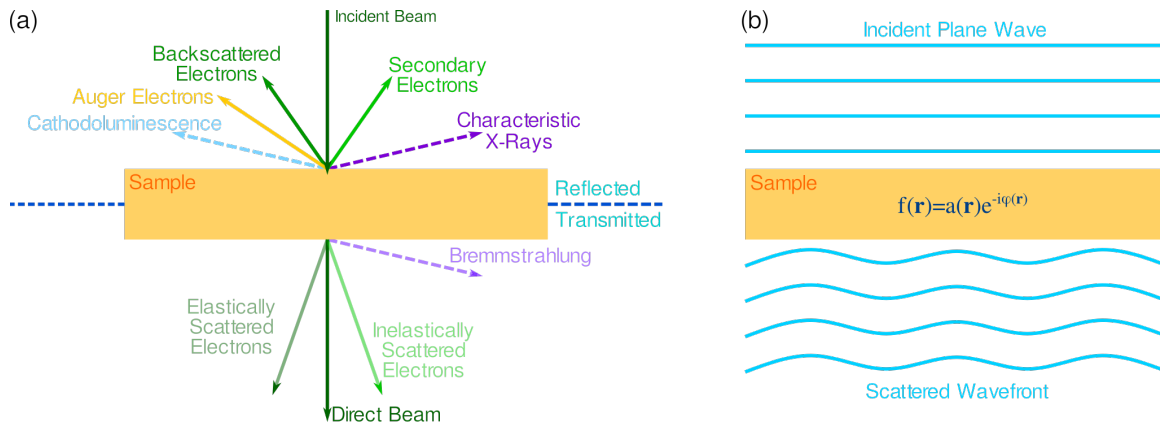


Figure 2.4: Diagrams illustrating the ways in which electrons can be thought of as interacting with samples. In (a), electrons are shown as a beam of incident particles some of which pass straight through the sample, while others are scattered and in some cases produce secondary quanta, while in (b), the way in which the sample modulates the amplitude and phase of the incident electron wave is described by the sample transmission function $f(\mathbf{r})$. Adapted from reference [20].

when incident electrons promote electrons in the valence band of a semiconductor sample to the conduction band, which can be used to study variations in the bandgap. The signals due to Auger electrons, cathodoluminescence, secondary electrons and backscattered electrons are usually utilised in scanning electron microscopy (SEM); though they can be used in (S)TEM [56–59].

The final advantages of working with electrons is the relative ease with which high-energy, monochromatic electrons can be produced and the ease with which they can be manipulated by electromagnetic fields as described by Equation 2.6, the Lorentz Equation. This means it is easy to accelerate electrons to a desired energy (thereby reducing their wavelength) and focus them using electric and magnetic fields, using relatively compact apparatus. It also means, in addition to all the signals discussed above, that electrons can be used to probe electric and magnetic fields at atomic resolution respectively [60–62]³.

$$\mathbf{F} = -e(\mathbf{E} + \mathbf{v} \times \mathbf{B}) \quad (2.6)$$

2.3 Constituent Components of Electron Microscopes

Fundamental to any kind of electron microscope is a source of electrons and the means by which to manipulate and focus those electrons i.e. electron lenses. This section describes these different components as well as the physics underpinning how

³ The difference in resolution is not due to any fundamental difference in the action of magnetic and electric fields on electrons (although these do differ), but instead arises due to the need to reduce the strength of the magnetic lens (described in Section 2.3.2) studying magnetic samples, though atomic resolution imaging of magnetic fields is an area of ongoing research [63, 64].

they work. It begins in Section 2.3.1 with an overview of how different electron guns function and metrics of comparison. This is followed by a discussion of electron lenses and the various aberrations that they display in Section 2.3.2.

2.3.1 Electron Sources and Guns

Electron sources used in electron microscopes can be divided into two categories: thermionic emitters and sources that are based on field-emission. For both types of sources, the aim is to enable electrons in the source to overcome the potential barrier due to the source's work function and escape to the vacuum level. The electrons produced by the source are then accelerated to the desired voltage and focused into the first crossover, which is the image of the source that is propagated down the microscope column and becomes the illumination incident upon the sample.

In the case of thermionic emission, the working principle is simply that any material will emit electrons if heated to a sufficiently high temperature, due to a broadening of the Fermi distribution that describes the distribution of electron energies in the emitter. The temperature to which a material must be heated for thermionic emission to occur will depend on the material's work function. Equation 2.7 states Richardson's Law, which describes the dependence of the current density, j , due to thermionic emission on temperature for a given work function, Φ [65]. This is similar in form to Equation 1.43, the expression for the saturation current density of a Schottky contact. However, Equation 2.7 differs from the earlier expression in that the source workfunction is used rather than the difference in the metal workfunction and semiconductor electron affinity. Although the emission current can in principle always be increased by increasing the temperature to which the source is heated, in practice operating at higher temperatures shortens the source lifetime as it increases the rate of evaporation and oxidation. Ultimately, the temperature at which the source is operated is fundamentally limited by the temperature at which it ceases to be solid [20].

$$j = A^*T^2 e^{-\frac{\Phi}{k_B T}} \quad (2.7)$$

Choice of thermionic emitters is therefore restricted to materials with a high melting point or those with a small work function. Consequently, there are two kinds of thermionic sources: thin W wires shaped like a hairpin-style filament and LaB₆ crystals. This latter kind have a low work function and, among their various advantages compared with W filaments, is their longer lifetime as, unlike W filaments, they do not evaporate while in use [66]. The Tecnai T20 TEM used for the majority of the experimental measurements presented in this thesis has, over the period during which these measurements were performed, been equipped with a W filament and a LaB₆ source at different times.

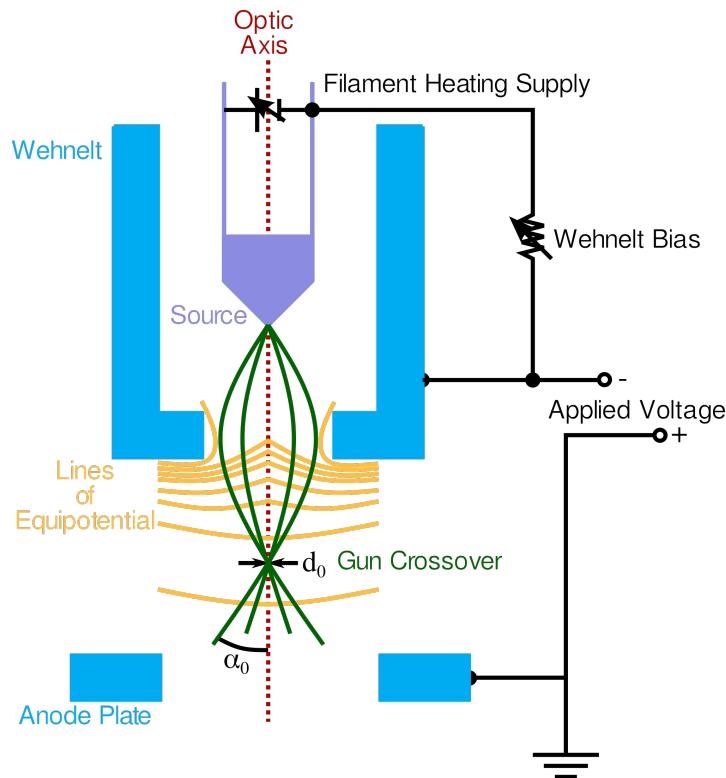


Figure 2.5: A schematic of the gun assembly of a typical thermionic emitter. The primary potential difference is between the source (cathode) and anode plate, while the bias on Wehnelt modifies the electric field so that electrons are focused into a crossover with diameter d_0 with a divergence angle of α_0 . Redrawn from reference [20].

The gun assembly of a thermionic source is (largely) independent on the type of thermionic source used, and Figure 2.5 illustrates a typical thermionic gun assembly. A high voltage is applied between the source, which takes the role of a cathode, and an anode which is kept at ground. Between the source and the anode is a grid known as a Wehnelt cylinder. The potential V between the cathode and the anode accelerates electrons to the desired velocity, while the Wehnelt, which is held at a small negative potential, focuses the electrons coming from the source into the first crossover. As the bias applied to the Wehnelt is negative, it repels electrons, and the potential applied to the cathode must account for this.

Field-emission sources, usually called field-emission guns (FEGs) operate on an entirely different principle from thermionic guns. The operational principle of a FEG is that applying a high electric field to the W tip reduces the width of the potential barrier at the metal-vacuum interface. When the width is sufficiently small, electrons that are at the Fermi level in the tip are able to quantum tunnel through the potential barrier and escape from the tip into the vacuum. This is known as “cold” field emission, as the source is kept at ambient temperature. A W tip is used due to the ease with which W wires can be manufactured to processed a fine ($<0.1\mu\text{m}$ in radius) tip, making it possible to exploit the high electric field that can be obtained at a sharp point. This tip is bonded to a W hairpin through which a current can be passed to

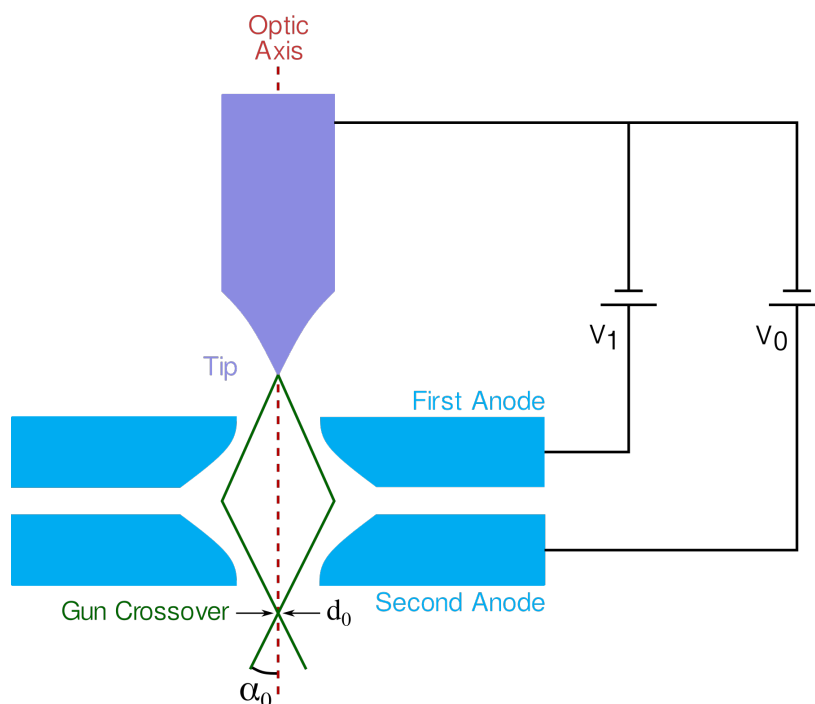


Figure 2.6: A basic diagram of a FEG. The two anodes together act as an electrostatic lens that focuses electrons into a very small crossover. An extra lens may sometimes be added underneath the two anodes. Redrawn from reference [20].

heat the tip for the purposes of driving off contaminants (field emission requires that the tip be completely free of contamination or any oxide) or reshaping the tip. The Glasgow Atomic Resolution Microscope (ARM) 200cF (S)TEM used to obtain results presented in Chapter 5 was equipped with a cold FEG.

Although Schottky sources are often grouped with FEGs, they are strictly speaking thermionic sources that are facilitated by the application of an electric field, rather than field emitters that are facilitated by heating. The electric field applied to the tip of a Schottky source (also a W tip as in a FEG) is sufficiently strong to lower the work function of the tip through the Schottky effect but not strong enough to enable quantum tunnelling (the defining feature of a field-emitter). Equation 2.8, in which ϵ_0 is the permittivity of free space, describes the dependence of the reduced work function Φ_{Red} on the applied electric field. The reduced work function can then be substituted into Equation 2.7 to find the dependence of the current density of a Schottky emitter on the reduced work function (and hence applied electric field). The Karlsruhe 80 - 300 Titan (S)TEM also used to obtain results reported in Chapter 5 was equipped with a Schottky source.

$$\Phi_{red} = \Phi - \Delta\Phi = \Phi - e\sqrt{\frac{e|\mathbf{E}|}{4\pi\epsilon_0}} \quad (2.8)$$

In the gun assembly of a FEG or Schottky emitter, there are two anodes located in front of the W tip, the first of which is at a positive bias of a few kV with respect

to the tip and which extracts electrons from the tip in the case of a field emitter and lowers the tip work function in the case of a Schottky emitter. The second anode accelerates the extracted electrons to the desired energy. This arrangement is shown in Figure 2.6. The current density produced by field emission is described by Equation 2.9, the Fowler-Nordheim formula, in which the constants k_1 and k_2 weakly depend on the electric field and the work function of the tip [67].

$$j = \frac{k_1 |\mathbf{E}|^2}{\Phi} \exp\left(-\frac{k_2 \Phi^{3/2}}{|\mathbf{E}|}\right) \quad (2.9)$$

There are multiple ways in which illumination sources, including electron sources, can be characterised. One of the key performance metrics is source brightness, B , defined as the current density per unit solid angle, $\Delta \Omega = \pi \alpha_0^2$, where α_0 is the semi-angle of the cone of emission. This is defined in Equation 2.10. Additionally, both spatial and temporal coherence of the electron source are also important.

Spatial coherence is important because it is a necessary condition for observing the interference of electron waves with themselves, which underpins phase-contrast methods of imaging (discussed in Section 2.4). Spatial coherence of a source depends on the size of the source, with it decreasing with increasing source size [20, 68]. The smaller size of FEG and Schottky sources mean these sources are more spatially coherent than LaB_6 and W hairpin sources.

$$B = \frac{j}{\pi \alpha^2} \quad (2.10)$$

Temporal coherence is in effect a measure of the energy spread of the source, a dependence that arises due to the time-energy formulation of the Heisenberg Uncertainty Principle stated in Equation 2.11. It follows from this that the longer the temporal coherence length the more monochromatic the electron beam. Thermionic sources have an energy spread described by a Maxwell-Boltzmann distribution due to the fact that the electrons that escape the emitter are those at the tail-end of the Fermi distribution [13]. This is typically on the order of a few eV, though it depends on the operating voltage. There is a further spread in energy caused by the electrostatic repulsion between electrons due to the Boersch effect [69]. The shape of the Wehnelt can also effect the energy spread of the gun [70]. FEG and Schottky sources have significantly lower energy spread, in the range of 0.2 - 0.7 eV, with there being some variation depending on the tip orientation, temperature and operating voltage [71].

$$\Delta E \Delta t \geq \frac{h}{2\pi} \quad (2.11)$$

From the perspective of characterising detectors however, even thermionic sources can be regarded as monochromatic as their energy spread is much smaller than the spread in energies introduced by the finite energy resolution of semiconductor-based

sensors, discussed in Section 1.5.1. For example, assuming a detector that has an energy resolution limited only by the statistical fluctuations of charge carriers (equation 1.46), which is a best case scenario, 60 keV electrons will be measured as having energies ranging from $\sim 59 - 61$ keV. Relative to the detectors studied in this thesis, the electrons produced even by thermionic source are effectively monochromatic.

2.3.2 Electron Lenses

The ability to focus electrons using electric fields configured to act as a lens has already been referred to in the previous section. While electrostatic lenses are used in gun assemblies, magnetic lenses are preferred for use in the microscope column itself, in part due to their reduced susceptibility to high voltage breakdown [20]. Magnetic lenses are composed of a cylindrically symmetric core made from a magnetically soft material (e.g. soft Fe), which is known as a polepiece. This has a hole through it, known as the bore. The polepiece is surrounded by a copper coil, through which current can be passed, magnetising the polepiece and thereby inducing a magnetic field. By varying the current, the strength and hence focal length of the lens can be changed. Typically, two polepieces are used to make one lens, and the ratio of the size of the bore to the size of the gap between the two polepieces is a key characteristic in determining the focusing action of a lens. Polepieces are also sometimes manufactured so as to have a cone shape, and if this is the case then the angle of the cone is also important in determining the behaviour of the lens. Figure 2.7(a) shows an example of a two polepiece magnetic lens. More complex lenses can be constructed by using multiple polepieces with alternating polarities. For example, quadrupole and hexapole lenses can be made by using four and six polepieces respectively. Lenses such as these, along with octapole lenses can be used to correct for aberrations in the principle magnetic lenses of a microscope.

The magnetic field of a lens is rotationally symmetric, while along the optic axis it can be approximated by a bell-shape, sometimes referred to as a “Glockenfeld” [72]. Mathematically, this is described by Equation 2.12, where a is half the full width half maximum of the bell-curve. The radial magnetic field, B_r , experienced by paraxial electrons is stated in Equation 2.13, from which it can be seen that the radial component of the field is determined by the axial component of the magnetic field, B_z . The magnetic field increases in strength away from the optic axis so that the further off-axis electrons travel, the more strongly they are deflected. Due to the action of the magnetic field, electrons have a helical trajectory illustrated in Figure 2.7(b). The full trajectory of a paraxial electron due to a magnetic lens is described by Equations 2.14 and 2.15, in which θ_1 is the angle of the electron’s velocity v relative to z -axis, also marked in 2.7. In these Equations, the factor η is $\sqrt{e/2m_0c^2}$ and V the microscope accelerating voltage.

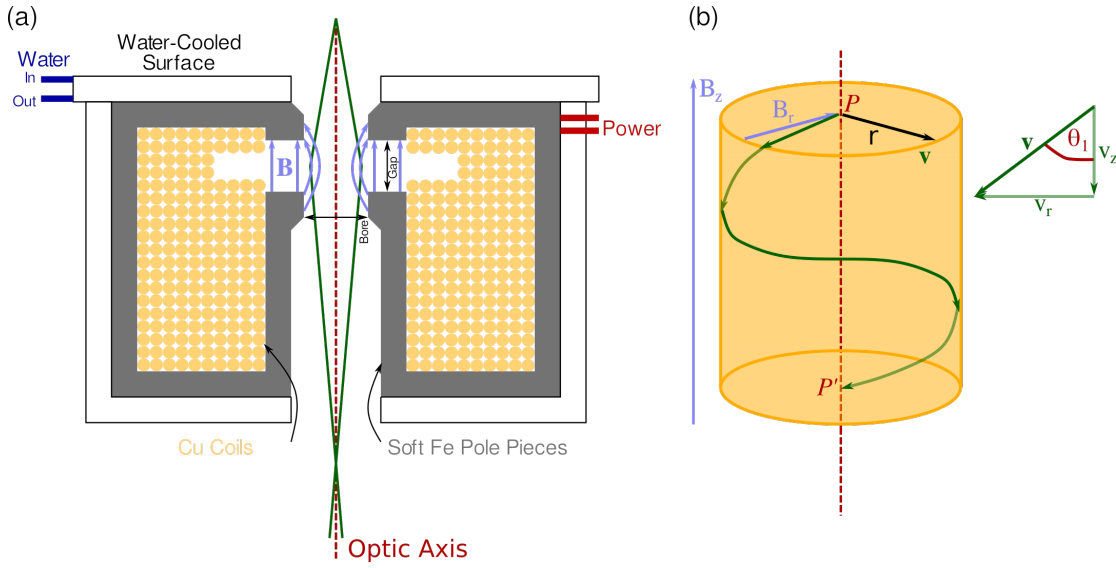


Figure 2.7: (a) Cross-section of a typical magnetic lens composed of two polepieces. These are in the hole down the centre of the lens. Due to resistive heating of the copper coils water cooling is also a key component of the lens system. Although (a) shows the ray paths as straight lines, in reality electrons have a helical trajectory as shown in (b). The effect of the magnetic field is that electrons pass through points P and P' on the optic axis, spiralling round the optic axis once in between [20].

$$B_z = \frac{B_0}{1 + (z/a)^2} \quad (2.12)$$

$$B_r \approx -\frac{r}{z} \frac{\partial B_z}{\partial z} \quad (2.13)$$

$$\frac{d^2 r}{dz^2} = -\frac{\eta^2 r B_z^2(z)}{2\sqrt{V}} \quad (2.14)$$

$$\frac{d\theta_1}{dz} = \frac{\eta B_z^2(z)}{2\sqrt{V}} \quad (2.15)$$

Magnetic lenses feature a variety of aberrations that adversely impact image quality and microscope resolution. For lenses that have rotational symmetry, there are five types of isotropic aberration possible: spherical aberration, astigmatism, field curvature, distortion and coma. Additionally, there are three anisotropic aberrations possible: anisotropic coma, anisotropic astigmatism and anisotropic distortion. Assuming that the electron source is not monochromatic or that electrons lose a significant range of energies due to interactions with the sample, then chromatic aberration will also affect image quality. Finally, deviations in the rotational symmetry of the magnetic field of a lens will cause axial astigmatism. The most important aberrations are spherical aberration, coma, axial astigmatism and chromatic aberration [13]. Axial astigmatism and coma can be corrected relatively easily, so that it is usually spherical aberration that limits the resolution of a microscope, unless it is equipped

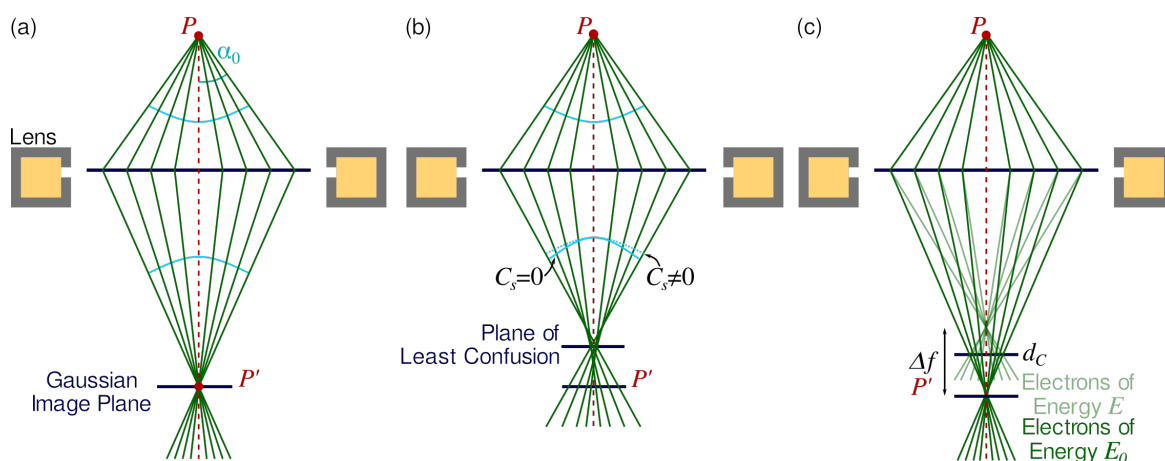


Figure 2.8: Ray diagrams showing the effects of spherical and chromatic aberration. In an ideal lens (a), the ray paths that emanate from point P in the object plane converge at point Gaussian image plane and there is no deformation in the form of the wave front. In (b) the further off-axis the wave front is, the more strongly focused it is, so that point P in the object plane expands to a disk at point P' in the Gaussian image plane of the lens. The diameter of the disk in the Gaussian image plane is larger than of the disk associated with P in the Plane of Least Confusion, which is the plane in which electrons are best focused. Chromatic aberration in (c) means that electrons with the primary energy E_0 are focused to point P' , but electrons with less energy are focused to a point in planes closer to the lens. The plane in which the disk associated with point P is narrowest is therefore prior to the Gaussian Image Plane.

with a corrector, in which case it is chromatic aberration. As spherical and chromatic aberration are the two most significant aberrations, these are the ones that will be discussed in detail.

Spherical aberration means that the further off-axis the electron wavefront is when it is acted upon by the lens, the more strongly focused they are towards the optic axis. As illustrated in Figure 2.8, this has the consequence that electrons originating from a single point P broaden into a disk in the Gaussian image plane of the lens, with diameter $2C_s\alpha_0^3$, where C_s is the coefficient of spherical aberration and α_0 the angle of the associated ray path with the optic axis, labelled in Figure 2.8. The plane of least confusion, which lies in front of the Gaussian image plane is the plane in which the diameter of the disk of intensity due to electrons originating from point P is at its smallest. In this plane, the diameter of the disk of intensity is $0.5C_s\alpha_0^3$. A lens can, in principle, be defocused so as to bring the plane of least confusion into the position of the Gaussian image plane thereby minimising the blurring caused by spherical aberration. However, the above treatment of spherical aberrations assumes fully incoherent illumination (which is not the case in TEM or STEM). Furthermore, to take the disk diameter in the plane of least confusion as defining the impact of spherical aberration on resolution neglects the dependence of resolution on the contrast transfer capabilities of the lens. The impact of spherical aberration on resolution in TEM and STEM is discussed more fully in Section 1.3 including why the disk size in the Gaussian image plane is a better measure of the effect of spherical aberration [73].

Chromatic aberration arises because electrons of different energies (and hence velocities) experience different forces due to the magnetic field produced by a lens as per Equation 2.6. Consequently, the focal point to which electrons are directed depends on electron energy. The spread in focal lengths Δf (marked in Figure 2.8(c)) and relation to the spread in electron energy ΔE is described by Equation 2.16, where I refers to the lens current, which determines the lens strength. Deviations from a perfectly monochromatic electron beam arise due to the intrinsic energy spread of the electron source; instability in the high voltage supply of the electron gun and energy losses in the sample. For paraxial electrons the diameter of the disk in the plane in which electrons of all energies are best focused is d_c , defined in Equation 2.17 where C_c is the coefficient of chromatic aberration and the other symbols have their usual meanings.

$$\frac{\Delta f}{f} = \frac{\Delta E}{E} - 2 \frac{\Delta I}{I} \quad (2.16)$$

$$d_c = \frac{1}{2} C_c \frac{\Delta E}{E} \frac{1 + E/E_0}{1 + E/2E_0} \alpha_0 \quad (2.17)$$

2.4 Anatomy and Operation of a (S)TEM

A (S)TEM can broadly speaking be divided into three parts: the electron gun, the optical column and the camera chamber. This final part contains the viewing screen (coated with ZnS or Zn/CdS powder which fluoresces in response to incident electrons) and detectors and cameras used to view and record images and diffraction patterns. The optical column can be further divided into three parts: the illumination optics, the objective lens and the post-specimen optics. In this section the different optical assemblies of the microscope are described as well as how they are used depending on the mode of operation. As can be seen in Figure 2.9, there is considerable overlap in components between TEM and STEM, and a single instrument can act as both a TEM and a STEM.

In both TEM and STEM, the role of the illumination system is to control the parameters of the electron beam incident upon the sample. The two key parameters in both modes of operation is the beam current and the semi-angle of convergence of the beam upon the sample [13]. It consists of a minimum of two condenser lenses, Condenser 1 (C1) and Condenser 2 (C2) and an aperture. In a simple two-lens condenser system, C1 controls the spot size and the current reaching the sample. The C2 lens controls the semi-angle of convergence of the beam at the sample, determining whether the illumination is parallel or convergent. For more modern instruments, including the JEOL ARM 200 cF used to acquire data presented in Chapter 5 of this thesis, the upper polepiece of the objective lens is used as a third condenser lens. This

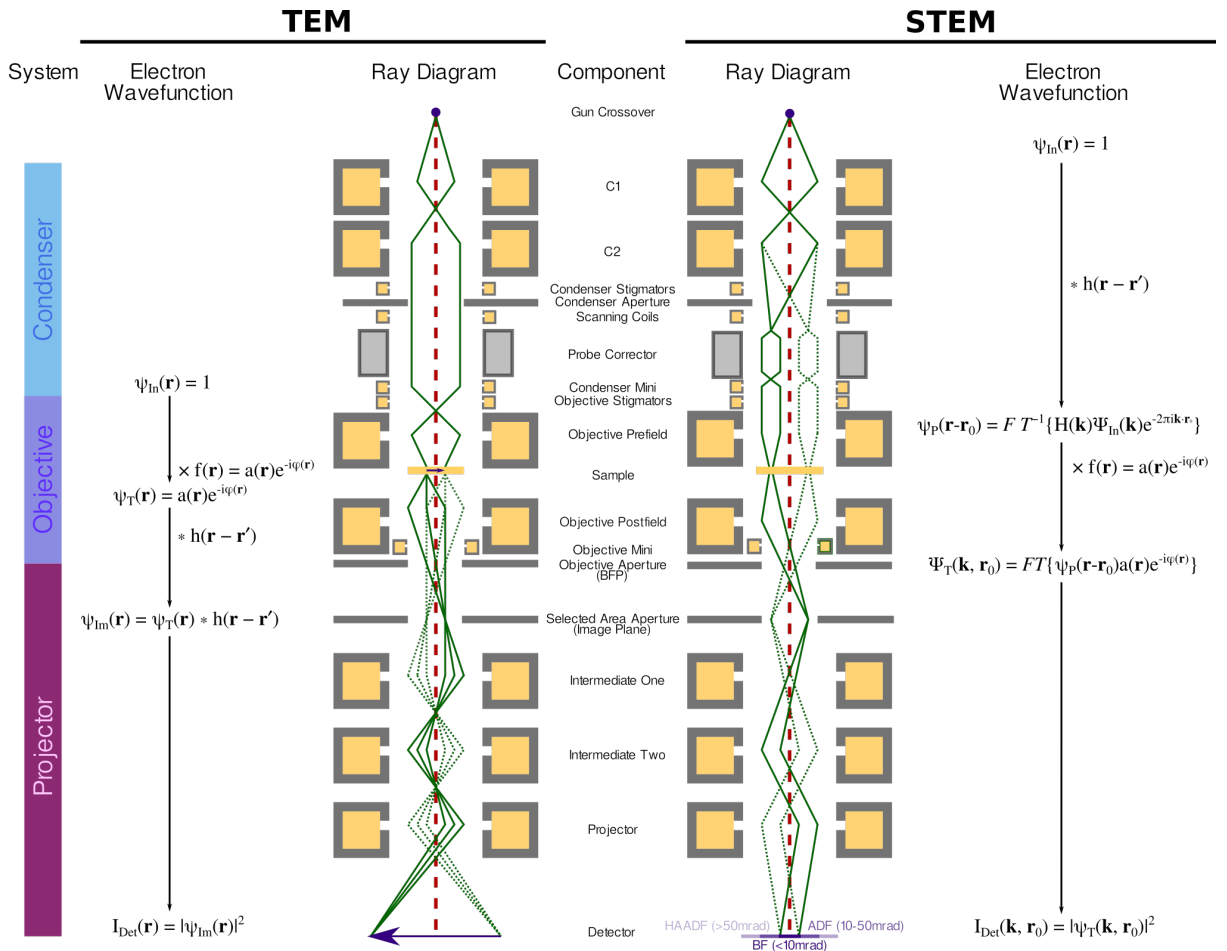


Figure 2.9: Illustration of the key components of a TEM and STEM and the ray paths associated with electron waves in the two instruments. The electron wavefunction formalism describing how images are formed in the two instruments is also noted. Whereas in a TEM the sample can be directly imaged in the detector plane, in a STEM, the image formed depends on the intensity of the electrons scattered into different regions of the detector plane. Note that the column depicted here is a generic one and does not correspond to any particular microscope, though it largely mimics that of the ARM 200 cF at the University of Glasgow. Inspired by reference [74].

makes both more parallel illumination and smaller, more convergent probes possible. The use of the prefield of the objective lens to form a smaller probe can be understood as the objective lens having a focal point of the in the sample plane between the two polepieces [13]. Such objective lenses are sometimes known as condenser-objective lenses and, when operating in TEM, require the introduction of an extra “mini-lens” to maintain the parallelism of the illumination when not using a convergent mode [20]. Other microscopes, such as the Titan 80 - 300 (S)TEM also used to acquire data presented in Chapter 5, feature a three lens condenser system.

Independently of how it is used, the objective lens is the most important lens of the microscope, as it is the primary image-forming lens. Image formation by a lens is a two-step process according to the Abbe theory of imaging [75]. A wave emanating from a point on the sample is effectively propagated to infinity in the

back focal plane (BFP) of the lens. The process of wave propagation is described by Huygen's principle [76]. This states that every point on a wavefront produces a secondary spherical wave weighted by the value of the original wavefront at that point. The propagated wave is the result of the interference of all the secondary spherical waves, so that it is, in effect, the result of diffraction.

Consequently, in the BFP, the electron wave can be described by the Fraunhofer approximation of diffraction, as it can be regarded as being in the far-field. Effectively the BFP of a lens contains the Fourier transform of the wave that leaves the sample. From the BFP, the electron wave continues to propagate. The distance to the image plane is the product of the lens magnification factor and the lens focal length. Assuming these are sufficiently large, the image plane can be regarded as in the far field of the BFP. The wavefront in the image plane of the lens is therefore described as Fraunhofer as diffraction from the wavefront in the BFP. Consequently, the image wave is therefore the inverse Fourier transform of the diffraction pattern in the BFP. The objective lens assembly also includes an aperture that can be used to limit the angle through which electrons are scattered by the sample and still contribute to the diffraction pattern in the BFP and hence the formation of any image.

The post-sample optics, which consist of a projector lens and at least one intermediate lens, control whether the BFP or the image plane of the objective lens is further magnified and projected onto to the viewing screen of the microscope (or selected camera or detectors). In STEM, it is always the BFP, with image formation depending on which part of the diffraction pattern is recorded and, in some cases, how this data is processed. For TEM, changing the strength of the projector lens makes it possible to select between imaging (magnifying and projecting the image plane) and diffraction (magnifying and projecting the BFP) modes. Figure 2.10 shows the post-sample optics of a TEM in diffraction mode to demonstrate the difference from an instrument in imaging mode as in Figure 2.9(a).

Although the differences in microscope alignment between TEM and STEM may appear slight, the differences in image formation become apparent considering the wavefunction formalism presented in Figure 2.9. Spherical electron waves produced by the source can be approximated as plane waves once they reach the condenser system. This initial, incident wave, $\psi_{In}(\mathbf{r})$, can be regarded as unity for simplicity without specifying a particular set of circumstances. In TEM, this wavefront is focused onto the sample, but maintains its general form. The sample is described by the sample transmission function $f(\mathbf{r}) = a(\mathbf{r})e^{-i\phi(\mathbf{r})}$, in which $a(\mathbf{r})$ represents the sample as an amplitude object (in the sense that it affects the amplitude of the incident wave), while $e^{-i\phi(\mathbf{r})}$ describes its properties as a phase object. $\psi_T(\mathbf{r})$, the transmitted, or exit, wave, can be regarded as the product of product of the incident wave and the sample transmission function, leading to Equation 2.18.

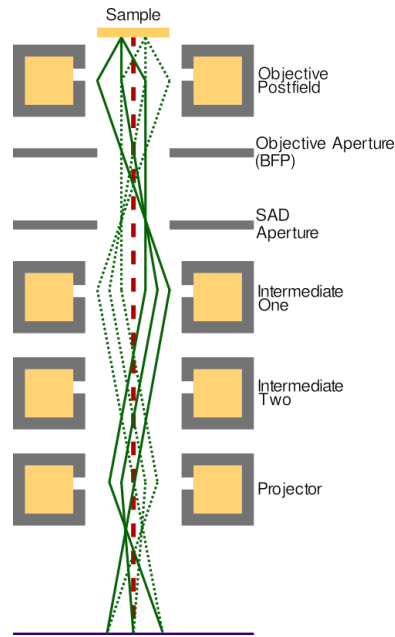


Figure 2.10: A ray diagram showing post-sample alignment for a TEM operating in diffraction mode. The key difference between the microscope in imaging and diffraction mode is the strength of the intermediate lenses. To select the area of the sample that contributes to the diffraction pattern, an aperture is inserted in the image plane of the objective lens (which is conjugate with the sample plane) known as the selected area diffraction (SAD) aperture. Adapted from reference [20].

$$\psi_T(\mathbf{r}) = a(\mathbf{r})e^{-i\phi(\mathbf{r})} \quad (2.18)$$

The ability of the lens to transfer ψ_T is described by its OTF⁴, which in the context of electron microscopy is normally referred to as $H(\mathbf{k})$. This is defined in Equation 2.19, in which $A(\mathbf{k})$ is the aperture function; $E(\mathbf{k})$ is the envelope function and $X(\mathbf{k})$ is the aberration function. $A(\mathbf{k})$ describes the way in which the lens aperture sets an upper limit on the maximum angle that electrons can be scattered by and still contribute to image formation and so sets a cut-off to the maximum spatial frequency that can be present in the image, while the envelope function describes the attenuation of the wave due to the lens. The aberration function describes the affect of lens aberrations and is defined in Equation 2.20. It should be noted that there are higher-order aberrations than those included in Equation 2.20, but the expression holds in cases where (third-order) spherical aberrations dominate as in a standard microscope without any correction for spherical aberration.

$$H(\mathbf{k}) = A(\mathbf{k})E(\mathbf{k})e^{iX(\mathbf{k})} \quad (2.19)$$

$$X(\mathbf{k}) = \pi\Delta f|\mathbf{k}|^2 + \frac{1}{2}\pi C_s\lambda^3|\mathbf{k}|^4 \quad (2.20)$$

⁴ Although this concept was introduced in Chapter 1 in the context of detector performance, the same linear systems theory can be used to describe image formation in a microscope

In real space, $H(\mathbf{k})$, corresponds to the lens IRF, $h(\mathbf{r})$ ⁵. The image wave, ψ_{Im} is then the convolution of $h(\mathbf{r})$ and $\psi_T(\mathbf{r})$. This is equivalent to multiplying $\Psi_T(\mathbf{r})$, the Fourier transform of $\psi_T(\mathbf{r})$ and the wave in the BFP, by $H(\mathbf{k})$ as in Equation 2.21. The intensity recorded in the detector plane, $I_{Det}(\mathbf{r})$, is then the product of $\psi_{Im}(\mathbf{r})$ with its complex conjugate.

$$\Psi_{Im}(\mathbf{k}) = H(\mathbf{k})\Psi_T(\mathbf{k}) = A(\mathbf{k})E(\mathbf{k})e^{i\chi(\mathbf{k})}\Psi_T(\mathbf{k}) \quad (2.21)$$

In STEM, the condenser system focuses ψ_{In} into a probe $\psi_P(\mathbf{r} - \mathbf{r}_0)$ incident on the sample at \mathbf{r}_0 . The effect of the lens on shaping the wave front is again described by $H(\mathbf{k})$ ⁶, and the probe can be modelled as the convolution of $h(\mathbf{r})$ with $\psi_{In}(\mathbf{r})$ in Equation 2.22. To account for the fact that the probe moves over the sample, a shift term, $e^{-i2\pi\mathbf{k}\cdot\mathbf{r}_0}$ is included in Equation 2.22. Again, the wave that exits the sample can be modelled as the product of the incident wave, in this case that of the probe, and the sample transmission function. This is defined in Equation 2.23. As the post-sample optics project the BFP of the objective onto the detector plane, the intensity at the detector plane is the product of $\Psi_T(\mathbf{k}, \mathbf{r}_0)$ with its complex conjugate, rather than $\psi_T(\mathbf{r} - \mathbf{r}_0)$ [77, 78]. It should be noted that the intensity recorded in STEM depends on the detector arrangement, which dictates the characteristics of the recorded image.

$$\psi_P(\mathbf{r} - \mathbf{r}_0) = FT^{-1}\{H(\mathbf{k})\Psi_{In}(\mathbf{k})e^{-i2\pi\mathbf{k}\cdot\mathbf{r}_0}\} \quad (2.22)$$

$$\psi_T(\mathbf{r} - \mathbf{r}_0) = FT^{-1}\{H(\mathbf{k})\Psi_{In}(\mathbf{k})e^{-i2\pi\mathbf{k}\cdot\mathbf{r}_0}\}a(\mathbf{r})e^{-i\phi(\mathbf{r})} \quad (2.23)$$

The above discussion of image formation has been as general as possible without reference to specific contrast mechanisms, though the form of the sample transmission function is suggestive of the two ways contrast can arise in images: through modulation of the amplitude of the electron wave and or through modulation of the electron wave's phase. Contrast mechanisms in both TEM and STEM can therefore be divided into two categories: amplitude contrast and phase contrast. As discussed above, the latter arises from the way in which the sample modulates the incident electron wave, which in turn is due to coupling of the electron wave with the electric potential of the sample (and magnetic vector potential in the case of magnetic samples).

The former can be further sub-divided into mass-thickness contrast and diffraction contrast. Diffraction contrast arises due to the variation in the structure of the sample (e.g. defects, strain and bending of the sample), so that there is localised variation in the diffraction pattern produced by the interactions of incident electrons

⁵ The Fourier domain forms of real-space functions being denoted by a capital letter, while the real-space are denoted with the lowercase

⁶ Though it should be noted that the aperture function in this is defined by the microscope's condenser aperture, though it is strictly speaking correct in STEM to refer to this aperture as the objective aperture as it defines the image resolution [77].

with the sample. Mass-thickness contrast arises because samples that are thicker and/or more massive (by being composed of higher- Z atoms) will scatter more electrons off-axis at high scattering angles due to the increased likelihood of Rutherford scattering. As discussed in Chapter 1, this is strongly dependent on Z and, as the mean free path of the electron is fixed for a given material, the likelihood of Rutherford scattering increases with sample thickness. Phase contrast requires interference of the transmitted electron waves with themselves, so acquiring a phase contrast image means portions of the electron wave that have been scattered differently must be able to contribute to the final image intensity.

In TEM, images with mass-thickness contrast can be obtained to use the objective aperture to select electrons that have been scattered into a certain angular range as is shown in Figure 2.11. In images formed using the direct beam i.e. bright field (BF) images, areas of high intensity correspond to portions of the sample that are thinner and/or composed of lower- Z atoms while the reverse is true in an image formed from electrons in a DF image. DF images in TEM that are based on the selecting a particular Bragg spot inherently contain information about specific sets of lattice planes as the areas that are bright in such a DF image correspond to those areas of the sample for which the corresponding Bragg condition is satisfied [20]. Phase contrast images can be obtained in TEM by using the objective aperture to let both on-axis and off-axis electron waves propagate to the image plane, as is shown in 2.11(c), in a technique known as high resolution TEM (HRTEM). It should be noted that it is not possible to recover the phase of the object from a single HRTEM image, as only the intensity of the exit wave is recorded by the detector. To recover the phase of the object, more advanced techniques such as focal series reconstruction and holography are necessary [79, 80].

In STEM, the interpretation of image contrast is somewhat more complex, if only due to how the signal collected depends on the detector configuration, for which there are a variety of options. However, the theorem of reciprocity links STEM contrast with that obtained in TEM, simplifying interpretation somewhat. Assuming conditions of elastic scattering, the propagation of electrons in the microscope is, in principle, time-reversible. Consequently, in a TEM, the electron source could be replaced with a detector and the detector plane swapped with an array of sources and the same intensity distribution would be observed. Comparing the ray diagrams for a STEM and a TEM, it can be seen that electron ray-paths prior to the sample in STEM are equivalent to those post-sample in TEM. In TEM, a point on the sample is illuminated by an image of the source as defined by the condenser aperture, while in STEM, a point on the source illuminates the detector plane, the portion of which is used in image formation is defined by the detector geometry. Note that in TEM, whether the image is coherent or incoherent depends on the coherency of the illumination, whereas in STEM it depends on the detector (assuming that the probe can itself be regarded as coherent).

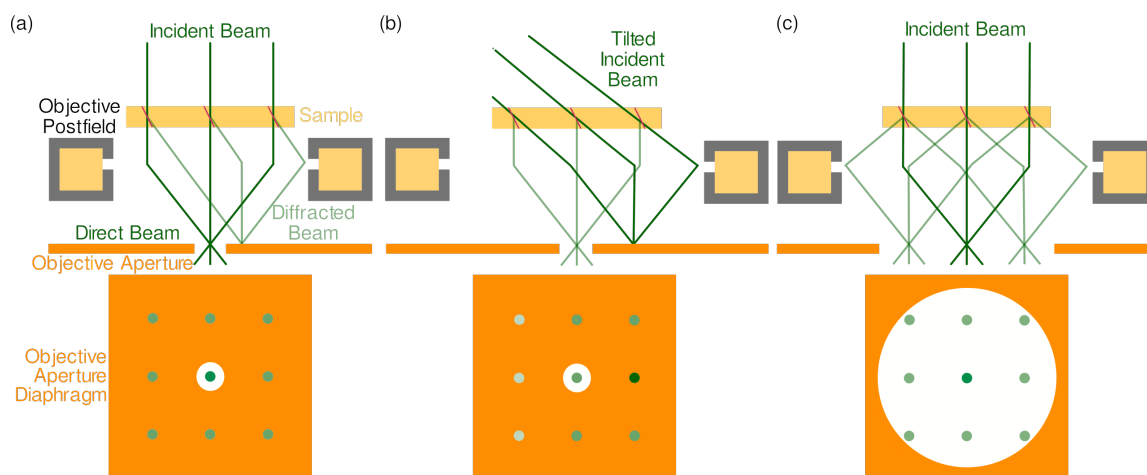


Figure 2.11: Optical arrangements for (a) bright-field (b) dark-field and (c) phase-contrast imaging in TEM. In (a) the electrons that pass through the objective aperture and contribute to image formation are those that have been transmitted directly through the sample while in (b) the incident beam has been tilted so that the electrons that are on-axis (and therefore least affected by lens aberrations) post sample are those that have been scattered by the sample. In (c) both on and off-axis electrons contribute to image formation. Adapted from [20].

One of the simplest examples of the principle of reciprocity is the equivalency between conventional HRTEM and BF STEM, illustrated in the simplified ray-diagram in Figure 2.12. Contrast obtained in STEM images acquired using a small, on-axis detector (in principle point-like, in practice so it subtends an angular range of ≤ 1 mrad) that records only those electrons that have remained on-axis can therefore be interpreted as equivalent to contrast observed in conventional HRTEM images with coherent, parallel illumination. The use of an annular bright field (ABF) detector that subtends a larger scattering angle (< 10 mrad) forms an incoherent image with reduced phase contrast and is equivalent to an HRTEM image formed with a larger condenser aperture and therefore incoherent illumination. More generally, the contrast obtained using the annular detectors traditionally used in STEM, which subtend a given angular range the diffraction pattern, α_0 is, by the theorem of reciprocity, equivalent to the contrast in a TEM image obtained using illumination defined by a condenser aperture that subtends a semi-angle α_0 at the sample.

There are several specific detector geometries and their associated contrast that it is worth describing in more detail. The first is an annular detector that subtends the angular range > 50 mrad, which is therefore illuminated only by those electrons that are scattered through large angles by the sample. Such large-angle scattering is attributable to Rutherford scattering. Consequently, the signal recorded by such high-angle annular dark field (HAADF) detectors provides a form of mass-thickness contrast. ABF and annular dark field (ADF) detectors (the latter of which typically subtends a range of 10-50 mrad) detect coherently scattered electrons and so less sensitive to changes in sample mass or thickness while still being sensitive to diffraction and phase contrast, making image interpretation more complicated.

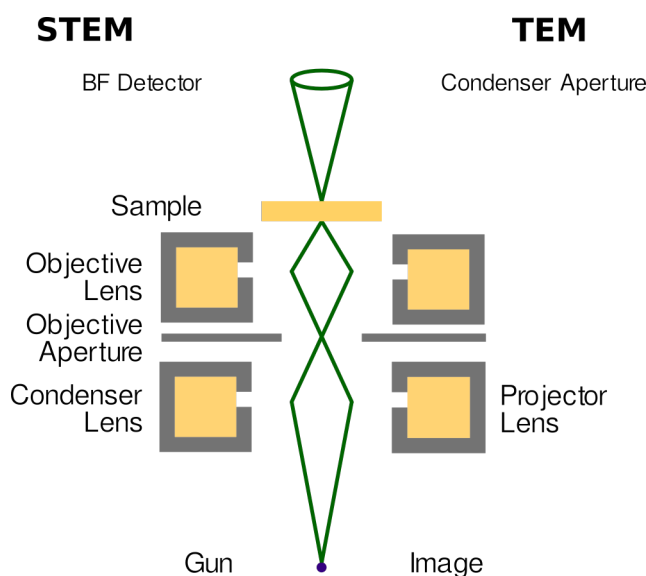


Figure 2.12: Ray diagram illustrating the principle of reciprocity as it applies to BF STEM and conventional HRTEM. Redrawn from reference [78].

The second noteworthy detector geometry is that of segmented on-axis detectors that do not have rotational symmetry, which can be used to form differential phase contrast (DPC) images. These typically consist of quadrant or octant segments, sometimes further divided into inner and outer segments. When the size of the electron probe is of a similar size to the lengthscales over which electric and magnetic fields in the sample operate, these fields will partially or fully deflect the probe. By calculating the difference in intensity recorded by different segments, the deflection of the probe can be measured which in turn permits measurement of the sample's magnetic or electric field.

The most versatile detector option, assuming one is willing to forgo recording the EELS signal, which is obtained from admitting the direct beam into a dedicated spectrometer, is using an on-axis pixelated detector. Recording the full 2D diffraction pattern (using an imaging detector) at each dwell point in the 2D STEM scan is known as four-dimensional STEM (4D-STEM). This makes it possible to generate 2D images of the sample with contrast based on any arbitrary detector geometry i.e. based on how a specific part or parts of the diffraction pattern changes as the incident beam is scanned across the sample. This is an incredibly powerful and versatile technique, which has rapidly become widespread in the past few years, largely enabled by the development of new detector technologies, which will be discussed in more detail in Section 2.5.2.

As a final point in this section, it is worth considering how aberrations affect the resolution that is obtainable in TEM and STEM. The probe size that is possible in STEM is of particular relevance to the current work given the confocal STEM alignment used for detector characterisation in this thesis (and which is described in Chapter 3). Resolution can be maximised in both TEM and STEM by appropriate choice of aperture collection semi-angle α_0 . In STEM, the optimal probe size is obtained by

defocusing the objective lens prefield so as to partially compensate for the effects of spherical aberration. For STEM, Equation 2.24 describes how electron source size (d_0), spherical (d_s) and chromatic (d_c) aberration and the limitations imposed by diffraction (d_A) determine probe size in an entirely uncorrected microscope [68].

$$d_P = \sqrt{\left(d_0^{1.3} + (d_A^4 + d_s^4)\right)^2 + d_c^2} \quad (2.24)$$

Both the JEOL ARM 200cF and the Titan 80 - 300 (S)TEM used in the course of the work presented in this thesis are equipped with correctors that mitigate the effects of spherical aberration in the formation of the probe when operating in STEM. Specifically they are both equipped with a CEOS CESCOR corrector [81]. This uses an arrangement of hexapole lenses to correct for all aberrations up to third-order. As these microscopes are limited by fifth-order aberrations, the optimal aperture semi-angle of collection is defined by Equation 2.25, and the corresponding probe diameter by Equation 2.26. In these expressions, C_5 is the coefficient of the fifth-order spherical [77].

$$\alpha_{opt,5} = \left(\frac{12\lambda}{C_5}\right)^{1/6} \quad (2.25)$$

$$d_{opt,5} = 0.45\lambda^{5/6}C_5^{1/6} \quad (2.26)$$

2.5 Survey of Detector Technologies Used in Electron Microscopy

2.5.1 Traditional Detector Technologies

The earliest medium for recording images and diffraction patterns in TEM was photographic plates and, more latterly, photographic film. This consisted of a photographic emulsion layer that was sensitive to incident electrons supported by a glass plate, or, in the case of film, a transparent plastic support. The emulsion was composed of gelatin in which were suspended fine silver halide particles. Incident electrons ionised the silver halide grains, causing them to develop into silver. The energy required to trigger the conversion of silver halide to silver is $\sim 7\text{eV}$, so a single electron (given the energies typically used in TEM), was able to ionise several silver halide grains. Film was therefore sensitive to individual electrons, but counting individual electrons was not possible due the “integrating” mode of acquisition inherent to using film cassettes. Even when using a short exposure, fogging of the film due to low-level stray scatter of electrons and secondaries in the camera chamber meant it was not possible to isolate individual electron events and thereby count them. After development of the film to develop the silver grains to metallic silver and remove

undeveloped silver halide grains, quantitative measurement of the electron intensity film could be performed using a film scanner. With the appropriate knowledge of the particular kind of film used, it was possible to convert the optical density of the film to an electron dose [13,82]. An important advantage of film was its large area and small effective pixel size (as determined by grain size and optical scanner parameters) [83], giving it an excellent field of view (FOV). However, film had only a reasonably good dynamic range and its response is only linear at intermediate intensities [84].

Imaging plates were a kind of reusable, electronic film, consisting of a layer of a photostimulable phosphor (BaFX:Eu , where $\text{X}=\text{Cl, Br, I}$) 50 - 100 μm thick on a supportive plastic layer that was covered by an elastic protective layer [13]. Incident electrons ionised Eu^{2+} to Eu^{3+} , with some of the escaped secondary electrons produced as part of this process becoming trapped in F^+ centres in the crystal, storing the energy of the incident electrons. Illuminating the imaging plate with a He-Ne laser provided enough energy for the trapped electrons to escape and convert the Eu^{3+} to excited Eu^{2+} [82]. As part of the de-excitation process, Eu^{2+} releases visible light, which could be recorded to create a copy of the image originally recorded by the imaging plate. In addition to their slightly increased convenience compared to film (in that they were reusable and could be exposed to light prior to exposure to electrons), another important advantage of imaging plates was their greatly improved linearity of response and dynamic range compared to film while still having reasonable spatial resolution and number of pixels for a given area. The pixel size of imaging plates was determined by the spot size of laser-scanning readout device as well and is typically about 19 μm [85].

Nevertheless, in spite of the positive qualities of film and imaging plates, they were fundamentally limited compared with digital methods of recording data, due to the need to develop and then digitise the data after acquisition for the purposes of analysis. Additionally, loading a plate or film into position, exposing it and then moving it to a canister for exposed plates/film took several seconds, so that time-resolved studies were not feasible. The finite size of the film cassettes placed an upper limit on the number of exposures that could be acquired before the camera chamber had to be brought up to air to exchange the cassettes. This imposed an upper limit on the size of the datasets that could be acquired without significantly disturbing the microscope and experimental set-up and, by extension, what experiments were feasible. Additionally, the plastic supports used in film tended to outgas and shrink, while the original photographic plates had the disadvantage of being very heavy and fragile [20]. Furthermore, the gelatin in the emulsion contained a significant quantity of water so that in the case of both plates and film it was necessary to dehydrate the recording medium in a desiccator and to then load the microscope with the film or plates as quickly as possible [13].

The introduction of charge-coupled device (CCD) cameras, which are digital recording devices, represented a significant step forward in the recording of images in TEM. The semiconductor based devices, shown in Figure 2.13, consist of p-type bulk with n-type strips above which is a SiO₂ interface and segmented metal electrodes. At the interface of the n-type and p-type material there is a depleted space-charge region sensitive to incident radiation. The segmented metal-oxide-semiconductor (MOS) structures form potential wells at the surface of the semiconductor, the depth of which can be manipulated by applying an appropriate potential to the corresponding electrode. During acquisition, electrons produced in the space-charge region are drifted to the nearest potential well, while during read-out, the potentials on the electrodes are varied so as to sequentially move the charge in each well to the neighbouring one along the column. Charge is then moved along to the readout anode using the same mechanism [31]. This process of applying clocked potentials to read-out the CCD camera is illustrated in Figure 2.14. Figure 2.14 shows a schematic of a standard CCD pixel. It is worth noting that more advanced CCD cameras are capable of transferring charge to a separate, but parallel matrix from which readout is performed so as to increase the frame rate of such devices [20, 31], though the maximum frame rates of those used in TEM have tended to < 100 fps [86].

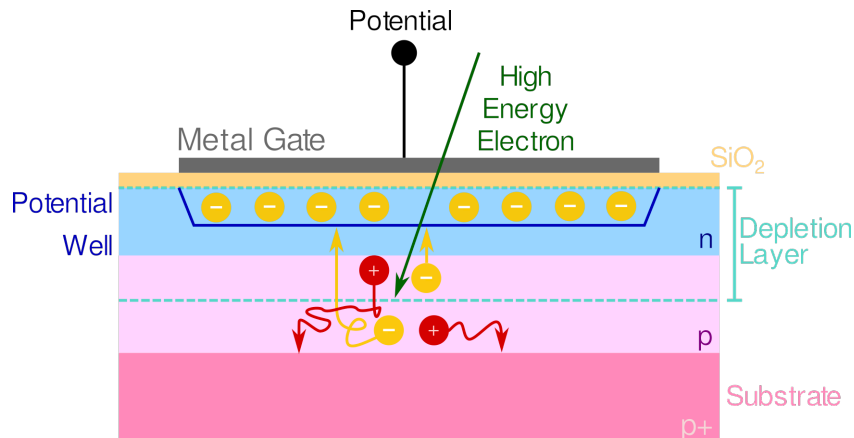


Figure 2.13: Schematic of a CCD pixel. Charge generated in the thin sensor layer is collected by potential wells defined by a MOS structure. The depth of the well can be altered by changing the potential applied to the gate.

However, the potential wells of CCD cameras are relatively shallow and are quickly saturated by high-energy electrons, which can damage the MOS structures at the surface of the camera [87]. Consequently, to improve the dynamic range of CCD cameras and protect them from damage, they are typically used in conjunction with a scintillator (either a powder layer or a single YAG crystal 50 μm thick) that is optically coupled to the CCD camera with a fibre plate or a light-optical tandem objective [88–90]. This has an adverse impact on the spatial resolution and efficiency of CCD cameras. Not only does the primary electron scatter long distances in the

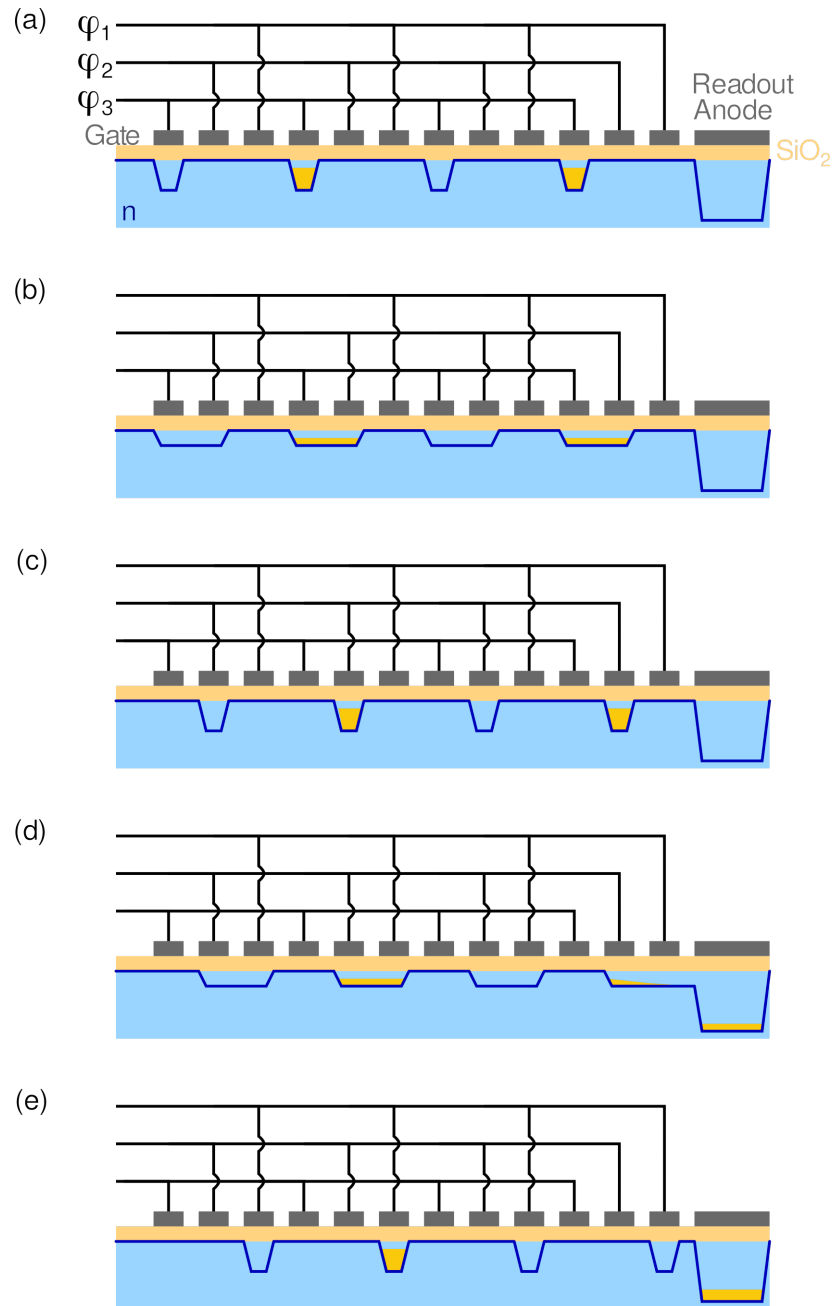


Figure 2.14: Illustration of the readout scheme for a CCD camera. Every third gate in the row of pixels is connected to the same potential (ϕ_0 , ϕ_1 and ϕ_2 , thereby creating a periodic potential underneath the gates. Electrons are collected in the minima of these (the potential wells) as seen in (a). By changing the potential at the gates, the shape and depth of the wells can be altered, moving electrons along the row to the readout anode, as seen in (b)-(e). Adapted from reference [31].

scintillator, which has relatively low stopping power, but low-energy photons produced by the interaction of the primary electron with the scintillator also scatter laterally in the scintillator, as illustrated in Figure 2.15. Consequently, signal due to the primary electron can be registered in pixels quite distant from the point at which the electron entered the sensor, leading to blurring in the image recorded [91]. Additionally, the indirect detection scheme is inherently lossy (as discussed in Section 1.3) and

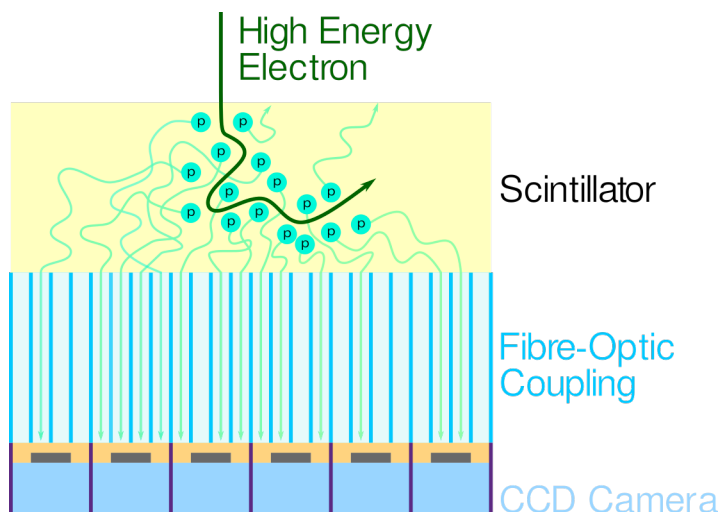


Figure 2.15: Figure of an optically-coupled CCD camera showing how photons produced by the interaction of the incident electron with the scintillator scatter laterally and are collected by CCD pixels remote from the entry point of the electron in the scintillator causing blurring in the images recorded.

degrades the detector's efficiency.

The annular detectors used in STEM have tended to be composed of YAG scintillators optically coupled to a photo-multiplier tube (PMT) [13, 20, 82]. Low-energy optical photons produced by the interaction of the primary electron with the scintillator are directed to a photocathode at the entrance of the PMT. At the photocathode, incident low-energy photons are converted to low-energy electrons by means of the photoelectric effect. These electrons are accelerated by a potential that is applied across the PMT so that they hit a series of dynodes at high speed, thereby producing more electrons that are also accelerated towards the subsequent dynodes and multiplied and then, finally, the readout anode [6]. In this way, illustrated in Figure 2.16 the electrical signal is amplified so that it is large enough for readout and digitisation, with the intensity recorded for a dwell point proportional to the height of the analogue electrical pulse produced by the PMT. While the scatter of photons in the scintillator does not have an adverse impact on spatial resolution as was the case for optically-coupled CCD camera, the process is still lossy and therefore reduces the overall efficiency of the system.

Annular and on-axis dedicated STEM detectors (i.e. not pixelated imaging detectors) that are semiconductor-based have tended to consist of a circular Si surface-barrier type or pn-junction type device usually divided into four quadrants though more specialised configurations are possible [92, 93]. While semiconductor-based dedicated STEM detectors are very efficient at detecting incident electrons, their large capacitance means they are slow to respond to variations in signal intensity as happen over the course of a STEM scan (and detection of which is crucial for generating contrast). A key advantage of scintillator-coupled PMTs is the rapid response of

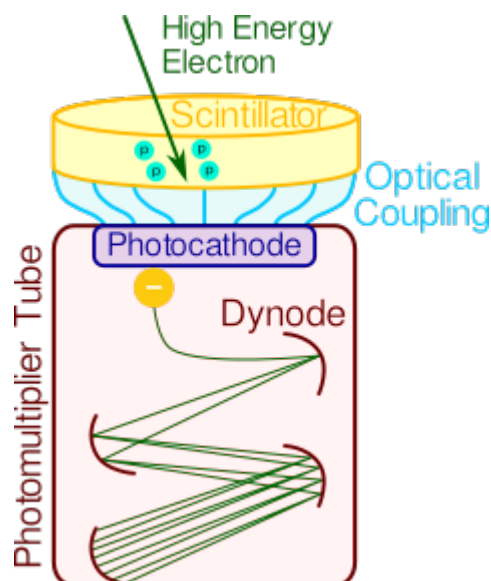


Figure 2.16: Schematic of a scintillator optically-coupled to a PMT such as might be used as a BF detector in STEM. Electrons produced at the photocathode via the photoelectron effect are multiplied by being accelerated into and colliding with a series of dynodes. The electrons produced at each dynode being also being multiplied at subsequent dynodes via the same process.

the scintillator, so that the bandwidth of such systems is in the MHz regime [20]. Semiconductor-based STEM detectors have therefore tended to be used only when a segmented detector has been required e.g. for DPC imaging [94].

As mentioned in Section 2.4, imaging i.e. pixelated detectors can be used in STEM to record the full contents of the BFP of the objective lens in a technique known as 4D-STEM due to the dimensions of the resulting datasets. The earliest demonstrations of this used scintillator-coupled CCDs [95], but the widespread adoption of this technique has only been made feasible by the development of direct electron detectors (DEDs), due to the poor SNR of optically-coupled CCD cameras and their limited frame rates.

2.5.2 The Direct Electron Detector Revolution

The introduction of pixelated detectors that are capable of converting incident electrons directly into an electrical signal, without an intermediary conversion step using a scintillator, can be credited with enabling a wide variety of experimental techniques within (S)TEM and electron microscopy more widely. The recent, widespread uptake of 4D-STEM [96] and the particular resurgence in ptychography [97–100] can be accredited to the development of high-speed DEDs that have high, linear dynamic range that that makes them capable of recording the full diffraction pattern using a reasonable (i.e. $\sim \mu\text{s}$) dwell time. Similarly, recent breakthroughs in cryogenic electron microscopy (cryoEM) [101, 102] can be attributed to the development of suitable DEDs with small pixels and large FOV that have superseded the performance of film [48].

However, different experimental modalities place a premium on different aspects of detector performance and at present there is no single, universal DED that offers excellent performance for all experimental modalities at all electron energies. In this section, the two types of DED that currently dominate (S)TEM are described. Also discussed is their suitability for different experimental techniques, with a particular focus on hybrid pixel detectors (HPDs), as the focus of this thesis is how the performance of such detectors can be better understood and enhanced.

For cryoEM which is usually used to mean single-particle analysis (SPA) applied to the study of macromolecular complexes in the life sciences, the key detector requirements are an excellent DQE combined with large field-of-view (FOV). This latter requirement arises because such experiments entail imaging many instances of a given molecule, frozen within vitrified ice at different orientations relative to the incident beam, to reconstruct the 3D structure of the molecule. At the same time, the number of electrons that biological samples can be exposed to without deteriorating due to radiolysis-induced damage (i.e. chemical bonds breaking due to primary electrons inelastically scattering with the sample, causing a change in sample structure) is extremely limited, typically $10 \text{ electrons}/\text{\AA}^2$ [14, 49, 103]. A premium is therefore placed on the detector's ability to reproduce the SNR of the images incident upon it at high spatial frequencies.

Given these requirements, monolithic active pixel sensors (MAPS) have become the detector of choice for cryoEM. Other imaging-based applications that also benefit from a large FOV and high DQE, and which have also tended to adopt MAPS detectors include (cryo-)electron tomography (ET), whereby tomographic reconstructions of a sample are obtained by acquiring a series of images of the sample tilted at a range of angles relative to the incident beam.

Monolithic devices consist of thin epilayer of lightly-doped p-type Si, which acts as the volume sensitive to incident radiation, that is supported by p⁺ type substrate with pixels defined by n-type wells. Their on-pixel electronics are relatively simple, typically consisting of at most four complementary metal-oxide semiconductor (CMOS) transistors, as is shown in Figure 2.17 [104]. This means their pixels can be very small, typically <

The exposed nature of the on-pixel electronics means that their radiation hardness is limited and the maximum electron flux that pixels can be exposed to without damage is finite [97, 138, 139]. This, in addition to the preference for small pixel pitches, also limits the sophistication of their on-pixel signal-processing electronics. Consequently, electron-counting, which further improves the imaging performance of DEDs, must be done in post-processing rather than being on-pixel. Although the incident electrons deposit only a small fraction of their energy in the thin sensors of monolithic devices, the fact they directly produce electrical signal in the sensors means distinguishing legitimate events from background noise in the detector is still feasible [104, 140]. The

Developer/ Commercial Vendor	Name	Intended/ Demonstrated Application(s)	Intended Electron Energy (keV)	Pixel Pitch (μm)	FOV	Frame Rate (fps)
Gatan	K2 Summit [49]	cryoEM (SPA [105], (cryo-)ET [106], microED [107])	≥ 200	5	3840 \times 3712 pixels 19.2 \times 18.56 mm ²	400
	K3 [108]	cryoEM (SPA [109], (cryo-)ET [106], microED [107])	300	5	5760 \times 4092 pixels 28.8 \times 20.46 mm ²	> 1500
	K3 Base [108]	cryoEM (SPA, (cryo-)ET, microED)	300	5	3456 \times 4092 pixels 17.28 \times 20.46 mm ²	> 1500
	K3 IS [110]	high-speed <i>in situ</i> studies [111], low-dose/beam damage studies [112], 4D-STEM [113], (cryo-)ET	200 - 300	5	5760/3456 \times 4092 pixels 28.2/17.28 \times 20.46 mm ²	150 (full frame) - 3500 (binned to 256 \times 256 pixels)
	Metro [114]	cryoEM, 4D-STEM	60 - 200	5	2048 \times 2048 pixels 10.24 \times 10.24 mm ²	1477
	Alpine [115]	cryoEM (SPA)	100 - 200	5	2304 \times 3240 pixels	> 1500
Thermo Fisher	Falcon 3 [116]	cryoEM (SPA [101], microED Hat- tne2019)	200 - 300	14	4096 \times 4096 pixels 57.34 \times 57.34 mm ²	40
	Falcon 4 [117]	cryoEM (SPA [101], (cryo-)ET [118], microED [119])	200 - 300	14	4096 \times 4096 pixels 57.34 \times 57.34 mm ²	250
	Falcon 4i [120]	cryoEM (SPA [121], (cryo-)ET)	200 - 300	14	4096 \times 4096 pixels 57.34 \times 57.34 mm ²	320
	4D-Camera [122]	4D-STEM [123]	30 - 300	10	576 \times 576 pixels 5.76 \times 5.76 mm ²	87 k
Direct Electron	Celeritas [124]	4D-STEM [125], HRTEM,	200 - 300 (optimised, sensitive to 60 - 1025)	15	1024 \times 1024 pixels 15.36 \times 15.36 mm ²	87 k
	Apollo [126]	cryoEM (SPA, microED, (cryo-)ET)	200 - 300	8	4096 \times 4096 pixels 32.8 \times 32.8 mm ²	data-driven
	DE-16 [127]	<i>in situ</i> /dynamical TEM [128], cryo- oEM (SPA, (cryo-)ET microED), 4D- STEM [129]	200 - 300 (standard) 30 - 300 (ER)	6.5	4096 - 4096 pixels 26.63 - 26.63 mm ²	92 (full-frame) - 4237 (2048 \times 128 pixel ROI)
	DE-64 [130]	cryoEM (SPA [131], microED [132], (cryo-)ET [133])	200 - 300 (optimised, sensitive to 80 - 1025)	6.5	8192 \times 8192 pixels 53.25 \times 53.25 mm ²	42 (full-frame) 4512 (4096 \times 128 pixel ROI)
	DE- DIRECTVIEW [134]	<i>in situ</i> studies, cryoEM (SPA), general low-dose imaging, 4D-STEM	120 - 300 (optimised) (sensitive to 80 - 1025)	6	4096 \times 3072 pixels 24.58 \times 24.58 mm ²	40 (full-frame) - 960 (4096 \times 128 pixel ROI)

Table 2.1: Table summarising the current generation of MAPS devices for use in (S)TEM. The 4D-Camera is not presently commercially available, being a custom, system developed in-house for use on the TEAM 0.5 microscope for the Molecular Foundry at the Lawrence Berkeley National Laboratory [135]. At the same time, the K2 and K3 series of detectors grew out of in-house systems built for the TEAM project [136], while the Falcon series of detectors arose from developments in monolithic device technologies made at the UK STFC Detector Group at the Rutherford Appleton Laboratory [137]. It is therefore possible there will be a commercial version of the 4D-Camera in the not distant future. Note that those applications listed for which there is no citation associated are included on the basis that the manufacturer advertises the detector for this application. A lack of citations is not necessarily cause for skepticism regarding the suitability of the detector for the application in question being in some cases is attributable to the newness of the product.

imaging performance of monolithic devices has been further improved by localising the entry point of incident electrons to individual pixels by finding the centre-of-mass of pixel clusters that register signal due to an incident electron, weighted by the amount of energy each individual pixel has registered [116, 141]. This approach to electron localisation is possible with monolithic devices when working with high-energy electrons, as the majority of the lateral spread in signal is due to diffusion of charge carriers, with the primary electron tending to pass straight through the sensor with minimal lateral scatter. Key to the success of detectors such as Gatan's K2 detector (and, more recently, their K3 series of detectors) has been a reduction in the effective pixel pitch by localising the electron point to sub-pixel accuracy using such an approach [142, 143], a unique feature among monolithic devices as seen in Table 2.1.

The frame rates of monolithic devices have improved rapidly in the past five years, with the current generation of monolithic devices being capable of kHz frame rates, as seen in Table 2.1. The previous generation of devices, of which the K2 was the most advanced, had only sub-kHz frame rates. However, given the way in which they count incident quanta, these frames must be sparsely populated to avoid undercounting of incident electrons. Coincidence loss, whereby one or more electrons strike the sensor near where another electron has already been registered in quick succession, so that the subsequent electron(s) are not registered, has a negative effect on device DQE and linearity [49, 144]. The improvement in the frame rates of monolithic devices therefore comes with an improvement in their count rate.

However, for some devices, including some of the K3 series of detectors, a distinction must be made between the raw frame rate of the device and the number of frames that are written to disk. Although the raw frame rate of the K3 is > 1500 fps, these raw frames are processed to identify electron events and corrected for motion drift before being summed and written to disk at a rate of > 75 fps. For the K3 and K3 Base the degree of compression going from the raw frames to the frames as written to disk is 20 and 60:1 respectively. Many monolithic devices increase their frame-rate by binning pixels or by only reading out a select region of interest (ROI) e.g the DE-16 as noted in Table 2.1. These techniques make it possible for such devices to achieve kHz though at the cost of a reduced counting ability and reduced FOV for a given magnification [145]. The fastest available device, the 4D-Camera [122], is able to achieve full (i.e. without reading out only a selected ROI or using binning) frame rates of 87 kHz, though this has a much smaller pixel matrix than most monolithic devices, as can be seen in Table 2.1, being intended for use recording the low-angle (i.e. coherent) scattering in a 4D-STEM experiment.

Monolithic devices have been regarded, due to their limited linearity when counting electrons, radiation hardness and frame rates, as less suitable for diffraction-based modalities, especially those using a parallel beam. This includes micro-electron diffraction (microED), another important technique in the life sciences, which entails

rotating crystalised macromolecules, such as proteins, and reconstructing their 3D structure from the resulting diffraction patterns. Due to the high intensity of the direct beam in such diffraction patterns, a detector with a large and linear dynamic range is necessary. Furthermore, a high-frame rate is preferred as this dictates the speed at which the crystal is rotated, which in turn determines the total acquisition time. For similar reasons, monolithic devices have tended not to be the detector of choice for many 4D-STEM experiments nor EELS. While they were the first type of DED successfully used for EELS [146, 147], they have to be used under specific conditions for their performance to surpass that of traditional CCD cameras [148]

They are, however, used for diffraction-based experiments which use a convergent beam, as the demands placed on the detector in terms of dynamic range are reduced, particularly those detectors that are capable of high-frame rates [96]. Similarly, while they are not presently the preferred type of detector for microED studies, they are beginning to show potential for use in such experiments. Until recently, microED had only been successfully performed with monolithic devices operating in integrating mode [149–151]. High quality microED datasets have been obtained using both the Falcon 4i, K2 and K3 detectors [107, 119, 152]. In the case of the K3 detector, it was possible to acquire data without using a beamstop to block the transmitted beam without any damage to the detector being observed. However, it is not yet clear to what extent the K3 could be routinely used for such experiments without sustaining damage or a substantial reduction in its lifetime. Nevertheless, combined with the improved frame rate of the K3 compared with that by the K2 (noted in Table

For experiments requiring high frame rates, radiation hardness and linear response under high incident flux, hybrid pixel detectors (HPDs), the other kind of DED, have generally been regarded as preferable to monolithic devices. These are composed of an application specific integrated circuit (ASIC), which contains sophisticated on-pixel signal processing circuitry, that is bump-bonded to a sensor. A schematic of an HPD pixel is shown in Figure 2.18, while a summary of the characteristics of current generation HPDs used in (S)TEM is given in Table 2.2). The sensors of such HPDs are typically 300-500 μm thick in order to protect the ASIC from incident. This makes them very robust. Combined with their high count-rates (and consequent highly linear response even under high electron flux) and frame-rates, this makes them particularly suitable for a variety of diffraction-based experiments including microED [155, 156], 4D-STEM [99, 157, 158] and EELS [40] as well time-resolved imaging [159, 160]. HPDs can be divided into two categories of detector previously discussed in Section 1.3: integrating and counting.

Integrating HPDs tend to have sufficient dynamic range so that they can record the signal due to multiple incident electrons arriving in a pixel over the course of a single acquisition. They can then distinguish between and count multiple electrons that arrive simultaneously though their ultimately finite dynamic range means their count

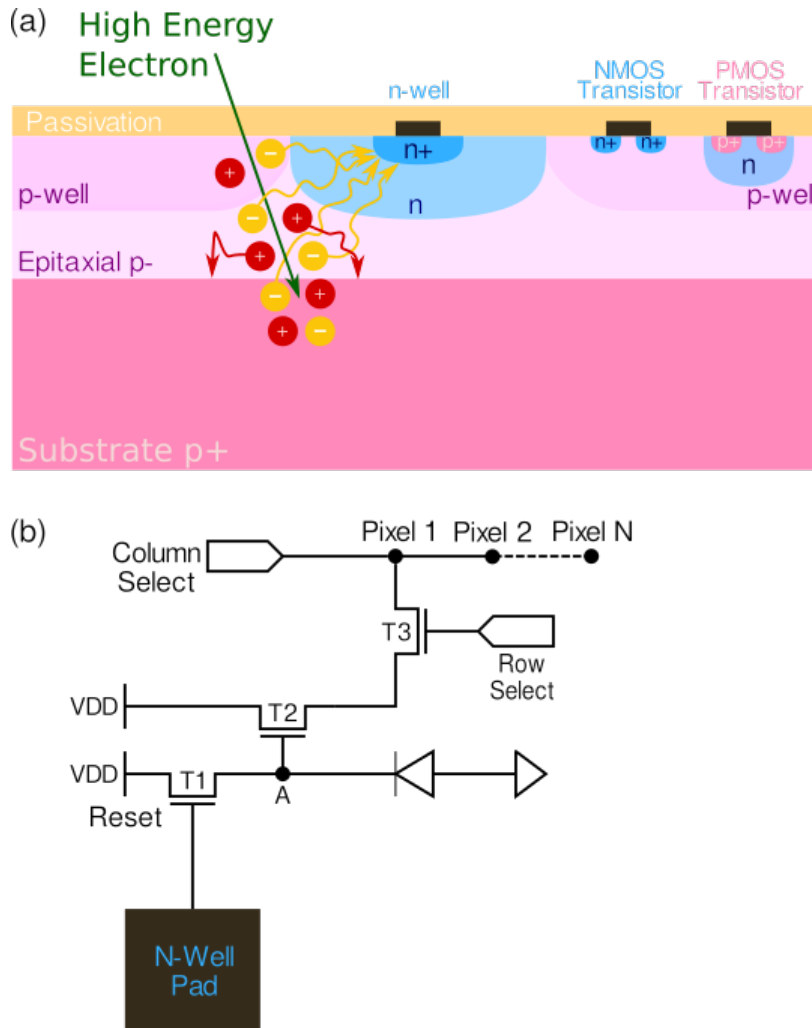


Figure 2.17: Views of a MAPS pixel using three transistors: (a) shows a cross section of a typical MAPS pixel, which is defined by the n-type well that collects electrons, is shown while (b) shows a simplified circuit diagram.. Electrons generated in the epitaxial p^- diffuse to the n-well. Prior to device exposure, transistor T1 is switched on, which charges the stray capacitance at node A. During exposure, the capacitor is discharged by an amount proportional to the signal induced on the n-well diode. T2 and T3, the row and column-select transistors read-put the signal to the external ADC [153]. Both panels adapted from reference [154].

rate is still limited by their frame-rate. This is typically in the kHz range. Devices in this category include the Electron Microscope Pixel Array Detector (EMPAD), the large dynamic range of which is due to its larger ($150\mu\text{m}$ pitch) pixels with large capacitance [161]. Another strategy to obtain a large dynamic range, implemented with the JUNGFRÄU ASIC is to use an adaptive gain [162, 163], whereby once the signal induced on a pixel exceeds a certain threshold, additional capacitance is brought on-line within the pixel. This means noise is low-enough that sensitivity to single-events is possible in the low-flux regime, while in the high-flux regime there is sufficient dynamic range to register the signal due to multiple incident electrons, which can then be converted into an electron count based on device calibration. The successor to the EMPAD, the EMPAD-G2 adopts a similar scheme in combination with

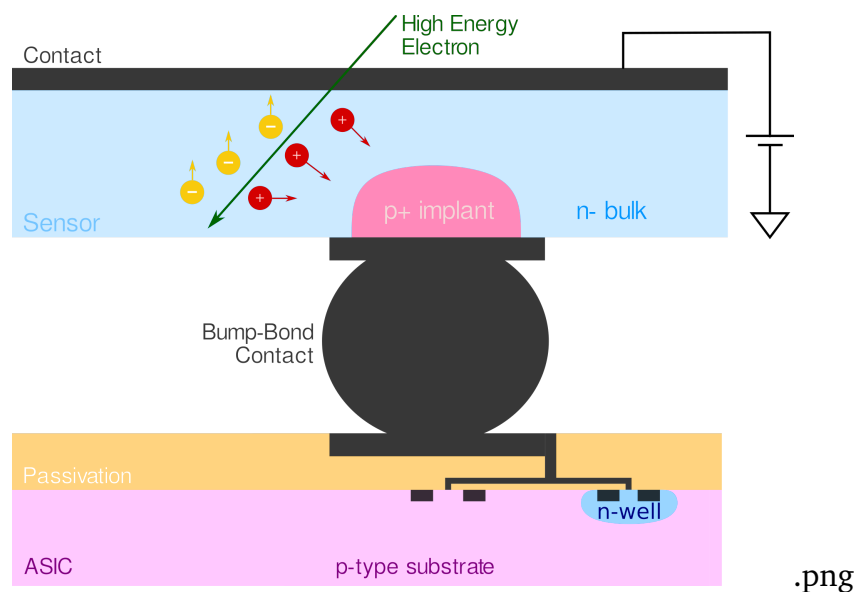


Figure 2.18: Figure showing a single HPD pixel. An external bias is applied to the backside of the sensor, which ensures rapid readout of charge carriers produced by incident electrons. For devices used in electron microscopy, the sensor is typically at least $300\ \mu\text{m}$ thick, though when using, 300 keV electrons a thicker sensor is required. The pixel pitch is defined by the spacing of the bump-bond pads. The ASIC contains all the signal-pro is bump-bonded to the ASIC. Not drawn to scale.

its large capacitance, incrementing a counter whenever a pixel’s capacitor is saturated and is emptied. This has enabled it to maintain a linear response to 300 keV electron flux $> 100\ \text{pA}$ per pixel and reach frame rates of 10 kHz [164].

The name of the second kind of detector i.e. the term “counting” is arguably somewhat misleading as depending on the exact kind of signal processing implemented, such devices can register other details about the signals that surpass the user-set threshold. In addition to counting the number of events that surpass the threshold, they can record time signals are over the threshold i.e. the time-over-threshold (ToT) or the time at which the induced signal surpasses the threshold, usually referred to as the time-of-arrival (ToA). The majority of the counting devices used in electron microscopy, including the Medipix3 [177] devices studied as part of the present work operate simply as counting detectors. While the original Timepix detector [185], can operate in counting, ToT or ToA modes of operation, when it has been used in electron microscopy, it has typically been used in counting mode [186–188]. Its successor, Timepix3 [180], can simultaneously record the ToT and ToA data associated with a hit and is notable for being the first DED able to operate in a data-driven mode of operation. For counting detectors, on-pixel count rates are typically in the kHz regime, though this is not linked to the device frame-rate, but instead to the deadtime of the on-pixel electronics [40].

HPDs have been shown to offer excellent performance in terms of MTF and DQE when using low-energy ($\leq 120\text{keV}$) electrons [50, 174, 184]. However, as the thick

Manufacturer/ Commercial Vendor	Name	Intended/ Demonstrated Application(s)	Intended Electron Energy (keV)	Pixel Pitch (μm)	FOV	Frame Rate (fps)
Gatan	Stela [165]	4D-STEM [166]	30 - 200	75	512 \times 512 or 1024 pixels 38.4 \times 38.4 or 76.8 mm ²	2000 (16-bit full frame) - 16000 (8-bit, binned 128 \times 128)
PNDetector/ JEOL	pn-CCD/4D- Canvas [167]	4D-STEM [168], high-speed, dynamical and <i>in situ</i> studies [169]	5 - 300	48	264 \times 264 pixels 12.62 \times 12.64 mm ²	1150 (full-frame) 4000 (4 \times binning)
Thermo Fischer	EMPAD [161]	4D-STEM [170]	60 - 300	150	128 \times 128 pixels 19.2 \times 19.2 mm ²	1100
	EMPAD-G2 [164]	4D-STEM	60 - 300	150	128 \times 128 pixels 19.2 \times 19.2 mm ²	10 k
	ARINA [171]	4D-STEM	30 - 300	100	192 \times 192 pixels 19.2 \times 19.2 mm ²	120 k
DECTRIS	ELA [172]	EELS [40]	30 - 200	75	512 \times 1024 38.4 \times 76.8 mm ²	2250 (16-bit full frame) - 18 k (8-bit ROI)
	SINGLA [173]	cryoEM (SPA [174] & microED [175])	30 - 200	75	1062 \times 1028 79.65 \times 77.1 mm ²	2250 (16-bit) - 4500 (8-bit)
	QUADRO [176]	Materials Science (4D-STEM, <i>in situ</i> /dynamic TEM, LEEM/PEEM)	30 - 200	75	512 \times 512 38.4 \times 38.4 mm ²	2250 (16-bit full frame) - 18 k (8-bit ROI)
Medipix3 Collaboration (CERN)	Medipix3 [177]	4D-STEM [157], high-speed, <i>in situ</i> studies [159], EELS [178], microED [179]	5 - 300	55	56/512 \times 256/1024 pixels 14.08/28.16 \times 14.08/56.32 mm ²	1 k (12-bit)- 12.5 k (1-bit)
	Timepix3 [180]	cryoEM (SPA) [51], 4D-STEM [181], EELS [182]	5 - 300	55	(single-chip/typical tiling) 256/512 \times 256/1024 pixels 14.08/28.16 \times 14.08/56.32 mm ²	Data-Driven
PSI Detector Group	EIGER [183]	microED [184], diffraction-based studies generally	8 - 300	75		2 k (32-bit) 23 k (4-bit)
	JUNGFRAU [162]	microED & diffraction-based studies generally [163]	2 - 120 000	75	256/512 \times 256/1024 pixels 19.2/38.4 \times 19.2/76.8 mm ² (single-chip/single module)	2000

Table 2.2: Table summarising the current generation of HPDs for use in (S)TEM. Note that in the case of the Medipix3 and Timepix3 detectors that there are a number of commercial vendors that have licensing agreements to sell systems based around the Medipix3 and/or Timepix3 technology into their detector systems. Likewise, several of the DECTRIS products (the ELA, SINGLA and QUADRO) are based around the EIGER ASIC developed at the Paul Scherrer Institut, with Gatan's STELA in turn being based around the ELA. The same caveats attached to those applications that are listed without a citation noted for Table 2.1.

sensors of HPDs entirely stop even 200 and 300 keV electrons, high-energy electrons travel laterally (i.e. perpendicular to the initial direction of travel of the electron when it enters the sensor) over large distances HPD sensors. They typically scatter over and are registered by multiple pixels [18, 184]. This introduces blurring into the images recorded, and the spatial resolution of HPDs is significantly poorer than that of monolithic devices when using high-energy electrons [48]. Furthermore, their pixel pitch is usually much larger than that of monolithic devices (as can be seen by comparing Tables 2.1 and 2.2). Consequently, although the magnification can be changed such that the smallest feature that is resolvable is the same for a given HPD as it is for a given monolithic device (by increasing the magnification) the FOV of the former will be more limited than that of the latter. While in principle the FOV of HPDs could be improved by increasing the number of pixels on a given device (e.g. by tiling several chips together to create a single device), the device size is ultimately constrained by the design of current generation TEMs as well as the effect of lens aberrations which increase the further off-axis the electrons are. As a result, HPDs have generally never been regarded as a competitive alternative to MAPS for imaging applications, in particular cryoEM.

The spatial resolution of HPDs can be improved by localising the entry point of electrons as has been possible with monolithic devices since at least 2013 [143, 144]. However, this is a much more challenging task with HPDs than it is with monolithic devices. As discussed above, in monolithic devices, the lateral spread in signal is largely due to the diffusion of charge-carriers in the sensor, with their being relatively little lateral spread in signal due to the scatter of the primary electron itself (at least when using primary electron energies ≥ 200 keV). In HPD sensors, when using high-energy electrons, the lateral spread in signal is largely due to the scatter of the electron itself. The stochastic nature of the trajectories of high-energy electrons in the thick sensors of HPDs mean that an electron is sometimes not registered by the pixel in which it enters the sensor [18]. Furthermore, electrons tend to deposit most of their energy towards the end of their trajectory [184], so that the entry point of incident electrons cannot be determined through using the (weighted-)centre-of-mass of pixel clusters as is true for monolithic devices used in electron microscopy [189] (or indeed HPDs in other contexts [190]). Consequently, it is only recently (2020) that electron localisation in the context of TEM was successfully demonstrated with an HPD. The first such demonstration of this used a convolutional neural network, trained on simulated data, to determine the entry point of the electron based the ToT and ToA data recorded by a Timepix3 detector [51].

It should be noted that, in addition to monolithic devices and HPDs, there is a third kind of DED. Fully depleted CCD cameras, known as pn-CCDs, whereby a bias is applied to the sensor, do not require a scintillator to increase the dynamic range of the pixel wells and are also more radiation hard [167]. These were initially

developed for X-ray imaging in astronomy [191] and for use in X-ray free electron lasers (XFEL) [192] but have been used successfully in electron microscopy for 4D-STEM [168, 193] and filming dynamical processes [169] and have been evaluated for use in cryoEM [194]. To a certain extent, the pn-CCD can be grouped with HPDs (for the sake of dividing detectors on the basis of the electron microscopy applications for which they are well suited) as its thick sensor ($450\ \mu\text{m}$) and relatively large pixel pitch ($48\ \mu\text{m}$) mean its response is broadly similar to that of HPDs that are able to record the energy deposited in each pixel. Also noteworthy is the fact it has proven possible to localise the entry point of high-energy electrons in the pn-CCD just by using the energy information recorded by individual pixels combined with an auto-encoder neural network architecture [195]. This demonstrates both that there are multiple approaches to electron localisation for devices with thick sensors and that, in keeping with the work performed with Timepix3, ToA information is less important for the purposes of localising the entry point of electrons (in the spatial domain) as ToT/energy information.

Given that monolithic devices are beginning to become more competitive for those applications that HPDs have tended to be preferred, combined with the seeming unsuitability of HPDs for those applications that MAPS detectors have dominated, it is worth considering future trends and whether MAPS devices will come to be the default kind of detector or whether it will continue to be the case that there are some applications for which HPDs are preferred, especially in light of recent advances in extending electron localisation to HPDs to improve their spatial resolution. Although the frame-rates of monolithic devices have improved they are still (for the most part) not comparable with those of HPDs. Likewise, their count-rates are still not on the same order as those of HPDs: whereas the count-rate of a HPD can be on the order of $10^6 - 10^9$ depending on electron energy, device architecture and settings [40, 164], the count-rates of monolithic devices continue to be on the order $< 20\ \text{e}^-/\text{pixel}/\text{s}$ [107, 126].

Additionally, data-driven readout, whereby hit information is read-out of individual pixels as soon as the hit is registered by the pixel is easier to implement in HPDs than it is in monolithic devices. This is because thresholding and hit identification can be done by individual pixels on an HPD, whereas for monolithic devices this must be implemented in the periphery of the ASIC or else in the DAQ system, requiring increased computational requirements to process and compress the data once it is off-chip [126, 196], Operating in a data-driven mode of operation reduces (if not eliminates) the read out of redundant data (i.e. empty pixels that record no electrons), increasing device speed and, in principle, throughput of useful data. It should be noted that the data-driven operation comes with the drawback of an increase in dead-time, as in addition to the time the pixel is not receptive to further hits because it is already processing a signal there is also the time it is sending the processed signal off-chip.

Nevertheless, data-driven operation has the potential to open-up time-resolved studies at a temporal resolution that would be unfeasible when operating in a frame-based, due to the increased amounts of data that need to be read out. Additionally, reading out only isolated electron clusters facilitates the identification of individual hits. For instance, the data-driven mode of Timepix3, which was the first DED to be able to operate in this way, was exploited in the work described above that successfully identified the entry point of 200 keV and 300 keV electrons using Timepix3. It has also been utilised to achieve STEM scan dwell times on the order of [181] and has also opened up the prospect of EELS at nanosecond resolution [182].

In light of the above, the improved frame rates and monolithic devices are likely, for the foreseeable future, to make it easier for such devices to be used for diffraction-based experiments (including 4D-STEM, microED and EELS) or time-resolved studies, though they may be intended and purchased primarily for high-resolution imaging. However, cases where a detector is intended primarily for time-resolved studies or diffraction-based modalities where a linear response to high flux and high frame-rates are the priority, HPDs will continue to be the detector of choice. Ongoing efforts to improve the spatial resolution of HPDs with machine-learning based approaches may in the long-term make them more competitive for imaging applications, though it is more likely, at least in the mid-term to make it easier to perform imaging experiments with detectors that have been purchased primarily for use in other experiments.

An exception to this, is in low-energy (100 keV) SPA cryoEM, which in recent years has been recognised as offering an improved level of contrast for a given level of sample damage compared with when using 200 keV and 300 keV electrons [197]. When using 100 keV electrons, monolithic devices lose their advantage compared with HPDs as, even in very thin sensors, 100 keV electrons will scatter laterally, rather than pass through the sensor. Relative to the pixel pitch of monolithic device, the lateral spread of signal due to the scatter of 100 keV electrons is much larger than is the case for HPDs. HPDs therefore offer enhanced imaging performance compared with monolithic devices for 100 keV cryoEM and are likely to be preferred to monolithic devices for this application [174].

In addition to using neural networks to identify the entry point of electrons, another approach to improving the performance of HPDs lies in investigating alternative sensors. Unlike both monolithic devices and the pn-CCD, HPDs can have sensors from materials other than Si, as the readout electronics are manufactured separately from the sensor. There has been extensive research into using high- Z sensors with HPDs with high- Z sensors for use in photon science, motivated by the reduction in quantum efficiency of Si sensors for photons with energies above 2 keV (i.e. “hard” X-rays and γ -rays) [198]. This is due to the decreased cross-section for photoelectric absorption with increasing photon energy for a given value of Z , as well as the

relatively low density of Si crystals. Consequently, the mean-free path of hard X-rays and γ -rays in Si is sufficiently long that the probability of interaction is low in even the thickest practicable Si sensors. The development of fourth-generation synchrotron sources as well as the increasing prominence of XFELs as a scientific tool require devices with good quantum efficiency at high photon energies [199] that are able to handle high photon flux, with up to 10^5 photons incident in a single pixel within a few tens of femtoseconds in XFELs [200]. This latter requirement of course has its counterpart in electron microscopy, with diffraction-based experiments and time-resolved experiments needing detectors that are able to withstand high incident electron flux. Other fields that either require or would benefit from HPDs with high- Z sensors to make HPDs beneficial are high-energy X-ray and γ -ray imaging in astronomical nuclear and medical contexts [201–203].

The motivation for investigating high- Z sensors for TEM is somewhat different from that in photon science. As electrons interact strongly with matter, the quantum efficiency of even thin Si sensors is not usually of concern (assuming an appropriately thin entrance window), hence the success of MAPS devices with epitaxial Si sensors outlined above. Instead, as discussed in Chapter 1, the increased stopping power of high- Z sensor materials is of interest for their potential to reduce the range of incident electrons and thereby improve the device PSF. Improvement in HPD performance for high-energy electrons has been expected since the earliest studies characterising HPDs with Si sensors for TEM, which established that their performance, while excellent for low-energy electrons, deteriorated at higher energies due to the lateral scatter of electrons across multiple pixels [18]. At the same time, it has been anticipated that increased backscatter from high- Z materials may mitigate any improvement in performance due to a reduced PSF by reducing the device quantum efficiency and DQE [48]. There is also the need to understand how the differences in material properties and processing technologies, leading to e.g. greater leakage currents, defects present in the sensor and different entrance window composition due to different contact structures being necessary, affect device performance and system design specifically in the context of electron microscopy.

2.5.3 HPDs and High- Z Sensors

Considering the physics of semiconductors and of electron interactions with matter, as well as principles of detector theory outlined in Chapter 1, there are several desirable properties in a semiconductor used as the sensor of a radiation detector. First, a sufficiently large bandgap so that thermally generated electron-hole pairs are kept to a minimum without cooling being necessary, or at least, only minimal cooling being necessary. At the same time, the band gap should still be small enough that each incident quanta of radiation produces a large number of electron-hole pairs so

it is easy to distinguish a hit from background noise and to ensure the best possible energy resolution (as is discussed in Section 1.5.1). Energy resolution is maximised if incident quanta deposit all of their energy in the sensor, with none escaping due to backscatter, or otherwise escaping, as it reduces the variation in the signal produced by each incident quantum of radiation. Consequently, to reduce the likelihood of electron backscattering (largely due to high-angle Rutherford scattering), low values of Z are preferable. This also reduces the likelihood of Compton scattering, which has a similar effect for X-rays that Rutherford scattering has for electrons in that it enables X-rays to scatter out of the sensor.

However, a low value of Z is in tension with high values of Z having increased stopping power. This is desirable in imaging detectors both from the perspective of improved spatial resolution (for electron microscopy) but also from improved energy resolution as it reduces the likelihood that charge is “lost” due to lateral drift to a pixel that registers very little charge so that it is obscured by the detector’s noise level. At the same time, high- Z materials tend to be compound ones (with the exception of Ge, which needs to be cooled to cryogenic temperatures due to its very small bandgap), which tend to have poorer charge carrier properties due to their increased density of defects. Poor values of $\mu\tau$ can also have an adverse impact on energy resolution and efficiency as they lead to incomplete collection of charge from the sensor.

There is no single “perfect” detector material, though some materials are more suitable for some applications than others depending on the balance of the trade-offs that have to be made. Table 2.3 summarises some of the key properties of various semiconductor materials that have been used or have been investigated for use with HPDs. It can be seen that there is significant range of values for the different properties and even variability between different “versions” of the same material, as with the different varieties of CZT or different generations of GaAs:Cr. Another point that is apparent is the disparity between the charge-carrier transport properties of the compound semiconductors compared with the single-element semiconductors. The electron $\mu\tau$ product is notably better than that of the holes for the compound semiconductors, so that HPD ASICs that are bonded to such sensors need to be sensitive to signals produced by the electrons produced in the sensor by incident radiation, not only that due to holes.

Si has been the dominant choice of sensor material for use in HPDs due to the relative ease with which, large, homogeneous crystals can be grown and the well-developed planar processes for manufacturing Si sensors⁷. For tracking experiments in HEP, the application for which HPDs were initially developed, the principle drawback of Si is its limited radiation hardness [210]. Thus far, the demands made on Si

⁷ Of course, this must be recognised as the result of extensive research into semiconductors, in particular Si, and associated technologies in the latter half of the 20th century as well as the intense effort made to develop processing technologies specifically for detectors within HEP [209].

Material	Average Z	Density (g cm^{-3})	Band Gap E_g (eV)	Resistivity ($\Omega \text{ cm}$)	$\epsilon_{e,h}$ (eV)	$\mu_e \tau_e$ ($\text{cm}^2 \text{V}^{-1}$)	$\mu_h \tau_h$ ($\text{cm}^2 \text{V}^{-1}$)
Si [203]	14	2.33	1.12	10^4	3.61	>1	1
Ge [203]	32	5.44	0.66	50	2.96	>1	>1
2014 GaAs:Cr [204]	32	5.32	1.43	10^9	4.2	10^{-5}	10^{-6}
2016 GaAs:Cr [205]	32	5.32	1.43	8.5×10^8	4.2	1.83×10^{-4}	2.4×10^{-7}
2017 GaAs:Cr [206]	32	5.32	1.43	1.69×10^9	4.2	4.73×10^{-4}	5×10^{-7}
epi-GaAs [203]	32	5.32	1.43	10^7	4.2	10^{-6}	10^{-6}
CdTe [207]	50	5.86	1.44	10^9	4.35	3×10^{-3}	2×10^{-4}
Redlen CZT [208]	50	5.78	1.6	10^{10}	4.6	10^{-2}	2×10^{-5}
“High-Flux” CZT [208]	50	5.78	1.6	10^{10}	4.6	11×10^{-4}	2.9×10^{-4}

Table 2.3: Table summarising key properties of semiconductors suitable for the detection of ionising radiation and that have been investigated for use with HPDs. Properties listed include the energy required to create an electron-hole pair $\epsilon_{e,h}$ and the charge carrier mobility lifetime products for electrons ($\mu_e \tau_e$) and holes ($\mu_h \tau_h$). It should be noted that in references [205] and [206] that the $\mu_h \tau_h$ product is inferred on the basis of simulation, as the small values of μ_h mean proper determination of $\mu_h \tau_h$ is not feasible.

sensors in terms of radiation hardness have been met and the effects of radiation damage have been thoroughly investigated to the point where effective strategies for managing radiation damage have been developed [16]. However, the need for alternatives to Si when using HPDs for other applications was recognised early on. Initial attempts to assess their suitability for use in medical imaging included testing an Omega3 chip (one of the first HPDs developed at CERN for use in HEP) to a GaAs sensor [211]. The original Medipix chip, the first ASIC designed to apply the benefits of HPDs to a field outside HEP, again, medical X-ray imaging, was initially characterised bonded to both Si and GaAs sensors [212–214].

Of the various alternatives to Si, the most extensively studied for use with HPDs are various forms of GaAs, CdTe and CZT [198, 199]. Ge has also been investigated but, although there are many advantages associated with Ge, including the ability to grow large high-purity crystals, the cooling required to render the sensor functional makes the overall system impractical [215]. CdTe and CZT, formed by replacing a small amount of Cd with Zn to create a crystal with a $\text{Cd}_{1-x}\text{Zn}_x\text{Te}$ composition, where $x = 0.08 - 0.2$ [199, 202], in principle should offer the greatest improvement in PSF for the highest-energy electrons due to their high density and high average value of Z as seen in table 2.3. Table 2.3 also shows that the charge transport properties of CdTe and CZT are also better than those of modern forms of GaAs, namely GaAs:Cr, being investigated for use with HPDs (discussed below). However, the high, average value of Z means that CdTe and CZT may suffer the greatest reduction in efficiency due to backscattering.

Beyond this, CdTe and CZT have other drawbacks compared with GaAs and Si. These include increased brittleness, which makes the manufacture and hybridisation of thin sensors challenging [199], which, on the basis of the results presented in Chapter 4 and 6, may be preferable for electron imaging, though how important this is likely depends on the maximum bias that can be applied to the sensor. CZT shows increased resistivity compared with CdTe, which means the maximum bias that can be applied without the leakage current becoming too high for the device to be usable is higher, though the thinnest sensors currently available are at least 2mm thick [208] while for CdTe the thinnest sensors are $750\mu\text{m}$ [216]. For both materials, the lack of research into the manufacture of thinner sensors is likely because the focus has been on sensor development for high-energy photon imaging, for which thicker ($500\mu\text{m}$) sensors are preferred to improve device quantum efficiency. This may therefore be something that could be improved if there were sufficient incentive due to e.g. high demand for thinner CdTe or CZT sensors for use in electron microscopy.

Another challenge associated with CdTe and CZT when working with photons is fluorescence from Cd and Te in the 20 - 30 keV range, leading to increased lateral spread in signal as well as the loss of signal due to the escape of fluorescence photons. Fluorescence, strictly speaking, refers to situations whereby, an atom that has

photoelectrically absorbed an incident photon returns to the ground state by emitting a characteristic X-ray. In addition to fluorescence triggered by an external source of photons, in compound semiconductors there can be a particular issue whereby characteristic X-rays of one atom species that are close in energy to the binding energy of electrons in the shells of the other atom species leads to high number of fluorescence events. This is also an issue for GaAs sensors, though the lower energy of fluorescence photons from Ga and As means their range and likelihood of escape is reduced compared with Cd and Te fluorescence photons [217]. Experimental and theoretical studies seem to confirm that the impact of fluorescence on the imaging performance of GaAs sensors is greatly reduced compared with the impact in CdTe sensors and can be regarded as negligible [218, 219]. For example, in CdTe, the Te K_{α_1} X-rays with energy 27.47 keV trigger the production of significant levels of Cd K_{α_1} X-rays with energy 23.17 keV. Likewise, in GaAs, the cross-section for the photoelectric absorption of As K_{α_1} X-rays with energy is significant.

In the context of electron microscopy, fluorescence is not expected to contribute significantly to the spread of signal generated by incident primary electrons. The low levels of Bremsstrahlung produced by incident electrons of the energies currently used in TEM is unlikely to trigger significant levels of fluorescence. At the same time, the extent to which the production of characteristic X-rays and other secondaries contribute to the lateral spread of signal in the sensor (be that a high- Z one or standard Si) is unclear, and one of the questions this thesis seeks to answer.

The main drawback associated with CdTe and CZT is polarisation, whereby the electric field in the sensor deteriorates over time due to the trapping of charge carriers in defects in the sensor, which leads to a build up in space charge. There are two mechanisms by which polarisation can be induced. Firstly, it can be induced by the application of a bias to device with Schottky contacts [220]. Over time, charge carriers are trapped under the contacts, leading to a build-up of space charge that leads to an electric field counter to that due to the applied bias. The electric field and by extension device performance can be restored by refreshing the bias, and the frequency with which this must be done ranges from minutes to hours depending on device operating conditions [220–222]. CdTe sensors with Ohmic contacts and CZT sensors with both kinds of contacts are not susceptible to this kind of polarisation, though they can display flux-induced polarisation [223]. This second kind of polarisation arises when the sensor is exposed to a high flux of incident radiation, leading to large number of charge carriers in the sensor and, consequently, a high number of trapped holes. The only way to remedy this kind of polarisation is to remove or reduce the external source of radiation [224].

Recently, a new kind of dedicated “high-flux” CZT has been developed, which has improved hole lifetime and, therefore, a reduced propensity to build-up space-charge in the sensor [208]. It has shown to be highly stable for photon fluxes of up

to [225, 226]. This improvement in high-flux performance does come at the cost of reduced spectroscopic performance, as photons that are absorbed close to the pixel electrode induce a signal with opposite polarity on neighbouring pixels, leading to a so-called “crater” effect. However, this can be compensated for applying corrections based on the depth of the photon interaction [227]. This is an effect that has also been observed in GaAs:Cr sensors [205, 206], though for both CZT and GaAs:Cr this is an issue that is only seen when using integrating ASICs. It should be noted that it is not a phenomenon that has been encountered in any of the measurements presented as part of the present work. While this can be attributed to the fact that most of the measurements presented herein have been acquired with a counting detector, it may also point to the fact that as electrons deposit their energy close to the high voltage contact, this crater effect is unlikely to be encountered except in sensors thinner than those currently being manufactured.

The GaAs used in early studies with HPDs tended to use semi-insulating GaAs grown via the liquid encapsulated Czochralski (LEC) method [213, 228, 229]. This material displayed instabilities in the electric field and suffered from poor charge-transport properties. These were largely due to the EL2 trap, a complex of an interstitial As atom and an As atom on a Ga lattice site. The EL2 trap determined the electric field within the sensor and limited the sensitive volume that could be depleted by applying a bias, though initial characterisation suggested that this could be improved upon with cooling [229]. When ionised, these traps gave rise to EL2⁺ defects that act as recombination centres due to a large electron trapping cross-section. Epitaxial GaAs was also investigated [230], but while this material featured fewer traps and had better charge transport properties, the thickness of the depletion volume of such sensors was limited to $\approx 100\mu\text{m}$ [231, 232]. The development of GaAs:Cr by researchers at Tomsk State University [233–237] represented a significant breakthrough, making possible thick sensors with good electron $\mu\tau$ product due to the Cr dopants compensating the EL2 vacancy. This rapidly attracted significant interest within the photon science community and the material has now been extensively studied bonded to a number of different ASICs (both counting [230, 238] and charge integrating [204, 239]) under a range of experimental conditions. Among the counting HPD ASICs with which it has been characterised are several members of the Medipix-series of detectors [230, 240–242], including the Medipix3 ASIC that is used in this work [238]. It is produced by growing n-type GaAs via the liquid encapsulated Czochralski method which is then diffused with Cr at high temperature.

Like CdTe and CZT it features defects, the precise nature of which are dependent on the exact growth process. The lines observed in the 2014 [204] and 2016 [205] generations of GaAs:Cr are not dissimilar to the defects observed in CdTe and CZT, which consist of dislocations at grain boundaries that manifest as lines along which the electric field is distorted leading to increased count rates and bubbles associated

with Te inclusions that are associated with higher leakage currents [243]. These different generations of GaAs:Cr arise due to variations in the LEC method used to grow the n-type GaAs due to changes on the part of the manufacturer (either in the process used by the manufacturer or a change in the manufacturer themselves). A newer generation of GaAs:Cr, the 2017 generation, does not appear to display any line defects though it still displays a granular structure [206]. The sensors characterised as part of the present work are from the 2014 and 2017 generations of GaAs:Cr.

Independent of the generation of GaAs:Cr used, the response of GaAs:Cr sensors have been shown to be highly stable at lower fluxes of incident radiation and radiation hard for incident fluxes of 12 keV photons of up to 3×10^8 photons $\text{mm}^{-2}\text{s}^{-1}$ [244]. This means that flat field corrections can be used to reliably correct for variation in response across the pixel matrix, albeit with the caveat that a such a correction does not mitigate for the variations in pixel shape and the geometric distortions these introduce into images [240]. However, when exposed to high incident photon flux, flux-induced polarisation observed, with this increasing with photon energy. This has an adverse impact on the charge-collection-efficiency of sensors and their performance [245]. The extent to which polarisation is an issue in the context of electron microscopy is unclear, given the different mechanisms by which electrons and photons interact with a sensor. It seems likely, however, that it will be an issue when using high electron energies and/or high fluxes of incident electrons. Nevertheless, given the overall stability of GaAs:Cr sensors and their extensive characterisation for photons with ASICs from the Medipix series of detectors, GaAs:Cr represents a natural choice as a starting point for beginning to consider alternatives to Si for use with counting DEDs.

2.6 Summary

TEM and STEM are powerful tools for studying nature at nanoscale and below resolutions. Underpinning their value and operation are the small wavelength of accelerated electrons; the range of signals produced by the interaction of electrons with matter and the relative ease with which electrons can be produced by electron sources as well as manipulated with electric and magnetic fields. The detector system used in a microscope is the final stage in the image forming process and as such places a limit on the types of signal that can be acquired as well as the quality of the data recorded. Traditional, indirect detector technologies have unnecessarily limited the data that can be acquired and by extension the experiments that can be performed. The development of direct detection devices has led to a step-change in electron microscopy, opening up range of experimental possibilities including cryoEM in the life sciences, time-resolved studies of dynamical processes and the burgeoning sub-field of 4D-STEM.

Two types of DED have developed in parallel. Monolithic devices offer excellent performance for applications requiring high spatial resolution with a large FOV when using high-energy electrons, but their performance deteriorates at lower electron energies. Given the advantages of HPDs in terms of speed and radiation hardness compared with monolithic devices, as well as their excellent imaging performance using low-energy electrons, it is natural to speculate as to whether their performance at high-energies can be enhanced, further increasing their versatility and the range of applications for which they are suitable. One obvious avenue of investigation is the use of alternative high- Z materials to replace the Si sensors of HPDs, which should in principle improve device performance by reducing the range of the lateral scatter of electrons in the sensor. Such materials have been the subject of extensive study within the photon science community, and while CdTe, CZT and GaAs:Cr all have drawbacks compared to Si in the form of defects, variations in response or polarisation, they are nevertheless sufficiently stable that their use in electron microscopy can be countenanced. GaAs:Cr is particularly promising, due to its apparent overall stability, though thorough investigation of its behaviour when working with electrons is required and this represents one of the key areas of investigation of the present work.

3

Methods and Materials

3.1 Introduction

In this chapter, an overview is given of the experimental procedures and computational methods used to obtain the results presented in Chapters 4-7. As the majority of the experimental work consisted of characterising devices based on the Medipix3RX ASIC, Section 3.2 presents an outline of how the ASIC operates and its key features, as well as the associated hardware and the specific devices characterised. The methods used to determine the detector performance metrics outlined in Chapter 1 are described in Section 3.3, along with an outline of how the devices' counting thresholds were calibrated, which is crucial for the accurate evaluation and comparison of detector response. Complementary to the experimental measurements have been simulations of the response of HPDs with Si sensors and the interactions of electrons with various high-Z sensor materials. The computer packages used for these simulations are described in Section 3.4.

3.2 Detectors and Associated Hardware

3.2.1 The Medipix3RX ASIC

The Medipix3RX ASIC [177] (henceforth referred to as the Medipix3 ASIC) was the principle ASIC used in this work, providing a platform to investigate the characteristics of different sensors in the context of TEM. The Medipix series of ASICs was developed with the aim of applying advances in detector technology at CERN for the LHC to medical X-ray imaging. However, as alluded to in Chapter 2, they have gone on to be used in a wide range of fields for a plethora of applications. This includes electron microscopy, in which they have been adopted for use in SEM [187, 188],

high-speed filming of dynamical processes [159, 160], 4D-STEM [3, 4], EELS [178] and microED [155, 156, 179].

Medipix3 ASIC is a counting detector with a single chip consisting of a 256×256 array of nominally $55 \mu\text{m}$ pitch square pixels. The chips are buttable on three sides so that multiple chips can be arranged in $2 \times M$ arrays to create larger devices. Additionally, not every pixel need be bump-bonded to the sensor and by bonding only one in four it is possible to create devices with a pitch of $110 \mu\text{m}$. The on-pixel electronic circuitry is composed of an analogue front-end which processes the signal induced on the pixel by incident radiation and digital back-end, which handles the counting and readout of signals that surpass the counting threshold. Both the analogue and digital portions of the pixel circuitry are marked in Figure 3.1. The primary components of the analogue front-end are an amplifier and semi-gaussian shaper that amplify and convert the signal induced in a pixel into a voltage pulse, while the key components of the digital back-end are two linear feedback shift registers, two discriminators and an arbitration logic. The analogue front-end is based on a Krummenacher architecture [246], whereby the return of the shaper output to baseline is controlled by a bias current referred to as I_{Krum} , as shown in Figure 3.2. In the case of the Medipix3 ASIC, the value of I_{Krum} is controlled by an 8-bit depth digital-to-analogue converter(DAC) with a current range of 0-60 nA. Each DAC step therefore represented a change of 234 pA in the value of I_{Krum} . It is usual when discussing I_{Krum} to state its value in terms of DAC on the understanding that these map linearly to the current. The value of I_{Krum} also controls the maximum leakage current that can be induced on a pixel prior to it becoming unresponsive [247] Another important feature of the pixel circuitry is that the linear feedback shift registers can be configured to act as counters (with a variable bit-depth ranging from 1-bit to 12-bit) during data acquisition or, when the chip is read out, shift registers .

In the Medipix3's most basic mode of operation, single-pixel mode (SPM), each pixel operates independently and compares the voltage pulse due to the signal induced on the pixel to one of the two discriminators. The threshold that a voltage pulse has to surpass for the signal to be counted is set by the user for the entire pixel matrix. To minimise variation in response across the pixel matrix due to imperfections in the manufacturing process, each pixel of the ASIC has its own 5-bit DAC to allow local threshold adjustment. If the voltage pulse surpasses the user-set threshold, then one of the shift registers is incremented. When the two linear feedback shift registers are configured to operate independently, the device can have two independent thresholds in SPM (referred to here, and in Figure 3.1, as TH0 and TH1), in which case, each of the two discriminators have a different threshold and are associated with one of the two linear feedback shift registers. Alternatively, the two registers can be configured to operate in tandem so that while one is being used as a counter during the current acquisition the other behaves as a shift register for the simultaneous readout of data

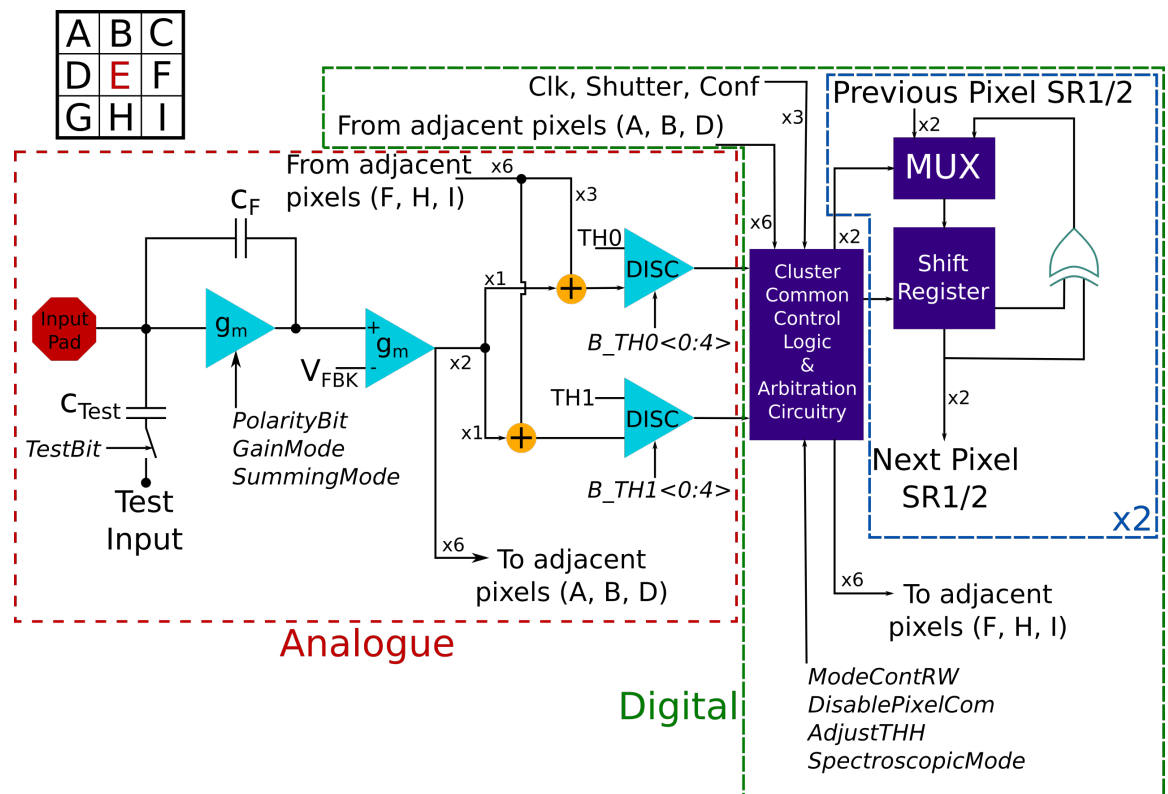


Figure 3.1: Schematic of the circuitry of a single Medipx3 pixel. Pixels can communicate with their immediate neighbours (at both their corners and along their edges) depending on the mode of operation it is set to work in. For example, the schematic shows how the central pixel “E” can communicate with its neighbours A, B, D, F, H, and I at its top left and bottom right corners when the detector is operating in CSM. Redrawn from references [177, 248, 249].

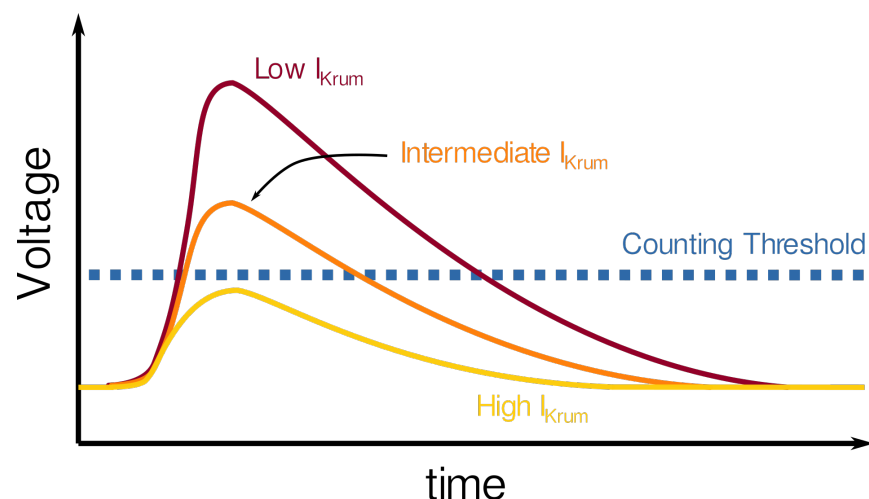


Figure 3.2: Illustration of how different values of I_{Krum} affect the voltage pulse produced by the semi-gaussian shaper. For a given signal induced on a pixel, and assuming all other pixel settings remain the same, then higher values of I_{Krum} will cause the voltage pulse to return to baseline more quickly, leading to a shorter pulse with a reduced peak. If the counting threshold voltage remains the same, then using a higher value of I_{Krum} can cause signals that would otherwise surpass the threshold to not be counted.

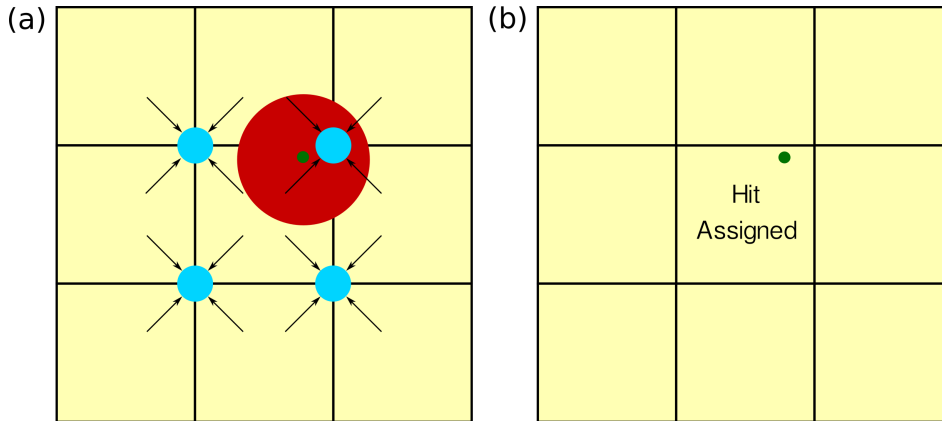


Figure 3.3: An illustration of how the CSM algorithm works. In (a), an incident photon has arrived in the central pixel but the charge it has created has been registered by three neighbouring pixels as well. Copies of the voltage pulses that are produced in each pixel are sent to summing nodes that can effectively be regarded as being at the corners of each pixel. The summed voltage pulses in the top right node surpass TH1, and the central pixel is the one that has registered the longest voltage pulse, so that in (b) the hit is assigned to the central pixel. Redrawn from reference [177].

from the previous acquisition, thereby enabling continuous acquisition and readout of data with no gap time between successive frames. The two registers may also be configured to act as a single counter with a 24-bit depth.

When the detector operates in charge-summing mode (CSM), copies of the voltage pulse produced in the analogue front-end of a pixel are sent to four summing nodes that are effectively located at the pixel's corners. These summing nodes are shared between sets of four pixels that share a corner, permitting more advanced signal processing. The voltage pulses that are received at each node are added together and compared with TH1 to determine if the signal should be counted. Hits are allocated to the pixel that has the individual voltage pulse that falls below TH0 last as the duration of the voltage pulse is proportional to the amount of the signal induced on the pixel. The underlying logic of the CSM circuitry, illustrated in Figure 3.3, is that incident radiation will deposit the majority of its energy in the pixel in which it enters the sensor, which is true for the scenario envisioned when the CSM algorithm was developed, namely low-energy photons interacting with Si sensors which usually deposit their energy in one interaction via photoelectric absorption. For such events, the sharing of charge between multiple pixels is due to the lateral dispersion of electron-hole pairs as they are drifted towards the electrodes. Of course, this does not hold true for all types of incident radiation.

If only one in four pixels are bump-bonded to the sensor, it can, in some circumstances, be advantageous to operate the device in the 'colour' versions of SPM or CSM. In colour modes of operation, the discriminators and linear feedback shift registers of the unbonded pixels are applied to the bonded pixels. Consequently, in colour SPM, the detector can have up to eight independent thresholds, depending on the

configuration of the linear feedback shift registers, whereas in colour CSM, there are four independent thresholds against which the summed voltage pulses from sets of four pixels are compared. A $55\ \mu\text{m}$ device can also be used in a colour mode of operation, with the drawback that three out of four pixels are not sensitive to incident radiation.

3.2.2 Overview of Devices and Associated Hardware

The sensors of the Medipix3 devices characterised as part of this work are as follows:

- A $300\ \mu\text{m}$ thick Si sensor with $55\ \mu\text{m}$ pitch with p-in-n implants and 500 nm Al backside¹ contact.
- A $300\ \mu\text{m}$ thick Si sensor with $110\ \mu\text{m}$ pitch with p-in-n implants and 500 nm Al backside contact.
- A $500\ \mu\text{m}$ thick Si sensor with $55\ \mu\text{m}$ pitch with p-in-n implants and 500 nm Al backside contact.
- A $500\ \mu\text{m}$ thick GaAs:Cr sensor with $55\ \mu\text{m}$ pitch with Ohmic Ni contacts, the backside one of which is 500 nm thick.

Although the primary difference between the four devices was their sensor, they also differed in the form of the printed circuit board (PCB) on which they were mounted. The two devices with $300\ \mu\text{m}$ thick Si sensors were assembled at CERN, while the two devices with $500\ \mu\text{m}$ thick sensors were assembled with boards designed at Diamond Light Source Ltd. (DLS). This difference in PCB merely reflects the different origins of the devices. The two different PCB layouts are shown in Figure 3.4. The two PCBs conformed to the same specification and were operationally identical, aside from the fact that only the DLS PCB was equipped with a Lemo connector for the purposes of supplying a bias to the detector beyond that which could be supplied by the data acquisition (DAQ) system via the VHDCI connection. Additionally, the chassis used to install different devices on the Tecnai T20 TEM, used for the majority of the measurements presented in this thesis, had to be adaptable to accommodate the different footprints of the types of PCB. Photographs of this chassis are seen in Figure 3.5, while Figure 3.6 shows a photograph of the Tecnai T20 with the port used to install detectors marked.

The DAQ used to control and readout all the Medipix3 devices characterised in this work was the Merlin [250, 251] readout system developed by the DLS Detector Group for use with Medipix3 devices and commercialised by Quantum Detectors Ltd. This can

¹ Despite the name, this is the contact that is on the surface of the sensor that is not bonded to the ASIC and that is (usually) the side that is illuminated with incident radiation. This naming convention, which is standard within the community, is based on regarding the face of the sensor that is bonded to the ASIC as the “front”.

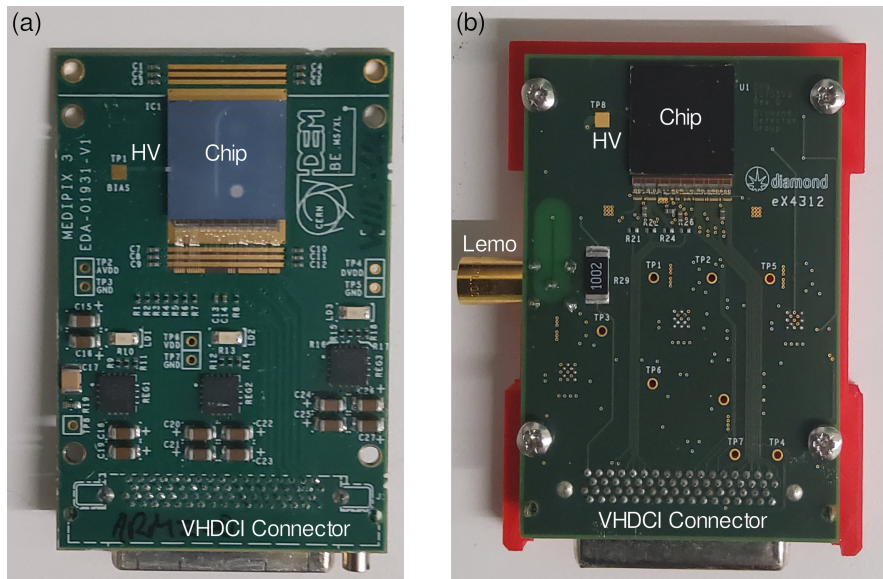


Figure 3.4: Photographs of (a) the CERN Medipix3 chipboard and (b) the DLS Medipix3 chipboard. In both (a) and (b) the detector (chip) is glued to the PCB, with power, commands and readout of the chip occurring through the bump bond wires that connect the PCB electronics to input/output pads on the chip. The bias to the sensor is supplied through a separate wire marked "HV". Power to the board itself as well as connection to the DAQ system is via a very-high density cable interconnect (VHDCI) connector. In the case of (a), the bias voltage is limited to that which can be supplied via the VHDCI connector, while in (b) the lemo connector can be used to supply a bias sourced from an external high voltage unit.

read-out detectors at rates of 100 Hz continuously or 1 KHz in bursts of 1200 frames. It connects to a given PCB by means of a VHDCI connection, through which it can supply a bias to the detector's sensor of 0-120 V. Consequently, devices that require a bias outside this range must be biased using an external high voltage supply. In the case of the three Si devices, the bias to the sensor was supplied from the Merlin DAQ. This was set 90 V for the 300 μm thick sensors and 110 V for the 500 μm thick device. These are the standard operational biases for p-in-n Si sensors of these thicknesses, which ensure that the sensors are over-depleted, so that signal produced by incident quanta is quickly drifted to the readout electrodes [252]. For the GaAs:Cr sensor an external power supply was used to supply a bias of -300 V via a lemo connection. This bias was used as it has been shown to maximise the charge collection efficiency of 500 μm thick GaAs:Cr sensors [238]. The Merlin DAQ can be operated using a local graphical user interface or remotely using TCP/IP commands, which can be integrated into scripting languages such as the Digital Micrograph $\text{\textcircled{C}}$ scripting language [253].

Installing devices on the Tecnai T20 made it possible to acquire data for electrons with energies in the range of 60 keV to 200 keV for the purposes of spectral measurements, MTF, NPS, DQE and linearity of response. In Figure 3.5, a Faraday cup mounted at the end of the chassis can be seen. This was connected to a Keithly 485 Picoammeter, in order to measure the beam current for those experiments for

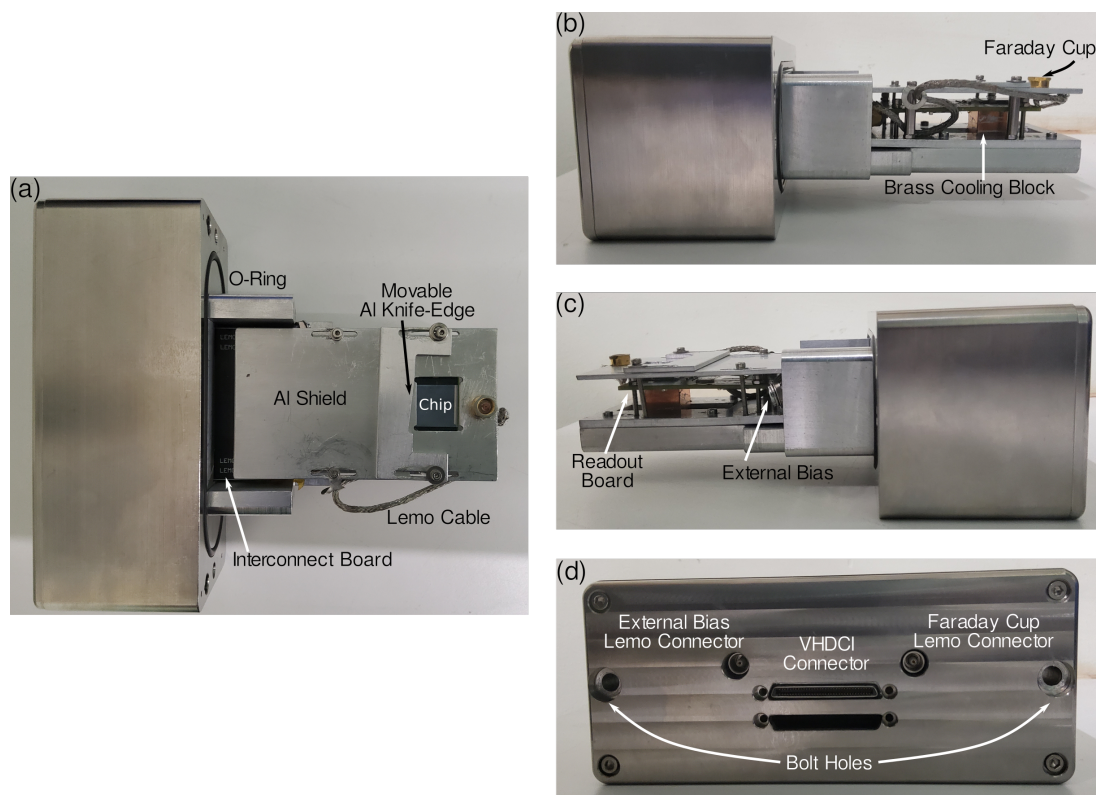


Figure 3.5: Photographs of the assembly used to install Medipix3 devices on a Tecnai T20 TEM: (a) shows an overhead view; (b) and (c) show side views while (d) shows the view of the chassis that faces outward when it is installed on a microscope. A knife-edge that can be slid in front of the chip for MTF measurements (described in Section 3.3.2) is marked in (a) as is an interconnect board which acts as a vacuum feed through connecting the detector PCB to the external VHDCI connector. Also marked in (a) and (d) are the Lemo cable and external Lemo connections used to provide an external bias to the sensor (marked in (c)) and connecting to the Faraday cup (marked (b)). The brass block marked in (b) is positioned in a recess and secured with Ag thermal vacuum paste so it acts as an efficient heat sink while still being movable to accommodate different PCB layouts.

which this was necessary, namely measurement of the detector gain and dead time, as is described in Sections 3.3.2 and 3.3.3.

To acquire 300 keV data with a GaAs:Cr Medipix3 device, the detector was mounted in a special chassis shown in Figure 3.7. This was installed on the Gatan camera block of a FEI Titan 80 - 300 (S)TEM at Karlsruhe Institute of Technology (KIT), opposite the Gatan Ultrascan CCD Camera that was permanently installed there so that it was in the same plane. Unlike the chassis used to install detectors on the Tecnai T20 TEM, this chassis does not feature a Faraday cup. Consequently, for the measurements acquired at KIT, the beam current used for determining the detector DQE was measured by acquiring images of the full beam spot with the Gatan Ultrascan, for which a manufacturer-provided analogue-to-digital units (ADU) to dose calibration was available.

This chassis was also used to install the GaAs:Cr Medipix3 device on the Glasgow ARM 200 cF (S)TEM for the purposes of confocal STEM scans outlined in Section 3.3.4,



Figure 3.6: Photograph of the Tecnai T20 at the University of Glasgow, used for the majority of experimental measurements presented in this thesis. The components of the microscope column described in Chapter 2 are labelled, along with the camera chamber and the SIS Megaview Camera. For the purposes of acquiring data with Medipix3 devices, the SIS Megaview Camera was removed and the 35mm port that it normally occupied used for the temporary installation of the chassis shown in Figure 3.5.

using the left-hand side 35mm port above the viewing screen. This experimental set-up was also used for investigating how the efficacy of applying a flat field correction to data acquired by the GaAs:Cr detector depended on the difference in the electron flux when the correction data and the corrected images were acquired. These results are described in Chapter 6. For beam current measurements for the purposes, the Keithly 485 Picoammeter was connected to the small viewing screen, with beam current measurements acquired when the electron beam was incident upon the Al edge of the screen. These measurements were then corrected on the basis of the backscattering coefficient of Al for electrons of a given energy [254].

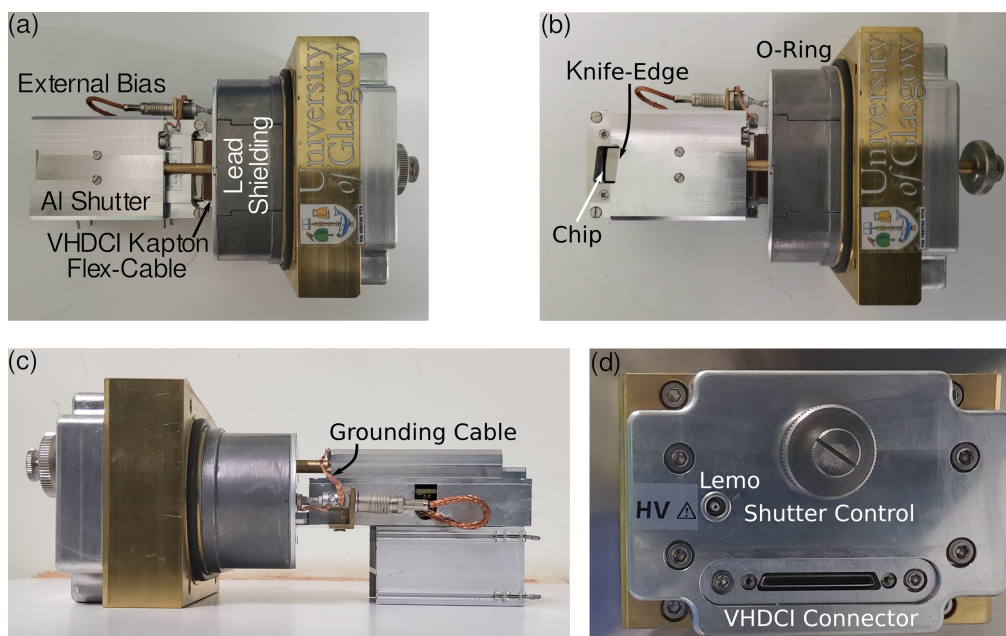


Figure 3.7: Photographs of the chassis used to install a Medipix3 device with GaAs:Cr sensor on the Karlsruhe Titan 80 - 300 (S)TEM and Glasgow ARM 200 (S)TEM: (a) and (b) show overhead views while (c) shows a side view and (d) the outward facing part of the chassis when installed on a microscope. The shutter (marked in (a)) has an edge which is at an angle to the chip (marked in (b)) so that it can be used as a knife-edge for MTF measurements, as described in Section 3.3.2. This shutter can be moved back and forth while the detector is in vacuum using the mechanism marked in (d). The bias to the sensor is provided by a Fast ComTech SHQ124M high voltage power supply, connected by a series of Lemo connections incorporating a vacuum feed-through. The feed-through connecting the PCB and the external VHDCI connector took the form a Kapton flex-cable.

3.3 Experimental Methods

3.3.1 Spectral Measurements and Calibration of Detectors

Although counting detectors cannot directly record an energy spectrum of the particles incident upon it, they can record a spectrum indirectly by recording data at a range of counting thresholds. With exposure to a constant distribution of quanta, measuring the number of counts recorded for a given while scanning the counting threshold over its full range, is equivalent to measuring the distribution of pulse heights induced on detector (as a count is only registered if the pulse exceeds a given counting threshold). As the pulse height is proportional to the amount of energy deposited in a pixel, this also provides a distribution of the energies deposited on a detector. It is usual to differentiate the number of counts recorded by a counting detector as a function of threshold to create a differential pulse height spectrum for the purposes of displaying energy spectrum data. Peaks in such distributions correspond to a large number of pulse heights being found at that energy, while minima indicate relatively few pulse heights at that energy [6].

In order for a differential pulse height spectrum to have any physical meaning, it is necessary to calibrate the counting thresholds in terms of energy. This is done by obtaining differential pulse height spectra with a detector for a range of quanta of well-known energies. The position of peaks in the spectra which correspond to the incident quanta can be identified in terms of counting threshold. A calibration curve is then obtained by plotting the energies of the quanta against the position of the peaks they give rise to in the recorded spectra in terms of the counting threshold in DAC units.

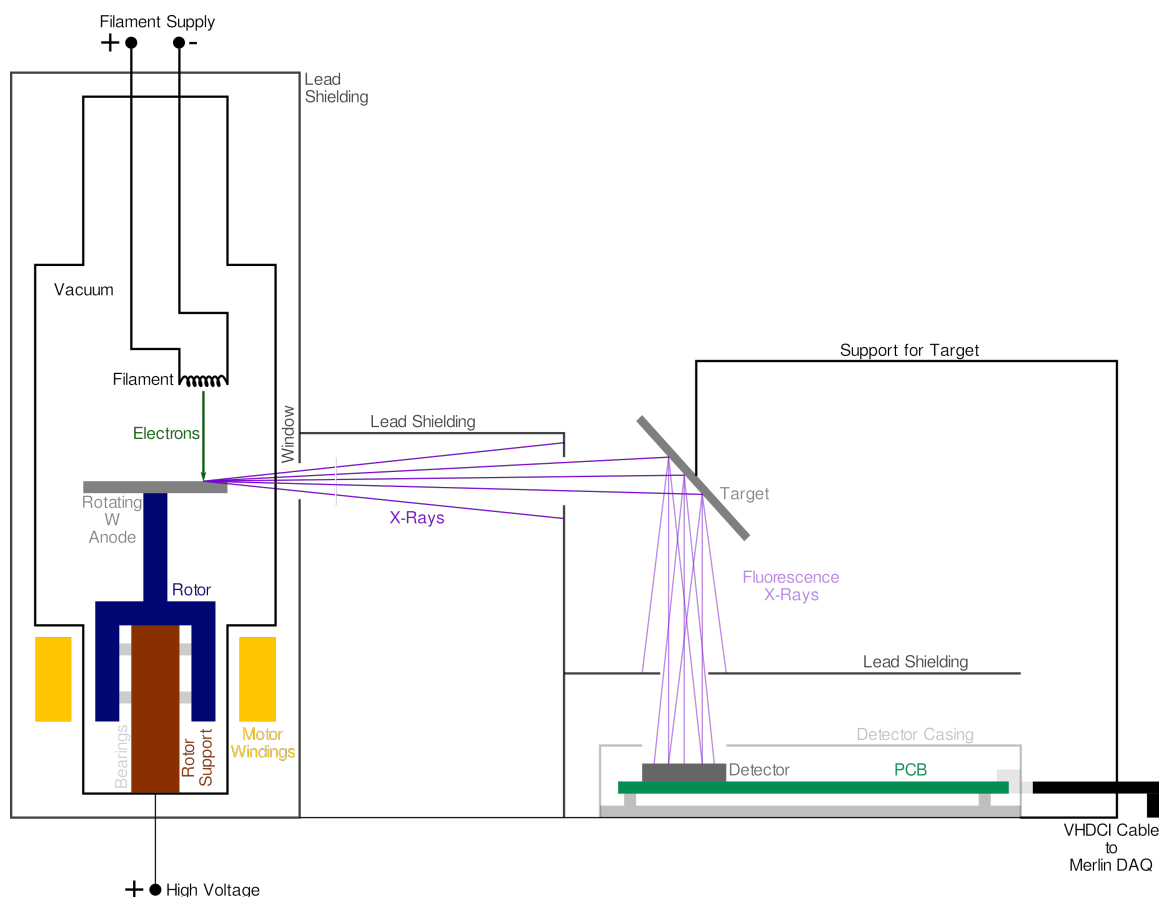


Figure 3.8: Schematic of an X-ray tube and diagram of the experimental set-up used for calibrating the counting threshold of Medipix3-type devices with fluorescence X-rays. X-rays are produced by electrons accelerated towards a W anode (the spinning of which increases the area with which the electron beam has to interact). Those X-rays that escape the tube through a window in the lead shielding strike a fluorescence target which is at an angle of approximately 45° to both the tube and the detector. Lead shielding with appropriately placed pinholes minimised the exposure of the detector to stray X-rays. Note that experimental apparatus is not drawn to scale.

Using lower-energy photons, it is possible to obtain an absolute energy calibration as they typically deposit their energy in a single interaction with the sensor, rather than depositing their energy over multiple pixels, as is the case for electrons with the energies used in TEM. The counting thresholds of the Medipix3 devices characterised in this thesis were therefore calibrated using fluorescence X-rays produced using an X-ray tube and series of targets. The working principle of the X-ray tube used in

the calibration of the Medipix3 devices, shown in Figure 3.8, is that electrons are accelerated through a potential difference and then strike an anode (made usually of either Mo, or as in the current work, W). This produces X-rays with a range of energies up to that of the accelerated electron. The X-rays produced are characteristic X-rays of the target that have energies lower than that of the incident electron with a background of Bremsstrahlung X-rays.

As shown in Figure 3.8, an arrangement of Pb bricks and pinholes was used to direct X-rays produced by the tube to the fluorescence target while shielding the detector from stray scatter. The fluorescence targets were positioned above the detector at an angle of $\approx 45^\circ$ (relative to the tube and the detector), so that fluorescence X-rays, characteristic of the target and produced by the interactions of the X-ray tube X-rays with the target are directed towards the detector. For the acquisition of the spectra, the peak voltage of the X-ray tube (i.e. the potential through which electrons are accelerated prior to striking the anode) was varied to ensure that there was sufficient overvoltage to be able to distinguish the characteristic fluorescence X-rays produced by the fluorescence target above the background X-rays while also using as high an X-ray tube current as possible to increase the visibility of the photopeaks (as the operational current was reduced when using higher peak voltages).

The choice of fluorescence targets used to calibrate a given device depended on which characteristic X-rays were discernible in the spectra recorded by that detector, which in turn depended on device characteristics. For example, the photopeaks of high-energy X-rays, such as those from Pb², were clearly discernible in the GaAs:Cr detector, due to the high stopping power of the sensor material, whereas the same was not true of the Si detectors. Table 3.1 lists targets used for the calibration of the different sensors characterised as part of the present work.

Figure 3.9 illustrates the key steps of the calibration procedure. An example of a threshold scan recorded by one of the Medipix3 devices is shown in Figure 3.9(a). The number of counts recorded for each counting threshold is differentiated to produce the corresponding differential pulse height spectrum shown in Figure 3.9(b). To identify the position of the photopeaks in a given spectrum, a single or double-Gaussian function (as appropriate for the peak shape) was fitted to. To determine the relationship between counting threshold and energy for the Medipix3 devices, a single or double Gaussian function (as appropriate for the peak shape) was fitted to each photopeak in the spectrum using a least-squares method. The photopeak(s) in the spectrum using a least-squares method. Figure 3.9(b) shows an example of a Gaussian fitted to a photopeak in the differential pulse height spectrum. The mean position(s) of the peaks were taken to be the threshold that corresponded to the fluorescence photon energy or energies. In cases where a double-Gaussian function was used, the

²The fluorescence of which could be obtained using Bremsstrahlung X-rays produced by the W X-ray tube when using an operating voltage greater than the K-edge of Pb, 88.008 keV.

Sensor	Mode	Threshold	Targets
300 μm Si 55 μm pitch	SPM	TH0	Ba, Nb, Sn, Se
300 μm Si 110 μm pitch	SPM	TH0	Ba, Nb, Sn
500 μm Si 55 μm pitch	SPM	TH0	Ba, Nb, Sn
500 μm Si 55 μm pitch	CSM	TH0	Ba, Sn
500 μm Si 55 μm pitch	CSM	TH1	Ba, Sn
500 μm GaAs:Cr 55 μm pitch	SPM	TH0	Ba, Nb, Sn, W
500 μm GaAs:Cr 55 μm pitch	CSM	TH0	Ba, W
500 μm GaAs:Cr 55 μm pitch	CSM	TH1	Ba, Sn, W, Pb

Table 3.1: Table listing fluorescence targets used for the calibration of the thresholds of Medipix3 devices in various modes of operations. Where possible, the K_α and K_β peaks would be fitted separately in order to increase the number of points in the calibration curve; even in instances where only two targets are listed, there were a minimum of three points in the calibration curve.

second, higher energy peak was taken to be due to K_β fluorescence photons and the lower energy peak to be due to K_α photons. For spectra where only a single peak was observed, the energy was taken to be the average of the K_α and K_β edges, weighted by their relative intensity. Where necessary, a linear background was also included in the function fitted to the data to account for any background to the spectrum.

The photon energies and positions of the corresponding photopeaks in terms of DAC units were then plotted. The resulting curve was fit with a straight line using a least-squares method, weighted by the errors on the peak position in terms of counting threshold, to determine the intercept and slope of the calibration curve. Figure 3.9(c) shows the calibration curve obtained on the basis of the peak fitted in (b) as well as peaks fitted in spectra acquired by the same device for different photon energies. The differential height spectra recorded by the detector can then be plotted in terms of energy, by converting the counting thresholds in terms of DAC units to energy. Figure 3.9(c) to the spectrum in Figure 3.9(d) shows an example of this.

It was observed that the reduced χ^2 values associated with fits to the photopeaks in the spectra for the purposes of determining the photopeak position were $\gg 1$, suggesting an underestimate of systematic errors. Rather than use the error(s) of the peak position(s) determined on the basis of the covariance matrix produced as part of the least-squares fitting procedure, the initial estimates of the function parameters fed to least-squares routine were systematically varied, and error(s) on the peak position(s) were taken to be the standard deviation of the range of peak position values obtained in this way.

3.3.2 Measurement of MTF, NPS and DQE

As discussed in Chapter 1, for pixelated, digital detectors, it is necessary to distinguish between the presampling and digital forms of MTF, NPS and DQE. The digital forms

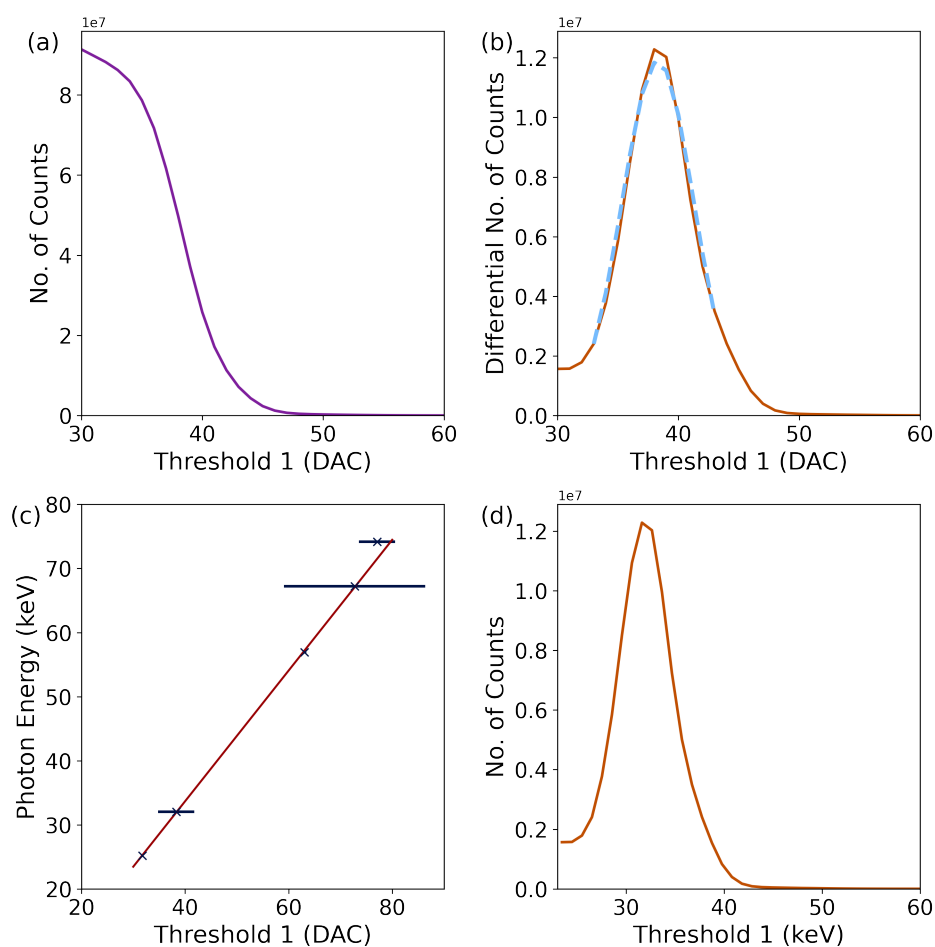


Figure 3.9: Examples of the key steps of calibrating the threshold energy of a Medipix3 device. In (a) a plot of the sum counts recorded of TH1 values in terms of DAC when the device was exposed to fluorescence X-rays produced from a Ba target. (b) shows the absolute value of the associated differential of (a). The photopeak in (b) is fitted with a Gaussian distribution, and this peak photon energy along with those from two other spectra are plotted in (c). A straight line is fit to this to determine the calibration, which is applied to the data in (b) to produce a spectrum in terms of energy in (d).

include the effect of sampling on the detector's ability to transfer noise and contrast, which may be regarded mathematically as evaluating the presampling forms at the centre of each pixel [41]. The presampling forms of the MTF and NPS quantify the effects of the scatter of incident electrons and of any secondary quanta produced by the primary electron in the sensor; the lateral dispersion of signal-carriers as they drift to the electrodes have on detector performance; and integrating over the effective pixel area. The finite pixel size sets a limit on the smallest size of features in the input image that can be resolved; those features with lengthscales smaller than the pixel pitch are undersampled. This leads to aliasing of both the image features and of the noise in the image produced by the detector, including those images used in the calculation of the MTF and NPS. Aliasing in the MTF and NPS means that they are overestimated at high spatial frequencies [255].

Determining the presampling forms is possible if the incident signal can be sampled at a rate greater than that permitted by the detector pixel pitch. In the case of the MTF, the presampling MTF means oversampling the incident signal that approximates a δ -function or, alternatively, a Heaviside function if characterising a square pixel detector. Oversampling generally requires some knowledge of the signal incident upon the detector. In the case of the MTF, this is possible as one can have knowledge of the object used to approximate a delta-function or Heaviside function (as appropriate) and its positioning relative to the detector. However, it is generally not feasible to know the profile of the noise incident upon the detector [41]. Consequently, characterisation of a digital detector is limited to measurement of the presampling MTF and digital NPS and the DQE that is calculated from these quantities, using Equation 3.1 must also be regarded as a digital one.

$$\text{DQE}_{dig}(\omega) = \frac{d_n^2 \text{MTF}_{pre}^2(\omega)}{n \text{NPS}_{dig}(\omega)} \quad (3.1)$$

There are several ways of measuring the presampling MTF of a detector. The knife-edge method [91] was used in the current work, informed by the approaches of other authors that have applied the technique to HPDs [18, 184]. For this technique, a sharp, electron-opaque edge (the “knife-edge”) is set at an angle relative to the pixel rows or columns. By combining individual line profiles, each with a known sub-pixel edge position, the knife-edge profile, which approximates a Heaviside function, is effectively oversampled and an edge-spread function (ESF) is produced, as illustrated in Figure 3.10. In the case of the present work, the knife-edge was a 2mm thick piece of Al set at an angle of 7° relative to the pixel rows at a distance of 0.5cm in front of the detector. A region of the knife-edge without defects 40 pixels wide in the middle of the sensor (so as to discount any edge effects) was identified and used in all analyses. For each column of pixels perpendicular to the edge in this region, the knife-edge location was identified as the position where the intensity was equal to midway between the average intensity in the uniformly illuminated and obscured regions of the sensor. This position was identified with sub-pixel accuracy via piecewise, linear interpolation. The profiles along pixel columns in this region were then aligned by the knife-edge position to create an oversampled ESF, as shown in Figure 3.10(b).

Differentiating the ESF yields the detector’s line spread function, which is the one-dimensional (1D) PSF. The ESF data can either be differentiated directly, or it can be fitted with a function which is then differentiated, which has the advantage of minimising the effects of noise on measurement of the MTF. The ESF can often be fitted with a sum of (complementary) error functions [135, 256]. For the measurements, presented in the current work Equation 3.2 was used to fit the ESF data. In this Equation, μ is the mean position of the function, which is set to 0, σ is the width of the error function and A is a normalisation factor. This has been used for the

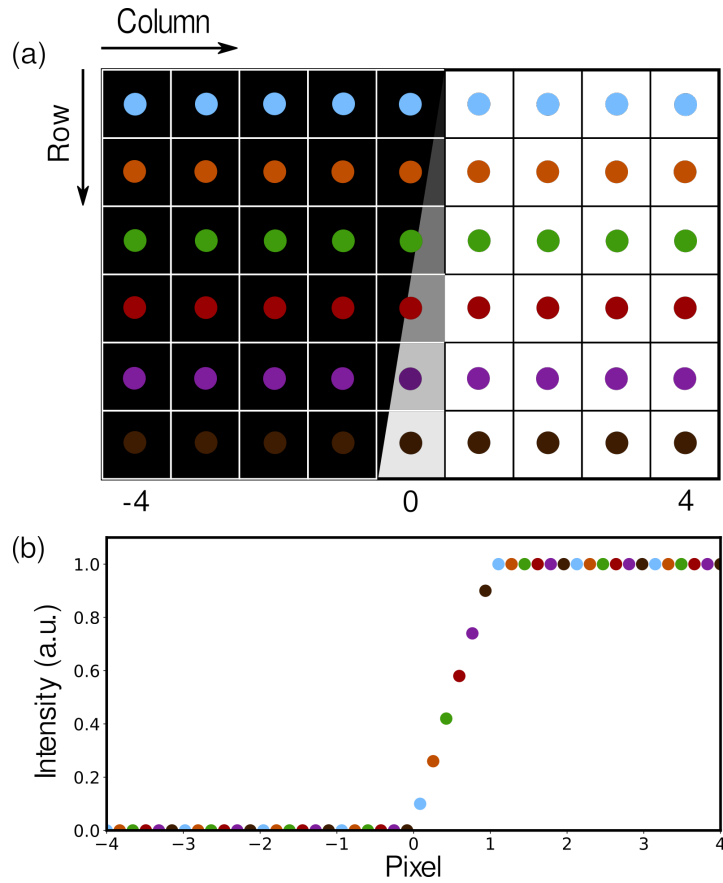


Figure 3.10: Illustration of how a knife-edge set at an angle to the rows or columns of a pixelated detector makes it possible to measure an oversampled ESF. In (a), a perfectly straight edge is set at angle relative to the pixel rows, so that rearranging the intensities recorded by pixels in order of the distance of the pixel from the edge-position is equivalent to plotting the intensities of the pixels in each column in order of the row they are located as seen in (b).

determination of the MTF of HPDs by other authors [18, 184]. To find the MTF, the modulus of the Fourier transform of the LSF, normalised to its value at a spatial frequency of 0, was calculated in accordance with Equations 3.3 and 1.50. An example of the process used to calculate the MTF is shown in Figure 3.11.

$$\text{ESF}_{fit}(x) = \frac{A}{2} \left(1 + \text{erf} \left(\frac{\mu - x}{\sigma} \right) \right) \quad (3.2)$$

$$T(\omega) = FT\{\text{PSF}(x)\} = FT\{\text{LSF}(x)\} = FT \left\{ \frac{d}{dx} \text{ESF}(x) \right\} \quad (3.3)$$

To measure the NPS of a detector, a series of flat field images (specifically 128 frames) was acquired at low electron flux to minimise the effects of coincidence loss. Equation 3.4 was then used to calculate the 2D digital NPS [41], in which N_x and N_y are the number of pixels in the detector's x - and y -axis respectively, while x_0 and y_0 are the pixel pitch in x and y respectively. The value represented by $\Delta d_{n_x, n_y}$ is the difference between the number of counts registered by a pixel with coordinates (x, y) , given a mean dose per pixel n , and the expected value of the number of counts

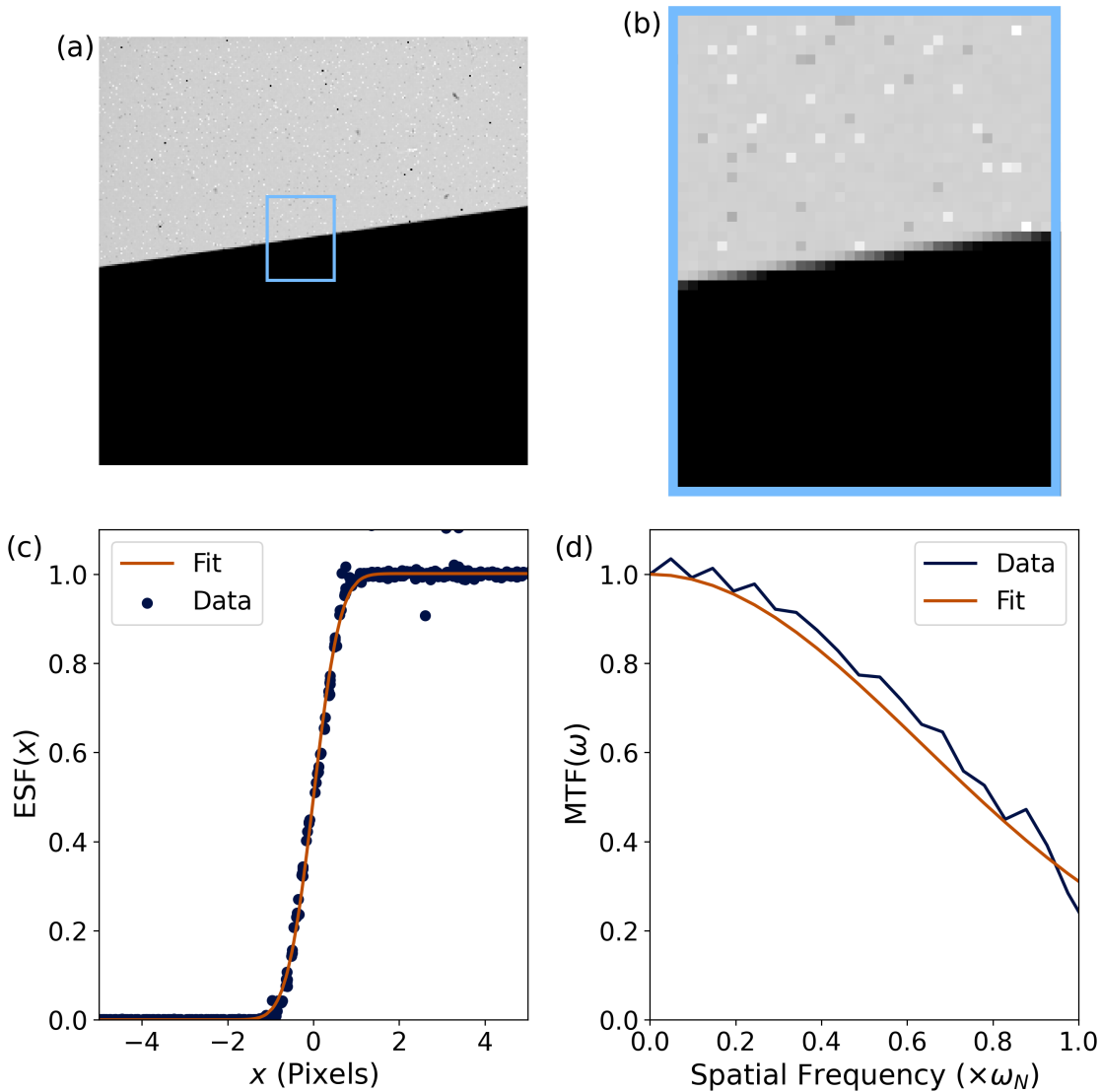


Figure 3.11: An illustration of the process by which a given detector’s MTF was measured. Beginning with (a), an image of the knife-edge with a flat field correction applied, an appropriate portion of a knife-edge image is identified, which is shown in close-up in (b). The pixel values are rearranged in order of their distance from the knife-edge and are plotted as in (c). This is then fit with Equation 3.2, which is used to calculate the MTF according to Equation 3.3, seen in (d). For comparison, the MTF obtained by using the raw ESF data in 3.3 is also plotted in (d).

recorded by the pixel. This was measured by calculating the mean image of the series of flat field values to find the expected image of d_n , which was then subtracted from each of the flat field images to acquire a series of images of $\Delta d_{n_x, n_y}$. The Fourier transform of each of these noise images was calculated, and the square modulus of these were averaged to find the expected value and hence the 2D NPS. Calculating the radial average of the 2D NPS provides the 1D NPS.

$$NPS_{dig}(\omega_x, \omega_y) = \frac{x_0 y_0}{N_x N_y} E\left\{|\text{FT}(\Delta d_{n_x, n_y})|^2\right\} \quad (3.4)$$

A problem in calculating the 1D NPS from the radial average of the 2D NPS is that the low-frequency NPS is noisier than the high-frequency NPS as there are fewer pixels over which to average, with this tending to an extreme for NPS(0). It is therefore beneficial to calculate NPS(0) separately to reduce the effects of noise on it and on the calculation of DQE(0). In principle, NPS(0) should be the variance, $\sigma_{d_n}^2$, of $\Delta d_{n_x, n_y}$. However, as electrons scatter over multiple pixels, there are correlations in the number of counts recorded by each pixel and hence correlations in the noise. The variance therefore typically underestimates the value of NPS(0). Instead, to find NPS(0), the images of $\Delta d_{n_x, n_y}$ were first binned by progressively larger factors, b and then the variance of the images normalised by the square of the binning factor was calculated. As b increases, $\sigma_{d_n}^2/b^2$ reaches a plateau as the correlations between neighbouring pixels are removed by effectively enlarging the pixels. This plateau value can be taken to be NPS(0) [48]. DQE(0) was then calculated using this independently calculated value of NPS(0) using Equation 3.6, which is then used in the calculation of DQE(ω) using Equation 3.7. In this Equation, NNPS(ω) is NPS(ω) normalised to the independently calculated value of NPS(0) (i.e. the normalised noise power spectrum). Figure 3.12 illustrates the steps taken to calculate the NNPS.

To ensure that the values of d_n and n in Equation 3.6 correspond to the NPS measured, d_n was taken to be the mean number of counts in the images used to calculate the NPS. To find n , the beam current I was measured, and a series of images with the entirety of the beam incident on the detector with a frame time t recorded. The detector gain factor, G , was calculated using Equation 3.5, where d_{n_m} is the mean number of counts recorded by the m -th pixel and M the total number of pixels. The value of n for the flat field exposures was then found by calculating d_n for these images and using the fact that $n = d_n/g$.

$$G = \frac{\sum_{m=0}^{M-1} d_{n_m} e}{I t} \quad (3.5)$$

$$\text{DQE}_{dig}(0) = \frac{d_n^2}{n \text{NPS}_{dig}(0)} \quad (3.6)$$

$$\text{DQE}_{dig}(\omega) = \text{DQE}_{dig}(0) \frac{\text{MTF}_{pre}^2(\omega)}{\text{NNPS}_{dig}(\omega)} \quad (3.7)$$

3.3.3 Linearity of Response

To measure the linearity of the Medipix3 detectors over a range of incident electron fluxes, and by extension their deadtime, for different primary electron energies, images with the entirety of the electron beam incident upon the detector were acquired. For each image, a different electron flux was used, with this being controlled through a combination of changing the microscope's condenser aperture; the excitation of the

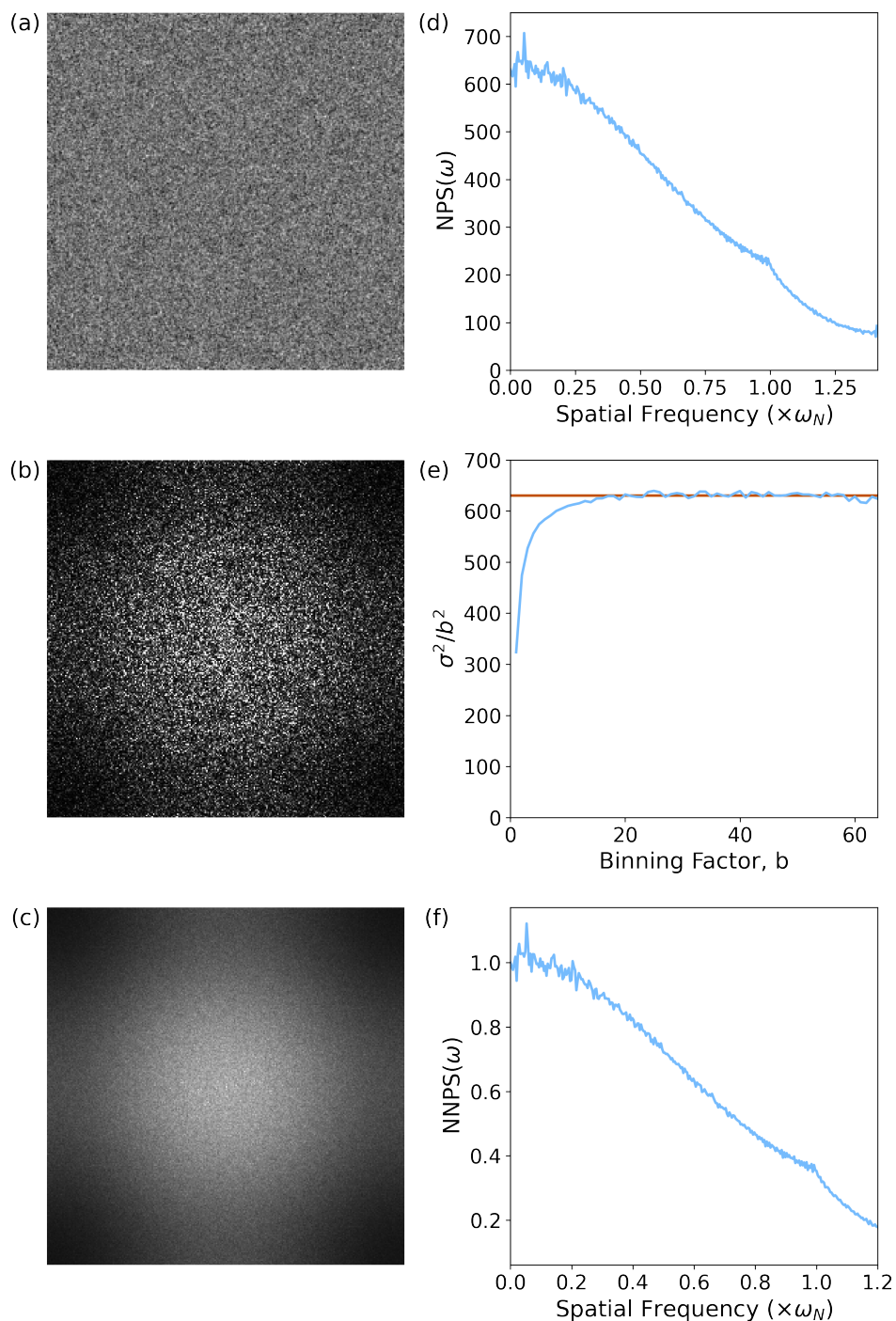


Figure 3.12: The process by which the NNPS of a detector was determined: (a) a single noise image and (b) the corresponding 2D noise power spectrum and (c) the 2D NPS obtained by averaging over the 2D NPS of 128 noise images. The contrast limits of (b) and (c) are the same, and it can be seen that (b) is much noisier than (c), highlighting the importance of averaging over many individual NPS. The radial average of (c) yields the 1D NPS in (d). The peak seen at ω_N in (d) is indicative of aliasing and this can also be seen in (b) and (c) in the middle of the edges of the 2D NPS. (e) shows a plot of the normalised variance of binned noise images plotted against binning factor. It can be seen that this reaches a plateau value, taken to be $NPS(0)$. The value of $NPS(0)$ was calculated as the average of the final thirty points, and is marked in orange. Along with (e), this is used to produce the NNPS shown in (f).

C1 and C2 lenses (which control the spot size and beam convergence respectively); and the current heating the thermionic emitter of the Tecnai T20 on which the detectors being studied were installed. The beam current was measured for each set of illumination conditions using the Faraday cup mounted on the chassis and a Keithly 485 Picoammeter. To try to ensure that approximately the same area of the detector was irradiated for each set of measurements, the beam was re-centered and the beam convergence adjusted after changing the spot size or condenser aperture.

A difficulty encountered when analysing the beam spot images to determine the incident electron flux per pixel was the determination of the area of the sensor that the beam illuminated. Due to stray scatter and the tails of the incident beam, the edge of the beam spot is not necessarily clearly defined. Additionally, when the incident flux is very high, there can be undercounting of the incident electrons within the disk. In extreme cases, pixels at the edge of the disk, which are only partially illuminated, register more events than pixels within the disk, which are fully illuminated. The edge of the disk therefore appears brighter than the main body of the disk, so that the profile of the beam spot resembles a caldera. This introduces a degree of uncertainty in the determination the area of the sensor illuminated by the beam, making it necessary to estimate an error on the illuminated area.

The procedure that was adopted to estimate the beam spot area and the error thereof was as follows:

- In an image, such as that shown in Figure 3.13(a), the beam spot was identified as being the area with counts above the threshold that best divided the beam spot image into two distinct regions (in this case, inside and outside the beam spot) based on recorded intensity using Otsu's method [257].
- The area that was identified as being above the Otsu threshold was used to define a mask. To remove any regions within the disk that had not been identified as being above threshold due to dead pixels or sensor defects a two-step process of binary opening (using a cross-shaped footprint) and closing was applied. The resulting mask, shown in Figure 3.13(b) was taken to be the area of the sensor the beam was incident upon.
- To find the error in the area estimate, a process of binary dilation using a disk with a radius of one pixel was applied to the mask to generate a second, incrementally larger mask.
- The difference in area between the two masks (an example of which is seen in Figure 3.13(d) was taken to be the error in the beam spot area.

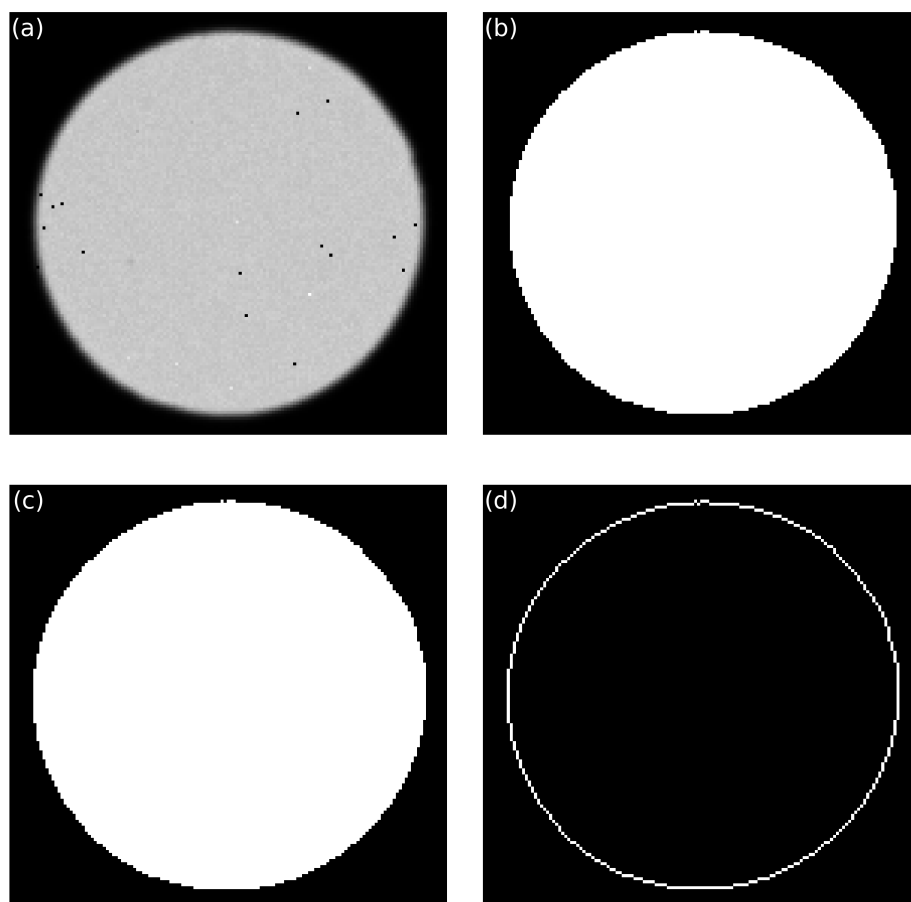


Figure 3.13: Illustration of how the area of the beam spot and its error. In (a) a close-up of an image of the beam spot is seen and in (b) the Otsu thresholded image. The image in (c) shows the result of applying a binary dilatation process to the mask in (b), while (d) shows the difference between (b) and (c). The sum of the pixels marked in white in (d) is taken to be the error in the area of (b).

Converting the total beam current into electrons/s, and dividing this by the area of the beam spot provides a value for the incident electron flux. The error on this was found by propagating the measurement error of the beam current (0.5 pA) and the error estimated for the beam spot area.

As mentioned above, an effort was made to keep the portion of the sensor that was illuminated constant under different illumination conditions. However, this was difficult to achieve consistently and, in some cases, it was necessary to converge the beam to obtain a high incident flux with measurements where significant undercounting was observed, which facilitated fitting the linearity data to obtain the deadtime (discussed in more detail in Chapters 4 and 6). Consequently, when plotting the average electron counts per pixel against electron flux per pixel, the average counts per pixel were determined only from the area of the detector that was illuminated in all datasets, determined as the overlap of the masks determined from each individual measurement. This avoided the introduction of errors due to

the average number of counts being determined from different areas of the sensor, which could differ due to variation in pixel response across the pixel matrix.

3.3.4 Detector Mapping with Confocal STEM

A common technique in photon science for investigating the pixel response of detectors is to record a series of images of a micro-focused beam of monochromatic X-rays located over a range of sub-pixel positions. Manipulation and deflection of X-rays is challenging and so, in practice, the detector is displaced in a raster pattern by moving the stage on which the detector is mounted using stepping motors. This technique also enables investigation of how the sensor response varies across the pixel matrix, which may be influenced by the presence of defects in the sensor and other inhomogeneities in the detector. This has permitted characterisation of effective pixel size [223, 243]; how the spectral response and degree of charge sharing depends on the photon entry point [258, 259] as well as the charge collection efficiency [260]; and the uniformity of the shape and size of pixels both between different versions of a given material [206] and in proximity to different types of defects [240].

Similarly, within electron microscopy, the uniformity of ADF detectors has been characterised for the purposes of calibrating their response for quantitative STEM by scanning them with a focused electron beam [261–263]. There are at least two ways of aligning an electron microscope to do this. In the first method, a (near) parallel beam is rocked through an angle by the scanning or beam tilt coils. The detector plane is coupled to the objective lens BFP, so that this deflection angle is translated into a lateral displacement in the detector plane with the post-sample optics aligned as they would be for STEM [264–266]. This has the advantage of more closely matching the alignment used when a microscope is operating as a STEM, so that there is a conformity in the scattering angles propagated through the post-sample optics when characterising the detector and performing a STEM scan. The second method, which has been referred to as a “confocal” alignment [267], entails aligning the pre-sample optics as for a standard STEM scan, and then aligning the post-sample optics for conventional TEM. In this way, the detector plane is coupled with the image plane of the objective lens, and the scanned probe is imaged directly. This has the drawback that there is a mis-match in microscope alignment when calibrating the detector and acquiring the STEM data to which the calibration is applied, which may affect the accuracy of that calibration.

To investigate the variation in pixel shape and response observed in the GaAs:Cr Medipix3 detector when recording electrons, the confocal STEM approach to performing sub-pixel scans was adopted. The confocal STEM alignment was preferred due to the greater ease with which it could be obtained, as well as because the priority was to ensure a small, sub-pixel sized beam was present in the detector plane rather

than to calibrate the detector response for the purposes of quantitative STEM. Figure 3.14 illustrates the microscope alignment for the confocal STEM mode of operation used to characterise an imaging detector. As the detector being characterised in this instance was itself a 2D pixelated detector, unlike the ADF detectors studied in earlier works which are single-channel detectors, this series of experiments were effectively 4D-STEM studies where the sample under investigation was the detector itself.

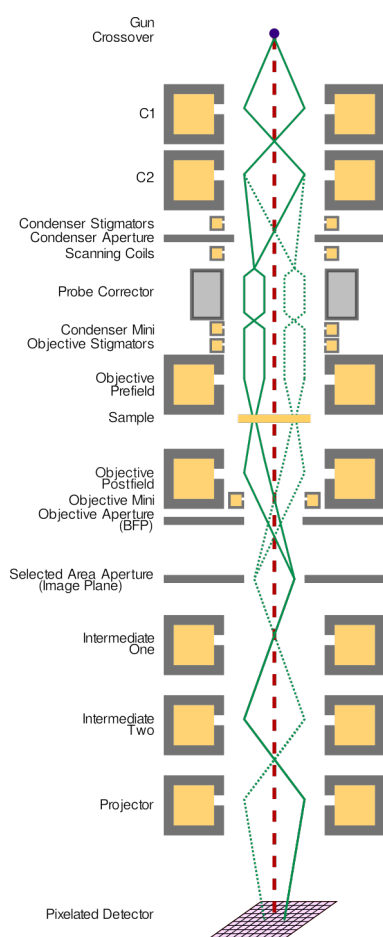


Figure 3.14: Ray diagram of a microscope aligned for the purposes of a confocal STEM scan of a pixelated detector. The pre-sample optics are aligned as in STEM, while the post-sample optics are aligned as they would be in TEM, so that an image of the scanned probe in the sample plane is projected onto the detector.

Confocal STEM experiments were conducted with both the Karlsruhe 80-300 FEI Titan STEM, operated with an accelerating voltage of 300 kV, and the Glasgow JEOL ARM cF 200 (S)TEM, operated at 200 kV. For the former microscope, a confocal STEM alignment could be obtained as part of the standard STEM alignment procedure. Consequently, the size of the probe in the detector plane could be estimated on the basis of prior characterisation of the probe size in the sample plane and prior calibration of the magnification factor for the Gatan Ultrascan Camera that was installed on the microscope (and which sat in the same plane as the Medipix3 GaAs:Cr detector). The probe size scanned across the Medipix3 GaAs:Cr detector was estimated

to be $9.1\ \mu\text{m}$. In the case of the Glasgow ARM, a confocal STEM alignment had to be obtained manually, by aligning the microscope for low-magnification STEM and then setting the strength of the projector and intermediate lenses to the level used when the microscope was aligned for TEM.

As there had been no prior calibration of the magnification factor for a detector mounted in the 35 mm port above the viewing screen for the Glasgow ARM, it was necessary to determine its value to estimate the size of the probe in the detector plane and ensure it was sub-pixel in size. This was done by performing a confocal STEM scan with a standard magnification calibration sample inserted in the sample plane, so that the detector recorded a STEM scan of the calibration sample superimposed upon a confocal STEM scan of the detector itself, shown in Figure 3.15(a)³. The calibration sample consisted of amorphous carbon with Au shadowing in a cross-grating pattern of 2160 lines per millimetre, equivalent to a repeat distance was 462.96 nm. Consequently, the magnification factor could be determined by comparing the known grid spacing to the equivalent spacing measured in a line profile from the image of the cross-grating in the confocal STEM scan recorded by the detector, shown in Figures 3.15(b) and(c). On this basis, the magnification factor was determined to be 1708. The FWHM of the probe in the detector plane was estimated as being $\sim 10\ \mu\text{m}$, as it was known to be 6 nm FWHM in the sample plane, given the $10\ \mu\text{m}$ condenser aperture used, based on prior characterisation of the microscope.

A challenge encountered when performing the confocal STEM scans on both the Glasgow ARM and the Karlsruhe Titan was obtaining a sufficiently low beam current so that the pixel in which the probe was incident did not begin to undercount, producing a caldera-like intensity profile. The most obvious indication of this occurring was the pixel in which the beam was incident recording fewer counts than its neighbours. Neither experimental set-up permitted an independent measurement of the beam current as it was too low for the Keithly 485 Picoameter or the Gatan Ultrascan Camera to reliably measure it, thereby preventing the setting of a current value that was known to be sufficiently low so that undercounting would be avoided. Consequently, direct observation of a caldera in a test pixel was used as a guide as to whether or not the beam current was too high. In the case of the measurements performed with the Karlsruhe Titan, the smallest physical spot size was used and the extraction voltage of the Schottky source was reduced to 3.5 kV from its usual value of 3.95 kV to reduce the emission current. Similarly, when acquiring data with the GaAs:Cr detector installed on the Glasgow ARM, the smallest physical spot size was also used and the voltage on

³ Due to the defects present in the GaAs:Cr sensor (discussed in Chapter 2), which would make measurement of the repeat distance difficult, and as the nature of the experiment meant that suitable flat field correction data could not be acquired, the calibration data was acquired with the Si Medipix3 detector that is permanently installed on the Glasgow ARM. This detector was temporarily removed, so that data could be acquired with the GaAs:Cr detector using the same microscope alignment and detector position.

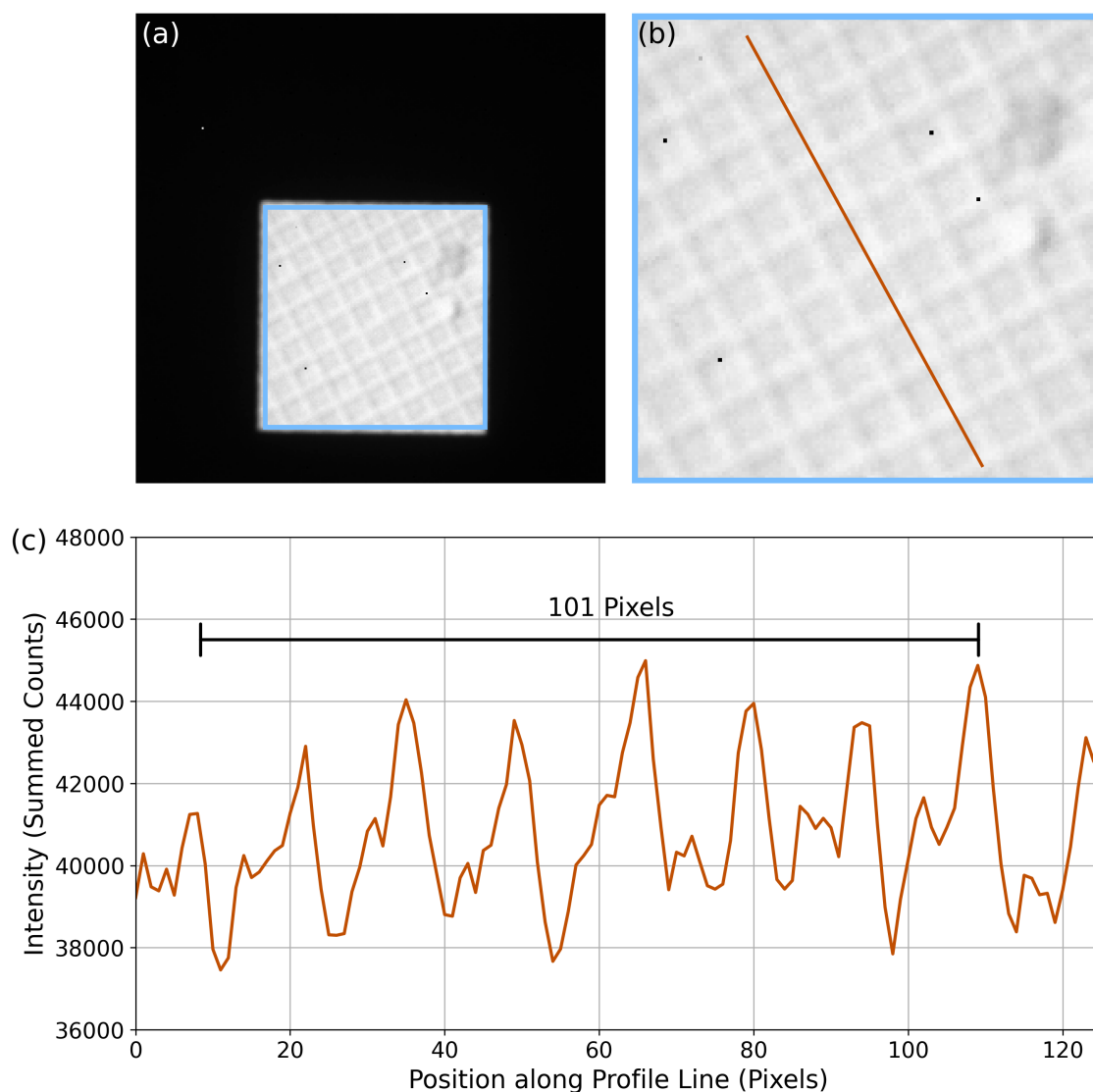


Figure 3.15: Illustration of the procedure used to calibrate the magnification of the probe when imaged in the plane of the Medipix3 detector. In (a), the sum of the images recorded by the detector over the course of the confocal STEM scan of the calibration sample is shown; this is akin to the summed diffraction pattern of a 4D-STEM scan and is the full scan of the sample projected onto the detector. A close-up of the scan area marked in (a) is shown in (b), which is annotated with the line along which the intensity was measured, which is plotted in (c). The variation in the intensity profile in (c) due to the repeats used to calculate the average size of one of the repeats in the detector plane is marked. Along the measured profile line, the average repeat distance was measured as being 14.4 pixels. This corresponded to a distance of $791 \mu\text{m}$ in the detector plane, taking into account the pixel pitch.

the extraction anode of the cFEG reduced to 3.3 kV. For the data acquired with the Si detector, a higher extraction voltage was used: for the calibration data presented in Figure 3.15 it was 3.58 kV and for the data presented in Figure 3.16 it was 3.6 kV.

The dataset produced by the confocal STEM scan is 4D, with two detector axes, detY and detX, and two scan axes, scanY and scanX. To generate pixel maps from this data, the weighted-centre of mass of the intensity recorded in each frame, and, by extension, each dwell point with scan coordinates scanY and scanX, was identified and

taken to be the position where the beam was incident. An example of this is shown in Figures 3.16(a) and (b). Although the probe is sub-pixel in size and incident in a single pixel, the scatter of incident electrons in the sensor and the lateral dispersion of the charge carriers produced by incident electrons, means that multiple pixels are able to record each incident electron. This has the consequence that the profile of the probe, as imaged by the detector, appears to spread over multiple pixels. It also means that the position of the beam can be determined to sub-pixel accuracy, on the basis of the measured intensity profile, which would not be possible if only the entry pixel registered the incident electrons. An alternative strategy for identifying the entry point of incident electrons by fitting the intensity profile in each frame with a 2D Gaussian using a least squares method, but the fitting procedure failed to work reliably across the full dataset.

A map of the pixel matrix showing the total number of counts recorded by the detector for each scan position (i.e. a summed scan image) may be obtained by summing all counts recorded by the detector at each dwell point and assigning that value to that dwell point in the scan. Figure 3.16(c) shows a sample of the data produced by processing the confocal 4D-STEM scan: associated with each scan point are coordinates in the detector plane as well as the scan coordinates and the total number of counts recorded by the detector at that scan point. Points in the scan were grouped on the basis of the (appropriately rounded) value of detY and detX ascribed to them, so that all points in the scan where the beam is incident in the same detector pixel are ascribed the same pixel label. A map of the pixel boundaries was produced by generating a scan image where each scan pixel/scan dwell point is assigned the value of the pixel label associated with it. Detector pixels in the scan image were then determined by identifying regions in the image with the same value and the boundaries between them, as shown in Figure 3.16(d). These boundaries could then be superimposed onto the sum image (as shown in Figure 3.16(e)) to show how the number of counts recorded by the detector varies depending where within the pixel the electron beam was incident.

The data presented in Figure 3.16 was acquired with the Si Medipix3 detector usually mounted on the Glasgow ARM while developing the confocal STEM procedure on this microscope, as the lack of defects makes it is more suitable as an exemplar. In Figure 3.16(e) the uniformity of the number of counts recorded across the scan map is indicative both of the homogeneity of the Si sensor as well as the large PSF of the Si detector when recording 200 keV electrons (discussed further in Chapter 4). This latter factor means that variations in the number of counts recorded due to charge sharing, which would manifest itself as an increase in the number of counts when the beam is located at the edges and corners of the pixel, is not observed, as it is not only when the beam is incident upon the edges of the pixel that that incident electrons are counted by more than one pixel. The pixel boundaries identified in the

example in Figures 3.16(e) and (f) are reasonably regular, although only two pixels are perfectly square. This potentially points to limitations in the way in which the data was acquired. The scan spacing was chosen so that it was approximately equal to the pixel pitch divided by the beam size and each pixel sampled over the course of the scan. However, the irregularities in the pixel boundaries suggest that the scan coordinates and axes may not not be completely aligned to the detector pixel matrix.

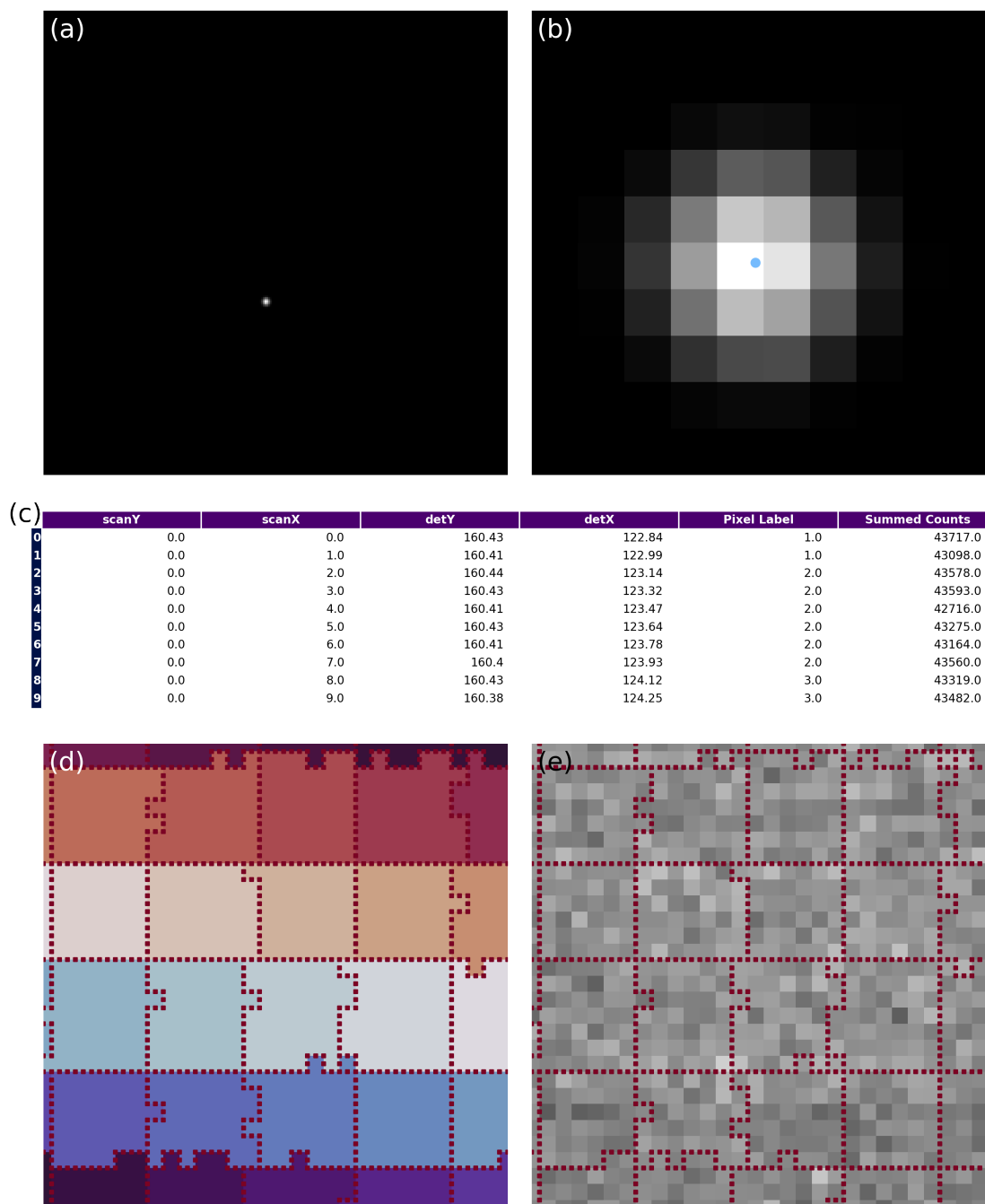


Figure 3.16: Figures showing how the raw 4D confocal STEM scans were processed to produce pixel maps. (a) shows a single frame recorded by the detector, which corresponds to a single dwell point in the scan, while (b) shows a close-up of the beam spot seen in (a), with the weighted centre-of-mass marked. (c) shows a sample of the data set obtained by processing the frames recorded by the detector. Note that all points in the scan for which the beam is identified as having been incident in a given pixel, i.e. as having the same (floored) values of detY and detX, have the same pixel label. An image of the pixel label value at each scan point, as shown in (d) can be used to identify the boundaries of the detector pixels in the scan, which can then be overlaid on the sum image as a guide as shown in (e).

3.4 Electron-Matter Interactions and Detector Response Simulation

Although experimental measurements permit quantification of detector response, they do not necessarily provide insight into the underlying mechanisms that give rise to the observed detector behaviour. Simulations are therefore a valuable counterpart to experimental measurements. Section 3.4.1 describes the software packages used to simulate the interactions of electrons with matter as well as the response of HPDs to incident electrons. Furthermore, an overview of the finite element package used to simulate the physical and electrical properties of Si sensors of HPDs is given in Section 3.4.2.

3.4.1 Simulation Packages Based on the Geant4 Framework

To complement the experimental characterisation of HPDs, simulations were performed using two software packages built using the Geant4 (GEometry ANd Tracking) framework [268–270]. The Geant4 toolkit was developed for the simulation of particle interactions with matter, originally in the context of high-energy particle physics, though it has been utilised in a range of fields including medicine [271] and space science [272]. It is an object-orientated toolkit written in C++ that can be used to build applications for the simulation of a range of specific scenarios.

The key components of a Geant4 simulation are a geometry, which describes the layout of the experiment, including the definition of physical volumes; the tracking of particles after they are generated as they pass through the different volumes defined by the geometry, and a run manager that initialises the simulation (potentially several times with different configurations) and records the output of the events. An event is defined as being a full simulation chain starting from the creation of a primary particle and terminating when no particles remain (with the termination of a given particle occurring when its energy falls below a user-set threshold). Physical volumes in the simulation can be defined using a comprehensive range of materials based on the National Institute of Standards and Technology's materials database, with users also able to define their own materials if need be. Simulation of the passage of particles uses Markov Chain Monte Carlo methods, whereby each step of the particle trajectory is randomly selected from a probability distribution based on the cross-sections of the various physical processes that the particle can participate in (given its current state), to determine its next state. In more sophisticated simulations, a physical volume may be designated as “sensitive” so as to enable the registration of particles that pass through the volume as ‘hits’ which can then be used to simulate the full response of a detector including the creation of and propagation of charge/signal carriers produced by incident particles and the digitisation of these to mimic a detector's signal

processing electronics. There are a number of applications built using the Geant4 framework for the simulation of detector response in various different contexts. These include the Geant4Medipix package [273, 274], dedicated to simulating Medipix-type detectors, and Allpix [275], for the simulation of detectors with Si sensors in HEP.

Allpix² [276] (read as “Allpix Squared”) is the successor of Allpix and provides a highly flexible framework for the simulation of both monolithic devices and HPDs. It has been used extensively to simulate the response of devices with Si sensors in the current work. During the time period over which the research presented in this thesis was conducted, only Si sensors could be simulated within the Allpix² package, though the package has since been officially expanded to include alternative materials including high- Z sensor materials. Consequently, a simpler programme adapted from one of the advanced Geant4 examples [1] was used to simulate the interaction of electrons with GaAs and CdTe sensors, though this was not capable of simulating the full detector response. This is described in more detail in Chapter 5.

Given that both simulation packages rely on Geant4 for the simulation of particle interactions with a sensor, it is worth outlining how Geant4 models the relevant physical processes. The framework includes a wide variety of physical models for the purposes of calculating the cross-section of different processes. This enables simulations to be fine-tuned by using the most appropriate models for a given scenario while also maximising computational efficiency. Geant4 comes packaged with pre-defined “physics lists”, combinations of physical models that have been developed for use in a certain field e.g. interactions of high-energy particles with biological material for simulations in a medical physics context [277]. For the energy range of primary electrons considered in this thesis (≤ 300 keV), the Livermore version of electromagnetic physics was deemed to be most appropriate as it is valid for materials for which $1 \leq Z \leq 99$ and for energies down to 10 eV [278]. This draws upon the Lawrence Livermore National Laboratory data libraries for the atomic, electron and photon cross-sections, interpolating between the data available in these libraries to calculate the cross-sections and sample the final outcome of an interaction process. At energies < 100 GeV (which within the context of the applications for which Geant4 was originally developed is considered “low”) the effects of atomic shell structure become more important, making it necessary to use shell cross-section data. So-called “low-energy” processes that make use of these tables in the Livermore physics list include for the photoelectric effect, Compton and Rayleigh scattering and Bremsstrahlung production.

This choice of physics list was guided by the fact that the Livermore physics list has been shown to offer the best match with experimental data of the rate of energy loss of electrons with energies down to < 100 eV [278]. Other physics lists that are recommended for use in the energy regime relevant to electron microscopy, such as the Penelope variation of the electromagnetic physics list [279, 280], were also

tested. However, no significant difference in the results obtained with these other lists and the Livermore list was observed.

The tables also provide the binding energies of electrons in all subshells and transition probabilities between different atomic subshells for the production of fluorescence X-rays and Auger electrons. To improve computational performance, individual elastic scattering events of electrons are aggregated and modelled using a multiple scattering process, based on the Goudsmit-Saunderson model [281]. Ionisation by electrons uses data from the Livermore tables at energies of 100 keV or less and the Møller model [282] of electron-electron scattering for energies in the range of 100 keV to 100 TeV⁴. Bremsstrahlung production is simulated using the Seltzer-Berger tables of Bremsstrahlung cross-sections [283, 284]. Simulation of the photoelectric effect, Compton and Rayleigh scattering, fluorescence and Auger generation scattering also make direct use of the Livermore data tables, interpolating where necessary. By default, fluorescence is enabled when using the Livermore physics list while Auger generation is not. The simulations performed in this thesis had the production of Auger electrons enabled.

In Allpix², the simulation chain is defined by the user's selection from the modules included in the framework. The core executable initialises the simulation chain and geometry and manages communication between the different modules. Figure 3.17 illustrates the structure of the simulation framework as well as how a standard simulation chain maps onto a physical detector. A minimally functional simulation chain for a single detector, illustrated in Figure 3.17, consists of the following modules:

- A geometry builder module to define the geometry of the simulation.
- A deposition module to manage the creation of electron-hole pairs in a sensor in response to incident radiation, depending on the electron-hole pair creation energy of the sensor and its Fano factor.
- A propagation module to propagate charge carriers in the sensor on the basis of specified models of charge diffusion, drift and recombination as well as physical properties of the sensor and any electromagnetic fields present in the sensor.
- A transfer module to describe how propagated charge carriers induce signal on pixels of the simulated device.
- A digitizer module to simulate the response of the detector electronics and the signal produced by the simulated detector.

⁴The TeV energy range is far above that which is relevant in the present work, and the fact this model is specified as being suitable for use at such high energies reflects the fact that Geant4 and the standard physics lists were originally developed for use in HEP.

A notable feature of the framework is its ability to import fields describing how physical quantities vary in the volume of a sensor that were simulated or generated using other software packages, so that the effects of these fields can be incorporated into the simulation. The fields that can be imported (or otherwise generated according to analytic expressions by the relevant “Reader” module) are electric fields, magnetic fields, doping profiles and weighting potentials (used to determine the charge induced on pixels by the motion of charge carriers described by the Shockley-Ramo theorem, discussed in Chapter 1). Those modules that generate or read these fields must be instantiated for each simulated detector. For example, the Electric Field Reader module associated with a particular detector provides information about the electric field within the sensor of that detector, which can be used by the propagation module associated with that detector. Imported fields usually take the form of a field simulated for a sub-volume of the sensor that can be repeated across the pixel matrix, e.g. a single pixel. For the simulations presented within this thesis, an electric field and doping profile were simulated using Synopsys Technology Computer Aided Design (TCAD) for each type of simulated detector. This is discussed in more detail in Section 3.4.2. Weighting potentials were generated using the weighting potential generator utility included with Allpix², which determines a weighting potential by solving Equation 1.17 for a specified geometry with the pixel-of-interest set to have a potential of 1 V and all other electrodes held at ground.

Messages passed between modules consist of objects that, to a certain extent, correspond to the signal carriers that exist at different points in the detector signal processing chain. An `MCTrack` object contains information about the initial and final states of a particle, while a corresponding `MCParticle` object contains information about the start and end point of a part the particle’s trajectory in a given sensor. `DepositedCharge` and `PropagatedCharge` objects represent charge created in the sensor due to the deposition of charge and that same charge after it has been propagated through through the sensor by diffusion or the action of an applied electric field. Finally, `PixelCharge` and `PixelHit` objects represent the charge induced on a pixel and digitised signal produced by the pixel in response to that charge. These objects also compose the simulation output and, assuming that all objects produced in a simulation are written to file, their relationships can be reconstructed as part of the data analysis e.g. one can identify which particles contributed to the signal induced on particular pixel.

Construction of the detector and broader simulation geometry is implemented by the `GeometryBuilderGeant4` module, which interfaces with Geant4 and translates the geometry defined by the user in Allpix² configuration files to a Geant4 geometry. Two basic detector geometries are available within Allpix²: monolithic devices and HPDs. Aspects of these, such as the sensor thickness, pixel pitch and number of pixels, can be defined by the user. Definition of a geometry then consists of defining

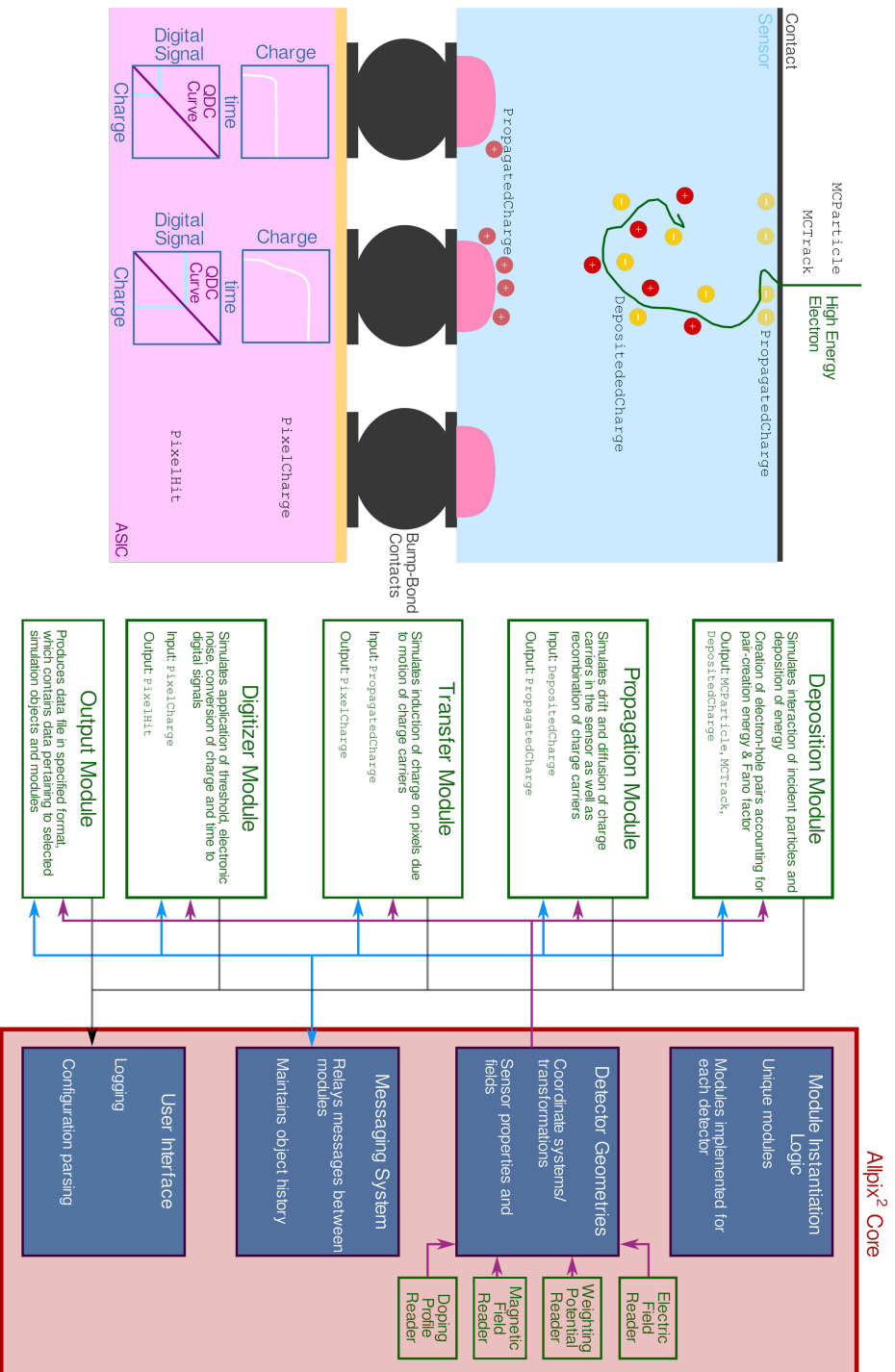


Figure 3.17: Schematic showing how the different components of the Allpix² framework relate to one another and how they relate to the detector and physical processes being simulated. The framework core includes components common to all modules used in a simulation chain both those that are instantiated once for a simulation (i.e. unique modules) and those that are instantiated for each detector in the simulation. An example of the former is the module that defines the simulation geometry, while those modules in green are all modules that must be instantiated for each individual detector, with the exception of the output module. Pink arrows indicate information relating to detector modules; the grey arrows correspond to logging information; and the blue arrows represent the bi-directional exchange of messages between the core and individual modules in the simulation chain. Adapted from reference [276].

the position, orientation and dimensions of the detectors being simulated as well as any other volumes such as support structures or shielding for the detectors. Each individual simulation consisted of a single detector with a circular, monochromatic electron source with a radius of $6\mu\text{m}$, so that the full beam was incident upon the simulated detector. The detectors simulated corresponded to those characterised experimentally i.e. devices with $300\mu\text{m}$ thick Si sensor and $55\mu\text{m}$ and $110\mu\text{m}$ pixel pitch as well as a device with a $500\mu\text{m}$ thick Si sensor and $55\mu\text{m}$ pitch. Examples of the configuration files that define the simulation geometry as well as list the modules used in the simulation chain and the specific parameters used for these modules are given in Appendix A. The simulation output was written to ROOT [285, 286] files using the `ROOTObjectWriter` module and analysed using custom scripts written in Python using the PyROOT, Python bindings for the ROOT analysis framework.

3.4.2 Simulation of Si Sensors with Synopsys TCAD

The ability of Allpix² to import profiles of the electric field, weighting potential and doping profiles of a sensor makes it possible to simulate the response of Si sensors with significantly enhanced accuracy [287]. In principle, the Equations dictating the electrical behaviour in a sensor (or a repeating unit of such a sensor such as an individual pixel) and which describe the dependence of the electric field and electrostatic profile on the sensor characteristics can be solved analytically. However, in practice this is only possible for very simple devices and in most cases numerical methods must be used. One option is to use finite-element modelling packages for semiconductor technologies such as Synopsys TCAD. This is a suite of tools for simulating the manufacture and behaviour of semiconductor devices. The current work used the `sde` [288] and `sdevice` [289] tools to simulate the planar processes used to manufacture Si sensors of the kind studied experimentally and thence determine the electric field, weighting potential and doping profile of such devices for use in Allpix² simulations.

In TCAD, a device is defined by a mesh, at each point of which is a value of the device properties. Such properties can include the underlying material at that point in the device (and associated characteristics); concentration of dopant atoms (either net or of a particular type or species); and the electrical characteristics, such as the electrostatic potential at that point. The mesh spacing can be made to be irregular in order to ensure that there is a sufficiently high density of nodes in regions of the device where an important property of interest varies significantly over short distances, ensuring behaviour of interest is properly modelled, while a low density can be used in regions where device properties are constant, reducing the amount of unnecessary computation.

Using Synopsys *sde*, a device is first defined as a volume (or set of volumes) with constant physical properties e.g. a volume of Si with constant doping and resistivity that represents a single HPD sensor pixel. A mesh (or meshes, as appropriate) can then be defined for the specified volume(s). Localised doping profiles may then be specified using analytic expressions. Additionally, planar regions representing metal contacts, for the purposes of defining regions where an electrostatic potential is applied in subsequent simulations can be specified. For the present work, individual pixels for each of the three Si devices were simulated, initially being defined by a cuboid volume of Si with a constant doping of 10^{11} P atoms cm^{-3} . The doping profile along the depth of the device for the frontside pixel implant was defined for a $38\mu\text{m}\times 38\mu\text{m}$ region in the centre of the pixel, using a Gaussian profile with a peak value of 10^{19} B atoms cm^{-3} at the device surface (and interface with the contact) and a standard deviation of $0.17\mu\text{m}$. Similarly, the backside implant for the HV contact was defined using a Gaussian profile with a peak value of 10^{19} P atoms cm^{-3} at the interface and a standard deviation of $0.15\mu\text{m}$. The parameters for the Gaussian distributions were chosen as they generated an overall device doping profile that matched the manufacturer's estimate of the same doping profile [252]. Contacts were then specified, in the case of the pixel contact this was a $35\mu\text{m}\times 35\mu\text{m}$ surface centred on the pixel, while for the high voltage contact the dimensions were those of the pixel pitch, so that the contact covered the entirety of the backside surface of the pixel. A mesh was then generated, the spacing of which varied from a maximum spacing of $10\mu\text{m}$ in all directions in the bulk where the doping concentration was constant, to a minimum spacing of $0.1\mu\text{m}$ in regions at the interface where the doping profile changed significantly over small distances. The mesh spacing was determined by iteratively evaluating the maximum difference in the hyperbolic arcsin of the doping concentration profile at the vertices of each mesh element. If the maximum difference was greater than 0.5 cm^{-3} then that element was refined and broken down into smaller elements with finer meshing.

The doping profile and choice of meshing was guided by data provided by Advacam, the manufactures of the Si sensors, regarding the concentration of Ph and B dopants at different depths of the sensors. The meshing strategy was also dictated by the limitations of the computational resources available; considering the disparity between the experimental results and simulation results seen in Chapter 4, it would be worth attempting to repeat the TCAD simulations using a finer meshing strategy. Although it was not possible to directly compare the simulated electric fields with experimental measurements of the electric field in the sensor, comparison with the published results of simulations of the electric field in the sensors of other Medipix-type devices performed with the Medici TCAD package [Kraphol2016] indicated that the simulation results were reasonable.

In `sdevice`, discrete, approximate forms of the equations describing the electrical properties of a device, namely Equations 1.17, 1.30 and 1.31, are solved for each node to simulate the electric field and electrostatic field in a device due to the application of a potential at one of the contacts. This gives rise to a system of coupled Equations g . A Newton-style solver is used to solve the system $g(z) = 0$ of non-linear Equations that results from a given set of boundary conditions, where \mathbf{z} represents a potential solution. An initial solution \mathbf{z}_n is attempted, which is used to calculate the gradient $(\nabla g)_{\mathbf{z}=\mathbf{z}_n}$ and hence a new solution \mathbf{z}_{n+1} using Equation 3.8, in which λ is a regularisation parameter with a value between 0 and 1 and \mathbf{k} a unit vector in the direction of $(\nabla g)_{\mathbf{z}=\mathbf{z}_n}$. This process is continued until the system of Equations reaches convergence.

At the boundaries of the device, reflecting i.e. Neumann boundary conditions are used which mean the electric field and current densities normal to the boundaries are zero. As long as the device simulation is that of a regular, repeating unit of the sensor (e.g. a pixel or group of pixels), these will correspond to the planes of symmetry that occur in a real device where these conditions would arise naturally. The application of a potential to a contact (or setting a contact to a potential of 0V) represents another boundary condition for the system of Equations. However, these boundary conditions are Dirichlet ones, for which the value specified at the boundary is the value the solution must have at that boundary.

$$\mathbf{z}_{n+1} = \mathbf{z}_n - \lambda \frac{g(\mathbf{z}_n)}{|(\nabla g)_{\mathbf{z}=\mathbf{z}_n}|} \mathbf{k} \quad (3.8)$$

In principle, boundary conditions as represented by the potentials applied to the contacts can be used and the system of Equations solved directly for any chosen set of potentials. However, in practice it facilitates convergence if the system of Equations is solved with all contacts held at a potential of 0V before beginning to ramp up the potential(s) that are applied, solving the system of Equations for each set of potentials until the final (and actually desired) potentials are applied to the contacts. To speed up computation, the initial solution used for each set of potentials is the solution arrived at for the previous set of potentials (aside from the first set of potentials attempted where the initial state of the system is used).

For each of the devices simulated for the work presented in this thesis (specifically those in Chapter 4), the pixel implant contact was held at ground while the backside, high voltage contact was set to the value of the bias used for the real device to which the simulated device corresponded, i.e. the $300\mu\text{m}$ thick Si sensors had a potential of 90 V applied to the backside contact, while the $500\mu\text{m}$ thick one had a 100 V potential applied to the backside contact. The scripts used for the simulation of devices using `sde` and `sdevice` are given in Appendix B, along with the specific device parameters used in the simulations.

3.5 Summary

The study and characterisation of HPDs for use in TEM entails a range of experimental techniques and apparatus, as well as a number of computational tools. This chapter has given an overview of the devices studied as part of the present work as well as the techniques and experimental apparatus used to characterise them. It has included a description of the Medipix3 ASIC and how it operates, along with a description of the specific devices based on this ASIC that are characterised in Chapters 4 and 6. The experimental procedure used to calibrate the counting thresholds of the Medipix3 detectors have been described along with the procedures used to determine their MTF, NPS, DQE and linearity of response. Additionally, an alignment for performing confocal STEM scans of detectors has been described, along with the methods used to determine the size of the probe incident upon the detector and the approach used to process the 4D confocal STEM scans to obtain sub-pixel maps of a detector. Finally the software packages used for the simulation of detectors and the interactions of electrons with different sensor materials have been outlined.

4

Counting Detectors with Si Sensors

4.1 Introduction

In this chapter, the results of measurements characterising the performance of the three Medipix3 detectors with different Si sensors are presented. Points of comparison include the energy spectra recorded by the three devices exposed to electrons with energies ranging from 60-200 keV; MTF and DQE measurements for 60 keV and 200 keV electrons; and detector deadtime for 200 keV electrons. All measurements were performed with the detectors operating in SPM unless otherwise stated. Simulations performed with the Allpix² framework were used in an attempt to gain further insight into the experimental measurements.

Section 4.2 compares the spectra recorded by the three detectors with one another as well as with the results of simulations. This provides a means by which to attempt to validate the simulations. While the comparison of the simulation results with experimental measurements indicated that further refinement of the simulations was necessary, the simulation results nevertheless provided insight into how the interactions of the incident primary electrons and the secondary quanta they produce give rise to the measured spectra. MTF and DQE measurements of the three detectors as a function of counting threshold are discussed in Section 4.3, presenting an opportunity to explore how MTF and DQE depend on sensor thickness and pixel pitch as well as electron energy. Finally the detectors' deadtime and their linearity of response are investigated in Section 4.4.

4.2 Spectral Measurements

The spectrum recorded by a detector along with its energy resolution for a given electron energy are indicative of the extent to which a detector is able to fully and

accurately measure the energy of electrons incident upon it. This is potentially important from the perspective of correctly identifying and distinguishing between different particles. For example, when developing strategies for localising the entry point of electrons, it may be helpful to distinguish between those electrons that have been absorbed by the sensor and those that have been backscattered. The lateral spread in energy for the two types of events is likely to be quite different, and it may make sense to process pixel clusters due to these two type of event differently when attempting to identify the electron entry point.

More generally, the spectra recorded by the three detectors, in principle, helps to elucidate the interactions of electrons with the sensors, which in turn give insight into the differences in the MTF and DQE measured for the three detectors. For example, to what extent does the scatter of secondary quanta produced by the primary electron contribute to the spread of signal at a significant distance from the region the primary electron interacts with the sensor and does this cause a deterioration in MTF and DQE? As one of the simplest ways of characterising a detector's response, it also provides a basic dataset for the purposes of validating any simulations or models of detector response. Section 4.2.1 therefore reports and discusses the spectra recorded for the three detectors, while in Section 4.2.2, a selection of the experimental spectra are compared with the results of simulations.

4.2.1 Experimental Measurements

Figure 4.1 shows the spectra recorded by the three detectors when they operate in SPM, while Figure 4.2 shows the spectra recorded when they operate in CSM. The spectra in Figure 4.1(a) feature periodic patterns that are not visible in the spectra seen in Figures 4.1(b) and (c) or any of the spectra seen in Figure 4.2. This is likely due to a higher than usual level of electronic noise on the threshold and counter that were active when these spectra were acquired.

In Figures 4.1(a) and (c), it is not possible to discern peaks corresponding to the incident electron energy, aside from when the primary electron energy is 60 keV or 80 keV. Even in the 60 keV and 80 keV spectra in Figures 4.1(a) and (c), the peaks are difficult to distinguish from the low-energy range of the spectrum in which they appear. This is due to incident electrons depositing their energy over multiple pixels so that no pixel records the entirety of the electrons energy. As each pixel operates independently, this gives rise to a tail to the primary electron peak. The greater the number of pixels over which the primary electron's energy is deposited, the larger the tail. For the 120 keV and 200 keV spectra in Figures 4.1(a) and (c), the spread in energy is so great that the tail dominates entirely and there is no peak. This effect is less pronounced for the spectra recorded by the $110\ \mu\text{m}$ pitch device in Figure 4.1(b).

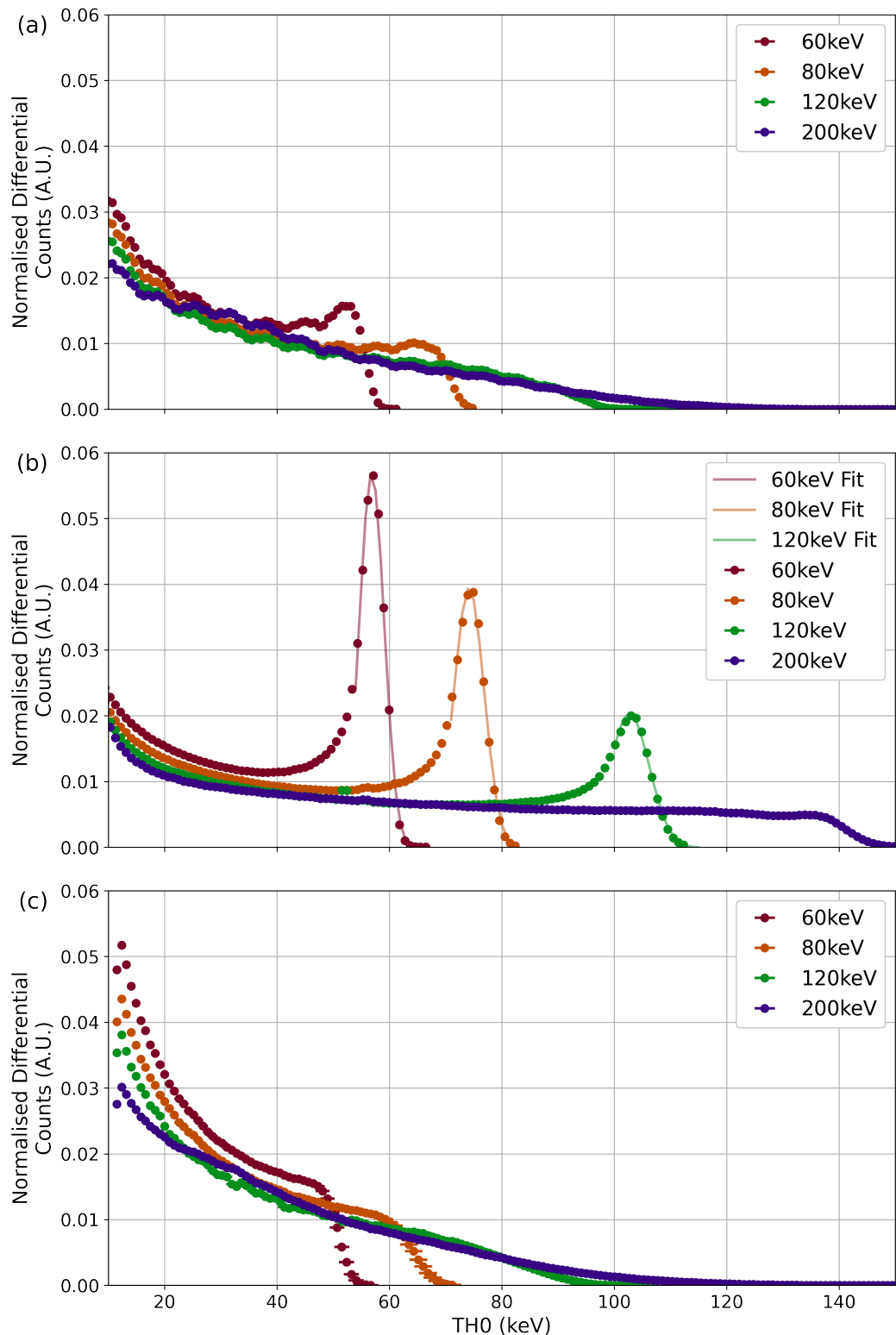


Figure 4.1: Spectra for electrons with energies from 60 keV - 200 keV recorded by Medipix3 detectors operating in SPM with (a) 300 μm thick and 55 μm pitch (b) 300 μm thick and 110 μm pitch and (c) 500 μm thick 55 μm pitch Si sensors.

Peaks corresponding to the primary electron energy are readily visible in the spectra for electrons with energies of 60 to 120 keV, though these still exhibit a tail.

These peaks were fitted with Gaussian functions using a least-squares ODR procedure to determine the energy measured by the detector for each electron energy and to calculate the detectors' energy resolution for each energy. Errors on the peak energy and standard deviation were calculated using the same approach used to estimate errors on the peaks fitted in the X-ray spectra used to calibrate the detectors' counting thresholds described in Chapter 3. The measured energies obtained using this procedure and their resolutions are listed in Tables 4.1 and 4.2.

In Figure 4.1(b), the 200 keV spectrum is similar to the 60 keV and 80 keV spectra in Figures 4.1(a) and (c), and it was not possible separate the primary electron peak from its tail and fit it with with a Gaussian. This indicates that the distance over which 200 keV electrons scatter in $300\ \mu\text{m}$ thick Si sensors, and the resulting lateral dispersion of signal, is sufficiently large that, even in devices with $110\ \mu\text{m}$ pitch pixels, significant amounts of energy are deposited on more than one pixel. Consequently, there is a deterioration in the spectral response and difficulty in distinguishing any kind of peak from the low-energy tail, as is the case for the $55\ \mu\text{m}$ pitch devices for all primary electron energies considered in Figures 4.1(a) and (c). Lower energy electrons, however, deposit most of their energy in a single $110\ \mu\text{m}$ pitch pixel, leading to the well-defined peaks observed in Figure 4.1(b). The improved spectral response of the $110\ \mu\text{m}$ pitch device is simply because incident electrons deposit more of their energy on each pixel, so that the variation in the energy recorded by individual pixels is reduced. This is also reflected in the fact the difference between E_0 and the measured maximum energy is smaller in the spectra recorded by the $110\ \mu\text{m}$ pitch device than it is in the spectra recorded by the $55\ \mu\text{m}$ pitch devices.

Were the devices being tested capable of registering the total amount of energy deposited in each pixel then, in principle, it would be possible to reconstruct the total energy deposited by each electron which would reduce the difference between the measured energy and the known primary electron energy. However, even in this instance, some disparity is likely to remain due to electrons losing some energy in the entrance window of the sensor [184] and some pixels receive some portion of the primary electron's energy registering insufficient energy to be distinguishable from the detector noise (so that the energy is effectively lost).

Looking at the spectra shown in Figure 4.2, the CSM algorithm improves the spectral response and energy resolution of all three devices. In the spectra recorded by all three devices, the low-energy tail is greatly reduced. Furthermore the 60 keV and 80 keV peaks in all three sets of spectra are readily apparent and can be fit with individual Gaussian functions. Tables 4.1 and 4.2 record the positions of these peaks and the detectors' energy resolution for these primary electron energies.

However, the peaks corresponding to 120 keV and 200 keV electrons appear somewhat distorted. For the 120 keV spectrum in Figure 4.2(a), the primary electron

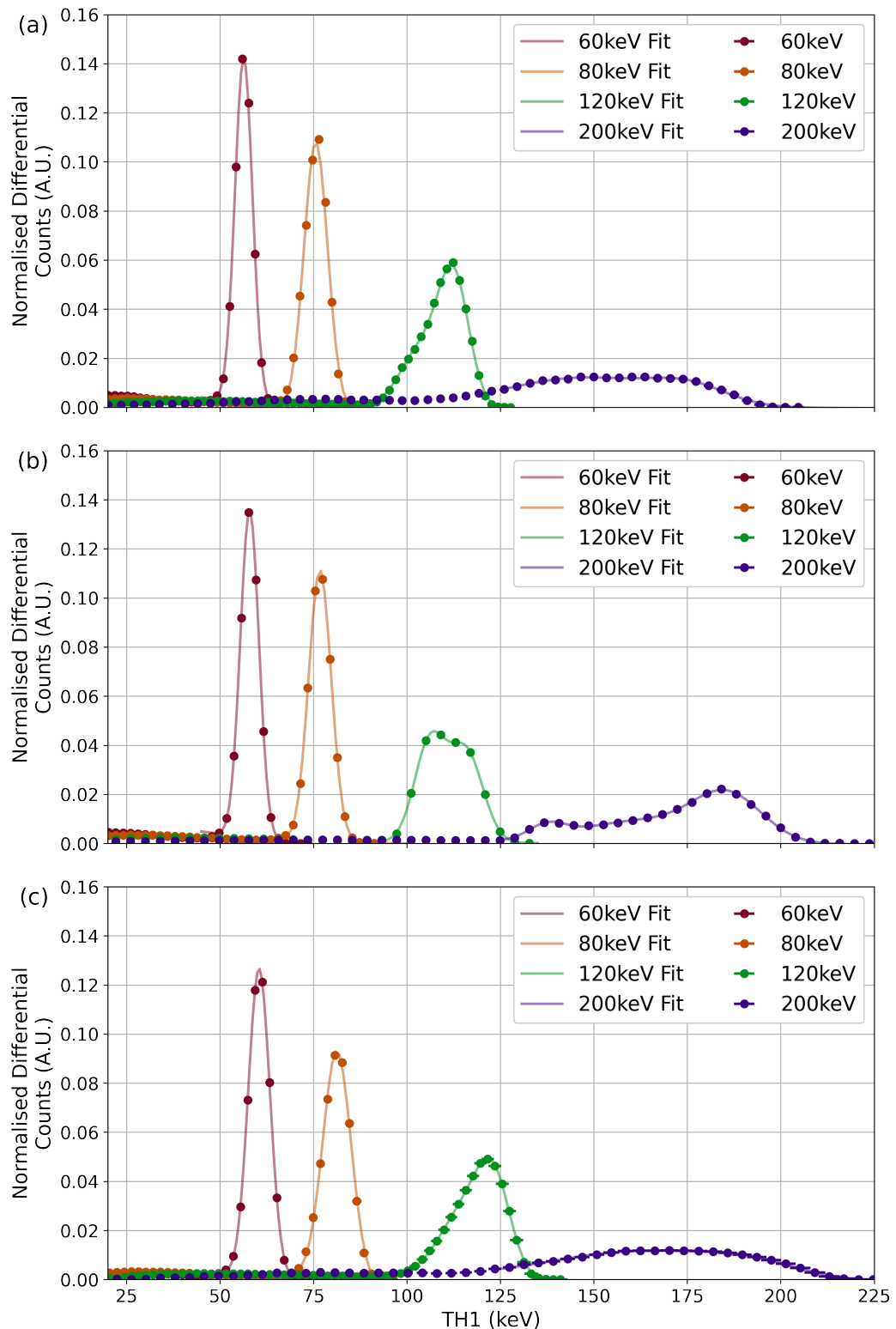


Figure 4.2: Spectra for electrons with energies from 60-200 keV recorded by the Medipix3 detector with (a) a $300\mu\text{m}$ thick Si sensor and $55\mu\text{m}$ pixel pitch; (b) a $110\mu\text{m}$ pixel pitch and $300\mu\text{m}$ thick Si sensor; and (c) a $500\mu\text{m}$ thick Si sensor and $55\mu\text{m}$ pixel pitch. All devices were set to operate in CSM.

peak appears to have low-energy “shoulder”, which is suggestive of a second, lower-

energy peak that cannot be distinguished from the primary electron peak. The peak in the 120 keV spectrum in Figure 4.2(c) is similar in appearance, although the shoulder is not so pronounced as those seen in the SPM spectra in Figures 4.1(a)-(c). In the case of the 120 keV spectra recorded by the $110\ \mu\text{m}$ pitch detector, the primary peak almost appears to be divided into two, with the height of the low-energy one being greater than the high-energy one. However, as was the case for the 120 keV spectra in Figures 4.2(a) and (c), if there are two peaks present in this spectrum they cannot be fully resolved. For the 200 keV spectra in Figures 4.2(a)-(c), there is significant broadening of the primary electron peak, though in both cases it is possible to identify a region corresponding to the peak (or peaks) and a lower-energy tail. In Figure 4.2(b), the 200 keV peak appears to feature a low-energy shoulder with the primary peak itself having also broadened significantly.

It was found that the regions corresponding to the primary electron peak in the 120 keV spectra in Figures 4.2(a)-(c) were best fit with a function describing a pair of Gaussian functions. The high-energy region in the 200 keV spectrum in Figure 4.2(b) was fit with a triple Gaussian function. Although the peaks in the 200 keV spectra recorded by the $55\ \mu\text{m}$ pitch detectors in Figures 4.2(a) and (c) do not show the same structure observed in the 200 keV spectra recorded by the $110\ \mu\text{m}$ pitch detector in Figure 4.2(b), these peaks were still best fit with a triple Gaussian function. The positions of both the primary (i.e. highest-energy) and any secondary peaks identified in the 120 keV and 200 keV spectra in Figure 4.2 are listed in Table 4.1. As none of the peaks identified in these spectra could be fit with a single Gaussian, it was not possible to determine the detectors' energy resolution for these values of E_0 .

Although the peaks in the 120 keV and 200 keV CSM spectra have been fit with more than one Gaussian function, this is not to claim that quanta of more than one energy is incident upon the detector. The position of these "secondary" peaks is noted in Table 4.1 on the basis that they provide a measure of the extent to which the spectra are distorted and the spread in the energies recorded.

Considering the energies associated with the peaks identified in the spectra in Figures 4.1 and 4.2 in Table 4.1, it can be seen that as the primary electron energy increases so to does the disparity between the electron energy and the measured energy, at least for the devices with $300\ \mu\text{m}$ thick sensors. For 60 keV and 80 keV electrons, the greatest mismatch between the primary electron energy is 4 ± 1 keV ($300\ \mu\text{m}$ thick sensor with $55\ \mu\text{m}$ pixel pitch) and 6 ± 1 keV ($300\ \mu\text{m}$ thick sensor with $110\ \mu\text{m}$ pixel pitch operating in SPM) respectively. The device with the $300\ \mu\text{m}$ thick Si sensor and $110\ \mu\text{m}$ pixel pitch when operating in SPM continues to display the greatest difference between the measured energy and E_0 for 120 keV and 200 keV electrons. This is likely because, unlike the other measurements which are acquired with the detectors operating in CSM, there is no attempt to reconstruct the total energy deposited by individual electrons.

E_0 (keV)	Sensor	Primary Peak Position (keV)	Secondary Peak Position(s) (keV)
60	300 μm , 55 μm	56 \pm 1	-
	300 μm , 110 μm (SPM)	57 \pm 1	-
	300 μm , 110 μm (CSM)	58 \pm 1	-
	500 μm , 55 μm	60 \pm 1	-
80	300 μm , 55 μm	76 \pm 1	-
	300 μm , 110 μm (SPM)	74 \pm 1	-
	300 μm , 110 μm (CSM)	77 \pm 1	-
	500 μm , 55 μm	81 \pm 1	-
120	300 μm , 55 μm	113 \pm 3	104 \pm 1
	300 μm , 110 μm (SPM)	103 \pm 3	-
	300 μm , 110 μm (CSM)	116 \pm 3	106 \pm 3
	500 μm , 55 μm	123 \pm 3	116 \pm 3
200	300 μm , 55 μm	176 \pm 3	77 \pm 1, 147 \pm 3
	300 μm , 110 μm (SPM)	135 \pm 3	-
	300 μm , 110 μm (CSM)	186 \pm 3	138 \pm 3, 163 \pm 3
	500 μm , 55 μm	192 \pm 3	80 \pm 1, 164 \pm 3

Table 4.1: Positions of peaks identified via fitting of the spectra recorded by the different Si sensors and presented in Figures 4.1(b) and Figures 4.2(a)-(c).

Looking at the energy resolution of the detectors for those combinations of primary electron energy, detector and operational mode for which it was possible to fit the primary electron peak with a single Gaussian, it can be seen that there is no obvious dependence on energy. Assuming the energy resolution of the detectors' was limited by the variations in the number of charge carriers produced by incident electrons in the sensor, their resolution would be 0.6%, 0.5% and 0.4% for 60 keV, 80 keV and 120 keV electrons respectively. The detectors' energy resolution is therefore over two orders of magnitude worse than that predicted by Equation 1.46. This can be attributed to the deposition of energy over multiple pixels as well as the backscatter of primary electrons.

E_0 (keV)	Sensor	Energy Resolution (%)
60	300 μm , 55 μm	10 \pm 6
	300 μm , 110 μm (SPM)	9 \pm 6
	300 μm , 110 μm (CSM)	10 \pm 6
	500 μm , 55 μm	11 \pm 6
80	300 μm , 55 μm	10 \pm 4
	300 μm , 110 μm (SPM)	9 \pm 4
	300 μm , 110 μm (CSM)	9 \pm 4
	500 μm , 55 μm	11 \pm 4
120	300 μm , 110 μm (SPM)	8 \pm 3
	300 μm , 110 μm (CSM)	9 \pm 3

Table 4.2: Resolution of those peaks identified in Figures 4.1(b) and Figures 4.2(a)-(c) for which a single peak could be identified and fit with a single Gaussian.

4.2.2 Comparison with Simulations

Turning to the results of simulations, Figure 4.3 presents a comparison of the spectra recorded by the device with a $300\ \mu\text{m}$ thick Si sensor with $55\ \mu\text{m}$ pixel pitch and its simulated counterpart for 60 keV and 200 keV electrons. Although simulations were performed for all three Si sensors, the results shown in Figure 4.3 were those that came closest to agreeing with the experimental spectra. The simulated SPM spectra were generated by applying the same counting thresholds used when acquiring the experimental data to the signal associated with the `PixelCharge` objects produced for each of the 20 000 simulated events. For each threshold, the total number of pixels that remained above threshold for all simulated events were noted to mimic a threshold scan. These were then differentiated to obtain a differential spectrum. For the CSM simulated spectrum, the signal associated with `PixelCharge` objects produced for each individual event were processed to identify which pixels registered the highest reconstructed charge locally, thereby mimicking the CSM algorithm. The values of TH1 used when acquiring the experimental CSM spectra were then applied to the reconstructed sum associated with these pixels, and the total number of pixels that exceeded each counting threshold differentiated to obtain a CSM spectrum.

An important point regarding the way in which the simulated spectra were generated is that, as the signal associated with `PixelCharge` objects were used rather than associated with the `PixelHit` objects, the effects the pixel electronics and the noise associated with them are not included. This choice was motivated by the fact that an accurate simulation of the effects of the signal processing electronics would have required running simulations for each desired threshold rather than one set of simulations and applying the thresholds in post-processing. The failure to incorporate this electronic noise represents a potential cause of the observed divergence between the experimental measurements and simulation results. However, the simulation of electronics noise is not essential for the accurate simulation of the response of HPDs to electrons. Instead, factors such as the incorporation of the entrance window has been found to be more important [184, 290, 291].

Comparing the simulation and experimental data in Figures 4.3(a) and (b), they are not entirely in agreement with one another. For the former, the peak in the simulated data is more pronounced than is the case in the experimental data, while in the latter the peak is smaller and at a lower energy in the simulated data than is the case for the experimental data. Although the experimental data and simulated data appear to be in relatively good agreement in Figure 4.3(c), in Figure 4.3(d) there is again a notable disparity. This disagreement between experiment and simulation indicates that further refinement of simulation parameters is required before simulations can be relied upon for quantitative insight into detector behaviour.

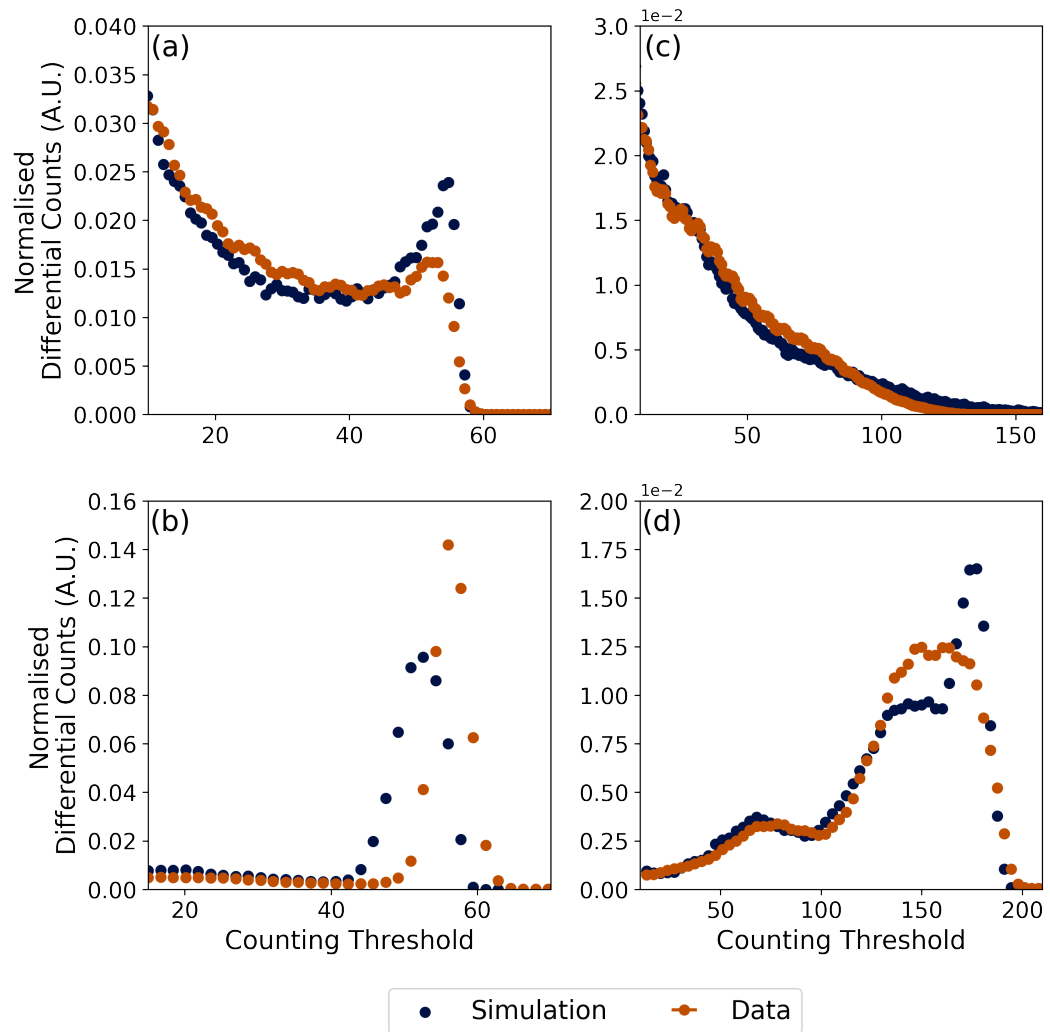


Figure 4.3: Comparisons of the simulated and experimental spectra for a Medipix3 detector with a $300\mu\text{m}$ thick Si sensor and $55\mu\text{m}$ pixel pitch exposed to 60 keV electrons with the detector operating in (a) SPM and (b) CSM; exposed to 200 keV and the detector operating in (c) SPM and (d) CSM.

In Allpix², charge carriers deposited in the sensor are grouped together when simulating their propagation through the sensor due to drift and diffusion. A key parameter in determining the accuracy of the simulation is the maximum number of charge carriers that can be grouped together for the purposes of the simulation. A smaller maximum should lead to an improvement in simulation accuracy at the cost of greatly increased computational demands. An improper choice in this parameter could be responsible for not accurately accounting for the effects of diffusion, thereby giving rise to the observed disparity between simulation and experiment. As the (average) total number of charge carriers produced by 60 keV electrons is much smaller than that produced by 200 keV electrons, the maximum number of charge carriers that could be grouped together for the purposes of propagation was correspondingly smaller. The maximum number of charge carriers that could be grouped together for the purposes of propagation were 50 and 200 for the 60 keV and 200 keV simulations

respectively. These values were chosen so as to restrict the total number of groups of charge carriers that had to be propagated to ~ 300 , a limit that was dictated by the available computational resources. Nevertheless, it appears that the maximum number of grouped charge carriers was too high in the case of the 60 keV simulations. This is likely because, due to the shorter length of the trajectories of 60 keV electrons compared with those of 200 keV electrons, as well as the fact that the average depth of energy deposition is reduced for 60 keV electrons compared with 200 keV electrons, the effect of the diffusion of charge carriers in determining the lateral spread of signal is more important for 60 keV electrons than it is for 200 keV electrons.

However, the observed differences between the experimental and simulated data in Figures 4.3(a) and (b) are somewhat contradictory. In Figure 4.3(a), the fact that the peak in the simulated data is more pronounced than is the case in the experimental data implies that the extent to which signal is lost to neighbouring pixels due to the diffusion of charge carriers is underestimated in the simulation. Contrary to this hypothesis is the fact that the simulated peak occurs at a lower energy than expected based on the experimental data in Figure 4.3(b). This implies that the effects of diffusion are overestimated.

Consequently, it seems likely that another factor contributes to the observed disparities between simulation and experiment. A likely candidate for this is the composition of detector's entrance window. In the simulations, the detector entrance window consisted of a $0.5\ \mu\text{m}$ thick Al contact and a $1\ \mu\text{m}$ thick layer of Si to mimic the layer of highly doped n-type material at the sensor's backside that ensures a good electrical contact but that is insensitive to incident radiation. If there were, variations in the thickness of this entrance window, this would increase the variation in the total amount of energy deposited in the sensor while not decreasing the maximum deposited energy. This would in turn lead to a broadening of the peak in any spectra without a decrease in the maximum registered energy. The fact that the simulation did not include this variation in entrance window thickness could then explain the disparity between experiment and simulation seen in Figure 4.3(a) while still being consistent with the simulation overestimating the effects of diffusion. This would, in turn, explain the differences in the experimental and simulated results in Figure 4.3(b). Additionally, the simulated CSM results may be more sensitive to the effect of an inaccurate simulation of charge-carrier transport as the CSM signal depends on the sum of signal registered on neighbouring pixels. If, on average, the signal registered on each individual pixel is less than it should be, then the CSM signal will see this same average reduction scaled by the number of pixels over which the signal is reconstructed.

Although no direct experimental evidence of there being variation in the backside entrance window of the $300\ \mu\text{m}$ thick sensor with $55\ \mu\text{m}$ pixel pitch was collected, it has been observed in other devices. This includes the GaAs:Cr HEXITEC device discussed in

Chapter 7 and the detector installed on the Glasgow ARM cF 200 (S)TEM. In the case of the latter example, confocal STEM scans of the device acquired while developing the technique (seen in close-up in Figure 3.16(e)) showed variations in intensity that are not visible in flat field images of the sensor and that are best explained by variations in the thickness of the entrance window. Figure 4.4 shows the full confocal STEM map where this is apparent. Without further measurements, variation in the entrance window cannot be discounted as a contributing factor to the divergence of the simulations from experimental measurements. Confocal STEM maps of the sensors could help to determine whether there is significant variation in the thickness of their entrance window that is otherwise not visible, thereby helping to further refine the simulation configurations. Additionally, although this would not be advisable with a working device, in principle this hypothesised variation in contact thickness could be confirmed and measured by using an atomic force microscope (AFM). As the sensor manufacture process is, in the case of Si sensors, a wafer-scale process, this could be done using a portion of a wafer that was surplus to requirements given the layout of sensors or, alternatively, the sensor of a non-functioning device could be used.

Further simulations which investigated how the thickness of the backside contact, and variations thereof, affect detector response including the spectral response would, in principle be straightforward. This simply requires modifying the simulation geometry, which can be done by editing one of the configuration files that compose the simulation input. Some initial simulations where the thickness of the backside contact was varied were performed, with a view to determining whether this proposed variation in backside contact thickness was responsible for the disparity between the experimental and simulation results. However, these were quite limited and consisted in replacing a single backside contact that was 0.5 μm thick with three strips of Al (covering the same area i.e. the entirety of the sensor surface), with thicknesses of 0.45 μm , 0.5 μm and 0.55 μm , to mimic a situation where there the backside contact thickness varied by $\pm 10\%$ of the expected value. The results of these simulations were not significantly different from the results obtained using a single contact of constant thickness. It would be advisable to perform AFM measurements, as discussed above, to determine experimentally the extent to which there was any variation in contact thickness. Such measurements could then inform a refined specification of the backside contact geometry in future simulations.

A key point about these simulation results is the fact that the 200 keV CSM spectrum in Figure 4.3(d) features distortions that are consistent with those observed in the experimental data. Rather than a single peak being observed, a peak with two low-energy shoulders is observed. While this does not agree completely the experimental results, which show what appears to be a single, broader peak with one low-energy shoulder, it does agree well with the fact that the single peak in the experimental data was best fit with a triple Gaussian function. Overall, the simulation

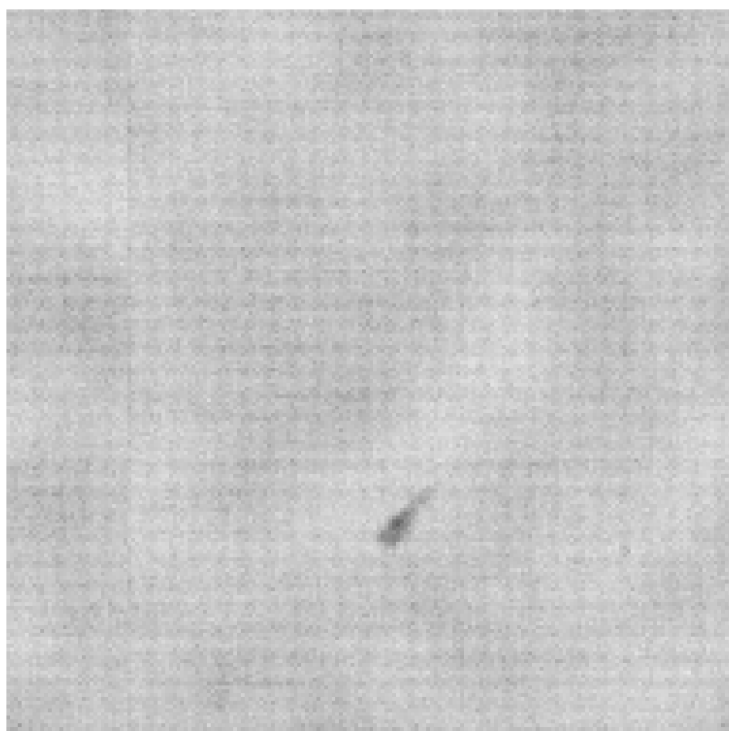


Figure 4.4: Sum confocal STEM scan image of the Medipix3 detector installed on the Glasgow ARM 200 cF (S)TEM using 200 keV electrons. The detector operated in SPM and used a low counting threshold just above the detector's intrinsic noise level. The same scan was shown in close-up in Figure 3.16(e). While variation in the number of counts due to increased number of pixels recording incident electrons when the beam is at the edge of a pixel, there is also a variation in the intensity at lengthscales on the order of a few pixels that are likely due to variation in the thickness of the entrance window. This is not seen in flat field images of the same sensor. There also appears to be a region with fewer counts due to a piece of detritus on the sensor.

results would seem to favour the idea that the distortions in the 120 keV and 200 keV CSM spectra in Figure 4.2 are due to the CSM algorithm itself. The disparity between the SPM and CSM spectra in Figure 4.3(c) would be consistent with there being a variation in the thickness of the entrance window in the real detector that is not accounted for in the simulation. This could cause a broadening of the peak and higher-energy shoulder so that these cannot be fully distinguished in the experimental data.

If the contact is thinner, on average, than is thought to be the case based on the data provided by Advacam, then this would account for the peak at a higher energy than is predicted by the simulations in Figure 4.3(b). The consequences of reduced energy loss in a thinner contact would be most pronounced in the 60 keV results as low-energy electrons, on average, lose a greater fraction of their energy in the sensor entrance window. In SPM, the deposition of incident electrons' energy over multiple pixels means that an increase in the average total amount of energy deposited in the sensor is not necessarily apparent. However, the effectiveness of the CSM algorithm in reconstructing the total charge deposited in the sensor by individual 60 keV electrons

could lead to an upwards shift of the energy peak. This would account for the obvious difference in the energy of the simulated and experimental peaks in Figure 4.3(b). A thinner, on average, backside contact would also be consistent with the narrower peak in the experimental data due to reduced variation in the energy of incident electrons as they enter the sensor (having lost a variable amount of energy in the backside contact).

Simulated spectra can also be generated on the basis of the total energy recorded by individual pixels and pixel clusters. The former is equivalent to a SPM spectrum, while the latter represents the that would be recorded were the detector an energy resolving one that was exposed to a low incident flux so that the total energy recorded over pixel clusters due to incident electrons could be reconstructed. By identifying the types of particles that deposited charge in individual pixels and by extension pixel clusters, it is possible to gain a better understanding of how electron interactions with the sensor give rise to the distribution of energy registered by the detector as well as the detector's performance more generally. Figure 4.5 shows both types of spectra for a detector with a $300\ \mu\text{m}$ thick Si sensor and $55\ \mu\text{m}$ pixel pitch for 60 keV and 200 keV electrons.

It can be seen that for all spectra in Figure 4.5 that most pixels, and by extension clusters, register energy that is due to a combination of that directly deposited by primary electrons and indirectly through the creation of secondary electrons. The low energy tail seen in the unclustered spectra in Figures 4.5(a) and (c) is largely due to primary electrons and the secondary electrons they create depositing their energy over multiple pixels. In the clustered spectra in Figures 4.5(b) and (d), the primary electron peak corresponds to those events where the primary electron has been absorbed, with very few such events contributing to the low energy tail. This indicates that the individual pixels over which primary electrons deposit their energy are largely contiguous, so that summing the energy deposited over them reconstructs the total energy deposited by the primary electron. The low energy tails in both Figures 4.5(b) and (d) are largely due to electrons that have backscattered from the sensor. It does not appear to be the case that a significant number of pixels register energy due to secondary quanta that travel a significant distance from where the primary electron enters the sensor, giving rise to a separate, secondary pixel cluster (even of only a single pixel). This would be indicated by pixels and clusters due entirely to secondary electrons or X-rays.

However, a small fraction of clusters lie in the low-energy tail although they are identified as having been absorbed by the sensor rather than backscattered. This suggests that there some instances of the pixels that register energy due to a single primary electron (and the secondary electrons that it produces) that are not direct neighbours. One possible cause of this may be the primary electron scattering out of the sensor into the entrance window and then back into the sensor. A very small fraction of pixels and clusters register energy that is deposited in the sensor through a more complex series of interactions than just the production of secondary electrons.

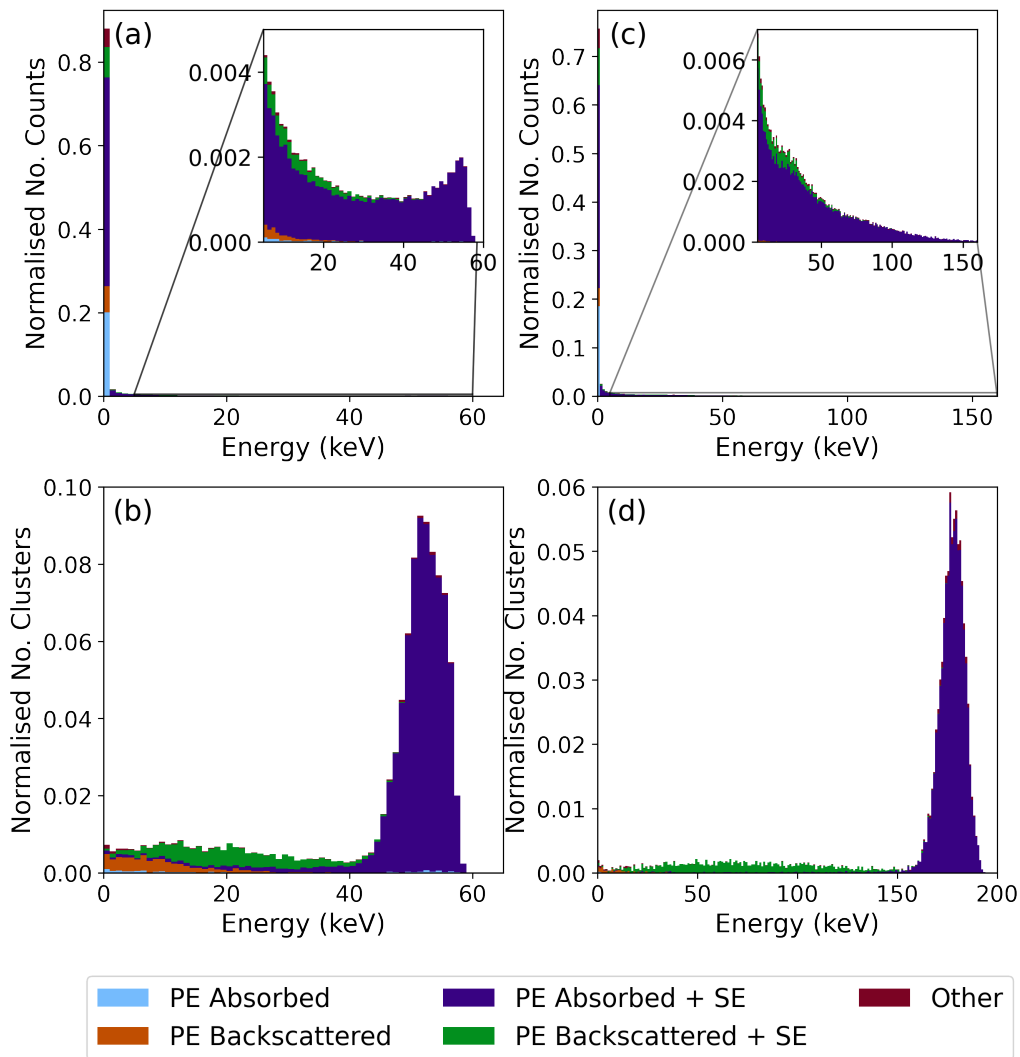


Figure 4.5: Spectra produced by simulating the response of a $300\mu\text{m}$ thick Si sensor with $55\mu\text{m}$ pitch exposed to (a) and (b) 60 keV electrons and (c) and (d) 200 keV electrons. In (a) and (d), spectra have been generated on the basis of the energy registered by individual pixels. For (c) and (d), spectra were constructed based on the sum signal recorded by pixel clusters, which identified as those pixels that recorded any signal and were neighbouring in a two-connected sense. Spectra have been broken down on the basis of whether or not the energy deposited in the pixel or cluster (as appropriate) was due to the primary electron (PE) that was absorbed or backscattered by the sensor; a combination of the primary electron (absorbed or backscattered) and secondary electrons that are absorbed by the sensor (SE) or another combination of particle and interaction types (labeled “Other”)

These include the production of X-rays or the deposition of energy by secondary electrons that escape from the sensor etc.

An important point regarding the 200 keV clustered spectra in Figure 4.3(d) is that by summing the energy deposited in clusters of neighbouring pixels gives rise to an evident peak corresponding to the primary electron energy. The same dataset, when processed in such a way as to mimic the operation of the CSM algorithm produces a spectrum that resembles the corresponding experimental CSM spectrum. This is further evidence in favour of the hypothesis that it is the CSM algorithm

introduces distortions into the spectra recorded when the Medipix3 detectors are exposed to electrons with sufficient energy to deposit their energy over more than one 2×2 pixel block.

4.3 MTF and DQE Measurements

The MTF and DQE of HPDs used with electrons are the result of the interplay between various factors, namely electron energy, sensor thickness and physical pixel pitch. In Section 4.3.1 the results of MTF and DQE measurements of the three Si sensors for 60 keV and 200 keV electrons using various counting thresholds are presented, while Sections 4.3.2-4.3.4 consider how each of the above factors influences detector performance in turn.

4.3.1 Experimental Measurements

Figure 4.6 shows the MTFs and DQEs of the three Si sensors operating in SPM exposed to 60 keV electrons using selected counting thresholds. These selected thresholds are the lowest threshold common to all three devices; a threshold equal to half the primary electron energy and the highest threshold at which it was possible to fit the ESF data common to all three detectors. The MTFs and DQEs of the three detectors are expressed in terms of the Nyquist frequency of $55 \mu\text{m}$ pitch devices, 9.09 lp mm^{-1} . In Figure 4.6(a), the MTF of the device with the $300 \mu\text{m}$ thick sensor and $55 \mu\text{m}$ pixel pitch is greater than that of the device with a $500 \mu\text{m}$ thick Si sensor. However, in Figure 4.6(b), the MTF of the two devices are almost identical, while in Figure 4.6(c) the MTF of the thicker sensor surpasses that of the thinner. The MTF of the detector with the $300 \mu\text{m}$ thick sensor and $110 \mu\text{m}$ pixel pitch is consistently poorer than that of the other two devices in Figures 4.6(a) - (c), when considered in terms of the Nyquist frequency of the smaller pixel device. Compared in terms of their own respective Nyquist frequencies, the $110 \mu\text{m}$ pitch device only fails to outperform the other two devices for the high threshold MTF measurement in Figure 4.6(c) and the low threshold DQE in Figure 4.6(d), for which it is comparable with the DQE of the other $300 \mu\text{m}$ thick sensor.

For the DQE in Figures 4.6(d) - (f), that of the $300 \mu\text{m}$ thick sensor with $55 \mu\text{m}$ pitch pixel is consistently greater than that of the $500 \mu\text{m}$ thick sensor. While there is a significant decrease in the DQE of the two detectors with a $55 \mu\text{m}$ pitch in Figure 4.6(e) compared with in Figure 4.6(d), the reduction the DQE of the $110 \mu\text{m}$ pitch device is slight. For the highest threshold DQE measurements in Figure 4.6(f), the DQE of the $110 \mu\text{m}$ pitch device exceeds that of both the other two detectors across all spatial frequencies (up until its respective Nyquist frequency of $0.5\omega_N$). In the lower threshold measurements in Figures 4.6(d) and (e), the DQE of the $110 \mu\text{m}$ pitch

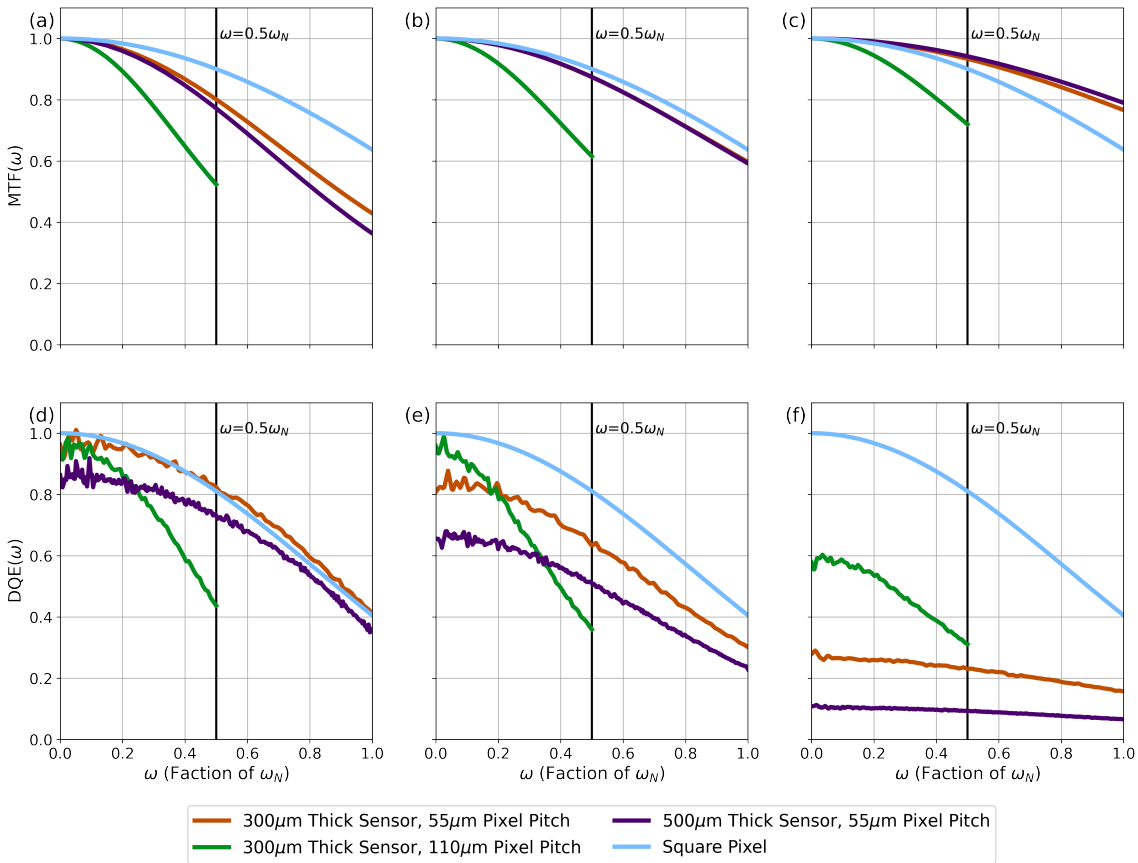


Figure 4.6: MTFs of the three Si Medipix3 devices exposed to 60 keV electrons when operating in SPM using counting thresholds of (a) ~ 12 keV, (b) ~ 30 keV and (c) ~ 48 keV. The corresponding DQE are shown in (d) - (f). Spatial frequencies are stated in terms of ω_N of the $55\ \mu\text{m}$ pitch detectors; $0.5\omega_N$ therefore represents the Nyquist frequency of the $110\ \mu\text{m}$ pixel pitch. The MTF of an idealised square pixel detector with is plotted in (a)-(c) and the corresponding DQE plotted in (d)-(f) as a cooperator.

device exceeds or matches that of the other two devices only at low spatial frequencies when compared in terms a common frequency scale but consistently surpasses or matches them when compared in terms of their respective Nyquist frequencies. It is worth noting that the low threshold DQE of the $300\ \mu\text{m}$ thick sensors in Figure 4.6(d) surpasses that of the ideal square pixel detector. This is an instance of greater suppression of deterministic blurring suppressing the NPS to a greater extent than the MTF leading to an improved DQE, as discussed in Chapter 1.

In Figure 4.7, the MTF and the DQE of three detectors when exposed to 200 keV electrons for selected counting thresholds are shown. The counting thresholds are the lowest counting threshold common to all three devices, the highest threshold common to all three devices for which the ESF data could be fit and the threshold equal to half this highest threshold. This different choice of thresholds is due to the greater disparity in the maximum amount of energy deposited in an individual pixel and the primary electron energy so that using a threshold equal to half the primary

electron energy would be too close to the highest threshold used to make the selected thresholds representative of device performance across the full threshold range. As expected given the increased area over which 200 keV electrons deposit their energy compared with 60 keV electrons, the detectors' MTFs are poorer in Figures 4.7(a)-(c) than they are in Figures 4.6(a)-(c). This also leads to a corresponding deterioration in DQE in Figures 4.7(d)-(f). The trends observed in the MTF data in Figures 4.7(a)-(c) are broadly similar to those observed in Figure 4.6(a)-(c).

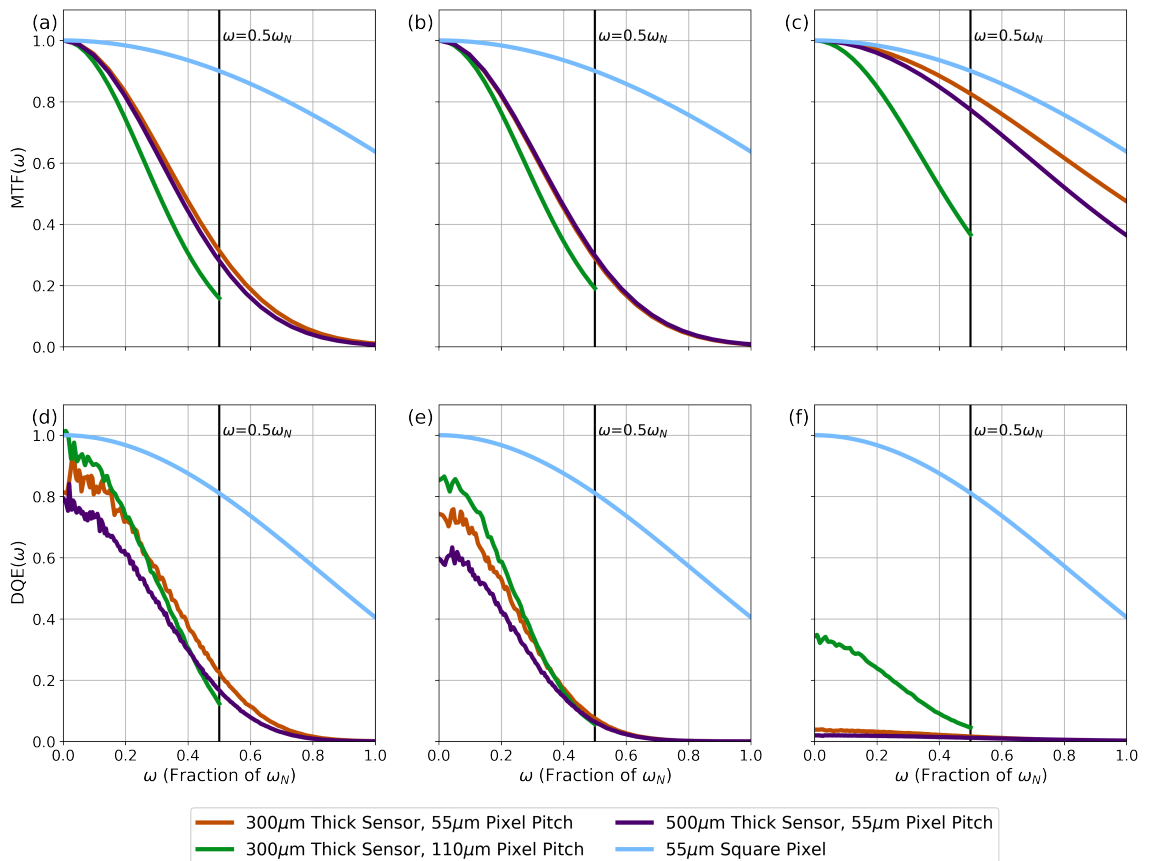


Figure 4.7: MTFs of the three Medipix3 detectors with Si sensors in SPM when using a counting threshold of (a) ~ 12 keV, (b) 59 keV and (c) ~ 118 keV. (d) - (f) show the devices' DQE for the same counting thresholds. As in 4.6, frequencies are stated in terms of ω_N of the $55\mu\text{m}$ pitch detectors and the MTF and DQE of a "ideal" square pixel detector is plotted as appropriate for ease of comparison. The primary electron energy was 200 keV.

The plots of the detectors' MTF at selected threshold in Figures 4.6(a)-(c) and Figures 4.7(a)-(c) indicate that the MTF of all three devices improves as the counting threshold increases for both 60 keV and 200 keV electrons, though the improvement is more pronounced for 60 keV electrons. As mentioned in Chapter 1, the effective pixel pitch dictates the MTF of a detector, and this can differ from the physical pixel pitch. The improvement observed in the MTF with increasing counting threshold is because, as the counting threshold increases, the amount of energy that an incident electron must deposit on a pixel for it to be registered by that pixel increases. Assuming that

incident quanta deposit most of their energy at or close to the point at which they enter the sensor, this means the distance from the centre of the pixel that incident quanta can enter the sensor, and still be counted by that pixel, decreases as the counting threshold is raised. At low counting thresholds, the effective pixel pitch for 60 keV and 200 keV electrons is larger than the sensors' physical pixel pitch, so that the measured MTFs are poorer than that predicted for an "ideal" square pixel detector. Though, as noted, the spread of signal can improve the DQE as in Figure 4.6(d). Whereas when a high counting threshold is used, the effective pixel size is smaller than that of the physical pixel, so that the measured MTF surpasses the expected

This reduction in effective pixel size as the counting threshold increases also accounts for the deterioration in the DQE observed as the counting threshold increases. As the amount of energy that incident quanta have to deposit on an individual pixel to be counted increases, so to does the probability of their not being counted at all, having deposited their energy over multiple pixels. As noted in Chapter 1, this dependence of MTF and DQE on threshold, and the origin thereof, has previously been documented for counting HPDs used both in photon science [292–295] and TEM [18, 50].

To better understand how the performance of the three detectors depends on counting threshold, the value of $MTF(\omega_N)$, $DQE(0)$ and $DQE(\omega_N)$ for all three detectors is plotted as function of counting threshold in Figures 4.8 for 60keV and 200 keV electrons. For the 60 keV results in Figures 4.8(a), the value of $MTF(\omega_N)$ for all three devices increases monotonically (almost linearly) with counting threshold. This is not the case for the 200 keV results in Figures 4.8(b). For the $55\mu\text{m}$ pitch devices, the value of $MTF(\omega_N)$ initially decreases as the counting threshold increases. However, at a counting threshold approximately equal to 60 keV, the value of $MTF(\omega_N)$ for these two devices begins to increase rather than decrease as the counting threshold is increased. The dependence of $110\mu\text{m}$ $MTF(\omega_N)$ on counting threshold is different in that it never exhibits a negative dependence on counting threshold. However, it is similar in that after initially increasing as the threshold does, the rate at which it increases with respect to the counting threshold becomes smaller, before beginning to increase again at high counting thresholds. There is in effect, something akin to a point of inflection at a threshold of ~ 60 keV.

Considering the behaviour of the two $55\mu\text{m}$ pitch devices in Figures 4.8(a), at low thresholds, the MTF of the $500\mu\text{m}$ thick sensor is poorer than that of the $300\mu\text{m}$ thick sensor, while the reverse is true at high counting thresholds. The extent to which the performance of the $300\mu\text{m}$ thick sensor (as summarised by the value of $MTF(\omega_N)$) surpasses that of the $500\mu\text{m}$ thick sensor at low counting thresholds is greater than the extent to which the performance of the latter surpasses that of the former at high counting thresholds. The threshold at which the difference between the values of $MTF(\omega_N)$ of the two $55\mu\text{m}$ pitch detectors is smallest is ~ 35 keV, i.e. approximately half the primary electron energy of 60 keV. Similarly the $110\mu\text{m}$ pitch

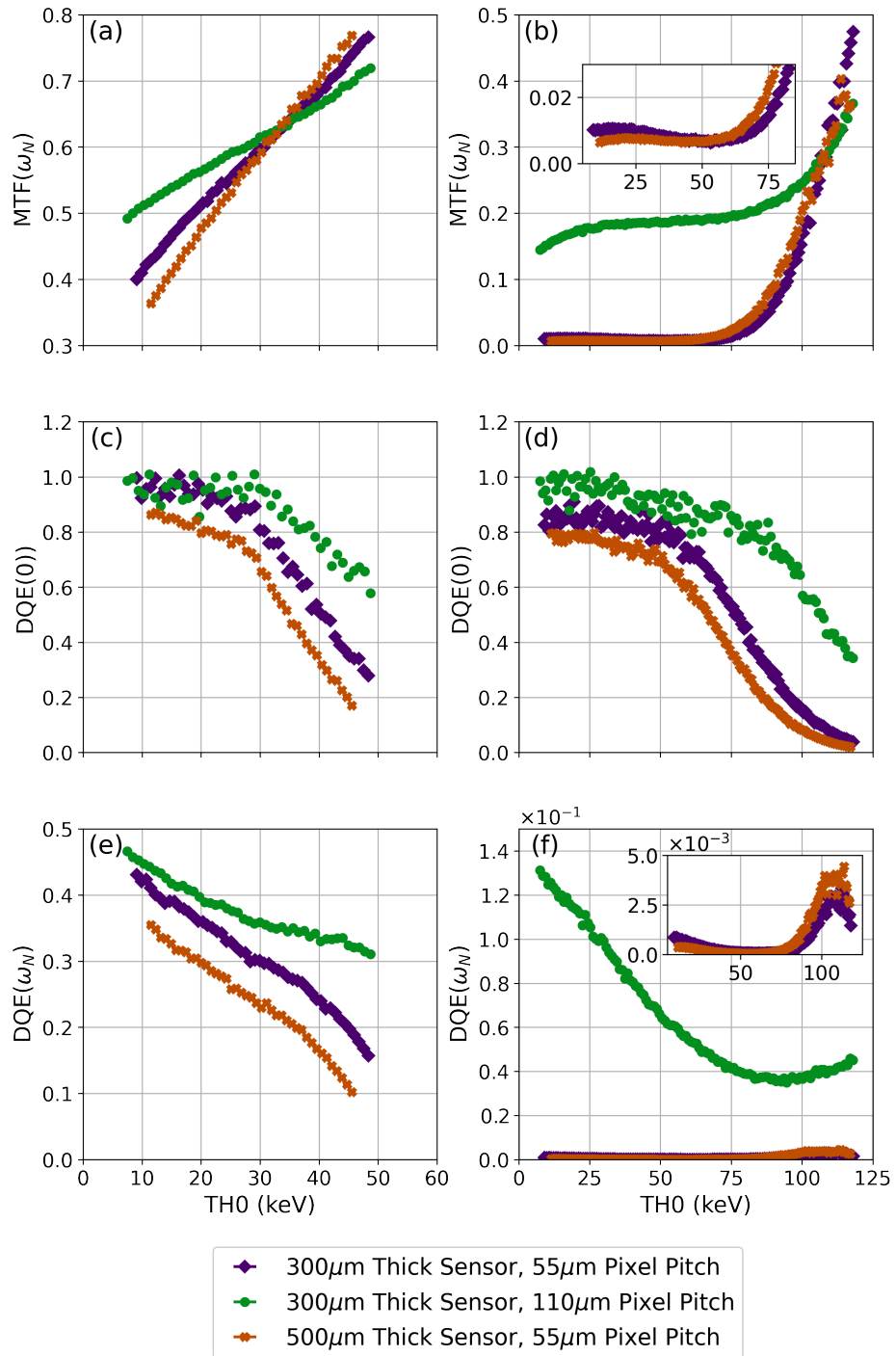


Figure 4.8: Plots of the dependence of the MTF and DQE as summarised by the values of $\text{MTF}(\omega_N)$, $\text{DQE}(0)$ and $\text{DQE}(\omega_N)$ on counting threshold for the three Si Medipix3 devices. In turn, the panels show the dependence of $\text{MTF}(\omega_N)$ for (a) 60 keV and (b) 200 keV electrons; the dependence of $\text{DQE}(0)$ on threshold for (c) 60 keV and (d) 200 keV electrons; and the dependence of $\text{DQE}(\omega_N)$ on counting threshold for (e) 60 keV and (f) 200 keV electrons. The insets of panels (b) and (f) show close-ups of the data for the 55 μm pitch results.

detector performs better than the other two detectors up until the threshold is about half the primary electron energy, above which it is poorer than the other two sensors.

For the 200 keV results in Figures 4.8(b), the difference in $\text{MTF}(\omega_N)$ between the

two $55\ \mu\text{m}$ pitch devices is largely negligible across most counting thresholds, with the largest difference being 0.09 at a counting threshold of $\sim 118\ \text{keV}$. It can be seen that there is a slight decrease in the value of $\text{MTF}(\omega_N)$ for the $500\ \mu\text{m}$ thick sensor at the highest counting thresholds used, which accounts for the (relatively, compared with the rest of the data in Figure 4.8(b)) large difference in $\text{MTF}(\omega_N)$ between the two detectors at this threshold. This is indicative of increased noise in the high threshold ESF data due to fewer counts in the illuminated region of the sensor. The thicker sensor is affected by this to a greater extent at a given threshold than the thinner sensor due to increased diffusion, which is discussed in more detail below. In contrast, the value $\text{MTF}(\omega_N)$ for the $110\ \mu\text{m}$ is consistently higher than that of the other two detectors for most of the threshold range, aside from the highest counting thresholds used when it is again worse than that of the other two devices. This reflects the fact that at thresholds above $\sim 35\ \text{keV}$ the effective pixel pitch is smaller than the physical pixel pitch. More generally, the rate at which the value of $\text{MTF}(\omega_N)$ decreases with respect to the counting threshold increasing reflects the differences in the average amount of energy deposited on individual pixels. The greater this is, the more gradual is the reduction in effective pixel pitch as the threshold is increased.

In the case of the $60\ \text{keV}$ results in Figure 4.8(c), the value of $\text{DQE}(0)$ for the two $300\ \mu\text{m}$ thick sensors is close to unity at low counting thresholds, with both decreasing at high thresholds, though the reduction is more pronounced in the case of the $55\ \mu\text{m}$ pitch device than it is the case of the $110\ \mu\text{m}$ pitch detector. The value of $\text{DQE}(0)$ for the $500\ \mu\text{m}$ pitch detector is consistently poorer than that of the other two detectors, though its dependency on threshold is otherwise similar to that of the other two devices. The most notable difference when comparing the $200\ \text{keV}$ data in Figure 4.8(d) with the $60\ \text{keV}$ data in Figure 4.8(c), is that while the value of $\text{DQE}(0)$ at low counting thresholds for the $110\ \mu\text{m}$ pitch detector is close to unity as it was for $60\ \text{keV}$ electrons, the value of $\text{DQE}(0)$ for the two $55\ \mu\text{m}$ pitch detectors is reduced. For all three detectors, the value of $\text{DQE}(0)$ in Figure 4.8(d) is initially constant, before initially decreasing gradually with respect to counting threshold before there rate of decrease becomes larger at high thresholds. At high thresholds, when at most one pixel registers each incident electron, $\text{DQE}(0)$ is equivalent to the probability of the incident electron being detected at all. The less energy that is deposited on average in each individual pixel, the lower this is for a given threshold.

Whether or not an electron is counted in a pixel is a stochastic process. There is therefore variation in the number of pixels that count each incident electron at a given counting threshold. As has been pointed out by McMullan et al [18], this means that HPDs can be modelled as Zweigian amplifier [296]. If the detector gain g is the average number of counts registered per incident electron (i.e. the average number of pixels that register an incident electron), then the variance of the detector gain is σ_g . The value of $\text{DQE}(0)$ for such a detector can be calculated using g and σ_g per Equation

4.1. This indicates that at zero spatial frequency, the key factor determining the DQE is the variance in the number of pixels that register an incident electron. At low counting thresholds, increased lateral spread in signal in the sensor leads to an increase in the variance of the number of registered counts, which causes a deterioration in $DQE(0)$. The larger PSF of the $500\ \mu\text{m}$ thick sensor compared to its $300\ \mu\text{m}$ thick counterparts means also means that the variance in the number of pixels that register incident electrons is increased, so that its value of $DQE(0)$ is consistently poorer than that of the other two for both electron energies and across all counting thresholds.

$$DQE(0) = \frac{\bar{g}^2}{\bar{g}^2 + \sigma_g^2} \quad (4.1)$$

While the dependency of $DQE(\omega_N)$ on counting threshold for 60 keV electrons for all three detectors in Figure 4.8(e) appears to mimic the dependency of $DQE(0)$ on counting threshold, the dependence of the 200 keV results in Figure 4.8(f) is more complex. The decrease and subsequent increase in the value of $DQE(\omega_N)$ for the $55\ \mu\text{m}$ pitch detectors corresponds to the decrease and increase in the value of $MTF(\omega_N)$ in Figure 4.8(b), with the decrease at very high thresholds likely being due to the deterioration in $DQE(0)$ dominating any improvement due to the MTF. For the $110\ \mu\text{m}$ pitch device, the initial decrease in $DQE(\omega_N)$ for 200 keV electrons in Figure 4.8(f) reflects the deterioration in $DQE(0)$ with increased counting threshold, while the increase at high thresholds reflects the improvement in MTF at high thresholds.

4.3.2 Electron Energy and Trajectory

The 60 keV MTF results for all three sensors indicate that the effective pixel pitch progressively decreases in size as the counting threshold increases, conforming to the expectations set out above for quanta that deposit most of their energy at or close to the point at which they enter the sensor. However, the 200 keV MTF results seem to suggest that, in the case of the $55\ \mu\text{m}$ pitch devices that the effective pixel pitch initially increases in size as the counting threshold is raised, before beginning to decrease at a threshold of ~ 53 keV. The behaviour of the $110\ \mu\text{m}$ pitch device is more consistent with the previously outlined model of the effective pixel pitch consistently decreasing as the counting threshold is increased. Nevertheless, the trend observed suggests that the effective pixel pitch initially rapidly decreases as the counting threshold is first increased, before remaining relatively constant for intermediate thresholds (between ~ 40 keV and ~ 60 keV) and then rapidly decreasing in size as counting threshold is further increased. This is still somewhat different from the consistent decrease in effective pixel pitch with increasing counting threshold that matches the measured MTF for all three detectors for 60 keV.

Similar trends to those observed in the 200 keV MTF results have been observed in the dependence of the MTF on counting threshold for the Eiger detector for 200 keV and 300 keV electrons [184]. The explanation put forward for this was that, per Equation 1.1, the rate at which electrons lose energy via Coulomb interactions with bound atomic electrons in the sensor increases as the energy of the primary electron decreases. Consequently electrons tend to deposit the majority of their energy towards the end of their trajectory. Depending on the primary electron energy and pixel pitch, this can mean that, on average, the pixel in which the electron enters the sensor is not the one to register the most energy. Consequently, an initial increase in counting threshold can cause a deterioration in MTF, as the entry pixel is discounted. However, an improvement can still be observed when using a high counting threshold, as the only pixels that remain above threshold are those that correspond to events where the trajectory of the primary electron has kept it within or close to the pixel in which it enters the sensor, so that the entry pixel records of the most energy. Consequently there is a decrease in the effective pixel pitch and improvement in MTF, as seen in the high threshold 200 keV MTF results for all three detectors.

To confirm this as the underlying cause of the trends observed in the MTF data, the trajectories of 60 keV and 200 keV electrons in the simulations performed with Allpix² were analysed determine the probability of primary electrons directly depositing a certain amount of energy at a given $1\ \mu\text{m}$ length along their trajectory. The results of this analysis are shown in Figure 4.9. It should be noted that these results neglect energy loss due to the production of secondaries and are based on the generation of electron-hole pairs due to the primary electron only. For both 60 keV results in Figure 4.9(a) and the 200 keV results in Figure 4.9(b), the most probable amount of energy to be deposited along a $1\ \mu\text{m}$ length along the trajectory is consistently less than 4 keV. However, the further along their trajectory electrons of both energies are, the more likely they are to deposit more energy in a given $1\ \mu\text{m}$ length. This is indicated by the high-energy tails seen in the probability distributions of the energy deposition for a given distance along the electron's trajectory. The further along electrons trajectory for both electron energies, the broader the distribution is, with this becoming noticeable when the electron has travelled $\sim 10\ \mu\text{m}$ when the primary electron energy is 60 keV and $\sim 100\ \mu\text{m}$ when it is 200 keV.

Comparing Figures 4.9(a) and (b), a significant difference between them is the total distance travelled by 60 keV electrons and by 200 keV in a Si sensor; the maximum distance of the latter is almost 6 times that of the latter. The full trajectory of a 60 keV electron could in principle be contained in a single $55\ \mu\text{m}$ pitch pixel even if its entire trajectory was entirely parallel to the sensor electrodes and entirely straight i.e. with no reduction in net displacement due to e.g doubling back on itself. However, the same would not be true for the full trajectory of a 200 keV electron in even a $110\ \mu\text{m}$ pitch pixel. Thus, although both 60 keV and 200 keV electrons are both

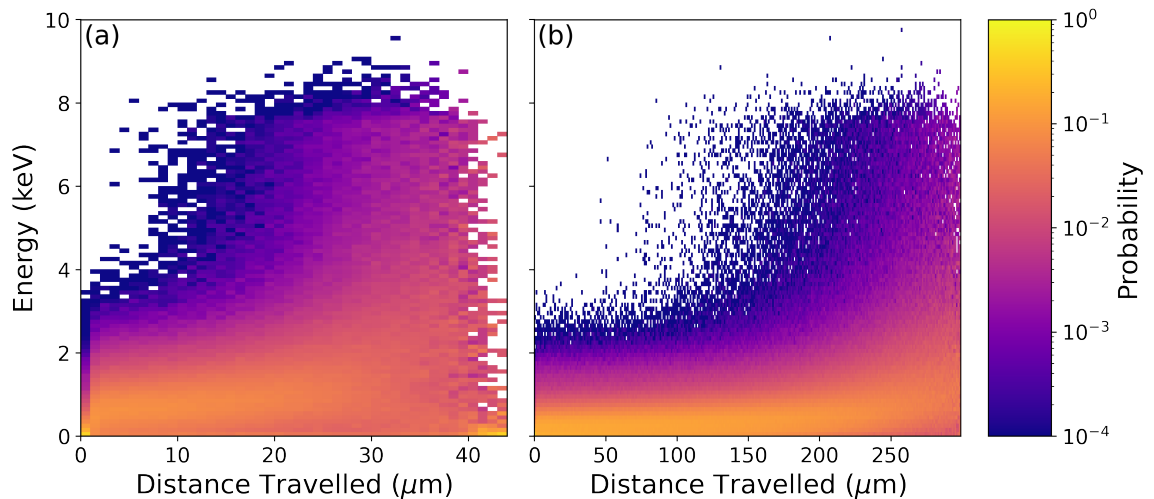


Figure 4.9: Probability distributions of the deposition of a certain amount of energy at a given point along the trajectory of the primary electron in Si for primary electron energies of (a) 60 keV and (b) 200 keV. Each column has been normalised to its own sum, so that for each position along the x -axis, the distribution in y represents the probability of depositing a given amount of energy at that position along the electron's trajectory.

more likely to deposit more energy towards the end of their trajectory, the dependency of the effective pixel pitch for the two electron on counting threshold is very different.

60 keV electrons still deposit most of their energy relatively close to where they enter the sensor (if not mostly in the pixel in which they enter the sensor), one of the requirements for the previously outlined dependence of the effective pixel pitch on counting threshold. 200 keV electrons, however, due to their longer trajectories, deposit more energy at a significant distance away from their entry point, potentially several pixels away, depending on pixel pitch. Thus, when the counting threshold of the $55\ \mu\text{m}$ pitch devices is initially increased in the 200 keV measurements, the pixels that are discounted are the pixels in which the incident electrons have entered the sensor but have deposited only a small amount of energy. This causes a deterioration in the MTF for the $55\ \mu\text{m}$ pitch detectors, as discussed above.

For the $110\ \mu\text{m}$ pitch device, the larger pixel pitch means that even 200 keV electrons deposit a significant portion of their energy in the entry pixel, so that the pixels that are discounted when the counting threshold is initially increased tend not to be the entry pixel. This is why the MTF of the $110\ \mu\text{m}$ device initially improves with an increase in the counting threshold. However, the plateau observed in the dependence of $\text{MTF}(\omega_N)$ on threshold suggests that at intermediate thresholds the pixels that are discounted at a given threshold are a roughly equal mixture of those containing the entry point and those that do not.

4.3.3 Sensor Thickness

Another notable difference in the MTF and DQE results in Figures 4.6 - 4.8 is that observed between the two $55\ \mu\text{m}$ pitch devices. This can be attributed to increased

lateral spread in charge due to diffusion in the thicker sensor. Assuming there is no significant difference in the average thickness of the entrance windows of sensors of differing thickness, then the depth at which incident electrons deposit their energy remains the same and is independent of how thick the sensors are. If the biases applied to sensors are such that the velocity of the charge carriers in both sensors is comparable, then in a thicker sensor the increased travel time of the charge carriers means that the lateral spread of charge carriers will be greater.

The notable difference in performance prompts speculation as to the extent to which the effects of diffusion differ between the two sensors as well as the extent to which it can be reduced. A Gaussian distribution with standard deviation $\sigma = \sqrt{2Dt}$ can be used to approximate the spatial spread of charge created at a point due to diffusion [16]. This depends on the diffusion constant D , which was introduced in Chapter 1, the charge-carrier type, sensor material, and the time t that it takes the charge to travel from the point in the sensor at which it is created to the read-out electrode. The collection time for holes created at depth d in a Si sensor can be calculated using Equation 4.2, in which V_{di} is the sum of the depletion bias and built-in bias of the sensor and V_b the bias applied to the sensor [32]. The depletion bias and built-in bias can be calculated using Equations 1.36 and 1.37. Figure 4.10 shows plots of the dependence of σ for holes in Si on the depth at which the hole is created for 300 μm and 500 μm sensors with the bias applied to the devices when performing the experimental measurements presented in this chapter (90 V and 110 V respectively, ensuring devices of both thicknesses are suitably over-depleted as discussed in Section 3.2.2). Also plotted is the theoretical dependence of σ on charge creation depth when a higher bias, 150 V for the thin sensor and 200 V for the thicker, is applied, for the purposes of investigating to what extent increasing the bias applied to the sensor may reduce the effects of diffusion. These alternative values of the bias are beyond the range of the power supply built into the Merlin DAQ used to control the detectors, but within the range of biases that could be applied to both sensors without the leakage current becoming excessively high [252, 291].

$$t_p = \frac{(W - d)^2}{2\mu_p V_{di}} \log\left(\frac{V_b + V_{di}}{V_b - V_{di}}\right) \quad (4.2)$$

Comparing the predictions made when using the biases used to acquire experimental data, the maximum difference in σ between the 300 μm sensor and the 500 μm thick sensor is 9.8 μm , occurring, as would be expected, when the hole is created at the far-side of the sensor from the pixel electrodes. Also marked in Figure 4.10 are the average depths at which 60 keV and 200 keV electrons deposit energy, weighted by the amount of energy deposited. At these depths, the predicted difference in σ for the 300 μm and 500 μm thick sensors with the biases used experimentally is also 9.8 μm . This increased diffusion in the 500 μm thick sensor compared with the 300 μm thick

sensor accounts for the differences in the MTF of the two devices with $55\mu\text{m}$ pitch. At low counting thresholds, the MTF of the thicker sensor is poorer due to increased diffusion causing a greater lateral spread in signal. However, at higher counting thresholds, this increased diffusion in the thicker sensor means that the maximum amount of energy deposited in a single pixel is smaller than is the case in the thinner sensor. Consequently, at lower counting thresholds, the effective pixel pitch of the thicker sensor is greater than that of the thinner sensor, as more pixels register enough signal to count the incident electron due to increased diffusion. For higher counting thresholds, the effective pixel pitch of the device with the thicker sensor is smaller, as electrons need to enter the sensor closer to the centre of the pixel in order to deposit sufficient energy to be above threshold, due to the increased diffusion leading to less energy being deposited on each individual pixel on average.

Returning briefly to the spectral measurements presented in Section 4.2, this interpretation is consistent with the SPM spectra presented in Figures 4.1 (a) and (c). Increased diffusion in the thicker sensor accounts for the greater disparity in the maximum energy recorded (i.e. maximum energy deposited in an individual pixel) and the actual primary electron energy for the $500\mu\text{m}$ thick sensor compared with the $300\mu\text{m}$ thick sensor in these figures. However, for the CSM spectra recorded by the two detectors in Figures 4.2(a) and (b), the thicker sensor consistently records a higher energy than the thinner sensor, which is in contradiction with this hypothesis. This may be accounted for by the fact that there were fewer fluorescence energies used in the calibration of the thicker sensor device, so that the error on the calibration is greater, which becomes more apparent applying that calibration to data acquired with incident quanta with much higher energies those used to determine the calibration. The reduced number of fluorescence energies used in the calibration of the thicker sensors was due to the lack of readily available targets that produced photons of sufficiently low energy that they were fully stopped by the thicker sensor while being sufficiently high energy that they were clearly distinguishable from the detector noise, which was higher for the thicker sensor, particularly when operating in CSM.

Increasing the bias to 150 V for the $300\mu\text{m}$ thick sensor and 200 V for the $500\mu\text{m}$ sensor respectively reduces the maximum value of σ by $4.4\mu\text{m}$ to $15\mu\text{m}$ and by $7.5\mu\text{m}$ to $21.6\mu\text{m}$. The reduction in σ for the depths at which 60 keV and 200 keV electrons on average deposit their energy is similar. As both the $300\mu\text{m}$ and $500\mu\text{m}$ thick sensors are sufficient to absorb the full energy of 60 keV and 200 keV electrons, the greatest potential reduction in σ (based on range of parameters considered here) is obtained when comparing the predictions made for a $500\mu\text{m}$ thick sensor with a bias of 110 V applied to those made for $300\mu\text{m}$ thick sensor with a bias of 150 V applied. Comparing the predictions for these two sets of parameters, the reduction in σ at the average energy deposition depths for 60 keV and 200 keV electrons and the surface of the sensor is $14.2\mu\text{m}$.

However, while using a thinner sensor and increasing the bias applied reduces the value of σ for holes created at the average depths of energy deposition of both 60 keV electrons and 200 keV electrons, the extent to which this may affect device performance depends on how large σ is compared to the spread in signal due to the scatter of the primary electron itself. For 60 keV electrons, the total distance travelled by the primary electron itself is on the order of $\sim 50\mu\text{m}$, while for 200 keV electrons it is on the order of $\sim 300\mu\text{m}$ based on the results in Figure 4.9. Consequently, while the value of σ in any of the discussed scenarios and the potential reductions in σ obtained by using one configuration in place of another is significant relative to range of 60 keV electrons, this is not so for 200 keV electrons. This is why the difference in MTF between the between the two $55\mu\text{m}$ pitch devices is more pronounced when the primary electron energy is 60 keV than it is when it is 200 keV.

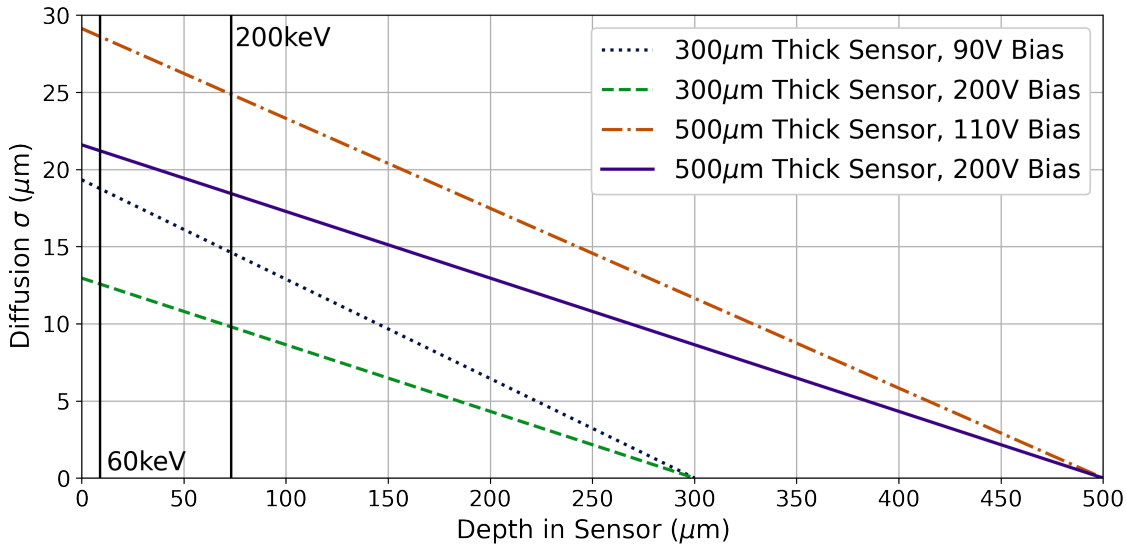


Figure 4.10: Plots of σ , the standard deviation σ of the Gaussian distribution describing the effects of diffusion on the position of a hole in a Si sensor depending on the depth at which the hole was created in the sensor, depending on the sensor thickness and the applied bias.

4.3.4 Pixel Pitch

The physical pixel pitch of a device is the final factor that determines device performance. Considering the results in Figures 6.2-4.8, in the $110\mu\text{m}$ pitch device, incident electrons deposit their energy over fewer pixels, leading to a corresponding improvement in MTF and DQE compared with the devices with a smaller pixel pitch. However, increasing the physical pixel pitch suppresses the MTF at a given spatial frequency as quantified in absolute terms (rather than in terms of the Nyquist frequency that corresponds to the increased pixel pitch). This can be understood by considering, as an example, two detectors, both of which only count incident quanta in the pixel in which the quanta enter the sensor, one of which has a physical

pixel pitch that is twice that of the other. The MTF of these two detectors, in terms of the Nyquist frequency of the device with the smaller pixel pitch, are $|\text{sinc}(\omega)|$ and $|\text{sinc}(2\omega)|$. Consequently, the MTF of the device with the larger pixel pitch device is that of the smaller pixel device compressed by a factor of 2. This entails a corresponding reduction in the transfer of contrast at frequencies $< 0.5\omega_N$ for the device with the larger pixel pitch in addition to no transfer of contrast at spatial frequencies $\geq 0.5\omega_N$. This is illustrated in Figure 4.11(a).

Although this follows quite trivially from the definition of a detector's MTF, due partly to the tendency to report the MTF of different detectors in terms of their own respective Nyquist frequencies, it is a fact that it is easy to overlook and is a fundamental drawback when using larger pixel devices for imaging. At the same time, the larger larger pixel pitch does not preclude the lateral spread in signal due either to diffusion or to scatter of the primary electron and any secondaries it produces having an adverse impact on performance, as can be seen in the low threshold MTF and DQE of the $110\mu\text{m}$ pitch detector for 200 keV electrons, which do not conform to behaviour of a perfect square pixel detector. This prompts the questions as to what pixel pitch optimises device MTF and DQE for a given electron energy and how this can be determined.

For X-ray detectors, there exists an extensive body of work modelling their performance, as quantified by their MTF and DQE, as a linear system [297–302]. One model for the effective pixel pitch of HPDs as a function of counting threshold E_T that has been validated in the context of imaging with X-rays for a variety of detectors including one based on the Medipix3 ASIC is defined in Equation 4.3 [292, 303]. This assumes that the lateral spread in signal in the sensor is due to diffusion only and can be regarded as uniformly distributed along a distance Δ [304]. As will be discussed in more detail below, this model for the effective pixel pitch is likely not suitable for electrons in the full energy range used in TEM and considered in this thesis. However, it represents a reasonable starting point for modelling the performance of detectors when imaging with electrons and aids understanding how the combination of pixel pitch and a given degree of lateral signal spread gives rise to the effective pixel pitch and MTF of a device.

$$a(E_0, E_T) = x_0 - 2\Delta \left(\frac{E_T}{E_0} - \frac{1}{2} \right) \quad (4.3)$$

Figures 4.11(b)-(c) show the MTFs on the basis of an effective pixel calculated using Equation 4.3 and a selection of different values of Δ and E_T/E_0 for detectors with a physical pitch of unity and twice unity (which can taken to correspond to the $55\mu\text{m}$ and $110\mu\text{m}$ pitch detectors with $300\mu\text{m}$ thick sensors and are described as such). Comparing Figures 4.11(b)-(d), it can be seen that for a given set of conditions (i.e. lateral spread in signal, counting threshold, sensor thickness) the detector with

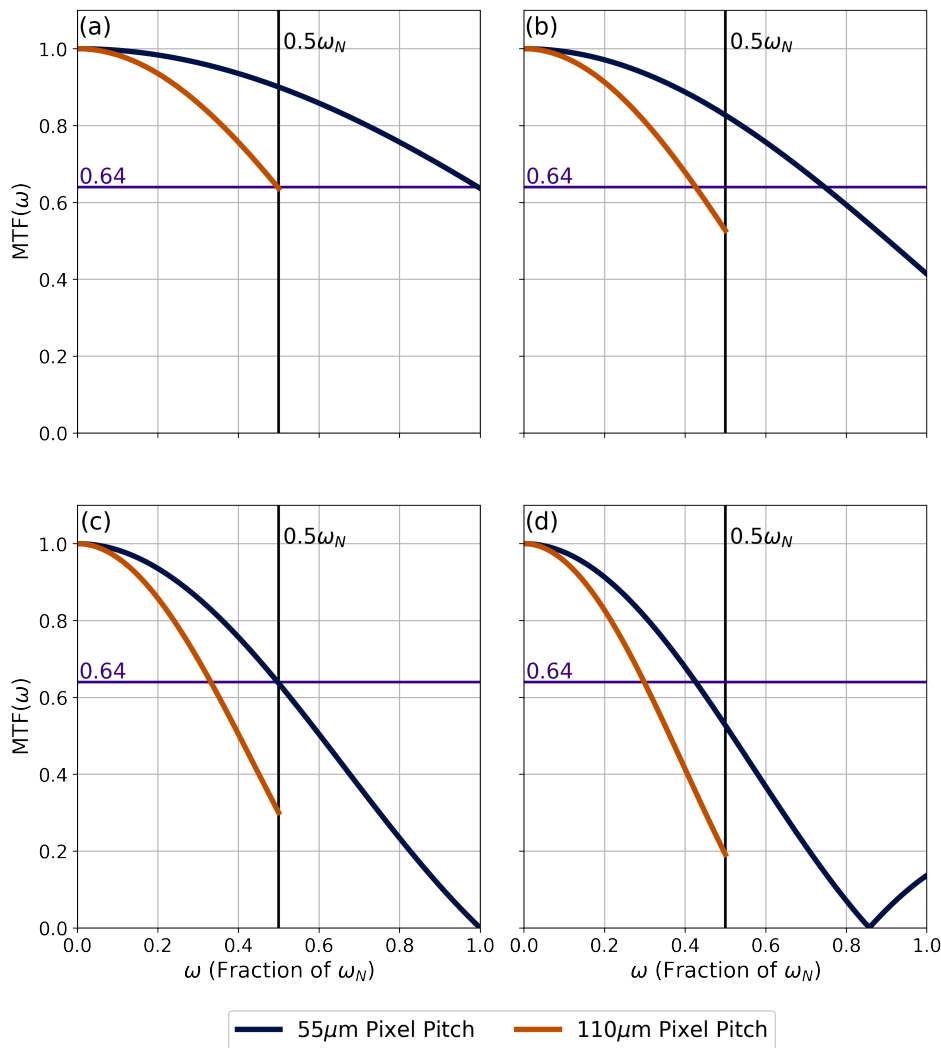


Figure 4.11: MTFs of devices with $110\ \mu\text{m}$ and $55\ \mu\text{m}$ pixel pitch when (a) both devices register incident quanta only in the pixel in which they enter the sensor; their effective pixel pitch is calculated using Equation 4.3 with $E_T/E_0=1/6$ for (b) $\Delta=0.5$, (c) $\Delta=1.5$ and (d) $\Delta=2$, where Δ is expressed as a fraction of the width of the smaller physical pixel pitch. This ratio of E_T/E_0 could represent a threshold of 10 keV for 60 keV electrons or, given the maximum amount of energy deposited in individual pixels by 200 keV electrons, ~ 20 keV for 200 keV electrons.

the smaller pixel pitch should have the better MTF when the spatial frequency is given in terms of an absolute value. Of course, for a given combination of parameters, the value of $\text{MTF}(0.5\omega_N)$ of the larger pixel device will be greater than the value of $\text{MTF}(\omega_N)$. As discussed in Chapter 2, one can increase the magnification of the image incident upon the detector so that the features in the incident image with spatial frequencies just below the ω_N have spatial frequencies just below $0.5\omega_N$. These features could then be recorded with better contrast than they would be by the smaller pitch device at lower magnification, though at the cost of reducing the detector's FOV.

The MTFs in Figure 4.11(a) and (b) look similar to those measured for the Si sensors for 60 keV electrons in Figure 4.6(a) and (b). However, in Figure 4.11(d), the

limitation of this model when modelling the performance of HPDs for high-energy electrons is apparent. When using a large value of Δ , in this example twice the smaller pixel pitch, which is a reasonable estimate for 200 keV electrons incident on a $55\ \mu\text{m}$ pitch device, the MTF of the smaller pixel device increases at high spatial frequencies. This reflects the absolute value of the sinc function through which the effective pixel pitch is passed, and does not match the way in which the MTF of the $55\ \mu\text{m}$ pitch devices tend to 0 at high spatial frequencies when using a low threshold as in Figure 4.7(a). Being more conservative and using $\Delta = 1.5$ and the same ratio of E_T/E_0 , as in Figure 4.11(c), the MTF of the smaller pixel pitch device equals 0 at ω_N . However, it is generally too high at higher spatial frequencies and does not display the same decay to 0 that is observed in the experimental data in Figure 4.7(a). Additionally the shape of the MTF of the larger pixel device in Figure 4.11(c) and (d) differs from that of the 200 keV MTF of the $110\ \mu\text{m}$ pitch device at lower counting thresholds in Figure 4.7(a) and (b), which feature a more gradual decrease at high spatial frequencies.

Although one might think that, in the case of the larger pixel device, this model for the effective pixel might serve as a reasonable approximation or starting point for modelling detector response to 200 keV electrons this would appear to not be the case. This indicates that even when using a larger pixel pitch, the spatial spread in energy due to the scatter of high-energy electrons must be accounted for to accurately model device performance. The divergence between the experimental MTFs and the theoretical ones implies that the effective pixel of HPDs used in TEM cannot be modelled as a top-hat function. It is likely, given the stochastic nature of electron interactions, that the edge of the effective pixel has a gradual profile, rather than sharp, profile. This would reflect the fact that electrons can enter the same point in a pixel and give rise to a different pixel clusters, which may or may not include the entry pixel.

4.4 Linearity of Response

In addition to the MTF and DQE of a detector, the other key performance characteristic of a detector is its deadtime. Indeed, this is not unrelated to the DQE as, the longer the detector deadtime, the greater the risk of incident quanta not being detected because they have entered a pixel while it is processing an earlier event, causing a deterioration in device efficiency and DQE. The deadtime of detectors based on the Medipix3 ASIC with Si sensors has previously been determined for 10 keV photons [39]. However, these measurements were not performed with the detectors operating in the ASIC's lowest gain mode, as this is not suitable for use with photons in this energy range. Whereas, when imaging with electrons with the energies typically used in TEM, it is necessary to use the lowest gain mode, as otherwise the maximum counting threshold will much smaller than the maximum amount of energy deposited on an individual

pixel. Furthermore, as the deadtime, in principle, depends on the time that the voltage pulse is above threshold, it is proportional to the average amount of energy deposited in a single pixel by incident quanta. The average amount of energy deposited by e.g. a 200 keV electron is obviously substantially larger than that deposited by a 10 keV photon. For both these reasons, it is necessary to perform separate measurements of the detectors' deadtime for electrons, as that measured for photons is not a reliable guide of the detectors' performance in this respect.

To determine the upper limit of the detectors' deadtime for the range of electron energies considered in this chapter, the deadtime of the three devices was determined for 200 keV electrons (the maximum electron energy which was available when performing these measurements) using a I_{Krum} setting of 10 DAC and a counting threshold of ~ 12 keV. The I_{Krum} setting of 10 DAC is the standard operational setting; all other measurements presented in this chapter were acquired with the detectors using an I_{Krum} setting of 10 DAC. Increasing the value of value of I_{Krum} would reduce the time the voltage pulse produced by the analogue front end of the detector's pixel electronics and hence deadtime, while using a lower electron energy would reduce the average amount of energy deposited on individual pixels, causing a reduction in measured deadtime.

Data was collected with all three detectors using the method outlined in Section 3.3.3, and the average count rate as a function of incident electron flux for all three was plotted, seen in Figure 4.12. Initial attempts to fit the data with Equations 1.47 and 1.48 were unsuccessful. It was found necessary to modify Equation 1.48 to include a term to account for the fact that, as incident electrons were registered by multiple pixels, the number of counts recorded for a given incident flux was greater than would be predicted by Equation 1.48. This represents a kind of gain, though it is not necessarily the gain a detector has at a given incident flux, and is denoted as the "deadtime gain", g_τ . The modified expression for the behaviour of a paralyzable detector, which was used to fit the linearity data of the three detectors using a least-squares ODR routine, is stated in Equation 4.4, where the other symbols have the same meanings that they had in Equations 1.47 and 1.48. This means that the deadtime τ determined by fitting the count rate curve represents an average deadtime per event per pixel. The fitted curves are also plotted in Figure 4.12, along with the response of a perfectly linear detector that counts all incident quanta in one pixel only.

$$n_{out} = n_{in} g_\tau e^{-n_{in} \tau} \quad (4.4)$$

In Figure 4.12, the detector that begins to undercount at the lowest incident flux (as quantified on a per pixel basis) is the $500 \mu\text{m}$ thick sensor, which deviates from a linear response above an incident flux of $\sim 2.5 \times 10^4$ electrons/pixel/s or $\sim 8 \times 10^6$ electrons/ mm^2/s . Of course, it must be recognised that, for the $110 \mu\text{m}$ pitch

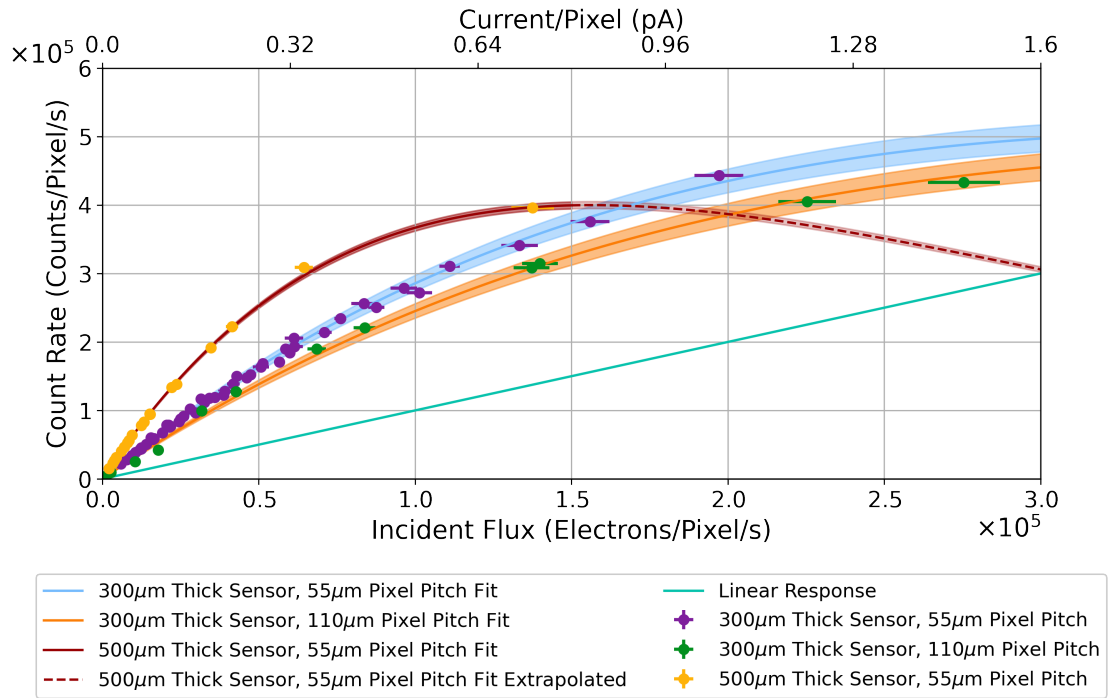


Figure 4.12: Plots of the count rate curves for the three Medipix3 detectors as a function of incident 200 keV electron flux when operating in SPM with a counting threshold of 12 keV and an I_{Krum} setting of 10 DAC. Also plotted are the predicted count rates as a function of incident flux based on the fitted values of τ and g_τ for the three detectors as well as the response of a perfectly linear detector. The shaded regions indicate the uncertainty of the predicted count rates due to the errors on the fitted parameters. As no data was collected with the 500 μm thick sensor above an incident flux of 1.5×10^5 electrons/pixel/s, the predicted count-rate for this device at higher levels of incident electron flux is an extrapolation based on the fit made to the lower incident flux data. This has been plotted as a dashed line to distinguish it from the predicted count-rate for the regime in which experimental data was acquired.

device, the incident flux per unit area is, for any given measurement, a quarter of that incident on the 55 μm pitch devices due to the larger pixel area. Consequently, if one considers the incident flux per unit area, it is the 110 μm pitch device that begins to undercount first, at an incident flux of $\sim 7.5 \times 10^4$ electrons/pixel/s or $\sim 6 \times 10^6$ electrons/ mm^2/s . Viewed in these terms, it is the 300 μm thick sensor with 55 μm thick device that best maintains a linear response, beginning to undercount at an incident flux of $\sim 6 \times 10^4$ electrons/pixel/s ($\sim 1.9 \times 10^7$ electrons/ mm^2/s).

The fitted values of τ and g_τ for the three detectors are listed in Table 4.3. As the scatter of 200 keV electrons over multiple pixels means that they deposit their energy over multiple pixels, the fitted value of τ for each detector represents the average deadtime given the average amount of energy deposited on each pixel. This average amount of energy differs depending on sensor thickness and pixel pitch.

One might expect that the 110 μm pitch detector would have the largest deadtime due to the larger pixels recording, on average more energy than the smaller pixels of the 55 μm pitch detectors. Along similar lines, one would think that, of the

Detector	τ (μs)	g_τ	τg_τ (μs)
300 μm Thick Sensor, 55 μm Pitch	2.7 ± 0.1	3.75 ± 0.03	10.2 ± 0.4
300 μm Thick Sensor, 110 μm Pitch	2.40 ± 0.08	3.1 ± 0.1	7.5 ± 0.3
500 μm Thick Sensor, 55 μm Pitch	6.40 ± 0.07	6.96 ± 0.04	44.5 ± 0.6

Table 4.3: Fitted values of the deadtime (τ) and the deadtime gain (g_τ) and their product for the three Medipix3 detectors operating in SPM with an I_{Krum} setting of 10 DAC and a counting threshold of ~ 12 keV for 200 keV electrons.

two 55 μm pitch devices, the one with the thinner sensor would have the longer deadtime. In the thinner sensor, each individual pixel should, on average, register more energy for a given electron energy than is the case for the thicker sensor, due to the reduced lateral spread of charge-carriers due to diffusion in the thinner sensor (as discussed in Section 4.3.3).

It is therefore somewhat surprising that the device with the largest deadtime is the device with the 500 μm thick sensor, which is also the one with the largest PSF (based on the MTF measurements in Section 4.3 and the fitted value of g_τ) as well as the measured values of g made for the purposes of calculating the devices' DQE. Furthermore 110 μm pixel pitch device has the shortest deadtime as well as smallest value of g_τ . Although the number of examples is small, it appears that the deadtime and the value of g_τ (and by extension PSF) of a detector are correlated.

One possible explanation for this apparent correlation between PSF and deadtime is that the more pixels that register an incident electron, the lower the flux at which undercounting begins to occur. This is reflected in the fact that the count rate curve of the 500 μm thick and 55 μm pitch device deviates from a linear response (given its PSF and, by extension, gain) at a lower incident flux than is the case for the other two devices. If this is the case, the measured deadtimes may be better regarded as a measure of the incident flux at which a device ceases to respond linearly, rather than a direct measurement of the average amount of time it takes for a pixel to process the signal induced on it by an incident electron, making it unable to register other incident electrons.

It might be expected that by including g_τ in the exponent of Equation 4.4, the average deadtime per pixel could be recovered. However, attempts to fit the datasets with Equation 4.4 modified in this way produced values of g_τ and τ that were not significantly different from those obtained using Equation 4.4 itself. This is with the exception of the 110 μm pitch dataset, in which case using the modified form of Equation 4.4 gave larger values for both g_τ and τ . If including g_τ in the exponent permitted determination of the true average deadtime per electron per pixel, then the obtained for τ should be smaller than that obtained using Equation 4.4, not larger or the same.

For lack of better alternatives, Equation 4.4 represents the most satisfactory function with which to fit the datasets. Although it is not clear that the measured values of τ presented in Table 4.3 truly represent the average deadtime per electron per pixel, the form of Equation 4.4, which is the most satisfactory function with which to fit the datasets at present implies that this is the way in which the values of τ should be interpreted. It is therefore worthwhile considering the product of τ and g_τ on the basis that this, theoretically, reflects the full extent to which a detector is insensitive to incident electrons. This product is also listed in Table 4.3. That of the $500\mu\text{m}$ pitch detector is more than four times that of either of the devices with thinner sensors.

The deadtime measured by other authors [39] for Medipix3 devices with $300\mu\text{m}$ thick sensors $55\mu\text{m}$ and $110\mu\text{m}$ pitch pixels ranged from 0.69 to $0.40\mu\text{s}$ for 10 keV photons. The devices were operated in high gain mode and in SPM with I_{Krum} ranging in value from 5-100 DAC. When the same devices operated in CSM with otherwise identical operating conditions, the deadtime increased to 3.5 - $2.02\mu\text{s}$. Consequently, the measured average deadtime per electron per pixel for each of the three devices is similar to those measured for other Medipix3 devices with settings fine-tuned for photons. They are still an order of magnitude larger than that measured for a device based on the Eiger ASIC [183] with a $450\mu\text{m}$ thick Si sensor and $75\mu\text{m}$ pitch pixels for 60 keV electrons with a counting threshold of 20 keV ($0.1\mu\text{s}$) [40]. However, this disparity is reasonable given the PSF for such a device (with a larger pixel pitch and higher counting threshold) and lower energy electrons. Overall, the deadtimes measured as part of the present work are comparable with other published values.

4.5 Summary

The focus of this chapter has been to develop a better understanding how sensor characteristics such as thickness and pixel pitch affect the performance of HPDs used in TEM. To this end, the performance of three detectors based on the Medipix3 ASIC, each of which had a Si sensor with a different combination of pixel pitch and sensor thickness, in response to electrons with energies ranging from 60 - 200 keV has been investigated. Points of comparison have included the energy spectra recorded by the three detectors operating in both SPM and CSM; the MTFs and DQE of the detectors operating in SPM for 60 keV and 200 keV electrons; and the deadtime of the detectors in SPM for 200 keV electrons.

In the SPM spectra of all three devices, a significant low-energy tail was observed that makes it difficult to identify the primary electron peak in the spectra, with the exception of the 60 keV , 80 keV and 120 keV peaks in the spectra recorded by the $110\mu\text{m}$ pitch detector. This is due to incident electrons depositing their energy over multiple pixels, with this effect becoming more pronounced with increasing

electron energy and decreasing pixel size. Although the CSM algorithm improves the quality of the spectra recorded by all three detectors for 60 keV and 80 keV electrons, it appears to introduce artefacts into the spectra. Spectra obtained by simulating the response of an HPD with $300\ \mu\text{m}$ thick sensor with $55\ \mu\text{m}$ pixel pitch displayed some divergences from comparable experimental data. This is likely due to limited time and computational resources imposing limits on the degree of accuracy with which the propagation of charge-carriers in the sensor could be simulated. While this meant quantitative comparison of the experimental and simulated was not possible, the simulation results still offered valuable insight into the detectors' behaviour. In particular, they provided evidence that the artefacts observed in the high-energy CSM spectra are indeed due to the CSM algorithm. This is likely due to the limited number of pixels over which the CSM algorithm operates, so that, for high-energy electrons, the total energy deposit is not properly reconstructed and multiple pixels can still register incident electrons.

Further analysis of the spectra produced by the simulated device indicated that the low-energy tail observed in the SPM spectra was, in addition to the scatter of primary and secondary electrons over multiple pixels, due to the backscatter of primary electrons. Summing the energy deposited over multiple pixels in the simulations resulted in spectra for which the low-energy tail was composed of events where the primary electron had backscattered from the sensor, depositing only part of their energy. The low-energy tails seen in the CSM spectra are therefore likely attributable to backscattered electrons depositing only part of their energy in the sensor. Additionally, the fraction of pixel clusters or even individual pixels that register energy deposited by secondaries only, with no contribution from the primary electron, is negligible. The production and subsequent interactions of secondary electrons and X-rays does not appear to play a significant role in the spread of signal in the sensor. Furthermore, they do not give rise to significant numbers of isolated pixel hits isolated from the main cluster of pixels that register incident electrons in the vicinity of where they enter the sensor.

Results of the MTF and DQE measurements of the detectors were, for the most part, consistent with the spectral measurements as well as the observations of other authors and the explanations put forward for those observations [18, 50, 184]. Just as the increased lateral scatter of electrons with increasing primary energy led to a deterioration in the quality of the spectra recorded, so too did it lead to a decrease in imaging performance as quantified by the detectors' MTF and DQE. The MTF and the DQE of the larger pixel device did not display the same level of deterioration, due to the fact that more of the lateral scatter of the primary electron was contained within a single pixel for this device. This is also in accordance the spectra recorded by the $110\ \mu\text{m}$ device being better (i.e. improved resolution with reduced disparity between the measured and actual electron energy) than those of the $55\ \mu\text{m}$ pitch devices.

While the value of $\text{MTF}(\omega_N)$ of the three detectors increased monotonically with counting threshold for 60 keV electrons, the dependency of $\text{MTF}(\omega_N)$ on counting threshold was more complex for 200 keV electrons. As described by Tinti et al. [184], if the primary electrons' trajectories are such that it tends to deposit most of its energy in a pixel away from the one in which it entered the sensor, then the PSF will initially decrease as the counting threshold is increased, due to the pixels in which the electron has entered the sensor being discounted. It will then improve when a very high counting threshold is used, as the only pixels that will register enough signal to be above threshold are those that are the entry pixels for events where the electron has doubled back on itself, depositing most of its energy in the entry pixel. Simulations confirmed the tendency of electrons of both energies to deposit most of their energy towards the end of their trajectory, a fundamental feature of electrons' interactions with thick targets. However, the shorter distances travelled by 60 keV electrons mean that they still deposit most of their energy sufficiently close to their entry point that the effective pixel pitch of all three consistently decreases as the counting threshold is increased. For 200 keV electrons this is not the case. For the smaller pitch devices, the 200 keV value of $\text{MTF}(\omega_N)$ and $\text{DQE}(\omega_N)$ initially decreased as the counting threshold increased, before increasing again at very high counting thresholds. Even in the case of the $110\mu\text{m}$ pitch pixel, the effect of the increased range of 200 keV electrons was still visible in the dependence of $\text{MTF}(\omega_N)$ on counting threshold, which was no longer (largely) linear. It was also apparent in the dependence of $\text{DQE}(\omega_N)$ on counting threshold for the larger pitch device, which was similar to that of the two smaller pitch devices for 200 keV electrons.

A previously underexplored factor in determining detector response has been the sensor thickness and, relatedly, the bias applied. Use of a thicker sensor increased the degree to which signal-carriers produced in the sensor spread laterally due to diffusion, so that the MTF of the $500\mu\text{m}$ thick sensor was poorer than its $300\mu\text{m}$ counterpart (in terms of pixel pitch) at low counting thresholds, and better at higher thresholds. Increased diffusion in the thicker sensor meant that the maximum energy registered in a pixel was smaller, so that the effective pixel pitch was a smaller (relative to the physical pixel pitch) at higher counting thresholds, while at lower counting thresholds more pixels registered enough energy to be above threshold. This increased number of pixels that are able to register an incident electron combined with the reduced maximum amount of energy deposited on a pixel accounted for the consistently poorer value of $\text{DQE}(0)$ for the thicker sensor compared with that of the thinner sensor. The extent to which diffusion increased the total signal spread depends on the energy and range of the primary electron. Consequently, while sensor thickness has a noticeable impact on both MTF and DQE for 60 keV electrons, its effect is less pronounced for the 200 keV results. Nevertheless, calculations of the dependency of diffusion on sensor thickness and applied bias indicate that there is merit in investigating thinner sensors

for those electron energies that permit it as well as the possibility of applying biases greater than 120 V (the maximum permitted by the Merlin DAQ in its current form).

It should be noted that the one way in which the MTF and DQE results are inconsistent with the spectral measurements is that, in CSM the energy measured by the $55\ \mu\text{m}$ pitch $300\ \mu\text{m}$ thick device is consistently lower than that measured by the $500\ \mu\text{m}$ thick device across all electron energies considered. One would expect the increased diffusion in the thicker sensor would mean that the energy recorded by the thicker sensor would be less than that measured by the thinner sensor. This is indeed observed when the devices operate in SPM and may reflect a greater degree of error in the calibration of the device with the thicker sensor.

Although it has not been possible to develop a comprehensive model of detector performance such as those that have been developed for HPDs when imaging with X-rays, the recorded datasets represent a comprehensive source of data for the purposes of developing and validating such a model. Comparison of a standard model for detector MTF developed for HPDs used in photon science with the experimental results suggests that, while this model could be adapted for modelling the response of the HPDs to low-energy electrons (given appropriate knowledge of the signal spread of 60 keV electrons), more significant modification is likely necessary to fully model device response to high-energy electrons, even for large pixel devices. This is again likely due to the tendency of high-energy electrons to deposit most of their energy a significant distance away from the point at which they enter the sensor. Additionally, consideration of this model highlights that, although a larger pixel pitch improves detector response in terms of spectral response, MTF and DQE, the latter two quantities are only improved in relative terms (i.e. when considering the MTF and DQE of devices with different pixel pitches in terms of their respective Nyquist frequencies).

Attempts to fit the detectors' count rate curves using the models for both paralyzable and unparalyzable detectors proved unsuccessful. It was found necessary to adapt the model of a paralyzable detector to account for the fact incident electrons were counted by multiple pixels. Using this model, an attempt was made to determine an average deadtime per electron per pixel for each detector for 200 keV electrons. It is not clear that this was entirely successful, as the average deadtime per electron per pixel increased with the average number of pixels that counted the incident electron. Due to incident electrons being counted by multiple pixels, all three devices record an inflated count rate at lower incident flux and deviate from a linear response at a lower incident flux than would be otherwise the case. Rather than τ representing the average deadtime per electron per pixel, it appears better to interpret as a measure of the extent to which a given detector is able to maintain a linear response (given the average number of pixels that register the primary electrons). The τg_τ product represents the maximum extent to which a detector is occupied with processing the signal due to an electron and unable to record another incident electron.

The smaller the detector PSF, the higher the flux the detector is able to be exposed to while maintaining a linear response. Although the $110\ \mu\text{m}$ had the smallest deadtime, the total number of electrons that are incident on each pixel is four times that incident on each $55\ \mu\text{m}$ for a given incident flux so that it actually begins to undercount at a lower flux than the other two devices. This is consistent with the MTF of the $110\ \mu\text{m}$ pitch detector being poorer than that of $55\ \mu\text{m}$ pitch devices when comparing their performance in terms of a common pixel pitch and Nyquist frequency. For a given incident flux, it was the $300\ \mu\text{m}$ thick sensor with $55\ \mu\text{m}$ pitch that was best able to maintain a linear response, which is also the device with the best PSF (for the low counting threshold used for the linearity measurements).

5

Simulations of High-Z Sensor Materials

5.1 Introduction

Prior to presenting experimental measurements characterising devices with high- Z sensors in Chapters 7 and 8, this chapter records simulations investigating the differences between the interactions of electrons with various high- Z sensor materials. This establishes baseline expectations for the performance of devices with sensors manufactured from these materials. It also provides context for the experimental results presented in Chapters 7 and 8 and facilitates the interpretation of these results. A description of the simulation geometry and the methods used to analyse the simulation data are presented in Section 6.2. In Section 6.3, results for the extent of the energy spread due to the scatter of primary electrons, as well as secondary quanta, in different materials are presented for primary electrons with energies ranging from 30-300 keV. Also considered are the differences in the extent to which electrons within this energy range are backscattered from the various sensor materials, and the effect that has on the distribution of the energy deposited in the sensor volume. The analysis also includes a breakdown of the energy deposited in different materials on the basis of type of quanta (i.e. primary electron, secondary electron or X-ray).

5.2 Methods

The simulations presented in this chapter were performed with an adapted version of the Geant4 advanced “microelectronics” example [1] as discussed in Chapter 3. The basic simulation geometry consisted of a target (i.e. sensor) that was $500\mu\text{m}$ thick and 3 cm in width and length with an electron source $650\mu\text{m}$ away, pointing towards the sensor. This source had no spatial extent and, as there were no other objects between the source and target, all electrons initially interacted with the

sensor at its centre. Behind the sensor was located a block of Si 700 μm thick with the same length and width as the sensor, which mimicked the ASIC that would be present in the case of a real device.

The material used in the construction of the target could be changed in order to investigate the potential trade-offs between increased lateral spread in signal and reduced efficiency in different sensor materials when working with different electron energies. The materials used for the target were Si, GaAs and CdTe, as defined by the NIST materials database, used for the definition of materials within the Geant4 framework. It should be noted that GaAs can be taken to stand for GaAs:Cr and CdTe for both CdTe and CZT as the material properties relevant to the simulations are the same. For the range of primary electron energies considered in these simulations (30 - 300 keV), all the simulated targets were of sufficient dimensions to absorb the full trajectory and energy deposition both perpendicular and parallel to the direction of incidence, excepting that lost due to backscatter of the primary electron or the escape of secondaries. For each set of simulation parameters (i.e. each combination of primary electron energy and sensor material) 20 000 events were simulated.

The simulation output consisted of the coordinates of all interactions for each particle, including the amount of energy lost in each interaction and the information about the interaction type. Processing this entailed grouping the trajectory data for each individual particle for each event and, on the basis of this, determining whether the particle's energy had been deposited entirely in the sensor or whether the particle had been backscattered from, transmitted through or had otherwise escaped from the sensor. Having labelled all simulated particles appropriately, calculating the fraction of energy deposited by each type of particle (e.g. primary electron, secondary electron and X-ray; escaped or absorbed) in the sensor averaged over all events was trivial. Likewise, it was straight forward calculating the probability of the primary electron backscattering from the sensor, which was of particular interest given speculation that the increased backscatter from high- Z sensors would have adverse effects on their performance compared with Si sensors [48].

Errors on the fraction of primary electrons that had backscattered from the sensor, were calculated by regarding the simulation results as following a Binomial distribution. Each simulated event is an independent trial for which there is probability p of the electron being backscattered, which is equal to the fraction backscattered when many events are simulated. The error of this probability p can be calculated using Equation 5.1, in which M is the number of trials/simulated events.

$$\sigma = \sqrt{\frac{p(1-p)}{M}} \quad (5.1)$$

To estimate the error on the average amount of energy deposited in the sensor (be that in total or a particular type of particle) a bootstrapping method was implemented.

This entailed sampling, with replacement, the output corresponding to individual simulated events (i.e. sampling from the range 1 to M , the number of events and then selecting the corresponding event data sets). For that selection of events, the average energy deposition (be that in total or for a particular particle type) was calculated. This process was repeated 10 000 times, with sample sizes equal to the total number of simulated events. The error was then calculated as the standard deviation of the sample means.

To investigate the lateral spread in signal at different primary electron energies, as well as how the lateral spread related to different particle types, 2D histograms of the trajectories of interest per unit area in the plane perpendicular to the direction of incidence (i.e. the xy -plane) were generated. These were weighted by the energy deposited by particles at that point in their trajectory, normalised to the total number of simulated events, to create a probability distribution of the average energy deposited in the sensor as a function of position. With appropriate binning to smooth the energy deposition at the edges of the energy deposition, contour lines containing a given percentage of the total average energy deposit could be determined and their average radius calculated. As an example, Figure 5.1 shows binned histograms of the total average energy deposited by incident 300 keV electrons for three different sensors, with the contours containing 50%, 90% and 99% of the total average energy deposited. Note that the binning factor used in the case of the Si sensor data in Figure 5.1(a) is greater than that used for the GaAs or CdTe data in Figures 5.1(b) and (c). It was observed that position of the contour varied slightly depending on the number of bins used. To estimate the error on the average radius of a given energy deposition contour, the average radii of the contours was calculated when using ± 1 the number of bins, and the standard deviation of these different averages calculated.

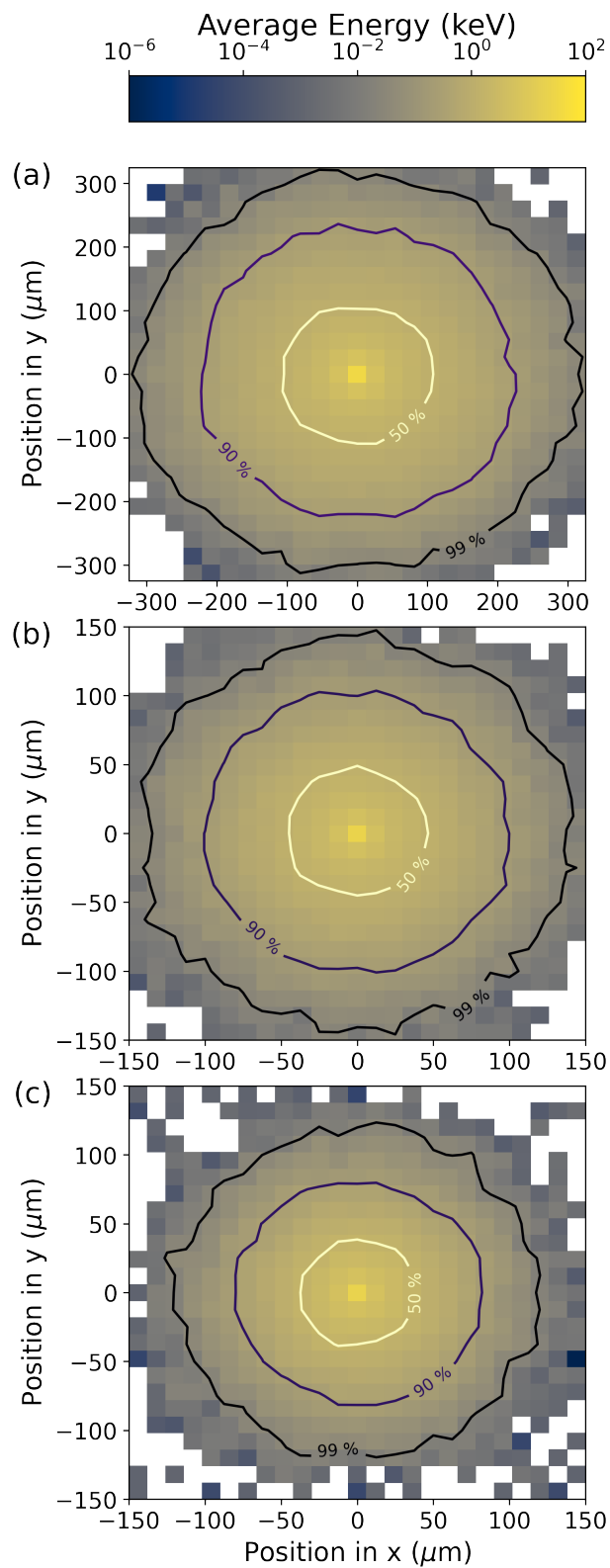


Figure 5.1: 2D histograms of the energy distribution of 300 keV electrons averaged over the 20 000 simulated events in (a) Si, (b) GaAs and (c) CdTe. The contour lines mark the distance from the impact point at which 50%, 90% and 99% of the energy is deposited.

5.3 Results and Discussion

Consistent with expectations, the area over which incident electrons deposit their energy is greatly reduced in the high- Z materials compared with in Si. This can be seen just from considering Figure 5.1, in which the lateral extent of the energy deposition by 300 keV electrons is double that in Si when compared with the GaAs and CdTe targets. Looking at Figure 5.2, it can be seen that this reduction in range in high- Z sensors relative to Si holds true across all energies.

Comparing the average radii of the contours containing 50%, 90% and 99% of the primary electrons' energy for different materials, for a given fraction of energy and primary electron energy, the radius in the Si sensor (figure 5.2(a)) is at least double that in GaAs (Figure 5.2(b)). The difference between GaAs and CdTe (Figure 5.2(c)) is much less pronounced and less consistent than the difference between Si and the other two materials. While the radius of a given contour at a given primary electron energy is always larger in GaAs than it is in CdTe, there is significant variation in the extent to which it is larger. In the case of the contours containing 50% of the energy deposited by 60 keV electrons, the radius of the contour for the CdTe sensor is equal to that of the GaAs target (with an error of $\pm 10\%$), whereas for 120 keV electrons, the radius corresponding to the CdTe sensor is $73 \pm 5\%$ that of the GaAs sensor. For the contours containing 90% and 99% of the primary electron energy, there is greater consistency in the difference between the GaAs and CdTe simulation results. The radius of the 90% contour for the CdTe sensor ranges between $84 \pm 1\%$ that of the GaAs sensor for 30 keV electrons to $80 \pm 2\%$ for 120 keV electrons, while the radius of the 99% contour varies between (at 30 keV) $87 \pm 3\%$ that of the GaAs radius and $83 \pm 4\%$ that of the GaAs radius using 120 keV electrons.

Overall, these simulations results confirm the expectation that the lateral spread in signal due to incident electrons can be greatly reduced by using a high- Z sensor in place of a Si one. At the same time, the difference in the lateral spread of signal between the GaAs and CdTe sensors is not nearly so large as the difference in signal spread in these materials and in the Si target, suggesting that the improvement in performance obtained by using a CdTe or CZT sensor in place of a GaAs one may be limited. The trends in the ratio of the GaAs radius to the CdTe for a given level of energy deposition indicate that the difference in the maximum extent of the lateral deposition of energy is consistent independent of electron energy, but that the difference in the intermediate extent of the lateral deposition is dependent on E_0 . As the PSF of a detector is dependent on the full extent of the average lateral dispersion of energy due to an incident electron, this suggests that, when using a lower counting threshold, the ratio of the performance of a GaAs detector to a CdTe one should be fairly consistent, without a strong dependence on primary electron energy, all else being equal. However, if using a high counting threshold,

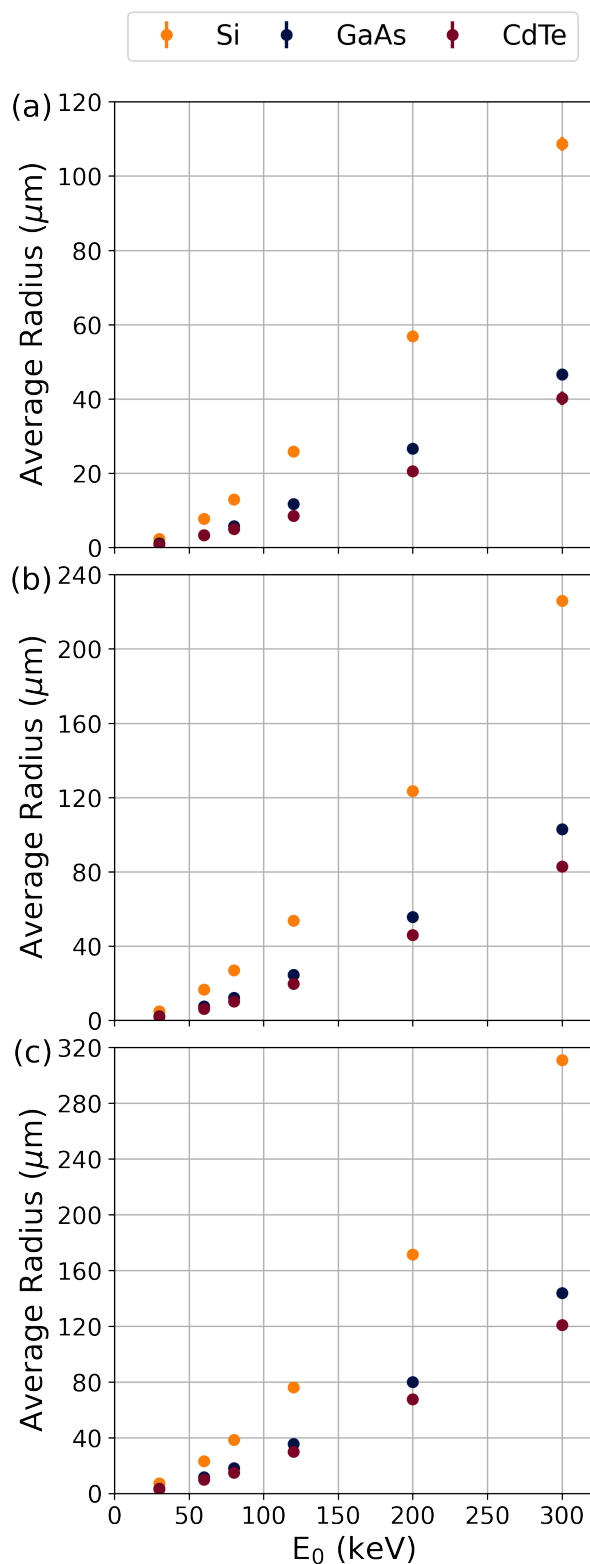


Figure 5.2: Average radii of the contours containing (a) 50%, (b) 90% and (c) 99% of the energy deposited by electrons ranging in primary energy from 30 keV to 300 keV in Si, GaAs and CdTe sensors.

the performance difference between a GaAs and CdTe device may be more strongly linked to primary electron energy, due to the greater disparity in the lateral extent

to which 50% of the electron's energy is deposited.

In Figure 5.3(a), the fraction of primary electrons that are backscattered from different materials is plotted as a function of primary electron energy. The fraction of backscattered electrons is very clearly linked to the sensor material, increasing with the average value of Z , as expected given the background discussion in Chapter 1. There also appears to be a weak dependence on primary electron energy, with the fraction of backscattered electrons decreasing as electron energy increases. This is most pronounced in the case of Si, for which the backscattering coefficient is 0.164 ± 0.003 for 30 keV electrons, decreasing to 0.138 ± 0.002 for 300 keV electrons. Similarly, the backscattering coefficient ranges between 0.323 ± 0.003 for 30 keV electrons and 0.308 ± 0.003 for GaAs. For CdTe, the dependence on energy appears to be minimal, as the maximum degree backscattering (0.418 ± 0.003), occurs for a primary electron energy of 120 keV while the fraction backscattered for 30 keV and 300 keV electrons is 0.411 ± 0.003 and 0.410 ± 0.003 respectively. For a given electron energy, the fraction of electrons backscattered from GaAs is approximately double that backscattered from Si, whereas the fraction backscattered from CdTe is close to three times the proportion that are backscattered from Si.

The increase in backscattering coefficient with Z is less problematic if incident electrons still deposit most of their energy in the sensor prior to being backscattered. In Figure 5.3(b), the ratio of the average amount of energy deposited to primary electron energy is, like the fraction of backscattered electrons, strongly dependent on the average value of Z and weakly dependent on primary electron energy. In the case of the CdTe target, the average amount of energy deposited is less than 70% that of the primary electron energy, while for the GaAs target this ranges between $76.7 \pm 0.2\%$ and $79.0 \pm 0.2\%$ of the primary electron energy. The average energy deposited in the Si sensor was at least $89.6 \pm 0.1\%$ of the primary electron energy.

Figures 5.3(c) and (d) plot the average amount of energy deposited in the sensor, normalised to the primary electron energy for events where the primary electron is absorbed or backscattered. It is apparent that the backscatter of primary electrons causes the reduction of average energy deposited, seen in Figure 5.3(b), and that backscattered electrons on average deposit less than half their energy in the sensor. When the primary electron is absorbed, the average amount of energy deposited is $> 98\%$ that of the primary electron energy across all values of E_0 for all three sensor materials. However, when the primary electron is backscattered, the average amount of energy is strongly dependent on the sensor material, with it decreasing for higher values of Z . For the CdTe sensor, backscattered electrons deposit less than a third of their energy on average, while for Si it is less than 45%. In the case of both absorbed and backscattered electrons, there appears to be a slight dependence in the average fraction of energy deposited on primary electron energy. For absorbed electrons, the average fraction of primary electron energy decreases with increasing

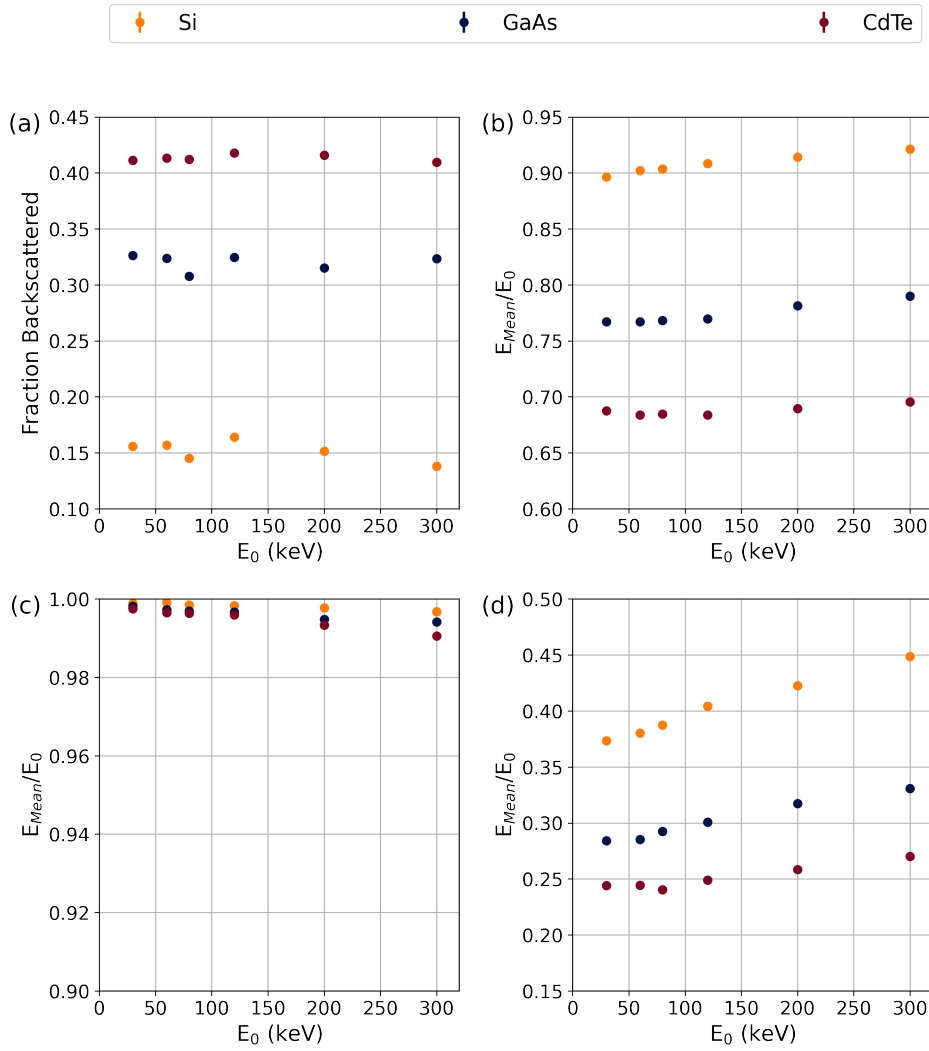


Figure 5.3: Results of the analysis of simulations investigating how electron backscatter depends on primary electron energy (E_0) and sensor material. In (a), the fraction of electrons backscattered for different sensor materials and values of E_0 are plotted, while in (b), the ratio of the average energy deposited E_{Mean} to E_0 is plotted. The data in (b) can be broken down further on the basis of whether the primary electron is (c) absorbed or (d) backscattered from the sensor.

electron energy, while for backscattered electrons it increases. The former trend may reflect the increased generation of higher energy secondaries for higher values of E_0 , which have a higher probability of escaping from the sensor, while the latter trend is likely due to the greater penetration of higher energy energy electrons into the sensor prior to being backscattered (with the cross-section for Rutherford scattering being inversely proportional to electron energy as per Equation 1.7).

Taken together, these results indicate that the primary mechanism by which energy is “lost” in an event, i.e. not registered by a sensor, is the backscatter of primary electrons. These results also show that significantly more energy as a fraction of the incident electrons’ total energy is not deposited in GaAs and CdTe sensors than in Si ones. Consequently, incident electrons will deposit a broader range of

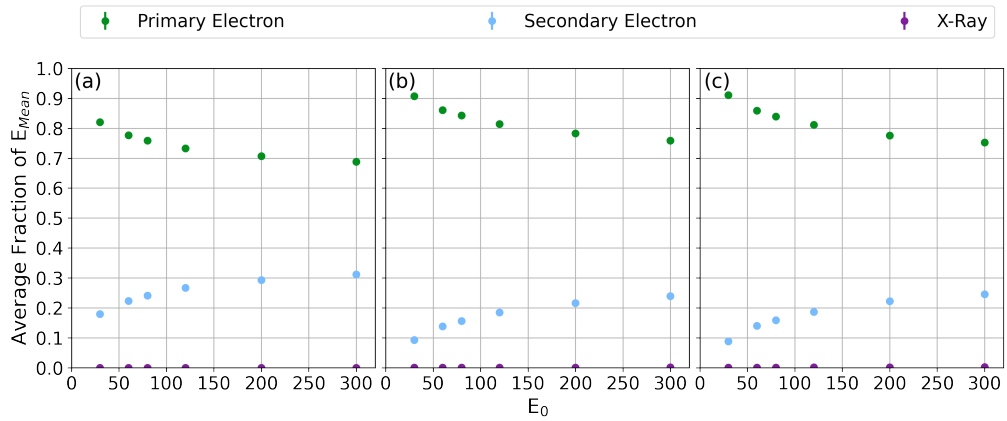


Figure 5.4: Fraction of the average amount of energy deposited in the target by the incident primary electrons, secondary electrons and X-rays produce for primary electron energies ranging from 30 keV to 300 keV in (a) Si, (b) GaAs and (c) CdTe sensors.

energies in these materials, potentially leading to a deterioration in energy resolution compared with Si (contingent on other device parameters, e.g. charge collection efficiency and pixel pitch).

To better understand how the interactions of different types of secondary radiation produced by primary electrons depend on the sensor material, the results in Figures 5.2 and 5.3 were broken down on the basis of the type of quanta (primary electron, secondary electron and X-ray) that deposited the energy. Figure 5.4 shows the fraction of the average amount of energy deposited in a given simulated event by the three categories of quanta for a range of primary electron energies for Si, GaAs and CdTe targets. It can be seen that for all energies and in all three materials, the average amount of energy deposited by X-rays negligible. Additionally, for all three materials, the proportion of energy deposited by secondary electrons increases with primary electron energy, though it appears to tend towards a plateau at values of E_0 above 200 keV. In the case of the Si results, the minimum fraction of energy deposited by secondary electrons is 0.180 ± 0.001 for 30 keV electrons, while the maximum is 0.312 ± 0.001 for 300 keV electrons. For the GaAs, the corresponding values are 0.093 ± 0.002 and 0.240 ± 0.001 , while for the CdTe results they are 0.089 ± 0.003 and 0.246 ± 0.002 . There is therefore a slight decrease in the fraction of energy deposited by secondary electrons with increasing average value of Z .

In Equations 1.12 and 1.13, which define the cross-sections of slow and fast secondary electrons, there is no dependence on Z , only an inverse dependence on the energy of the secondary electron and, in the case of slow secondary electrons, the energy of the Fermi level. As the cut-off energy applied to the production of particles in the simulation rules out slow secondary electrons from making up a significant proportion of the electrons produced in the simulation, the differences seen between the three materials cannot be attributed to differences in their respective

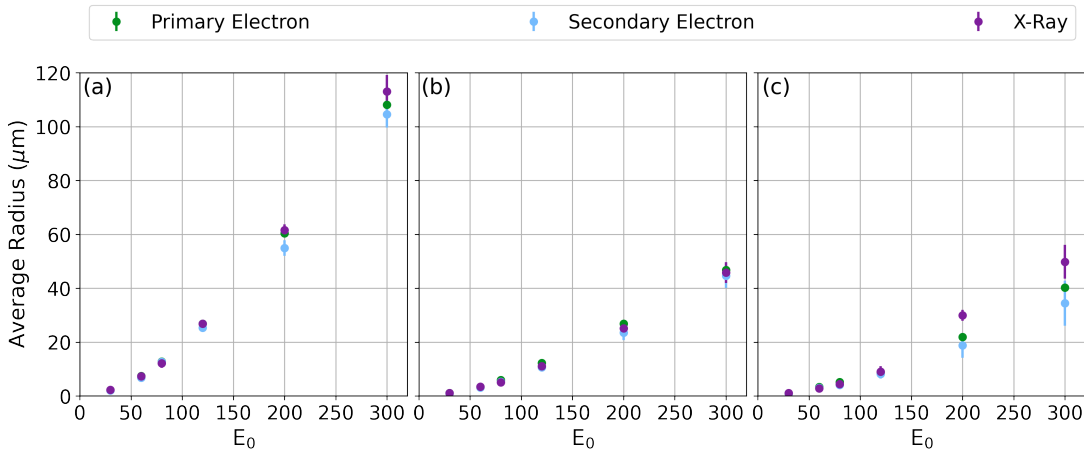


Figure 5.5: Radii of the contours containing 50% of the energy deposited by primary electrons, secondary electrons and X-rays in (a) Si, (b) GaAs and (c) CdTe targets.

Fermi levels. Of course, even if slow electrons were not below the simulation cut-off energy, Equations 1.12 and 1.13 both refer to the cross sections for generating secondary electrons of a given energy (relative to the primary electron energy), rather than the average fraction of energy deposited via the generation of secondary electrons in a thick target. The reason for this difference in energy deposition is therefore not obvious.

Of course, more relevant to this thesis is the extent to which secondaries may contribute to the further lateral spread in signal produced by incident primary electrons, thereby potentially leading to a deterioration in detector PSF. In Figures 5.5-5.7 the radii of the contours containing 50%, 90% and 99% of the energy deposited by primary electrons, secondary electrons and X-rays for Si, GaAs and CdTe sensors are plotted.

Comparing the 50% radii results for all targets in Figure 5.5, the differences in the energy deposition for different types of particle are negligible in all three materials for primary electron energies below 100 keV. For Si (Figure 5.5(a)), the 50% energy deposition radii for X-rays is greater than or equal to that due to primary electrons, while the secondary electron radii are smaller than that of the primary electrons when E_0 is above 100 keV. A similar trend is seen for the CdTe sensor (Figure 5.5(c)) at energies above 120 keV, and is in fact more pronounced than in the case of the Si sensor. This is in contrast with the results for GaAs in Figure 5.5(b), in which the difference between the 50% energy deposition radii for different types of particle with increasing values of E_0 is negligible.

Considering the 90% radii in Figure 5.6, there is only a significant difference in the radii associated with different types of quanta when the primary electron energy is above 100 keV. Even at higher values of E_0 , the difference between the radii associated with different quanta in Si (figure 5.6(a)) is small, though the X-ray radius tends to be the largest, and the secondary electron the smallest (although this does not hold

true in the case of the 200 keV data). For both GaAs and CdTe (Figures 5.6(b) and (c)), the 90% energy deposition X-ray radii are larger than that due to both primary and secondary electrons at primary electron energies ≥ 200 keV, while at lower primary electron energies there is little difference. As was the case for the 50% energy deposition radii results in Figure 5.5(c), the secondary electron 90% energy deposition radii for CdTe is smaller than the primary electron 90% energy deposition radii when there is a significant difference i.e. at primary electron energies ≥ 200 keV. This is not the case for the GaAs data, for which the secondary electron radius is consistently larger than that due to the primary electron for values of $E_0 \geq 200$ keV.

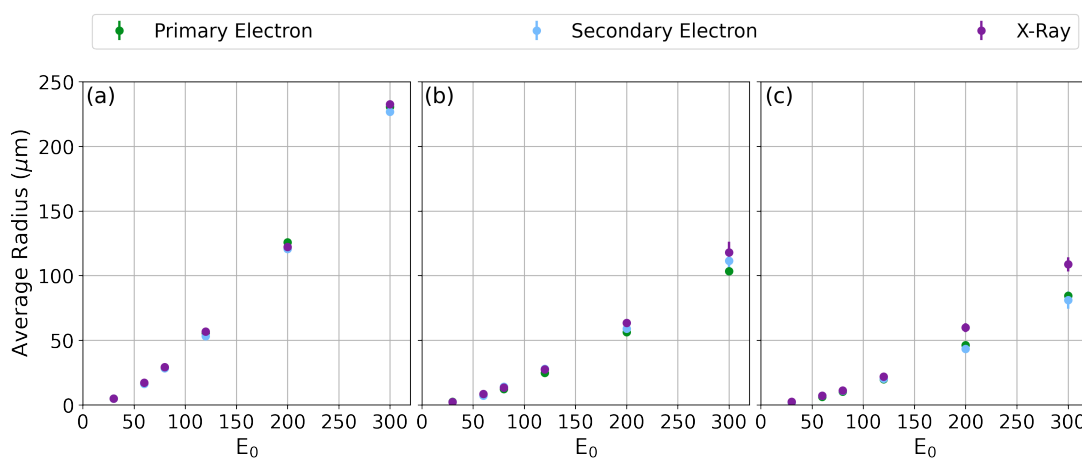


Figure 5.6: Radii of the contours containing 90% of the energy deposited by primary electrons and secondary quanta in (a) Si, (b) GaAs and (c) CdTe targets.

For the 99% energy deposition radii results in Figure 5.7, the differences in the energy deposition radii by the various quanta are again minor in the Si sensor (figure 5.7(a)), and most pronounced in the CdTe sensor (figure 5.7(c)). For the GaAs (figure 5.7(b)) and CdTe sensors, the X-ray radius is again the largest, while now in both cases the primary electron radius is the smallest for any given primary electron energy. There is a significant degree of variability in the extent to which the radius of the X-ray energy deposition exceeds that due to the other quanta for both the GaAs and CdTe sensors. This is most apparent in the case of the CdTe sensor, for which the X-ray radii when $E_0 \geq 200$ keV is disproportionately high relative to the difference between the X-ray radius and radii associated with other quanta for lower energy electrons. It is also true in the case for the X-ray radius in the GaAs sensor for 120 keV electrons.

There are several trends that emerge when grouping the results in Figures 5.5-5.7 together and considering them as a whole along with the data presented in Figure 5.2. Generally, the energy deposition radius due to primary electrons is equal to that of the radius due to the total energy deposition for a given combination of parameters (i.e. E_0 , sensor material and percentage energy deposition) being considered. It is usually not the case that the X-ray radius is smaller than that of the primary electron for a

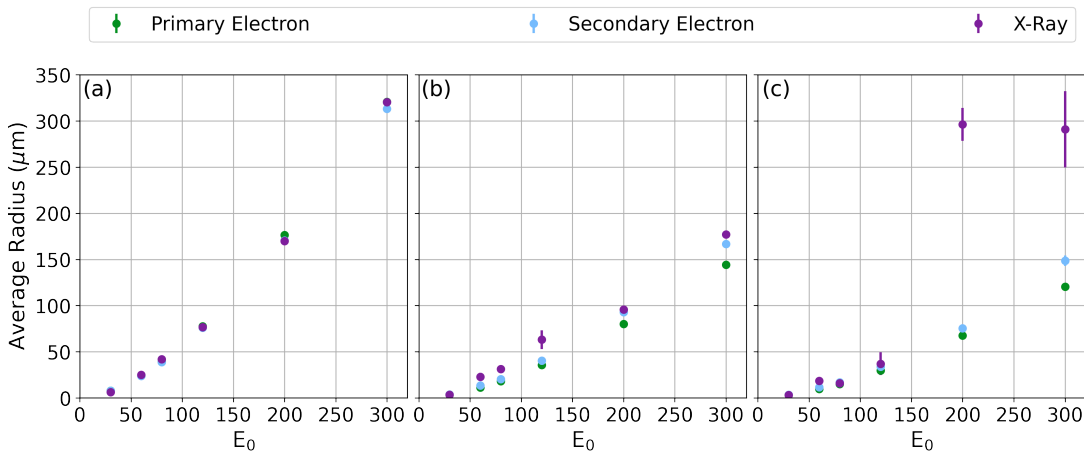


Figure 5.7: Radii of the 99% energy contours for primary electrons, secondary electrons and X-rays in (a) Si, (b) GaAs and (c) CdTe targets.

given set of parameters (a notable exception being the 99% energy deposition radii for 200 keV electrons in Si). Additionally, the radii of the secondary electron energy deposition is equal to or greater than that due to primary electrons as the fraction of energy deposited increases. Overall, this is consistent with the majority of the energy being deposited directly by primary electrons and the scatter of the primary electrons themselves. Nevertheless, it also points to an increase in lateral spread of signal due to the action of secondary quanta, causing a significant increase in the net lateral spread of signal beyond that due to the scatter of the primary electrons themselves.

The relative increase in lateral spread increases with both E_0 and Z , and the greatest increase in lateral energy deposition is due to X-rays rather than secondary electrons. This is consistent with the production of Bremsstrahlung X-rays being proportional to Z^2 and E_0 . It is also consistent with the fact that the CdTe K_α X-rays are higher in energy than both those of GaAs and Si, as discussed in Chapter 2. It may also reflect the increased stopping power of CdTe for high-energy X-rays relative to GaAs and Si. However, this would be contrary to an increase in energy lost due to the escape of secondaries for higher values of Z that was put forth as an explanation for reduction in average amount of energy with increasing primary electron energy in Figure 5.3(c), which also increased with the value of Z . Unfortunately, the simulation does not include information about how much energy the secondary particles have when they are first created, nor how much energy they have at the end of their trajectory. It is therefore not possible to compare the energy distributions of those secondary quanta that escape from the sensor and those that are absorbed to further investigate how much energy is lost by the escape of secondaries and how this relates to the value of Z of the sensor.

Considering the extent to which the interactions of X-rays far from the electron entry point affect detector PSF when using sensors made from CdTe and GaAs, it should be noted that the maximum X-ray radius at these energies for the GaAs and

CdTe targets does not exceed the maximum primary electron radius of the Si target. Furthermore, the relatively small fraction of energy that is deposited by X-rays means that this effect is small. Therefore, while there will be a small number of individual events for which the lateral spread in signal will be significantly increased due to the production of an X-ray that travels a significant distance away from the entry point of the electron, this is unlikely to cause a significant deterioration in the average response of the detector and hence its PSF.

At the same time, some of the results themselves indicate that the number of X-rays produced over the course of the simulation run is too low for the average radii results to be reliable. Due to the low number of X-rays produced over the course of the simulation run, a single X-ray travelling a larger than average distance skews the average radii calculations. This would account for the disproportionately large 99% radius for X-rays in the GaAs target when the primary electron energy is 120 keV (figure 5.7(b)) and in the CdTe target when E_0 is 200 keV or 300 keV, as well as the disproportionately small 99% radius for 80 keV electrons in the CdTe target (figure 5.7(c)).

Figure 5.8 shows the distribution of the average energy deposited in the xy -plane for 200 keV electrons in CdTe, both in total and broken down by different particle types. This makes it readily apparent that the interactions of secondary electrons and X-rays increase the lateral spread of the energy deposited in the sensor beyond that due to primary electrons only. Comparing the average energy distribution due to all particles and due to primary electrons (Figures 5.8(a) and (b)) with that due to just secondary electrons (Figure 5.8(c)) and X-rays (Figure 5.8), the former is much smaller in its spatial extent than is the case in the latter. Comparing the distribution of the energy deposited by X-rays and secondary electrons, it can be seen that, on average, secondary electrons actually deposit more energy further away from the entry point of the primary electrons at the origin. However, as the average amount of energy deposited by X-rays in any given event is so small, the diffuse deposition of energy far away from the origin is not negated by a large average amount of energy deposited close to the origin as is the case for secondary electrons, such that the 99% radius for X-rays is over three times that for secondary electrons.

It is also possible to observe a spatial correlation in the energy deposited by secondary electrons and by X-rays, looking at the average energy deposition further away from the electron entry point (i.e. beyond the 99% energy deposition radii for secondary electron). Tracing the origin of secondary electrons in the simulation output to either the primary electron or an X-ray confirms that the generation of secondary electrons by X-rays does contribute to the further spatial spread of signal. However, the average amount of energy deposited by secondary electrons produced by X-rays is never more than 1% of the total average amount of energy deposited,

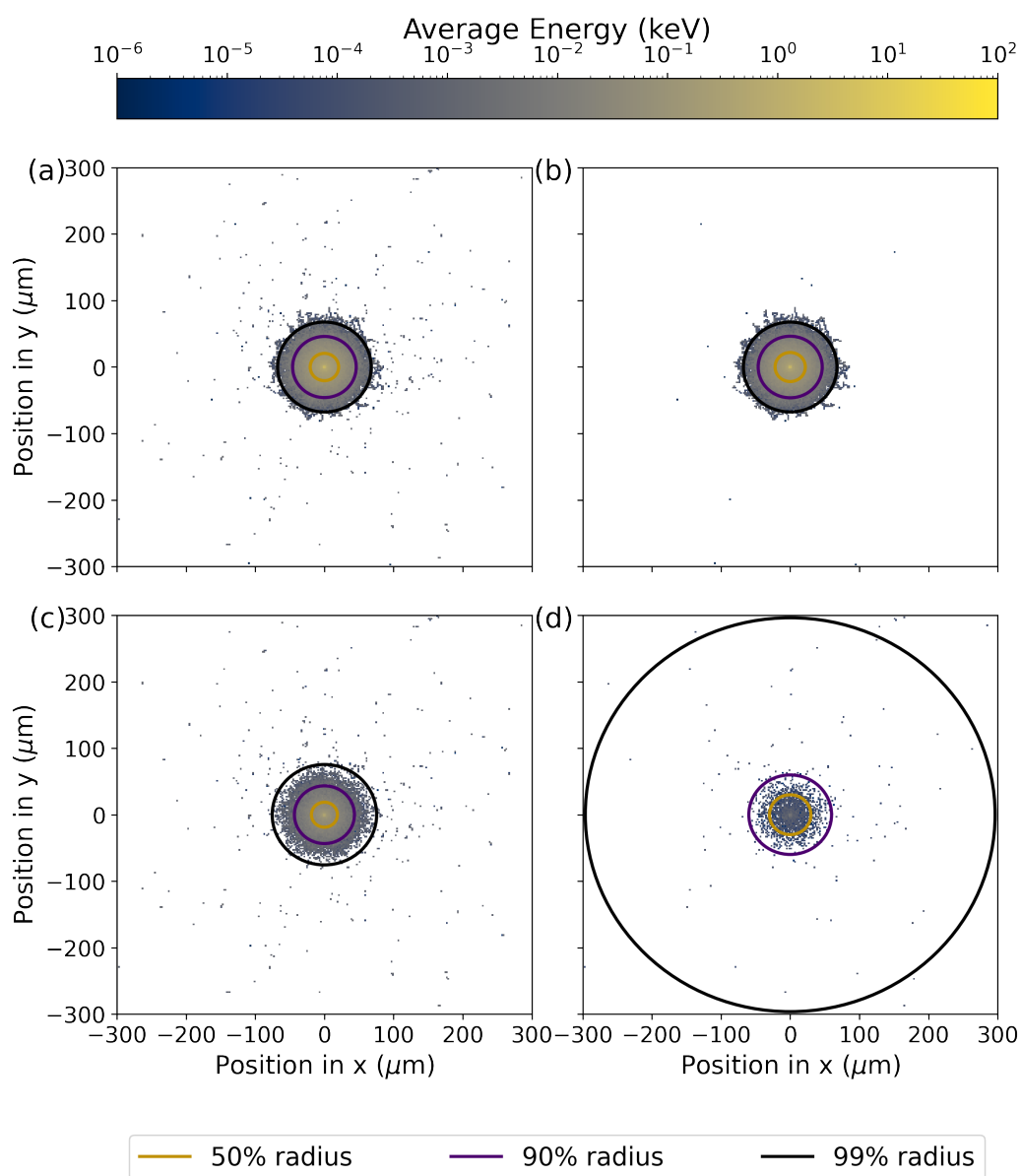


Figure 5.8: Figure showing the average energy deposition due to (a) all particles; (b) primary electrons; (c) secondary electrons and (d) X-rays. In (a)-(d), the circles plotted have radii corresponding to the average radii of the contours containing 50%, 90% and 99% of the average amount deposited by the appropriate type of particles for that Figure.

so the extent to which this mechanism contributes to the overall lateral spread in energy deposition is negligible.

The fact that the radii of the 50% energy deposition due to secondary electrons tends to be smaller than that of the primary electrons for all three sensor materials reflects the isotropic production of the secondary electrons by primary electrons over the course of their trajectory. This means that some secondary electrons travel back towards the entry point after being created, leading to an increased deposition of energy close to the primary electron entry point. It does not follow from this, however, that secondary electrons reduce the lateral spread of energy or cause an increase

in energy deposited in the vicinity of the entry point. Considering the trajectory of individual primary electrons, secondary electrons are emitted in random directions along the length of the primary electrons' paths, so the effect of emitting secondary electrons is an increase in the lateral deposition along the trajectory of the primary electron, not a preferential deposition of energy back towards the entry point. That similar behaviour is not also seen with X-rays likely reflects the fact that secondary electrons will begin to interact with and deposit their energy in the sensor as soon as they are created, whereas X-rays can travel significant distances prior to interacting with the sensor. Consequently, an X-ray of a given energy that is emitted back in the direction of the entry point is able to continue travelling past the entry point and deposit its energy a significant away from the entry point in a way that is not possible for a secondary electron of the same energy.

5.4 Summary and Conclusions

This Chapter has described simulations performed using the Geant4 framework of the interactions of primary electrons with Si, GaAs and CdTe sensors. It began with a description of the simulation geometry and broad outline of the methods used to process the particle trajectories that composed the simulation output. Initial analysis of the simulation output confirmed that the use of GaAs and CdTe significantly reduced the lateral spread in the energy deposited by electrons with energies ranging from 30 - 300 keV, with the relative reduction in the lateral spread in high- Z sensor materials increasing with primary electron energy. These results also showed that the reduction in the lateral spread of energy achieved by using a CdTe sensor in lieu of a GaAs sensor was only a small fraction of that achieved by using a GaAs sensor.

Analysis of the average amounts of energy deposited in different sensor materials, both overall and broken down on the basis of whether the primary electron backscattered from the sensor or not, indicated that the backscatter of primary electrons is the primary mechanism by which energy is lost and not absorbed by the sensor. The fraction of electrons backscattered from a sensor increases with the sensor's average value of Z , while the average amount of energy deposited in the sensor by backscattered electrons decreased with Z .

Investigation of the energy deposition due to different types of particles indicated that, X-rays do increase the lateral spread in average energy deposited both by their own direct interactions with the sensor and by producing secondary electrons at increased distances from the entry point of the primary electron. Additionally, it appears that the extent to which X-rays increase the maximum lateral spread of signal increases with the value of Z . However, the total amount of energy deposited by X-rays, either directly or through the generation of secondary electrons, is overall negligible.

Consequently, the production of and interactions of X-rays are unlikely to have a significant impact on device performance. Significant amounts of energy are deposited by secondary electrons, and this also causes an increase in the lateral spread of energy deposition relative to that due to primary electrons themselves. Nevertheless, the primary cause of the lateral spread of energy deposition is the scatter of the primary electrons themselves. This is with the significant caveat that these simulations have not included the effects of the diffusion of charge carriers, which would likely also contribute significantly to the lateral spread of signal produced by incident electrons.

Rather than being dependent directly on the properties of different sensor materials, the degree of diffusion is dependent more on the thickness of the sensor; the bias applied; and the temperature of the sensor. The first of these parameters is the most important, with the width of the diffusion kernel exhibiting a linear dependence on sensor thickness, while it increases only with the square root of the temperature and the inverse square root of the bias. That high-Z sensors tend to be thicker (due to the difficulty in manufacturing thinner sensors) than their Si counterparts can, to a certain extent be compensated for by applying a higher bias. At the same time, this suggests that further modelling and simulations that take into account the effects of diffusion would be worthwhile to determine the extent to which the (likely) increased diffusion in thicker high-Z sensors mitigates the improvement in PSF due to reduced lateral scatter of the primary electron and secondary quanta in such sensors. This would in turn determine how critical the development of processes to produce thinner high-Z sensors are to fully exploiting the benefits of high-Z materials in detectors used for TEM.

6

Characterisation of a Counting Detector with GaAs:Cr Sensor

6.1 Introduction

Following on from simulations investigating the differences in electron range and energy deposition in high- Z sensor materials compared with Si, this chapter records the experimental characterisation of a Medipix3 detector with a GaAs:Cr sensor. As mentioned in Chapter 3, this device has a $500\mu\text{m}$ thick sensor and $55\mu\text{m}$ pixel pitch and is operated with a bias of -300 V . Measurements performed include spectral measurements, which are discussed in Section 6.2; MTF and DQE measurements which are Section 6.3 and measurements of the detector's deadtime in Section 6.4. In the latter two sections, the Medipix3 device with a SI500 thick Si sensor and $55\mu\text{m}$ pixel pitch is used as a comparator, as an example of a standard, current generation HPD suitable for use in TEM for electron energies up to 300 keV with the same pixel pitch. The Medipix3 device with GaAs:Cr sensor is also used as a platform to investigate how defects in the sensor material affect the response of individual pixels and the device's performance overall. Results from this investigation are presented in Section 6.5.

6.2 Spectral Measurements

Figure 6.1 shows spectra acquired with the Medipix3 GaAs:Cr detector exposed to various different electron energies at low incident flux. As was the case for the $55\mu\text{m}$ pitch devices studied in Chapter 4, it is not possible to distinguish clear peaks in the spectra recorded when the detector operated in SPM. For the CSM spectra, single peaks due to incident electrons of a given primary energy can be identified and fitted with a Gaussian distribution for energies up to and including 120 keV . In the case of

the CSM spectra for 200 keV and 300 keV electrons, the peaks identified could not be fit with a single Gaussian and instead double Gaussians had to be used. Peaks in the spectra, and the errors on the relevant peak parameters, were calculated using the same procedure outlined in Chapter 3. The energy resolution calculated for the electron energies for which single peaks could be clearly identified and for which an energy resolution measurement is meaningful are listed in table 6.1, while the position of the fitted peaks are listed in table 6.2.

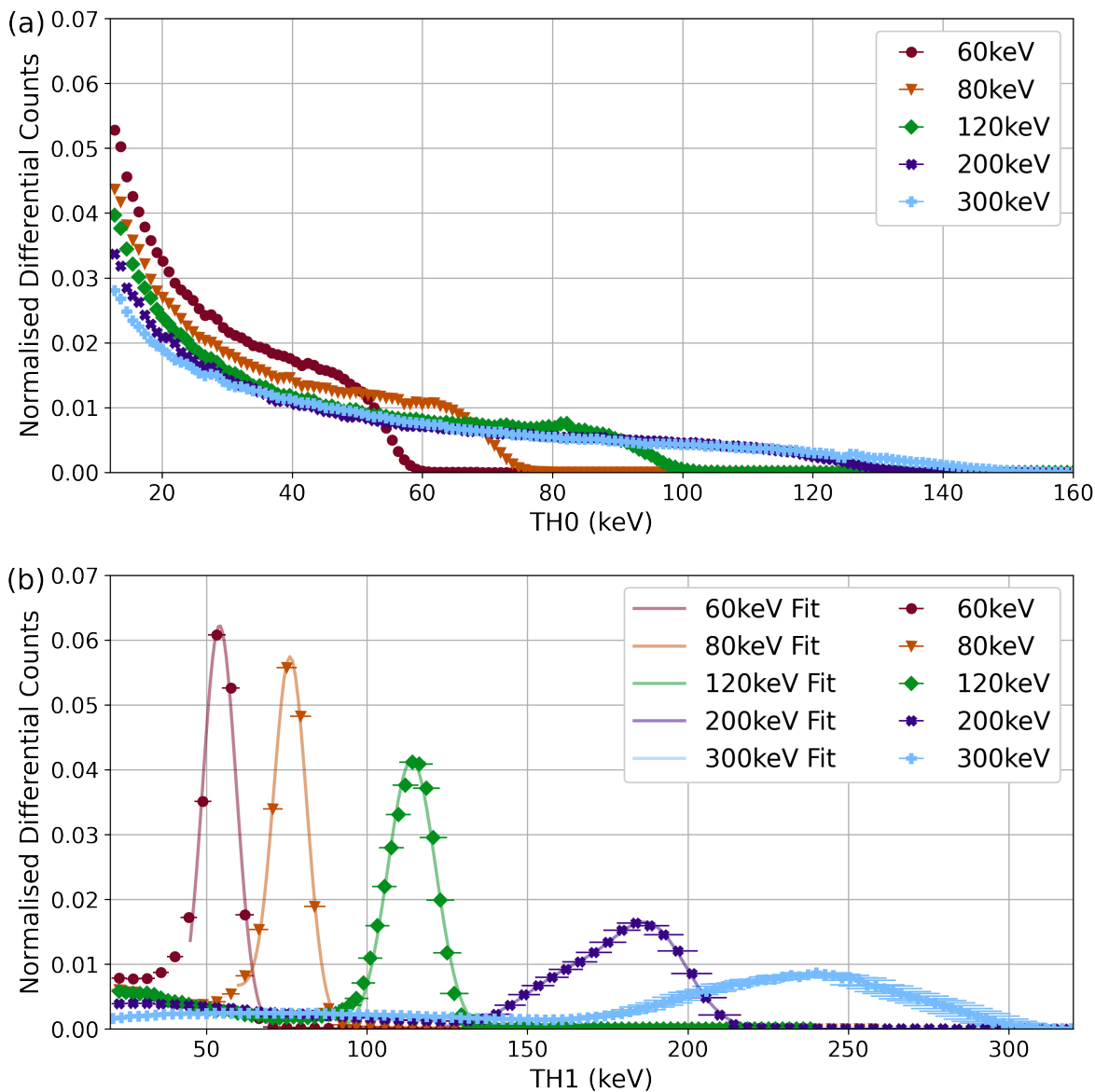


Figure 6.1: Spectra recorded by the Medipix3 device with a GaAs:Cr sensor operating in (a) SPM and (b) CSM. The spectra have been normalised so that the area under each of them is unity.

Comparing the results in Table 6.1 with that in Table 4.2, it can be seen that the energy resolution of the GaAs:Cr detector operating in CSM for 60 keV and 80 keV electrons is worse than both of the Si detectors with $55\mu\text{m}$ pitch in the same

operational mode and for the same electron energies. This is not surprising in itself, as taking into account the different Fano factors and charge creation energies of the two materials, then on the basis of Equation 1.46, for a given energy of incident quanta, the resolution of a GaAs sensor should be 19% greater (i.e. worse) than that of a Si sensor. Of course, the Si sensors do not themselves conform to the predictions made by Equation 1.46 and are instead limited by the deposition of energy over multiple pixels. However, the difference in energy resolution between the GaAs:Cr sensor and all the Si sensors surpasses this. The closest that the experimental measurements come to agreeing with this theoretical prediction is for 80 keV electrons; the resolution of the GaAs:Cr detector in CSM is $42 \pm 4\%$ greater than that of the $500 \mu\text{m}$ thick Si detector with $55 \mu\text{m}$ pitch pixel. The poorer energy resolution of the GaAs:Cr sensor is consistent with both increased backscatter from the GaAs:Cr sensor compared to the Si and the poorer $\mu_e \tau_e$ -product of GaAs:Cr relative to the $\mu_h \tau_h$ -product of Si.

Energy (keV)	Energy Resolution (%)
60	23 ± 1
80	15.7 ± 0.6
120	15.3 ± 0.4

Table 6.1: Resolution of the Medipix3 GaAs:Cr detector operating in CSM for those primary electron energies for which a single peak corresponding to the primary electron energy could be identified.

Considering the results in Table 6.2 and comparing them with the results in Table 4.1, it can also be seen that the disparity in measured primary electron energy, based on the position of the (primary) peak, and actual primary electron energy is greater for the GaAs:Cr sensor than it is for the $500 \mu\text{m}$ thick Si sensor with $55 \mu\text{m}$ pitch pixel and the $300 \mu\text{m}$ thick Si sensor with $110 \mu\text{m}$ pixel pitch when operating in CSM. This is consistent with the average amount of energy deposited in a GaAs sensor being less than that deposited with a Si sensor simulation results in the previous chapter due to backscatter (Figure 5.3). Another potential contributing factor, not included in the simulations in Chapter 5 is an increase in energy loss in and backscatter from the backside contact of the GaAs:Cr sensor compared with the Si sensor. As this is $0.5 \mu\text{m}$ of Ni, compared with $0.5 \mu\text{m}$ of Al and an entrance window of $1 \mu\text{m}$ Si for the Si devices, there is likely to be increased backscatter from and energy deposition in the GaAs:Cr backside contact. Also not included in the simulations, as previously noted, are the differing charge carrier properties in the two materials. The reduced $\mu_e \tau_e$ -product GaAs:Cr compared with the $\mu_h \tau_h$ -product of Si may mean that charge collection in the GaAs:Cr sensor is incomplete, leading to a reduction in the measured energy. This reduction in the average energy deposited/measured likely contributes to a deterioration in energy resolution.

It is noteworthy, however, that in the CSM spectra recorded for higher (≥ 200 keV) electron energies by the GaAs:Cr sensor, the maximum number of Gaussians needed to fit the spectra is two, rather than three in the case of the Si sensors. Additionally, in the case of the 120 keV CSM spectrum, only one peak is observed, unlike in the Si spectra for which there two “peaks” are observed, even for the $110\mu\text{m}$ pitch device. This represents a substantial improvement in response. The fact that the CSM algorithm does not introduce distortions into the spectra to the same extent as it did for the Si sensors in Chapter 4 is an initial indication of the reduced lateral spread of signal in the GaAs:Cr sensor compared with the Si.

Electron Energy (keV)	Primary Peak Position (keV)	Secondary Peak Position (keV)
60	54 ± 1	-
80	76 ± 1	-
120	114 ± 3	-
200	189 ± 3	168 ± 3
300	240 ± 3	200 ± 3

Table 6.2: Positions of peaks identified via fitting the spectra recorded by the Medipix3 GaAs:Cr detector operating in CSM.

6.3 MTF and DQE Measurements

It is helpful, for the sake of quantifying how the performance of a GaAs:Cr device differs from established detector technologies using Si sensors, to benchmark the results of the GaAs:Cr Medipix3 assembly using a comparable device with a Si sensor. For this reason, the results of the MTF and DQE measurements taken with the Medipix3 device with a $500\mu\text{m}$ sensor and $55\mu\text{m}$ pitch Si sensor presented in Chapter 3 are reproduced in this section where appropriate for ease of comparison. This choice of Si sensor as a comparator is motivated by the fact that of the three Si sensors characterised, it is the only one that is sufficiently thick to fully absorb 300 keV electrons. As it is expected that high- Z sensors will offer the greatest improvement in performance compared with Si sensors at higher electron energies, the thicker sensor better represents the devices that the GaAs:Cr sensor might come to supplant.

Figures 6.2-6.6 present an initial comparison of the MTF and DQE of the Si and GaAs:Cr detectors operating in SPM at selected counting thresholds for primary electron energies ranging from 60-300 keV. Comparing the MTF and DQE at selected thresholds makes it possible to fully compare the detectors’ performance across all spatial frequencies up to ω_N at representative counting thresholds. The selected thresholds are the lowest threshold above both detectors’ noise levels; a threshold equal to half the primary electron energy, when the primary electron energy ≥ 120 keV, or half the maximum threshold common to both devices otherwise for which the

ESF data was fit; and the highest threshold common to both devices at which the knife-edge data could be fit with Equation 3.2. As in Chapter 4, this final threshold is usually somewhat less than the initial energy of electrons incident on the sensor, as it is relatively rare for an electron to deposit all its energy in a single pixel. Figures 6.2 - 6.6 also show the theoretical MTF and DQE of a square pixel detector that counts all incident quanta once in the pixel of entry is plotted, as another standard comparator of detector performance.

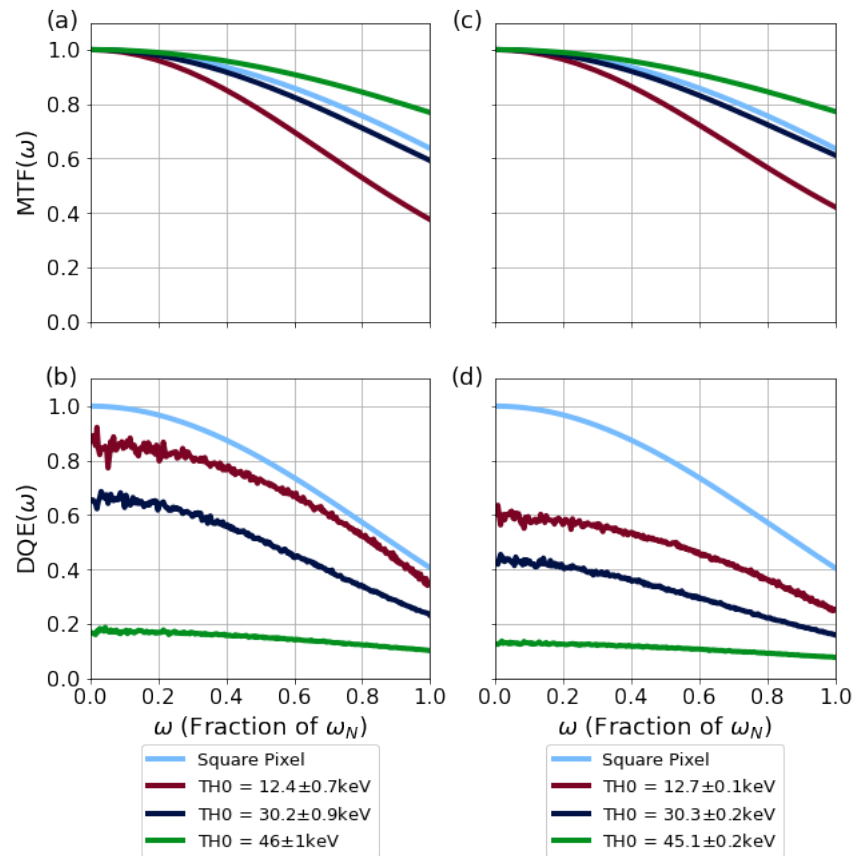


Figure 6.2: (a) MTF and (b) DQE measurements at selected thresholds with the Si device operating in SPM for 60 keV electrons; (c) MTF and (d) DQE measurements for the GaAs:Cr detector under the same conditions.

Beginning with low primary electron energies for which HPDs with Si sensors typically offer excellent MTF and DQE performance, Figure 6.2 shows results for the two devices operating in SPM and exposed to 60 keV electrons. For a given threshold, the MTF of the Si device (Figure 6.2(a)) is slightly lower than that of the GaAs:Cr device (Figure 6.2(c)), with the greatest difference always occurring at ω_N . The maximum difference is 0.05, and occurs when using the lowest counting threshold. With increasing threshold, the maximum difference (i.e. difference at ω_N in MTF between the two devices) decreases.

However, for each counting threshold, the GaAs:Cr DQE in Figure 6.2(d) is significantly lower than that of their Si counterpart in Figure 6.2(b). The maximum

difference (0.33) occurs when using the lowest counting threshold, though unlike the MTF results this occurs at a low spatial frequency ($0.02\omega_N$). At this threshold, the minimum difference in DQE is 0.09 at a spatial frequency of $0.99\omega_N$. Similarly, the maximum difference of 0.26 between the intermediate threshold DQE measurements also occurs at a low spatial frequency ($0.01\omega_N$). In the case of the high threshold measurement the difference in DQE is negligible. This suggests that at lower counting thresholds, the discrepancy in DQE between the two devices is largely due to a significant difference in efficiency, likely due to increased backscatter from the GaAs:Cr device. DQE(0) in effect acts as a scaling factor (as can be seen when considering how $DQE(\omega)$ is calculated in Equation 3.7), leading in turn to a significant difference in $DQE(\omega)$. With increasing threshold, this underlying difference in device efficiency due to the properties of the different sensor materials becomes less important, and the DQE is in both cases is dominated by undercounting of incident electrons due to a reduction in effective pixel size. Such an interpretation would be consistent increased backscatter and poorer charge collection in the GaAs:Cr sensor (relative to the Si one).

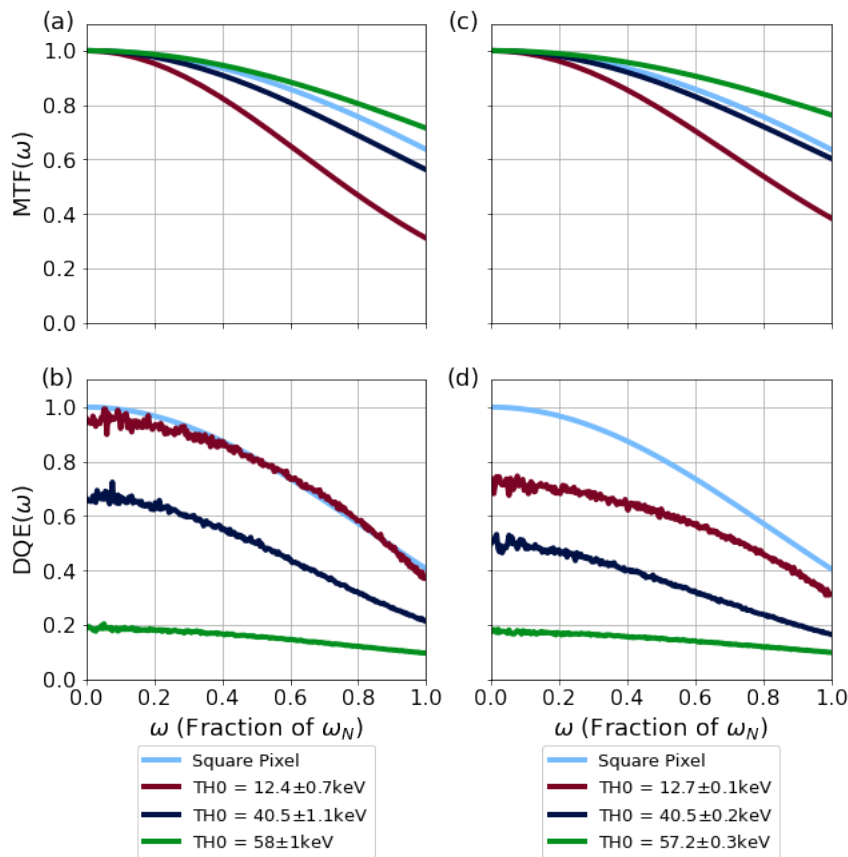


Figure 6.3: MTF for (a) Si and (c) GaAs:Cr detectors operating in SPM with selected counting thresholds for 80 keV electrons; the corresponding DQE results for (b) the Si device and (d) the GaAs:Cr device.

Increasing in energy to 80 keV, the MTF and DQE of the Si and GaAs:Cr devices for selected thresholds can be seen in Figure 6.3. As was the case for 60 keV electrons,

the MTFs of the GaAs:Cr device in Figure 6.3(c) are marginally better than those of the Si detector in Figure 6.3(a). For the MTF results, the maximum difference between the two devices, 0.07, again occurs using the lowest counting threshold though, though it occurs at $0.93\omega_N$ rather than ω_N . The difference in MTF between the two devices at a given threshold continues to be greatest at high ($>0.9\omega_N$) spatial frequencies. While the difference in MTF is slight, the difference in DQE is more substantial, with the Si detector (Figure 6.3(b)) again outperforming the GaAs:Cr sensor (Figure 6.3(d)). The maximum difference in DQE between the two is 0.32, occurring at a spatial frequency of $0.05\omega_N$ when using a low counting threshold. For the low threshold DQEs, the smallest difference between the two devices occurs at a spatial frequency of $0.06\omega_N$, at which the Si detector DQE is 0.06 greater than that of the GaAs:Cr device. For both the MTF and DQE, the difference between the two devices decreases with increasing counting threshold.

Evaluating the 60 keV and 80 keV electrons collectively, any benefits of the GaAs:Cr sensor appear to be marginal, consisting in only a slight improvement in MTF. Taking into account the considerably poorer DQE of the GaAs:Cr detector compared with that of the Si detector, the GaAs:Cr sensor does not appear to be the optimal choice for experiments using low-energy electrons. Experiments that benefit from low-energy (< 200 keV electrons) include studies of 2D materials that are sensitive to knock-on damage, whereby incident electrons transfer enough energy to atoms in the sample that the atoms break free. The minimum primary electron energy necessary for this type of damage to occur is typically $\gtrsim 80$ keV, depending on the composition of the material [305]. CryoEM studies conducted at 100 keV, for which HPDs are likely particularly suitable as discussed in Section 2.5.2, may also fall into the category of experiments for which Si sensors are preferable. However, given the results obtained for 120 keV electrons presented below, further studies characterising the response of GaAs:Cr sensors to 100 keV electrons are necessary.

The benefits of the GaAs:Cr sensor become apparent with increasing electron energy. Figure 6.4 shows the MTF and DQE for the Si and GaAs:Cr devices in SPM at 120 keV. For each threshold shown, both the MTF and the DQE of the GaAs:Cr detector (Figures 6.4(c) and (d)) is greater than that of the Si device (Figures 6.4(a) and (b)). In the case of the MTF, that of the GaAs:Cr device is at least 0.19 higher than the MTF of the Si device at ω_N for each threshold. The greatest difference is 0.32 for the intermediate threshold MTF at ω_N . For the DQE, the greatest difference occurs when using the low counting threshold, for which the DQE of the GaAs:Cr detector is 0.42 greater than that of the Si detector at a spatial frequency of $0.87\omega_N$. The difference in DQE between the devices tends to get smaller as the counting threshold increases. This is the inverse of the trend noted previously for the DQE of 60 keV electrons, and suggests that, at the higher electron energies the difference in DQE is driven

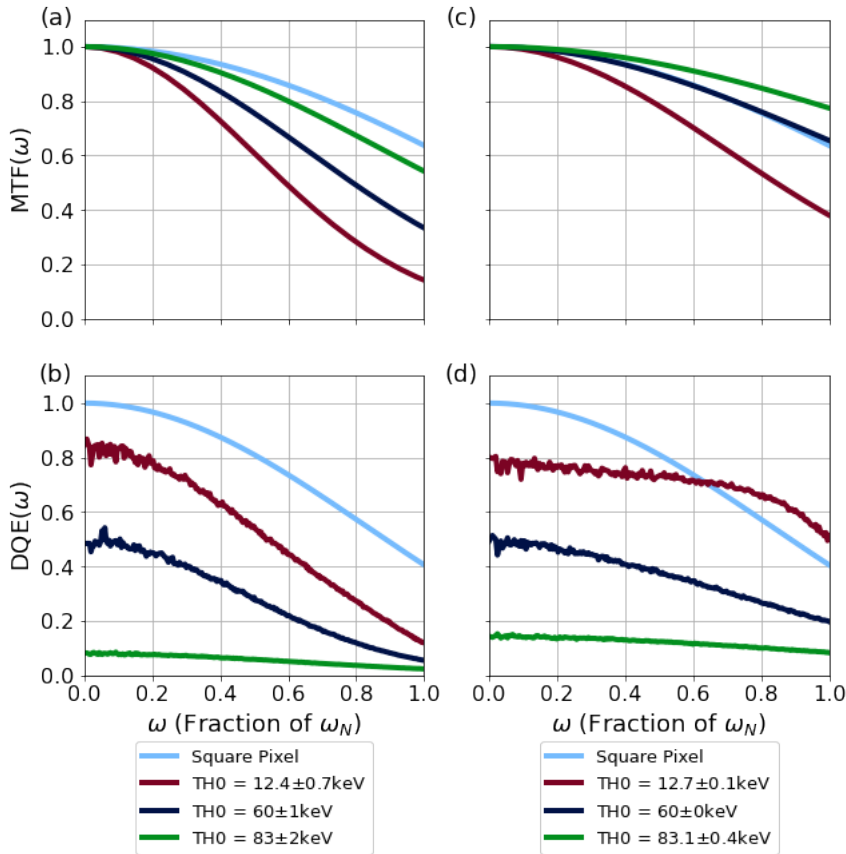


Figure 6.4: (a) MTF and (b) DQE at selected thresholds for a Si device operating in SPM for 120 keV electrons; (c) MTF and (d) DQE for a GaAs:Cr detector in SPM for 120 keV electrons at selected thresholds.

more by the difference in MTF between the two devices, rather than a difference in $DQE(0)$ due to underlying differences in sensor efficiency.

At 200 keV, the GaAs:Cr device clearly offers significant advantages compared to the Si sensor, surpassing it significantly in terms of both MTF and DQE in Figure 6.5. When using an intermediate threshold, the MTF of the GaAs:Cr device is 0.54 greater than its Si counterpart at $0.64\omega_N$. This is the greatest difference in the MTFs of the two devices shown in Figures 6.5(a) and (c). The greatest difference between the DQE of the two devices occurs using a low threshold, as was the case in the lower electron energy results. This occurs at a spatial frequency of $0.71\omega_N$, with the DQE of the GaAs:Cr sensor (Figure 6.5(d)) being 0.74 higher than that of the Si sensor in Figure 6.5(b). Although the difference in DQE decreases with increasing counting threshold, it continues to be substantial for the higher threshold measurements at 200 keV. The maximum differences in DQE for the intermediate and high threshold measurements are 0.43 and 0.06, occurring at spatial frequencies of $0.5\omega_N$ and $0.02\omega_N$ respectively.

It is worth noting that the extent to which the GaAs:Cr device's performance surpasses that of the Si detector for 200 keV electrons is greater than the extent to which it outperforms the Si detector when using 120 keV electrons. The maximum

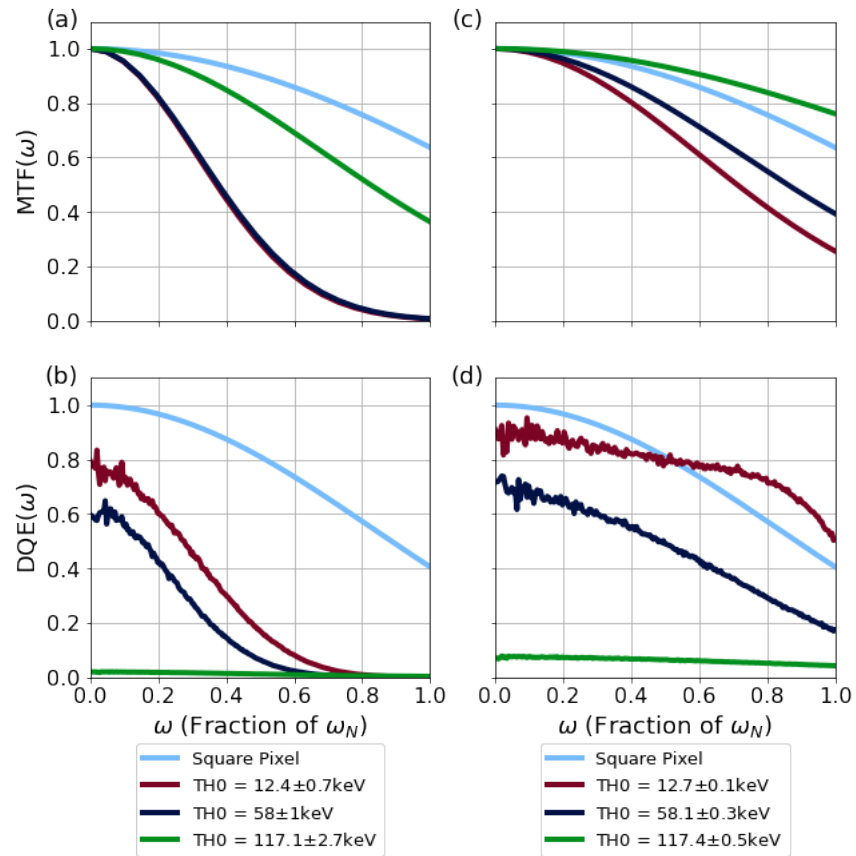


Figure 6.5: 200 keV SPM (a) MTF and (b) DQE at selected thresholds for a Si detector at selected thresholds and selected (c) MTF and (d) DQE for a GaAs:Cr device under the same conditions.

difference between the low threshold MTF and DQE of the two devices for 200 keV electrons is almost 1.8 times that of the maximum differences in the low threshold MTF and DQE for 120 keV electrons. Similarly, for the intermediate and high counting thresholds, the maximum differences in MTF for 200 keV electrons is 1.7 times the maximum difference in MTF for 120 keV electrons. The maximum difference in DQE for the intermediate counting threshold for 200 keV electrons is 2.8 times that for 120 keV electrons. At a high counting threshold the difference in DQE for 200 keV electrons is only 0.8 times that of the difference for 120 keV electrons.

An important feature of Figures 6.4(d) and 6.5(d), is the fact the low threshold DQE of the GaAs:Cr detector for 120 keV and 200 keV electrons benefits from the anti-aliasing effect of incident electrons being counted by multiple pixels. As discussed in Section 1.5.2, the effect of an electron being counted by multiple pixels is a suppression at high spatial frequencies of both the MTF and the NPS. This in turn, leads to an increase in the DQE at high spatial frequencies, as the NPS is suppressed to a greater extent than the MTF, relative to their idealised forms for a square pixel detector.

Indeed, this effect can be discerned in all the low-threshold SPM datasets presented in this thesis, but as the value of $DQE(0)$ is always less than unity, and as $DQE(0)$

acts as a scaling factor for the entire DQE, it is usually the case that the high-spatial frequency DQE is less than its corresponding MTF and does not exceed the theoretical DQE for a square pixel. Nevertheless, this effect was visible in the 60 keV low threshold DQE results for the Medipix3 devices with $300\ \mu\text{m}$ thick Si sensors in Chapter 4 as well as the 80 keV low threshold DQE results for the $500\ \mu\text{m}$ thick Si sensor in Figure 6.3(b). However, this effect is much more pronounced for the 120 keV and 200 keV DQE low threshold measurements for the GaAs:Cr sensor.

For instance, in Figure 6.3(b) the low threshold DQE only just exceeds the square pixel DQE by 0.03 at a spatial frequency of $0.69\omega_N$. Whereas in Figures 6.4(d) and 6.5(d), the low threshold value of $\text{DQE}(\omega_N)$ is 0.50 and 0.51, which is in good agreement with the maximum value of $\text{DQE}(\omega_N)$ possible due to this effect, as discussed in Chapter 1 as well as by other authors [48]. The greatest extent to which the low threshold DQE of the GaAs:Cr detector surpasses the DQE of a square pixel detector (without this anti-aliasing effect being considered) is by 0.12 at a spatial frequency of $0.9\omega_N$ for 120 keV electrons and by 0.17 at $0.86\omega_N$ for 200 keV electrons. Ultimately, this high level of performance can be attributed to the range of 120 keV and 200 keV electrons in GaAs:Cr corresponding to a favourable degree of blurring combined with a good overall device efficiency for electrons of these energies.

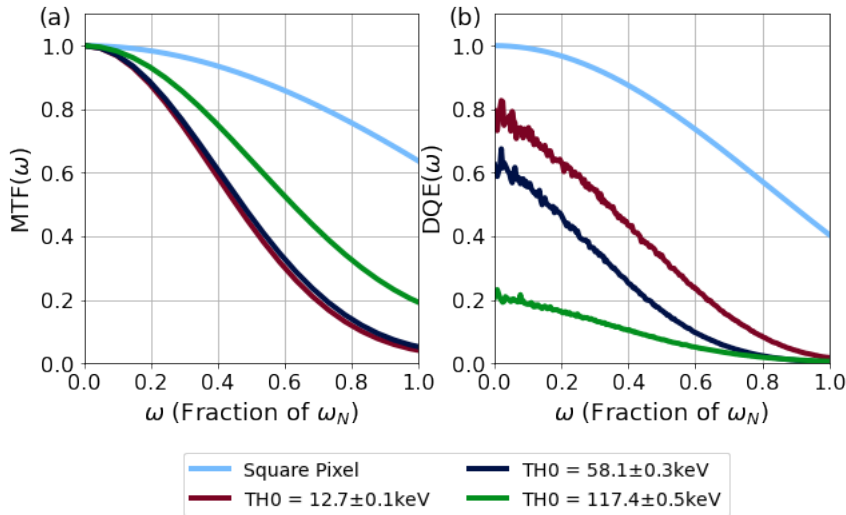


Figure 6.6: (a) MTF and (b) DQE at selected thresholds for a GaAs:Cr Medipix3 device operating in SPM for 300 keV electrons.

For 300 keV electrons, the performance of the GaAs:Cr detector deteriorates and is comparable with that of the Si sensor for 200 keV electrons. This can be seen by comparing Figures 6.5(a) and Figure 6.6(a), which show the 200 keV MTF results for the Si sensor and the 300 keV MTF results for the GaAs:Cr sensor at the same selected thresholds respectively. Comparing the low threshold MTFs of the GaAs:Cr detector at 300 keV and the Si detector at 200 keV in Figure 6.5(a), the maximum extent to which the former exceeds the latter is 0.15, at a spatial frequency

of $0.49\omega_N$. The maximum difference between the MTF of the Si detector at 200 keV and the GaAs:Cr device at 300 keV increases with the counting threshold: for the intermediate threshold measurement the maximum difference is 0.16, again occurring at a spatial frequency of $0.49\omega_N$. It is only for the high threshold measurement that the MTF of the Si detector for 200 keV electrons exceeds that of the GaAs:Cr device for 300 keV electrons. For the high threshold MTF measurements, the maximum difference between the Si device for 200 keV electrons and the GaAs:Cr device for 300 keV electrons is 0.19 at a spatial frequency of $0.83\omega_N$.

The DQE of the GaAs:Cr device for 300 keV electrons tends to be better than that of the Si sensor for 200 keV electrons. For the selected thresholds shown in Figures 6.5(b) and 6.6(b), the maximum difference in DQE is always such that GaAs:Cr detector DQE is higher than that of the Si detector, though it is only for the highest counting threshold that the GaAs:Cr 300 keV DQE is consistently higher than that of the Si 200 keV DQE. Unsurprisingly, given the increased lateral spread in deposited energy for 300 keV electrons compared with 200 keV electrons, the MTF of the GaAs:Cr device is always better at 200 keV (Figure 6.5(c)) than it is at 300 keV. The same is not true for the DQE: at the low and intermediate thresholds the 200 keV DQE (Figure 6.5(d)) is better than the DQE achieved using 300 keV electrons, but for the high counting threshold the DQE is better for 300 keV electrons than it is for 200 keV electrons across all spatial frequencies. This is likely due to reduced undercounting of the higher energy electrons at high threshold as the maximum amount of energy they deposit in a single pixel is greater. Overall, although the performance of the GaAs:Cr detector is markedly poorer at 300 keV than it was at 200 keV, it is still better than that of the Si detector at 200 keV.

Considering the dependence of $\text{MTF}(\omega_N)$ as a function of counting threshold for the two devices across the full electron energy range makes it possible to simultaneously compare how the performance of the devices depends on electron energy and counting threshold. Figure 6.7 shows how $\text{MTF}(\omega_N)$ varies with counting threshold for different electron energies with the two devices operating in SPM. Several points become more apparent when the data is presented in this way. For 60 keV electrons, the MTF performance of the GaAs:Cr sensor (Figure 6.7(b)) surpasses that of the Si detector (Figure 6.7(a)) at low counting thresholds, but the MTF of the two devices converges at high thresholds. The difference at low counting thresholds is small, with a maximum value of 0.06 when the GaAs:Cr detector has a threshold of 14.6 ± 0.2 keV. For electrons with energies ≥ 80 keV, $\text{MTF}(\omega_N)$ of the GaAs:Cr device is consistently greater than that of the Si detector across all counting thresholds.

Comparing the trends for the lower set of electron energies (up to 120 keV), for the GaAs:Cr sensor the low threshold $\text{MTF}(\omega_N)$ decreases only slightly as the primary electron energy increases. However, for the Si detector there is a consistent decrease in performance (even within this reduced range of lower electron energies)

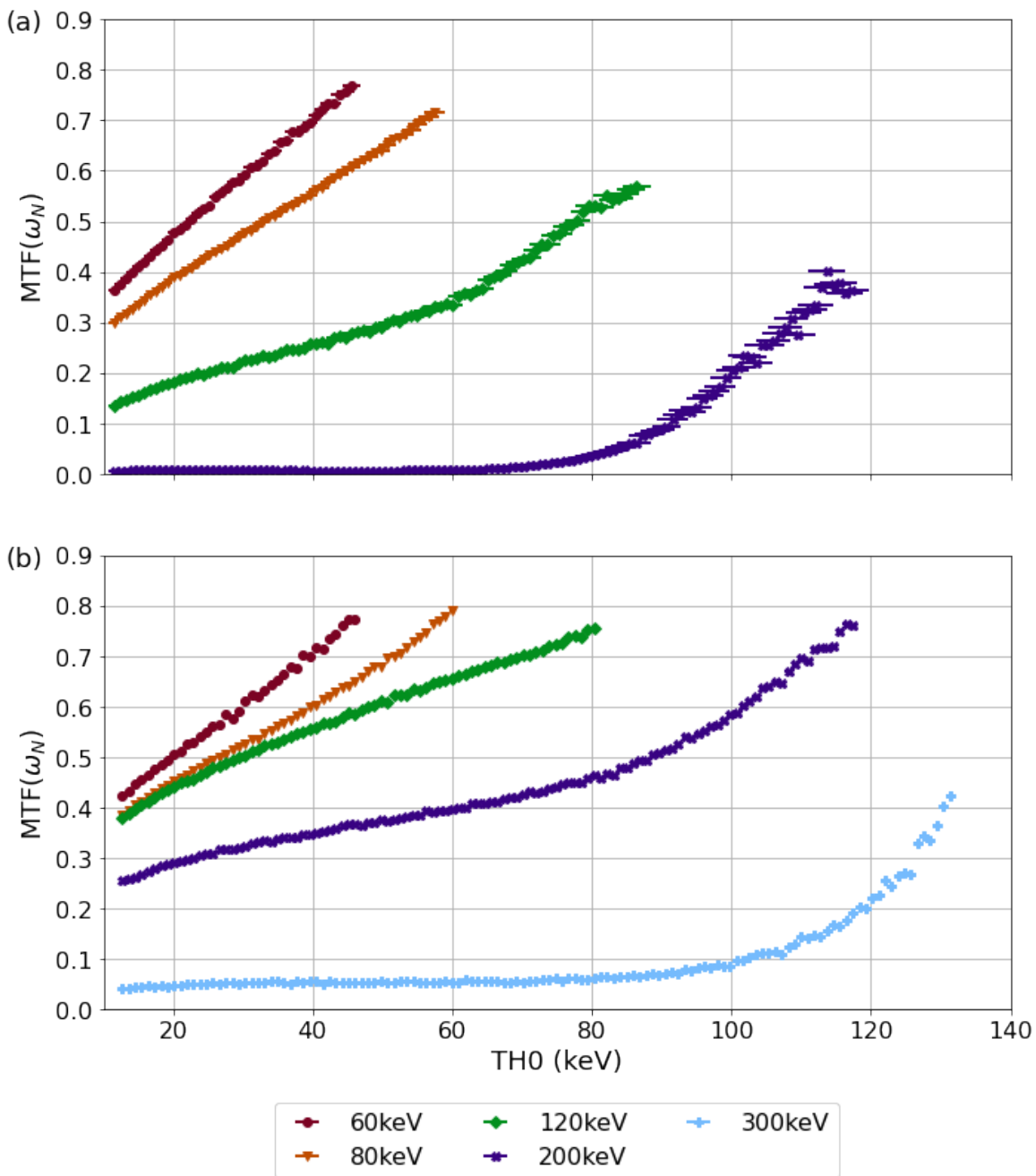


Figure 6.7: $MTF(\omega_N)$ for (a) Si and (b) GaAs:Cr devices as a function of counting threshold when operating in SPM for electrons with energies ranging from 60-300 keV.

with increasing primary electron energy. Considering the higher electron energies, it can be seen that not only does the MTF of the GaAs:Cr for 300keV electrons surpass that of the Si detector for 200keV electrons, but that the MTF of the GaAs:Cr detector for 200keV electrons surpasses that of the Si detector for 120keV electrons at low counting thresholds.

Figure 6.8 shows the dependence of $MTF(\omega_N)$ on counting threshold when the Si and GaAs:Cr devices operate in CSM for 60 keV, 200 keV and (for the GaAs:Cr sensor) 300 keV electrons. The relationship between threshold and $MTF(\omega_N)$ is quite different

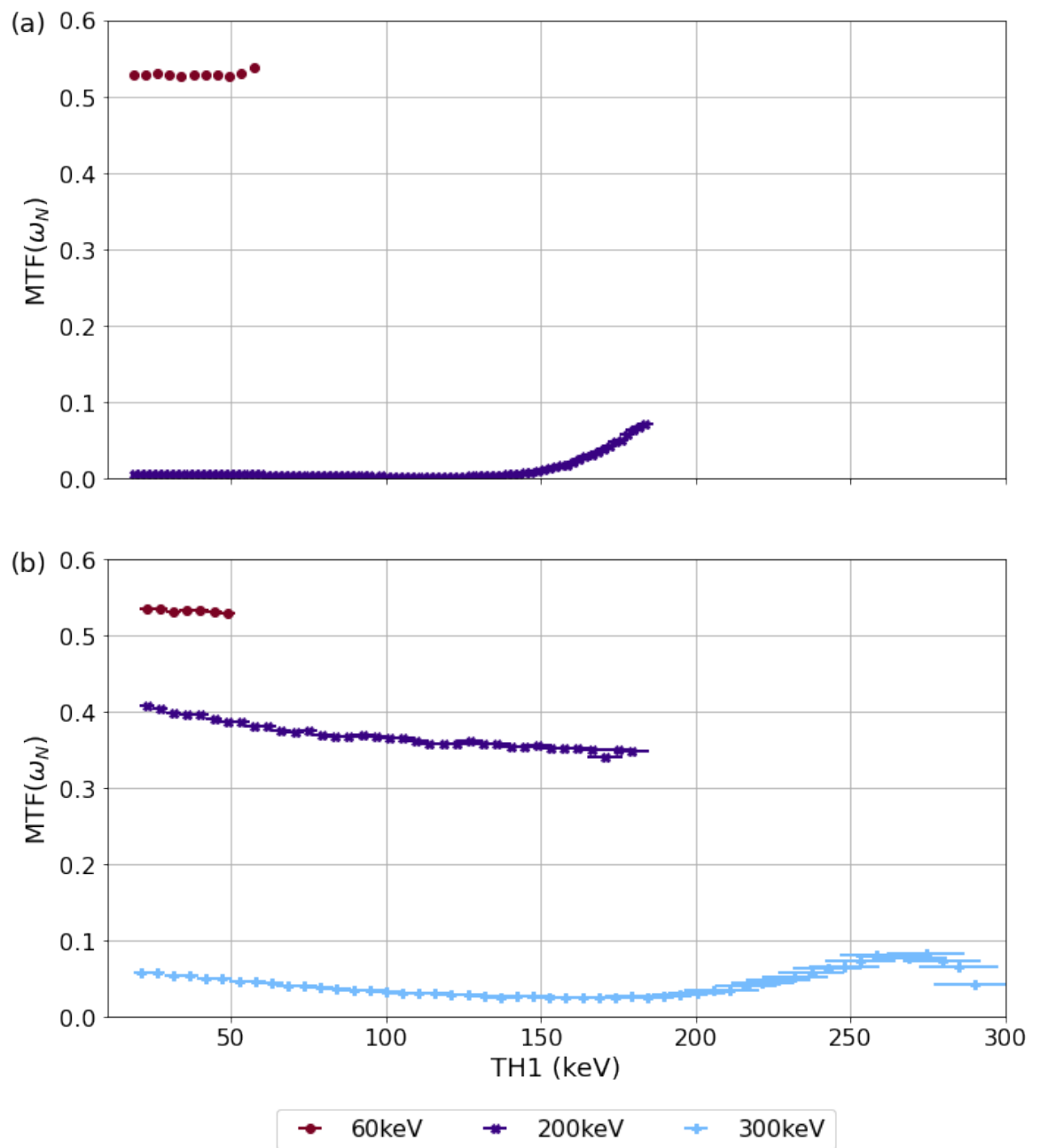


Figure 6.8: $MTF(\omega_N)$ as a function of counting threshold when operating in CSM with electrons energies in the range of 60 keV - 300 keV for (a) the Si sensor and (b) the GaAs:Cr device.

when the detectors operate in CSM compared with the behaviour seen when they operate in SPM in Figure 6.7. In SPM, the value of $MTF(\omega_N)$ generally increases with increasing threshold at a consistent rate for low-energy electrons, while for higher energy electrons $MTF(\omega_N)$ initially increases gradually with counting threshold or is approximately constant until it begins to increase rapidly with counting threshold above a certain critical threshold. Whereas, in CSM, $MTF(\omega_N)$ is relatively constant for both detectors across the full counting threshold range when using low energy electrons. For 60 keV electrons, $MTF(\omega_N)$ fluctuates around 0.53 for both devices.

There is again a shift in behaviour for higher electron energies. For 200 keV electrons, $MTF(\omega_N)$ for the GaAs:Cr detector starts at 0.41 at a threshold of 24 ± 2 keV and decreases to a value of 0.34 at the highest threshold used, which was 184 ± 6 keV. Whereas for the Si detector $MTF(\omega_N)$ is 0.01 at a threshold of 18.9 ± 0.5 keV and decreases to a minimum of 0.00 at a threshold of 112.2 ± 2 keV before increasing at thresholds above ~ 130 keV to a maximum value of 0.07 at a threshold of 179.1 ± 2 keV. For 300 keV electrons, the value of $MTF(\omega_N)$ for the GaAs:Cr sensor is 0.06 at a threshold of 19 ± 2 keV. As the counting threshold increases, this also decreases, reaching a minimum of 0.03 at a threshold of 166 ± 8 keV before increasing to a maximum of 0.08 at a threshold of 290 ± 13 keV before decreasing again.

This difference in behaviour when operating in CSM stems from the fact that, in this mode of operation, whether or not an electron is counted depends on the sum of the charge induced in neighbouring pixels. For low-energy electrons, which typically deposit all their energy across one of the 2×2 pixel blocks that the CSM algorithm operates across (as indicated by the spectra in Figures 4.2(c) and 6.1(b)), this summed charge is consistently above threshold until the threshold is equal to the energy of the incident electron. However, for both Si and GaAs:Cr sensors, electrons with energies ≥ 200 keV have sufficient range that they deposit their energy over more than one 2×2 pixel block, as can be seen referring back to the simulation results in Figure 5.2. Consequently, at low thresholds more than one pixel can register an incident electron, as more than one pixel block can register enough signal so as to be above the counting threshold. Additionally, it is not necessarily the case that the pixel block across which incident electrons deposit the majority of their energy contains the entry pixel. Given the propensity of electrons to deposit more energy towards the end of their trajectory (as discussed in Chapter 4), it is often not the pixel block that contains the entry pixel that registers the highest signal.

As the counting threshold increases, the pixel block that contains the entry pixel tends to be discounted, leading to the observed decrease in $MTF(\omega_N)$ for low-energy electrons. The improvement in $MTF(\omega_N)$ at higher thresholds observed for 300 keV and 200 keV electrons in the GaAs:Cr sensor reflects the fact that, at high thresholds, the only pixel blocks that continue to register enough signal to be above threshold are those recording events where the trajectory of the incident electron terminates in the pixel block in which it entered the sensor. In such events, the incident electron deposits most of its energy in the pixel block in which they enter the sensor. It is still relatively unlikely that the pixel in which the electron entered the sensor is also the one that registers the highest signal. Consequently, the overall effect of the CSM algorithm is to (usually) allocate the incident electron to the wrong pixel, thereby introducing blurring into the recorded image. This is analogous to the detectors' behaviour when they operate in SPM, though with the energy deposition over 2×2 pixel blocks being the key consideration, rather than individual pixels.

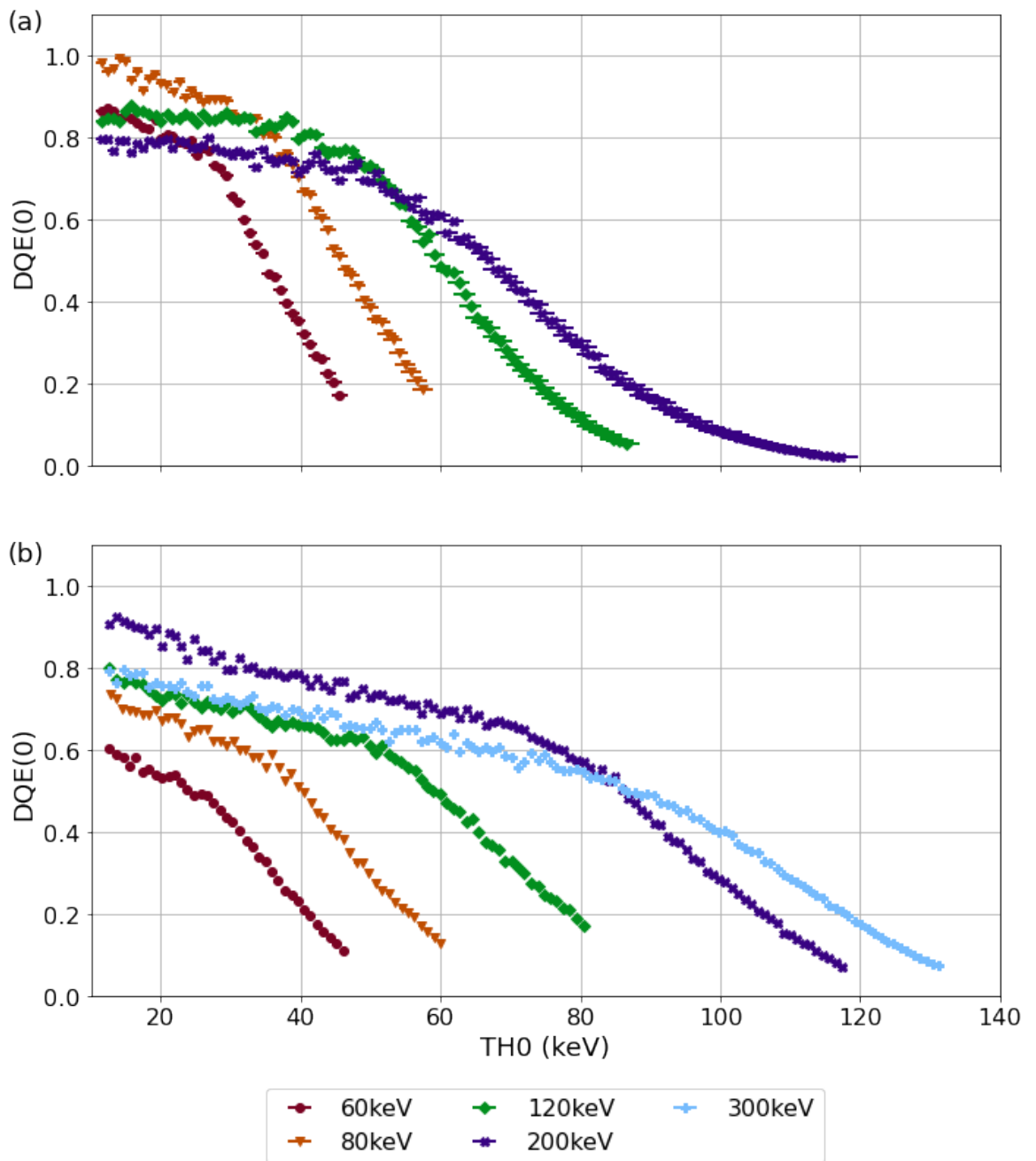


Figure 6.9: Dependence of DQE(0) on counting threshold for (a) the Si Medipix3 device and (b) the Medipix3 detector with GaAs:Cr sensor, both operating in SPM for incident electrons with energies from 60 keV to 300 keV.

The dependence of DQE(0) on counting threshold for both devices operating in SPM can be seen in Figure 6.9. There is an improvement in DQE(0) going from 60 keV to 80 keV for both the Si (Figure 6.9(a)) and GaAs:Cr (Figure 6.9(b)) detectors. However, for the Si device, DQE(0) decreases when the primary electron energy increases to 120 keV and 200 keV, whereas for the GaAs:Cr detector there is further improvement in DQE(0) up until a primary electron energy of 200 keV before there is a decrease for primary electrons with an energy of 300 keV. The initial improvement in DQE(0) with increasing electron energy can be explained by a reduction in the

backscatter of electrons from the sensor, as per the simulation results in Figure 5.3(a), leading to only partial energy deposition such that incident electrons are not registered. However, the increased variance in the number of pixels that register an incident electron leads to a deterioration of $DQE(0)$.

For both sensors, when using 60 keV and 80 keV electrons, $DQE(0)$ decreases gradually with increasing threshold up to approximately half the primary electron energy. At higher thresholds, the effective pixel pitch is less than that of the physical pixel pitch, so $DQE(0)$ decreases rapidly with the increase in threshold. For 200 keV and 300 keV electrons, the threshold at which there is a change in gradient in the dependence of $DQE(0)$ on threshold is approximately half the maximum energy deposited by the primary electron on a single pixel, rather than approximately half the primary electron energy. In the case of 120 keV electrons, the threshold at which there is a change in the dependence on threshold appears to be part way between half the primary electron energy and half the maximum energy deposited. This is due to the previously discussed increased disparity in primary electron energy and maximum signal deposited in a single pixel for higher electron energies.

Likewise, the differences in the rate at which $DQE(0)$ decreases as the counting threshold is raised for each primary electron and for each detector reflects the underlying differences lateral spread of energy. At high counting thresholds, the Si sensor's $DQE(0)$ for 200 keV electrons is higher than its $DQE(0)$ for 120 keV electrons. Similarly, the $DQE(0)$ of the GaAs:Cr for 300 keV electrons at high counting threshold is higher than the $DQE(0)$ for 200 keV electrons at the same counting threshold. This reflects the fact that the higher the primary electron energy is, the greater is the maximum amount of energy that can be deposited in a single pixel is. Consequently, the fraction of incident electrons that are not counted when the counting threshold is high (i.e. high enough for all primary electrons of a given energy to be counted by one pixel only) is smaller the higher the electron energy.

When the devices operate in CSM, the dependence of $DQE(0)$ on counting threshold is somewhat different from that observed when the detectors operate in SPM. The dependency of $DQE(0)$ on electron energy shows a similar dependency to that seen in SPM: for the GaAs:Cr sensor, $DQE(0)$ improves when increasing in energy from 60 keV to 200 keV but deteriorates with a further increase in energy to 300 keV. For 60 keV electrons in the Si sensor (Figure 6.10(a)), the value of $DQE(0)$ decreases slightly with increasing threshold and the range of $DQE(0)$ values is relatively small. In contrast to the $DQE(0)$ results when the detector operates in SPM in Figure 6.9(a), it is not obvious that there is a change in the gradient when the counting threshold is set to half the primary electron energy. However, for the 60 keV $DQE(0)$ of the GaAs:Cr sensor, shown in Figure 6.10(b), there does appear to be a change in the dependence of $DQE(0)$ at a counting threshold of half the primary electron energy. Likewise, for high electron energies in both sensors (seen in Figures 6.10(a) and (b)),

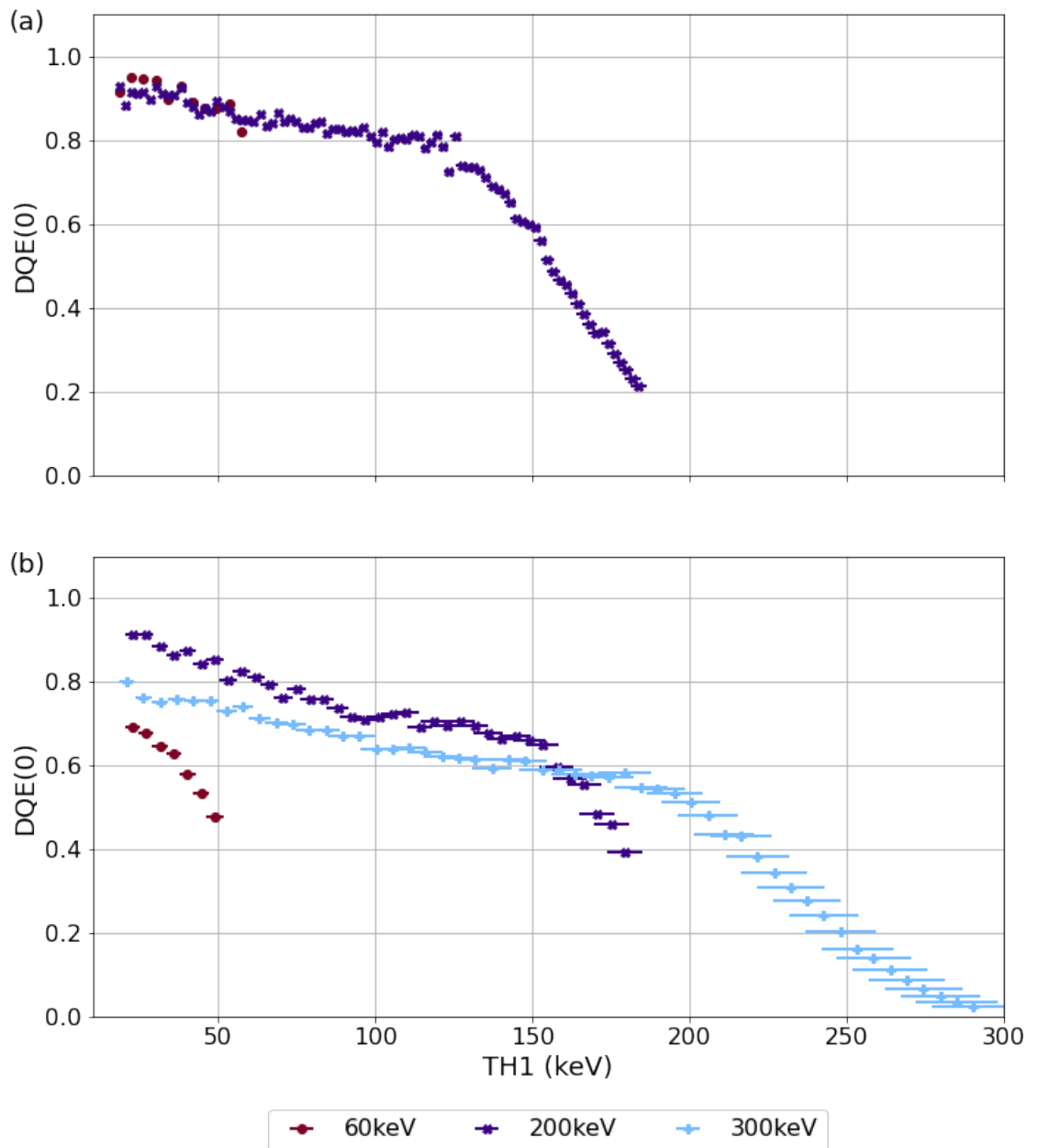


Figure 6.10: DQE(0) as a function of counting threshold using electrons ranging in energy from 60 keV to 300 keV for (a) the Si device and (b) GaAs:Cr device operating in CSM.

the dependence of DQE(0) on threshold is similar to that seen for all electron energies when the devices operate in SPM, although the threshold at which the dependency on threshold changes does not correspond to half the maximum deposited energy or half the primary electron energy.

However, in the case of the 200 keV Si DQE(0) and the 300 keV GaAs:Cr DQE(0) results, the thresholds at which the dependency of DQE(0) on counting threshold changes does correspond to the threshold at which $MTF(\omega_N)$ begins to improve in Figure 6.8. The trends observed in the dependency of DQE(0) on counting threshold are consistent with the interpretation of the dependency of $MTF(\omega_N)$ on threshold when the devices operate in CSM. 60 keV electrons deposit most of their energy

in a single pixel block and it is only when the threshold is close to the primary electron energy that there is a deterioration DQE(0) due to incident electrons not being counted. With the GaAs:Cr sensor, the increased backscatter from the sensor likely accounts for the greater dependency on threshold for the 60 keV DQE(0), as more electrons deposit only part of their energy in the sensor.

In both sensors, high energy electrons are counted by multiple pixels having deposited energy across multiple 2×2 pixel blocks and there is therefore a gradual decrease in the number of incident electrons that are not counted. Although the electrons deposit their energy across multiple pixel blocks, the summed charge in each block must still be above threshold for a pixel to register the incident electron. At high counting thresholds, electrons are only counted in a single pixel block and as the counting threshold increases, the greater the energy deposited in that block must be for the electron to be counted. The threshold at which there is a change in the gradient of the dependency of DQE(0) on threshold is indicative of the threshold at which a single 2×2 , and hence single pixel, records enough energy to exceed TH1. Whereas in SPM the threshold above which only single pixels record electrons is half the primary electron energy or half the maximum energy deposited in a single pixel, this is not the case in CSM. For 200 keV electrons in the Si sensor this threshold is ~ 125 keV, while for 300 keV electrons in the GaAs:Cr sensor in the GaAs:Cr sensor it is ~ 200 keV.

It is worth noting that, in general, CSM appears to improve the value of DQE(0). Comparing, for example, the value of DQE(0) for 60 keV electrons in Figures 6.9(b) and 6.10(b), the low threshold ($TH1 = 22.8 \pm$ keV) value of DQE(0) in CSM is 0.69. When operating in SPM with TH0 is set to approximately the same value (22.9 ± 0.2 keV), the value of DQE(0) is 0.54. Even for the lowest threshold used for the SPM measurements (12.7 ± 0.1 keV, the value of DQE(0) is only 0.60. One likely explanation for this improvement is that the CSM algorithm reconstructs small amounts of energy that are deposited by backscattered electrons which would otherwise not be registered as, due to the scatter of the electron in the sensor and diffusion, no individual pixel registers enough energy to count the event

Figure 6.11 shows how $DQE(\omega_N)$ depends on counting threshold when the detectors operate in SPM. For 60 keV, 80 keV and 120 keV electrons in both sensors, $DQE(\omega_N)$ largely tracks the dependence DQE(0) on threshold, although the change in the rate of dependence at half the primary electron energy is less apparent. Similar behaviour is also seen in the dependence of $DQE(\omega_N)$ on threshold for 200 keV electrons in the GaAs:Cr sensor in Figure 6.11(b). However, in the case of 200 keV electrons incident on the Si sensor (Figure 6.11(a)) and 300 keV electrons incident upon the GaAs:Cr sensor (Figure 6.11(b)), the dependence of $DQE(\omega_N)$ on threshold appears to match the dependence of $MTF(\omega_N)$ on counting threshold. This would seem to confirm the earlier hypothesis that, at higher electron energies, the dominant

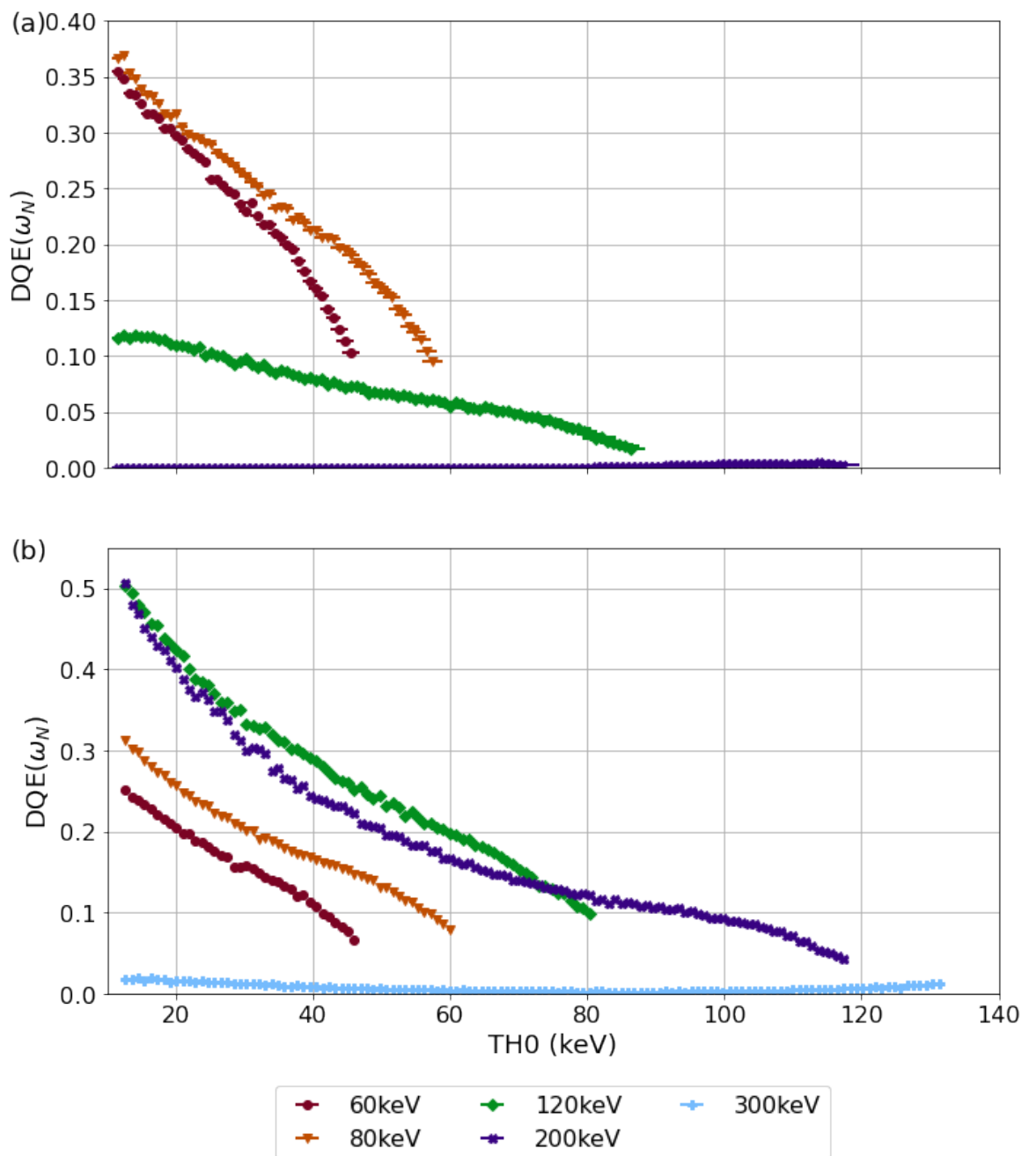


Figure 6.11: Dependence of $DQE(\omega_N)$ on counting threshold for (a) Si and (b) GaAs:Cr devices operating in SPM for electrons with energies ranging from 60 keV to 300 keV.

factor in determining the DQE at high spatial frequencies is the MTF, rather than the zero spatial frequency signal-to-noise ratio.

Similar trends are observed in the dependence of $DQE(\omega_N)$ on counting threshold when the detectors operate in CSM. In Figure 6.12, the dependence of threshold of $DQE(\omega_N)$ largely corresponds to the dependence of $DQE(0)$ on threshold in Figure 6.10.

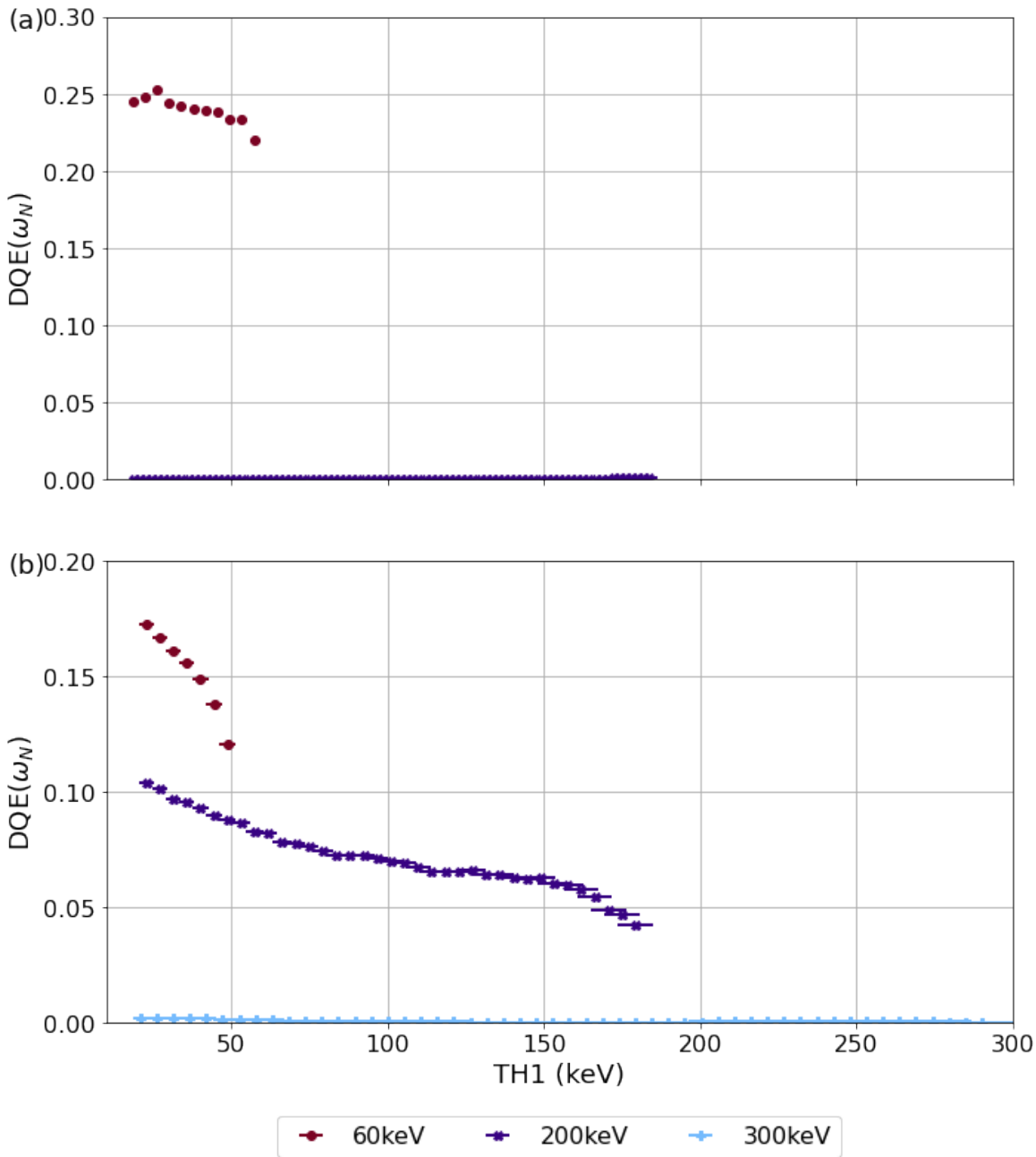


Figure 6.12: Dependence of $DQE(\omega_N)$ on counting threshold for (a) Si and (b) GaAs:Cr detectors in CSM for electrons with energies from 60 keV to 300 keV.

6.4 Linearity of Response

In this section, the linearity of response and deadtime of the Medipix3 device equipped with a $500\mu\text{m}$ thick GaAs:Cr sensor using a counting threshold of 12.7 ± 0.1 keV is compared with that of the Medipix3 detector with a $500\mu\text{m}$ thick Si sensor using a counting threshold of 12.4 ± 0.7 keV. All measurements were performed with the devices operating in SPM, using the same settings as for the measurements previously outlined with the exception that the value of I_{Krum} has been varied to investigate how its value affects the linearity of the detectors' response, as in Chapter 4. As the

GaAs:Cr detector appears to offer the best performance (and be a potentially more suitable option than Si) when using 120 keV and 200 keV electrons, measurements comparing the linearity of the detectors' response have been performed for both these electron energies. In spite of the limitations discussed in Chapter 4, Equation 4.4 was fit to the experimental linearity curves to extract values of g_τ and τ , as it was the model that was found to best fit the data.

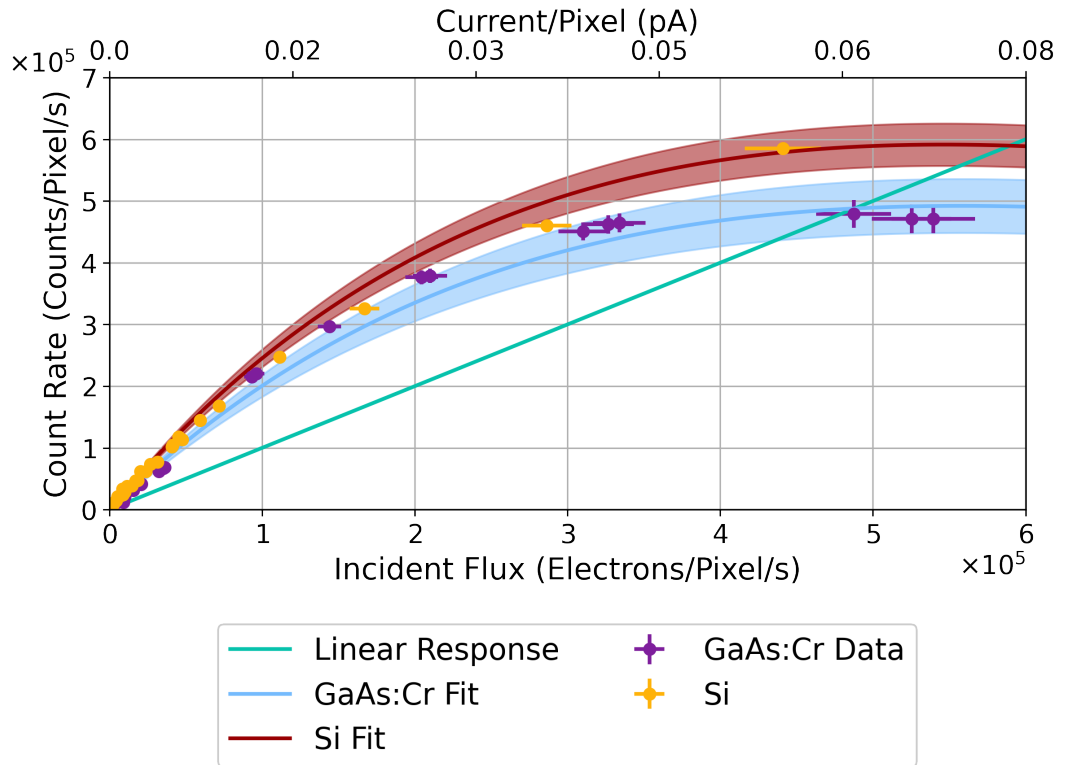


Figure 6.13: Count rate of the Si and GaAs:Cr Medipix3 devices exposed to increasing incident flux of 120 keV electrons with both devices using an I_{Krum} setting of 10 DAC. The shading indicates the error on the fit to the data, based on the propagation of the errors calculated for the fitted parameters.

Figure 6.13 shows the average count rate recorded by the two detectors exposed to various levels of incident electron flux when the primary electron energy was 120 keV and when both detectors had an I_{Krum} setting of 10 DAC, while Figure 6.14 shows the same when using 200 keV electrons, for selected values of I_{Krum} . In both figures, the expected detector response given the value of τ and g_τ obtained by fitting the data with Equation 4.4 using least-squares ODR, as well as the response of a perfectly linear detector are plotted.

Comparing the results of in Figures 6.13 and 6.14(a), several similarities and differences can be observed. For both 120 keV and 200 keV electrons, the Si detector registers a greater count rate for a given incident electron flux when the incident flux is low. This of course reflects the larger PSF of the Si detector for 120 keV and 200 keV electrons. However, while the count rate of the Si detector continues to

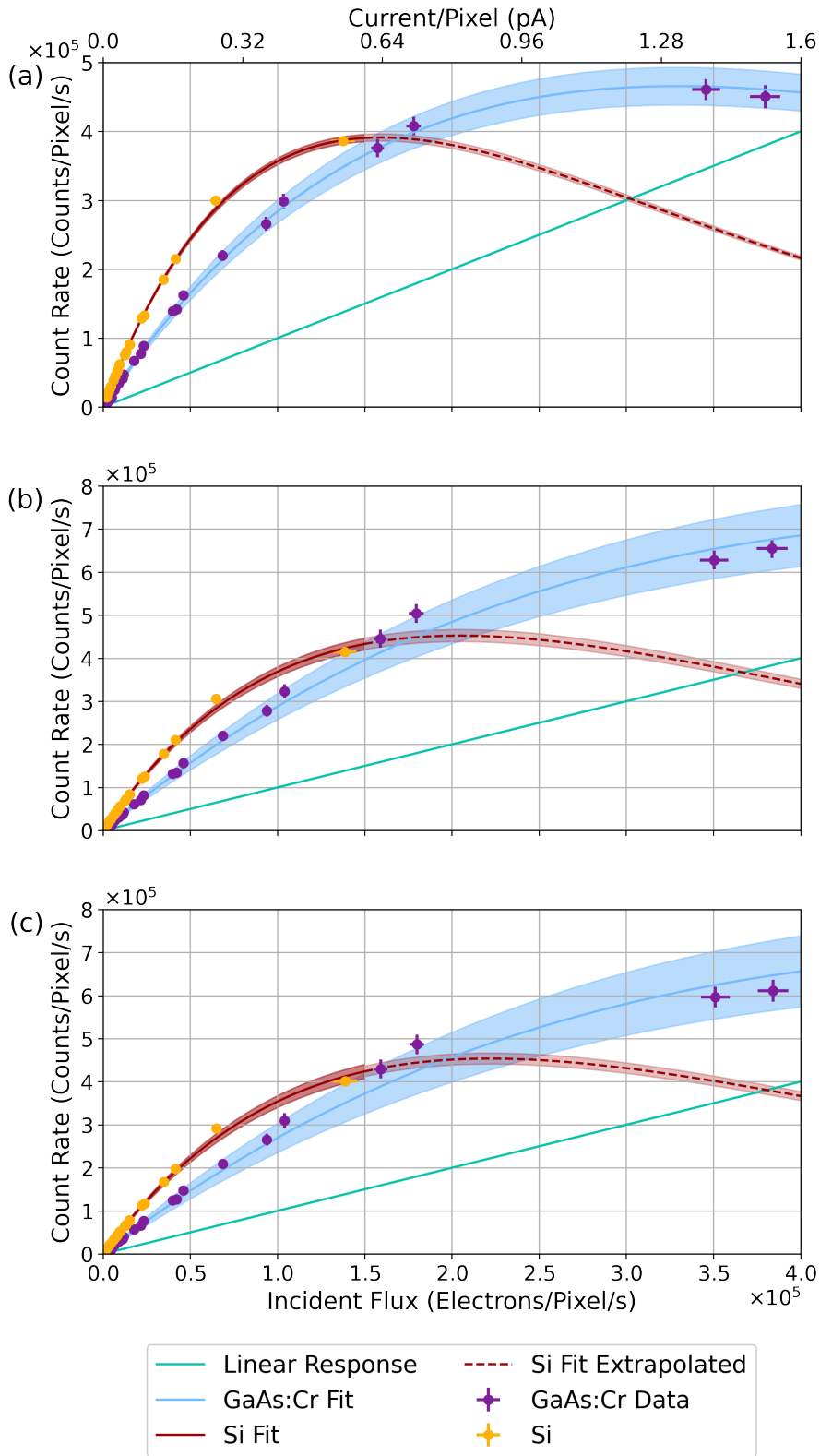


Figure 6.14: Count rate of the Si and GaAs:Cr Medipix3 detectors as a function of incident flux of 200 keV electrons when I_{Krum} is set to (a) 10 DAC, (b) 130 DAC and (c) 250 DAC. The uncertainty on the fit to the data was determined by propagating the errors on the fitted parameters. As in Figure 4.12, the predicted count rate for the Si sensor at incident flux above 1.5×10^5 electrons/pixel/s is an extrapolation based on the parameters found by fitting Equation 4.4 to the data points obtained at lower incident flux. For clarity, the predicted count rate of the sensor at incident flux $> 1.5 \times 10^5$ electrons/pixel/s has been plotted as a dashed line in (a)-(c)

surpass that of the GaAs:Cr detector at higher fluxes when using 120 keV electrons, that of the GaAs:Cr detector appears to supersede that of the Si detector at high flux when using 200 keV electrons.

It should of course be noted that this is with the considerable caveat that the datasets do not include any measurement of the Si detector's count rate when using an incident flux $> 1.5 \times 10^5$ electrons/pixel/s when using 200 keV electrons. This assertion is therefore based entirely on the expected count rate based on the fitted values of τ and τg . It is possible that rather than decrease, the count rate of the Si detector might reach a plateau as the GaAs:Cr detector's appears to do so at for 200 keV electrons or as both detectors appear to do for 120 keV electrons in Figure 6.13, that may be greater than the count rate of the GaAs:Cr detector.

However, considering how the count-rate behaviour of the two detectors changes with increasing I_{Krum} , this seems unlikely. Comparing Figures 6.14(b) and (c) with 6.14(a), the dependence of the GaAs:Cr detector's count rate on incident flux evolves as I_{Krum} increases so that at high incident flux a plateau is no longer observed and the count rate continues to increase. The GaAs:Cr detector's count rate at an incident flux of $1.58 \pm 0.04 \times 10^5$ electrons/pixel/s increases by $18 \pm 7\%$ when I_{Krum} is set to 130 DAC and by $14 \pm 7\%$ when I_{Krum} is equal to 250 DAC compared to when I_{Krum} is 10 DAC. In contrast, the Si detector's count rate at the comparable incident flux of $1.38 \pm 0.07 \times 10^5$ electrons/pixel/s increases by only $9 \pm 1\%$ when using an I_{Krum} setting of 130 DAC and by $7 \pm 1\%$ when I_{Krum} is set to 250 DAC. This suggests that the Si detector's count rate is unlikely to surpass that of the GaAs:Cr at incident fluxes above 1.5×10^5 electrons/pixel/s for the higher values of I_{Krum} shown in Figure 6.14, even if it does not decrease as predicted. In turn, this suggests that the same may hold true when I_{Krum} is set to 10 DAC. Furthermore, the predicted decrease in count rate for the Si detector at high incident flux is entirely consistent with the undercounting expected of a paralyzable detector. The greater reduction in count rate expected for the Si detector compared with the GaAs:Cr detector at high flux can be explained by the greater PSF of the Si detector. Just as this leads to an inflated count rate at low incident flux, at high flux this may mean that the pile-up of events is more pronounced.

Figure 6.15 shows the dependence of the detectors' deadtime for 120 keV and 200keV electrons on I_{Krum} , as well as the dependence of their τg_τ product on I_{Krum} . As in Chapter 4, this is on the basis that this product best represents the full extent to which the detectors are unresponsive due to an incident electron of a given energy. It can be seen that the deadtime of the Si detector is consistently higher than that of the GaAs:Cr detector for both primary electron energies, though the average deadtime for 120 keV electrons is very similar when both detectors use an I_{Krum} setting of 10 DAC and smaller than the error calculated for both detectors' deadtimes. Increasing I_{Krum} reduces the deadtime of the detectors and the measured value of g_τ due to the effective increase in counting threshold, as expected. For very high values of I_{Krum} ,

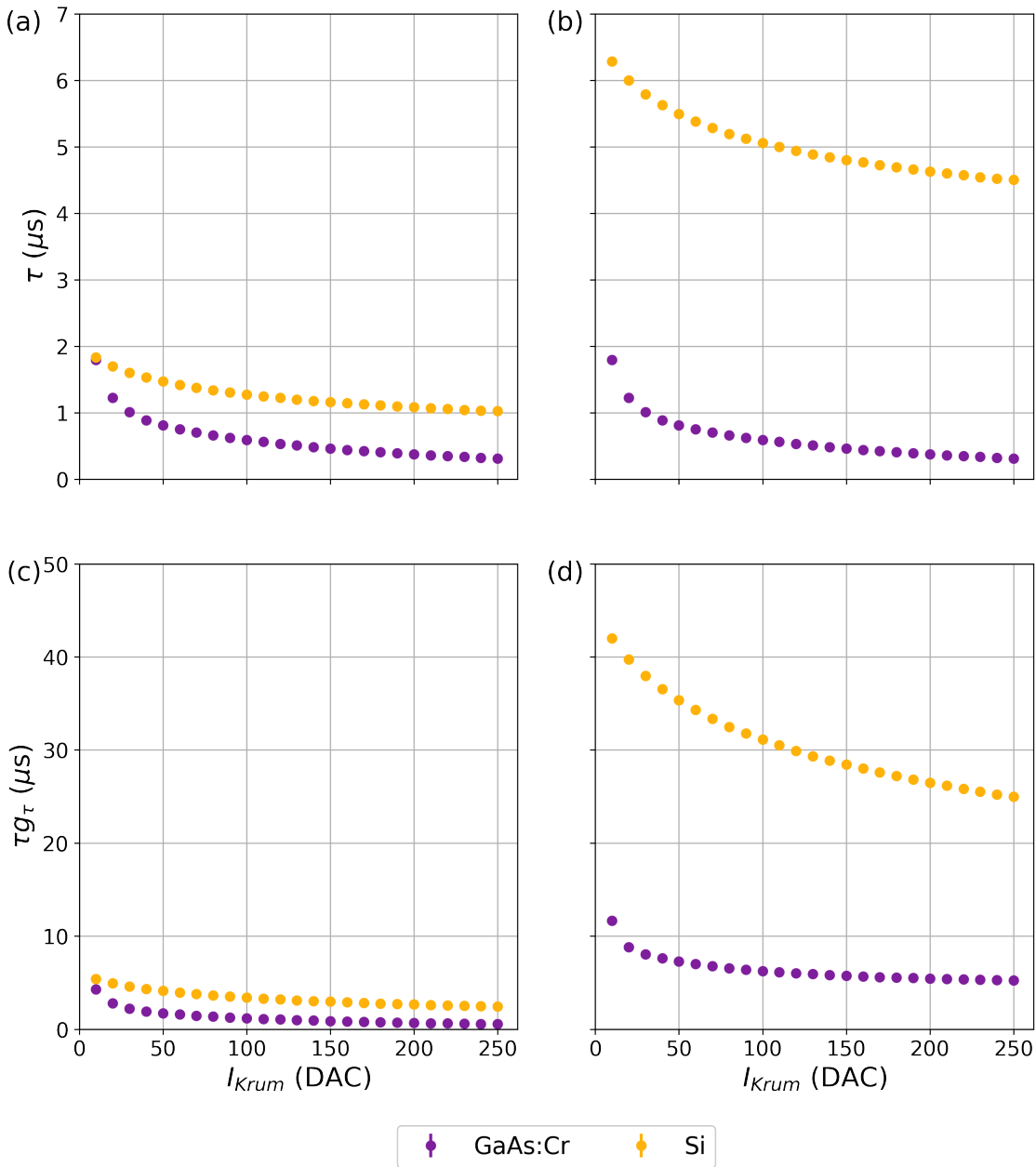


Figure 6.15: Dependence of the Si and GaAs:Cr detectors deadtime (τ), on I_{Krum} for (a) 120 keV electrons and (b) 200 keV electrons; the dependence of the τg_{τ} product of the two detectors for (c) 120 keV and (d) 200 keV electrons.

the average deadtime per electron per pixel is comparable to the deadtime measured by other Medipix3 devices with Si sensors to 10 keV photons and to that measured for a device based on the Eiger ASIC for 60 keV electrons [39, 40].

Likewise, the τg_{τ} product also decreases as the value of I_{Krum} increases. As was discussed in Chapter 4, τg_{τ} is more representative of the extent to which a detector is unresponsive due to a single incident electron. The difference between the GaAs:Cr and Si detectors for 120 keV electrons is smaller than it is when using 200 keV electrons. For 120 keV electrons the maximum difference in τg_{τ} is 2 ± 0.5 μs when I_{Krum} is ≥ 20 DAC), while the maximum difference for 200 keV electrons is 32 ± 0.9 μs

when I_{Krum} is set to 10 DAC. In the case of 200 keV electrons, this difference decreases with increasing I_{Krum} to a minimum of $21 \pm 1 \mu\text{s}$ when $I_{Krum} \geq 240$ DAC.

The increase in count rate obtained by increasing I_{Krum} comes at the cost of an effective increase in counting threshold, as some signals no longer surpass the counting threshold because of the more rapid return to baseline. Consequently, above a certain value of I_{Krum} no improvement in count rate is possible as it is accompanied by an increase in undercounting and, if the incident flux is too low for the increase in count rate to be beneficial, it can be the case that increasing I_{Krum} causes a decrease in the count rate. In Figure 6.16(c), the plateau observed in the high count rate results at high values of I_{Krum} indicates that the incident flux is sufficiently high that the maximum benefit possible by increasing I_{Krum} has been obtained. The plateau begins at an I_{Krum} setting of ≈ 150 DAC, for which the increase in count rate is $22.7 \pm 0.2\%$ what it was when I_{Krum} was set to 10 DAC for the Si detector and $61 \pm 9\%$ for the GaAs:Cr detector. For the low flux measurements, the reduction in count rate when using a value of I_{Krum} of 150 DAC in Figure 6.16(a) is $15 \pm 3\%$ (GaAs:Cr) and $14 \pm 1\%$ (Si). The increase in count rate at high incident obtained by using a high value of I_{Krum} therefore outweighs the undercounting at low flux that a high value of I_{Krum} entails, particularly in the case of the GaAs:Cr sensor.

For the high count rate results for 200 keV electrons in Figure 6.16(d), no plateau in the dependence of count rate on I_{Krum} is observed for either detector. This suggests that the highest 200 keV flux incident upon the detectors was insufficiently high for the increase in count rate at high levels of I_{Krum} to be equal to the decrease in counts due to undercounting. The maximum count rate of the GaAs:Cr detector occurs when I_{Krum} is set to 90 DAC, while for the Si detector it is when I_{Krum} is set to 100 DAC. At these values of I_{Krum} , the increase in count rate is $37 \pm 6\%$ (GaAs:Cr) and $10 \pm 1\%$ (Si) relative to when a value of 10 DAC is used. For the low flux measurements in Figure 6.16(a), the decrease in count rate at these I_{Krum} settings is $9 \pm 2\%$ (GaAs:Cr) and $8 \pm 1\%$ (Si) relative to a setting of 10 DAC. Therefore, even at what are instances of relatively low flux incident upon the detectors, it can be seen that an appropriate choice of the value of I_{Krum} can lead to an improvement in count rate that outweighs the decreased count rates at low incident flux.

One final point worth noting when considering the results in Figure 6.16 collectively, is that the improvement in count rate observed by using a high value of I_{Krum} with the GaAs:Cr detector is significantly higher than the improvement observed with the Si detector. This is a point that will be revisited in Section 6.5.

To summarise, the values of τ and τg_τ extracted from datasets acquired for both 120 keV and 200 keV electrons at a range of I_{Krum} settings were consistently lower for the device with the GaAs:Cr sensor than those for the Si sensor device (when comparing a given I_{Krum} setting and electron energy). The difference in the detectors' performance was smallest when I_{Krum} was set to 10 DAC, and, in the case of thd

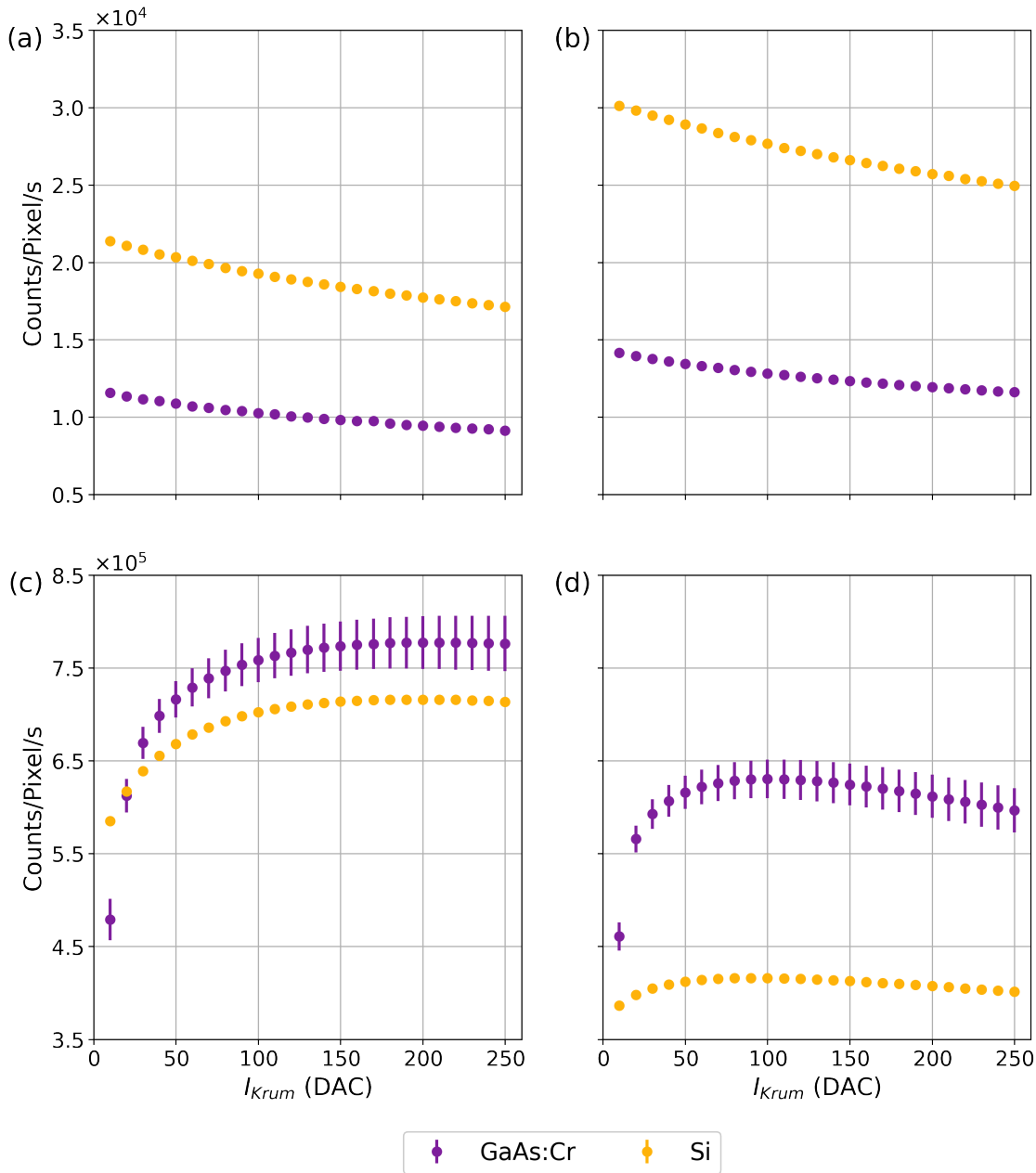


Figure 6.16: Dependence of the count rate of the GaAs:Cr and Si detectors on I_{Krum} for (a) 120 keV electrons at an incident flux of $5.3 \pm 0.9 \times 10^3$ electrons/pixel/s (GaAs:Cr) and $5.4 \pm 0.1 \times 10^3$ electrons/pixel/s (Si) (b) 200 keV electrons at an incident flux of $4.8 \pm 0.2 \times 10^3$ electrons/pixel/s (GaAs:Cr) and $4.5 \pm 0.1 \times 10^3$ electrons/pixel/s (Si), (c) 120 keV at an incident flux of $4.9 \pm 0.2 \times 10^5$ electrons/pixel/s (GaAs:Cr) and $4.4 \pm 0.2 \times 10^5$ electrons/pixel/s (Si) and (d) 200 keV electrons at an incident flux of $3.49 \pm 0.08 \times 10^5$ electrons/pixel/s (GaAs:Cr) and $1.38 \pm 0.07 \times 10^5$ electrons/pixel/s (Si).

120 keV electron data, the difference in τg_τ is within error. The smaller values of τ and τg_τ do not automatically equate to a higher count rate for a given incident flux for the GaAs:Cr sensor. Instead, as in Chapter 4, these value of τ is indicative as how low or high a flux to which the detector can be exposed while maintaining a linear response. This is due to the way in which the detectors' count rates are inflated by incident electrons being counted by multiple pixels. Nevertheless, the effect of the smaller (for

a given primary electron energy) PSF of the GaAs:Cr sensor (compared with the Si sensor) means that it is able to maintain a more linear response for higher incident flux than is the case for the Si sensor. The improvement possible in count rate at high incident flux when using a high value of I_{Krum} is greater for the GaAs:Cr detector than it is for the Si detector. Furthermore, the improvement in count rate at high flux obtained by using a high value of I_{Krum} outweighs the loss of counts to a greater extent for the GaAs:Cr detector than is the case for the Si detector. It can therefore be argued that the GaAs:Cr detector surpasses the Si detector in terms of linearity of response for 120 keV and 200 keV electrons in addition to surpassing it in terms of MTF and DQE. Consequently, for these electron energies, the GaAs:Cr detector is, overall, a better choice than the Si when working at these energies, offering better imaging performance and better linearity of response for experiments that involve a high electron flux incident upon the detector.

6.5 Investigation of Defects

As discussed in Chapter 2, the GaAs:Cr sensor material features defects that are visible in the images recorded by a detector using GaAs:Cr for the sensor. The 2014 generation of GaAs:Cr, which is the variety studied as part of the present work, features lines and a granular structure, both of which are associated with networks of dislocations that arise when the crystal is being grown. Figure 6.17 shows a comparison of the flat fields recorded by Medipix3 devices with Si and GaAs:Cr sensors. While the Si sensor in Figure 6.17(a) is highly homogeneous, the GaAs:Cr sensor in Figure 6.17(b) displays all the defects typical of the 2014 version of GaAs:Cr. These are visible in the flat field images as the defects distort the electric fields in the sensor which define the pixel shape and size and affect the charge collection properties of the sensor. Figures 6.17 show some of these defects in close-up. Looking at the histograms of the pixel intensities in the flat fields in Figure 6.17(c) confirms the greater variation in the response of the GaAs:Cr sensor compared with the Si sensor; the standard deviation of the distribution of mean-normalised intensities for the former is almost four times that of the latter.

Figures 6.18(a) and (b) show flat field images of the GaAs:Cr detector exposed to 200 keV and 300 keV electrons, with the regions from which confocal STEM maps were acquired at both electron energies marked. The full, summed confocal STEM maps acquired using 200 keV and 300 keV electrons are shown in 6.18(c) and (d). It can be seen that the contrast of the 200 keV confocal STEM map is more pronounced than that of the 300 keV map, with the regions of high and low numbers of counts more clearly delineated in the 200 keV map than they are in the 300 keV map. This reflects the improved PSF of the GaAs:Cr detector for 200 keV electrons relative

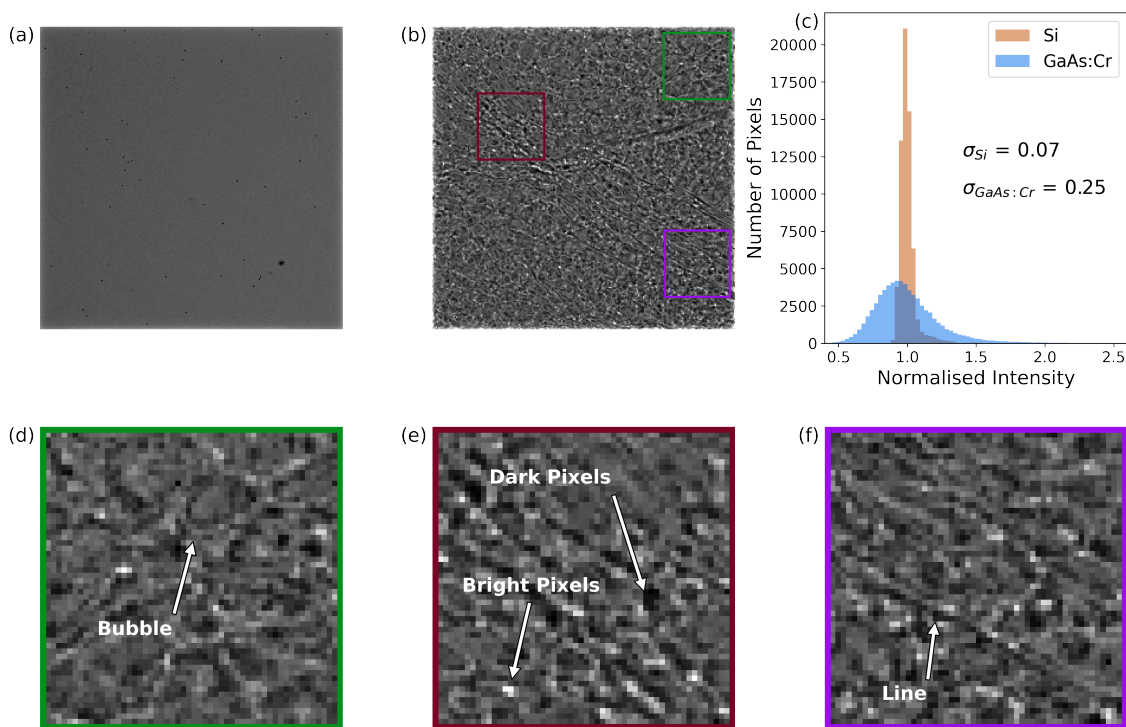


Figure 6.17: Mean-normalised flat field images recorded by (a) the Medipix3 device with $500\ \mu\text{m}$ Si sensor and $55\ \mu\text{m}$ pitch characterised in Chapter 3 (b) the Medipix3 GaAs:Cr device, both exposed to 200 keV electrons; (c) shows histograms of the intensities in (a) and (b); (d) - (e) show close-ups of ROI marked in (b) that showcase examples of different types of defects seen in the GaAs:Cr sensor.

to 300 keV electrons. Nevertheless, features identifiable in one map are generally visible in the other, the most obvious being the line defects that run across the sensor which manifest as bright lines in both maps.

The regions of the sensor from which the confocal STEM maps were acquired are shown in close-up Figure 6.19(a) and (b). Within these close-ups, selected ROIs are marked. That marked marked in blue, ROI B, represents a portion of the sensor that was common to both the confocal STEM maps as well as all images acquired as part of the 120 keV linearity dataset. Is shown in close-up in Figures 6.19(c) and (d), in which several selected pixels of interest (POI) are marked. These pixels have been chosen for being the largest in the ROI (marked in blue); the pixel in the ROI that has recorded the greatest number of counts (marked in red); the pixel that recorded an average (relative to the entire pixel matrix) number of counts (marked in purple); the pixel with an average area (again, calculated on the basis of the pixel area (marked in green); and the pixel that recorded the fewest counts in ROI B in both datasets (marked in yellow). It is worth noting that the pixel marked in yellow is not the pixel that An additional POI is marked in Figures 6.19(g) and (i). This is located on one of the line defects that run across the sensor and is of interest due to the behaviour it displays in the 200 keV linearity datasets, discussed further below.

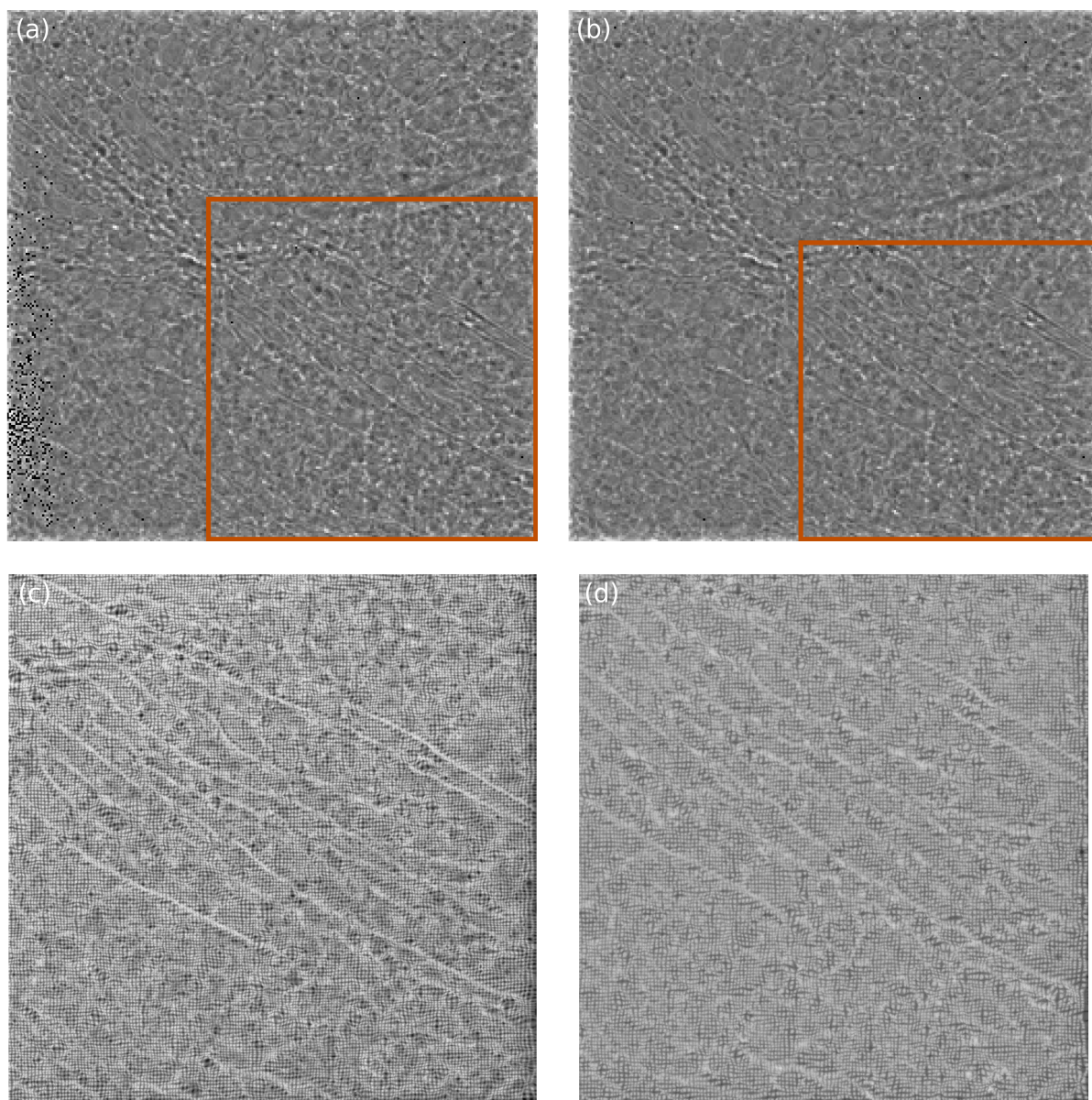


Figure 6.18: Flat field exposures of the GaAs:Cr detector operating in SPM with a counting threshold of 12.7 ± 0.1 keV when using (a) 200 keV and (b) 300 keV electrons with the regions from which sub-pixel confocal STEM maps were obtained marked. (c) shows the map acquired with 200 keV electrons and (d) that acquired with 300 keV electrons. Images in (a) - (d) are all normalised to their mean pixel intensity value and set to have the same contrast limits.

The corresponding confocal STEM maps of ROI B and C are shown Figures 6.19(d), (f), (h), and (j), and the regions of these that correspond to the POI are marked in the same colours that they are marked in Figure 3.15(c), (e), (g) and (i). It can be seen that the shapes and the areas of the POI are not consistent between the 200 keV (Figures 6.19(c) and (g)) and 300 keV (Figures 6.19(e) and (i)) confocal STEM maps. Although none of the POI in either the 200 keV or 300 keV confocal STEM maps are regular in shape, some are more distorted than others. In the 300 keV maps in Figure 6.19(f) and (j), the pixels marked in green and light purple are close to being regular squares. For both pixels, the lower and left-hand edges are straight, while the right-hand and upper edges which appear to be more proximate to a defect are distorted. The pixels marked in red, purple and yellow are recognisable as distorted pixels, while that in blue is almost circular. In the 200 keV confocal STEM maps, the shapes of the POI are more distorted than they are in the 300 keV map, with the regions identified as belonging to the POIs marked in dark blue and red no longer being entirely contiguous with one another. Even the light purple and green pixels are distorted, with the latter much reduced in size. This is also true for the dark purple pixel and for the pixel marked in yellow, though in the case of the yellow the reduction in size (relative to that observed in the 300 keV map) is less than is the case for the pixels marked in green and dark purple.

A similar increase in distortion can be seen when comparing the confocal STEM maps of ROI D, which was a region of the sensor identified as being relatively uniform (compared with other areas of the sensor). For the 300 keV confocal STEM map of ROI D in Figure 6.19(h), the pixels are close to being squares in shape, with pixel corners usually corresponding to the regions of the map where the greatest number of counts are recorded. This follows from the fact that when incident quanta enter the sensor at the corner of a pixel, it is, when a low counting threshold is used, counted by more pixels than is the case when it enters near the centre of the pixel, if only due to increased charge-sharing caused by the lateral dispersion of charge carriers due to diffusion in the sensor. The centre of the pixel therefore appears as a region where fewer counts are recorded. Some pixels, for example those in the middle of the second row from the top, are irregular in shape, but nevertheless the pixel boundaries correspond to the sum confocal STEM map in a way that largely matches expectations. However, although the two datasets have been processed in the same way, the pixel boundaries identified for the same region of the sensor on the basis of the 200 keV confocal STEM scan are highly distorted in Figure 6.19(l), with areas identified as belonging to one (detector) pixel appearing within an area of the sensor belonging to another.

Pixel response maps generated from both the 200 keV and 300 keV maps are shown in Figure 6.20. In these images, the number of counts in each (STEM scan) pixel is the number of counts recorded by a specific (detector) POI at that STEM scan

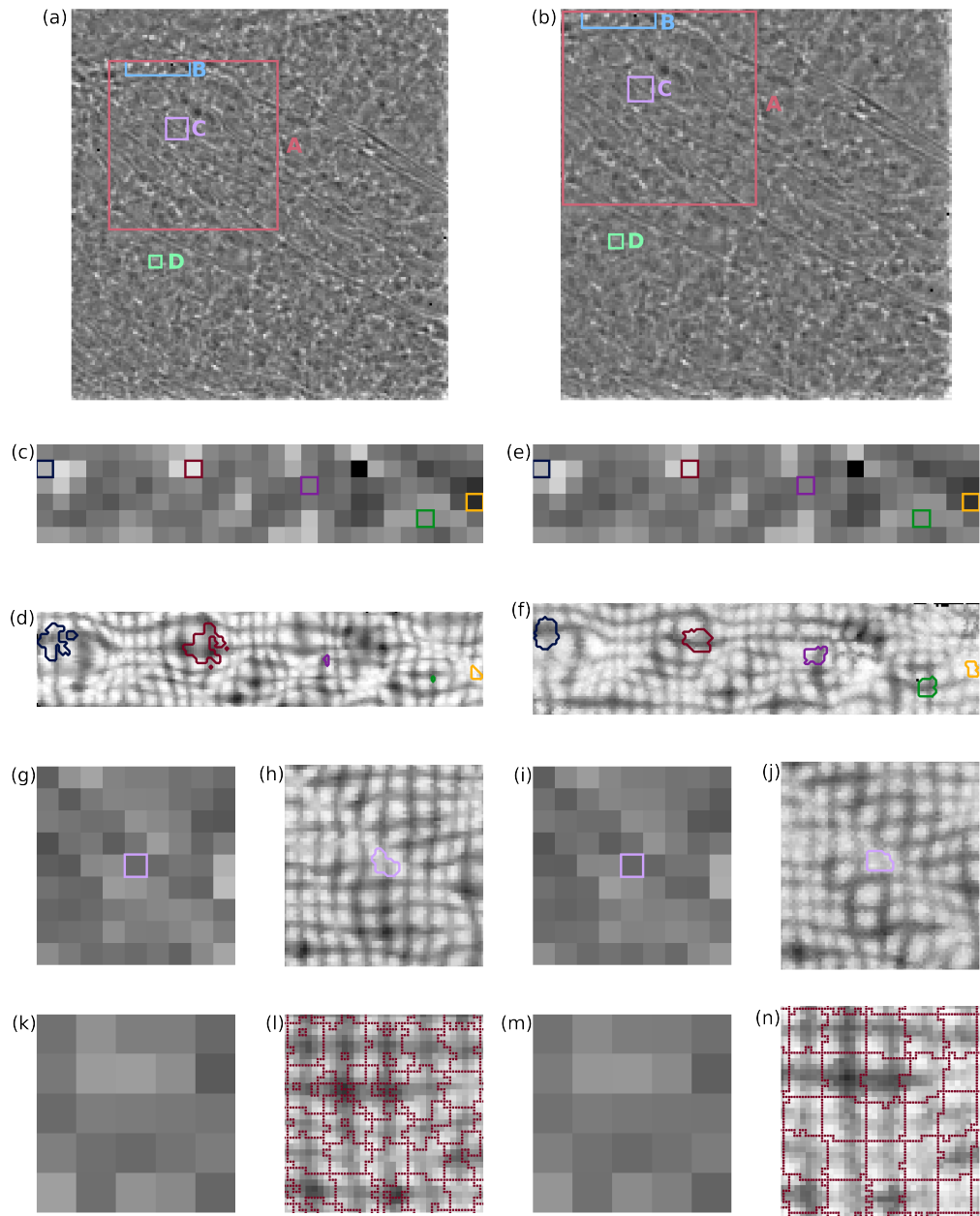


Figure 6.19: Close-ups of the regions of the sensor from which confocal STEM maps were acquired for the (a) 200 keV and (b) 300 keV datasets. Marked in (a) and (b) are several ROI. ROI B is shown in close-up in (c) for 200 keV electrons, (e) 300 keV electrons; ROI C is shown in close-up in (g) for 200 keV electrons and (i) 300 keV electrons; and ROI D is shown in close-up in (k) for 200 keV and (m) 300 keV electrons. Also shown are sum confocal STEM maps of ROI B for (d) 200 keV and (f) 300 keV electrons; of ROI C for (h) 200 keV and (j) 300 keV electrons; of ROI D for (l) 200 keV and (n) 300 keV electrons.

dwell point. The specific pixels to which these maps pertain to the pixels marked in Figure 6.19(c)-(f). It can be seen that the pixel response maps for the pixels marked in blue, red, dark purple and green in Figures 6.19(c) - (f) display a reduction in the number of counts recorded when the beam is incident in the centre of the pixel. This is most pronounced for the 200 keV confocal STEM maps, as can be seen by comparing the pixel maps in Figures 6.20(a), (c), (e) and (g) with their counterparts in Figures 6.20(b), (d), (f) and (h) acquired using 300 keV electrons.

The greater range of values in the 200 keV POI response maps (compared with the 300 keV maps) has the effect of making the shapes of the pixels seem more distinct when using 200 keV rather than 300 keV electrons, an effect which may be exacerbated by the reduced PSF of the detector for 200 keV electrons as opposed to 300 keV electrons. However, the pixel maps recorded using 300 keV electrons are more representative of the true shape of the pixels and, overall, the pixel shapes determined using the 300 keV data are better-defined than those determined using 200 keV electrons. The improved PSF for 200 keV electrons may also explain the fact when there is a reduction of counts in the centre of the POI response map it is more pronounced in the 200 keV dataset than it is for the 300 keV dataset. However, the more significant cause in to the reduction in counts in the 200 keV POI response maps is likely that, while the beam current used in both the 200 keV and 300 keV measurements appears to have been too high to avoid undercounting, the electron flux used when acquiring the 200 keV map was particularly high, causing increased undercounting. It is only the pixel marked in yellow that does not display this reduction of counts when the electron probe is incident upon the centre of the pixel in both the 200 keV and 300 keV confocal STEM datasets, while the pixel marked in light purple displays a reduction in counts in the 200 keV dataset but not in the 300 keV electron dataset.

It seems likely that the increased distortion in the confocal STEM maps acquired using 200 keV electrons is indicative of a failure to accurately identify the position of the electron probe and accurately assign dwell points in the scan to the correct detector pixel. This in turn appears to be caused by undercounting by the pixel in which the beam is incident, primarily when the beam is in the centre of the pixel. While the pixel shapes and areas determined using the 300 keV confocal STEM datasets appear more sensible, and it is tempting to think that these represent an accurate measurement of the pixel area and shapes of the GaAs:Cr sensor, with the observed distortions in pixel shape and size being comparable to that observed by other authors [205, 206, 240]. However, the fact that undercounting is observed in the 300 keV POI response maps in Figures 6.20(b), (d), (f), and (h) and as this undercounting is a likely cause for the failure to accurately identify the position of the electron probe, it seems unlikely that there are not inaccuracies in the pixel shapes and sizes as determined using the 300 keV dataset. Consequently, the pixel areas and

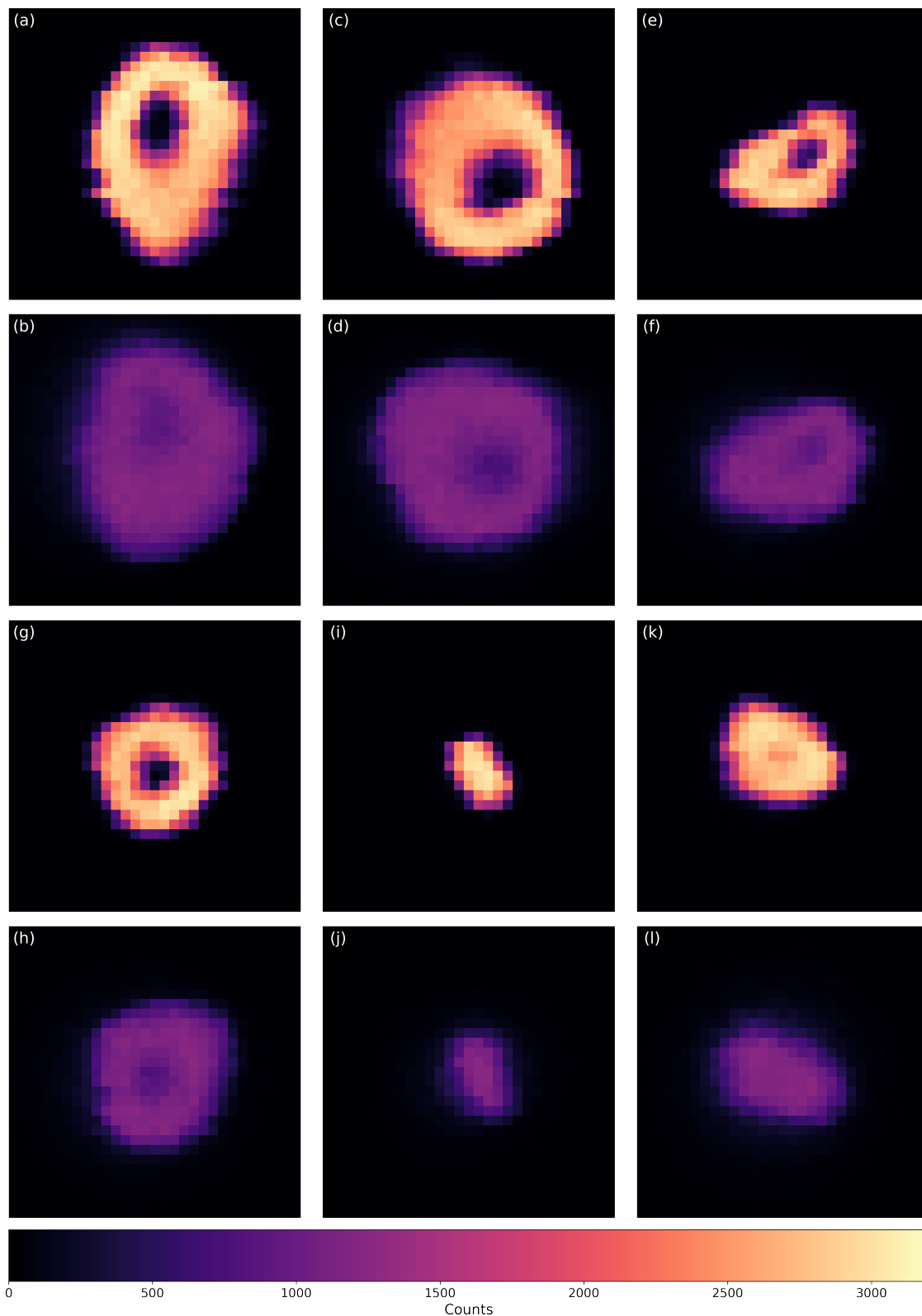


Figure 6.20: Pixel response maps for the pixel marked in (a) light blue, (c) red, (e) purple, (g) green and (i) yellow in Figures 6.19(c)-(f) generated from the 200 keV confocal STEM scans. (b), (d), (f), (h) and (j) show the same again but generated from the 300 keV dataset. The pixel response map for the pixel marked in dark blue in Figures 6.19(g)-(j) is seen in (k) for 200 k and (l) for 300 eV electrons.

shapes determined on the basis of the 300 keV confocal STEM dataset can at best be regarded as broadly indicative of general trends in the shapes and sizes of the GaAs:Cr detector's pixels, rather than rigorous, quantitative measurements.

Nevertheless, it is informative to compare the pixel areas as calculated by multiplying the number of dwell points assigned to a given pixel by the beam size in the detector plane for the 300 keV dataset and comparing this to the intensities recorded across the pixel matrix. Figure 6.21(a) shows maps of the pixel areas determined in this way for the whole region of the sensor, while close-ups of the area maps for ROIs B, C and D are seen in Figures 6.21 (b), (c) and (d). Comparing these area maps with their flat field counterparts in Figure 6.19, there appears to be a positive correlation between the pixel area and the number of counts it registers. This is not always consistently the case. As previously alluded to, the pixel that records the greatest number of counts in ROI B (marked in dark blue) is not the pixel that was identified as having the largest area (marked in red). This is apparent when comparing the counts recorded by these two pixels in Figure 6.19(e), with the areas they are identified as having in Figure 6.21(b).

However, there is overall a positive correlation between pixel size and counts recorded in the low flux flat field exposure, as can be seen by plotting the normalised intensity recorded by pixel in the 300 keV flat field image against. This can straightforwardly be attributed to the fact the larger a pixel is, the more electrons are incident upon it for a given flux. Additionally, larger pixels will register more of the charge deposited by electrons that enter neighbouring pixels (as defined by the nominal pixel pitch of $55\ \mu\text{m}$), as their larger volume means there is a greater probability of electrons that have entered the sensor in a neighbouring pixel depositing charge in them, either by scattering into them or by the diffusion of charge carriers produced in neighbouring pixels.

While acquiring data for the purposes of determining the various detector performance metrics for the GaAs:Cr Medipix3 detector, it was often observed that, when the flux incident upon the detector was high, individual pixels would begin to undercount and, at very high flux, become unresponsive until the incident flux was reduced. This behaviour was not uniform across the pixel matrix, and there appeared to be correlations between the defects in the sensor and which pixels would undercount for a given incident flux. Figures 6.23(a) - (e) shows an example of this behaviour. A small increase in the incident flux, as there is between Figures 6.23(a) and (b) causes no apparent change in the response of individual pixels. However, with a more substantial increase in incident flux, as occurs going from Figures 6.23(a) or (b) to Figure 6.23(c), the distribution of normalised pixel intensities begins to shift. This change in intensity distribution is indicative of a change in the mean number of counts recorded across the ROI due to some pixels beginning to undercount. In Figure 6.23(d) several pixels have

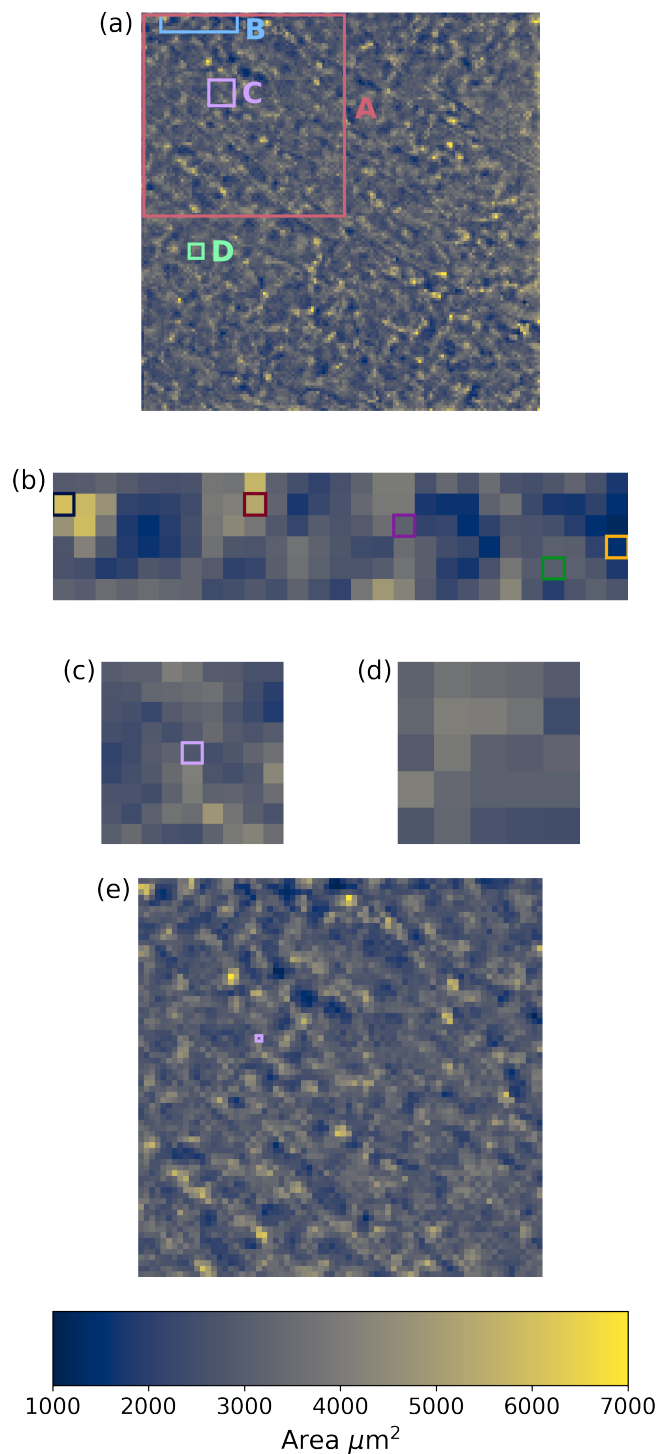


Figure 6.21: Maps of pixel areas as determined on the basis of the 300 keV confocal STEM dataset for (a) the full portion of the sensor form from which the 300 keV confocal STEM dataset was acquired, (b) ROI B, (c) ROI C, (d), ROI D and (e) ROI A. The selected POI previously marked in Figures 6.19(c) - (j) are also marked where appropriate in (b), (c) and (e). The light purple pixel marked in ROI C in (c) is also marked in ROI D in (d) to aid comparison with Figures 6.24.

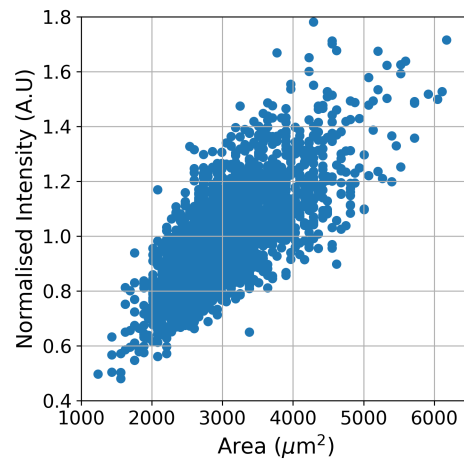


Figure 6.22: Plot of the mean-normalised pixel intensities in the region of the 300 keV flat field image shown in Figure 6.18(b), against the corresponding pixel area as determined from the 300 keV confocal STEM scan of that same region of the GaAs:Cr sensor.

ceased counting, including the pixel marked in red, with the number of unresponsive pixels increasing as the incident flux is further increased in Figure 6.23(e).

The fact that the pixel marked in red has ceased counting is confirmed by considering the count rate of the pixel as a function of incident flux in Figure 6.23(h), which falls to 0 counts/pixel/s at incident flux above 2.5×10^5 electrons/pixel/s when I_{Krum} is set to 10 DAC, as was the case for the measurements presented in Figure 6.23(a)-(e). Looking at the count rate as a function of incident flux for the pixel marked in blue in Figure 6.23(g), it can be seen that this pixel also becomes unresponsive at an incident flux greater than that used in Figures 6.23(a)-(e). For the count rate curves in both Figures in 6.23(g) and (h), increasing the value of I_{Krum} causes these pixels to have non-zero count rates at levels of incident flux that, when using an I_{Krum} setting of 10 DAC, cause the pixels to become unresponsive. Recovery of the responsiveness of those pixels that cease to count in Figure 6.23(e) by increasing the value of I_{Krum} is confirmed in Figure 6.23(f), which shows ROI B exposed to the same incident flux as in Figure 6.23(e), but with an I_{Krum} set to 50 DAC. Those pixels that had stopped in counting in Figure 6.23(e) have begun to count again.

This phenomenon of pixels turning off in response to high incident flux has previously been observed in a Timepix detector with GaAs:Cr sensor [241, 306]. In those instances, this effect was explained by the incident flux producing sufficient charge in the sensor that the current induced on pixels never fell below the counting threshold, which is a precondition for the counter to be incremented and thereby record an event. In effect, a particularly extreme instance of pile-up for a paralyzable detector was posited. However, this explanation is inconsistent with the fact that similar behaviour is not observed in the Si detector at a comparable electron flux to that at which it is observed in the GaAs:Cr sensor, particularly given that the

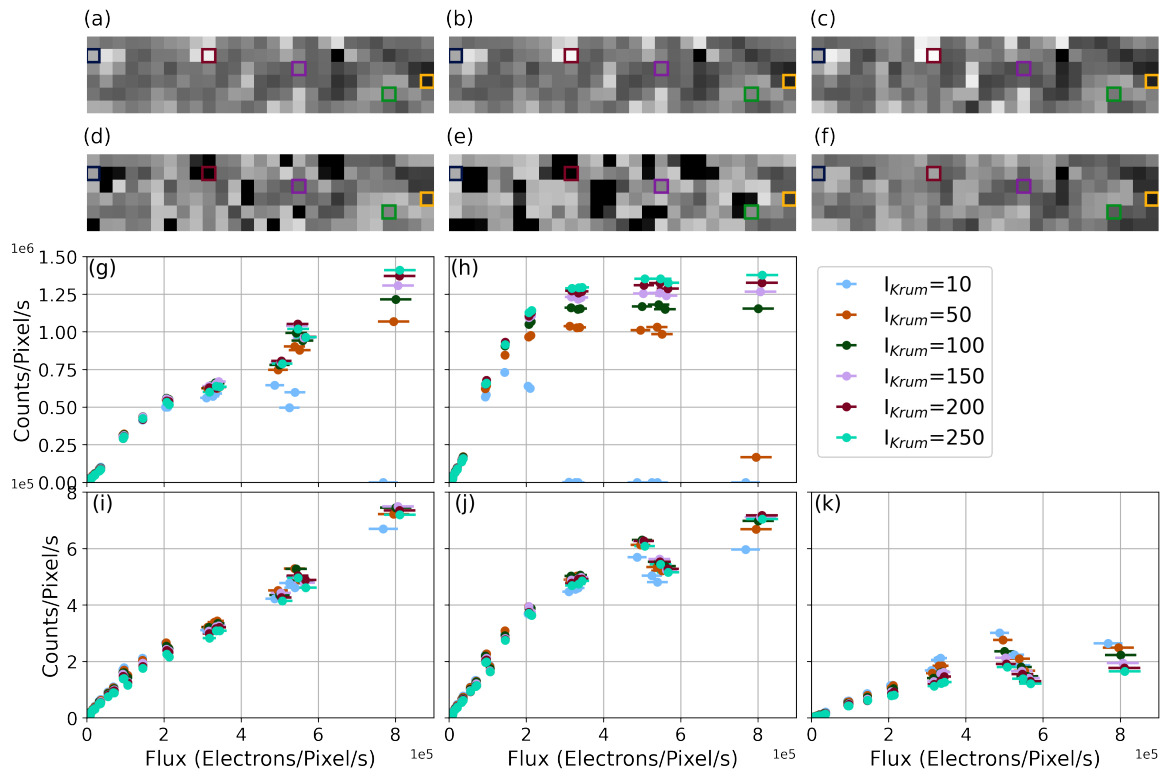


Figure 6.23: Close-ups of ROI B of the GaAs:Cr exposed to 120 keV electrons at an incident flux of (a) $1 \pm 0.1 \times 10^4$ electrons/pixel/s, (b) $3.2 \pm 0.2 \times 10^4$ electrons/pixel/s, (c) $1.44 \pm 0.08 \times 10^5$ electrons/pixel/s, (d) $3.3 \pm 0.2 \times 10^5$ electrons/pixel/s and (e) $5.4 \pm 0.3 \times 10^5$ electrons/pixel/s, all with I_{Krum} set to 10 DAC. The same ROI still exposed to incident flux of $5.4 \pm 0.3 \times 10^5$ electrons/pixel/s but with I_{Krum} set to 50 DAC is shown in (f). Plots of the count rate of the pixels marked in (g) blue, (h) red, (i) purple, (j) green and (k) yellow are plotted as a function of incident 120 keV electron flux for selected values of I_{Krum} .

deadtime for the GaAs:Cr detector is shorter than that of the Si for both 120 keV and 200 keV electrons.

While pile-up is inevitably a factor in the GaAs:Cr detector's response at high incident flux, this particular effect is better explained by the leakage compensation circuitry that is present on individual pixels being overwhelmed when the current induced on a pixel is too high. This behaviour has been observed for a Medipix3 device with a Ge sensor, for which pixels were observed to turn off and become unresponsive as the detector's temperature increased, which in turn increased the device's leakage current [215]. The disparity in the behaviour of the Si and GaAs:Cr Medipix3 devices can then be explained by the fact that the dark current of the GaAs:Cr sensor is higher than that of the Si sensor due to the higher bias and different material properties. Additionally, and perhaps more critically, the maximum leakage current that can be compensated for depends on whether the ASIC is set to collect holes or electrons. In hole collecting mode, used for the Si sensors, the maximum current is equal to the value of I_{Krum} ; in electron collecting mode, the maximum leakage current is equal to half the value of I_{Krum} . Therefore, for a given value of I_{Krum} , the maximum

leakage current that can be compensated for in a pixel of a device with a GaAs:Cr sensor is half that of a device with a Si sensor. A consequence of the role that I_{Krum} plays in determining the maximum leakage current of a pixel is that increasing I_{Krum} increases the maximum leakage current that can be compensated for on an individual pixel. This accounts for the fact that increasing the value of I_{Krum} causes those pixels that are unresponsive at high incident flux to begin counting again. It also explains the disproportionate increase in count rate for high values of I_{Krum} for the GaAs:Cr detector compared with the Si detector observed in Section 6.4.

Considering the count rate curves of the pixels marked in purple, and yellow in Figure 6.23(i) - (j), it can be seen that the way in which a pixel's count rate depends on I_{Krum} varies from pixel to pixel. For the pixel marked in purple, the count rate does not appear to strongly depend on I_{Krum} whereas for the pixel marked in green, increasing I_{Krum} causes a slight improvement in count rate at high incident flux. Finally, for the pixel marked in yellow, which for a given incident electron flux typically has a much lower count rate than any of the other POI (excepting the pixels marked in dark blue and red when they begin to undercount and become unresponsive), the count rate decreases as I_{Krum} increases. Together, the results in Figures 6.23(g)-(k) indicate, perhaps somewhat unsurprisingly, that the linearity of a pixel's response strongly depends on the pixel's area, which in turn has implications on the detector's linearity overall.

The behaviour of the pixel marked in yellow suggests that the count rate for smaller pixels is limited by their area, rather than pile-up, as their area reduces the number of electrons to which they are exposed. As there is limited scope for pile-up in the electronics of a small pixel, increasing I_{Krum} does not cause an improvement in count rate, instead causing an increase in undercounting due to the effective increase in threshold. Larger pixels, such as that marked in red, undercount at lower incident flux and become unresponsive at lower levels of incident flux than smaller pixels. This is consistent with the POI scans presented in Figure 6.20, in which it is the smaller pixels that do not display a reduction in registered counts when the beam is incident upon their centre, while the largest pixels display the most pronounced reduction.

The maximum benefit in increasing I_{Krum} is therefore observed in the behaviour of larger pixels. The plateau observed in the count rate curves of the pixel marked in red in Figure 6.23(h) for values of $I_{Krum} \geq 100$ DAC suggests that, for this pixel, the increase in count rate at higher levels flux is balanced by the undercounting caused by the increase value of I_{Krum} . Consequently, its count rate is limited by the effective increase in counting threshold, and for these pixels there could be a benefit in re-calibrating the counting threshold of the detector for increased values of I_{Krum} . The fact that the pixel marked in red is measured as having a smaller area than the pixel marked in blue, which does not display such a high count rate as the red pixel nor the same plateau behaviour suggests that the area of the pixel

marked in red is underestimated, which is further evidence for the fact that the pixel areas determined from the 300 keV dataset are only estimates that are indicative of general trends across the pixel matrix.

In the case of intermediate sized pixels, such as those marked in purple and green, the have count rate is limited by the ASIC deadtime (at least for the range of incident flux considered here). Their area is not so large that they register enough signal so as to become unresponsive, though they do deviate from a linear response at high incident flux, but also not so small that there is no benefit obtained by increasing the value of I_{Krum} , though the maximum possible benefit is not obtained.

The region of the sensor that was contained within all images acquired as part of the measurement of the detector's deadtime for 120 keV electrons and the 300 keV confocal STEM scan is relatively small and does not necessarily display all behaviour of interest as the flux upon the detector is varied. It is therefore informative to consider a larger portion of the sensor that overlaps with both the 300 keV confocal STEM and all images acquired as part of the measurement of the detector's deadtime for 200 keV electrons, although the maximum flux incident on the detector for these measurements is less than that incident upon the detector for the 120 keV measurement. Figure 6.24(a)-(d) shows ROI A of the GaAs:Cr sensor exposed to increasing incident flux of 200 keV electrons with I_{Krum} set to 10 DAC, while Figures 6.24(e) - (f) show ROI A exposed to a high ($3.80 \pm 0.09 \times 10^5$ electrons/pixel/s) incident flux of 200 keV electrons when I_{Krum} is set to 50 DAC and 100 DAC. The trend observed is similar to that seen for the 120 keV results for ROI B in Figure 6.23. As the incident flux increases, pixels begin to undercount (though none of them becomes entirely responsive). Increasing I_{Krum} reduces the detector deadtime, improving the overall count rate of the detector with the improvement in count rate generally being greater for those pixels that display the greatest degree of undercounting at high flux.

However, the increase in count rate, for those pixels that undercount significantly at high incident flux, is not consistent. It appears that those pixels that undercount significantly at high flux can be separated into two categories: individual pixels, the count rate of which improves when I_{Krum} is increased; and clusters of pixels, the count rate of which does not appear to recover when using a high value of I_{Krum} . An example of the pixel of the latter type is that which is marked in light purple in Figures 6.24(a)-(f) (as well as Figures 6.19(g)-(j) and 6.21(c)). Considering its count rate as a function of incident flux, in Figure 6.24(i), it can be seen that, like the pixel marked in yellow, increasing I_{Krum} causes a reduction in count rates. This pixel is measured as having a below average area of $2795 \mu\text{m}^2$, and so this behaviour may simply be attributable to the small area of the pixel. However, the fact that it appears to be part of a cluster of pixels that show similar behaviour, of which there are a number and which do not exactly correspond to regions with consistently smaller pixels, suggests that some of this behaviour maybe attributable to localised variations

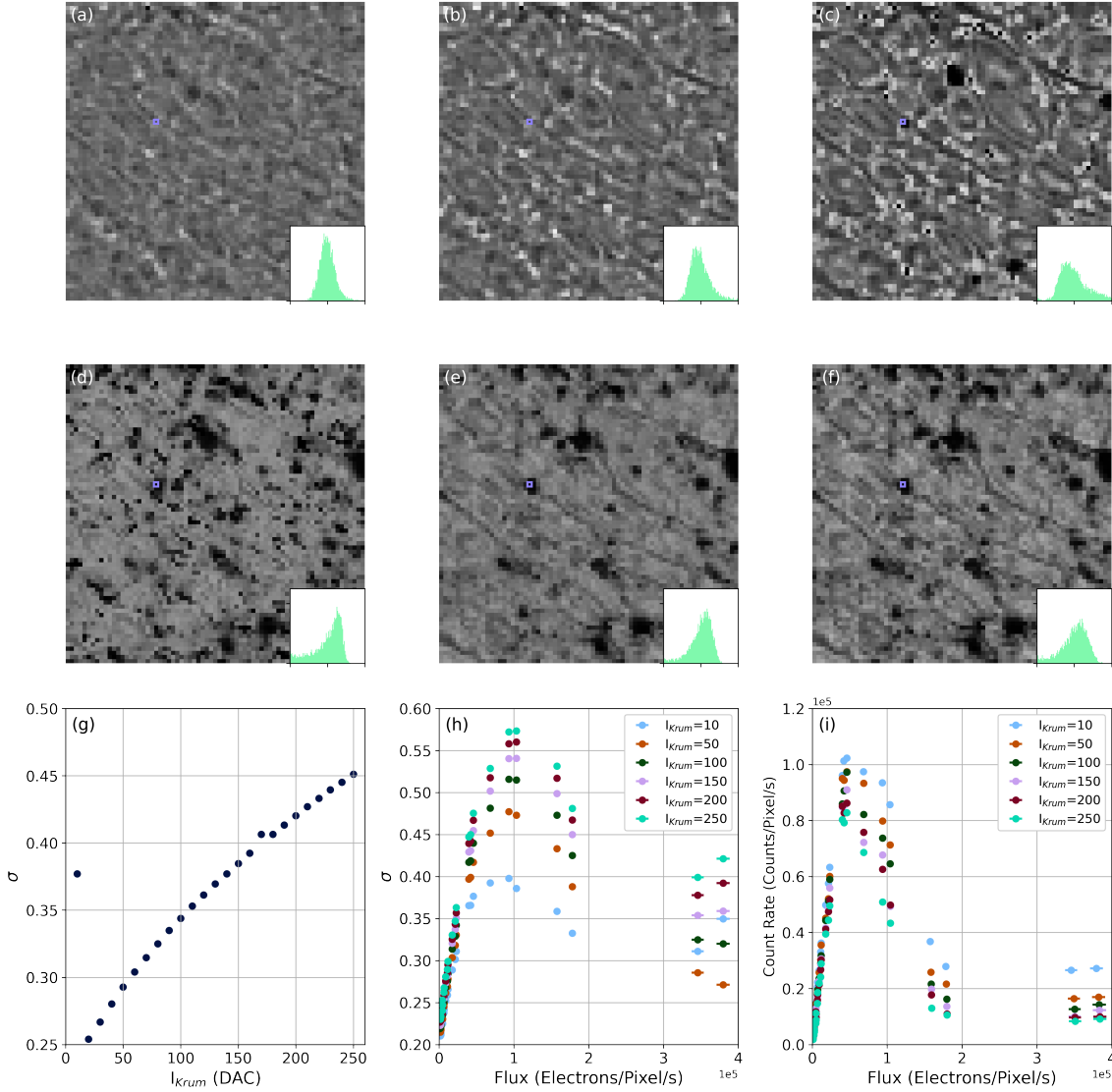


Figure 6.24: Close-ups of ROI A of the GaAs:Cr detector when I_{Krum} is set 10 DAC exposed to incident flux of 200 keV electrons of (a) $1 \pm 0.2 \times 10^3$ electrons/pixel/s, (b) $1.78 \pm 0.04 \times 10^4$ electrons/pixel/s, (c) $1.03 \pm 0.02 \times 10^5$ electrons/pixel/s, (d) $3.80 \pm 0.09 \times 10^5$ electrons/pixel/s; an incident flux of $3.80 \pm 0.09 \times 10^5$ electrons/pixel/s with I_{Krum} set to (e) 50 DAC and (f) 100 DAC. The images in (a)-(f) are all normalised to their mean value and have the same contrast limits set; the inset histograms of the normalised pixel intensities have x -limits of 0-2 normalised counts and y -limits of 0-200 pixels. (g) shows a plot of the standard deviation of the mean-normalised intensities recorded in ROI A as a function of the I_{Krum} setting used; in (h) plots of the standard deviation of the mean normalised intensities recorded in ROI A as a function of incident 200 keV electron flux for selected I_{Krum} settings are shown; while in (i) plots of the count rate of the pixel marked in purple in (a)-(f) as a function of incident 200 keV electron flux for selected values of I_{Krum} are plotted.

in the properties GaAs:Cr material. Those clusters of pixels that display a reduced count rate at high flux even when using a high value of I_{Krum} may be indicative of flux-induced polarisation within the material, which would be expected in GaAs:Cr for high incident flux of high energy quanta [245]. This may be highly localised as it depends on the density of the traps present in the material.

The larger area of ROI A, compared with ROI B, means that it is worth considering how the distribution of pixel intensities changes for different values of I_{Krum} as well as incident flux. Considering the histograms of the mean-normalised pixel intensities inset in Figures 6.24(a)-(f), it can be seen that as the flux increases, while I_{Krum} is kept constant, the range of intensities recorded increases, with a pronounced tail emerging at very high incident flux in Figure 6.24(d), indicative of the increased number of pixels counting less than the average within the ROI. While increasing I_{Krum} reduces this tailing in Figure 6.24(e), it does not decrease the width of the intensity distribution. Indeed, a further increase in the value of I_{Krum} causes an increase in the width of the intensity distribution in Figure 6.24(f). This is confirmed when considering Figures 6.24(g) and (h), which show the standard deviation of the normalised pixel intensities (σ) when a flux of $(3.80 \pm 0.09) \times 10^5$ electrons/pixel/s is incident upon the detector for different values of I_{Krum} and σ as a function of incident flux. While increasing I_{Krum} initially causes a decrease in σ at high incident flux in Figure 6.24(g), further increases in the value of I_{Krum} causes an increase in σ . At an I_{Krum} setting of 150 DAC, the value of σ is greater than it was when using an I_{Krum} setting of 10 DAC. Considering Figure 6.24(h), it can be seen that high value of σ observed when I_{Krum} was set to 10 DAC and the detector exposed to a high incident flux in Figure 6.24(g) is actually somewhat anomalous. The general trend is that the higher the value of I_{Krum} , the greater is the value of σ for a given incident flux. Overall, these results indicate that, although an increased value of I_{Krum} improves the detector count rate, the interplay between the reduced deadtime and increased effective counting threshold for individual pixels across the pixel matrix as I_{Krum} is increased, tends to decrease the overall uniformity of the detector's response across the pixel matrix.

Given the variability of individual pixels' response to different incident electron flux, the question naturally arises as to how the efficacy of a standard flat field correction depends on the flux of incident electrons. To investigate this, pairs of image datasets were acquired with the GaAs:Cr sensors exposed to 120 keV electrons at various different levels of incident flux. Each dataset consisted of a series of frames to be used as an image of the sensor and a series of images to be used to calculate a flat field correction image. At each flux, the total number of frames and acquisition time were varied so that the average number of counts in the "raw" sensor images and the flat field were the same, independent of flux. The mean counts per pixel in the final sensor images was between 4200 and 4300 counts, while the mean counts per pixel in the final flat field correction images was between 423540 and 423560

counts. Flat field corrections calculated from all the flat field correction images were then applied to the sensor images, including those that were acquired at different incident flux. This created a selection of images where there were varying degrees of mismatch between the flux incident upon the detector when the image data was acquired and when the flat field data was acquired.

Figure 6.25 shows a selection of these images. Specifically, it shows ROI A of the GaAs:Cr sensor obtained by applying the flat field corrections acquired when the incident flux was $9.2 \pm 0.2 \times 10^3$ electrons/pixel/s and $1.57 \pm 0.02 \times 10^5$ electrons/pixel/s to images acquired when the detector was exposed to a flux ranging from $9.2 \pm 0.2 \times 10^3$ electron/pixel/s to $1.57 \pm 0.002 \times 10^5$ electrons/pixel/s. The greater the divergence between the flux to which the detector was exposed when collecting the flat field data and the image data, the less effective the correction. This is confirmed by the fact that the greater the mismatch in the flat field and image fluxes, the greater the increase in the standard deviation of the mean-normalised pixel intensities, seen in Figures 6.25(j) and (k). When the mismatch in flat field and image flux is the same, the range of normalised intensities in the resulting image was the same even if the mismatch was inverted, so that e.g. the histograms of Figures 6.25(d) and (e) were the same. In the images for which the flat field flux is greater than the image flux, the contrast is inverted relative to the contrast in the images for which the flat field flux is less than the image flux. This is apparent comparing the line profiles taken across Figures 6.25(d) and (e), plotted in 6.25(f), which are mirrors of each other. These trends can be explained by the fact that the pixels that record lower or higher than average counts in the low-flux data are reversed in the high-flux images.

A final point that must be considered in relation to the defects present in the GaAs:Cr sensor is the extent to which their variation in pixel shape and size may introduce distortion into features recorded by the GaAs:Cr sensor. This point has been raised by Ponchut et al. [240] as a particular issue for compound high- Z sensor materials as these distortions, which are common in such materials cannot be corrected for using standard techniques such as a flat field correction. The knife-edge used to measure the MTF of the GaAs:Cr detector for 300 keV electrons was the shutter of the chassis (specifically designed for this purpose) used to mount the detector on the Titan 80 - 300 at KIT. This could be moved while the detector was installed on the microscope, making it very easy to record images with the knife-edge in multiple locations relative to the sensor. These are shown in Figure 6.26, along with close-ups in the vicinity of the knife-edge with and without flat field corrections applied.

Distortions are readily apparent in the profile of the knife-edge, in particular in Figures 6.26(f) and (g), though to a lesser extent Figures 6.26(d) and (e). In Figures 6.26(h), the distortions are difficult to discern, and it is only the uncorrected close-up in Figures 6.26(i) that some variation in the profile of the edge is apparent. That these deviations from a straight line differ for each of the three locations

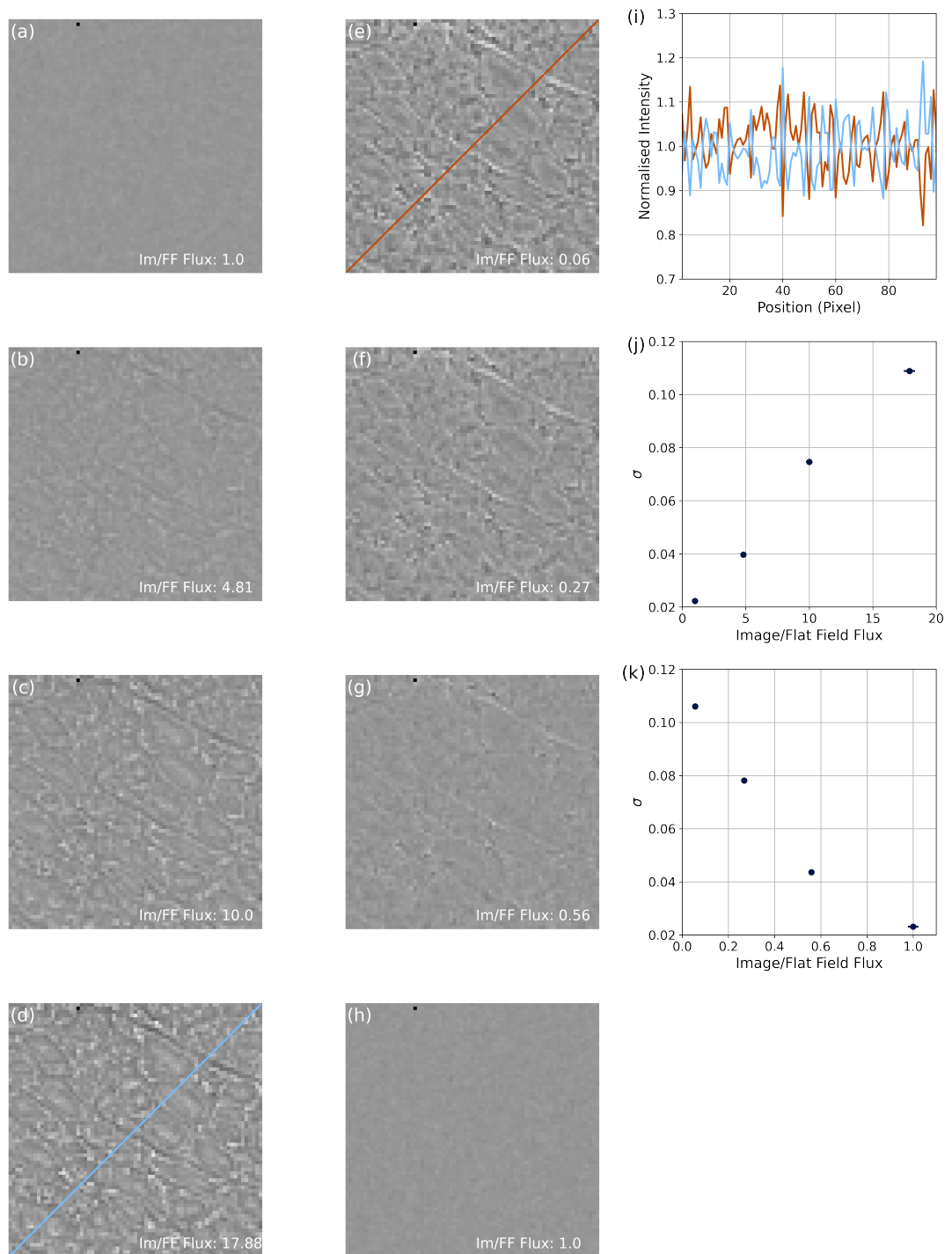


Figure 6.25: Images same ROI A exposed to 120 keV electrons at a flux of (a) and (e) $9.2 \pm 0.2 \times 10^3$ electrons/pixel/s; (b) and (f) $4.41 \pm 0.07 \times 10^4$ electrons/pixel/s; (c) and (g) $8.5 \pm 0.1 \times 10^4$ electrons/pixel/s; and (d) and (h) $1.57 \pm 0.02 \times 10^5$ electrons/pixel/s. Images (a) - (d) have had a flat field correction applied for which the flat field has been acquired under an incident flux of $9.2 \pm 0.2 \times 10^3$ electrons/pixel/s, while images in (e) - (h) have had a flat field correction applied for which the flat field data was acquired with an incident electron flux of $1.57 \pm 0.02 \times 10^5$ electrons/pixel/s. All images have been normalised to their average pixel value. In (d) and (e), lines along which the intensity profile was measured are marked, and these are plotted in (i). The standard deviations of the images in (a) - (d) are plotted as a function of image to flat field flux in (j), while those of images (e) - (h) are plotted in (k).

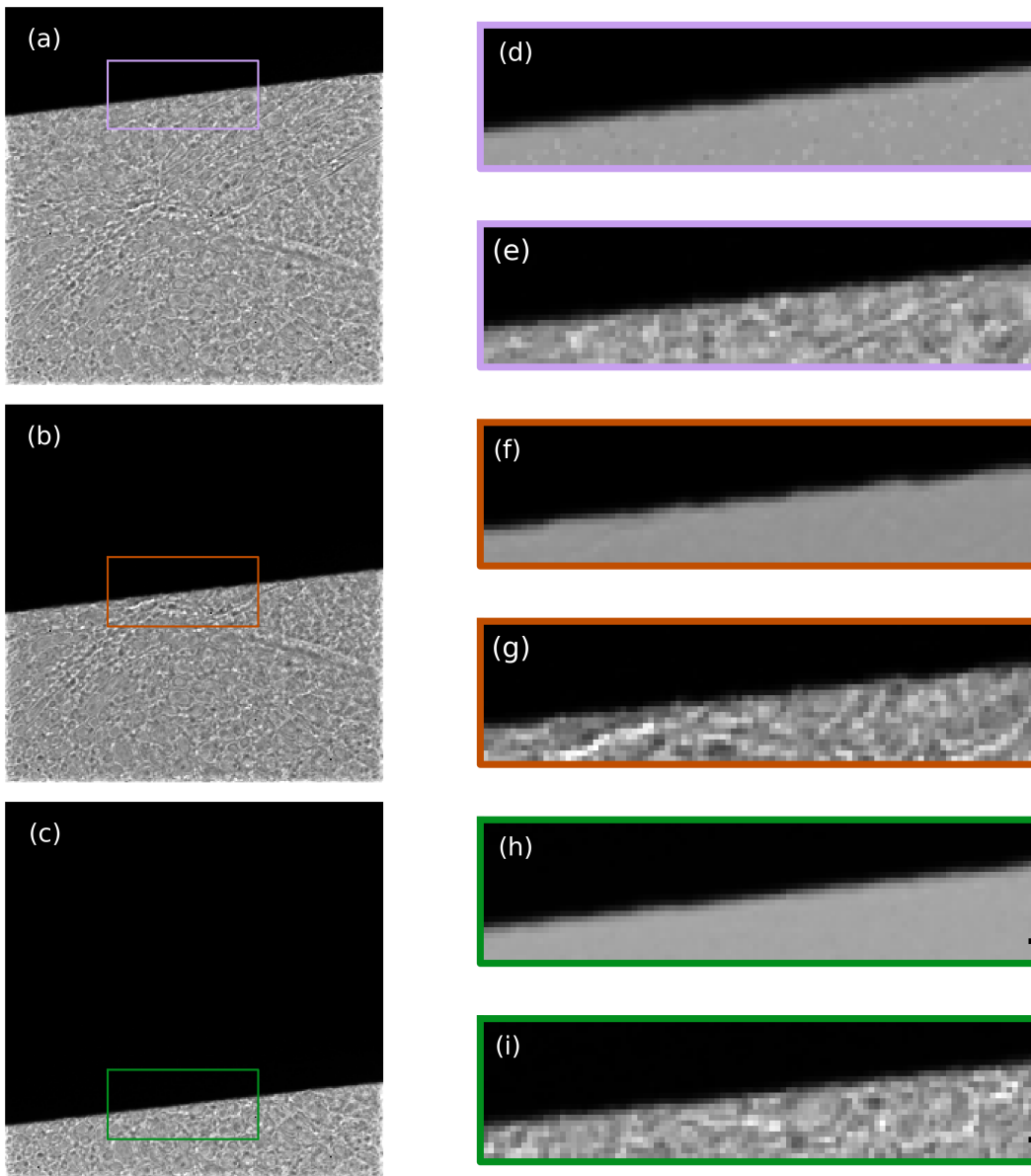


Figure 6.26: (a)-(c) Images of the knife-edge placed at three different positions relative to the GaAs:Cr detector and acquired with 300 keV electrons; (d), (f) and (h) show close-ups of the ROIs marked in (a)-(c) with a flat field correction applied; (e), (g) and (i) show the same ROI in (d), (f) and (g) without the flat field correction applied.

demonstrate that they are not due to imperfections in the edge itself (which was manufactured to a high level of precision and which showed no imperfections when expected visually). For the ROI marked in Figure 6.26(c), the flat field correction appears to mitigate the worst of the distortions, as correcting for the variations in the counts recorded by each pixel results in a clearer definition of the profile of the knife-edge. In Figure 6.26(d) and (f), it can be seen that the flat field correction does not compensate for the distortions in the shape of the knife-edge that the variable shape and size of individual pixels have introduced. This indicates that the distortions present in Figure 6.26(i) have only been obscured by the flat field correction and are still present in Figure 6.26(h).

Looking at these images, it is easy to envision how defects present in the sensor could distort the features of the objects recorded in an image, particularly at high spatial frequencies. In spite of this, the MTF appears to be largely independent of the position at which it is measured, as seen in Figure 6.27. This can be accounted for by the fact that oversampling the ESF averages over the effects of any distortions introduced by any defects. The impact of the distortions introduced by the defects may also not be reflected in the MTF because the method does not distinguish between features that are present in the image that impinges upon the sensor and features that are present in the recorded image because they have been introduced by the sensor. When recording a flat field image, an image of the sensor is in effect recorded, and when imaging a sample, the data acquired is simply that pertaining to the sample with the image of the sensor superimposed upon it. Consequently, it is not so much that there is reduction in the contrast transferred at a given spatial frequency, but an alteration of the information contained within the image.

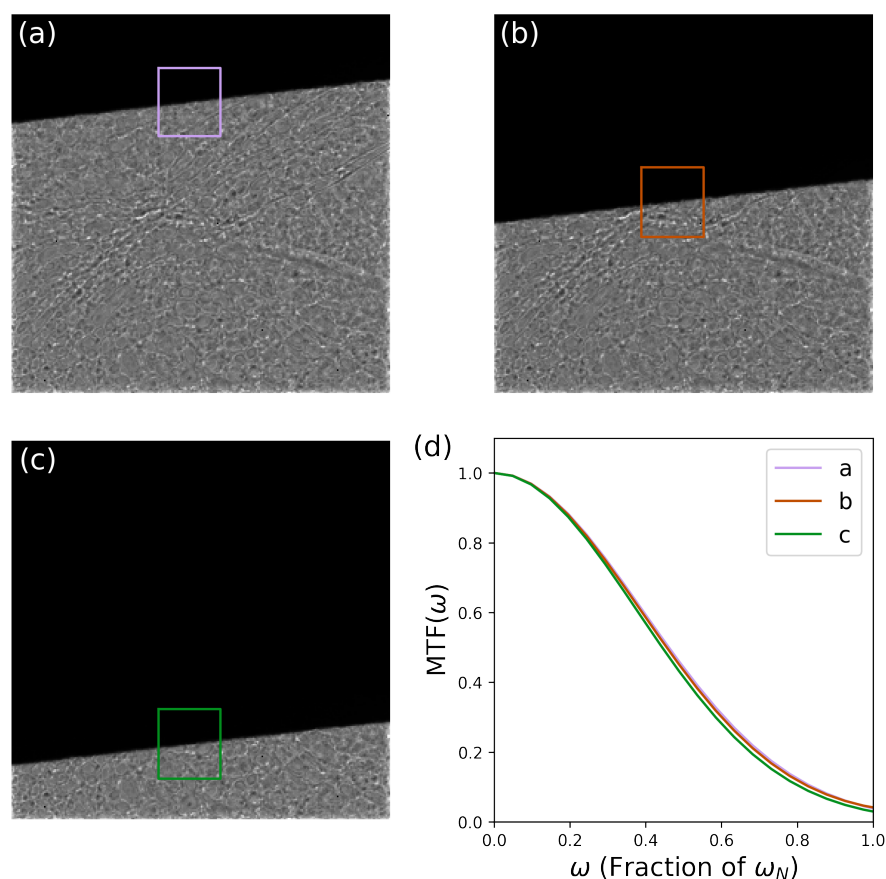


Figure 6.27: (a)-(c) show the different positions at which the knife-edge was positioned relative to the GaAs:Cr sensor when it was mounted on the Titan 80-300 (S)TEM and exposed to 300 keV electrons with the regions that were used to determine the MTF marked, while (d) shows the corresponding MTFs.

6.6 Summary

In this chapter, the response of a Medipix3 detector with a $500\ \mu\text{m}$ thick GaAs:Cr sensor and $55\ \mu\text{m}$ pixel pitch to electrons with energies ranging from 60 keV to 300 keV has been investigated. Where appropriate, its response has been compared with that of a Medipix3 detector with a $500\ \mu\text{m}$ thick Si sensor and $55\ \mu\text{m}$ pixel pitch. Measurements have included detector MTF, DQE and device deadtime.

It was found, when the detectors operated in SPM, that the MTF of the GaAs:Cr detector compared favourably with that of the Si detector across all primary electron energies, with the improvement in MTF relative to that of the Si sensor for a given counting threshold increasing with primary electron energy, to the extent that the performance of the GaAs:Cr device for 200 keV electrons surpassed that of the Si detector for 120 keV electrons. At low (< 120 keV) primary electron energies, the DQE of the GaAs:Cr detector was poorer than that of the Si sensor, though for higher electron energies its DQE clearly surpasses that of the Si detector. When using a low counting threshold, the DQE of the GaAs:Cr detector for 120 keV and 200 keV electrons also surpasses that of an idealised square pixel detector, and comes close to matching the maximum DQE possible when accounting for the effects of aliasing. At the higher end of the primary electron energy range considered in this work, the performance of the GaAs:Cr detector deteriorates, though its MTF and DQE for 300 keV electrons still surpasses that of the Si sensor when using 200 keV electrons.

Broadly similar trends were observed when the detectors operated in CSM. Operating in CSM lead to an improvement in MTF and $\text{DQE}(0)$ for the detectors relative to operating in SPM and using a low counting threshold. However, the value of $\text{DQE}(\omega_N)$ when operating in SPM and using a low threshold was better than that which could be obtained using CSM.

The linearity of the GaAs:Cr detector for 120 keV and 200 keV when operating in SPM was also found to compare favourably with that of a Si sensor. Furthermore, it was observed that the extent to which the deadtime of the GaAs:Cr detector was shorter than that of the Si detector was greater when using 200 keV electrons than it was when using 120 keV electrons. The MTF (and hence PSF) of the GaAs:Cr detector surpasses that of the Si detector to a greater extent when using 200 keV electrons than it does when working with 120 keV, so the average number of pixels triggered in the GaAs:Cr detector relative to the number triggered in the Si detector is smaller when using 200 keV electrons than it is for 120 keV electrons. Consequently, there is a corresponding relative decrease in the average deadtime of the GaAs:Cr detector relative to that of the Si detector when using 200 keV electrons compared with when working with 120 keV electrons.

The improved PSF of the GaAs:Cr sensor also means that the average energy deposited on an individual pixel is higher, so that, when using a higher value of I_{Krum} ,

the incidence of undercounting, due to the increased counting threshold, is less in the GaAs:Cr sensor than it is in the Si. This means the trade-off in between the benefit to the count rate at high flux obtained by using a high threshold and the loss of counts at low flux is reduced. Increasing the value of I_{Krum} was also shown to improve the count rate of the GaAs:Cr detector to a greater extent that was the case with the Si detector. This likely relates to the increase in the maximum current that can be induced on a Medipix3-based device by increasing I_{Krum} , which is more significant when collecting electrons (as when using a GaAs:Cr sensor) rather than holes (as for a Si sensor).

In spite of all these positive points, the GaAs:Cr material still features several drawbacks that must be overcome if it is to become a viable alternative to Si for the sensors of HPDs used in TEM. The defects present in the GaAs:Cr material cause considerable variation in response across the pixel matrix. While the variations in the intensity recorded can be compensated for by using a standard flat field correction, for this to be effective, the flux incident upon the detector when acquiring the images to be correct must be similar to that when the flat field data was acquired. This is due to the area of individual pixels varying considerably, leading to a corresponding variation in the effective flux incident on individual pixels. Consequently, the linearity of the response of individual pixels for a given incident electron flux differs from pixel to pixel depending on area. Furthermore, the effect of increasing I_{Krum} affects each pixel differently depending on their area, generally causing a decrease in the uniformity of the pixel's response for a given incident flux. Polarisation may also affect detector response in regions of the sensor where there is a high density of traps when the detector is exposed to a high flux of high-energy (200 keV) electrons.

Matching the flux of flat field data and image data will likely present challenges when imaging samples with variable thickness and/or density or working in diffraction-based modalities, due to the wide range of intensities incident on the sensor. In principle, using different flat field corrections for different parts of the sensor depending on the flux incident upon that part of the sensor when conducting an experiment might be one way to proceed, but this requires (ideally) independent knowledge of the flux incident upon the detector, which may not be available.

A more fundamental issue with flat field corrections is that they only (when effective) correct for the variation in the number of counts recorded across the pixel matrix. They do not compensate for the distortions introduced by the irregular shape of individual pixels. Though they do not appear to have an adverse impact on the MTF, their presence likely alters the information contained in the images recorded by the detector, with this being a particular issue at high spatial frequencies. The MTF therefore does not appear to entirely capture the impact of defects on device performance.

7

Investigating a Spectroscopic Detector with GaAs:Cr Sensor

7.1 Introduction

Moving away from the characterisation of devices based on the Medipix3 ASIC, which represents the primary focus of this thesis, this chapter documents preliminary measurements of the response of a detector based on the HEXITEC ASIC to electrons. Detectors based on the HEXITEC ASIC are not in themselves suitable for use in TEM due to its large pixel pitch, though there may be scope to utilise it in STEM. However, due to its spectroscopic capabilities and large pixel pitch, as well as the fact that it has been bonded to Si, GaAs:Cr, CdTe and CZT, in some cases with a variety of different backside contact configurations, it represents an ideal platform for developing a better understanding of the behaviour different sensor materials. These measurements were curtailed due to disruption caused by the COVID-19 pandemic.

Nevertheless, this chapter records preliminary measurements, the results of which provide insight into the importance of the backside contact in determining device efficiency. Chapter 7 begins with a description of the HEXITEC ASIC in Section 7.2. This is followed by an overview of the experimental apparatus and methods used in Section 7.3. This includes a description of the specific device used in the present work; the hardware used to install it on the Tecnai T20 TEM at the University of Glasgow; and the method used to calibrate it. Section 7.4 describes the aforementioned experiments with electrons and also includes a presentation and discussion of the results of these experiments. The results of the experimental measurements prompted simulations similar to those described in Chapter 4, but incorporate backside contacts of various different compositions. Results of these simulations are presented in Section 7.5.

7.2 Overview of the HEXITEC ASIC

HEXITEC [204, 307] is a spectroscopic ASIC developed for the purposes of spectroscopic imaging with intended applications including synchrotron-based diffraction experiments and tomography. Each ASIC consists of 80×80 $250 \mu\text{m}$ pixels, each of which contains a CSA, CR-RC-shaper and a second-order low-pass filter. Figure 7.1 shows a schematic of the circuitry of a single HEXITEC pixel. The gain on the amplifier can be selected such that dynamic range of a pixel is 4-200 keV or 12-600 keV. Rather than comparing the height of the voltage pulse being compared with a threshold on pixel, a peak hold circuit maintains the peak voltage of the pulse until readout. The shaper and peak hold voltages are sampled sequentially using three track-and-hold buffers prior to readout to prevent incorrect peak hold data (arising due to partly developed voltage pulses or incorrect reset of the peak hold circuitry). During readout, one buffer samples the output of the peak hold circuit while the other two sample the shaper output, one before and one after the peak hold output is sampled. This makes it possible to reject those events where the peak hold circuit output is sampled before the voltage pulse has fully developed or false events due to peak hold output not being reset to the correct voltage.

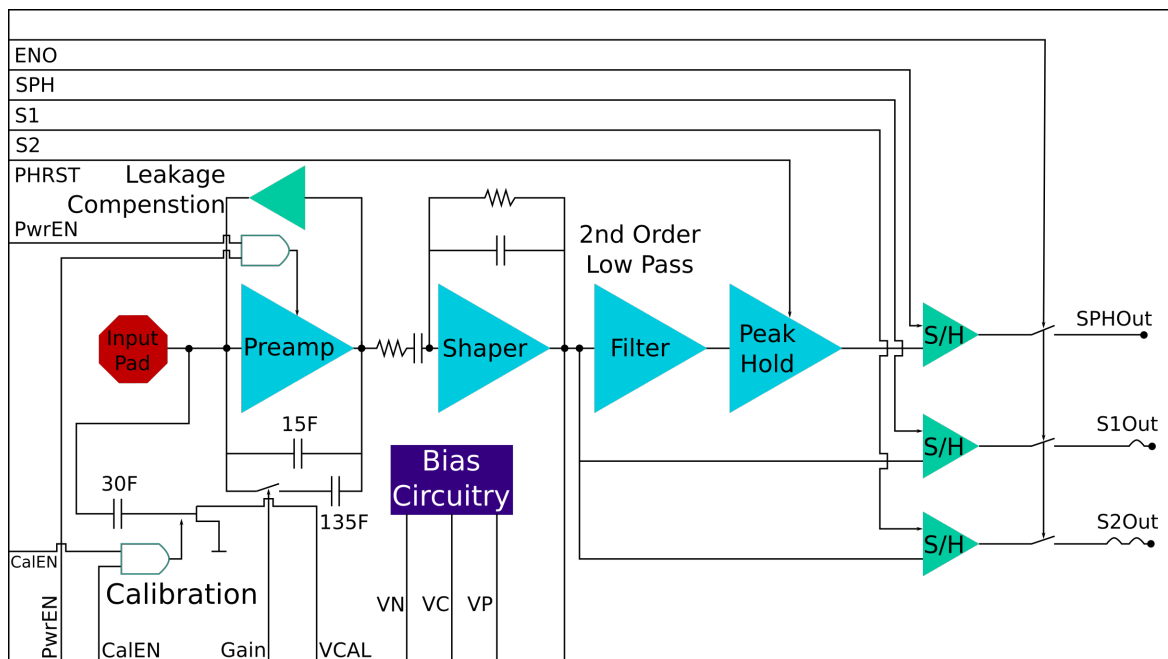


Figure 7.1: Schematic of the signal processing circuitry present on a single HEXITEC pixel. Charge induced on the pixel Input Pad is amplified and converted into a voltage step by the preamplifier (marked as “Preamp”), which is shaped and filtered by a CR-RC shaper (labelled “Shaper” and “Filter”). The risetime of the resulting voltage pulse is $\sim 2 \mu\text{s}$, while the return to baseline is $8 \mu\text{s}$ [308]. Redrawn from [307].

Readout is by a rolling shutter system that reads the pixel array row by row in four parallel block of 20 pixels per column. The signal readout of the chip for each pixel is analogue, taking the form of the peak voltage registered by the peak-hold, and is digitised off-chip by a 14-bit ADC. The maximum frame rate of the system is 8.9 kHz, though this can be limited by the data bandwidth of the DAQ used with a given device [309].

7.3 Methods and Experimental Apparatus

7.3.1 Detector and Associated Hardware

The device used to acquire data presented in this chapter was bonded to a $500\mu\text{m}$ thick GaAs:Cr sensor, manufactured from the 2016 generation of GaAs:Cr. This tends to feature bubble-like defects, though line defects are not so common. Given the large pixel pitch of the HEXITEC device, these defects, though present, are difficult to discern in flat field exposures of the detector. It had Ohmic contacts, the backside one of which consisted of $0.1\mu\text{m}$ thick Ni followed by $0.5\mu\text{m}$ Au, such that the layer of Au that was the outermost layer. The sensor was bonded to the HEXITEC ASIC using an Au stud process [310].

Whereas the Merlin DAQ used with the Medipix3 devices studied as part of the current work is largely separate from the detector assembly, the DAQ of the HEXITEC system is integrated into the same unit as the detector. Photographs of the assembly used to install the HEXITEC detector on the Tecnai T20 TEM at the University of Glasgow are shown in Figure 7.2. The PCB includes four 14-bit ADC units to digitise the signal read-out from each of the pixels. Also located on the PCB are a field-programmable gate (FPGA) which packages the raw data for transmission to the control PC via an ethernet connection (labelled in Figure 7.2(b)) and a HV power supply that supplies the bias to the sensor.

To regulate the temperature of the components on the PCB, thermally conductive tape (an example of which is marked in Figure 7.2(a)) is used to connect the components to the Cu cold-finger that is used to remove heat from both the detector and the PCB. The cold-finger, which is visible in Figure 7.2(b), extends to a Cu pad external to the detector chassis, which is in thermal contact with a pad that is cooled by a chiller. The DB15 connector marked in Figure 7.2(b) could be connected to two temperature probes that could be used to monitor the temperature the PCB and the detector.

The chip, seen in Figures 7.2(a) and (c), unlike the Medipix3 devices, is not glued to the PCB, but is instead mounted on an Al module that is fixed to the PCB. Consequently, devices with different sensors swapped in and out of a single assembly. This also meant that when acquiring calibration data (as described below in Section

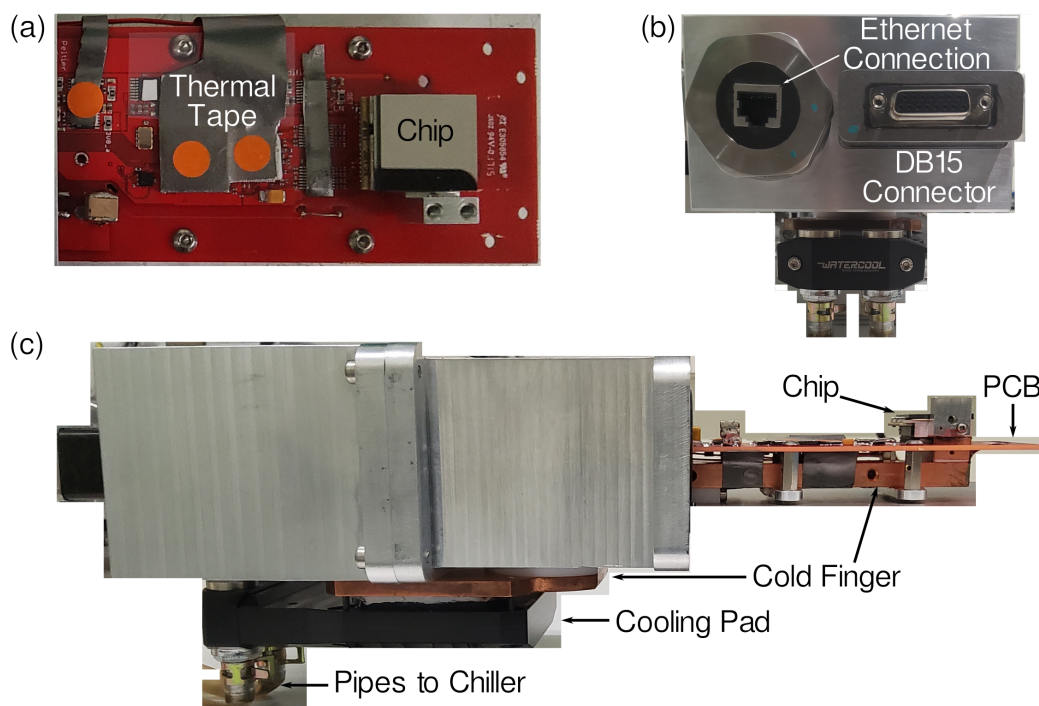


Figure 7.2: Photographs of the assembly used to install a HEXITEC detector on the Tecnai T20 TEM: (a) overhead shot of the PCB on which the chip is installed and which is within the vacuum of the microscope’s detector chamber; (b) photograph of the exterior face of the assembly facing away from the microscope, with the ethernet and DB15 connectors for interfacing with the DAQ computer and external temperature monitoring units respectively; and (c) side-view of the full assembly. The photographs have been cropped close to the objects of interest to remove extraneous background details.

7.3.2, the detector could be integrated with a different unit more suited for acquiring this data, rather than that pictured in Figure 7.2, which was specifically designed for installing devices on the Tecnai T20 TEM.

The initial measurements acquired with the HEXITEC detector consisted of illuminating the detector with 60 keV and 80 keV electrons. For these measurements, a bias of -200V was applied with the device cooled to a temperature of 31.1°. This is slightly higher than the standard operational temperature of $\leq 30^\circ\text{C}$, but it was not possible to cool the detector further, possibly due to the thermal contact between the chip and the cold-finger that was in contact with the chiller being substandard. Consequently, it was not possible to apply the usual full bias of -300V for a sensor of this thickness [238], without the leakage current becoming too high and obscuring the signal due to incident quanta. Under the operating conditions used, the leakage current was 5.24 μA .

Individual acquisitions consisted of $\sim 4.77 \times 10^5$ frames acquired at a frame rate of ~ 1.6 kHz. The current incident on the detector was controlled with appropriate choice of spot size, condenser aperture and heating current of the thermionic source so that the total number of pixels registering any signal was approximately 10% of the total number of pixels in the matrix in a given frame. Given the frame rate

used, this meant that the maximum current that could be incident on the detector without compromising the quality of the spectra acquired (due to pile-up) was $< 1\text{pA}$, which was too low to measure using the available apparatus while the detector was installed on the microscope. Consequently, measurements of the detector's overall efficiency in response to electrons were not feasible.

7.3.2 Calibration with γ -rays

As the HEXITEC detector measures the energy deposited in each pixel by incident quanta, it is possible to calibrate the relationship between pulse height (as quantified by ADU channel) and energy for each individual pixel. This has the advantage of compensating for variations in gain across the pixel matrix, resulting in an overall more accurate calibration. These variations arise due to imperfections in the ASIC manufacturing process as well as variations in the properties of the sensor material. Calibration data (described below) was acquired with the HEXITEC detector prior to installing it on the Tecnai T20 TEM under the similar operational conditions as when collecting data with electrons. The operational conditions differed only in that, as the calibration data was not acquired when the device was under vacuum, so that maintaining a temperature of 30° was possible.

A pixel-by-pixel calibration of GaAs:Cr HEXITEC device was determined using a variation of the scaled search algorithm developed for calibrating detectors based on the HEXITEC ASIC [311]. This entails acquiring spectra from a source that produces quanta with a range of well-defined energies, which give rise to clear peaks in the data acquired by the device being calibrated. In the case of the present work, an ^{241}Am source was used, which produced spectra with well-defined peaks due to the 13.9 keV, 17.8 keV, 20.8 keV, 26.4 keV and 59.5 keV γ -rays produced as part of the decay of ^{241}Am to ^{239}Np . The source was positioned 7 cm away from the detector to make flat field illumination possible, with $\sim 4.77 \times 10^5$ frames acquired at a frame rate of ~ 1.6 kHz.

Using this data, a reference spectrum is generated by combining the spectra recorded by each individual pixel. To form this reference spectrum, a threshold of 100 ADU was applied to individual frames acquired by the HEXITEC detector while exposed to the ^{241}Am source to discount signal due to the dark current. Clusters of pixels due to individual quanta were then identified in each frame as pixels that neighboured one another either along the edge of a pixel or along the diagonal of a pixel (i.e. pixels are neighbours in a two-connectivity sense). The reference spectrum was then constructed by plotting the histogram of the total energy associated with single-pixel clusters in terms of ADU channel, as can be seen in Figure 7.3(a). The position of the photopeak due to 59.5 keV γ -rays, in terms of ADU, was then determined by fitting a Gaussian to the highest energy peak. Furthermore, search ranges in which it was expected to find the other photopeaks in the spectrum recorded by by

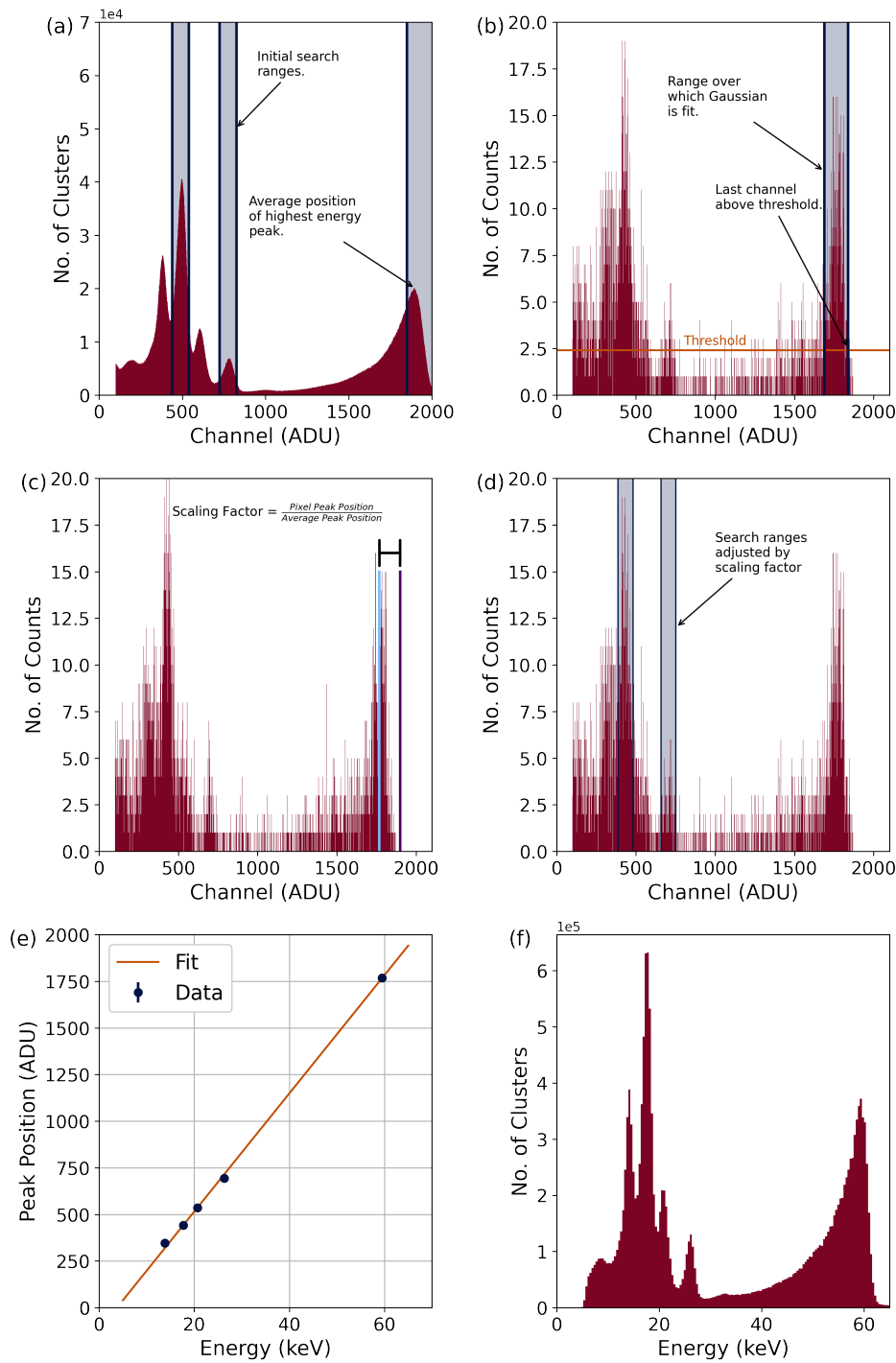


Figure 7.3: Illustration of the procedure used to perform a pixel-by-pixel calibration of the HEXITEC detector. (a) shows the reference spectrum formed by summing all pixel clusters due to individual events, with search ranges for selected photopeaks marked. In (b), the spectrum recorded by a single pixel is shown, along with the threshold used to determine the upper limit of the 59.5 keV photopeak, and hence the search range for this peak in the individual pixel spectrum. (c) shows the difference in the position of the 59.5 keV between the exemplar individual pixel spectrum (marked in blue) and the summed reference spectrum (marked in purple). In (d), the new, scaled search ranges for selected photopeaks in the individual pixel spectrum are shown. (e) shows the calibration curve based on the position of the photopeaks found in the individual pixel spectrum shown in (b)-(d), along with the line fitted to this data. In (f), the calibrated spectrum formed using all events registered by the detector is shown. Adapted from reference [311].

each individual pixel were defined. Examples of these for the photopeaks due to the 17.8 keV and 26.4 keV γ -rays are marked in Figure 7.3(a).

For each pixel, a spectrum was then formed using all single cluster events that had been recorded by that pixel. An example of this is shown in Figure 7.3(b). A threshold for the pixel was determined by calculating the average number of events per channel recorded by the pixel. The final channel that registered a greater number of events than this threshold is taken to be the upper limit of the range containing the 59.5 keV photopeak. Subtracting the size of the range defined for the 59.5 keV photopeak from this channel, provided a new range in which to find the position 59.5 keV photopeak in the individual pixel spectrum. This is also marked in Figure 7.3(b) The position of the 59.5 keV photopeak was then identified by fitting a Gaussian to the data within this range.

A scaling factor for the individual pixel spectrum was then determined by dividing the position of the 59.5 keV photopeak in the single-pixel spectrum by its position in the reference spectrum. Figure 7.3(c) shows an example of the difference that can arise between the peak position in an individual pixel spectrum and the reference spectrum. This scaling factor was then applied to the limits of the search ranges defined for the other photopeaks in the reference spectrum, to generate search ranges specific to the individual pixel. Examples of these are shown in Figure 7.3(d). Due to the small number of counts in the spectrum, fitting these peaks is challenging. Consequently, the peak position was taken to be the channel that recorded the highest number of counts within a given search range. In the event that the maximum number of counts was recorded by more than one channel in a search range, the peak position was taken to be the average of those channels that recorded the maximum number of counts. Errors for the peak positions were determined by grouping pixels on the basis of their scaling factor, and calculating the standard deviation of the position of each peak for a given scaling factor.

For each pixel, the positions of the photopeaks was plotted as a function of photon energy, and a calibration obtained by fitting the curve with a straight line using a least-squares algorithm, weighted by the error on the peak positions. The calibration curve obtained by plotting the photon energy against peak position in terms of ADU, as in Figure 7.3(b). The calibration coefficients acquired for each individual pixel can then be applied to all the events registered by each individual pixel. Clusters, which are now indicative of the energy that has been deposited by a single event, can then be identified in individual frames again, and a sum spectrum in terms of energy generated, such as that shown in Figure 7.3(f).

7.4 Results of Experiments with Electrons

Figure 7.4 show spectra and images recorded by a the HEXITEC sensor exposed to 60 keV and 80 keV electrons as well as the ^{241}Am used for calibrating the detector. For all three datasets shown in Figure 7.4, a threshold of 100 ADU was applied to the data, and the pixel-by-pixel calibration acquired using the method outlined in Section 7.3.2 was applied. Clusters of pixels due to individual interactions were then identified in each frame using the same two-connected method used in the calibration procedure. The summed energy of the clusters used to form the spectra. To form the images seen in Figures 7.4(a)-(c), which have been normalised to their mean value, the summed energy of each cluster was allocated to the pixel identified as containing the cluster's weighted centre of mass.

In Figure 7.4(b) and (c) there are regions in the top left quadrant of the beam spot where fewer counts are recorded than in the rest of the illuminated region of the sensor. This variation is not seen in the flat field image recorded by the same device when exposed to an ^{241}Am source (Figure 7.4(a)). Looking at the spectra, there is a pronounced tail to the peak that corresponds to the 59.5 keV γ -ray produced by the ^{241}Am source in Figure 7.4(d). This is contrary to the expectation that the resolution of the detector improves with increasing energy, as the peaks that correspond to the 13.9 keV, 17.8 keV, 20.8 keV and 26.4 keV γ -rays in the same spectrum are much narrower than the 59.5 keV peak and do not exhibit the same tailing. A similar tailing effect is seen in the peaks corresponding to the primary electron energy in the 60 keV and 80 keV spectra in Figures 7.4 (e) and (f), though it is more apparent in the 60 keV case. This tailing can, at least in part, be attributed to incomplete charge collection due to the low bias applied to the sensor.

Figure 7.5(d) shows the measured intensity along profile lines marked in Figures 7.5(a)-(c), which show the same images in Figure 7.4(a)-(c). Comparison of these profiles confirms that there is significant variation in the intensity recorded across the pixel matrix in the case of the electron measurement, whereas the variation in the case of the photon measurement is minimal. In the latter case, the variation can be likely explained by the source not being perfectly centred relative to the detector when the calibration data was acquired. This has resulted in a small decrease in the number of counts recorded in the bottom left-hand corner of the sensor relative the rest of the sensor.

The intensity profile across the sensor for the electron measurements cannot be attributed to a variation in the response of the sensor itself, as if this were the case the intensity profile would be the same for both electrons and photons. Nor can it be regarded as being due to a variation in the illumination. One likely explanation is a variation in the thickness of the backside contact over the surface of the sensor. The extent to which photons lose energy in the backside contact is limited due to the large

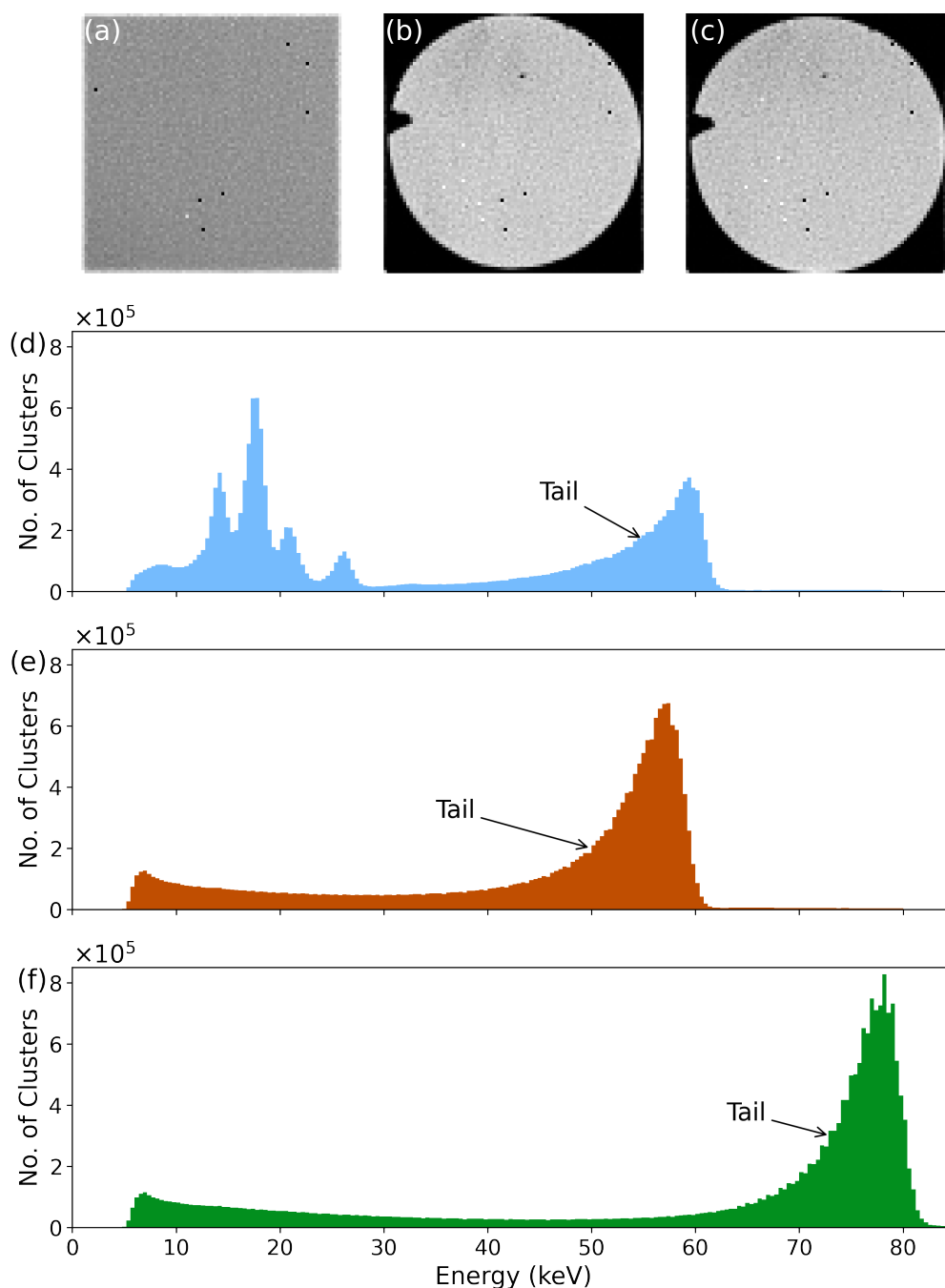


Figure 7.4: Images recorded by the HEXITEC device exposed to (a) ^{241}Am , (b) 60 keV electrons and (c) 80 keV electrons. These images have been formed by identifying the weighted CoM of each pixel cluster and assigning to each pixel the number of clusters identified as having their WCoM in that pixel. The resulting images were then normalised to their mean pixel value, and all three images in (a)-(c) have the same contrast limits. (e) - (f) show the spectra corresponding to the images in (a) - (c)

mean free path of photons with energies such as those of the γ -rays produced by the ^{241}Am source. Consequently, to observe any variation in the recorded number of γ -rays across the sensor, the variation in the mass-thickness of the backside contact must be substantial. However, this is not the case for electrons. The strongly interacting nature of electrons means that there can be significant difference in recorded intensity

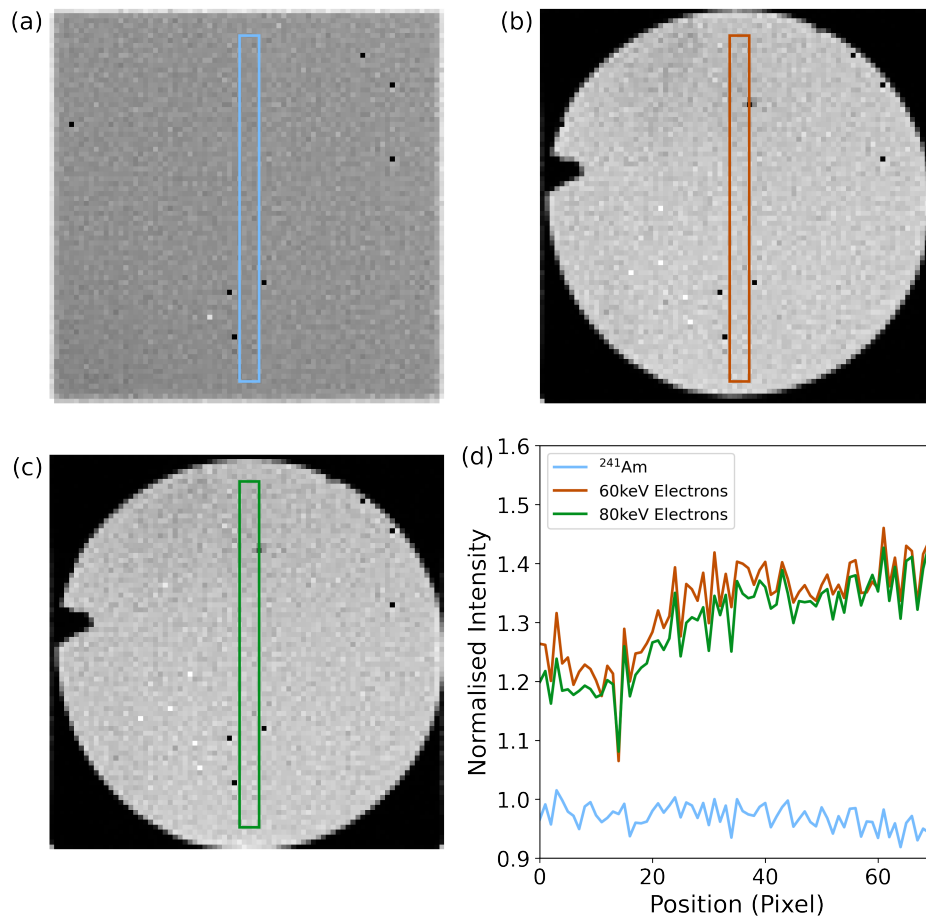


Figure 7.5: Mean-normalised sum images recorded by the HEXITEC detector exposed to (a) ^{241}Am source (b) 60 keV electrons and (c) 80 keV electrons with regions along which line profiles were measured shown in (d) marked. The width of these regions is the width over which the line profiles were averaged.

and energy straggling even with only modest variation in contact thickness.

Spectra acquired from specific ROI of the sensor when exposed to the ^{241}Am source and 60 keV and 80 keV electrons are presented in Figure 7.6. The locations of ROI 1 (in red) and ROI 2 (in purple) are marked in Figure 7.6(a)-(c), which show the same images as Figures 7.4(a)-(c) and Figures 7.5(a)-(c). There is no difference between the photon spectra, seen in Figures 7.6(d) and (g), recorded in these ROI. However, there is a pronounced difference in the electron spectra recorded in these two areas. Summing over the total number of counts in the spectra recording in the two ROI using electrons, the number of counts recorded in ROI 1 is 89% that recorded in ROI 2 for both electron energies. Taking the peak in the 60 keV spectra to be the whole portion of the spectrum to lie between 45 keV and 65 keV, the intensity of the 60 keV peak in ROI 1 is 80% that of the peak in ROI 2. For 80 keV electrons, defining the peak as beginning at 65 keV and ending at 85 keV, the intensity of the peak in ROI 1 is 85% that in the spectra associated with ROI 2. Considering the lower energy tails that lie below the lower energy limit of the primary peak, the number of counts recorded in

this region in the sensor in ROI 1 is 9.7% more than that recorded in ROI 2 for 60 keV electrons. For 80 keV electrons, the number of counts recorded in the low-energy tail in the spectra associated with ROI 1 and ROI 2 are within 1% of one another.

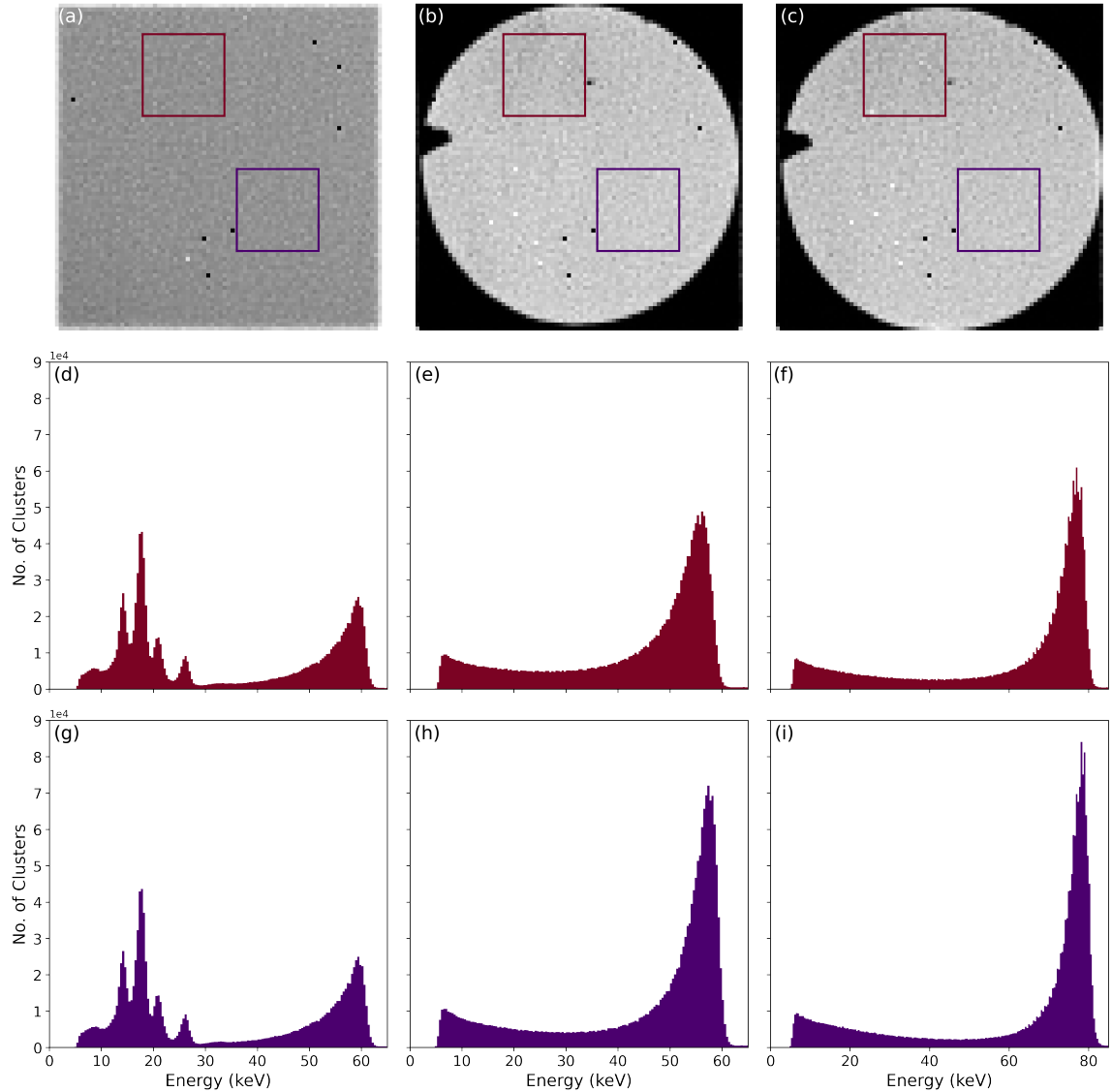


Figure 7.6: Images acquired by the HEXITEC detector when exposed to (a) ^{241}Am source (b) 60 keV and (c) 80 keV electrons showing the locations of ROI 1 (red) and ROI 2 (purple). ^{241}Am spectra recorded in (d) ROI 1 and (g) ROI 2; 60 keV electron spectra recorded in (e) ROI 1 and (h) ROI 2; 80 keV electron spectra recorded in (f) ROI 1 and (i) ROI 2.

This is indicative of a shift in the relative distribution of energies recorded in the two ROI when increasing in primary electron energy from 60 keV to 80 keV. The fraction of the number of counts recorded in ROI 1 to number of counts recorded in ROI 2 is consistent across the two primary electron energies, indicating that the fraction of electrons that are backscattered from the contact without interacting with the sensor are, for a given contact thickness, similar for the two energies. This is consistent with the simulation results presented in Figure 5.3(a), which indicated that while the backscattering coefficient strongly depended on the average value of Z , there

was, at most, a weak dependence on primary electron energy. For 60 keV electrons a reduction in the number of counts in the primary electron peak is accompanied by an increase in the number of counts in the low-energy tail.

However, for 80 keV electrons, the reduction in the number of counts in the primary peak for the spectra associated with ROI 1 compared with that measured in ROI 2 is not accompanied by a change in the number of counts in the low energy tail. This likely reflects the fact that, in an absorber of a given thickness, lower energy electrons will deposit a greater fraction of their energy in the absorber than electrons of a higher energy. While the primary electron peak is therefore broader in the spectrum recorded in the area with the thicker contact, the degree of straggling observed in the 60 keV spectrum is not observed. The variation in energy deposition, due to differences in the backside contact thickness across the sensor, is another factor that gives rise to the tails observed in electron spectra recorded by the whole sensor noted in Figure 7.4(e) and (f) in addition to incomplete charge collection.

Due to the tailing of the primary electron peaks, these had to be fit with double Gaussians, rather than single, so that it is not possible to calculate the detector's energy resolution for these electron energies. Nevertheless, it is evident to the eye that the FWHM of the peaks in both the 60 keV and 80 keV spectra recorded by ROI 1 are greater than the FWHM of the peaks in the spectra recorded by ROI 2. This represents a deterioration in performance that is consistent with increased energy deposition in the backside contact of the detector. Table 7.1 lists the measured energies of the peaks (based on the fitting thereof) in the spectra recorded by the two different ROI shown in Figures 7.6(e)-(f) and (h)-(i) as well as the spectra recorded by the full sensor shown in Figure 7.4(e) and (f). For both the 60 keV and 80 keV measurements, the measured energy of the primary peak is reduced in ROI 1 compared with in ROI 2, though the difference is slight and within the errors calculated for the peak energy. The measured peak energy for ROI 1 better matches that measured for the whole sensor for both primary electron energies. It is therefore tempting to think the thicker contact in ROI 1 is more representative of the average contact thickness. However, this is difficult to justify given the observed intensity distribution observed in e.g. Figures 7.4(b) and (c), which suggests the average contact thickness to be closer to that in ROI 2. The intensity distributions observed in the images of the beam spot are likely a more reliable guide, given the fact the differences in measured peak positions in Table 7.1 are within error of one another.

This variation in measured energy observed with the HEXITEC device suggests that one reason for the disparity in the energy measured by the GaAs:Cr Medipix3 device compared with its Si counterpart is due to more energy being lost in and/or increased backscatter from the entrance window of the GaAs:Cr device (a nominally $0.5\ \mu\text{m}$ thick Ni contact) compared with that of the Si sensor (with a nominally $0.5\ \mu\text{m}$ thick Al contact). However, it is worth noting that the difference in measured energy and

Electron Energy (keV)	Peak Energy (keV)
60 keV (Full Sensor)	57 ± 4
60 keV (ROI 1)	57 ± 1
60 keV (ROI 2)	58 ± 1
80 keV (Full Sensor)	78.1 ± 0.3
80 keV (ROI 1)	78 ± 2
80 keV (ROI 2)	79 ± 1

Table 7.1: Energy of the primary electron peaks in the spectra recorded by the GaAs:Cr HEXITEC assembly exposed to 60 keV and 80 keV electron when taking the spectra from the full sensor and for the selected ROI shown in Figures 7.4(b) and (c).

actual primary electron energy is smaller than is the case for the Medipix3 detector operating in CSM, even in the case of ROI 1. This is somewhat unexpected and contrary to the explanation just suggested for the differences observed between the two Medipix3 devices, given that the frontside contact of the HEXITEC sensor ($0.1 \mu\text{m}$ Ni and $0.5 \mu\text{m}$ Au) is thicker and has a higher average value of Z than that of the Medipix3 device and does not have a high enough bias to ensure full charge-collection.

One reason for this may be that the larger pixel pitch of the HEXITEC detector means that less charge is lost to neighbouring pixels for which the net registered charge of an event is below threshold. Although the radius of the 99% contours for 60 keV and 80 keV electrons (see Figures 5.2(b) and 5.7(b)) is less than the Medipix3 pixel pitch, which might lead one to expect that the full energy of 60 keV and 80 keV electrons would be collected across the $2 \times$ pixel block across which the CSM algorithm works, this may not be guaranteed in all cases, as for each event it depending on the trajectory of the individual electron. Additionally, the simulations presented in the previous section do not include the lateral dispersion of charge carriers due to dispersion as they travel to the electrodes.

7.5 Simulations Incorporating Contacts

Prompted by the experimental results presented in the previous section, simulations similar to those presented in Chapter 4 were performed with the change that a selection of different contact layers were included in the simulation geometry. These contact layers, which varied in thickness and composition were immediately adjacent to the face of the GaAs sensor that was exposed to electrons. The goal of this set of simulations was partly to confirm that the variation in response across the pixel matrix observed in Section 7.4 could be attributed to differences in the thickness of the backside contact across the sensor. A second aim was to understand to what extent the backside contact of GaAs:Cr sensors could be chosen so as to optimise detector response.

Research into the understanding the behaviour of GaAs:Cr sensors used with different types of contact, and thereby enhancing their performance, is an active

area of study. The composition of the contacts influences the leakage current and charge collection efficiency of a device, which both in turn affect device energy resolution [312]. However, the focus has primarily been on improving the response of GaAs:Cr sensors for use in photon science in which, as previously mentioned, attenuation of primary incident quanta is usually, though not always, less of a concern [313]. Consequently, there is merit in considering how the contacts of GaAs:Cr sensors can be optimised to enhance the performance of such devices, which may also be of benefit to those photon science applications for which the attenuation of high-energy photons is of concern.

Initial simulations consisted of a GaAs target with a $0.1\mu\text{m}$ thick layer of Ni followed by a layer of Au that varied in thickness from $0.45\text{-}0.55\mu\text{m}$ in thickness. Simulated thicknesses of the Au layer were therefore the nominal thickness of the Au layer of the device used in the experimental measurements $\pm 10\%$ variation. The aim of these simulations was to confirm the variation in contact thickness as the cause of the variation in recorded counts observed in Section 7.4. As such the simulated primary electron energies for this geometry were 60 keV and 80 keV electrons.

Analysis of the simulations of GaAs sensor with Ni/Au contacts are presented in Figure 7.7. In Figure 7.7(a), the fraction of 60 keV electrons backscattered from the backside contact, without having any direct interaction with the sensor ranges from 0.269 ± 0.003 to 0.324 ± 0.003 . For 80 keV electrons, this figure ranges from 0.163 ± 0.003 to 0.206 ± 0.003 . These represent a relative reduction in the number of electrons interacting directly with the sensor of $17\pm 1\%$ and $21\pm 2\%$ respectively. Considering the difference in the fraction of backscattered electrons when using a layer of Au that is $0.5\mu\text{m}$ thick rather than $0.45\mu\text{m}$ thick, the relative reduction in electrons that interact with the sensor is $10\pm 1\%$ for 60 keV electrons and $11\pm 2\%$ for 80 keV electrons. The relative reductions in the number of electrons reaching the sensor are similar for each electron energy when increasing the thickness of the Au layer from $0.5\mu\text{m}$ to $0.55\mu\text{m}$.

Looking at Figure 7.7(c), it can be seen that for both primary electron energies, the fraction of energy deposited in the sensor when the primary electron is backscattered by the backside contact is negligible. The small amount of energy that is deposited can be attributed to secondaries produced by the interactions of the primary electron with the contact going onto deposit a small fraction of the primary electron energy in the sensor. Consequently, electrons backscattered from the backside contact are highly unlikely to be registered by the sensor at all, so that the net smaller number of counts registered in ROI 1 compared with ROI 2 can be attributed to backscattering from the backside contact. On the basis of the differences in the degrees of backscattering for different thicknesses of Au in Figure 7.7(a), the difference in the number of counts measured between ROI 1 and ROI 2 for 60 keV and 80 keV electrons is consistent with the Au layer in ROI 1 being between 10% and 20% thicker than that in ROI 2.

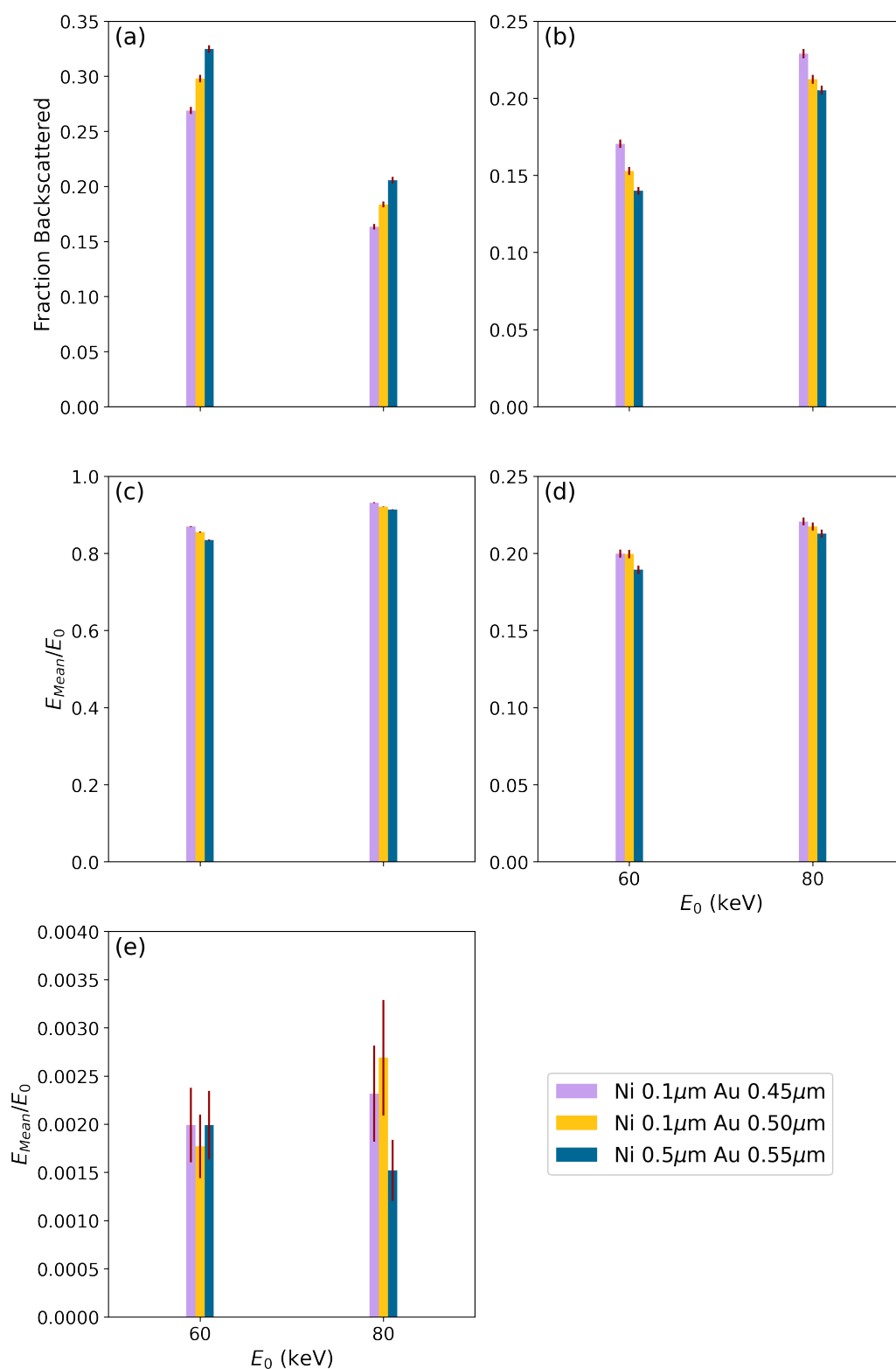


Figure 7.7: Results of simulations for which the GaAs target had backside contacts consisting of 0.1 μm thick layer of Ni and Au layers of varying thicknesses ranging from 0.45 μm -0.55 μm in thickness. The fraction of primary electrons backscattered from (a) the backside contact and (b) the sensor; the ratio of the average energy deposited E_{Mean} to primary electron energy when the primary electron is (c) absorbed by the sensor, (d) backscattered from the sensor or (e) backscattered from the backside contact.

In Figure 7.7(b), the fraction of electrons backscattered from the sensor decreases as the simulated contact becomes thicker. This can be attributed to the fact that the thicker the contact is, the more energy the electron will lose in the contact, and the less energy it has to then backscatter from the sensor. The increase in backscatter from the contact with increasing thickness of the Au layer is greater than the reduction in backscatter from the sensor. It is therefore not the case that an increase in backscatter from the backside contact is necessarily compensated for by a decreased backscatter from the sensor.

For 60 keV electrons, the average fraction of energy deposited in the sensor when the electron backscatters from the sensor in Figure 7.7(d) ranges from 0.199 ± 0.003 to 0.189 ± 0.003 . When the primary electron is absorbed, the average fraction of energy deposited increases from 0.855 ± 0.002 to 0.834 ± 0.002 in Figure 7.7(e). In the case of 80 keV electrons, the corresponding ranges in average fraction of energy deposited are 0.217 ± 0.003 to 0.212 ± 0.003 and 0.921 ± 0.001 to 0.914 ± 0.001 . Unsurprisingly, for both primary electron energies there is a reduction in the average fraction of the primary electron's energy deposited in the sensor as the thickness of the Au contact increases. This can be attributed to an increase in energy deposited in the contact with increasing contact thickness. The relative increase in energy lost when the thickness of the Au layer increases from $0.45 \mu\text{m}$ to $0.5 \mu\text{m}$ is greater for 60 keV electrons (both backscattered and absorbed) which is consistent with the increased straggling observed for 60 keV electrons in Figure 7.6(e) compared with 80 keV electrons in Figure 7.6(f).

Given that the degree of backscatter increases with the mass-thickness of a contact, it naturally follows that research into alternative backside contacts for GaAs should focus on structures that are as thin as possible and composed of low- Z materials. Ideally, Al contacts, like those used with Si devices and for Z is 13, would be used. Unfortunately, research investigating the behaviour of GaAs:Cr with an Al contact has found that this gives rise to inversion layer in the sensor below the contact, forming a barrier for the flow of electrons [314]. The same behaviour was also been observed for V and Cr contacts, which would also be of interest due to their relatively low values of Z (23 and 24 compared with 28 for Ni). Of the structures that have been found suitable for use as backside contacts with GaAs:Cr, one of the most promising, from the perspective of keeping the contacts as minimising the thickness and average Z of the contact, are Al/NiV ones [315].

While this work presented in this thesis was being undertaken, it was not possible to obtain information about the composition of the NiV alloy used in these contacts. Consequently, the simulations presented herein used Ni in place of NiV on the basis that this represented a worst case scenario, as V would lower the average value Z . The backside contact structures investigated therefore consisted of $0.1 \mu\text{m}$ Ni and $0.5 \mu\text{m}$ Ni, to investigate the benefits of using a thinner Ni contact, as well as structures consisting of $0.1 \mu\text{m}$ Ni with $0.1 \mu\text{m}$ of Al and $0.5 \mu\text{m}$ Al. The choice of the latter two

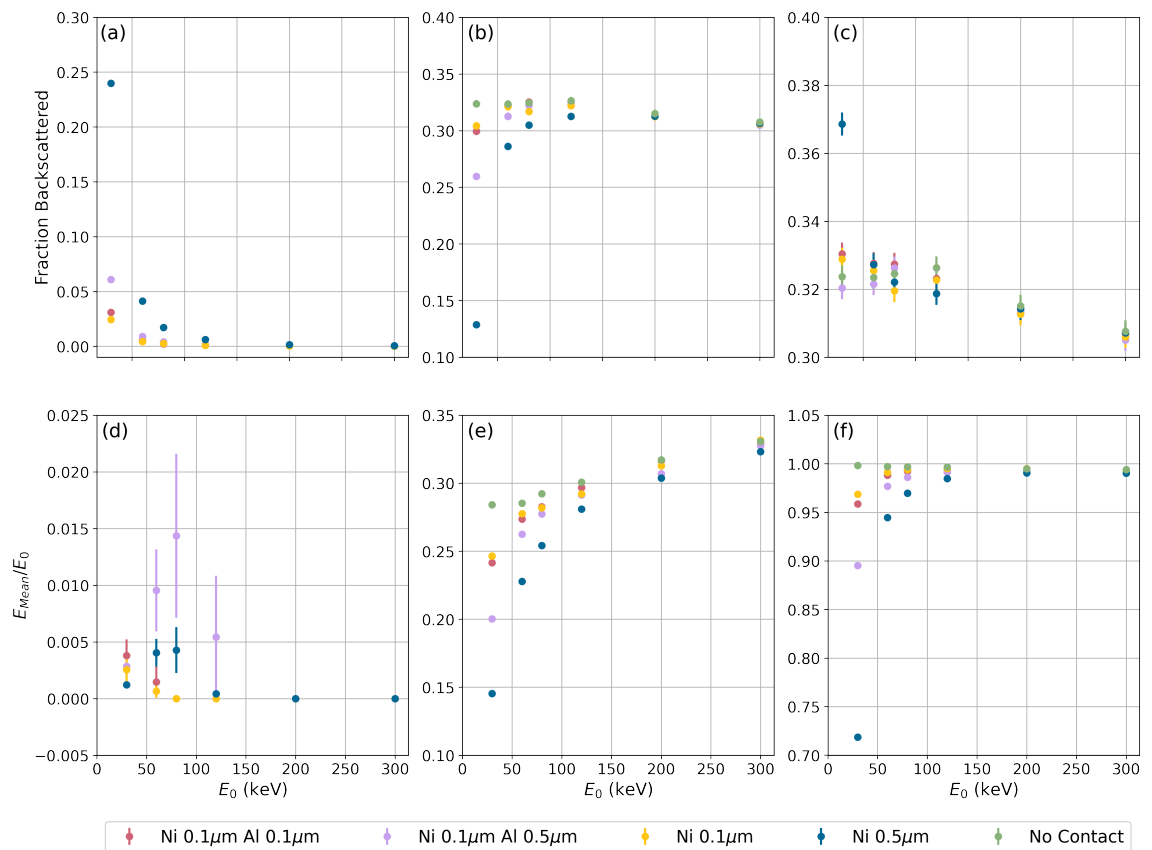


Figure 7.8: Analysis of simulations of a GaAs sensor equipped with backside contacts composed of varying thicknesses and combinations of Al and Ni. Plotted as a function of primary electron energy E_0 are (a) the fraction of electrons backscattered from the contact; (b) the fraction of electrons backscattered from the sensor; (c) the sum fraction of electrons backscattered from the device; the ratio of the average energy E_{Mean} to E_0 when electrons are (d) backscattered from the contact; (e) backscattered from the sensor; and (f) absorbed in the sensor. Relevant results from simulations of electron interactions with a GaAs sensor with no backside contact are reproduced from Figure 5.3 as a comparator.

structures is motivated by speculation as to whether using a top-most layer of Al may reduce the net backscatter of electrons due to electrons losing energy in the Al layer (so that it is more difficult for them to escape from the sensor). Figure 7.8 summarises the results of these simulations.

In Figure 7.8(a), it can be seen that there is no dependence in the fraction of electrons that are backscattered from the backside for electrons with energies ≥ 200 keV. Differences are only significant for primary electron energies below 200 keV, for which the fraction backscattered is greatest when using a 0.5 μm thick Ni contact and smallest with 0.1 μm thick Ni contact. Similarly, the fraction of electrons backscattered from the sensor only shows dependence on the contact composition for primary electron energies < 200 keV in Figure 7.8(b). For these lower electron energies, the fraction backscattered from the sensor is smallest when using a 0.5 μm thick Ni contact, increasing when using one of the thinner contacts. Unlike the results for the simulations with Ni/Au contacts shown in Figure 7.7, increased backscatter

from the contact(s) that are thicker or that have higher average values of Z appears to be mostly compensated for by reduced backscatter from the sensor. The total fraction of backscattered electrons is largely independent from either contact composition or primary electron energy in Figure 7.8, though there is slight reduction as the primary electron energy increases. A notable exception is 30 keV electrons, for which the total fraction of backscattered electrons when using a $0.5\ \mu\text{m}$ thick Ni contact is larger than the case where no contact is used. This indicates the increased backscatter from the contact is not fully compensated for by reduced backscatter from the sensor.

The energy deposited by electrons that are backscattered from the contact is negligible for all contact structures and primary electron energies in Figure 7.8. In Figures 7.8(e) and (f), the average fraction of primary electron energy deposited in the sensor for both electrons back scattered from and absorbed by the sensor is only dependent on the contact structure for electrons with energies lower than 200 keV. Below this energy, the average energy deposition is consistently smallest using a $0.5\ \mu\text{m}$ thick Ni contact and highest when using a $0.1\ \mu\text{m}$ thick Ni contact both for electrons backscattered from and fully absorbed by the sensor. Taken together, these results suggest that there is minimal benefit to be gained from using contacts where the topmost layer is composed from a low Z material such as Al in terms of reducing backscatter or reducing the amount of energy lost by interactions with the backside contact. Instead, the focus should be on making the backside contact be as thin as possible. Given that the only monolayer contact structures that have been found to be suitable for use with GaAs:Cr are Ni ones, this entails determining the minimal thickness of Ni needed to form a reliable contact.

The other way in which the choice of backside contact can be evaluated is the extent to which it changes the lateral scatter of the primary electron and hence the lateral deposition of energy. Figure 7.9 shows plots of the average radii of the 50%, 90% and 99% energy deposition radii for the various contact structures combined with a GaAs sensor for primary electron energies ranging from 30-300 keV. It can be seen that, for the range of backside contacts considered in these simulations, the backside contact makes no or little difference to the lateral deposition of energy. There are some datapoints for which some variation is seen in the average radius e.g. the 300 keV 50% energy deposition radius in Figure 7.9(a) or the 200 keV 90% energy deposition radius in Figure 7.9(b). However, these differences, when they do arise, are negligible.

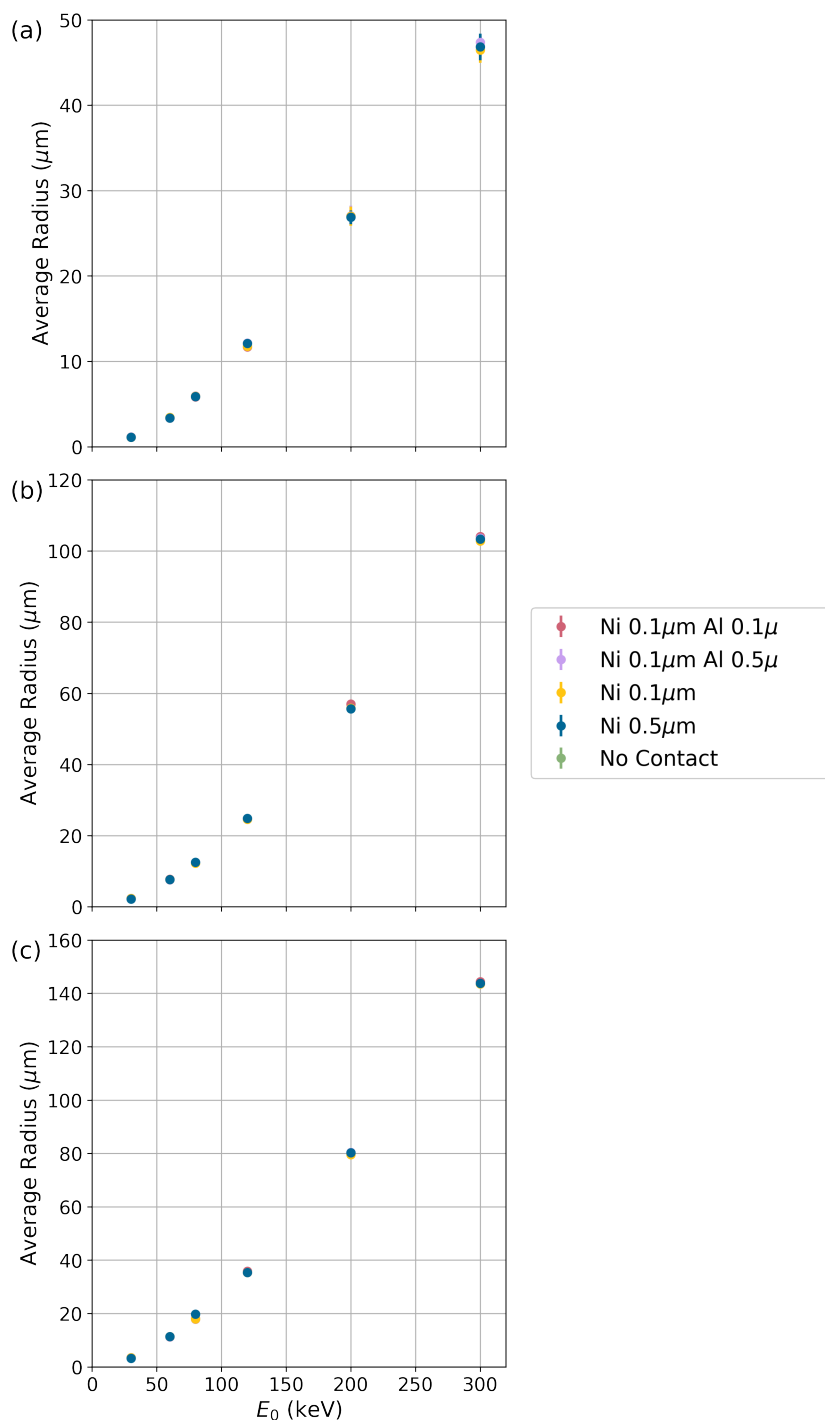


Figure 7.9: Plots of the average radii of the (a) 50% (b) 90% and (c) 99% deposition contours in a GaAs sensor with a selection of backside contacts composed of different combinations of Al and Ni. The average radii of the 50%, 90% and 99% energy deposition contours for a GaAs sensor with no backside contact are reproduced from Figure 5.2 for the sake of comparison.

7.6 Summary

A HEXITEC detector with a 500 μm thick GaAs:Cr sensor was successfully installed on the Tecnai T20 TEM at the University of Glasgow. This device had previously been calibrated using the γ -ray spectrum produced by an ^{241}Am source. Spectra

acquired when the GaAs:Cr detector was exposed to 60 keV and 80 keV electrons showed clear peaks that corresponded to the expected primary electron energies. A striking difference in the spectra and images acquired when the HEXITEC detector was exposed to γ -rays and electrons was that the latter showed variation across the sensor that was not repeated in former. This difference could be attributed to a variation in the thickness of the backside contact across the sensor, which to which electrons are more sensitive. Simulations investigating the backscatter of 60 keV and 80 keV electrons from a GaAs sensor with backside contacts composed of $0.1\ \mu\text{m}$ of Ni and a layer of Au ranging from $0.45\text{-}0.55\ \mu\text{m}$ in thickness provided further evidence in favour of this hypothesis.

These experimental results prompted further simulations investigating how the backscatter of primary electrons was affected by the composition of the backside contact of a GaAs:Cr sensor. Simulations of different possible backside contact configurations indicated that, for primary electron energies $\geq 120\ \text{keV}$, it would be beneficial to investigate alternatives to the $0.5\ \mu\text{m}$ Ni backside contact that is the thinnest/lightest contact currently used with GaAs:Cr sensors and which was used with the Medipix3 GaAs:Cr device characterised in Chapter 6. The most important factor, for the range of possible structures considered, appeared to be the overall thickness of the contact. There was no benefit to using a thin layer of a lighter element, in this case Al, prior to a layer of Ni to slow incident electrons and thereby reduce backscatter from the Ni and GaAs. While the thickness and composition of the backside contact had an effect on the fraction of electrons backscattered from the device and the fraction of energy deposited by electrons that interacted with the sensor (absorbed and backscattered), it was found that these factors had very little impact on the lateral spread in energy deposition in the sensor. Nevertheless, the results of these simulations indicate that using thinner Ni contacts has the potential to improve the performance of GaAs:Cr devices for electrons with energies $< 100\ \text{keV}$, potentially extending the range of energies for which GaAs:Cr sensors are a viable alternative to Si.

8

Conclusions and Future Work

8.1 Introduction

DEDs have enabled experiments that were previously impossible or impracticable, with HPDs proving particularly well-suited for a number of experimental modalities for which MAPS devices are not optimal. The work presented in this thesis was undertaken with the aim of developing a better understanding of how the interactions of electrons with the thick sensors of HPDs give rise to the observed performance. This was in addition to determining how the performance of HPDs used in TEM can be improved. These goals were both in service to a broader aim of informing the development of the next generation of HPDs designed for TEM. Section 8.2 summarises the main results obtained and the conclusions that can be derived from them, while Section 8.3 discusses the future work that would naturally follow on from these findings.

8.2 Results and Conclusions

8.2.1 Si Sensors

In Chapter 4, three HPDs based on the Medipix3 ASIC were characterised, each with a Si sensor with a different combination of pixel pitch and sensor thickness, to investigate how these factors affected device performance. Two sensors were $300\mu\text{m}$ thick, one with a $55\mu\text{m}$ pitch and one with a $110\mu\text{m}$ pitch, while a third sensor was $500\mu\text{m}$ thick with a $55\mu\text{m}$ pitch. The key performance metrics considered when comparing these detectors were their spectral response, MTF, DQE and deadtime.

There was little difference in the spectra recorded by the two $55\mu\text{m}$ pitch devices for electrons with energies ranging from 60-200 keV when the detectors operated in SPM. For both devices, these were dominated by low-energy tails that arose from

incident electrons depositing their energy over multiple pixels. However, in the spectra recorded by the $110\mu\text{m}$ pitch detector it was possible to identify peaks due to the primary electron in spectra recorded for electron energies up to and including 120 keV, though there was still a significant low-energy tail. Additionally, although the maximum amount of energy registered by an individual pixel was consistently greater for the $110\mu\text{m}$ pitch device, there was still a significant difference between this and the primary electron energy for 120 keV and 200 keV electrons.

Operating in CSM enhanced the quality of the spectra recorded by all three detectors when exposed to 60 keV and 80 keV electrons, to the extent that it was possible to measure and compare the detectors energy resolution. For these lower electron energies, there was little difference between the three detectors in terms of their energy resolution, which was limited by the deposition of energy over multiple pixels. However, for higher electron energies, it introduced artefacts into the spectra recorded as it failed to reliably fully reconstruct the energy deposited by incident electrons. Given the much larger area over which the CSM algorithm operates in the case of the $110\mu\text{m}$ pitch device, it is somewhat surprising that the spectra it recorded featured artefacts to the same extent as that seen in the spectra recorded by the smaller pitch devices. Overall, the advantages offered by the $110\mu\text{m}$ pitch device in terms of energy measurement, compared with the $55\mu\text{m}$ pitch devices, seem to be somewhat minimal.

Comparisons of the experimental spectra with those produced using simulations indicated that the simulations did not fully reproduce the physical processes that gave rise to the detector performance that was experimentally observed. Further refinement of the simulation configuration is necessary before the simulations could be used for reliable, quantitative insight into performance of HPDs used in TEM. The most important aspect that requires correction is likely the number of charge carriers that can be grouped together for the purposes of simulating their propagation through the sensor. Another aspect of the simulations that may need to be refined is the thickness and composition of the entrance windows of the simulated sensors. Nevertheless, some insight could be gained from decomposing simulated spectra on the basis of the type of interaction that had given rise to the signal induced on each pixel. Namely, that incomplete energy deposition appears to be largely due to incident electrons backscattering from the sensor. Additionally, it is backscattered electrons that give rise to isolated, individual pixel events, rather than secondary X-rays or secondary electrons traveling significant distances away from the point at which the primary electron interacts with the sensor.

MTF and DQE measurements of the three sensors for 60 keV and 200 keV electrons provided an opportunity to investigate how differences in electron energy, sensor thickness and pixel pitch affected device performance. The thicker sensor displayed the poorest performance of all three detectors when using a low counting threshold,

which is preferable from the perspective of maximising the DQE. This was due to increased diffusion of charge carriers in the thicker sensor, and consequently greater lateral spread of signal in the thicker sensor compared with the thinner ones. The effect of diffusion on performance was more significant in the case of the lower-energy measurements, as at higher energies the distance travelled by the primary electron was much greater than the lateral distance travelled by holes due to diffusion in the sensor.

Analysis of energy deposition along the simulated trajectories of electrons confirmed the increased probability of greater energy at the end of the trajectory. This added credence to the idea, proposed by other authors, that device MTF is not improved (initially) when using high-energy electrons by increasing the counting threshold because of the large range of high-energy electrons, combined with their tendency to deposit most of their energy towards the end of their trajectory.

Consideration of a model for effective pixel width and associated MTF developed for HPDs used with X-rays helped to highlight how the MTF is the result of the interplay of the lateral spread in signal in the sensor and the physical pixel pitch. Comparison of the MTF predicted by this model for various degrees of signal spread with experimental measurements indicated that this model might be successfully adapted for modelling the response of HPDs to low-energy electrons. However, a rather different model would be required for modelling the response of high energy electrons. It seems likely that the profile of the effective pixel, and hence overall performance, of an HPD for high-energy electrons cannot be properly modelled by top-hat function due to the extended region over which electrons deposit their energy and the stochastic nature of their trajectories.

Given the combined effects of electron trajectory, pixel pitch and sensor thickness, it seems sensors should be no thicker than is necessary to prevent electrons with the maximum energy that it is anticipated with which the sensor will be used from being transmitted through the sensor and damaging the ASIC. Additionally, the maximum bias that can be applied to the sensor should be applied. While this will likely have only a marginal effect on device performance for high electron energies, implementing these recommendations should improve device performance for lower electron energies. This indicates that the typical choice of $300\ \mu\text{m}$ and $500\ \mu\text{m}$ thick sensors for use with HPDs in TEM should be reviewed, particularly the latter choice in cases where the maximum beam energy is 200 keV (which is stopped by $300\ \mu\text{m}$ thick Si sensors). Furthermore, the power supply used with the Merlin DAQ should be reviewed. If it is not possible to supply a higher bias through the VHDCI connection, then the bias applied to devices with Si sensors should be supplied using an external power supply and the lemo connection to the PCB as was done for the GaAs:Cr Medipix3 device characterised as part of the present work. For very low electron energies i.e. $< 60\text{keV}$, it is probable that smaller pixels would be beneficial in light of the reduced range of electrons of these energies, if signal spread due to diffusion can be kept to a

minimum. Although the Medipix series of ASICs is, at $55\ \mu\text{m}$ towards the lower end of the pixel pitch size range of HPDs, the Mönch ASIC with a pitch of $25\ \mu\text{m}$ is smaller still [316, 317]. Combined with a Si sensor it would, in the first instance, likely be worthwhile exploring for use in SEM or low-energy TEM. (Furthermore, as will be discussed in Section 8.3, there are other potentially worthwhile studies that could be carried out with such a small pitch HPD as MÖNCH.)

The final set of results discussed in Chapter 4 was the linearity of count rate and deadtime of the detectors with Si sensors. A modified form of the model of a paralyzable detector that took into account the scatter of high-energy electrons over multiple pixels was proposed and used in an attempt to determine the deadtime of the three Si sensors for 200 keV electrons. In spite of the modifications made to the model for detector deadtime, the deadtime of the detectors appeared to scale with the number of pixels that registered incident electrons. Rather than the extracted values of τ providing a measure of the average length of time that a pixel was unresponsive to subsequent electrons, they appeared to provide a measure of the extent to which a detector was able to maintain a linear response, given the fact that multiple pixels ought to register incident electrons, under progressively higher incident electron flux. However, this had to be considered in tandem with the pixel pitch. While the $110\ \mu\text{m}$ pitch sensor had the shortest deadtime, the detector best able to maintain a linear response at high flux, as quantified in terms of a number of electrons per unit area per second, was the $300\ \mu\text{m}$ thick sensor with $55\ \mu\text{m}$ pitch.

8.2.2 High- Z Sensor Materials

In Chapter 5, the interactions of electrons with energies ranging from 30 keV to 300 keV with CdTe and GaAs were explored using simulations and compared with those of electrons of the same energies in Si. It was found that using GaAs in place of Si reduced the lateral spread of energy by more than 50% for a given electron energy. Use of a CdTe sensor led to a further reduction of less than 20%. However, the fraction of electrons backscattered from the sensor was consistently 30% greater than that backscattered by the GaAs device. Furthermore the average amount of energy deposited in the CdTe sensor by electrons that had been backscattered was slightly less than 90% that deposited by backscattered electrons in the GaAs sensor. Taken together, these results suggest the improvement in MTF that is obtained by using a CdTe/CZT sensor in place of a GaAs:Cr one is likely outweighed by the increase in backscatter.

Breaking down the energy deposited in the CdTe and GaAs sensors based on the type of particle that deposited it showed that X-rays produced by the interactions of electrons with the sensor do travel significant distances from the interaction site of the primary electron. Together with the secondary electrons they produce, these secondary X-rays deposit energy significant distances away from the region where

the primary electron enters the sensor and where most of its energy is deposited. However, the amount of energy deposited in this way was, on average, negligible and does not constitute a significant contribution to the lateral spread of signal.

In Chapter 6, the performance of a Medipix3 detector with GaAs:Cr sensor was characterised, with its performance compared to that of the Si sensor with the same pixel pitch and sensor thickness where appropriate. Spectra recorded by the GaAs:Cr sensor in SPM were dominated by a low energy tail and there was no obvious improvement compared to the SPM spectra recorded by the Si detectors with $55\mu\text{m}$ pixel pitch. The CSM algorithm did appear to be slightly more effective at reconstructing the energy deposited by incident electrons, with distortions only appearing in the 200 keV and 300 keV spectra and to a lesser extent than is the case in the Si CSM spectra.

It was found that, when the devices operated in SPM, the MTF of the GaAs:Cr sensor was consistently better than that of the Si sensor, aside from at high counting thresholds for 60 keV electrons when they were equivalent. With increasing electron energy, the extent to which the MTF of the GaAs:Cr detector at a given counting threshold surpasses that of the Si sensor increased. This is exemplified, for instance, by the fact that the MTF of the GaAs:Cr detector for 200 keV electrons surpassed that of the Si detector for 120 keV electrons. The DQE of both the detectors initially improved with electron energy, decreasing as the value of E_0 increased above energies of 80 keV for the Si detector and 120 keV for the GaAs:Cr detector. At energies below 120 keV the DQE of the GaAs:Cr sensor was poorer than that of the Si detector, though matched or surpassed the DQE of the Si sensor at higher energies.

The same general dependencies observed in the SPM MTF and DQE data for the two devices on electron energy held true when the devices operated in CSM, as did the relative difference in performance between the two devices. CSM improved the MTF of both devices and the value of $\text{DQE}(0)$ at low counting thresholds. However, at the same thresholds the value of $\text{DQE}(\omega_N)$ was poorer than if the device had been operating in SPM. This improvement in DQE at high spatial frequencies when the detectors operate with a low threshold in SPM is caused by deterministic blurring suppressing the NPS to a greater extent than the MTF in the presence of aliasing. The benefits of this effect are lost in the attempt to allocate the incident electron to a single pixel. However, one could apply an artificial blur to data in which the entry point of electrons had been localised to recoup this benefit (by e.g. convolving the data produced by the localisation process with a Gaussian kernel).

Consequently, if wanting to optimise device DQE at high spatial frequencies, operating in SPM with a low threshold is preferable, whereas, if MTF is critical and there are less stringent requirements on the dose to which the sample is exposed or the total acquisition time, then operating in SPM with a high counting threshold is better. If wanting to optimise MTF and the DQE simultaneously, particularly the DQE

at low spatial frequencies, then operating in CSM can be advantageous. For example, for 200keV electrons, the low threshold CSM $MTF(\omega_N)$ of the GaAs:Cr sensor is 0.41. The threshold at which its $MTF(\omega_N)$ operating in SPM is equal to this is 64.6keV, for which $DQE(0)$ is 0.68 and $DQE(\omega_N)$ is 0.15. However, the low threshold CSM $DQE(0)$ and $DQE(\omega_N)$ are 0.91 and 0.10 respectively; operating in CSM can therefore provide the same MTF and comparable high-frequency DQE as to when the detector operates in SPM while enhancing the low-frequency DQE. It may be worth investigating the extent to which applying a deterministic blurring to some CSM datasets could improve the DQE of the detectors when operating in this mode of operation.

The same modified model of the count rate of a paralyzable detector used in Chapter 4 was used to measure the deadtime of the GaAs:Cr and Si devices for 120 keV and 200 keV electrons as a function of I_{Krum} . It was found that GaAs:Cr detector's deadtime was consistently shorter than that of the Si detector, consistent with the earlier finding in Chapter 4 that a detector's deadtime (at low counting threshold) scaled with its PSF. The deadtime for both devices increased with electron energy and tended to decrease for higher values of I_{Krum} . As increasing I_{Krum} effectively increases the counting threshold, the decrease in deadtime with increasing I_{Krum} could be attributed, in part, to a reduction in the average number of pixels that register each electron due to an increase in the threshold.

For the two detectors operating in SPM with a counting threshold of ~ 12.5 keV, the optimal value of I_{Krum} for 120 keV electrons was determined to be ~ 150 DAC based on the count rate of the two detectors at the high incident flux as a function of I_{Krum} . The improvement in count rate compared to when I_{Krum} was set to 10 DAC for the GaAs:Cr device was $61 \pm 9\%$, and $22.7 \pm 0.2\%$ for the Si sensor; the corresponding reduction in count rate at low incident flux was $15 \pm 3\%$ for the GaAs:Cr sensor $14 \pm 1\%$ for the Si sensor. It was therefore established that the improvement in count rate at high incident flux obtained by using the optimal value of I_{Krum} was greater than the resulting reduction in count rate at low incident flux. In principle, the optimal value of I_{Krum} should be the same for other electron energies. However, it was not possible to confirm this as the maximum incident flux used for the 200 keV datasets was too low for the improvement in count rate to cancel out the undercounting due to the effective increase in counting threshold. Nevertheless, for the optimal values of I_{Krum} that could be determined for the 200 keV datasets, 100 DAC for the GaAs:Cr device and 90 DAC for the Si device, the improvement in count rate for both devices at high incident flux was still greater than the reduction in count rate at low incident flux.

Increasing the value of I_{Krum} reduced the deadtime of the GaAs:Cr sensor for both electron energies to a greater extent than it did the deadtime of the Si sensor. This was due, in part, to the fact that the value of I_{Krum} also controlled the maximum current that could be induced on each pixel before become unresponsive. However, the effect of I_{Krum} on the maximum current differs depending on whether the ASIC

operates hole-collecting mode (as for the Si sensor) or in electron-collecting mode (as for the GaAs:Cr sensor). For a given value of I_{Krum} , the maximum leakage current for the GaAs:Cr sensor was therefore half that of the Si sensor. A consequence of this is that pixels of the GaAs:Cr device become unresponsive at an incident flux at which no pixels in the Si sensor become unresponsive. Increasing I_{Krum} for the GaAs:Cr sensor therefore disproportionately improved the linearity of the GaAs:Cr response to high incident flux as it causes pixels that would otherwise be unresponsive at high flux to count again.

The Medipix3 GaAs:Cr device was also used to investigate the impact of defects present in the GaAs:Cr sensor due to its smaller pixel pitch (compared to the HEXITEC detector). These studies were also enabled by the fact it was possible to install it on different microscopes. Confocal STEM scans of a quarter of the GaAs:Cr detector with 200 keV and 300 keV electrons, in principle making it possible to measure the variation in pixel area and shape across the pixel matrix. However, the beam current used was too high, so that some pixels undercounted the number of incident electrons when the beam was within the pixel. This interfered with the identification of the pixel in which the beam was incident. The effect was more pronounced in the 200 keV dataset, which showed extensive distortion, though it was also present in the 300 keV dataset to a lesser extent. Consequently, while neither dataset could be used for quantitative determination of the pixel shapes and areas, the 300 keV electron dataset could be used to determine general trends in the pixel shapes and sizes.

Combined with analysis of the count rates of individual pixels, it was found that the linearity of larger pixels tended benefit from an increase in I_{Krum} more than small pixels. This was simply because the effective incident flux to which pixels were exposed depended on their area. Larger pixels are exposed to a greater number of electrons per second for a given incident flux, so increasing I_{Krum} caused an improvement in count rate at high flux. Smaller pixels are exposed to fewer electrons per second, and increasing I_{Krum} primarily led to increased rates of undercounting that were not balanced by a reduction in counts missed due to pile-up (unlike in the case of the larger pixels).

Investigations of the efficacy of flat field corrections for compensating for the effect of defects in the sensor indicated that flat field corrections were effective when the flux incident upon the detector was the same when the image being to be corrected and the flat field correction data. Otherwise, defects in the sensor were visible in the corrected data due to the disparity in the count rate of individual pixels at different levels of incident flux. Furthermore, a flat field correction does not compensate for the variation in pixel shape and area which introduces distortions into the features present in images incident upon the detector.

The final results chapter described the calibration of a HEXITEC detector with GaAs:Cr sensor; the successful installation of the detector on the Tecnai T20 TEM at

the University of Glasgow; and initial measurements of detector response to electrons. These were somewhat limited, firstly, because the maximum bias that could be applied to the sensor was less it should have been to ensure full charge collection and secondly because they only extended to measurements of detector response to 60 keV and 80 keV electrons. Nevertheless, significant differences in the spectra recorded in different regions of the sensor in the electron datasets that did not have a counterpart in the γ -ray dataset used to calibrate the sensor highlighted the extent to which the thickness of the backside contact could affect device efficiency. This led to further simulations of the interactions of electrons with a GaAs sensor with different contact configurations. These indicated, that given the contact structures that have been shown to be suitable for use with GaAs:Cr sensors, the optimal backside contact for GaAs:Cr sensors for use in electron microscopy Ni contacts that were as thin as possible.

8.3 Future Work

The next natural step for the work presented in Chapter 4 is to refine the simulations of the Si sensors so that they are more consistent with experimental measurements. This would then make it possible to further investigate how the diffusion and recombination of charge carriers in the sensor determine device performance. Although, the effect of the former can in principle be modelled in the manner described in Chapter 4, this still does not offer guidance into how much energy is lost to pixels that do not register sufficient energy for them to exceed even the lowest possible threshold, just above the noise level of a detector. More generally, accurate simulations of device response would facilitate the design of future detectors. They would aid the development of a more comprehensive, analytic model of detector performance such as those developed for photon science by providing insight into the form of the effective pixel area for different scenarios.

Development of such a model arguably represents the most significant objective of the present work that was not achieved and, given its utility in optimising sensor design for different applications, remains one of the most worthwhile outstanding goals to pursue. Achieving this hinges on developing an understanding of the form of the effective pixel area for a given combination of electron energy, threshold, sensor thickness and pitch. The primary challenge here is in modelling the deposition of energy by electrons, and this might be possible by adapting some of the mathematical formalism developed for modelling the fluorescence and Compton scattering in X-ray detectors [293, 300, 318].

Given the recent extension of the Allpix² simulation package to permit the simulation of HPDs with other materials, another sensible next step would be to build upon the simulations of electron interactions with CdTe and GaAs presented in this

thesis with more comprehensive simulations that incorporated device response using Allpix². This is likely to be particularly useful in developing an understanding of the optimal sensor design for devices using high-Z sensors, or extending any modelling work to devices with sensors made from materials other than Si, as trapping and recombination effects are more important in such materials. The measurements acquired with the Medipix3 GaAs:Cr sensor and presented in Chapter 6 could, in principle, be used for the purposes of validating any simulations and modelling of the performance of HPDs with GaAs:Cr sensors.

Regarding the measurements of the deadtime of the Medipix3 devices, it would be beneficial to acquire further data for all four detectors at higher levels of incident flux, particularly for 200 keV electrons. This would help to confirm the maximum flux for which the proposed model of detector count rate is valid and refine the determination of the detectors' deadtime. In the case of the devices for which the effect of increasing I_{Krum} was investigated, it would be sensible to calibrate the detectors' counting threshold for all values of I_{Krum} used, so that the extent to which reducing the deadtime affects MTF and DQE (due to the effective increase in counting threshold) can be established.

Further studies of HEXITEC detectors within the context of TEM would be beneficial, both for the purposes of acquiring data to validating simulations as well as for the insight that experimental measurements themselves would provide. Although simulations performed as part of the current work indicate that secondary quanta should not play a significant role in contributing to the spread of signal, measurements of the spectra recorded by HEXITEC devices for high electron energies would help to confirm this. If characteristic X-rays did deposit energy a significant distance away from the interaction point of their parent primary electron, this would give rise to peaks in the spectra recorded by the detector. As a first step, it would be desirable to repeat measurements with 60 keV and 80 keV electrons with a GaAs:Cr sensor to which the full bias could be applied to obtain measurements with the device operating under optimal conditions. Ideally, the sensor would also have a thinner backside contact composed of Ni only that was more consistent in its thickness than was the case of the device previously studied. Following on from this, would be measurements the detector's response to higher energy electrons, with the experimental apparatus that has been developed for the purposes of acquiring the data presented in this thesis. As the hardware makes it possible to swap-in other devices, other natural next steps in this line of enquiry would be to investigate the response of CdTe, CZT and Si sensors.

In addition to measurements of the spectra for individual electron energies, MTF and DQE measurements could be attempted. Although the assembly used to install devices on the Tecnai T20 TEM does not permit mounting a knife-edge in front of the sensor, nor does its position permit use of the beam-stop as a knife-edge as other authors have done, MTF measurements could be performed using the edge of one

of the microscope apertures [164, 291]. Measurement of the MTF from a circular aperture is relatively straightforward, assuming one can image the entire aperture. The ESF can then be formed by identifying the centre of the aperture image (i.e. the image of the beam spot as defined by the aperture) and rearranging the intensities recorded by pixels in order of the pixels' distance from the centre of the aperture image [319]. Once the ESF has been normalised, the MTF can then be calculated in the usual way.

Though acquiring data without coincidence loss with HEXITEC requires using a beam current that is too low to be measured with a picoammeter, beam current measurements for the purposes of calculating the HEXITEC system's gain factor for determining the DQE could, in principle, be performed by using one of the Medipix3 devices. This would require the gain factor of the Medipix3 device also be determined for the electron energies of interest, given the counting threshold used, using the set-up described in Chapter 3 for beam current and gain measurements. Of course, as this method would entail measuring the beam current with the Medipix3 device, removing it and then installing the HEXITEC device, this would require the beam current to be stable for an extended period of time, and so may not be feasible. If it were possible to acquire MTF and DQE measurements, it should then be possible to correlate changes in the MTF and DQE depending on the energy threshold applied to the data with features observed in the corresponding energy spectrum that were above and below a given energy threshold. For example, one could identify to what extent discounting any characteristic X-rays affects the MTF and DQE.

Further to measurements of the performance of materials such as CdTe and CZT with the HEXITEC ASIC, the improved spatial resolution, at least in terms of MTF, mean that it would also be desirable to investigate their performance with a smaller pixel ASIC, such as the Medipix3 ASIC. Recent measurements with the JUNGFRÄU ASIC (pixel pitch $75\mu\text{m}$) show a small improvement to the MTF for 200 keV and 300 keV electrons is possible by using a CdTe sensor in place of a GaAs:Cr sensor [291]. However, consistent with the simulations in Chapter 5, the improvement observed is much less than that obtained by using a GaAs:Cr sensor in place of a Si one. It may be expected that the relative improvement in MTF obtained by using a CdTe/CZT sensor in place of a GaAs:Cr sensor would be increased when using a device with a smaller pixel pitch, such as one of the Medipix series of detectors. To fully compare the performance of CdTe and CZT sensors with that of GaAs:Cr and Si sensors, MTF and DQE measurements of devices using the same ASIC (but different sensors) are necessary.

Given the reduced range of electrons in GaAs:Cr and CdTe, it may make sense to use high- Z materials with an ASIC with a smaller pixel pitch such as the MÖNCH ASIC. The increased information about the electron trajectories in high- Z sensors obtained by using a smaller pitch ASIC may make it possible to adapt the approaches used to localise the entry point of high-energy electrons in Si sensors [51, 195]. If done to a

sufficiently high degree of accuracy, this would mean an effective pixel pitch on the order of $\sim 10\ \mu\text{m}$, which would be comparable to the physical pitch of MAPS detectors.

This would open up the prospect of HPDs that can compete with monolithic devices for use in applications in which the latter kind of detector has traditionally dominated e.g. SPA cryoEM performed using 200–300 keV electrons. As noted in Chapter 2, for cryoEM performed using 100 keV electrons, HPDs already offer improved performance compared monolithic devices for this electron energy [174]. Furthermore, the suitability of HPDs for ptychography means they have already been used to successfully demonstrate the improvement in SPA cryoEM possible via ptychography [100]. The shift from MAPS to HPDs for cryoEM would nevertheless be greatly facilitated by a reduction in the pixel pitch of HPDs.

Although the smaller pixel pitch is not strictly necessary to attempt this with a high- Z sensor, it is likely that for a $55\ \mu\text{m}$ pitch device, the reduced number of pixels that register the incident electron will make identifying the electron point more challenging due to the reduced information about the electron's trajectory. Likewise, there would be merit in investigating the possibility of electron localisation and superresolution with a MÖNCH device with a Si sensor both for its own sake but also for comparison with electron localisation routines developed for the high- Z case. This would help to determine whether the increased information about electron trajectory obtained by using a Si sensor with small pixel pitch improves the accuracy of electron localisation routines or whether there is an optimal degree of scattering and track information relative to pixel pitch when reconstructing the electron entry point. Independent of sensor material and pixel pitch, machine learning algorithms used to identify the electron entry point in HPDs could, in principle, be improved by training them with confocal STEM data acquired when using a very low beam current so that pixel clusters due to individual electrons could be identified at each dwell point.

Beyond simply characterising the performance of devices with GaAs:Cr or CdTe and CZT sensors in terms of their MTF, DQE etc. another sensible next step would be to investigate their performance in real experiments. For instance, it would be interesting to compare a range of 4D-STEM datasets with both the Medipix3 GaAs:Cr detectors and one of the $55\ \mu\text{m}$ pitch Medipix3 Si detectors to investigate to how the extraction of different types of signals are affected (whether positively due to the improved PSF or negatively due to the defects in the sensor) by using a GaAs:Cr sensor in place of a Si one. Acquiring experimental data with the GaAs:Cr sensor would also help to determine to what extent the variation in detector response under different levels of incident flux is a substantive problem.

Assuming that the defects present in high- Z materials do present a problem as expected, then correcting for the artefacts introduced by these defects represents one of the key challenges that must be surmounted before the benefits of high- Z sensors can be fully exploited. Ideally, improvements in the crystal growth procedure

leading to increased uniformity would resolve this issue, and while there has been and continues to be improvement on this front, in the short to mid-term it is likely necessary to correct the effect of defects in post-processing. This is a challenging task as it requires an understanding of how the response of each individual pixel changes as a function of the incident flux. However, this still does not account for the effects of the variation in pixel shape. It seems plausible that knowledge of the shape of individual pixels acquired from confocal STEM scans could be used to correct for this somehow, though this would probably require measurements using a smaller spacing between dwell points, lower beam current and possibly also lower electron energy.

If confocal STEM scans are to be used for training electron localisation algorithms or for further investigation/correction of defects in compound high- Z sensors, then the technique requires further refinement. The most obvious improvement needed is identifying a safe level of emission from a given experimental set-up (i.e. combination of electron source, electron energy and alignment) so that significant levels of undercounting do not interfere with identification of the position of the electron beam in the sensor. Given the difficulty entailed in measuring the low beam currents necessary, this might be done by performing scans, starting at a low level of source emission and becoming progressively larger, covering selected sub-regions. These regions would center on pixels that were identified as recording the largest number of counts in a flat field image and an overly high emission could be identified as the lowest emission at which undercounting was observed in the pixel response maps of these pixels. Additionally, it may be the case that using a smaller spacing between dwell points would improve the accuracy with which the boundaries of pixels were identified. It would therefore be sensible to perform a series of scans of a selection of small regions of the sensor with progressively larger (scan) pixel spacing to identify the minimal scan spacing to accurately map the pixel shapes and sizes.

Future developments in HPDs for (S)TEM are likely to include the development of ASICs for specific applications within (S)TEM. Previously, HPDs used in electron microscopy have been adapted for those developed for photon science or X-ray imaging, with even the EMPAD detectors having been adapted from the XPAD [161, 320]. This is beginning to change, with DECTRIS developing the ARINA detector specifically for 4D-STEM [171]. Further specialisation is likely to be seen with the performance characteristics that are optimised depending on the envisioned application.

For TEM imaging, it is likely that there will be a push towards smaller pitch devices, towards the limit of what is permitted by bump-bonding methods, which is currently on the order of a few tens of micrometers [316]. This will probably be accompanied by further work in the refinement of electron localisation strategies. In general, developments will likely be along the lines of the work discussed in relation to the Mönch ASIC above. At the same time, spatial resolution and sensitivity to individual electrons are no longer the barriers they once were, and this line of investigation

is limited to refinement of previous work and technologies, rather than the next breakthrough in terms of insights enabled by advances in detector technology.

Enabling, time-resolved, dynamical studies is the next frontier for detector technologies, both in TEM and STEM. This requires the development of devices with high frame rates (in addition to high spatial resolution for TEM) with no gaps between frames for read-out. Alternatively, devices with data-driven readout and the ability to accurately record the ToA of incident electrons with a high level of precision but with high throughput would also be suitable for such studies. In both types of architecture, to maximise the temporal resolution, then the entry point of the electron must be localised in time as well as in space. The spatial scatter of electrons leads to electrons being recorded with different arrival times in different pixels and being recorded

Both good temporal resolution and high throughput are also desirable properties for detectors intended for STEM, even without the consideration of time-resolved 4D-STEM (i.e. 5D-STEM) and STEM-EELS. These qualities would permit shorter dwell times in STEM, comparable with those that are possible with conventional annular i.e. nanosecond dwell times, as well as minimising cross-talk between neighbouring dwell points due to electrons being registered in more than one frame. In the case of 4D-STEM and EELS, a high degree of linearity in response to high incident flux is also desirable, if only in the case of the former to maximise the range of 4D-STEM modalities for which the detector is suitable

The prospect of 5D-STEM and time-resolved STEM-EELS has already been raised by the successful use of a Timepix3 for EELS and 4D-STEM with sub-microsecond dwell times [181,182]. However, a significant limitation of the Timepix3 ASIC is its relatively low data bandwidth, with the maximum incident hit rate that it can process without corruption of data in its fastest mode of operation being 40 MHits/cm²/s [180]. As electrons are registered by multiple pixels, the maximum incident flux is less than this theoretical maximum, with the extent of the reduction depending on electron energy and sensor PSF. Its successor, Timepix4, has a maximum bandwidth of 360 MHits/cm²/s, an increasing the bandwidth by a factor of 9, and can apply a time stamp to events with a resolution of 200 ps, compared with 1.56 ns for Timepix3 [321]. This raises the prospect of time-resolved studies with (potentially) sub-nanosecond temporal resolution. Combining Timepix4 with a high- Z sensor would, nevertheless, maximise the incident electron flux by reducing the number of pixels that detect each electron. Additionally, given that a timestamp is recorded for each pixel that records an incident electron, reducing the spatial spread of signal would also maximise the temporal resolution [194]. If developing a detector specifically for 4D/5D-STEM and STEM-EELS, then Timepix4 combined with a high- Z sensor is a highly promising option.

There are two main challenges that would have to be overcome if this strategy were to be pursued. The first is the finite amount of time taken to read-out pixels

that have registered an event when the detector operates in data-driven mode, during which time those pixels are insensitive to incident electrons. This could be overcome by developing an ASIC that combines a Timepix4-like architecture with the ability to either store multiple events on pixel prior to a global readout at the end of the measurement, which be highly demanding in terms of ASIC design. More realistic, at least in the short to mid-term, is the prospect of using machine learning to separate overlapping events and recover events lost due to pile-up and coincidence loss.

The second challenge that must be overcome is the loss of events due to backscatter, particularly if using a high- Z sensor. This could be done by keeping device noise to a minimum, so that the counting threshold can be set as low as possible, thereby permitting detector of backscattered electrons that deposit only a very small fraction of their energy in the sensor. In turn, this would entail minimising the leakage current of high- Z sensors, which requires further improvements in the methods used to manufacture them. A more immediate solution may be active cooling of devices with high- Z sensors. Going forward, it would also be advisable to optimise the device settings to minimise any contributions to the noise and for this to be a consideration in the development of future ASICs.

8.4 Summary

The work presented in this thesis represents a small contribution to the development of future detector technologies for use in electron microscopy. It has been partially successful in achieving of the goals stated at the outset of the present work, the first of which was to develop a better understanding of the response of HPDs to electrons using Si sensors. This was hampered, in part, by difficulties in developing accurate simulations of device response and was, for the most part, limited to measurements of the MTF, DQE and deadtime of a selection of Si sensors. Nevertheless, this provided some insight into the role sensor thickness and pixel pitch play along with electron energy in determining device response. The work presented regarding HPDs with Si detectors potentially contributes to the foundation of a more comprehensive model for the response of HPDs to electrons, which may in turn guide the design of HPDs developed for specific applications within electron microscopy.

More successful has been the investigation of high- Z sensor materials. Use of a GaAs:Cr sensor has been shown to significantly improve the MTF performance of a Medipix3 detector compared with a Si sensor with the same pixel pitch and thickness for electrons with energies used in current generation TEM. It also improves the DQE for electrons with energies ≥ 120 keV, and there is scope to improve the DQE of the GaAs:Cr sensor for lower electron energies by using thinner backside contacts. Use of a GaAs:Cr sensor also improved device deadtime compared with when a Si sensor

was used. This was part of a general trend whereby the deadtime of devices based on the Medipix3 ASIC depended on their PSF. On the basis of simulation results, HPDs with CdTe and CZT sensors merit investigation, with measurement of the DQE being of particular interest. More generally, there is merit in investigating the performance of high- Z sensors, especially combined with ASICs with smaller pixels than those used in the present work. Devices with smaller pixels would be of interest from the perspective of understanding whether small pixel, high- Z sensors can lead to HPDs that can compete with monolithic devices for imaging applications. High- Z sensors combined with devices with larger pixels, such as those used in the present work, would be of interest for the sake of comparing their performance with HPDs with Si sensors for applications in which HPDs have traditionally excelled. This would permit determination of the advantages of high- Z sensors when used under real experimental conditions, as well as potentially maximising the value of the detailed information provided by advanced ASICs such as Timepix4. However, defects in high- Z sensor materials still represent a significant drawback and another focus for future work is in further improvement of the uniformity of high- Z alternatives to Si or correcting for the artefacts introduced by defects in post-processing.

Appendices

Appendix A

Examples of configuration files used for simulations of detectors with Si sensors performed with Allpix².

Executable Configuration File

```
[Allpix]
model_paths = "."
log_level = "STATUS"
log_format = "SHORT"
detectors_file = "Medipix3_Detector_Variable.conf"
root_file =
    "Modules_Medipix3_300um_55um_90V_200keV_ConstantContact.root"
purge_output_directory = false
number_of_events = 20000

[GeometryBuilderGeant4]
world_material = vacuum

[DepositionGeant4]
physics_list = FTFP_BERT_LIV
enable_pai = false
particle_type = "e-"
source_energy = 200keV
source_position = 0m 0mm -1m
source_type = "beam"
source_energy_spread = 0keV
flat_beam = true
beam_direction = 0 0 1
beam_divergence = 0 0
beam_size = 6mm
number_of_particles = 1
output_plots = false
range_cut = 0.001um

[ElectricFieldReader]
name="dut"
model = "mesh"
output_plots = true
field_scale = 1.0 1.0
field_offset = 0.0 0.0
depletion_depth = 300um
```

```

file_name = "./300um_55um_90V_ElectricField.apf"

[DopingProfileReader]
name="dut"
model = "mesh"
output_plots = true
field_scale = 1.0 1.0
field_offset = 0.0 0.0
doping_depth = 300um
file_name = "./300um_55um_90V_DopingConcentration.apf"

[WeightingPotentialReader]
name="dut"
model = "mesh"
output_plots = true
file_name = "./300um_55um_WeightingPotential.apf"

[TransientPropagation]
name="dut"
mobility_model = "arora"
recombination_model = "srh"
temperature = 311.15K
charge_per_step = 200
output_plots = true
integration_time = 0.5us
propagate_electrons = true
propagate_holes = true
induction_matrix = 3 3

[PulseTransfer]
output_plots = true

[ROOTObjectWriter]
file_name = "Medipix3_300um_55um_90V_200keV_ConstantContact.root"
include = MCParticle MCTrack DepositedCharge PixelCharge

```

Detector Configuration

```

[dut]
type = "medipix3"
position = 0 0 0mm
orientation_mode = "xyz"
orientation = 0deg 0deg 0deg

```

Configuration for “medipix3” Device

```
type = "hybrid"

number_of_pixels = 256 256
pixel_size = 55um 55um
implant_size = 38um 38um

sensor_thickness = 300um
sensor_excess = 1mm

bump_sphere_radius = 9.0um
bump_cylinder_radius = 7.0um
bump_height = 20.0um

chip_thickness = 100um
chip_excess_top = 1610um
chip_excess_bottom = 1610um
chip_excess_right = 10um
chip_excess_left = 10um

[support]
thickness = 1.76mm
size = 47mm 79mm
offset = 0 -22.25mm
material="G10"

[support]
# Frontside contact
thickness = 1000nm

size = 14080um 14080um
location = "absolute"
offset = 0 0 -250500nm
material= "Silicon"

[support]
# Frontside contact
thickness = 500nm
size = 14080um 14080um
location = "absolute"
offset = 0 0 -251250nm
material= "Aluminum"
```

Appendix B

Script for Simulating Pixel Structure with sde

```
(sde:clear)
(sdegeo:set-default-boolean "ABA")
(define num_x 1)
(define num_y 1)
(define pitch 55)
(define pad 35)
(define gap (- pitch pad))
(define thickness 300)
(define doping_width 38)
(define doping_gap (- pitch doping_width))
(define edge (* gap 0.5))
(define doping_edge (* doping_gap 0.5))

(sdegeo:create-cuboid (position 0 0 0) (position (* num_x pitch)
  (* num_y pitch) thickness) "Silicon" "bulk")

;Generating pad array - vanadium and nickel contact
;define x and y variables for loop

(define pix_X 0)
(define pix_Y 0)

(do ( (i 0 (+ i 1)) )

  ( (= i (* num_x num_y))

    (begin

      ;defining name of pad of particular pixel

      (define V_reg (string-append "V." (number->string i)))

      ;creating pad of particular pixel

      (sdegeo:imprint-rectangular-wire (position (+ edge (* pix_X
        pitch)) (+ edge (* pix_Y pitch) 0) (position (+ edge pad (*
        pix_X pitch)) (+ edge pad (* pix_Y pitch) 0))

      (if (= pix_X (- num_x 1))
        (begin
```

```

        (set! pix_X 0)
        (set! pix_Y (+ pix_Y 1))
    )
    (begin
        (set! pix_X (+ pix_X 1))
    )
)
)
)

;establishing the different contact types
(sdegeo:define-contact-set "Cathode" 4 (color:rgb 0 1 0 ) "##")

(do ( (i 0 (+ i 1)) )

    ( (= i (* num_x num_y)))

    (begin

        (sdegeo:define-contact-set (string-append "Pixel"
            (number->string i)) 4 (color:rgb 1 0 0 ) "##")

    )

)

;assigning each Ni region within a pixel as a contact
(set! pix_X 0)
(set! pix_Y 0)
(do ( (i 0 (+ i 1)) )

    ( (= i (* num_x num_y) ))

    (begin

        (sdegeo:set-contact(find-face-id (position (+ edge (* 0.5
            pad) (* pix_X pitch)) (+ edge (* 0.5 pad) (* pix_Y
            pitch) 0)) (string-append "Pixel" (number->string i)))

        (sdedr:define-refeval-window (string-append "Pixel"
            (number->string i)) "Rectangle" (position (+ (* pix_X
            pitch) doping_edge) (+ (* pix_Y pitch) doping_edge) 0.0)
            (position (+ (* pix_X pitch) doping_edge doping_width) (+
            (* pix_Y pitch) doping_edge doping_width) 0.0))

        (if (= pix_X (- num_x 1))

            (begin

                (set! pix_X 0)
                (set! pix_Y (+ pix_Y 1))
            )

            (begin

```

```

        (set! pix_X (+ pix_X 1))
      )
    )
  )
)

;assigning the bottom Al as a contact

(sdegeo:set-contact(find-face-id(position (* 0.5 num_x pitch) (*
  0.5 num_y pitch) thickness)) "Cathode")

;meshing the final structure
;global mesh

(sdedr:define-refeval-window "RefEvalWin_1" "Cuboid" (position -10
  -10 -10) (position (+ (* num_x pitch) 10) (+ (* num_y pitch)
  10) (+ thickness 10)))

(sdedr:define-refinement-size "RefinementDefinition_1" 10 10 10
  0.1 0.1 0.1)

(sdedr:define-refinement-placement "RefinementPlacement_1"
  "RefinementDefinition_1" (list "window" "RefEvalWin_1"))

(sdedr:define-refinement-function "RefinementDefinition_1"
  "DopingConcentration" "MaxTransDiff" 0.5)

;(sdegeo:define-refeval-window "OhmicImplant" "Rectangle" (position
  pitch pitch 0.0) (position (* 2.0 pitch) (* 2.0 pitch) 0.0))

(sdedr:define-refeval-window "JunctionImplant" "Rectangle"
  (position 0.0 0.0 thickness) (position (* num_x pitch) (* num_y
  pitch) thickness))

(sdedr:define-constant-profile "Prof.BulkPhosphorus"
  "PhosphorusActiveConcentration" 1.0e11)

(sdedr:define-analytical-profile "Prof.Phosphorus"
  "PhosphorusActiveConcentration" "a=1e+19;b=300;c=0.15"
  "a*exp((-1 *(b-z)^2)/(2*c^2))" 0 "general")

(sdedr:define-gaussian-profile "Prof.Boron"
  "BoronActiveConcentration" "PeakPos" 0.0 "PeakVal" 1e+19
  "StdDev" 0.17 "Gauss" "Factor" 0.0)

(sdedr:define-constant-profile-region "Place.BulkPhosphorus"
  "Prof.BulkPhosphorus" "bulk")

;(sdegeo:define-analytical-profile-placement "Place.Boron"
  "Prof.Boron" "OhmicImplant" "Both" "NoReplace" "Eval")

(set! pix_X 0)

```

```

(set! pix_Y 0)

(do ( (i 0 (+ i 1)) )
  ( (= i (* num_x num_y) ))

  (begin
    (sdedr:define-analytical-profile-placement (string-append
      "Place.Boron" (number->string i)) "Prof.Boron"
      (string-append "Pixel" (number->string i)) "Both"
      "NoReplace" "Eval")

    (if (= pix_X (- num_x 1))
      (begin
        (set! pix_X 0)
        (set! pix_Y (+ pix_Y 1))
      )
      (begin
        (set! pix_X (+ pix_X 1))
      )
    )
  )
)

(sdedr:define-analytical-profile-placement "Place.Phosphorus"
  "Prof.Phosphorus" "JunctionImplant" "Both" "NoReplace" "Eval")

; Meshing structure
(sde:build-mesh "snmesh" "" "n34_msh")

```

Script for Simulating Electrical Properties of a Pixel with sdevice

```

File {
  grid= "n34_msh.tdr"
  current= "n46_des.plt"
  plot= "n46_des.tdr"
  output= "n46_des.log"
}

Electrode {
  { Name= "Cathode" Voltage=0.0 WorkFunction= 4.06}
  { Name = "Pixel0" Voltage=0.0 WorkFunction= 4.06}
}

Physics{
  temperature= 311.15
  mobility (ConstantMobility)
  recombination (SRH)
}

```

```

DefaultParametersFromFile
EffectiveIntrinsicDensity (NoBandGapNarrowing)
}

Plot{
  eDensity hDensity
  ElectricField/Vector
  Potential
  SpaceCharge
  eTrappedCharge hTrappedCharge
  Doping DonorConcentration AcceptorConcentration
  HeavyIonChargeDensity
  CurrentPotential
  hInterfaceTrappedCharge
  eCurrent hCurrent
}

Math {
  ExitOnFailure
  Digits = 5
  Iterations = 16
  NotDamped = 100
  RHSMIn = 1e-6
  Extrapolate
  Method = ParDiSo
  NumberOfThreads= 16
}

Solve {
  Coupled(Iterations=500 LineSearchDamping = 1e-4){Poisson}
  Coupled(Iterations= 500 LineSearchDamping= 1e-4){ Poisson
    Electron Hole}
  Quasistationary ( InitialStep= 1e-2 MaxStep= 0.2 MinStep= 1e-9
    Increment= 1.5
    Goal { Name= "Cathode" Voltage= 90}
    Goal { Name = "Pixel0" Voltage=0.0})
  {Coupled{ Poisson Electron Hole }}
}

```

Bibliography

- [1] P. Caron, C. Inguibert, D. Lambert, and M. Raine-Theillet. Advanced example microelectronics. https://geant4-dev.web.cern.ch/collaboration/working_groups/advExamples/example_microelectronics.html#publications, (Last accessed: 01.07.2022).
- [2] K. A. Paton, M. C. Veale, X. Mu, C. S. Allen, D. Maneuski, C. Kübel, V. O'Shea, A. I. Kirkland, and D. McGrouther. Quantifying the performance of a hybrid pixel detector with GaAs:Cr sensor for transmission electron microscopy. *Ultramicroscopy*, 227:113298, 2021.
- [3] G. W. Paterson, R. W. H. Webster, A. Ross, K. A. Paton, T. A. MacGregor, D. McGrouther, I. MacLaren, and M. Nord. Fast Pixelated Detectors in Scanning Transmission Electron Microscopy. Part II: Post-Acquisition Data Processing, Visualization, and Structural Characterization. *Microscopy and Microanalysis*, 26(5):944–963, 2020.
- [4] M. Nord, R. W. H. Webster, K. A. Paton, S. McVitie, D. McGrouther, I. MacLaren, and G. W. Paterson. Fast Pixelated Detectors in Scanning Transmission Electron Microscopy. Part I: Data Acquisition, Live Processing, and Storage. *Microscopy and Microanalysis*, 26(4):653–666, 2020.
- [5] K. A. Paton, M. C. Veale, X. Mu, C. S. Allen, D. Maneuski, C. Kübel, V. O'Shea, A. I. Kirkland, and D. McGrouther. Quantifying the performance of a hybrid pixel detector with GaAs:Cr sensor for transmission electron microscopy [Data Collection]. [10.5525/gla.researchdata.1145](https://doi.org/10.5525/gla.researchdata.1145).
- [6] G. F. Knoll. *Radiation Detection and Measurement*. John Wiley & Sons Inc., 4th edition, 2010.
- [7] W. R. Leo. *Techniques for Nuclear and Particle Physics Experiments: A How-to Approach*. Springer-Verlag, 2nd edition, 1994.
- [8] R. Gauvin and G. L'Espérance. A Monte Carlo code to simulate the effect of fast secondary electrons on κ_{AB} factors and spatial resolution in the TEM. *Journal of Microscopy*, 168(2):153–167, 1992.

- [9] H. A. Bethe and W. Heitler. On the stopping of fast particles and on the creation of positive electrons. *Proceedings of the Royal Society of London. Series A*, 146(856):83 LP – 112, 1934.
- [10] H. A. Kramers. XCIII. On the theory of X-ray absorption and of the continuous X-ray spectrum. *The London, Edinburgh, and Dublin Philosophical Magazine and Journal of Science*, 46(275):836–871, 1923.
- [11] N. F. Mott and H. S. W. Massey. *The Theory of Atomic Collisions*. Clarendon Press, 3rd edition, 1965.
- [12] H. A. Bethe. Molière’s Theory of Multiple Scattering. *Physical Review Letters*, 89(6):1256–1266, 1953.
- [13] L. Reimer and H. Kohl. *Transmission Electron Microscopy: Physics of Image Formation*. Springer, 5th edition, 2008.
- [14] R. F. Egerton, P. Li, and M. Malac. Radiation damage in the TEM and SEM. *Micron*, 35(6):399–409, 2004.
- [15] C. Leroy and P-G. Rancoita. Particle interaction and displacement damage in silicon devices operated in radiation environments. *Reports on Progress in Physics*, 70(4):493–625, 2007.
- [16] L. Rossi, P. Fischer, T. Rohe, and N. Wermes. *Pixel Detectors: From Fundamentals to Applications*. Springer-Verlag, 2006.
- [17] M. Battaglia, D. Contarato, P. Denes, D. Doering, P. Giubilato, T. S. Kim, S. Mattiazzo, V. Radmilovic, and S. Zalusky. A rad-hard CMOS active pixel sensor for electron microscopy. *Nuclear Instruments and Methods in Physics Research, Section A: Accelerators, Spectrometers, Detectors and Associated Equipment*, 598(2):642–649, 2009.
- [18] G. McMullan, D M Cattermole, S Chen, R Henderson, X Llopart, C Summerfield, L Tlustos, and A R Faruqi. Electron imaging with Medipix2 hybrid pixel detector. *Ultramicroscopy*, 107(4-5):401–413, 2007.
- [19] D. Contarato, P. Denes, D. Doering, J. Joseph, and B. Krieger. Direct detection in Transmission Electron Microscopy with a 5 μm pitch CMOS pixel sensor. *Nuclear Instruments and Methods in Physics Research, Section A: Accelerators, Spectrometers, Detectors and Associated Equipment*, 635(1):69–73, 2011.
- [20] D. B. Williams and C. B. Carter. *Transmission Electron Microscopy: A Textbook for Materials Science*. Springer International Publishing, 2009.

- [21] H. Bethe. Bremsformel für Elektronen relativistischer Geschwindigkeit. *Zeitschrift für Physik*, 76:293–299, 1932.
- [22] E. J. Williams. Applications of the method of impact parameter in collisions. *Proceedings of the Royal Society of London. Series A, Containing Papers of a Mathematical and Physical Character*, 139(837):163–186, 1933.
- [23] H. W. Streitwolf. Zur Theorie der Sekundärelektronenemission von Metallen Der Anregungsprozeß. *Annals of Physics*, 458(3-4):183–196, 1959.
- [24] K. Murata, D. F. Kyser, and C. H. Ting. Monte Carlo simulation of fast secondary electron production in electron beam resists. *Journal of Applied Physics*, 52(7):4396–4405, 1981.
- [25] C. Møller. Über den Stoß zweier Teilchen unter Berücksichtigung der Retardation der Kräfte. *Zeitschrift für Physik*, 70(11-12):786–795, 1931.
- [26] C. M. Davisson and R. D. Evans. Gamma-Ray Absorption Coefficients. *Reviews of Modern Physics*, 24(2):79, 1952.
- [27] H. Spieler. Chapter 2 - Signal Formation and Acquisition. In *Semiconductor Detector Systems*. Oxford University Press, 2005.
- [28] S. Ramo. Currents Induced by Electron Motion. *Proceedings of the IRE*, 27(9):584–585, 1939.
- [29] B Mikulec. Development of segmented semiconductor arrays for quantum imaging. *Nuclear Instruments and Methods in Physics Research A*, 510:1–23, 2003.
- [30] C. Kittel. *Introduction to Solid State Physics*. John Wiley & Sons Inc., 8th edition, 2005.
- [31] G Lutz. *Semiconductor Radiation Detectors*. North-Holland, 2004.
- [32] H. Spieler. *Semiconductor Detector Systems*. Oxford University Press, 2005.
- [33] S. M. Sze. *Semiconductor Devices: Physics and Technology*. John Wiley & Sons Ltd., 2nd edition, 2002.
- [34] B. D. Cline, M. Bullough, K. Richardson, H. Thorpe, M. C. Veale, and M. D. Wilson. Characterisation of the performance of p-type Si detectors for hard X-ray spectroscopy. *Journal of Instrumentation*, 17(05):P05030, 2022.

- [35] G. Pellegrini, C. Fleta, F. Campabadal, S. Díez, M. Lozano, J. M. Rafí, and M. Ullán. Technology development of p-type microstrip detectors with radiation hard p-spray isolation. *Nuclear Instruments and Methods in Physics Research Section A: Accelerators, Spectrometers, Detectors and Associated Equipment*, 566(2):360–365, 2006.
- [36] Gianluigi Casse. Radiation hardness of p-type silicon detectors. *Nuclear Instruments and Methods in Physics Research Section A: Accelerators, Spectrometers, Detectors and Associated Equipment*, 612(3):464–469, 2010.
- [37] U. Fano. Ionization Yield of Radiations. II. The Fluctuations of the Number of Ions. *Physical Review*, 72:26–29, 1947.
- [38] S. Usman and A. Patil. Radiation detector deadtime and pile up: A review of the status of science. *Nuclear Engineering and Technology*, 50(7):1006–1016, 2018.
- [39] E. Frojdh, R. Ballabriga, M. Campbell, M. Fiederle, E. Hamann, T. Koenig, X. Llopart, D. de Paiva Magalhaes, and M. Zuber. Count rate linearity and spectral response of the Medipix3RX chip coupled to a 300 μ m silicon sensor under high flux conditions. *Journal of Instrumentation*, 9(4):C04028–C04028, 2014.
- [40] B. Plotkin-Swing, G. Corbin, S. De Carlo, N. Dellby, C. Hoermann, M. Hoffman, T. Lovejoy, C. Meyer, A. Mittelberger, R. Pantelic, L. Piazza, and O. Krivanek. Hybrid pixel direct detector for electron energy loss spectroscopy. *Ultramicroscopy*, 217:113067, 2020.
- [41] I. A. Cunningham. Chapter 2 Applied Linear-Systems Theory. In R. L. Van Metter, J. Beutel, and H. L. Kundel, editors, *The Handbook of Medical Imaging, Volume 1*, pages 79–96. SPIE Press, 2000.
- [42] A. Papoulis and S. U. Pillai. *Probability, Random Variables and Stochastic Processes*. McGraw-Hill Higher Education, 4th edition, 2017.
- [43] J. C. Dainty and R. Shaw. *Image Science: Principles, analysis and evaluation of photographic-type imaging processes*. Academic Press, 1974.
- [44] N. Wiener. Generalized harmonic analysis. *Acta Mathematica*, 55(1):117–258, 1930.
- [45] C.E. Shannon. Communication in the Presence of Noise. *Proceedings of the IRE*, 37(1):10–21, 1949.

- [46] H. Nyquist. Certain Topics in Telegraph Transmission Theory. *Transactions of the American Institute of Electrical Engineers*, 47(2):617–644, 1928.
- [47] R. Shaw. The equivalent quantum efficiency of the photographic process. *The Journal of Photographic Science*, 11(4):199–204, 1963.
- [48] G. McMullan, S. Chen, R. Henderson, and A. R. Faruqi. Detective quantum efficiency of electron area detectors in electron microscopy. *Ultramicroscopy*, 109(9):1126–1143, 2009.
- [49] R. S. Ruskin, Z. Yu, and N. Grigorieff. Quantitative characterization of electron detectors for transmission electron microscopy. *Journal of Structural Biology*, 184(3):385–393, 2013.
- [50] J. A. Mir, R. Clough, R. MacInnes, C. Gough, R. Plackett, I. Shipsey, H. Sawada, I. MacLaren, R. Ballabriga, D. Maneuski, V. O’Shea, D. McGrouther, and A. I. Kirkland. Characterisation of the Medipix3 detector for 60 and 80 keV electrons. *Ultramicroscopy*, 182:44–53, 2017.
- [51] J. P. van Schayck, E. van Genderen, E. Maddox, L. Roussel, H. Boulanger, E. Fröjdh, J-P. P. Abrahams, P. J. Peters, and R. B. G. Ravelli. Sub-pixel electron detection using a convolutional neural network. *Ultramicroscopy*, 218:113091, 2020.
- [52] L. de Broglie. Recherches sur la théorie des Quanta. *Annales de Physique*, 3:3–128, 1925.
- [53] G. B. Airy. On the diffraction of an annular aperture. *The London, Edinburgh, and Dublin Philosophical Magazine and Journal of Science*, 18(114):1–10, 1841.
- [54] P. P. Ewald. X-ray diffraction by finite and imperfect crystal lattices. *Proceedings of the Physical Society*, 52(1):167–174, 1940.
- [55] R. F. Egerton. *Electron Energy-Loss Spectroscopy in the Electron Microscope*. Springer, 3rd edition, 2011.
- [56] J. A. Venables, G. G. Hembree, J. Drucker, P. A. Crozier, and M. R. Scheinfein. The MIDAS project at ASU: John Cowley’s vision and practical results. *Journal of Electron Microscopy*, 54(3):151–162, 2005.
- [57] S. J. Pennycook, A. J. Craven, and L. M. Brown. Cathodoluminescence on a scanning transmission electron microscope. *Developments in Electron Microscopy and Analysis*, 1977.

- [58] D. Imeson, R.H. Milne, S.D. Berger, and D. McMullan. Secondary electron detection in the scanning transmission electron microscope. *Ultramicroscopy*, 17(3):243–249, 1985.
- [59] P. W. J. Linders and P. Hagemann. Mass determination of thin biological specimens using backscattered electrons: Application in quantitative x-ray microanalysis on an automated stem system. *Ultramicroscopy*, 11(1):13–19, 1983.
- [60] N. Shibata, S. D. Findlay, Y. Kohno, H. Sawada, Y. Kondo, and Y. Ikuhara. Differential phase-contrast microscopy at atomic resolution. *Nature Physics*, 8(8):611–615, 2012.
- [61] N. Shibata, T. Seki, G. Sánchez-Santolino, S. D. Findlay, Y. Kohno, T. Matsumoto, R. Ishikawa, and Y. Ikuhara. Electric field imaging of single atoms. *Nature Communications*, 2017.
- [62] S. McVitie, D. McGrouther, S. McFadzean, D.A. MacLaren, K.J. O’Shea, and M.J. Benitez. Aberration corrected lorentz scanning transmission electron microscopy. *Ultramicroscopy*, 152:57–62, 2015.
- [63] Y. Kohno, S. Morishita, and N. Shibata. New STEM/TEM Objective Lens for Atomic Resolution Lorentz Imaging. *Microscopy and Microanalysis*, 23(S1):456–457, 2017.
- [64] N. Shibata, Y. Kohno, A. Nakamura, S. Morishita, T. Seki, A. Kumamoto, H. Sawada, T. Matsumoto, S. D. Findlay, and Y. Ikuhara. Atomic resolution electron microscopy in a magnetic field free environment. *Nature Communications*, 10(1):2308, 2019.
- [65] H. Ibach and H. Lüth. *Solid-state physics: An introduction to principles of materials science*. Springer, 4th edition, 2010.
- [66] M. E. Haine, P. A. Einstein, and P. H. Borchers. Resistance bias characteristic of the electron microscope gun. *British Journal of Applied Physics*, 9(12):482, 1958.
- [67] L. W. Swanson and L. C. Crouser. Total-Energy Distribution of Field-Emitted Electrons and Single-Plane Work Functions for Tungsten. *Physical Review*, 163(3), 1967.
- [68] P. Kruit. Electron Sources. In C. B. Carter and Williams D. B., editors, *Transmission Electron Microscopy: Diffraction, Imaging, and Spectrometry*. Springer International Publishing, 2016.

- [69] H. Boersch. Experimentelle Bestimmung der Energieverteilung in thermisch ausgelösten Elektronenstrahlen. *Zeitschrift für Physik* 1954 139:2, 139(2):115–146, 1954.
- [70] M. Troyon and P. Zinzindohoué. Energy spread of different thermionic electron sources. In R. Uyeda, editor, *Electron Microscopy*, volume 1. Maruyen, 1966.
- [71] P. Zinzindohoué and M. Troyon. Energy spread of different field emission electron beams. In R. Uyeda, editor, *Electron Microscopy*, volume 1. Maruyen, 1966.
- [72] W. Glaser. Strenge Berechnung magnetischer Linsen der Feldform $H=H_0(1+(z/a)^2)$. *Zeitschrift für Physik* 1941 117:5, 117(5):285–315, 1941.
- [73] P. W. Hawkes. *Electron Optics and Electron Microscopy*. Taylor & Francis Ltd., 1972.
- [74] G. M. Macauley. *Skating on spin ice: On the application of Lorentz microscopy and numerical techniques to characterise phase transitions and non-equilibrium phenomena in artificial spin ices*. PhD thesis, University of Glasgow, 2020.
- [75] M. Lehmann and H. Lichte. Electron Waves, Interference & Coherence. In C. B. Carter and Williams D. B., editors, *Transmission Electron Microscopy: Diffraction, Imaging, and Spectrometry*. Springer International Publishing, 2016.
- [76] Eugene Hecht. *Optics*. Addison-Wesley, London, 4th edition, 2002.
- [77] S. J. Pennycook. Imaging in the STEM. In C. B. Carter and Williams D. B., editors, *Transmission Electron Microscopy: Diffraction, Imaging, and Spectrometry*. Springer International Publishing, 2016.
- [78] P. D. Nellist. The Principles of STEM Imaging. In S. J. Pennycook and P. D. Nellist, editors, *Scanning Transmission, Electron Microscopy: Imaging and Diffraction*. Springer, 2011.
- [79] M. Lehmann and H. Lichte. Electron Holography. In C. B. Carter and Williams D. B., editors, *Transmission Electron Microscopy: Diffraction, Imaging, and Spectrometry*. Springer International Publishing, 2016.
- [80] A. Thust. Focal-Series Reconstruction. In C. B. Carter and Williams D. B., editors, *Transmission Electron Microscopy: Diffraction, Imaging, and Spectrometry*. Springer International Publishing, 2016.
- [81] M. Haider, S. Uhlemann, and J. Zach. Upper limits for the residual aberrations of a high-resolution aberration-corrected STEM. *Ultramicroscopy*, 81(3), 2000.

- [82] J. M. Zuo and J. C. H. Spence. Electron Detectors. In *Advanced Transmission Electron Microscopy*. Springer, 2017.
- [83] A. R. Faruqi and G. McMullan. Electronic detectors for electron microscopy. *Quarterly Reviews of Biophysics*, 44(3):357–390, 2011.
- [84] J. M. Zuo. Electron detection characteristics of a slow-scan CCD camera, imaging plates and film, and electron image restoration. *Microscopy Research and Technique*, 49(3):245–268, 2000.
- [85] J. M. Zuo, M. R. McCartney, and J. C. H. Spence. Performance of imaging plates for electron recording. *Ultramicroscopy*, 66(1-2):35–47, 1996.
- [86] I. MacLaren, T. A. Macgregor, C. S. Allen, and A. I. Kirkland. Detectors—The ongoing revolution in scanning transmission electron microscopy and why this important to material characterization. *APL Materials*, 8(11):110901, 2020.
- [87] P. T. E. Roberts, J. N. Chapman, and A. M. MacLeod. A CCD-based image recording system for the CTEM. *Ultramicroscopy*, 8(4):385–396, 1982.
- [88] O. L. Krivanek and P. E. Mooney. Applications of slow-scan CCD cameras in transmission electron microscopy. *Ultramicroscopy*, 49(1-4):95–108, 1993.
- [89] I. Daberkow, K. H. Herrmann, L. Liu, and W. D. Rau. Performance of electron image converters with YAG single-crystal screen and CCD sensor. *Ultramicroscopy*, 38(3-4):215–223, 1991.
- [90] G. Y. Fan and M. H. Ellisman. High-sensitivity lens-coupled slow-scan CCD camera for transmission electron microscopy. *Ultramicroscopy*, 52(1):21–29, 1993.
- [91] R. R. Meyer and A. I. Kirkland. Characterisation of the signal and noise transfer of CCD cameras for electron detection. *Microscopy Research and Technique*, 49(3):269–280, 2000.
- [92] H. Yang, T. J. Pennycook, and P. D. Neillist. Efficient phase contrast imaging in STEM using a pixelated detector. Part II: Optimisation of imaging conditions. *Ultramicroscopy*, 2015.
- [93] S. Majert and H. Kohl. High-resolution STEM imaging with a quadrant detector—Conditions for differential phase contrast microscopy in the weak phase object approximation. *Ultramicroscopy*, 148:81–86, 2015.
- [94] J. N. Chapman. High resolution imaging of magnetic structures in the transmission electron microscope. *Materials Science and Engineering: B*, 3(4):355–358, 1989.

- [95] T. J. Pennycook, A. R. Lupini, H. Yang, M. F. Murfitt, L. Jones, and P. D. Nellist. Efficient phase contrast imaging in STEM using a pixelated detector. Part 1: Experimental demonstration at atomic resolution. *Ultramicroscopy*, 2015.
- [96] C. Ophus. Four-Dimensional Scanning Transmission Electron Microscopy (4D-STEM): From Scanning Nanodiffraction to Ptychography and Beyond. *Microscopy and Microanalysis*, 25(3):563–582, 2019.
- [97] W. Gao, C. Addiego, H. Wang, X. Yan, Y. Hou, D. Ji, C. Heikes, Y. Zhang, L. Li, H. Huyan, T. Blum, T. Aoki, Y. Nie, D. G. Schlom, R. Wu, and X. Pan. Real-space charge-density imaging with sub-ångström resolution by four-dimensional electron microscopy. *Nature*, 575(7783):480–484, 2019.
- [98] S. Fang, Y. Wen, C. S. Allen, C. Ophus, G. D. Han, A. I. Kirkland, E. Kaxiras, and J. H. Warner. Atomic electrostatic maps of 1D channels in 2D semiconductors using 4D scanning transmission electron microscopy. *Nature Communications*, 10(1):1127, 2019.
- [99] C. M. O’Leary, C. S. Allen, C. Huang, J. S. Kim, E. Liberti, P. D. Nellist, and A. I. Kirkland. Phase reconstruction using fast binary 4D STEM data. *Applied Physics Letters*, 116(12):124101, 2020.
- [100] L. Zhou, J. S. Song, J. and Kim, X. Pei, C. Huang, M. Boyce, L. Mendonça, D. Clare, A. Siebert, C. S. Allen, E. Liberti, D. Stuart, X. Pan, P. D. Nellist, P. Zhang, A. I. Kirkland, and P. Wang. Low-dose phase retrieval of biological specimens using cryo-electron ptychography. *Nature Communications*, 11(1):1–9, 2020.
- [101] T. Nakane, A. Kotecha, A. Sente, G. McMullan, S. Masiulis, P. M. G. E. Brown, I. T. Grigoras, L. Malinauskaite, T. Malinauskas, J. Miebling, T. Uchański, L. Yu, D. Karia, E. V. Pechnikova, E. de Jong, J. Keizer, M. Bischoff, J. McCormack, P. Tiemeijer, S. W. Hardwick, D. Y. Chirgadze, G. Murshudov, A. R. Aricescu, and S. H. W. Scheres. Single-particle cryo-EM at atomic resolution. *Nature*, 587(7832):152–156, 2020.
- [102] K. M. Yip, N. Fischer, E. Paknia, A. Chari, and H. Stark. Atomic-resolution protein structure determination by cryo-EM. *Nature*, 587(7832):157–161, 2020.
- [103] N. Grigorieff and S. C. Harrison. Near-atomic resolution reconstructions of icosahedral viruses from electron cryo-microscopy. *Current Opinion in Structural Biology*, 21(2):265–273, 2011.

- [104] A. C. Milazzo, P. Leblanc, F. Duttweiler, L. Jin, J. C. Bouwer, S. Peltier, M. Ellisman, F. Bieser, H. S. Matis, H. Wieman, P. Denes, S. Kleinfelder, and N. H. Xuong. Active pixel sensor array as a detector for electron microscopy. *Ultramicroscopy*, 104(2):152–159, 2005.
- [105] A. Merk, A. Bartesaghi, S. Banerjee, V. Falconieri, P. Rao, M. I. Davis, R. Pragani, M. B. Boxer, L. A. Earl, J. L. S. Milne, and S. Subramaniam. Breaking Cryo-EM Resolution Barriers to Facilitate Drug Discovery. *Cell*, 165(7):1698–1707, 2016.
- [106] F. Eisenstein, R. Danev, and M. Pilhofer. Improved applicability and robustness of fast cryo-electron tomography data acquisition. *Journal of Structural Biology*, 208(2):107–114, 2019.
- [107] M. T. B. Clabbers, M. W. Martynowycz, J. Hattne, B. L. Nannenga, and T. Gonen. Electron-counting MicroED data with the K2 and K3 direct electron detectors. *Journal of Structural Biology*, 214(4):107886, 2022.
- [108] Gatan Inc. K3 Direct Detection Cameras - Models 1025 and 1024. <https://www.gatan.com/datasheets/datasheet-k3-camera?modal=1>, Datasheet dated February 2022; downloaded 05.01.23.
- [109] J. R. Feathers, K. A. Spoth, and J. C. Fromme. Experimental evaluation of super-resolution imaging and magnification choice in single-particle cryo-EM. *Journal of Structural Biology: X*, 5:100047, 2021.
- [110] Gatan Inc. K3 IS Direct Detection Camera - Models 1026 and 1027. <https://www.gatan.com/datasheets/datasheet-k3-camera-0?modal=1>, Datasheet dated November 2020; downloaded 05.01.23.
- [111] A. A. Murthy, P. Masih Das, S. M. Ribet, C. Kopas, J. Lee, M. J. Reagor, L. Zhou, M. J. Kramer, M. C. Hersam, M. Checchin, A. Grassellino, R. dos Reis, V. P. Dravid, and A. Romanenko. Developing a Chemical and Structural Understanding of the Surface Oxide in a Niobium Superconducting Qubit. *ACS Nano*, 16(10):17257–17262, 2022.
- [112] P. A. Crozier. How to Get Something Out of Nothing (Almost!): Extracting Information from Noisy Data. *Microscopy and Microanalysis*, 28(S1):2976–2977, 2022.
- [113] S. Kanomi, H. Marubayashi, T. Miyata, K. Tsuda, and H. Jinnai. Nanodiffraction Imaging of Polymer Crystals. *Macromolecules*, 54(13):6028–6037, 2021.
- [114] Gatan Inc. Metro Counting Camera - Model 1130. <https://www.gatan.com/datasheets/datasheet-metro?modal=1>, Datasheet dated July 2022; downloaded 05.01.23.

- [115] Gatan Inc. Alpine Direct Detection Camera - Model 1124. <https://www.gatan.com/datasheets/datasheet-alpine?modal=1>, Datasheet dated July 2022; downloaded 05.01.23.
- [116] M. Kuijper, G. van Hoften, B. Janssen, R. Geurink, S. De Carlo, M. Vos, G. van Duinen, B. van Haeringen, and M. Storms. FEI's direct electron detector developments: Embarking on a revolution in cryo-TEM. *Journal of Structural Biology*, 192(2):179–187, 2015.
- [117] ThermoFischer Scientific. Falcon 4 Direct Electron Detector - Datasheet. <https://assets.thermofisher.com/TFS-Assets/MSD/Product-Information/Falcon-4-Detector-datasheet.pdf>, Datasheet dated June 2020, downloaded 05.01.23.
- [118] M. Obr, W. J. H. Hagen, R. A. Dick, L. Yu, A. Kotecha, and F. K. M. Schur. Exploring high-resolution cryo-ET and subtomogram averaging capabilities of contemporary DEDs. *Journal of Structural Biology*, 214(2):107852, 2022.
- [119] M. W. Martynowycz, M. T. B. Clabbers, J. Hattne, and T. Gonen. Ab initio phasing macromolecular structures using electron-counted MicroED data. *Nature Methods*, 19(6):724–729, 2022.
- [120] ThermoFischer Scientific. Falcon 4i Direct Electron Detector. <https://assets.thermofisher.com/TFS-Assets/MSD/Datasheets/falcon-detector-datasheet-ds0371.pdf>, Datasheet dated January 2022; downloaded 05.01.23.
- [121] Y. Yang, D. Arseni, W. Zhang, M. Huang, S. Lövestam, M. Schweighauser, A. Kotecha, A. G. Murzin, S. Y. Peak-Chew, J. Macdonald, I. Lavenir, H. J. Garringer, E. Gelpi, K. L. Newell, G. G. Kovacs, R. Vidal, B. Ghetti, B. Ryskeldi-Falcon, S. H. W. Scheres, and M. Goedert. Cryo-EM structures of amyloid-42 filaments from human brains. *Science*, 375(6577):167–172, 2022.
- [122] J. Ciston, I. J. Johnson, B. R. Draney, P. Ercius, E. Fong, A. Goldschmidt, J. M. Joseph, J. R. Lee, A. Mueller, C. Ophus, A. Selvarajan, D. E. Skinner, T. Stezelberger, C. S. Tindall, A. M. Minor, and P. Denes. The 4D Camera: Very High Speed Electron Counting for 4D-STEM. *Microscopy and Microanalysis*, 25(S2):1930–1931, 2019.
- [123] P. Ercius, I. Johnson, H. Brown, P. Pelz, S. Hsu, B. Draney, A. Fong, E. and Goldschmidt, J. Joseph, J. Lee, J. Ciston, C. Ophus, M. Scott, A. Selvarajan, D. Paul, D. Skinner, M. Hanwell, P. Harris, C. and Avery, T. Stezelberger, C. Tindall, R. Ramesh, A. Minor, and P. Denes. The 4D Camera – An 87 kHz Frame-rate Detector for Counted 4D-STEM Experiments. *Microscopy and Microanalysis*, 26(S2):1896–1897, 2020.

- [124] Direct Electron. Celeritas Camera - Ultra-Fast 4D STEM and *in situ* TEM. <https://directelectron.com/wp-content/uploads/2022/09/Celeritas-Product-Booklet.pdf>, Product booklet dated 20.07.22; downloaded 05.01.23.
- [125] S. Huang, C. Francis, J. Sunderland, V. Jambur, I. Szlufarska, and P. M. Voyles. Large Area, High Resolution Mapping of Approximate Rotational Symmetries in a Pd_{77.5}Cu₆Si_{16.5} Metallic Glass Thin Film. *Ultramicroscopy*, 241:113612, 2022.
- [126] Direct Electron. Apollo Camera - Ultra-Fast Electron Counting for cryoEM. <https://directelectron.com/wp-content/uploads/2022/09/Apollo-Product-Booklet.pdf>, Product booklet dated 19.07.22; downloaded 05.01.23.
- [127] Direct Electron. DE-16 Camera System - The Most Versatile Direct Detector Available. <https://directelectron.com/wp-content/uploads/2022/09/DE-16-Product-Booklet.pdf>, Product booklet dated 21.07.22; downloaded 05.01.23.
- [128] D. Chatterjee, A. Annamareddy, J. Ketkaew, J. Schroers, D. Morgan, and P. M. Voyles. Fast Surface Dynamics on a Metallic Glass Nanowire. *ACS Nano*, 15(7):11309–11316, 2021.
- [129] Barnaby D. A. Levin. Direct detectors and their applications in electron microscopy for materials science. *Journal of Physics: Materials*, 4(4):042005, 2021.
- [130] Direct Electron. DE-64 Camera System - Exceptional DQE Enormous Area for cryoEM. <https://directelectron.com/wp-content/uploads/2022/09/DE-64-Product-Booklet-1.pdf>, Product booklet dated 29.10.19; downloaded 05.01.23.
- [131] H. Sutherland, M. J. Conley, E. Emmott, J. Streetley, I. G. Goodfellow, and D. Bhella. The Cryo-EM Structure of Vesivirus 2117 Highlights Functional Variations in Entry Pathways for Viruses in Different Clades of the Vesivirus Genus. *Journal of Virology*, 95(13):10.1128/jvi.00282–21, 2021.
- [132] S. Inoue, K. Nikaido, T. Higashino, S. Arai, M. Tanaka, R. Kumai, S. Tsuzuki, S. Horiuchi, H. Sugiyama, Y. Segawa, K. Takaba, S. Maki-Yonekura, K. Yonekura, and T. Hasegawa. Emerging Disordered Layered-Herringbone Phase in Organic Semiconductors Unveiled by Electron Crystallography. *Chemistry of Materials*, 34(1):72–83, 2022.

- [133] J. Haney, S. Vijayakrishnan, J. Streetley, K. Dee, D. M. Goldfarb, M. Clarke, M. Mullin, S. D. Carter, D. Bhella, and P. R. Murcia. Coinfection by influenza A virus and respiratory syncytial virus produces hybrid virus particles. *Nature Microbiology*, 7(11):1879–1890, 2022.
- [134] Direct Electron. DE-DirectView Camera - Versatile and Economical Direct Detection. <https://directelectron.com/wp-content/uploads/2022/09/DE-DirectView-Product-Flyer.pdf>, Product booklet dated 29.10.19; downloaded 05.01.23.
- [135] M. Battaglia, D. Contarato, P. Denes, D. Doering, T. Duden, B. Krieger, P. Giubilato, D. Gnani, and V. Radmilovic. Characterisation of a CMOS active pixel sensor for use in the TEAM microscope. *Nuclear Instruments and Methods in Physics Research, Section A: Accelerators, Spectrometers, Detectors and Associated Equipment*, 622(3):669–677, 2010.
- [136] U. Dahmen. A Status Report on the TEAM Project. *Microscopy and Microanalysis*, 13(S02):1150–1151, 2007.
- [137] N. Guerrini, R. Turchetta, G. Van Hoften, R. Henderson, G. McMullan, and A. R. Faruqi. A high frame rate, 16 million pixels, radiation hard CMOS sensor. *Journal of Instrumentation*, 6(03):C03003, 2011.
- [138] A. R. Faruqi, R. Henderson, and J. Holmes. Radiation damage studies on STAR250 CMOS sensor at 300 keV for electron microscopy. *Nuclear Instruments and Methods in Physics Research, Section A: Accelerators, Spectrometers, Detectors and Associated Equipment*, 565(1):139–143, 2006.
- [139] M. Gallagher-Jones, C. Ophus, K. C. Bustillo, D. R. Boyer, O. Panova, C. Glynn, C. T. Zee, J. Ciston, K. C. Mancina, A. M. Minor, and J. A. Rodriguez. Nanoscale mosaicity revealed in peptide microcrystals by scanning electron nanodiffraction. *Communications Biology*, 2(1):1–8, 2019.
- [140] A. R. Faruqi, R. Henderson, M. Pryddetch, P. Allport, and A. Evans. Direct single electron detection with a CMOS detector for electron microscopy. *Nuclear Instruments and Methods in Physics Research, Section A: Accelerators, Spectrometers, Detectors and Associated Equipment*, 546(1-2):170–175, 2005.
- [141] J. Keizer, G. van Hoften, J. Mulder, and . van Duinen. Falcon 4 performance validation by single event analysis. *Microscopy and Microanalysis*, 27(S1):1338–1339, 2021.

- [142] P. L. Chiu, X. Li, Z. Li, B. Beckett, A. F. Brilot, N. Grigorieff, D. A. Agard, Y. Cheng, and T. Walz. Evaluation of super-resolution performance of the K2 electron-counting camera using 2D crystals of aquaporin-0. *Journal of Structural Biology*, 192(2):163–173, 2015.
- [143] X. Li, P. Mooney, S. Zheng, C. R. Booth, M. B. Braunfeld, S. Gubbens, D. A. Agard, and Y. Cheng. Electron counting and beam-induced motion correction enable near-atomic-resolution single-particle cryo-EM. *Nature Methods*, 10(6):584–590, 2013.
- [144] X. Li, S. Q. Zheng, K. Egami, D. A. Agard, and Y. Cheng. Influence of electron dose rate on electron counting images recorded with the K2 camera. *Journal of Structural Biology*, 184(2), 2013.
- [145] F. Wang, M. P. Echlin, A. A. Taylor, J. Shin, B. Bammes, B. D.A. Levin, M. De Graef, T. M. Pollock, and D. S. Gianola. Electron backscattered diffraction using a new monolithic direct detector: High resolution and fast acquisition. *Ultramicroscopy*, 220:113160, 2021.
- [146] J. L. Hart, A. C. Lang, A. C. Leff, P. Longo, C. Trevor, R. D. Twesten, and M. L. Taheri. Direct Detection Electron Energy-Loss Spectroscopy: A Method to Push the Limits of Resolution and Sensitivity. *Scientific Reports*, 7(1):8243, 2017.
- [147] Alan Maigné and Matthias Wolf. Low-dose electron energy-loss spectroscopy using electron counting direct detectors. *Microscopy*, 67:86–97, 2018.
- [148] M. Haruta, J. Kikkawa, K. Kimoto, and H. Kurata. Comparison of detection limits of direct-counting CMOS and CCD cameras in EELS experiments. *Ultramicroscopy*, 240:113577, 2022.
- [149] J. Hattne, M. W. Martynowycz, P. A. Penczek, and T. Gonen. MicroED with the Falcon III direct electron detector. *IUCrJ*, 6(5):921–926, 2019.
- [150] B. Bammes, W. Zhou, and W. Chiu. Sub-Ångström-resolution MicroED Using a Direct Detection Camera. *Microscopy and Microanalysis*, 26(S2):1524–1526, 2020.
- [151] K. Takaba, S. Maki-Yonekura, S. Inoue, T. Hasegawa, and K. Yonekura. Protein and Organic-Molecular Crystallography With 300kV Electrons on a Direct Electron Detector. *Frontiers in Molecular Biosciences*, 7, 2021.
- [152] M. T. B. Clabbers, M. W. Martynowycz, J. Hattne, and T. Gonen. Hydrogens and hydrogen-bond networks in macromolecular MicroED data. *Journal of Structural Biology: X*, 6:100078, 2022.

- [153] A. R. Faruqi and R. Henderson. Electronic detectors for electron microscopy. *Current Opinion in Structural Biology*, 17:549–555, 2007.
- [154] R. Coath, J. Crooks, A. Godbeer, M. Wilson, and R. Turchetta. Advanced pixel architectures for scientific image sensors. *Proceedings of the Topical Workshop on Electronics for Particle Physics*, pages 57–61, 2009.
- [155] M. T.B. Clabbers, E. van Genderen, W. Wan, E. L. Wiegers, T. Gruene, and J. P. Abrahams. Protein structure determination by electron diffraction using a single three-dimensional nanocrystal. *Acta Crystallographica Section D: Structural Biology*, 2017.
- [156] E. Van Genderen, M. T. B. Clabbers, P. P. Das, A. Stewart, I. Nederlof, K. C. Barentsen, Q. Portillo, N. S. Pannu, S. Nicolopoulos, and T. Gruene. *Ab initio* structure determination of nanocrystals of organic pharmaceutical compounds by electron diffraction at room temperature using a Timepix quantum area direct electron detector. *Acta Crystallographica Section A*, 72(2):236–242, 2016.
- [157] M. Krajenak, D. McGrouther, D. Maneuski, V. O’Shea, and S. McVitie. Pixelated detectors and improved efficiency for magnetic imaging in STEM differential phase contrast. *Ultramicroscopy*, 165:42–50, 2016.
- [158] J. Song, C. S. Allen, S. Gao, C. Huang, H. Sawada, X. Pan, J. Warner, P. Wang, and A. I. Kirkland. Atomic Resolution Defocused Electron Ptychography at Low Dose with a Fast, Direct Electron Detector. *Scientific Reports*, 9(1):3919, 2019.
- [159] G. W. Paterson, R. J. Lamb, R. Ballabruga, D. Maneuski, V. O’Shea, and D. McGrouther. Sub-100 nanosecond temporally resolved imaging with the Medipix3 direct electron detector. *Ultramicroscopy*, 210:112917, 2020.
- [160] A. I. Kirkland, C. S. Allen, E. Besley, C. Huang, J. Kim, S. Skowron, and J. Warner. Observing Structural Dynamics and Measuring Chemical Kinetics in Low Dimensional Materials Using High Speed Imaging. *Microscopy and Microanalysis*, 25(S2):1682–1683, 2019.
- [161] M. W. Tate, P. Purohit, D. Chamberlain, K. X. Nguyen, R. Hovden, C. S. Chang, P. Deb, E. Turgut, J. T. Heron, D. G. Schlom, D. C. Ralph, G. D. Fuchs, K. S. Shanks, H. T. Philipp, D. A. Muller, and S. M. Gruner. High Dynamic Range Pixel Array Detector for Scanning Transmission Electron Microscopy. *Microscopy and Microanalysis*, 22(1):237–249, 2016.

- [162] A. Mozzanica, A. Bergamaschi, S. Cartier, R. Dinapoli, D. Greiffenberg, I. Johnson, J. Jungmann, D. Maliakal, D. Mezza, C. Ruder, L. Schaedler, B. Schmitt, X. Shi, and G. Tinti. Prototype characterization of the JUNGFRÄU pixel detector for SwissFEL. *Journal of Instrumentation*, 9(05):C05010–C05010, 2014.
- [163] E. Fröjdh, J. T. C. Wennmacher, P. Rzepka, A. Mozzanica, S. Redford, B. Schmitt, J. A. van Bokhoven, and T. Gruene. Discrimination of Aluminum from Silicon by Electron Crystallography with the JUNGFRÄU Detector. *Crystals*, 10(12):1148, 2020.
- [164] H. T. Philipp, M. W. Tate, K. S. Shanks, L. Mele, M. Peemen, P. Dona, R. Hartong, G. van Veen, Y-T. Shao, Z. Chen, J. Thom-Levy, D. A. Muller, and S. M. Gruner. Very-High Dynamic Range, 10,000 Frames/Second Pixel Array Detector for Electron Microscopy. *Microscopy and Microanalysis*, 28(2):425–440, 2022.
- [165] Gatan Inc. Stela Hybrid-Pixel Camera - Model 1015. <https://www.gatan.com/datasheets/datasheet-stela-camera?modal=1>, Datasheet dated October 2021; downloaded 05.01.23.
- [166] A. A. Murthy, P. Masih Das, S. M. Ribet, C. Kopas, J. Lee, M. J. Reagor, L. Zhou, M. J. Kramer, M. C. Hersam, M. Checchin, A. Grassellino, R. dos Reis, V. P. Dravid, and A. Romanenko. Developing a Chemical and Structural Understanding of the Surface Oxide in a Niobium Superconducting Qubit. *ACS Nano*, 16:17257–17262, 2022.
- [167] H. Ryll, K. Müller, S. Ihle, H. Soltau, Ivan Ordavo, Andreas Liebel, Robert Hartmann, Andreas Rosenauer, and Lothar Strüder. Results of a pnCCD Based Ultrafast Direct Single Electron Imaging Camera for Transmission Electron Microscopy. *Microscopy and Microanalysis*, 19(S2):1160–1161, 2013.
- [168] M. Simson, H. Ryll, H. Banba, R. Hartmann, M. Huth, S. Ihle, L. Jones, Y. Kondo, K. Muller, P. D. Nellist, R. Sagawa, J. Schmidt, H. Soltau, L. Striider, and H. Yang. 4D-STEM Imaging With the pnCCD (S)TEM-Camera. *Microscopy and Microanalysis*, 21(S3):2211–2212, 2015.
- [169] H. Ryll, M. Simson, M. Den Hertog, R. Dunin-Borkowski, K. El Hajraoui, R. Hartmann, M. Huth, S. Ihle, V. Migunov, J. Schmidt, H. Soltau, and L. Striider. Imaging At the Timescale Of Micro- and Milliseconds With the pnCCD (S)TEM Camera. *Microscopy and Microanalysis*, 21(S3):1585–1586, 2015.
- [170] Y. Jiang, Z. Chen, Y. Han, P. Deb, H. Gao, S. Xie, P. Purohit, M. W. Tate, J. Park, S. M. Gruner, V. Elser, and D. A. Muller. Electron ptychography of 2D materials to deep sub-ångström resolution. *Nature*, 559(7714):343–349, 2018.

- [171] DECTRIS AG. DECTRIS ARINA - An ultra-fast 4D STEM hybrid-pixel detector. https://media.dectris.com/220712-Brochure-DECTRIS_ARINA.pdf, Customer brochure dated July 2022; downloaded 05.01.23.
- [172] DECTRIS AG. DECTRIS ELA - A new hybrid pixel electron detector. https://media.dectris.com/210605-Brochure-DECTRIS_ELA.pdf, Customer brochure dated 05.06.21; downloaded 05.01.23.
- [173] DECTRIS AG. DECTRIS SINGLA - A new hybrid pixel electron detector. https://media.dectris.com/220627-DECTRIS_SINGLA-Brochure.pdf, Customer brochure dated 05.06.21; downloaded 05.01.23.
- [174] K. Naydenova, G. McMullan, M. J. Peet, Y. Lee, P. C. Edwards, S. Chen, E. Leahy, S. Scotcher, R. Henderson, and C. J. Russo. CryoEM at 100keV: A demonstration and prospects. *IUCrJ*, 6(6):1086–1098, 2019.
- [175] T. Gruene, J. T. C. Wennmacher, C. Zaubitzer, J. J. Holstein, J. Heidler, A. Fecteau-Lefebvre, S. De Carlo, E. Müller, K. N. Goldie, I. Regeni, T. Li, G. Santiso-Quinones, G. Steinfeld, S. Handschin, E. van Genderen, J. A. van Bokhoven, G. H. Clever, and R. Pantelic. Rapid Structure Determination of Microcrystalline Molecular Compounds Using Electron Diffraction. *Angewandte Chemie International Edition*, 57(50):16313–16317, 2018.
- [176] DECTRIS AG. QUADRO - The fastest direct electron detector for Materials Science. https://media.dectris.com/220414-Brochure-DECTRIS_QUADRO.pdf, Customer brochure dated 14.04.22; downloaded 05.01.23.
- [177] R. Ballabriga, J. Alozy, G. Blaj, M. Campbell, M. Fiederle, E. Frojdh, E. H. M. Heijne, X. Llopart, M. Pichotka, S. Procz, L. Tlustos, and W. Wong. The Medipix3RX: A high resolution, zero dead-time pixel detector readout chip allowing spectroscopic imaging. *Journal of Instrumentation*, 8(02):C02016, 2013.
- [178] M. Tencé, J-D. Blazit, X. Li, M. Krajnak, E. Nebot del Busto, R. Skogeby, L. Cambou, M. Kociak, O. Stephan, and A. Gloter. Electron Energy-loss Spectroscopy Using MerlinEM - Medipix3 Detector. *Microscopy and Microanalysis*, 26(S2):1940–1942, 2020.
- [179] R. Bücker, P. Hogan-Lamarre, P. Mehrabi, E. C. Schulz, L. A. Bultema, Y. Gevorkov, W. Brehm, O. Yefanov, D. Oberthür, G. H. Kassier, and R. J. Dwayne Miller. Serial protein crystallography in an electron microscope. *Nature Communications*, 11(1):1–8, 2020.

- [180] T. Poikela, J. Plosila, T. Westerlund, M. Campbell, M. De Gaspari, X. Llopart, V. Gromov, R. Kluit, M. Van Beuzekom, F. Zappone, V. Zivkovic, C. Brezina, K. Desch, Y. Fu, and A. Kruth. Timepix3: A 65K channel hybrid pixel readout chip with simultaneous ToA/ToT and sparse readout. *Journal of Instrumentation*, 9(5):C05013–C05013, 2014.
- [181] D. Jannis, C. Hofer, C. Gao, X. Xie, A. Béch e, T. J. Pennycook, and J. Verbeeck. Event driven 4D STEM acquisition with a Timepix3 detector: Microsecond dwell time and faster scans for high precision and low dose applications. *Ultramicroscopy*, 233:113423, 2022.
- [182] Y. Auad, M. Walls, J-D. Blazit, O. St ephan, L. H. G. Tizei, M. Kociak, F. De la Pe na, and M. Tenc e. Event-based hyperspectral EELS: towards nanosecond temporal resolution. *Ultramicroscopy*, 239:113539, 2022.
- [183] I. Johnson, A. Bergamaschi, H. Billich, S. Cartier, R. Dinapoli, D. Greiffenberg, M. Guizar-Sicairos, B. Henrich, J. Jungmann, D. Mezza, A. Mozzanica, B. Schmitt, X. Shi, and G. Tinti. Eiger: A single-photon counting x-ray detector. *Journal of Instrumentation*, 9(5), 2014.
- [184] G. Tinti, E. Fr ojdh, E. van Genderen, T. Gruene, B. Schmitt, D. A. Matthijs De Winter, B. M. Weckhuysen, and J. P. Abrahams. Electron crystallography with the EIGER detector. *IUCrJ*, 5(2):190–199, 2018.
- [185] X. Llopart, R. Ballabriga, M. Campbell, L. Tlustos, and W. Wong. Timepix, a 65k programmable pixel readout chip for arrival time, energy and/or photon counting measurements. *Nuclear Instruments and Methods in Physics Research Section A: Accelerators, Spectrometers, Detectors and Associated Equipment*, 581(1-2):485–494, 2007.
- [186] R. Beacham, A. Mac Raighne, D. Maneuski, V. O’Shea, S. McVitie, D. McGrouther, A Mac Raighne, D. Maneuski, V. O’Shea, S. McVitie, and D. McGrouther. Medipix2/Timepix detector for time resolved Transmission Electron Microscopy. *Journal of Instrumentation*, 6(12):C12052–C12052, 2011.
- [187] S. Vespucchi, A. Winkelmann, G. Naresh-Kumar, K. P. Mingard, D. Maneuski, P. R. Edwards, A. P. Day, V. O’Shea, and C. Trager-Cowan. Digital direct electron imaging of energy-filtered electron backscatter diffraction patterns. *Physical Review B*, 92(20):205301, 2015.
- [188] S. Vespucchi, A. Winkelmann, K. Mingard, D. Maneuski, V. O’Shea, and C. Trager-Cowan. Exploring transmission Kikuchi diffraction using a Timepix detector. *Journal of Instrumentation*, 12(02):C02075–C02075, 2017.

- [189] M. Battaglia, D. Contarato, P. Denes, and P. Giubilato. Cluster imaging with a direct detection CMOS pixel sensor in Transmission Electron Microscopy. *Nuclear Instruments and Methods in Physics Research, Section A: Accelerators, Spectrometers, Detectors and Associated Equipment*, 608(2):363–365, 2009.
- [190] C. Teyssier, P. Allard Guérin, G. Bergeron, F. Dallaire, C. Leroy, S. Pospisil, and Y. B. Trudeau. *Exploitation of the charge sharing effect in Timepix device to achieve sub-pixel resolution in imaging applications with alpha particles.*, pages 681–687. World Scientific Publishing, 2012.
- [191] L. Strüder, U. Briel, K. Dennerl, R. Hartmann, E. Kendziorra, N. Meidinger, E. Pfeffermann, C. Reppin, B. Aschenbach, W. Bornemann, H. Bräuninger, W. Burkert, M. Elender, M. Freyberg, F. Haberl, G. Hartner, F. Heuschmann, H. Hippmann, E. Kastelic, S. Kemmer, G. Kettenring, W. Kink, N. Krause, S. Müller, A. Oppitz, W. Pietsch, M. Popp, P. Predehl, A. Read, K. H. Stephan, D. Stötter, J. Trümper, P. Holl, J. Kemmer, H. Soltau, R. Stötter, U. Weber, U. Weichert, C. von Zanthier, D. Carathanassis, G. Lutz, R. H. Richter, P. Solc, H. Böttcher, M. Kuster, R. Staubert, A. Abbey, A. Holland, M. Turner, M. Balasini, G. F. Bignami, N. La Palombara, G. Villa, W. Buttler, F. Gianini, R. Lainé, D. Lumb, and P. Dhez. The European Photon Imaging Camera on XMM-Newton: The pn-CCD camera. *Astronomy & Astrophysics*, 365(1):L18–L26, 2001.
- [192] L. Strüder, S. Epp, D. Rolles, R. Hartmann, P. Holl, G. Lutz, H. Soltau, R. Eckart, C. Reich, K. Heinzinger, C. Thamm, A. Rudenko, F. Krasniqi, K. U. Kühnel, C. Bauer, C. D. Schröter, R. Moshhammer, S. Techert, D. Miessner, M. Porro, O. Hälker, N. Meidinger, N. Kimmel, R. Andritschke, F. Schopper, G. Weidenspointner, A. Ziegler, D. Pietschner, S. Herrmann, U. Pietsch, A. Walenta, W. Leitenberger, C. Bostedt, T. Möller, D. Rupp, M. Adolph, H. Graafsma, H. Hirsemann, K. Gärtner, R. Richter, L. Foucar, R. L. Shoeman, I. Schlichting, and J. Ullrich. Large-format, high-speed, X-ray pnCCDs combined with electron and ion imaging spectrometers in a multipurpose chamber for experiments at 4th generation light sources. *Nuclear Instruments and Methods in Physics Research Section A: Accelerators, Spectrometers, Detectors and Associated Equipment*, 614(3):483–496, 2010.
- [193] M. Huth, S. Ihle, R. Ritz, M. Simson, H. Soltau, V. Migunov, M. Duchamp, R.E. Dunin-Borkowski, H. Ryll, and L. Strüder. Electric and Magnetic Field Mapping With the pnCCD (S)TEM Camera. *Microscopy and Microanalysis*, 22(S3):256–257, 2016.

- [194] A. Ziegler, R. Hartmann, R. Andritschke, F. Schopper, L. Strüder, H. Soltau, and J. M. Plitzko. Results of a pnCCD Detector for Direct Single-Electron Imaging in Cryo-TEM. *Microscopy and Microanalysis*, 13(S02):392–393, 2007.
- [195] B. Eckert, S. Aschauer, P. Holl, P. Majewski, T. Zabel, and L. Strüder. Electron Imaging Reconstruction for Pixelated Semiconductor Tracking Detectors in Transmission Electron Microscopes Using the Approach of Convolutional Neural Networks. *IEEE Transactions on Nuclear Science*, 69(5):1014–1021, 2022.
- [196] P. Pelz, P. Ercius, C. Ophus, I. Johnson, and M. Scott. Real-time interactive ptychography from electron event representation data. *Microscopy and Microanalysis*, 27(S1):188–189, 2021.
- [197] M. J. Peet, R. Henderson, and C. J. Russo. The energy dependence of contrast and damage in electron cryomicroscopy of biological molecules. *Ultramicroscopy*, 203:125–131, aug 2019.
- [198] M. Fiederle, S. Procz, E. Hamann, A. Fauler, and C. Fröjdh. Overview of GaAs und CdTe Pixel Detectors Using Medipix Electronics. *Crystal Research and Technology*, 55(9):2000021, 2020.
- [199] S. Tsigaridas and C. Ponchut. High-Z Pixel Sensors for Synchrotron Applications. In K. Iniewski, editor, *Advanced X-ray Detector Technologies: Design and Applications*, pages 87–107. Springer International Publishing, 2022.
- [200] A. Bergamaschi, A. Mozzanica, and B. Schmitt. XFEL detectors. *Nature Reviews Physics*, 2(7):335–336, 2020.
- [201] O. Grimm. CdTe Sensors for Space-Based X-ray Detectors. In K. Iniewski, editor, *Advanced X-ray Detector Technologies: Design and Applications*, pages 109–133. Springer International Publishing, 2022.
- [202] T. E. Schlesinger, J. E. Toney, H Yoon, E. Y. Lee, B. A. Brunett, L Franks, and R. B. James. Cadmium zinc telluride and its use as a nuclear radiation detector material. *Materials Science and Engineering: R: Reports*, 32(4-5):103–189, 2001.
- [203] S. Del Sordo, L. Abbene, E. Caroli, A. M. Mancini, A. Zappettini, and P. Ubertini. Progress in the Development of CdTe and CdZnTe Semiconductor Radiation Detectors for Astrophysical and Medical Applications. *Sensors*, 9(5):3491–3526, 2009.

- [204] M. C. Veale, S. J. Bell, D. D. Duarte, M. J. French, A. Schneider, P. Seller, M. D. Wilson, A. D. Lozinskaya, V. A. Novikov, O. P. Tolbanov, A. Tyazhev, and A. N. Zarubin. Chromium compensated gallium arsenide detectors for X-ray and γ -ray spectroscopic imaging. *Nuclear Instruments and Methods in Physics Research, Section A: Accelerators, Spectrometers, Detectors and Associated Equipment*, 752:6–14, 2014.
- [205] D. Greiffenberg, M. Andrä, R. Barten, A. Bergamaschi, P. Busca, M. Brückner, S. Chiriotti Alvarez, I. Chsherbakov, R. Dinapoli, P. Fajardo, E. Fröjdh, C. Lopez-Cuenca, A. Lozinskaya, M. Meyer, D. Mezza, A. Mozzanica, S. Redford, M. Ruat, C. Ruder, B. Schmitt, X. Shi, D. Thattil, G. Tinti, O. Tolbanov, A. Tyazhev, S. Vetter, A. Zarubin, and J. Zhang. Characterization of GaAs:Cr sensors using the charge-integrating JUNGFRU readout chip. *Journal of Instrumentation*, 14(05):P05020–P05020, 2019.
- [206] D. Greiffenberg, M. Andrä, R. Barten, A. Bergamaschi, M. Brückner, P. Busca, S. Chiriotti, I. Chsherbakov, R. Dinapoli, P. Fajardo, E. Fröjdh, S. Hasanaj, P. Kozłowski, C. Lopez Cuenca, A. Lozinskaya, M. Meyer, D. Mezza, A. Mozzanica, S. Redford, M. Ruat, C. Ruder, B. Schmitt, D. Thattil, G. Tinti, O. Tolbanov, A. Tyazhev, S. Vetter, A. Zarubin, and J. Zhang. Characterization of Chromium Compensated GaAs Sensors with the Charge-Integrating JUNGFRU Readout Chip by Means of a Highly Collimated Pencil Beam. *Sensors*, 21(4):1550, 2021.
- [207] C. Toyokawa, H. and Saji, M. Kawase, K. Ohara, A. Shiro, R. Yasuda, T. Shobu, A. Suenaga, and H. Ikeda. Development of CdTe Pixel Detectors for Energy-Resolved X-ray Diffractions. *Proceedings of the Second International Symposium on Radiation Detectors and Their Uses (ISR2018)*, 24(24), 2019.
- [208] B. Thomas, M. C. Veale, M. D. Wilson, P. Seller, A. Schneider, and K. Iniewski. Characterisation of Redlen high-flux CdZnTe. *Journal of Instrumentation*, 12:C12045, 2017.
- [209] E. H.M. Heijne. History and future of radiation imaging with single quantum processing pixel detectors. *Radiation Measurements*, 140:106436, 2021.
- [210] E. H.M. Heijne. Semiconductor micropattern pixel detectors: A review of the beginnings. *Nuclear Instruments and Methods in Physics Research, Section A: Accelerators, Spectrometers, Detectors and Associated Equipment*, 465(1):1–26, 2001.

- [211] C. Da Via, R. Bates, E. Bertolucci, U. Bottigli, M. Campbell, E. Chesi, M. Conti, S. D'Auria, C. DelPapa, M. E. Fantacci, G. Grossi, E. Heijne, E. Mancini, P. Middelkamp, C. Raine, P. Russo, V. O'Shea, L. Scharfetter, K. Smith, W. Snoeys, and A. Stefanini. Gallium arsenide pixel detectors for medical imaging. *Nuclear Instruments and Methods in Physics Research Section A: Accelerators, Spectrometers, Detectors and Associated Equipment*, 395(1):148–151, 1997.
- [212] M. Campbell, E. H.M. Heijne, G. Meddeler, E. Pernigotti, and W. Snoeys. A Readout Chip for a 64×64 Pixel Matrix with 15-bit Single Photon Counting. *IEEE Transactions on Nuclear Science*, 45:751–753, 1998.
- [213] C. Schwarz, M. Campbell, R. Goeppert, E. H.M. Heijne, J. Ludwig, G. Meddeler, B. Mikulec, E. Pernigotti, M. Rogalla, K. Runge, A. Söldner-Rembold, K. M. Smith, W. Snoeys, and J. Watt. X-ray imaging using a hybrid photon counting GaAs pixel detector. *Nuclear Physics B - Proceedings Supplements*, 78(1-3):491–496, 1999.
- [214] B. Mikulec, M. Campbell, G. Dipasquale, C. Schwarz, and J. Watt. Characterization of a single photon counting pixel system for imaging of low-contrast objects. *Nuclear Instruments and Methods in Physics Research, Section A: Accelerators, Spectrometers, Detectors and Associated Equipment*, 458(1-2):352–359, 2001.
- [215] D. Pennicard, B. Struth, H. Hirsemann, M. Sarajlic, S. Smoljanin, M. Zuvic, M.O. Lampert, T. Fritsch, M. Rothermund, and H. Graafsma. A germanium hybrid pixel detector with $55\mu\text{m}$ pixel size and 65,000 channels. *Journal of Instrumentation*, 9(12):12003–12003, 2014.
- [216] J. Becker, M.W. Tate, K.S. Shanks, H.T. Philipp, J.T. Weiss, P. Purohit, D. Chamberlain, and S.M. Gruner. Sub-microsecond x-ray imaging using hole-collecting Schottky type CdTe with charge-integrating pixel array detectors. *Journal of Instrumentation*, 12(06):06022–06022, 2017.
- [217] A. C. Thompson. *X-Ray Data Booklet*. Lawrence Berkeley National Laboratory, University of California, 3rd edition, 2009.
- [218] D. Pennicard and H. Graafsma. Simulated performance of high-Z detectors with Medipix3 readout. *Journal of Instrumentation*, 6(6):06007–06007, 2011.
- [219] S. Chiriotti, R. Barten, A. Bergamaschi, M. Brückner, M. Carulla, I. Chsherbakov, R. Dinapoli, E. Fröjd, D. Greiffenberg, S. Hasanaj, V. Hinger, T. King, P. Kozłowski, C. Lopez-Cuenca, A. Lozinskaya, F. Marone, D. Mezza, K. Moustakas, A. Mozzanica, C. Ruder, B. Schmitt, D. Thattil, O. Tolbanov, A. Tyazhev,

- A. Zarubin, and J. Zhang. High-spatial resolution measurements with a GaAs:Cr sensor using the charge integrating MÖNCH detector with a pixel pitch of 25 μm . *Journal of Instrumentation*, 17(04):04007, 2022.
- [220] Ad. Cola and I. Farella. The polarization mechanism in CdTe Schottky detectors. *Applied Physics Letters*, 94(10):102113, 2009.
- [221] E. N. Gimenez, V. Astromskas, I. Horswell, D. Omar, J. Spiers, and N. Tartoni. Development of a Schottky CdTe Medipix3RX hybrid photon counting detector with spatial and energy resolving capabilities. *Nuclear Instruments and Methods in Physics Research Section A: Accelerators, Spectrometers, Detectors and Associated Equipment*, 824:101–103, 2016.
- [222] V. , E. N. Gimenez, A. Lohstroh, and N. Tartoni. Evaluation of Polarization Effects of e^- Collection Schottky CdTe Medipix3RX Hybrid Pixel Detector. *IEEE Transactions on Nuclear Science*, 63(1):252–258, 2016.
- [223] S. Tsigaridas, C. Ponchut, S. Zanettini, and A. Zappettini. Characterisation of pixelated CdZnTe sensors using MAXIPIX. *Journal of Instrumentation*, 14(12):C12009–C12009, 2019.
- [224] M. Prokesch, S. A. Soldner, A. G. Sundaram, M. D. Reed, H. Li, J. F. Eger, J. L. Reiber, C. L. Shanor, C. L. Wray, A. J. Emerick, A. F. Peters, and C. L. Jones. CdZnTe Detectors Operating at X-ray Fluxes of 100 Million Photons/(mm^2sec). *IEEE Transactions on Nuclear Science*, 63(3), 2016.
- [225] M. C. Veale, P. Booker, S. Cross, M. D. Hart, L. Jowitt, J. Lipp, A. Schneider, P. Seller, R. M. Wheeler, M. D. Wilson, C. C T. Hansson, K. Iniewski, P. Marthandam, and G. Prekas. Characterization of the Uniformity of High-Flux CdZnTe Material. *Sensors*, 20(10):2747, 2020.
- [226] K. Iniewski. CZT sensors for Computed Tomography: from crystal growth to image quality. *Journal of Instrumentation*, 11(12):C12034–C12034, 2016.
- [227] M. C. Veale, L. L. Jones, B. Thomas, P. Seller, M. D. Wilson, and K. Iniewski. Improved spectroscopic performance in compound semiconductor detectors for high rate X-ray and gamma-ray imaging applications: A novel depth of interaction correction technique. *Nuclear Instruments and Methods in Physics Research Section A: Accelerators, Spectrometers, Detectors and Associated Equipment*, 927:37–45, 2019.
- [228] A. Zwerger, A. Fauler, M. Fiederle, and K. Jakobs. Medipix2: Processing and measurements of GaAs pixel detectors. *Nuclear Instruments and Methods in Physics Research, Section A: Accelerators, Spectrometers, Detectors and Associated Equipment*, 576(1):23–26, 2007.

- [229] L. Tlustos, M. Campbell, C. Fröjdh, . Kostamo, and S. Nenonen. Characterisation of an epitaxial GaAs/Medipix2 detector using fluorescence photons. *Nuclear Instruments and Methods in Physics Research, Section A: Accelerators, Spectrometers, Detectors and Associated Equipment*, 591(1):42–45, 2008.
- [230] L. Tlustos, G. Shelkov, and O. P. Tolbanov. Characterisation of a GaAs(Cr) Medipix2 hybrid pixel detector. *Nuclear Instruments and Methods in Physics Research, Section A: Accelerators, Spectrometers, Detectors and Associated Equipment*, 633:S103–S107, 2011.
- [231] A. Erd, C. aand Owens, G. Brammertz, M. Bavdaz, A. Peacock, V. Lämsä, S. Nenonen, H. Andersson, and N. Haack. Hard X-ray test and evaluation of a prototype 32×32 pixel gallium-arsenide array. *Nuclear Instruments and Methods in Physics Research, Section A: Accelerators, Spectrometers, Detectors and Associated Equipment*, 487(1-2):78–89, 2002.
- [232] C. Erd, A. Owens, G. Brammertz, D. H. Lumb, M. Bavdaz, A. J. Peacock, S. A. A. Nenonen, and H. Andersson. Measurements of the quantum efficiency and depletion depth in gallium-arsenide detectors. *X-Ray and Gamma-Ray Detectors and Applications IV*, 4784:386–393, 2003.
- [233] A. I. Ayzenshtat, D. L. Budnitsky, O. B. Koretskaya, L. S. Okaevich, V. A. Novikov, A. I. Potapov, O. P. Tolbanov, A. V. Tyazhev, and A. P. Vorobiev. GaAs as a material for particle detectors. *Nuclear Instruments and Methods in Physics Research, Section A: Accelerators, Spectrometers, Detectors and Associated Equipment*, 494(1-3):120–127, 2002.
- [234] D. Budnitsky, A. Tyazhev, V. Novikov, A. Zarubin, O. Tolbanov, M. Skakunov, E. Hamann, A. Fauler, M. Fiederle, S. Procz, H. Graafsma, and S. Ryabkov. Chromium-compensated GaAs detector material and sensors. *Journal of Instrumentation*, 9(7):C07011–C07011, 2014.
- [235] D. Budnitsky, V. Novikov, A. Lozinskaya, I. Kolesnikova, Z. Zarubin, A. Shemeryankina, T. Mikhailov, M. Skakunov, O. Tolbanov, and A. Tyazhev. Characterization of 4 inch GaAs:Cr wafers. *Journal of Instrumentation*, 12(1):C01063, 2017.
- [236] A. V. Tyazhev, D. L. Budnitsky, O. B. Koretskay, V. A. Novikov, L. S. Okaevich, A. I. Potapov, O. P. Tolbanov, and A. P. Vorobiev. GaAs radiation imaging detectors with an active layer thickness up to 1 mm. *Nuclear Instruments and Methods in Physics Research, Section A: Accelerators, Spectrometers, Detectors and Associated Equipment*, 509(1-3):34–39, 2003.

- [237] A. Tyazhev, V. Novikov, O. Tolbanov, A. Zarubin, M. Fiederle, and E. Hamann. Investigation of the current-voltage characteristics, the electric field distribution and the charge collection efficiency in x-ray sensors based on chromium compensated gallium arsenide. *Hard X-Ray, Gamma-Ray, and Neutron Detector Physics XVI*, 9213:92130G, 2014.
- [238] E. Hamann, T. Koenig, M. Zuber, A. Cecilia, A. Tyazhev, O. Tolbanov, S. Procz, A. Fauler, T. Baumbach, and M. Fiederle. Performance of a Medipix3RX Spectroscopic Pixel Detector With a High Resistivity Gallium Arsenide Sensor. *IEEE Transactions on Medical Imaging*, 34(3):707–715, 2015.
- [239] J. Becker, M. W. Tate, K. S. Shanks, H. T. Philipp, J. T. Weiss, P. Purohit, D. Chamberlain, and S. M. Gruner. Characterization of chromium compensated GaAs as an X-ray sensor material for charge-integrating pixel array detectors. *Journal of Instrumentation*, 13(1):01007–01007, 2018.
- [240] C. Ponchut, M. Cotte, A. Lozinskaya, A. Zarubin, O. Tolbanov, and A. Tyazhev. Characterisation of GaAs:Cr pixel sensors coupled to Timepix chips in view of synchrotron applications. *Journal of Instrumentation*, 12(12):C12023–C12023, 2017.
- [241] P. Smolyanskiy, D. Kozhevnikov, O. Bakina, G. Chelkov, D. Dedovich, K. Kuper, A. Leyva Fabelo, and A. Zhemchugov. Study of a GaAs:Cr-based Timepix detector using synchrotron facility. *Journal of Instrumentation*, 12(11):P11009–P11009, 2017.
- [242] P. Smolyanskiy, B. Bergmann, G. Chelkov, S. Kotov, U. Kruchonak, D. Kozhevnikov, Y. Mora Sierra, I. Stekl, and A. Zhemchugov. Properties of GaAs:Cr-based Timepix detectors. *Journal of Instrumentation*, 13(2), 2018.
- [243] M. Ruat and C. Ponchut. Characterization of a Pixelated CdTe X-Ray Detector Using the Timepix Photon-Counting Readout Chip. *IEEE Transactions on Nuclear Science*, 59(5):2392–2401, 2012. Conference Name: IEEE Transactions on Nuclear Science.
- [244] M. C. Veale, S. J. Bell, D. D. Duarte, M. J. French, M. Hart, A. Schneider, P. Seller, M. D. Wilson, V. Kachkanov, A. D. Lozinskaya, V. A. Novikov, O. P. Tolbanov, A. Tyazhev, and A. N. Zarubin. Investigating the suitability of GaAs:Cr material for high flux X-ray imaging. *Journal of Instrumentation*, 9(12):C12047–C12047, 2014.
- [245] P. Zambon. Simulation of polarization dynamics in semi-insulating, Cr-compensated GaAs pixelated sensors under high x-ray fluxes. *AIP Advances*, 11(7):075006, 2021.

- [246] F. Krummenacher. Pixel detectors with local intelligence: an IC designer point of view. *Nuclear Instruments and Methods in Physics Research Section A: Accelerators, Spectrometers, Detectors and Associated Equipment*, 305(3):527–532, 1991.
- [247] R. Ballabriga Suñé. *The Design and Implementation in 0.13 μm CMOS of an Algorithm Permitting Spectroscopic Imaging with High Spatial Resolution for Hybrid Pixel Detectors*. PhD thesis, Universitat Ramon LLull, 2009.
- [248] R. Ballabriga, M. Campbell, E. H. M. Heijne, X. Llopart, and L. Tlustos. The Medipix3 prototype, a pixel readout chip working in single photon counting mode with improved spectrometric performance. *IEEE Transactions on Nuclear Science*, 54(5):1824–1829, 2007.
- [249] R. Ballabriga, M. Campbell, E. Heijne, X. Llopart, L. Tlustos, and W. Wong. Medipix3: A 64k pixel detector readout chip working in single photon counting mode with improved spectrometric performance. *Nuclear Instruments and Methods in Physics Research Section A: Accelerators, Spectrometers, Detectors and Associated Equipment*, 633:S15–S18, 2011.
- [250] I. Horswell, E. N. Gimenez, J. Marchal, and N. Tartoni. A Medipix3 readout system based on the National Instruments FlexRIO card and using the LabVIEW programming environment. *Journal of Instrumentation*, 6:C01028–C01028, 2011.
- [251] R. Plackett, I. Horswell, E. N. Gimenez, J. Marchal, D. Omar, and N. Tartoni. Merlin: a fast versatile readout system for Medipix3. *Journal of Instrumentation*, 8(01):C01038, 2013.
- [252] S. Vahanen. Private Communication. Internal information regarding specification of Si sensors.
- [253] D.R.G. Mitchell and B. Schaffer. Scripting-customised microscopy tools for Digital Micrograph. *Ultramicroscopy*, 103(4):319–332, 2005.
- [254] P. Dondero, A. Mantero, V. Ivanchenko, S. Lotti, T. Mineo, and V. Fioretti. Electron backscattering simulation in Geant4. *Nuclear Instruments and Methods in Physics Research Section B: Beam Interactions with Materials and Atoms*, 425:18–25, 2018.
- [255] C. E. Metz and K. Doi. Transfer function analysis of radiographic imaging systems. *Physics in Medicine and Biology*, 24(6):1079–1106, 1979.

- [256] G. Deptuch, A. Besson, P. Rehak, M. Szelezniak, J. Wall, M. Winter, and Y. Zhu. Direct electron imaging in electron microscopy with monolithic active pixel sensors. *Ultramicroscopy*, 107(8):674–684, 2007.
- [257] N. Otsu. Threshold Selection Method from Gray-Level Histograms. *IEEE Trans Syst Man Cybern*, SMC-9(1):62–66, 1979.
- [258] C. Fröjdh, H. Graafsma, H. E. Nilsson, and C. Ponchut. Characterization of a pixellated CdTe detector with single-photon processing readout. *Nuclear Instruments and Methods in Physics Research, Section A: Accelerators, Spectrometers, Detectors and Associated Equipment*, 563(1):128–132, 2006.
- [259] M. C. Veale, S. J. Bell, P. Seller, M. D. Wilson, and V. Kachkanov. X-ray microbeam characterization of a small pixel spectroscopic CdTe detector. *Journal of Instrumentation*, 7(07):P07017–P07017, 2012.
- [260] R. M. Wheeler, L. Jowitt, S. Richards, M. C. Veale, M. D. Wilson, O. J. L. Fox, K. J. S. Sawhney, A. D. Lozinskaya, A. Shemeryankina, O. P. Tolbanov, A. Tyazhev, and A. N. Zarubin. X-ray microbeam characterisation of crystalline defects in small pixel GaAs:Cr detectors. *Nuclear Instruments and Methods in Physics Research Section A: Accelerators, Spectrometers, Detectors and Associated Equipment*, 999:165207, 2021.
- [261] J. M. LeBeau and S. Stemmer. Experimental quantification of annular dark-field images in scanning transmission electron microscopy. *Ultramicroscopy*, 108(12):1653–1658, 2008.
- [262] R. Fritz, A. Beyer, W. Stolz, K. Müller, M. Schowalter, A. Rosenauer, I. Häusler, H. Kirmse, A. Mogilatenko, H. Kirmse, W. Neumann, and K. Volz. Quantitative Analysis of Chemical Composition Using HAADF-STEM in a JEOL 2200FS. *Microscopy and Microanalysis*, 17(S2):1410–1411, 2011.
- [263] K. E. MacArthur, L. B. Jones, and P. D. Nellist. How flat is your detector? Non-uniform annular detector sensitivity in STEM quantification. *Journal of Physics: Conference Series*, 522:012018, 2014.
- [264] L. Jones. Quantitative ADF STEM: acquisition, analysis and interpretation. *IOP Conference Series: Materials Science and Engineering*, 109:012008, 2016.
- [265] F. F. Krause, M. Schowalter, T. Grieb, K. Müller-Caspary, T. Mehrrens, and A. Rosenauer. Effects of instrument imperfections on quantitative scanning transmission electron microscopy. *Ultramicroscopy*, 161:146–160, 2016.

- [266] S. D. House, Y. Chen, R. Jin, and J.C. Yang. High-throughput, semi-automated quantitative STEM mass measurement of supported metal nanoparticles using a conventional TEM/STEM. *Ultramicroscopy*, 182:145–155, 2017.
- [267] L. Jones, A. Varambhia, H. Sawada, and P.D. Nellist. An optical configuration for fastidious STEM detector calibration and the effect of the objective-lens pre-field. *Journal of Microscopy*, 270(2):176–187, 2018.
- [268] S. Agostinelli, J. Allison, K. Amako, J. Apostolakis, H. Araujo, P. Arce, M. Asai, D. Axen, S. Banerjee, G. Barrand, F. Behner, L. Bellagamba, J. Boudreau, L. Broglia, A. Brunengo, H. Burkhardt, S. Chauvie, J. Chuma, R. Chytracsek, G. Cooperman, G. Cosmo, P. Degtyarenko, A. Dell’Acqua, G. Depaola, D. Dietrich, R. Enami, A. Feliciello, C. Ferguson, H. Fesefeldt, G. Folger, F. Foppiano, A. Forti, S. Garelli, S. Giani, R. Giannitrapani, D. Gibin, J. J. Gomez Cadenas, I. Gonzalez, G. Gracia Abril, G. Greeniaus, W. Greiner, V. Grichine, A. Grossheim, S. Guatelli, P. Gumplinger, R. Hamatsu, K. Hashimoto, H. Hasui, A. Heikkinen, A. Howard, V. Ivanchenko, A. Johnson, F. W. Jones, J. Kallenbach, N. Kanaya, M. Kawabata, Y. Kawabata, M. Kawaguti, S. Kelner, P. Kent, A. Kimura, T. Kodama, R. Kokoulin, M. Kossov, H. Kurashige, E. Lamanna, T. Lampen, V. Lara, V. Lefebure, F. Lei, M. Liendl, W. Lockman, F. Longo, S. Magni, M. Maire, E. Medernach, K. Minamimoto, P. Mora de Freitas, Y. Morita, K. Murakami, M. Nagamatu, R. Nartallo, P. Nieminen, T. Nishimura, K. Ohtsubo, M. Okamura, S. O’Neale, Y. Oohata, K. Paech, J. Perl, A. Pfeiffer, M. G. Pia, F. Ranjard, A. Rybin, S. Sadilov, E. di Salvo, G. Santin, T. Sasaki, N. Savvas, Y. Sawada, S. Scherer, S. Sei, V. Sirotenko, D. Smith, N. Starkov, H. Stoecker, J. Sulkimo, M. Takahata, S. Tanaka, E. Tcherniaev, E. Safai Tehrani, M. Tropeano, P. Truscott, H. Uno, L. Urban, P. Urban, M. Verderi, A. Walkden, W. Wander, H. Weber, J. P. Wellisch, T. Wenaus, D. C. Williams, D. Wright, T. Yamada, H. Yoshida, and D. Zschesche. GEANT4 - A simulation toolkit. *Nuclear Instruments and Methods in Physics Research, Section A: Accelerators, Spectrometers, Detectors and Associated Equipment*, 506(3):250–303, 2003.
- [269] J. Allison, K. Amako, J. Apostolakis, H. Araujo, P. Arce Dubois, M. Asai, G. Barrand, R. Capra, S. Chauvie, R. Chytracsek, G.A.P. Cirrone, G. Cooperman, G. Cosmo, G. Cuttone, G.G. Daquino, M. Donszelmann, M. Dressel, G. Folger, F. Foppiano, J. Generowicz, V. Grichine, S. Guatelli, P. Gumplinger, A. Heikkinen, I. Hrivnacova, A. Howard, S. Incerti, V. Ivanchenko, T. Johnson, F. Jones, T. Koi, R. Kokoulin, M. Kossov, H. Kurashige, V. Lara, S. Larsson, F. Lei, O. Link, F. Longo, M. Maire, A. Mantero, B. Mascialino, I. McLaren, P. Mendez Lorenzo, K. Minamimoto, K. Murakami, P. Nieminen, L. Pandola, S. Parlati, L. Peralta, J. Perl, A. Pfeiffer, M.G. Pia, A. Ribon, P. Rodrigues, G. Russo, S. Sadilov,

- G. Santin, T. Sasaki, D. Smith, N. Starkov, S. Tanaka, E. Tcherniaev, B. Tome, A. Trindade, P. Truscott, L. Urban, M. Verderi, A. Walkden, J.P. Wellisch, D.C. Williams, D. Wright, and H. Yoshida. Geant4 developments and applications. *IEEE Transactions on Nuclear Science*, 53(1):270–278, 2006.
- [270] J. Allison, K. Amako, J. Apostolakis, P. Arce, M. Asai, T. Aso, E. Bagli, A. Bagulya, S. Banerjee, G. Barrand, B.R. Beck, A.G. Bogdanov, D. Brandt, J.M.C. Brown, H. Burkhardt, Ph. Canal, D. Cano-Ott, S. Chauvie, K. Cho, G.A.P. Cirrone, G. Cooperman, M.A. Cortés-Giraldo, G. Cosmo, G. Cuttone, G. Depaola, L. Desorgher, X. Dong, A. Dotti, V.D. Elvira, G. Folger, Z. Francis, A. Galoyan, L. Garnier, M. Gayer, K.L. Genser, V.M. Grichine, S. Guatelli, P. Guèye, P. Gumplinger, A.S. Howard, I. Hřivnáčová, S. Hwang, S. Incerti, A. Ivanchenko, V.N. Ivanchenko, F.W. Jones, S.Y. Jun, P. Kaitaniemi, N. Karakatsanis, M. Karamitros, M. Kelsey, A. Kimura, T. Koi, H. Kurashige, A. Lechner, S.B. Lee, F. Longo, M. Maire, D. Mancusi, A. Mantero, E. Mendoza, B. Morgan, K. Murakami, T. Nikitina, L. Pandola, P. Paprocki, J. Perl, I. Petrović, M.G. Pia, W. Pokorski, J.M. Quesada, M. Raine, M.A. Reis, A. Ribon, A. Ristić Fira, F. Romano, G. Russo, G. Santin, T. Sasaki, D. Sawkey, J.I. Shin, I.I. Strakovsky, A. Taborda, S. Tanaka, B. Tomé, T. Toshito, H.N. Tran, P.R. Truscott, L. Urban, V. Uzhinsky, J.M. Verbeke, M. Verderi, B.L. Wendt, H. Wenzel, D.H. Wright, D.M. Wright, T. Yamashita, J. Yarba, and H. Yoshida. Recent developments in Geant4. *Nuclear Instruments and Methods in Physics Research Section A: Accelerators, Spectrometers, Detectors and Associated Equipment*, 835:186–225, 2016.
- [271] S. Incerti, I. Kyriakou, M. A. Bernal, M. C. Bordage, Z. Francis, S. Guatelli, V. Ivanchenko, M. Karamitros, N. Lampe, S. B. Lee, S. Meylan, C. H. Min, W. G. Shin, P. Nieminen, D. Sakata, N. Tang, C. Villagrasa, H. N. Tran, and J. M. C. Brown. Geant4-DNA example applications for track structure simulations in liquid water: A report from the Geant4-DNA Project. *Medical Physics*, 45(8):722–739, 2018.
- [272] G. Santin, V. Ivanchenko, H. Evans, P. Nieminen, and E. Daly. GRAS: a general-purpose 3-D Modular Simulation tool for space environment effects analysis. *IEEE Transactions on Nuclear Science*, 52(6):2294–2299, 2005.
- [273] A. Schübel, D Krapohl, E. Fröjdth, C. Fröjdth, and G. Thungström. A Geant4 based framework for pixel detector simulation. *Journal of Instrumentation*, 9(12), 2014.
- [274] D. Krapohl, A. Schübel, E. Fröjdth, G. Thungstrom, and C. Fröjdth. Validation of Geant4 Pixel Detector Simulation Framework by Measurements With the Medipix Family Detectors. *IEEE Transactions on Nuclear Science*, 63(3):1874–1881, 2016.

- [275] M. Benoit. The allpix simulation framework. <https://twiki.cern.ch/twiki/bin/view/Main/AllPix>, (Last accessed: 01.07.2022).
- [276] S. Spannagel, K. Wolters, D. Hynds, N. Alipour Tehrani, M. Benoit, D. Dannheim, N. Gauvin, A. Nürnberg, P. Schütze, and M. Vicente. Allpix²: A modular simulation framework for silicon detectors. *Nuclear Instruments and Methods in Physics Research Section A: Accelerators, Spectrometers, Detectors and Associated Equipment*, 901:164–172, 2018.
- [277] L. de la Fuente Rosales, S. Incerti, and M. A. Francis, Z. and Bernal. Accounting for radiation-induced indirect damage on DNA with the Geant 4-DNA code. *Physica Medica*, 51:108–116, 2018.
- [278] J. Allison, J. Apostolakis, A. Bagulya, C. Champion, S. Elles, F. Garay, V. Grichine, A. Howard, S. Incerti, V. Ivanchenko, J. Jacquemier, M. Maire, A. Mantero, P. Nieminen, L. Pandola, G. Santin, D. Sawkey, A. Schälicke, and L. Urban. Geant4 electromagnetic physics for high statistic simulation of LHC experiments. *Journal of Physics: Conference Series*, 396(2):022013, 2012.
- [279] C. G. H. Walker, I. Konvalina, F. Mika, L. Frank, and I. Müllerová. Quantitative comparison of simulated and measured signals in the STEM mode of a SEM. *Nuclear Instruments and Methods in Physics Research Section B: Beam Interactions with Materials and Atoms*, 415:17–24, 2018.
- [280] J. Korpanty, K. Gnanasekaran, C. Venkatramani, N. Zang, and N. C. Gianeschi. Organic solution-phase transmission electron microscopy of copolymer nanoassembly morphology and dynamics. *Cell Reports Physical Science*, 3(3):100772, 2022.
- [281] S. Goudsmit and J. L. Saunderson. Multiple Scattering of Electrons. *Physical Review*, 57:24–29, 1940.
- [282] C. Møller. Zur Theorie des Durchgangs schneller Elektronen durch Materie. *Annalen der Physik*, 406(5):531–585, 1932.
- [283] S. M. Seltzer and M. J. Berger. Bremsstrahlung spectra from electron interactions with screened atomic nuclei and orbital electrons. *Nuclear Instruments and Methods in Physics Research Section B: Beam Interactions with Materials and Atoms*, 12(1):95–134, 1985.
- [284] S. M. Seltzer and M. J. Berger. Bremsstrahlung energy spectra from electrons with kinetic energy 1 keV–10 GeV incident on screened nuclei and orbital electrons of neutral atoms with $Z = 1–100$. *Atomic Data and Nuclear Data Tables*, 35(3):345–418, 1986.

- [285] R. Brun and F. Rademakers. ROOT — An object oriented data analysis framework. *Nuclear Instruments and Methods in Physics Research Section A: Accelerators, Spectrometers, Detectors and Associated Equipment*, 389(1-2):81–86, 1997.
- [286] I. Antcheva, M. Ballintijn, B. Bellenot, M. Biskup, R. Brun, N. Buncic, Ph Canal, D. Casadei, O. Couet, V. Fine, L. Franco, G. Ganis, A. Gheata, D. Gonzalez Maline, M. Goto, J. Iwaszkiewicz, A. Kreshuk, D. Marcos Segura, R. Maunder, L. Moneta, A. Naumann, E. Offermann, V. Onuchin, S. Panacek, F. Rademakers, P. Russo, and M. Tadel. ROOT — A C++ framework for petabyte data storage, statistical analysis and visualization. *Computer Physics Communications*, 180(12):2499–2512, 2009.
- [287] D. Dannheim, K. Dort, D. Hynds, M. Munker, A. Nürnberg, W. Snoeys, and S. Spannagel. Combining TCAD and Monte Carlo methods to simulate CMOS pixel sensors with a small collection electrode using the Allpix² framework. *Nuclear Instruments and Methods in Physics Research Section A: Accelerators, Spectrometers, Detectors and Associated Equipment*, 964:163784, 2020.
- [288] Synopsys Inc. *Sentaurus™ Structure Editor User Guide*.
- [289] Synopsys Inc. *Sentaurus™ Device User Guide*.
- [290] G. Tinti, H. Marchetto, C. A. F. Vaz, A. Kleibert, M. Andrä, R. Barten, A. Bergamaschi, M. Brückner, S. Cartier, R. Dinapoli, T. Franz, E. Fröjdth, D. Greiffenberg, C. Lopez-Cuenca, D. Mezza, A. Mozzanica, F. Nolting, M. Ramilli, S. Redford, M. Ruat, Ch. Ruder, L. Schädler, Th. Schmidt, B. Schmitt, F. Schütz, X. Shi, D. Thattil, S. Vetter, and J. Zhang. The EIGER detector for low-energy electron microscopy and photoemission electron microscopy. *Journal of Synchrotron Radiation*, 24(5):963–974, 2017.
- [291] E. Fröjdth, J. P. Abrahams, M. Andrä, R. Barten, A. Bergamaschi, M. Brückner, S. Chiriotti, R. Dinapoli, D. Greiffenberg, V. Hinger, L. Lovacik, T. King, P. Kozłowski, C. Lopez-Cuenca, M. Jürgen, D. Mezza, A. Mozzanica, C. Ruder, B. Schmitt, S. Hasanaj, D. Thattil, E. van Genderen, S. Vetter, and J. Zhang. Electron detection with CdTe and GaAs sensors using the charge integrating hybrid pixel detector JUNGFRU. *Journal of Instrumentation*, 17(01):C01020, 2022.
- [292] J. Marchal. Theoretical analysis of the effect of charge-sharing on the Detective Quantum Efficiency of single-photon counting segmented silicon detectors. *Journal of Instrumentation*, 5(1), 2010.

- [293] J. Marchal, J. McGrath, and K. Medjoubi. Analytical model of single-X-ray photon counting pixel-array detectors. *Journal of Instrumentation*, 9(3), 2014.
- [294] J. McGrath, J. Marchal, and K. Medjoubi. Sampling function of single-X-ray-photon counting hybrid pixel detectors: Combining an analytical approach to Monte-Carlo simulations and Finite-Element-Modeling. *Journal of Instrumentation*, 8(10):P10008–P10008, 2013.
- [295] J. McGrath, J. Marchal, R. Plackett, I. Horswell, D. Omar, E. N. Gimenez, and N. Tartoni. Comparisons between simulation and measurements taken with the Medipix3RX detector. *Journal of Instrumentation*, 9:C05007–C05007, 2014.
- [296] H.J. Zweig. Detective quantum efficiency of photodetectors with some amplification mechanisms. *Journal of the Optical Society of America*, 55(5):525–528, 1965.
- [297] J. Yao and I. A. Cunningham. Parallel cascades: New ways to describe noise transfer in medical imaging systems. *Medical Physics*, 28(10):2020–2038, 2001.
- [298] J. Tanguay, S. Yun, H. K. Kim, and I. A. Cunningham. The detective quantum efficiency of photon-counting x-ray detectors using cascaded-systems analyses. *Medical Physics*, 40(4):041913, 2013.
- [299] J. Tanguay, H. K. Yun, S. and Kim, and I. A. Cunningham. Detective quantum efficiency of photon-counting x-ray detectors. *Medical Physics*, 42(1):491–509, 2015.
- [300] J. Tanguay and I. A. Cunningham. Cascaded systems analysis of charge sharing in cadmium telluride photon-counting x-ray detectors. *Medical Physics*, 45(5):1926–1941, 2018.
- [301] J. Tanguay, J. Kim, H. K. Kim, K. Iniewski, and I. A. Cunningham. Frequency-dependent signal and noise in spectroscopic x-ray imaging. *Medical Physics*, 47(7):2881–2901, 2020.
- [302] J. Xu, W. Zbijewski, G. Gang, J. W. Stayman, K. Taguchi, M. Lundqvist, E. Fredenberg, J. A. Carrino, and J. H. Siewerdsen. Cascaded systems analysis of photon counting detectors. *Medical Physics*, 41(10), 2014.
- [303] J. Marchal and K. Medjoubi. Detective quantum efficiency model of single-X-ray-photon counting hybrid pixel detectors. *Journal of Instrumentation*, 7(11), 2012.

- [304] A. Bergamaschi, Ch. Broennimann, R. Dinapoli, E. Eikenberry, F. Gozzo, B. Henrich, M. Kobas, P. Kraft, B. Patterson, and B. Schmitt. Performance of a single photon counting microstrip detector for strip pitches down to $10\mu\text{m}$. *Nuclear Instruments and Methods in Physics Research Section A: Accelerators, Spectrometers, Detectors and Associated Equipment*, 591(1):163–166, 2008.
- [305] R.F. Egerton. Choice of operating voltage for a transmission electron microscope. *Ultramicroscopy*, 145:85–93, 2014.
- [306] E. Hamann, T. Koenig, M. Zuber, A. Cecilia, A. Tyazhev, O. Tolbanov, S. Procz, A. Fauler, M. Fiederle, and T. Baumbach. Investigation of GaAs:Cr Timepix assemblies under high flux irradiation. *Journal of Instrumentation*, 10(1):C01047–C01047, 2015.
- [307] L. Jones, P. Seller, M. Wilson, and A. Hardie. HEXITEC ASIC—a pixellated readout chip for CZT detectors. *Nuclear Instruments and Methods in Physics Research Section A: Accelerators, Spectrometers, Detectors and Associated Equipment*, 604(1-2):34–37, 2009.
- [308] L. Jowitt, M. Wilson, P. Seller, C. Angelsen, R. M. Wheeler, B. Cline, D. Schöne, F. Lauba, M. Goede, R. Ball, M. Verhoeven, G. Gottseleben, M. N. Boone, F. Van Assche, and M. C. Veale. HEXITEC 2×2 tiled hard X-ray spectroscopic imaging detector system. *Journal of Instrumentation*, 17(01):P01012, 2022.
- [309] M. C. Veale, P. Seller, M. Wilson, and E. Liotti. HEXITEC: A High-Energy X-ray Spectroscopic Imaging Detector for Synchrotron Applications. *Synchrotron Radiation News*, 31(6):28–32, 2018.
- [310] A Schneider, M C Veale, D D Duarte, S J Bell, M D Wilson, J D Lipp, and P Seller. Interconnect and bonding techniques for pixelated X-ray and gamma-ray detectors. *Journal of Instrumentation*, 10:C02010, 2015.
- [311] J. Scuffham, M. C. Veale, M. D. Wilson, and P. Seller. Algorithms for spectral calibration of energy-resolving small-pixel detectors. *Journal of Instrumentation*, 8(10), 2013.
- [312] I. Chsherbakov, P. Chsherbakov, I. Kolesnikova, A. Lozinskaya, T. Mihaylov, V. Novikov, O. Tolbanov, A. Tyazhev, and A. Zarubin. The influence of contact material and its fabrication on X-ray HR-GaAs:Cr sensor noise characteristics. *Journal of Instrumentation*, 14(01):C01026–C01026, 2019.
- [313] A. Lozinskaya, I. Chsherbakov, I. Kolesnikova, T. Mihaylov, V. Novikov, A. Shemeryankina, O. Tolbanov, A. Tyazhev, and A. Zarubin. Detailed analysis of quasi-ohmic contacts to high resistive GaAs:Cr structures. *Journal of Instrumentation*, 14(11):C11026–C11026, 2019.

- [314] D. L. Budnitskii, V. A. Novikov, I. A. Prudaev, P. Ibanov, and . . Yaskevich. A photovoltaic effect in the metal–high-resistive GaAs:Cr contact. *Russian Physics Journal*, 55(7):748–751, 2012.
- [315] I. Chsherbakov, I. Kolesnikova, A. Lozinskaya, T. Mihaylov, V. Novikov, A. Shemeryankina, O. Tolbanov, A. Tyazhev, and A. Zarubin. GaAs:Cr X-ray sensors noise characteristics investigation by means of amplitude spectrum analysis. *Journal of Instrumentation*, 13(1):1030, 2018.
- [316] R. Dinapoli, A. Bergamaschi, S. Cartier, D. Greiffenberg, I. Johnson, J. H. Jungmann, D. Mezza, A. Mozzanica, B. Schmitt, X. Shi, and G. Tinti. MÖNCH, a small pitch, integrating hybrid pixel detector for X-ray applications. *Journal of Instrumentation*, 9(05):C05015–C05015, 2014.
- [317] A. Bergamaschi, M. Andrä, R. Barten, C. Borca, M. Brückner, S. Chiriotti, R. Dinapoli, E. Fröjdth, D. Greiffenberg, T. Huthwelker, A. Kleibert, M. Langer, M. Lebugle, C. Lopez-Cuenca, D. Mezza, A. Mozzanica, J. Raabe, S. Redford, C. Ruder, V. Scagnoli, B. Schmitt, X. Shi, U. Staub, D. Thattil, G. Tinti, C. F. Vaz, S. Vetter, J. Vila-Comamala, and J. Zhang. The MÖNCH Detector for Soft X-ray, High-Resolution, and Energy Resolved Applications. *Synchrotron Radiation News*, 31(6):11–15, 2018.
- [318] X. Ji, R. Zhang, G. H. Chen, and K. Li. Impact of anti-charge sharing on the zero-frequency detective quantum efficiency of CdTe-based photon counting detector system: Cascaded systems analysis and experimental validation. *Physics in Medicine and Biology*, 63(9), 2018.
- [319] American National Standards Institute. American National Standard for Evaluating the Image Quality of X-ray Computed Tomography (CT) Security-Screening Systems. *ANSI N42.45-2011*, pages 1–58, 2011.
- [320] N. Boudet, J. F. Berar, L. Blanquart, P. Breugnot, B. Caillot, J. C. Clemens, I. Koudobine, P. Delpierre, C. Mouget, R. Potheau, and I. Valin. XPAD: a hybrid pixel detector for X-ray diffraction and diffusion. *Nuclear Instruments and Methods in Physics Research Section A: Accelerators, Spectrometers, Detectors and Associated Equipment*, 510(1-2):41–44, 2003.
- [321] X. Llopart, J. Alozy, R. Ballabriga, M. Campbell, R. Casanova, V. Gromov, E. H. M. Heijne, T. Poikela, E. Santin, V. Sriskaran, L. Tlustos, and A. Vitkovskiy. Timepix4, a large area pixel detector readout chip which can be tiled on 4 sides providing sub-200 ps timestamp binning. *Journal of Instrumentation*, 17(01):C01044, 2022.